Dissertation zur Erlangung des Doktorgrades
der Fakultät für Chemie und Pharmazie
der Ludwig-Maximilians-Universität München

LANTHANIDE DEPENDENT METHANOL DEHYDROGENASES: A THEORETICAL AND BIOMIMETIC INVESTIGATION

Henning Lumpe

aus Bad Wildungen, Deutschland

2019

Dissertation zur Erlangung des Doktorgrades
der Fakultät für Chemie und Pharmazie
der Ludwig-Maximilians-Universität München

Lanthanide Dependent Methanol Dehydrogenases: A Theoretical and Biomimetic Investigation

Henning Lumpe
aus
Bad Wildungen, Deutschland
2019

Erklärung

Diese Dissertation wurde im Sinne von § 7 der Promotionsordnung vom 28. November 2011 von Frau Prof. Dr. Lena J. Daumann betreut.

Eidesstattliche Versicherung

Diese Dissertation wurde eigenständig und ohne unerlaubte Hilfe erarbeitet.

München, 13.01.2020

……...

Henning Lumpe

Dissertation eingereicht am	08.11.2019
1. Gutachter	Prof. Dr. Lena J. Daumann
2. Gutachter	Prof. Dr. Hans-Christian Böttcher
Mündliche Prüfung am	10.12.2019

Diese Arbeit wurde in der Zeit von Juni 2016 bis November 2019 am Department für Chemie der Ludwig-Maximilians-Universität München unter Anleitung von Frau Prof. Dr. Lena J. Daumann durchgeführt.

Disclosure of Participation

The following people mentioned underneath contributed in the practical laboratory work of this thesis, as part of their research internships.

ARTHUR POLIAKOW assisted in the total synthesis of PQQ described in Chapter III.

ANNIKA MENKE prepared the PQQ-Ln complexes, presented in Chapter IV.2

SABRINA KRÄH supported in the synthesis of $PQQH_2$ and in the spectrophotometric analysis of PQQ redox processes described in Chapter V.2 and V.3.

VIOLETA VETSOVA contributed in precursor and ligand synthesis, described in Chapter VII.2 and VII.3.

LAURA SCHWABBAUER continued the project from Violeta Vetsova and assisted in ligand synthesis and UV-Vis metal titration experiments described in Chapter VII.2 and VII.3.

MARIANNE FRIEMERT synthesized the PQQ-crown ether compounds, prepared the dry stock solutions of metal perchlorates and conducted UV-Vis metal titration experiments described in Chapter VII.4.

Somewhere, something incredible is waiting to be known.

Carl Sagan

SUMMARY

Lanthanides were long considered non-biologically relevant. However, recent discoveries have shown that lanthanide utilizing bacteria exist and are widespread in nature.

The lanthanides are used as metal ions in the active sites of methanol dehydrogenases (MDH), enzymes metabolizing methanol for energy generation of the microbes. Here, lanthanides act as Lewis acids, a role that is commonly fulfilled by calcium in related enzymes.

Beside the metal ion, the enzyme's active site includes the organic molecule pyrroloquinoline quinone (PQQ), a redox cofactor, which gets reduced concurrent to methanol oxidation.

This thesis deals with lanthanide dependent methanol dehydrogenases, the specific role of lanthanides in enzymatic action and the advantage these metals provide over calcium. The active site is treated by theoretical approaches using DFT. The cofactor PQQ is interesting on its own and several aspects of its chemistry and interaction with biologically relevant calcium and lanthanides are elucidated.

Chapter I provides a brief introduction in the key concepts of this thesis – the role of metals in biology and the purpose of bioinorganic chemistry, a discourse about lanthanides in general and lanthanide utilizing bacteria, the MDH enzyme and features of PQQ.

Chapter II describes how DFT calculations can help to gain further insight into the mechanism of action and the role of lanthanides in MDH. These calculations demonstrate a preference of MDH for early lanthanides and discuss the reasons for this, concerning several aspects of lanthanide chemistry.

Chapter III recapitulates the known total synthesis of PQQ, points out easily accessible alternatives and presents several PQQ derivatives and their syntheses. The trimethylester $PQQMe_3$ is accessed in a one-step synthesis and the deprotection to formerly unknown dimethylester $PQQMe_2$ is described. $PQQMe_2$ provides a multitude of possibilities for the synthesis of PQQ containing biomimetics.

Chapter IV deals with the coordination chemistry of PQQ with lanthanides and calcium. It presents the experimental findings using NMR and UV-Vis spectroscopy that PQQ in solution, although possessing several possible coordination sites,

still coordinates in the same way as bound in MDH. The first crystal structure of a biological relevant metal ion (here calcium) with this cofactor is presented and the feature of PQQ to coordinate preferentially early lanthanides is validated by complexation experiments.

Chapter V deals with the in-depth redox chemistry of PQQ and its derivative $PQQMe_3$ in regard to the biological role as redox cofactor. Using UV-Vis spectroscopy and electrochemistry methods it was shown for the first time that lanthanides do have an influence on the redox chemistry of PQQ.

In solution, PQQ is prone to nucleophilic attack and several derivatives, formed by reactions of PQQ with small molecules are known. Chapter VI deals with this reactivity of PQQ, elucidates the formation of a cyanide adduct and further elucidates methanol adduct formation and the influence of lanthanides and calcium on this type of reaction. A previously unknown PQQ-ketal species is characterized by NMR, IR and mass spectrometry.

Chapter VII presents the synthesis of four different ligands, mimicking the structure of the MDH active site and deals with the coordination chemistry of these ligands with lanthanides and calcium. Two very promising biomimetics were identified and characterized by UV-Vis spectroscopy and mass spectrometry.

While this summary shall only provide a brief overview of the contents of this thesis, more detailed descriptions of the results are given in the conclusion found at the end of each chapter.

I. INTRODUCTION 1
1. Metals in Biology 1
2. Rare-Earth Elements 2
3. Lanthanide Dependent Microorganisms 4
4. Pyrroloquinoline Quinone (PQQ) 8
II. DFT STUDIES 9
1. Introduction 9
2. Impact of Different Lanthanides on the Structure of XoxF 10
2.1. DFT Calculations of the Active Site 11
2.2. Conclusion 12
3. Impact of the Lanthanide Contraction 12
3.1. Introduction 13
3.2. Results and Discussion 15
3.3. Conclusion 28
III. SYNTHESIS AND PURIFICATION OF PQQ AND ITS DERIVATIVES 29
1. Introduction 29
2. Total Synthesis of PQQ 30
3. Purification of Biological Produced PQQ 33
3.1. Introduction 33
3.2. Purification of Vitamin Capsule Derived PQQ 34
4. Synthesis of PQQ Derivatives 34
4.1. Synthesis of $PQQMe_3$ 34
4.2. Synthesis of $PQQMe_2$ 37
4.3. Synthesis of $PQQH_2$ 38
5. Conclusion 39
IV. COORDINATION CHEMISTRY OF PQQ 40
1. Interaction of PQQ with Lanthanides and Calcium 40
1.1. Introduction 40
1.2. Results and Discussion 43
1.3. Conclusion 51
2. Further Investigation of the PQQ Complexation 52
V. REDOX-CHEMISTRY OF PQQ 58
1. Introduction 58
2. Reduction of PQQ with Ascorbic Acid 59
3. Reoxidation of $PQQH_2$ 61

3.1. Solvent Selection 61
3.2. Spectrophotometric Measurements in DMF 62
3.3. Evaluation of the Reoxidation Kinetics 67
3.4. Conclusion 70
4. Electrochemistry of PQQ 71
4.1. Introduction 71
4.2. Measurements of $PQQMe_3$ in Non-aqueous Solvents 75
4.3. Measurements of PQQ in Non-aqueous Solvents 78
4.4. Measurements of PQQ in H_2O/DMF Solvent Mixtures 79
4.5. Spectroelectrochemistry of PQQ in H_2O/DMF Solvent Mixtures 80
4.6. Influence of Lanthanides and Calcium on the CV of PQQ in H_2O/DMF Mixtures .. 82
4.7. Influence of Acids and Bases on the CV of PQQ in H_2O/DMF Solvent Mixtures ... 86
4.8. Measurements of $PQQMe_3$ in H_2O/DMF Solvent Mixtures 87
4.9. Additional Measurements on a Metrohm Device 88
4.10. Conclusion 90
VI. SMALL MOLECULE INTERACTION 92
1. Introduction 92
2. Cyanide Adduct Formation 93
2.1. Introduction 93
2.2. Elucidation of PQQ Cyanide Adduct Formation 93
3. Methanol Adduct Formation 96
3.1. Introduction 96
3.2. PQQ Adduct Formation in MeOD-d_4 96
3.3. Isolation Attempts of the PQQ-ketal Species of unknown Structure 100
3.4. Influence of Metals on Hemiketal Formation 104
3.5. Kinetics of the Formation and Decay of PQQ-hemiketal 119
4. Conclusion 122
VII. BIOMIMETIC COMPLEXES 124
1. Introduction 124
2. Synthesis and Investigation of TREN-(1,2-HOPO)$_3$ 126
2.1. Precursor Synthesis 126
2.2. Synthesis of TREN-(1,2-HOPO)$_3$ 127
2.3. Complex Formation 127
3. Synthesis and Investigation of TREN-(1,2-HOPO)$_2$-TAM-N1-PDA 130
3.1. Introduction 130

3.2. DFT Calculation 131
3.3. Ligand Synthesis 132
3.4. Complex Formation 137
3.5. Conclusion 141
4. Synthesis and Investigation of PQQ-Aza-Crown Ether Complexes 142
4.1. Synthetic Approaches 142
4.2. Coordination with Ca and La 145
5. Conclusion 151
VIII. EXPERIMENTAL PART 153
1. General Considerations 153
2. Analytical Methods 153
2.1. Nuclear Magnetic Resonance (NMR) 153
2.2. FT-Infrared Spectroscopy 154
2.3. UV-Vis Spectroscopy 154
2.4. Mass Spectrometry 154
2.5. Elemental Microanalyses 154
2.6. Inductively Coupled Plasma Optical Emission Spectroscopy 155
2.7. Inductively Coupled Plasma Mass Spectrometry 155
2.8. Electrochemistry 155
2.9. Spectroelectrochemistry 156
2.10. X-Ray Crystallography 156
2.11. DFT Calculations 156
3. General Procedures 157
3.1. GP I: Benzyl Deprotection 157
3.2. GP II: Acyl Chloride Formation 157
3.3. GP III: Formation of Acyl Thiazolidine-2-thione 157
4. Experimental Procedures for Chapter II 158
5. Experimental Procedures for Chapter III 158
5.1. Precursor Synthesis 158
5.2. Total Synthesis of PQQ 160
5.3. Isolation and Purification of PQQ 166
5.4. Synthesis of PQQ Derivatives 168
5.5. Synthesis of $PQQMe_2$ 173
6. Experimental Procedures for Chapter IV 177
6.1. Complex Formation of $PQQNa_2$ With La/Ln or La/Ca Couple 177

7. Experimental Procedures for Chapter V 179
7.1. General Working Methods 179
7.2. Reduction of PQQ With Ascorbic Acid 179
7.3. Spectrophotometric Measurement in DMF 180
8. Experimental Procedures for Chapter VI 181
8.1. General Considerations 181
8.2. Influence of Metals on Hemiketal Formation 181
8.3. Synthesis of PQQ-hemiketal 185
8.4. Kinetics of the Formation and Decay of PQQ-hemiketal 186
9. Experimental Procedures for Chapter VII 187
9.1. Precursor Synthesis 187
9.2. Synthesis and Investigation of TREN-(1,2-HOPO)$_3$ 190
9.3. Synthesis and Investigation of TREN-(1,2-HOPO)$_2$-TAM-N1-PDA 192
9.4. Synthesis and Investigation of PQQ-Aza-Crown Ether Complexes 200
9.5. Preparation of Dry Metal Perchlorate Solutions in Acetonitrile 205
IX. APPENDIX 211
1. Supporting Information 211
1.1. Supporting Information of Chapter II.2 211
1.2. Supporting Information of Chapter II.3 214
1.3. Supporting Information of Chapter IV.1 234
1.4. Supporting Information of Chapter IV.2 258
1.5. Supporting Information of Chapter VII 260
2. List of Abbreviations 270
3. Table of Compounds 273
4. References 275
5. List of Publications and Statement of Contribution 281
5.1. Publications Published as Part of this Thesis 281
5.2. Publications Published as not Part of this Thesis 283
5.3. Publications Published Prior to this Thesis 283
6. Contributions to Conferences 284

I. INTRODUCTION

1. Metals in Biology

The by far most abundant elements out of which terrestrial life is formed are carbon, hydrogen, nitrogen and oxygen, followed by phosphorus and sulfur. Those elements are so ubiquitous, that they even got their own acronym, speaking of “CHNOPS” elements or combinations thereof.[1-2] Metals on the other side, although plentiful on earth, are only present to a lower extent in living organisms. Besides calcium being relevant for bones, sodium and potassium being important for signal transduction and magnesium being required for proper ATP functionality, biologically relevant metals are only present in traces and are needed as cofactors in proteins.

Iron for example, being the cofactor of oxygen transporting hemoglobin, only makes up 0.006 mass% or 4.2 g of a 70 kg human.[3] Table I.1 provides an overview over all elements, which were considered biorelevant in 2016.[4]

Table I.1: Periodic system of the elements indicating those elements that are essential for most living organisms in dark green and those that are essential for more restricted life forms in light green. The essentiality of Cr (blue) is still under debate.[5] f-block elements are not shown (asterisk after lanthanum (La) and actinium (Ac)). Adapted from W. Maret.[4] Cd is included based on findings from Lane *et al.*[6]

H																	He
Li	Be											B	C	N	O	F	Ne
Na	Mg											Al	Si	P	S	Cl	Ar
K	Ca	Sc	Ti	V	Cr	Mn	Fe	Co	Ni	Cu	Zn	Ga	Ge	As	Se	Br	Kr
Rb	Sr	Y	Zr	Nb	Mo	Tc	Ru	Rh	Pd	Ag	Cd	In	Sn	Sb	Te	I	Xe
Cs	Ba	La*	Hf	Ta	W	Re	Os	Ir	Pt	Au	Hg	Tl	Pb	Bi	Po	At	Rn
Fr	Ra	Ac*															

Although being of low abundance in organisms, metals play an important and irreplaceable role in metabolic processes.[7] Bioinorganic chemistry sheds light on those elements and sets out to investigate their specific role and function in biological reactions.[8] Often, this research goes along with the synthesis of small molecules and complexes. Those so called “Biomimetics”, a term which was introduced by Otto Schmitt in the 1950s,[9] mimic structural features of active sites to gain deeper knowledge about their function by structural simplification.

Elements, that were long thought to have no biological relevance are the rare-earth elements, and although not mentioned in Table I.1, recent discoveries show their widespread utilization in living organisms.[10-14]

2. Rare-Earth Elements

The rare-earth elements (REE) are a group of 17 elements, including the f-block series from lanthanum to lutetium (also called lanthanides – Ln) and the group III elements scandium and yttrium. These elements are sometimes further divided into light rare-earth elements (LRE), including ^{57}La – ^{63}Eu and heavy rare-earth elements (HRE), including ^{64}Gd – ^{71}Lu and ^{39}Y. The first discovered rare-earth element was yttrium, 1787 by Gadolin in the mineral "ytterbite" in Sweden. The name of these elements originates from "earth" being an early name for oxides and the thought that these elements would be scarce. Their name is actually misleading, since those elements are neither oxides nor particularly rare. In the earth crust, the most abundant REE lanthanum and cerium are more abundant than copper and even the occurrence of the least abundant ones, thulium and lutetium, is higher than the one of silver or gold (Figure I.1).[15]

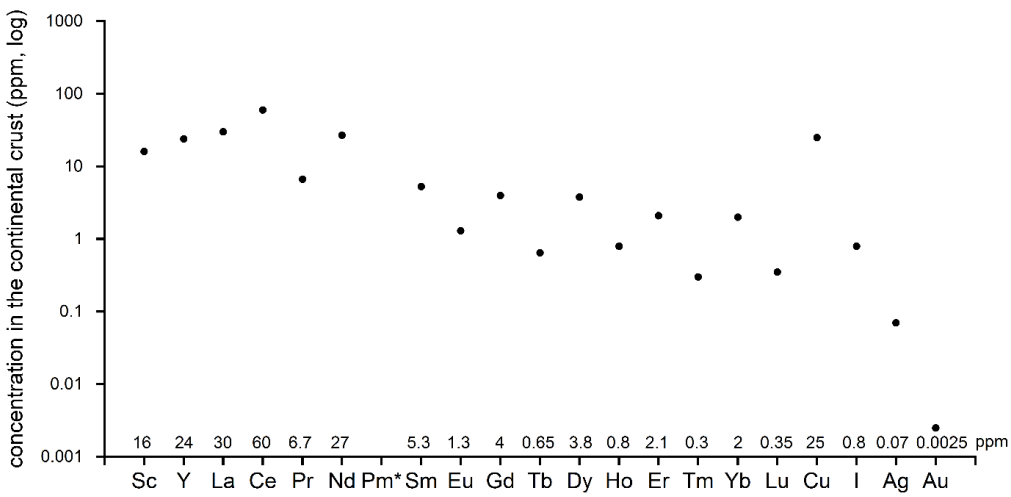

Figure I.1: Abundancies of rare-earth and other elements in the continental crust in ppm (logarithmic scale). Limited natural occurrence of Pm as radioactive fission product. Values provided by Wedepohl.[15]

REE with uneven numbers show lower contents than the even numbered ones. All REE are chemically very similar, a fact, which slowed research progression in the past, due to their occurence as mixed compounds in naturally occurring ores like bastnaesite ([(LRE)CO_3F]), monazite ([(LRE, Th)PO_4])) or xenotime ([(Y, HRE)PO_4)]). Due to their similar properties they are difficult to separate. Fractionized crystallization was the only method available until the first half of the 20th century, which was laborious and time-consuming. Praseodymium, one of the

metals being easier to purify, had to be recrystallized 5000 times to achieve a purity of 99%.[16] Broader chemical research on those metals was lacking before the development of more efficient purification methods such as ion exchange chromatography developed during the Manhattan project[17] and later the liquid-liquid extraction.[11] The latter is still used for industrial purification of REE but is environmentally harmful since producing large scales of acidic, toxic and even radioactive waste in addition to its enormous energy consumption.[18] The preferred oxidation state of REE is +III, by releasing two electrons from the s-, and one electron from the d-shell. However, several other oxidation states such as Eu^{II} or Ce^{IV} are known. From lanthanum to lutetium, the f-shell is continuously filled with electrons. However, those electrons do not participate in bonding, as the f-shell orbitals are more diffuse and distributed closer to the nucleus and therefore poorly shield the outer shells. Due to those unpaired electrons, all lanthanides, with the exception of La (empty shell) and Lu (full shell) are paramagnetic and show unique electromagnetic properties, making them interesting, especially for modern industrial applications (Figure I.2).[19]

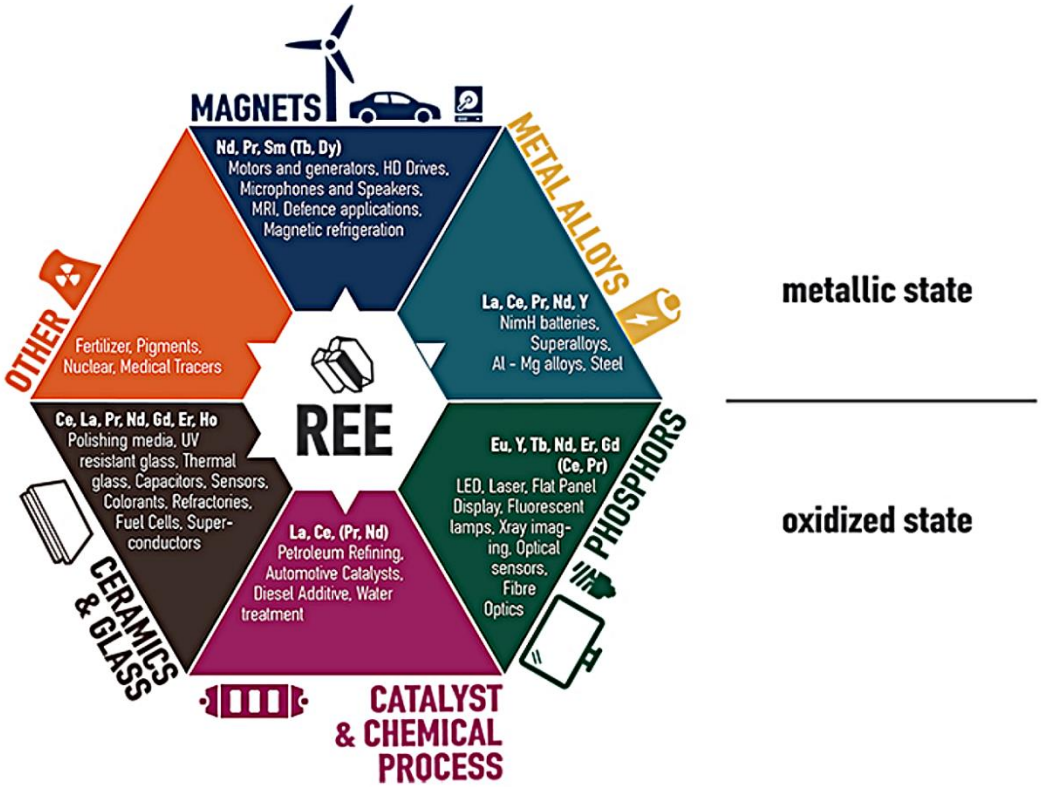

Figure I.2: Overview of applications of the rare-earth elements. Figure reproduced with kind permission of the EURARE project.[19]

The ionic radius of La^{3+} is similar to the one of Ca^{2+} (~ 1.03 – 1.22 *vs*. 1.00 – 1.18 Å for CN 6 – 9)[20] which is why lanthanides are often used for replacing calcium in the active site of proteins, for utilization of their superior spectroscopic properties.[21-22] Throughout the lanthanide series, the ionic radii decrease stepwise to 0.86 Å for lutetium.[20] This reduction in

radius is larger as it would be expected through the sole increase of nuclear charge and is known as the lanthanide contraction[23] – a phenomenon being partly explained by the poorly shielded outer electrons by the f-shell[24] and around 10% by relativistic effects.[25]

In comparison, lanthanides prefer relatively high coordination numbers of 7 – 12, a uniqueness resulting from the combination of relatively large ionic radii, a high charge of +3 and the interaction with ligands being mostly electrostatic.[11] The partly filled f-orbitals of lanthanides do not participate in bonding, whereas interaction with ligands relies mostly on electrostatic effects and electron pair acceptance as Lewis acid.[14]

Nowadays, lanthanides are found in a wide range of applications[18] (Figure I.2),[19] such as strong permanent magnets, catalysts, batteries, phosphors for LED and display devices or contrast agents in medicine. Lanthanides are even used in fertilizers[26] and animal feed.[27] However, the effect of the latter is currently not well understood, but the participation of microorganisms as symbionts has been proposed.[28]

3. Lanthanide Dependent Microorganisms

For a long time, the biorelevance of lanthanides was unknown. Although being present plentifully in the environment, their oxides and ores are poorly soluble and therefore their bioavailability is limited.[21] In 2004, Lim and Franklin hypothesized that lanthanides would be superior to calcium in various enzymes, but the low bioavailability of the lanthanides is said to have prevented expression of the respective enzymes.[31] However, starting in 2011, Kawai *et al.* reported in quick succession about a lanthanum dependent methanol dehydrogenase (MDH) in *Methylobacterium radiotolerans*[32] and *Methylorubrum* (formerly *Methylobacterium*) *extorquens* AM1[33], both encoded by the *xoxF* gene, and a cerium

Key Terms[29]

Protein – Biological macromolecule, build of chains of amino acids connected by peptide bonds.

Enzyme – Protein with catalytic function for substrate conversion. Reaction proceeds in the active site, which often includes a cofactor and/or a metal ion.

Active site – Region or cavity in an enzyme, where substrate binding and conversion proceeds.

Cofactor – Small organic molecule, which helps in enzymatic activity. Metal ions can be considered cofactors as well.

Operon – Group of genes, which are under the control of a single regulatory unit.

Nomenclature[30] – Gene: *xoxF*
Protein: XoxF

dependent MDH in *Bradyrhizobium sp.* MAFF211645.[34] It is unclear why these publications remained almost unnoticed. Three years later in 2014, Pol *et al.* reported a microorganism, originally found in 2007 in volcanic mudpots in the Solfatara crater, Naples Italy,[35] which turned out to be strictly lanthanide dependent.[36] The so called microorganism *Methylacidiphilum fumariolicum* SolV, or in short SolV could only be cultivated with its original mudpot water containing particular high amounts of dissolved lanthanides or in medium supplemented with lanthanide salts.[36] SolV expresses the same *xoxF* encoded MDH as mentioned above, metabolizing methanol for energy generation and containing a lanthanide ion in its active site.[36] Several clades of XoxF have evolved in different microorganisms, commonly named XoxF1-5.[37-39] The name is derived from the homology to calcium dependent MxaF-type MDH and the x stands for the unknown function at that time.[38] *xoxF* is positioned on an operon, together with *xox*G, encoding the natural electron acceptor for MDH and *xox*J, encoding a binding protein of unknown function.[40] The crystal structure of the enzyme isolated by Pol *et al.* was refined with cerium in the active site, although the metal ion in this enzyme was a Ln mixture due to mudpot water used. The central metal is coordinated by amino acids Glu172, Asn256, Asp299 and Asp301 and the known cofactor pyrroloquinoline quinone (PQQ), an organic heterocyclic molecule, functionalized with three carboxyl groups.[36]

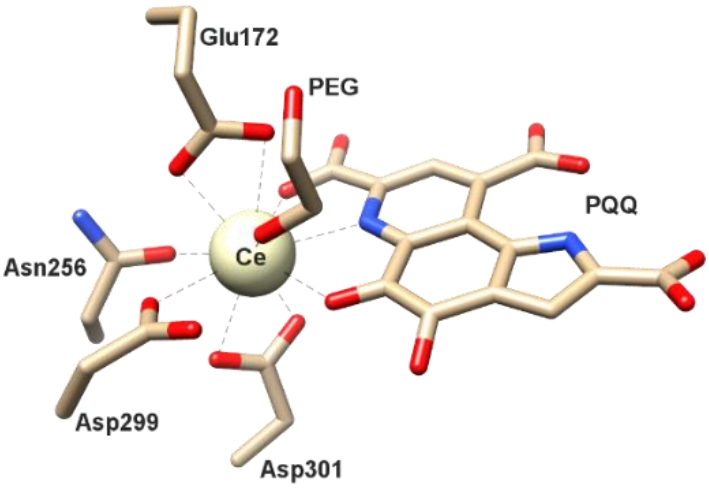

Figure I.3: Active site of the Ce-MDH from SolV strain (PDB ID: 4MAE) (co-crystallized with polyethylenglycol PEG).[36] Image generated with the UCSF Chimera package 1.12.[41]

This structure shows great similarity with an already known MDH, containing calcium in its active site, which is encoded by the gene *mxaF*. In comparison, the Ca-MDH lacks one aspartate, probably due to the generally smaller demand of coordination partners of calcium in comparison with lanthanides. This MDH-type was already discovered in 1964 by Anthony and Zatman[42-43] and is still subject of current research. PQQ acts as an electron acceptor and becomes reduced to $PQQH_2$, while methanol is oxidized to formaldehyde or even further to

formic acid in case of lanthanides.[36] The central metal acts as a Lewis acid, which activates the coordinating C=O group.[44-45] It is still subject of debate, whether a hydride is transferred from methanol to the PQQ C=O carbon (hydride transfer mechanism), or if methanol acts as a nucleophile and attacks the C=O position as a whole (hemiketal mechanism),[45-46] with DFT, model compound and crystallographic studies published.[47-51]

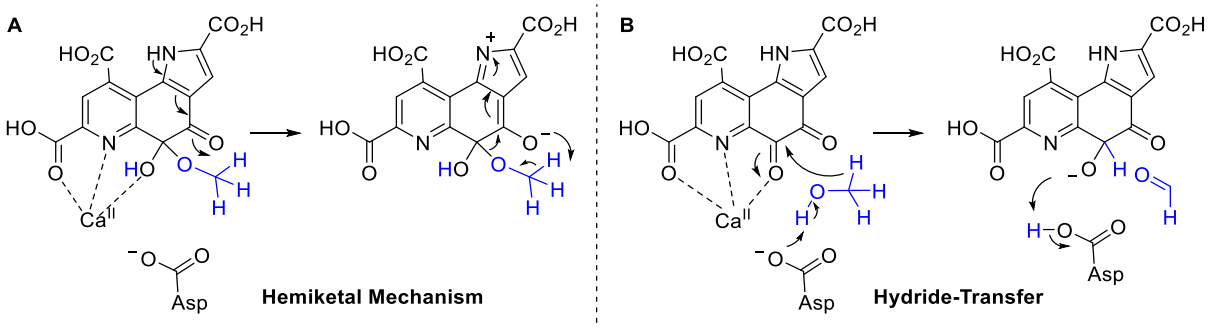

Scheme I.1: Possible mechanisms for methanol oxidation by calcium dependent MxaF MDH.

After the discovery of lanthanide dependent MDH enzymes, the presence of the *xoxF* gene and Ln utilization were verified in a wide range of microorganisms.[13] Such methanotrophic (= methane as carbon source) and methylotrophic (utilize C1 compounds such as methanol or methylamine for their metabolism) microorganisms are found in all kind of ecosystems such as soil, plants or ocean water[52-54] and are by far not restricted to extreme environments like SolV's volcanic mudpot.[36] Phylogenetic analysis revealed, that the *xoxF* gene is more widespread and evolutionary probably older than its Ca-counterpart.[39]

While some bacteria carry only the *xoxF* gene (like SolV), a wide range of bacteria carry both *xoxF* and *mxaF* genes.[54] An upregulation of the expression of *xoxF* concurrent to a down-regulation of *mxaF* when only nanomolar concentrations of Ln are present was described.[55-59] This mechanism was implemented as the so-called lanthanide switch.[55-59] Lanthanide dependent bacteria show a clear preference for the early lanthanides (Table I.2), as already discovered in cultivation experiments by Pol *et al.*[36] and was also noticed after the Deepwater Horizon (DWH) oil rig catastrophe.[60] Due to the enormous amounts of gas released into the ocean, methanotrophic bacteria started to bloom.[61] In return, this caused a significant depletion of the early lanthanides in the sea water,[62] which remained ununderstood for a long time.

Table I.2: Selected lanthanide utilizing bacteria cultivated with different lanthanides. Bottom: Observed depletion of selected lanthanides from seawater during DHW. Adapted from L. Daumann.[13] White squares indicate non-tested lanthanides, whereas fast growth or strong depletion is given in dark green, medium growth or depletion in light green and no or only poor growth stimulation / depletion in red. Orange: None of the tested lanthanides affected growth whereas La influenced *xoxF* and *mxaF* gene expression.

	Growth observed with														
Bacterial Strain	La	Ce	Pr	Nd	Pm	Sm	Eu	Gd	Tb	Dy	Ho	Er	Tm	Yb	Lu
M. extorquens AM1 (XoxF1)[63]															
P. putida KT244(PedH) [64]															
M. mobilis JLW8 mutant (XoxF4-1)[38]															
M. mobilis JLW8 (XoxF4-2)[38]															
Methylomonas sp. LW13 (XoxF5)[38]															
M. fumariolicum SolV (XoxF2)															
M. aquaticum 22A[58]	*														
	Depletion from ocean water observed														
Bloom of methanotrophic bacteria during DWH[62]															

Researchers only begin to understand how lanthanides are transported into and stored in cells. Experiments with AM1 already demonstrated, that this microorganism can harvest lanthanides even from scrap metal of hard drive magnets.[65] Recently, the Ln binding protein Lanmodulin was discovered, located in the periplasm of cells.[66] It has four metal coordination motifs (EF hands) showing a 10^8-fold selectivity to lanthanides over calcium.[66] However, its biological role remains to be elucidated.

It is postulated that bacteria must exhibit efficient uptake mechanisms for lanthanides. The existence of small chelators is suggested, which could be used for lanthanide availability by the bacteria and which were named “lanthanophores”,[13, 54] after the well studied “siderophores” which are responsible for iron uptake.

4. Pyrroloquinoline Quinone (PQQ)

The non-covalently bound redox cofactor of MDH enzymes, Pyrroloquinoline quinone, acts as an electron acceptor for the oxidation of methanol. It is comprised of an aromatic ring system, consisting of a pyrrol, a quinone and a pyridine and carries three carboxyl groups in total (Figure I.4).

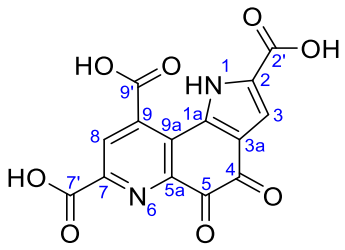

Figure I.4: Structure of PQQ and its numbering scheme according to Unkefer *et al.*[67]

As the key component in lanthanide supported methanol oxidation, studies on this cofactor will help to better understand lanthanide-utilizing bacteria in general. Interaction of PQQ with lanthanides will provide important information, which will help to elucidate the mechanism of Ln-MDH and the evolutionary advantage these elements provide over Ca.

Large parts of this thesis deal with the interesting and manifold chemistry of PQQ and cover its synthesis and purification (Chapter III), its coordination chemistry (Chapter IV), its redox chemistry (Chapter V), the interaction with small molecules (Chapter VI) and the synthesis of derivatives used for biomimetic model complexes (Chapter VII). Separate and more detailed introductions, covering each of those features are given at the beginning of the respective chapters. Chapter II deals with the active site of MDH enzymes and how DFT calculations can help to elucidate the impact of different lanthanides.

II. DFT STUDIES

1. Introduction

Density functional theory (DFT) has become a powerful tool for the calculation of structural and functional aspects of proteins.[68] Several calculations of the *mxaF* encoded Ca-MDH have been performed over the years.[47, 49, 69-75] From the calculations dealing with the methanol oxidation mechanism, almost all conclude the hydride transfer (see Scheme I.1) to be the energetically favored one.[47, 49, 72-73, 75] Leopoldini *et al.* state that both mechanisms are energetically rather unlikely and propose a third mechanism, being a modification of the addition-elimination mechanism.[70]

First calculation on the *xoxF* encoded Ln-MDH used the published crystal structure with cerium[36] and revealed the largest match with a semiquinone $PQQ^{\bullet-}$ configuration, possibly being the resting state of the enzyme.[76] Ce^{3+}–PQQ^{0} was defined to be the catalytically active form. On the basis of the calculations, Ce^{3+} influences the redox cycling of PQQ and promotes reduction to $PQQH_2$ more effectively than Ca^{2+}. The occurrence of a Ce^{4+} species was described to be rather unlikely. To simplify the calculation, only the active site of the enzyme was taken into account and present amino acids were truncated and fixed in their crystallographic position to model the steric imposed by the protein.[76]

A publication from Prejanò *et al.* deals with the possible reaction mechanism of the cerium containing XoxF active site by employing the quantum chemical cluster methodology.[77] The potential energy surfaces of the hydride transfer and the addition-elimination mechanism were calculated with the latter being the energetically favored one. Similar to the calculation described above, only the active site was taken into account with truncated and fixed amino acids.[77]

The latest theoretical approach from Tsushima combined molecular dynamics (MD) and fragment molecular orbital (FMO) calculations to model the whole protein instead of using truncated amino acids.[78] La^{3+}, Eu^{3+} or Yb^{3+} were used as central metals, leading to several structural changes in the active site. An additional H_2O molecule coordinated to the central metal in case of La^{3+}.

A coordinational change from bi- to monodentate Glu_{172} and from tri- to monodentate PQQ was observed from the larger La^{3+} and Eu^{3+} to the smaller Yb^{3+}, possibly explaining the preference of XoxF for LRE.[78]

2. Impact of Different Lanthanides on the Structure of XoxF

We followed the approach from Bogart *et al.*[76] in using a simplified active site of XoxF and compared calculated structures with either La^{3+}, Ce^{3+}, Pr^{3+}, Eu^{3+} or Yb^{3+} as central metal.

The following section is part of the publication:

Similar but not the same: First Kinetic and Structural Analyses of a Methanol Dehydrogenase Containing a Europium Ion in the Active Site

Bérénice Jahn, Arjan Pol, Henning Lumpe, Thomas R. M. Barends, Andreas Dietl, Carmen Hogendoorn, Huub J. M. Op den Camp and Lena J. Daumann

Published in: *ChemBioChem* **2018**, *19*, 1147-1153. DOI: 10.1002/cbic.201800130.
Reprinted under Creative Commons Attribution Non-Commercial License CC BY-NC.

Abstract

Since the discovery of the biological relevance of rare-earth elements (REE) for numerous different bacteria, the questions of the advantage of REE in the active site of methanol dehydrogenase (MDH) over calcium(II) and why bacteria prefer light REE have been a subject of debate. Here we report the cultivation and purification of the strictly REE-dependent methanotrophic bacterium *Methyl-acidiphilum fumariolicum* SolV with europium(III) as well as structural and kinetic analyses of the first Eu-substituted methanol dehydrogenase. Crystal structure determination of the Eu-MDH demonstrated that overall no major structural changes were induced by converting to this REE. Circular Dichroism (CD) measurements were used to determine optimal conditions for kinetic assays and inductively-coupled plasma mass-spectrometry (ICP-MS) showed 70% incorporation of Eu in the enzyme. Our studies explain why bacterial growth of SolV with Eu^{3+} is significantly slower than with La^{3+}/Ce^{3+}/Pr^{3+}: Eu-MDH possesses a decreased catalytic efficiency and affinity for the substrate. Although rare-earth elements have similar properties, the differences in ionic radii and coordination numbers across the series significantly impact MDH efficiency.

2.1. DFT Calculations of the Active Site

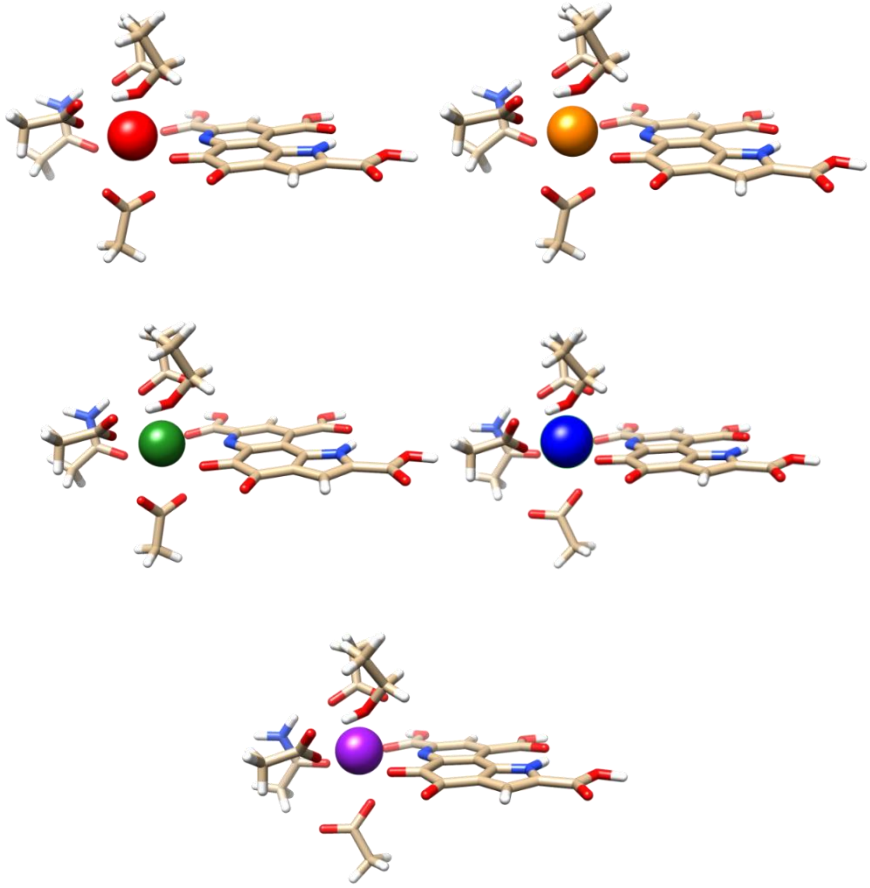

Figure II.1: Geometry optimized structures. Pictures generated with the UCSF Chimera package.[41] Carbon atoms in beige, oxygen in red, nitrogen in blue. Red sphere = La, orange sphere = Ce, green sphere = Pr, blue sphere = Eu, purple sphere = Yb. Asp301 becomes monodentate during the optimizations with the smaller REE Eu and Yb in the active site. Structure optimizations were performed using Gaussian 09[79] and the B3LYP functional with the 6-31G(d) basis set for C, H, N, O.[80-85] Quasi relativistic effective core potentials (ECP) were used for the central metal: MWB46 for La^{3+}, 47 for Ce^{3+}, 48 for Pr^{3+}, 52 for Eu^{3+}, 59 for Yb^{3+}.[86-88] Calculations were performed with 11 outer sphere electrons, as pseudo-singlets (f-electrons included in ECP) and restricted closed-shell calculations, a method, which is common for REE-complex calculations.[89] None of the frequency calculations showed negative values. Starting point of the geometry optimization was the active site of the crystal structure of Ce-MDH isolated from SolV (4MAE) with exchange of Ce^{3+} with La^{3+}, Pr^{3+}, Eu^{3+} and Yb^{3+} respectively. Based on the method from Schelter *et al.* the amino acid residues and the polyethylenglycol, present in the crystal structure were truncated and the anchoring carbon atoms were frozen in their crystallographic position to mimic the sterics imposed by the protein.[76] For simplification only the cofactor PQQ and the amino acids directly coordinating to the metal ions were included in the calculations and the calculations were done without models for solvent effects.

Notably, in DFT calculations with Eu^{3+} or Yb^{3+} in the active site, Asp_{301} became a monodentate ligand (Figure II.1 and Figure IX.2), when substrate was included in the calculations, but this residue is bidentate in the crystal structure in which no significant substrate density was present. It is known that the coordination number decreases within the REE series and this could provide one explanation for the differences observed during growth of SolV.[24, 36, 62, 90] The active site of MDH might display lower affinity for substrate as the size of the REE decreases.

2.2. Conclusion

The coordination chemistry of REE is known to show a high degree of structural diversity and the absence of strong ligand field effects can make predictions on the coordination numbers and geometry difficult.[91] In methanol dehydrogenase almost all ligands and the coordination geometry are determined by the protein environment and result in a coordination number of nine. Addition of the substrate as a tenth ligand might depend on the nature and characteristics of the REE ion in the active site. As Cotton and Raithby so appropriately describe it: "discontinuities can arise at any point in the lanthanide series, so where possible each of the elements should be examined in any particular study."[92] To conclude, we present the first structural and kinetic study of a methanol dehydrogenase isolated from a strictly REE-dependent bacterium with a europium ion in the active site. Our results show that while rare-earth elements have similar properties, the differences in ionic radii and coordination numbers across the series impact the catalytic efficiency of MDH, which might explain why bacteria depend on the larger, more abundant REE for growth.

3. Impact of the Lanthanide Contraction

Distinct structural changes were observed in calculations, depending on the lanthanide present in the active site. Therefore, the whole series of lanthanides from lanthanum to lutetium was analyzed, regarding enzymatic activity (biological assays) and structure of the active site (DFT calculations).

The following section is part of the publication:

Impact of the Lanthanide Contraction on the Activity of a Lanthanide-dependent Methanol Dehydrogenase – A Kinetic and DFT Study

Henning Lumpe, Arjan Pol, Huub op den Camp and Lena Daumann

Published in: *Dalton Trans.* **2018**, *47*, 10463-10472. DOI: 10.1039/c8dt01238e.
Reprinted under Creative Commons Attribution-NonCommercial 3.0 Unported Licence.

Abstract

Interest in the bioinorganic chemistry of lanthanides is growing rapidly as more and more lanthanide-dependent bacteria are being discovered. Especially the earlier lanthanides have been shown to be preferentially utilized by bacteria that need these Lewis acids as cofactors in their alcohol dehydrogenase enzymes. Here, we investigate the impact of the lanthanide ions lanthanum(III) to lutetium(III) (excluding Pm) on the catalytic parameters (v_{max}, K_M, k_{cat}/K_M) of a methanol dehydrogenase (MDH) isolated from *Methylacidiphilum fumariolicum* SolV. Kinetic experiments and DFT calculations were used to discuss why only the earlier lanthanides (La-Gd) promote high MDH activity. Impact of Lewis acidity, coordination number preferences, stability constants and other properties that are a direct result of the lanthanide contraction are discussed in light of the two proposed mechanisms for MDH.

3.1. Introduction

Calcium-dependent methanol dehydrogenases (MDH) have been known for over 50 years.[44] However, the recently discovered lanthanide (Ln)-dependent MDH are also widespread in bacteria inhabiting different ecosystems and this has sparked a growing interest in lanthanide-dependent metalloenzymes.[37, 93] These enzymes are mostly found in methanotrophic and methylotrophic bacteria, organisms that metabolize C_1 compounds such as methane or methanol. We recently reported the crystal structure of a Eu-MDH isolated from *Methylacidiphilum fumariolicum* SolV, a thermoacidophile that is strictly dependent on Ln for growth.[94] The structure reveals, in addition to the europium ion in the active site, the presence of pyrroloquinoline quinone (PQQ), a redox cofactor that is commonly found in many alcohol dehydrogenases (Figure II.2).[95] PQQ needs a Lewis acid for activation (Ca^{2+}, Ln^{3+}) and this cofactor is reduced to the quinol form ($PQQH_2$) concurrent with methanol oxidation. Further, the metal ion in the active site is proposed to be involved in proper substrate orientation and binding.[45] DFT calculations by Schelter and coworkers revealed that a trivalent lanthanide is superior to calcium(II) in cofactor activation.[76] For Ca-MDH, cytochrome C_L has been found to be the redox partner *in vivo*.[96-97] Some bacteria possess both genes for the Ca- as well as for the Ln-dependent enzyme.[58, 63-64, 98-100] In these bacteria lanthanides are also involved in gene expression and regulation and a sensing mechanism for Ln has been proposed but is still not well understood.[54-55, 63, 101-102] Not all lanthanide ions support growth of Ln-dependent bacteria equally and not all of them are able to produce an active MDH enzyme. A preference for the lighter, more abundant Ln has been noted both in laboratory and field experiments.[36, 58, 62, 64]

For example, during the Deepwater Horizon blowout in 2010, millions of moles of natural gas were released into the environment, leading to a bloom of methanotrophic bacteria.[60-61, 103-105] Analysis of water samples taken near the site revealed, that concurrent to the bacterial methane consumption, light lanthanides (La, Ce, Pr and Nd) were depleted during the event.[62] Masuda *et al.* recently reported that Ho^{3+} and Lu^{3+} did not support growth of *Methylobacterium aquaticum.* In addition, the Ln-dependent alcohol dehydrogenase from *Pseudomonas putida* did show catalytic activity upon addition of earlier lanthanides like La^{3+} but not with late Ln like Yb^{3+}.[58, 64] We recently reported that there is a link between the growth rate of strain SolV and the catalytic efficiency of the methanol dehydrogenase.[94] This enzyme is pivotal to the energy metabolism of methanotrophic and methylotrophic bacteria. The early Ln like La^{3+} and Pr^{3+} led to fast growth of strain SolV and high MDH activity while cultivation with Eu^{3+} was slower, albeit still exponential bacterial growth occurred, and this metal ion was able to produce an active MDH enzyme. However, addition of Yb^{3+} to purified MDH lead to a strong decrease in activity and this element did not support exponential growth of strain SolV. These results are surprising, as the later Ln^{3+} should be better Lewis acids owing to their decreased ionic radius, a result from the lanthanide contraction.[24]

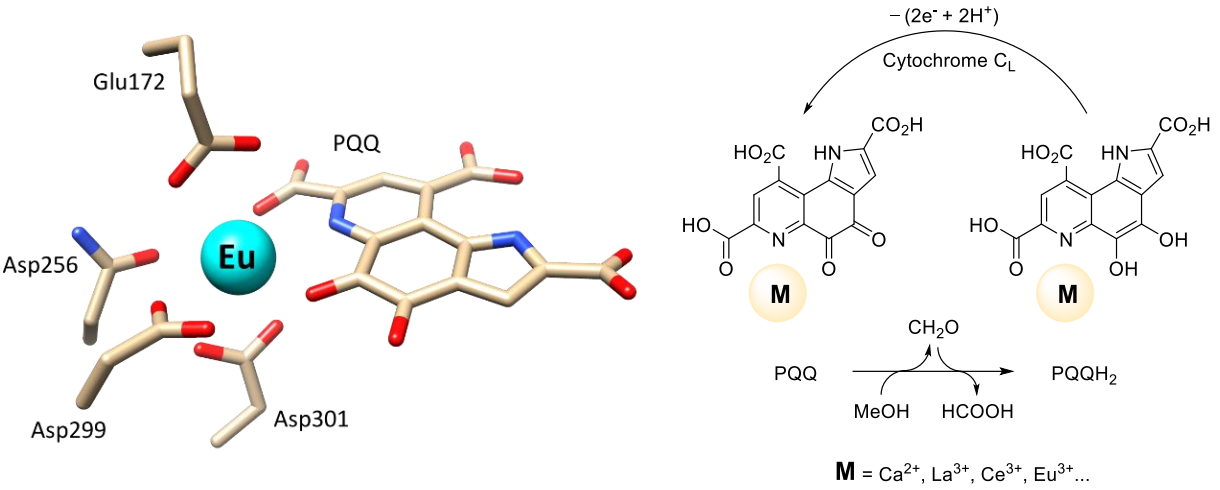

Figure II.2: Left: Active site of Eu-MDH from strain SolV (PDB 6FKW). Image generated with the UCSF Chimera package.[41] Right: Schematic overview of the MDH-methanol oxidation. MDH from strain SolV is also capable of oxidizing formaldehyde to formic acid.

Why are the chemically similar lanthanides not supporting growth and MDH activity equally? This question prompted us to study the activity of MDH isolated from *M. fumariolicum* SolV in the presence of the entire lanthanide series (La-Lu, excluding Pm). It should be noted that strain SolV is strictly dependent on Ln, as it does not possess the gene for Ca-MDH.[36] Kinetic investigations were complemented by DFT calculations of the active site and we drew from previously published studies in lanthanide coordination chemistry and the methanol

dehydrogenase literature to get a full picture of the impact of the lanthanide contraction and the resulting changes such as Lewis acidity and coordination number-preference along the series on the activity of MDH.

3.2. Results and Discussion

3.2.1 MDH Assay Optimization

The activity of MDH towards methanol was assessed with a dye-linked assay (Scheme II.1, Figure IX.3) using 2,6-dichlorophenolindophenol (DCPIP) as redox indicator, phenazine ethosulfate (PES) as artificial electron acceptor and PIPES buffer (20 mM, pH 7.2).[44, 106] The unfavorable solubility product of lanthanide phosphates precluded the use of phosphate buffer for our experiments.[107]

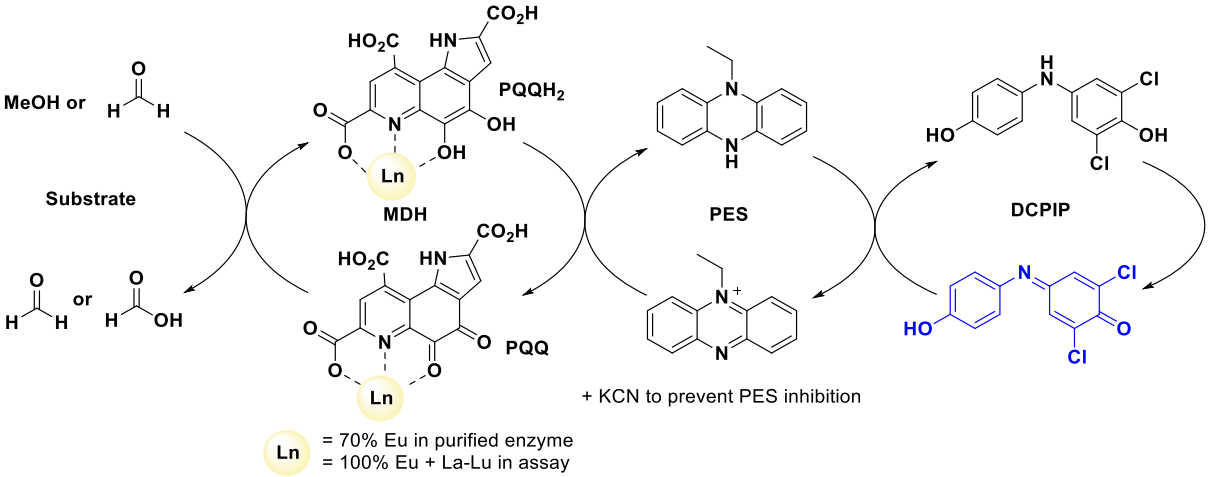

Scheme II.1: The assay components for assessing MDH activity.

Further, potassium cyanide was added to the assay. While cyanide prevents inhibition of MDH by PES it is also added to suppress endogenous substrate activity in MDH.[71, 108-109] It should be noted, that under the conditions of the assay (pH 7.2), the cyanide is present mainly in its protonated form (HCN) in solution and that the solubility of HCN is temperature dependent.[110] The nature of the endogenous substrate for methanol dehydrogenases has remained unresolved for the past decades but traces of alcohols and aldehydes present in the reagents used have been named.[44, 109] We further added a large excess of methanol (50 mM) to the assays to ensure this substrate was preferentially turned over. This assay is artificial in every way and prone to error, so it is important to investigate different systems under the same conditions and use caution when comparing results. The cultivation of strain SolV with Eu^{3+} and subsequent purification of Eu-MDH was reported recently.[94] The enzyme is obtained in a 'partial-apo' form after

purification where 70% of the active sites are substituted with Eu^{3+} and the remaining 30% are not occupied but can be reconstituted by adding additional Ln.[94] The addition of increasing amounts of europium(III) to 200 nM purified 'partial-apo' Eu-MDH led to a gradual increase in activity until saturation around 5 to 20 µM added metal was observed.[94] It is proposed that this excess of lanthanide ions will lead to a 100% occupation of the active site in MDH. The activity towards methanol oxidation upon La^{3+}, Pr^{3+} and Nd^{3+} addition to MDH follows the same saturation kinetics as the addition with Eu^{3+}, where, between 0 and 5 µM, a sharp increase in activity was observed, with saturation behavior for higher concentrations (Figure II.3). An investigation of a potential inhibiting effect of added lanthanide ions at higher concentrations than 20µM was precluded by a background reaction of the assay mix (PES, KCN, DCPIP in buffer) in the absence of MHD. It is worth noting here, that the determined affinity (of 'partial-apo' Eu-MDH) for the chosen lanthanides was not significantly different (K_{assoc}(La) = 0.55 ± 0.19 µM, K_{assoc}(Pr) = 0.52 ± 0.20 µM, K_{assoc}(Nd) = 0.49 ± 0.17 µM and K_{assoc}(Eu) = 0.53 ± 0.21 µM) but rather the specific activity (SA) of the enzyme in the presence of these different metal ions varied (Normalized SA: La = 0.13 ± 0.01, Pr = 0.17 ± 0.01, Nd = 0.18 ± 0.01, Eu = 0.08 ± 0.01).

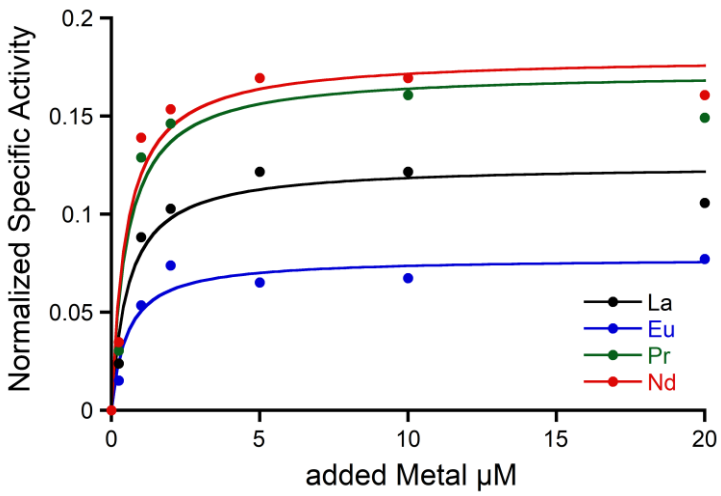

Figure II.3: Normalized specific activity (n = 3, for 5 and 10 µM n = 1) of 200 nM 'partial-apo' Eu-MDH in the presence of increasing amounts of $LnCl_3$, error bars were omitted for clarity, standard deviations from the mean were less than 10%. The data was normalized by subtracting the activity of Eu-MDH without added Ln from the data.

The metal ion affinity constant for Eu differed slightly from the one reported earlier (K_{assoc}(Eu) = 2.6 ± 0.6 µM) as we adjusted the assay for the use of a plate-reader instrument and the resulting variations in PES, DCPIP, methanol and 'partial-apo' Eu-MDH concentrations and ratios are known to have an impact on the assay values.[94] It is thus of importance to compare only results obtained under the exact same conditions, ideally obtained with the same stock solutions (artificial electron acceptor, redox indicator, methanol and and 'partial-apo' Eu-MDH

concentrations, temperature and pH and used buffer). We also conducted a titration with lutetium(III) under the same conditions as described in Figure II.3. However, increasing amounts of Lu^{3+} led to a gradual decrease of MDH activity. This indicates, that upon addition of an excess of lanthanide ions (20 µM Ln to 0.2 µM MDH), the active site metal (here Eu) can be replaced to some extent. Without the addition of MDH, the assay mixture did not show a background reaction in the presence of any of the Ln at the concentration used (20 µM).

3.2.2 Kinetic Experiments with the Entire Lanthanides Series

The differences in stimulated MDH activity by the early lanthanides La^{3+}, Pr^{3+}, Nd^{3+} compared to Eu^{3+} and Lu^{3+} prompted us to study the effect of equal concentrations of every lanthanide in the series to gain more insight into the differences caused by the lanthanide contraction on MDH activity. Based on the observations made in the titration experiment, we chose the same conditions for all lanthanides and added 20 µM (saturation conditions) of the respective chloride salts to 200 nM and 'partial-apo' Eu-MDH in a subsequent assay. Figure II.4 shows the differences in activity for 'partial-apo' Eu-MDH upon addition of the lanthanide series (La-Lu, Pm not included). The data was normalized to 1 for the MDH activity without added lanthanides (here 10 µL H_2O were added to achieve the same total volume in the sample well as in the Ln samples). Surprisingly, the addition of the late lanthanides (Tb^{3+} to Lu^{3+}) decreased the activity compared to when no additional lanthanide ions were added to Eu-MDH (entry H_2O in Figure II.4). Ln above Tb^{3+} increased activity gradually from Gd^{3+} to Nd^{3+}, while Pr^{3+} and La^{3+} were slightly lower in activity than Nd^{3+} but still among the three best metal ions for maximum activity.

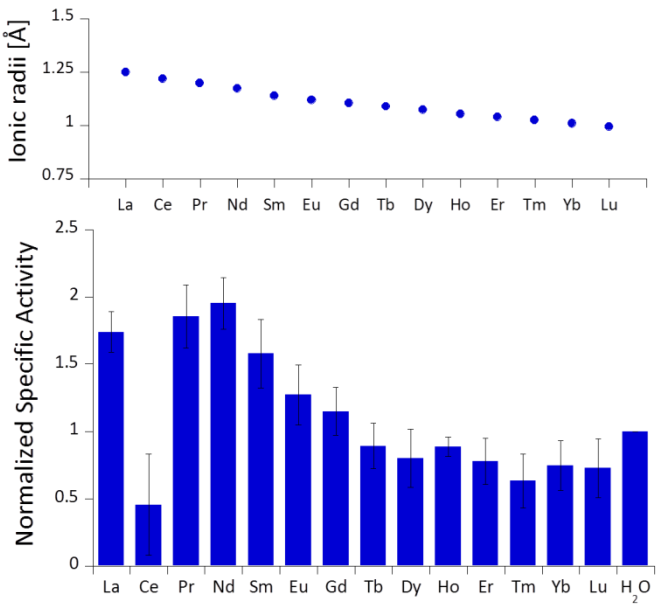

Figure II.4: Ionic radii of the lanthanides(III) in aqueous solution as determined by D'Angelo *et al.*[111] Normalized specific activity (n = 6) of 200 nM Eu-MDH in the presence of 20µM of $LnCl_3$. Conditions: 20 mM PIPES pH 7.2, 1 mM PES, 1 mM KCN, 100 µM DCPIP, 50 mM MeOH, 45°C.

The turnover point for an enhancing effect of an added Ln turning into a negative effect on catalysis occurs right after gadolinium(III). From our data, it is difficult to make a statement on whether the much discussed 'gadolinium break' is of relevance here.[112-113] The decrease of activity in the presence of some lanthanides suggests that the later Ln are able to exchange with europium(III) in the active site. This exchange might be dependent both on the external Ln^{3+} concentration as well as on the properties of the Ln^{3+} itself. The assay with Ce^{3+} did not yield reproducible results, despite several attempts. While the assay mix itself (buffer, PES, DCPIP, KCN) did not show a background reaction when cerium(III) was added, the DCPIP reduction varied greatly in the presence of 'partial-apo' Eu-MDH. We attribute this to the property of cerium to exist not only in the trivalent form but also in its tetravalent state.[24] Traces of Ce^{4+} present in the medium (not bound to the enzyme active site) might oxidize the reduced, colorless DCPIP dye back to the colored form and thus led to problematic results in the determination of MDH activity. This derivative was included in Figure II.4 for the sake of completeness but is not further discussed. It should be noted here again, that early (and larger) lanthanides are preferentially depleted by methanotrophic bacteria as demonstrated with samples collected during the Deepwater Horizon catastrophe.[60, 62] These studies could indicate that not only the activity of MDH is tuned to utilize the early lanthanides, but also the metal ion uptake mechanisms in these bacteria. This effect is most pronounced for La^{3+}, Ce^{3+}, Pr^{3+} and Nd^{3+}, Ln^{3+} that also yielded highly active MDH derivatives in our experiments and in enzymatic studies by others.[63] This observation is however not limited to MDH isolated from

methanotrophic and methylotrophic bacteria. Klebensberger and coworkes have shown that activity of an alcohol dehydrogenase isolated from *P. putida* (a non-methylotrophic organism) was observed with La^{3+}, Ce^{3+}, Pr^{3+}, Nd^{3+}, Sm^{3+}, Gd^{3+} and Tb^{3+}, and was highest with Pr^{3+} and Nd^{3+}. Lu^{3+}, Tm^{3+}, Ho^{3+} and Eu^{3+} were not investigated and Er^{3+} and Yb^{3+} as well as the two rare-earth elements Sc^{3+} and Y^{3+}, did not produce an active enzyme.[64] These findings together with our results suggest that these alcohol dehydrogenase systems are tuned by evolution to utilize and function with the earlier, more abundant lanthanides. However, why do Pr^{3+} and Nd^{3+} stimulate the highest activity? And why does the activity gradually decrease after Nd^{3+} albeit increasing Lewis acidity of the central metal ion? To answer these questions, the properties of the trivalent lanthanides along the series and the different mechanisms which have been proposed for methanol dehydrogenases, have to be considered.

3.2.3 MDH Mechanisms and Possible Impact of Ln Size

Specific Activity and Substrate Affinity. The redox cofactor PQQ needs a Lewis acid for activation of the C5 quinone C-O bond (Figure II.5).[44-45] However, the role of the Lewis acid in the active site might go beyond that purpose. Its additional involvement in cofactor (PQQ) orientation,[45, 70] cofactor redox cycling,[76] substrate orientation,[77] and substrate activation (by means of polarization of the O-H bond)[77] have been debated. Two general mechanisms (and variations thereof) have been proposed based on DFT, model and crystallographic studies: the hemiketal and the hydride transfer mechanism (key steps are shown in Figure II.5).[45, 49-51, 70, 77, 114] Through the series given that the coordination number does not change, Lewis acidity steadily increases, due to the decreasing ionic radius, caused by the lanthanide contraction (Figure II.4).[92] The specific activity (SA) of the enzyme should therefore steadily increase if this kinetic parameter were (solely) dependent on Lewis acidity of the metal ion in the active site. The low, or rather absence of any, SA for Lu^{3+} and the other late lanthanide ions (Figure II.4) however showed, that Lewis acidity and activation of the C5 carbonyl bond in PQQ is not the only factor that needs to be considered. Increased Lewis acidity might be the explanation why Pr^{3+} and Nd^{3+} led to more active enzyme derivatives than La^{3+}, but as we progress in the series, this positive impact is overruled by another factor.

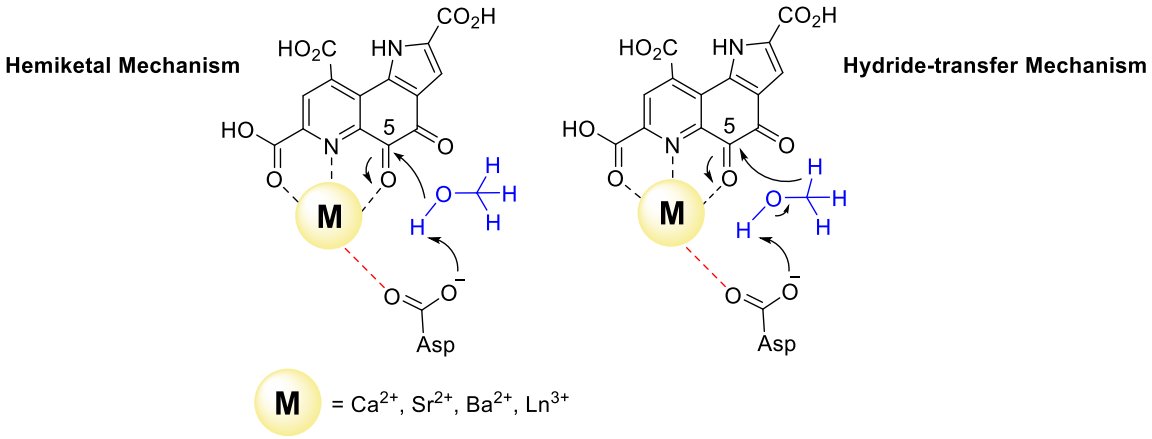

Figure II.5: Key steps of the two proposed mechanisms in methanol dehydrogenase enzymes.

Harris and Davidson reported a comparison of Ca-MDH and Sr-MDH isolated from *Methylobacillus glycogenes*. The authors demonstrated that Sr^{2+}, while having a 20% larger ionic radius than Ca^{2+}, produced the more active enzyme but with a decreased affinity for substrate (Table II.1).[115] Goodwin and Anthony reported the kinetic parameters of Ca-MDH, Sr-MDH and Ba-MDH from *Methylobacterium extorquens*.[116] Here, the same trend - the larger the alkaline earth ion, the higher the v_{max} but the lower the substrate affinity - was observed. (Table II.1). Increased Lewis acidity does not seem to necessarily have a positive effect on catalysis. It is interesting that in this study the native metal ion calcium(II) does produce the slowest enzyme. However it is the derivative with the best substrate affinity. The large decrease in substrate affinity upon substitution with barium(II) suggests that this 25 % larger, non-biologically relevant metal ion perturbs the active site and interferes with proper substrate binding. DFT calculations of the active site with Ca^{2+} or Ba^{2+} as the central metal were performed by Mainardi *et al.*[69] It was shown that the activation energy for methanol oxidation of Ca^{2+} containing MDH was doubled compared to the Ba^{2+}-derivative. By calculating the energy barriers for both the hemiketal- and the hydride-transfer mechanism, they further showed, that for both mechanisms almost all free-energy barriers were reduced in the presence of Ba^{2+}.[69] Within the lanthanide series, the larger derivatives are also superior to the smaller Ln and stimulate the highest activity. However, one has to keep in mind that with the lanthanide-dependent MDH, the larger Ln are the native metal ions and the later, less abundant Ln might play only a minor role in biological systems. Further, differences between Ln-MDH isolated from different bacteria have been noted.[36, 63] Ln-MDH isolated from strain SolV does not require activation by ammonia or methylamine in the dye-linked assay and has a pH optimum of 7 while the Ln-MDH isolated from *M. extorquens* does need methylamine and pH 9 to function properly (Table II.1).[36, 63, 98] Table II.1 also demonstrates the importance of the assay conditions such as temperature (30-60°C were reported), the chosen buffer and pH (phosphate,

PIPES or TRIS buffer, pH 7-9)[36, 63-64, 94, 98, 115-117], type of electron acceptor and redox indicator (PES, PMS, Wursters Blue, cytochrome C_L)[64, 71, 106, 118] and the presence of activators or competitive inhibitors (KCN, imidazole, ammonium ions, methylamine)[71, 98, 109, 115] for the kinetic parameters that are obtained. Further, some of the components e.g. PES and PMS are light sensitive and degradation during handling can impact the effective concentration of these reagents in the assay. Hence one should only compare kinetic parameters of systems that have been obtained under the same conditions.

Table II.1: Kinetic parameters of alcohol dehydrogenase enzymes.

Enzyme System (Substrate)	v_{max} [μmol min^{-1}mg^{-1}]	K_M [μM]	k_{eff} (k_{cat}/K_m) [mM^{-1}s^{-1}]
Ca-MDH[a,[115]] (MeOH)	7.3	15	-
Sr-MDH[a,[115]] (MeOH)	21.8	46	-
Ca-MDH[b,[116]] (MeOH)	0.81	3	-
Sr-MDH[b,[116]] (MeOH)	1.08	22	-
Ba-MDH[c,[116]] (MeOH)	1.61	3500	-
Ln-MDH[d] (MeOH)	4.4	0.8	5800
Eu-MDH[e,[94]] (MeOH)	0.189 ± 0.006	3.62 ± 0.44	55
Pr-ADH[f,[64]] (EtOH)	10.6 ± 0.4	177 ± 31	66 ± 12
La-ADH[g,[98]] (MeOH)	6.6	5980	2
La-ADH[g,[98]] (EtOH)	6.4	0.9	14500
Eu/Lu-MDH[h] (MeOH)	0.020 ± 0.002	0.82 ± 0.39	26
Eu-MDH[h] (MeOH)	0.043 ± 0.002	0.91 ± 0.24	50
Eu/La-MDH[h] (MeOH)	0.151 ± 0.005	1.30 ± 0.21	123

Conditions: [a]pH 9, 30°C, 6 mM $(NH_4)_2SO_4$, 3 mM Wursters blue, 6 mM KCN, MDH from *M. glycogenes* [b]pH 9.0, 10 mM NH_4Cl. [c]pH 9.0, 100 mM NH_4Cl, MDH from *M. extorquens* [d]Ln = mixture of La, Ce, Pr, Nd, 60°C, 100 nM MDH, pH 7, 2 mM PES, 40 μM DCPIP, MDH from *M. fumariolicum*. [e]pH 7.2, 45°C, 100 nM MDH, 1 mM PES, 1 mM KCN, 80 μM DCPIP, 20 μM $EuCl_3$, MDH from *M. fumariolicum*. [f]pH 8, 30°C, 0.5 mM PMS (phenazine methosulfate), 150 μM DCPIP, 25 mM imidazole, 1 μM $PrCl_3$, ADH = Alcohol dehydrogenase from *P. Putida*. [g]pH 9, 100 μM, $LaCl_3$, 5mM methylamine, 10 mM PQQ, 100 μM DCPIP, 100 μM PMS. ADH = Alcohol dehydrogenase from *M. extorquens*. [h]pH 7.2, 45°C, 200 nM MDH, 1 mM PES, 1 mM, KCN, 100 μM DCPIP, 20 μM $LnCl_3$, MDH from *M. fumariolicum*, this work.

Ideally, one could purify individual MDH derivatives with each of the different Ln in the active site and compare them under the same assay conditions. However, this endeavor is somewhat hampered by the absence of bacterial growth with the late lanthanides. In lieu of alternative purified Ln-MDH derivatives we nevertheless obtained catalytic parameters for some of the mixed Eu-MDH+Ln species in this study (Figure II.6 and Table II.1). 20 μM of Eu^{3+}, La^{3+} or Lu^{3+} were added to 200 nM Eu-MDH and increasing amounts of methanol were added (0, 1, 2, 5, 10, 20, 50 μM and 50 mM). As with the data in Figure II.3, the most striking difference among the derivatives (Eu + Lu, Eu + Eu and Eu + La) was the specific activity and the resulting difference in catalytic efficiency which increased with increasing size of the added metal ion (Table II.1). Methanol affinity was in this experiment the same within error, and if there are slight

differences between the derivatives they are not able to be detected due to the presence of mainly Eu^{3+} in the active site (Figure II.6). Previously, it was shown that MDH from SolV with a mixture of the larger Ln in the active site (La, Ce, Nd, Pr) exhibited a slightly increased affinity for substrate compared to Eu-MDH (Table II.1).[36, 94] However it should be mentioned here that the parameters of the assay were slightly different.

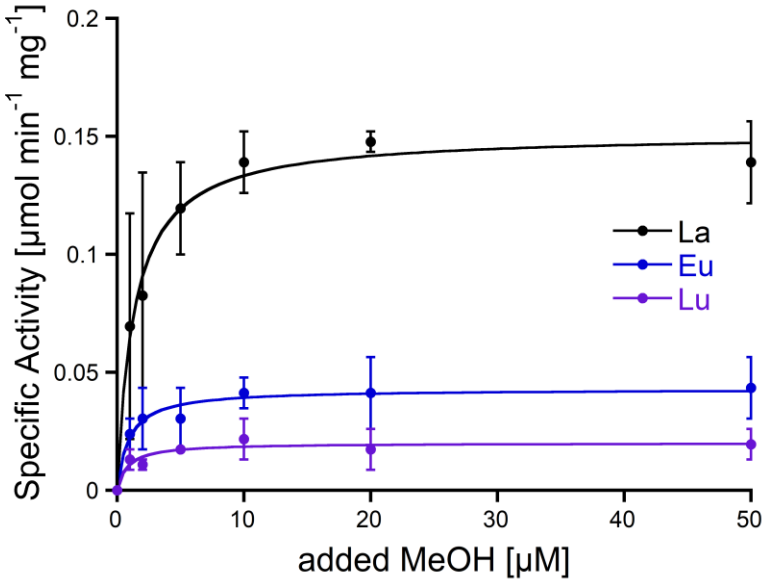

Figure II.6: Specific activity (n = 2) of 200 nM Eu-MDH in the presence of 20 µM $LnCl_3$ with increasing amounts of methanol. Conditions: 20 mM PIPES pH 7.2, 1 mM PES, 1 mM KCN, 100 µM DCPIP, 45°C.

We were further interested in how the specific activity would be influenced by a mixture of an early (La^{3+} or Nd^{3+}) and a late (Lu^{3+}) lanthanide. Since activity measurements included the addition of different Ln^{3+} to Eu-MDH which is already occupied to 70% with Eu^{3+}, a competition among the different metals for the active site has to be taken into account. Additional activity measurements were conducted in the presence of La^{3+}, Nd^{3+}, or Eu^{3+} together with increasing amounts of Lu^{3+} as competing metal for the active site (Figure II.7). The total amount of additional metal was kept constant at 20 µM. Hence, 100% in Figure II.7 stands for 100% La^{3+} (20 µM), 75% stands for 75% La^{3+} and 25% Lu^{3+} (15 µM and 5 µM, respectively) and so forth. 0 stands for 0% La^{3+} and 100% Lu^{3+} (20 µM). While the amount of Lu^{3+} decreased the MDH activity in the presence of La^{3+} and also, slightly, the one with Eu^{3+}, the activity of MDH in the presence of Nd^{3+} was relatively unaffected by lutetium(III) addition. Interestingly, all measurements showed a higher activity at 50% *e.g.* La^{3+}/Lu^{3+} (10 µM each) than the averaged values between 0 and 100% Lu^{3+}. The following paragraphs will discuss how the central metal ion could impact catalytic parameters and explain the differences among the lanthanides.

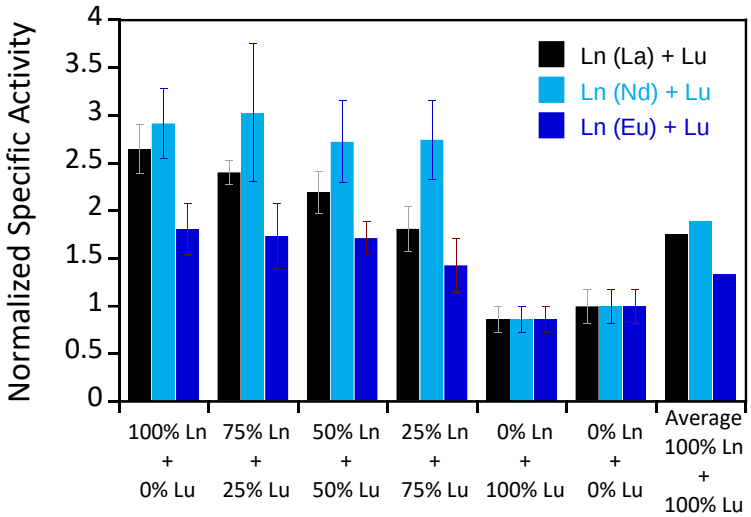

Figure II.7: Mixed Ln normalized specific activities (n = 3) of 200 nM Eu-MDH in the presence of 20 µM $LnCl_3$ (Ln = Lu + La/Nd/Eu). Conditions: 20 mM PIPES pH 7.2, 1 mM PES, 1 mM KCN, 100 µM DCPIP, 50 mM MeOH, 45°C.

Coordination Numbers and Substrate Orientation. The preferred coordination number (CN) of the active site ion could have an impact on substrate binding to the active site and on the surrounding amino acid/hydrogen-bond network that is important for proton abstraction during catalysis. The high SA of Nd^{3+} could be explained then as a compromise of a relatively high Lewis acidity while maintaining a high CN to bind the substrate. Drawing from lanthanide coordination chemistry, where researchers have studied the factors influencing the CN in simple lanthanides complexes, it has been shown that, regardless of other factors like the type of ligands or the used solvent, the preferred coordination number throughout the lanthanide series gradually decreases.[90, 92] For example, the number of water molecules in the complex $[Ln(NO_3)_3(terpy)(H_2O)_n]$ is reduced throughout the lanthanide series (*n* = 2 for La, 1 for Ce-Dy, 0 for Ho-Lu).[92] A lower coordination number preference of the late lanthanides could influence the ability to bind substrate and further disrupt the H-bond network around the active site to some extent. We investigated this for the entire series with DFT calculations. Generally, the influence of the protein environment on the CN and substrate orientation in enzyme active sites as well as solvent effects in lanthanide complexes have also been modelled in the past by molecular dynamics approaches.[49, 72-73, 119] As previously demonstrated for La^{3+}, Pr^{3+}, Eu^{3+} and Yb^{3+}, depending on the presence of substrate, the state of the cofactor and the Ln^{3+}, as well as the chosen calculation parameters, the coordination mode of the active sites amino acids in the geometry optimized structures does vary.[94] Calculations for the entire lanthanide series were conducted in a way similar to a previously published procedure reported by Schelter *et al.*[76] Detailed calculation methods and input files, as well as detailed information of the bond angles and distances for the optimized structures are given in the materials and methods section and

the ESI (Figure IX.4-6 and Table IX. -4). Calculations revealed that over the Ln series, the binding mode of the active site ligands and thus the coordination number of the metal ion change during geometry optimization (Figure IX.4-6 and Table IX.1-4). Over the lanthanide series, several turnover points were observed (Figure IX.6). A change in coordination mode of the (in the crystal structure) bidentate Asp301 residue (only present in Ln-MDH but not Ca- MDH) was also observed in the calculations of the Ce^{3+}PQQ derivative by Schelter and coworkers.[76] Further it was noted, that the catalytic base Asp299 displayed a high degree of flexibility. We have further tested the influence of different parameters such as solvent effects, a smaller ECP and free refinement (unfrozen) of the ligands on the final coordination number and these results are presented in Figure IX.7-9. Altering these parameters did not change the final coordination number of the active site metal.

In general, a preference for a lower coordination number in the active site, throughout the Ln series was shown by the DFT calculations in the gas phase, which would be in line with the observations made by coordination chemists studying the entire Ln-series.[24, 90-92] However, the CN in MDH is mostly set by the protein environment and the most flexible ligand would still be the substrate. In our experiments however, substrate affinity was hardly affected.

There are several other aspects to how the Lewis acid in the active site might influence methanol oxidation: (i) *Substrate deprotonation*. Proton abstraction from the substrate by the aspartate residue (here Asp299) is proposed to be assisted by the Lewis acid (Figure II.5).[77] In crystal structures of MDH, MeOH is often found coordinating to the Lewis acid and this ligation has been proposed to be beneficial for proton abstraction by lowering the pK_a value.[49] In our calculations of the active quinone PQQ form with substrate, the distance of the substrate oxygen to the PQQ C5 carbon was relatively constant between 3.41-3.42 Å. However, the distance of the substrate oxygen to the central metal decreased with decreasing ionic radius as expected throughout the lanthanide-series (2.67 Å for La, 2.56 Å for Lu, Table IX.). This is a common feature found in Ln-complexes. For the complex [Ln(TREN-1,2-HOIQO)(H_2O)], the sum of Ln-O bond lengths quadratically decrease throughout the Ln-series.[91] This pull towards the Lewis acid could hinder the H-transfer or the nucleophilic attack of the methanolate. Further it is interesting to note, that the distance of the aspartate residue in the active site (the one proposed to act as a general base to abstract the proton from the substrate) to the Lewis acid differs greatly in the reported structures of the Ca- and Ln-MDH derivatives. In Ca-MDH from *M. extorquens* (PDB: 1H4I, 1.94 Å resolution) the Asp303-Ca distance (shown as red dashes in Figure II.5) was reported to be 3.56 Å or 3.61 Å (PDB: 1W6S, 1.2 Å resolution) while in Ca-

MDH from *Methylophilus methylotrophus* W3A1 (PDB: 4AAH, 2.4 Å resolution) the Asp297-Ca distance is reported as 3.25 Å.[120-122] The two available Ln-MDH structures available to date are both enzymes isolated from strain SolV and show for Ce-MDH (PDB: 4MAE, 1.6 Å resolution) a significantly shorter Asp299-Ce distance of 2.86 Å and for Eu-MDH (PDB: 6FKW, 1.4 Å resolution) a Asp299-Eu distance of 2.95 Å.[36, 94] While the latter two values of Ln-MDH might be the same within the error of the experiment, the difference in distance from the Asp-residue to the metal ion between Ca and Ln is significant. However in calculations by Leopoldini *et al.* on the mechanism of Ca-MDH, this Ca-Asp distance was found to vary between 2.38 and 2.82 Å, showing a high degree of flexibility of this amino acid during catalysis.[70] We have also noted this flexibility in our calculations. The calculated distances of Ln-Asp in the active site with PQQ in the relevant resting state semiquinone form ($PQQ^{\bullet-}$) are found to be much shorter than the experimental values (Figure IX.11+13, Table IX.6). The nature of the metal ion (Ca, La-Lu) might affect the properties of this catalytic base (Asp297/303/299) during methanol oxidation and active site regeneration. For example, a stronger Lewis acid such as Lu^{3+}, interacting with Asp299 would hinder an efficient proton abstraction from methanol, but, in turn, once protonated, coordination of Asp by a stronger Lewis acid would lower the pK_a value and thus facilitate proton abstraction from this residue and regeneration of the active site. Given the high flexibility of this residue, it is unlikely that these two effects cancel each other as the distance to the Lewis acid and its positive or negative effect might vary during catalysis. (ii) *Ligand Exchange Rates and Complex Stabilities.* From decades-long research into the coordination chemistry of the lanthanides it is now well established that complex stabilities increase along the series.[24] Cotton *et al.* reported that the stability constants for EDTA lanthanide complexes significantly increase from the early to the late Ln, due to changes in charge density, coordination number and entropy.[123-124] These differences among the stability constants of Ln complexes are, for example, exploited in their separation by ion exchange methods. Further, Graeppi *et al.* measured the water exchange rates for the late Ln (Gd-Yb) in the complexes $[Ln(H_2O)_8]^{3+}$ and $[Ln(PDTA)(H_2O)_2]^-$ which decrease continuously throughout the series.[125] Transferring these concepts to the methanol oxidation in MDH, this could suggest that once product is formed (formaldehyde or formic acid) the higher stability of a resulting Ln-product (formaldehyde and especially formic acid, or more specifically, formate under the conditions of the assay) complex would make product release and ligand exchange less favorable for the late Ln and therefore would hinder the regeneration of the active site. This hypothesis could be tested with inhibition experiments of different derivatives of MDH. (iii) *The Redox Cycling of the Cofactor PQQ.* Schelter and coworkers

conducted DFT calculations of the active site of Ce-MDH and proposed that a stronger Lewis-acid would result in lowered virtual orbitals and would therefore facilitate PQQ reduction and in turn methanol oxidation.[76] Using their method, we investigated whether changing to a different lanthanide would influence this redox cycling in any way. For this we optimized the resting semiquinone $PQQ^{\bullet-}$ and the active quinone PQQ^{0} state for Ce^{3+} and the two "extremes" of the Ln series – La^{3+} and Lu^{3+} (Figure II.8) – and compared the molecular orbital (MO) energies for those derivatives.

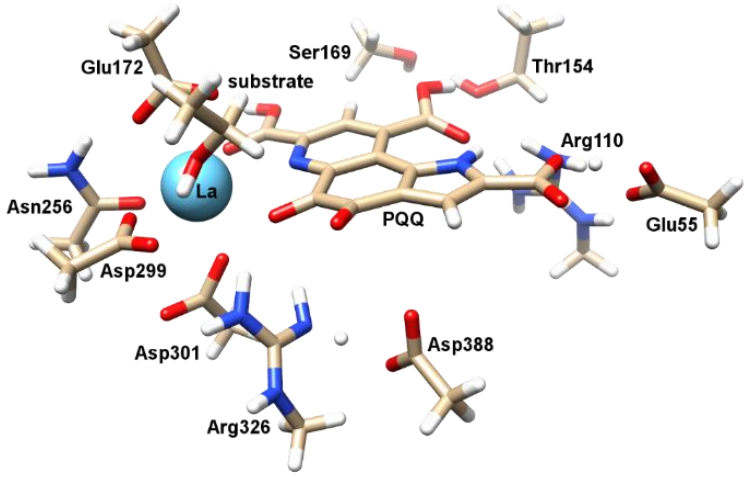

Figure II.8: Calculated extended active site of *xoxF* encoded MDH with La as the central metal and PQQ in its active PQQ^{0} form. Calculation details given in Figure IX.11 and Figure IX.12. Image generated with the UCSF Chimera package.[41]

While the bond lengths, the locations of the electron density as well as the MO energies of the Ce^{3+} PQQ^{0} derivative are in excellent agreement with the previously published results by Schelter, the bond lengths of the optimized structure of the published Ce^{3+} $PQQ^{\bullet-}$ species deviated from our calculated coordinates (Figure IX.11-14 and Table IX.5-7). However, as the input file and the keywords for the optimization were not given, it is difficult to comment on what caused this deviation. It should be noted that in our calculations no negative frequencies were observed.

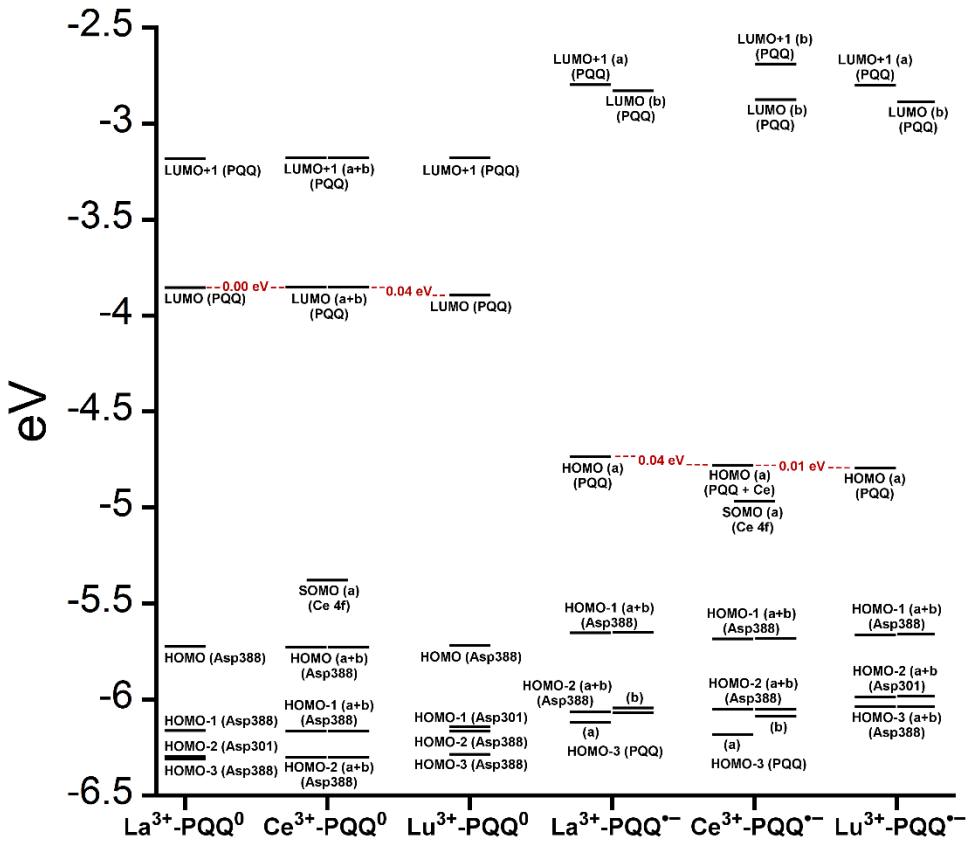

Figure II.9: Molecular orbital diagram of oxidized Ln PQQ^0 and the semiquinone form Ln $PQQ^{\bullet-}$. Ln = La^{3+}, Ce^{3+} and Lu^{3+}. Next to the MO description the location of electron density is shown in brackets.

The results presented in Figure II.9 suggest, that for the redox cycling, the nature of the lanthanide in the active site has only a small effect. The LUMO of the active PQQ^0 state is PQQ-based and would be filled during the methanol-oxidation. While the energy values for the La and Ce species differ only by 0.0016 eV, the Lu LUMO is slightly lowered by 0.0408 eV. In comparison, Schelter calculated the LUMO of the Ln-MDH active site with a Ca^{2+} central metal to be 0.81 eV higher than the Ce^{3+} species. The resting semiquinone state $PQQ^{\bullet-}$ shows the same PQQ-based MO which is now a single occupied HOMO. Also in this case, the Lu species is slightly lowered by 0.0590 eV compared to the La derivative. In both cases, the Lu species seems to be slightly favoured by means of energetic values, which is also in agreement with the conclusions made by Schelter and co-workers who stated that a better Lewis acid is beneficial for methanol oxidation. Protein electrochemistry with different MDH derivates could experimentally verify the conclusions drawn from these calculations. (iv) *Activation Energies.* Lastly, the activation energies of the rate-determining step could be affected by the different lanthanides in Ln-MDH similar to the Ca/Ba-MDH that was investigated by Mainardi *et al.*[69] This could be experimentally probed by determining kinetic parameters at different temperatures for different MDH derivatives. Efforts to purify and characterize such derivatives are currently underway.

3.3. Conclusion

Ten years ago, a biological relevance of lanthanides for living organisms was unthinkable.[31, 126-127] Now, studies of lanthanide-dependent bacterial metabolism is a quickly growing field. To answer the important questions of how these elements are made bioavailable, taken up into cells, regulate gene expression and what their advantages over calcium in the active site of enzymes are, it will take a strong collaborative effort by researchers working in the fields of microbiology, biochemistry, spectroscopy, computational and coordination chemistry. In this paper, we have investigated the methanol oxidation of a methanol dehydrogenase isolated from *M. fumariolicum* SolV with different lanthanides from a coordination chemists' point of view. While activity in the presence of early lanthanides was high, the decreasing size of the lanthanides caused by the lanthanide contraction had a negative effect on catalytic activity. Lewis acidity and co-factor activation are not the only important factors that have to be considered but coordination number preference, ligand exchange rates, substrate orientation and activation and hydrogen bonding are important factors as well.

III. SYNTHESIS AND PURIFICATION OF PQQ AND ITS DERIVATIVES

1. Introduction

In 1979, Salisbury *et al.* reported the first crystal structure of PQQ as its acetone adduct and proposed the underivatized structure of PQQ.[128] Based on this structural information, the first total synthesis was developed in nine steps by Corey and Tramontano in 1981.[129] Fourteen synthetic approaches were either published or patent-registered over the years, with a six-step synthesis from Glinkerman and Boger being the most recent one (2016).[129-142] Even a large scale synthesis was developed for kilogram amounts of PQQ.[138] However, all routes share the disadvantage of being time and chemical consuming, while showing low to medium yields with a maximum of 56%.[142] To overcome those limitations, biosynthesis of PQQ by microorganisms was established and developed alongside chemical production. Already in 1984, *M5* and uncharacterized methylotrophs were used to produce PQQ in a 10 µg/mL scale after two days of fermentation.[143] Later, the biosynthetic pathway of PQQ was elucidated in *Klebsiella pneumonia*, which involves six genes, PQQA-F, forming the so called PQQ-operon.[144] Distribution and properties of those genes were further elucidated by Shen *et al.*[145] A review about the biochemistry, physiology and genetics of PQQ, as well as PQQ producing microorganisms is given by Goodwin and Anthony.[146] Genes from *Klebsiella pneumonia* were even transferred to *E.coli* to produce ^{14}C labelled PQQ.[147] With *Methylovorus sp.*, the yields of PQQ were increased to a 125 mg/L scale after 6 days of fermentation.[148] Several studies indicate health benefits of a PQQ enriched nutrition.[149] Increasing numbers of companies produce PQQ containing nutritional supplement products, like “BioPQQ” from Mitsubishi Gas Chemical[150] or “PentaQQ” by Evonik.[151]

2. Total Synthesis of PQQ

Throughout the course of this thesis, the trimethyl ester of PQQ (**11**) was afforded in a 7-step-synthesis, based on a procedure described by Corey and Tramontano[129] which was later improved by two patents[139-140] (Scheme III-1). The alternative synthetic route by Glinkerman and Boger gives higher yields combined with reduced synthetic steps,[142] however, it does not include the key intermediate **10**, which is a known starting material for model complex syntheses[152] and valuable for further synthetic approaches.

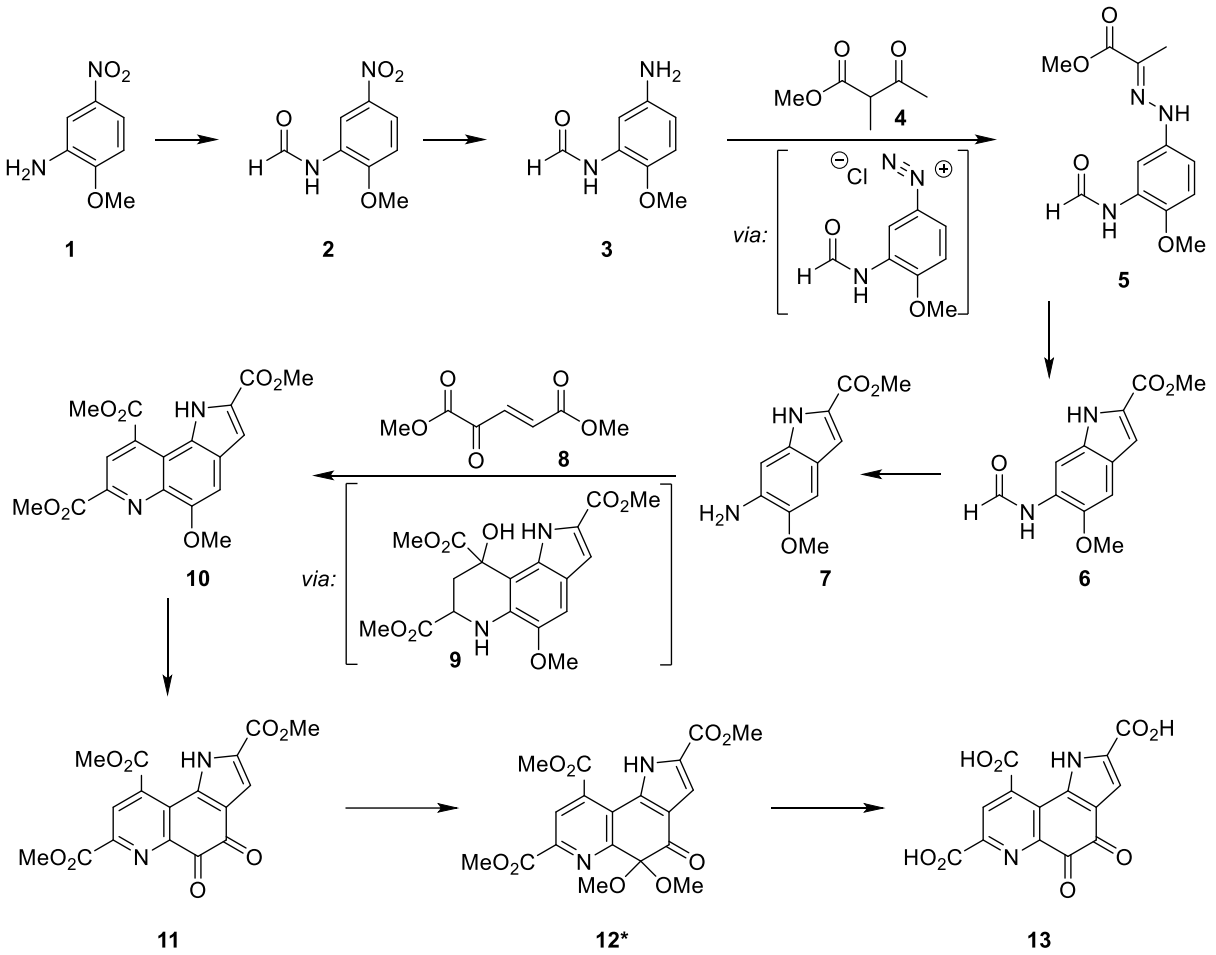

Scheme III-1: Total synthesis of PQQ, based on works from Corey and Tramontano[129]. *After treatment of **11** with methyl orthoformate and p-toluenesulfonic acid in refluxing methanol, ketal species was received which was described as the C5 adduct by the authors, but no analytical data was given.[129] The same reaction was later described by Itoh el al. to give the C4 ketal, which could be verified by X-ray crystal structure analysis. For more information about ketal formation, see Chapter VI.

First step of the reaction path was the amine protection from commercially available 2-methoxy-5-nitroaniline (**1**) by *in situ* generated acetic formic anhydride (Scheme III-2), leading to the N-formyl derivative (**2**) in 92% yield.

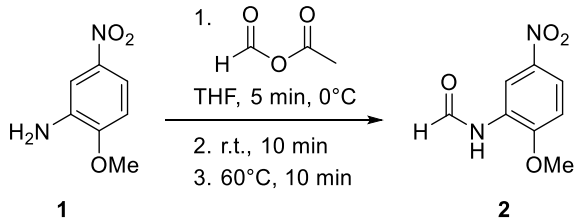

Scheme III-2: Formation of N-(2-methoxy-5-nitrophenyl)formamide (**2**).

In a next step, the nitro-group was hydrogenated in an autoclave by the addition of palladium on carbon as a catalyst (Scheme III-3). The reaction proceeded smoothly and led to the desired aniline **3** in 66% yield. Unreacted starting material could easily be separated and reused by washing the product with TCM. Attempts with the originally described conditions (PtO as catalyst in DMF) gave lower yields with higher amounts of unreacted starting material.

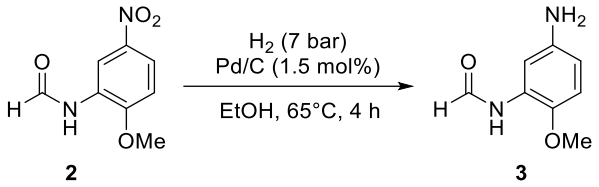

Scheme III-3: Hydrogenation of nitrobenzene **2**.

With sodium nitrite, the primary amine could be transformed into diazonium salt (**3'**), which was used for the addition of methyl 2-methyl-3-oxobutanoate (**4**) in 81% yield (Scheme III-4).

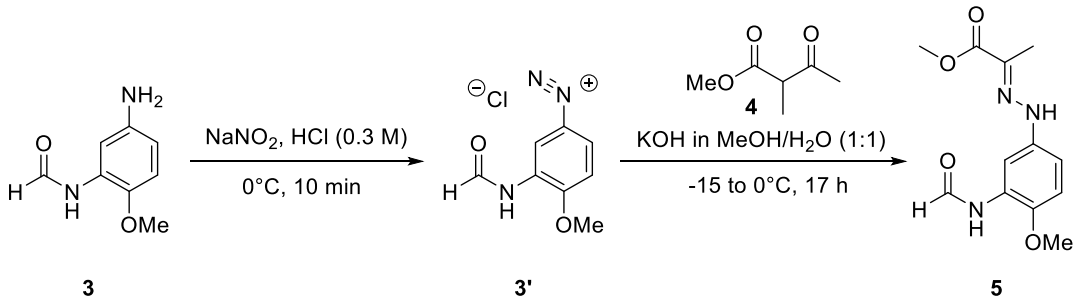

Scheme III-4: Addition of methyl 2-methyl-3-oxobutanoate (**4**) via diazonium salt (**3'**).

The precursor methyl 2-methyl-3-oxobutanoate (**4**) was synthesized by methylation of methyl 3-oxobutanoate (**4'**) with methyl iodide in 96% isolated yield after purification of the product by distillation.

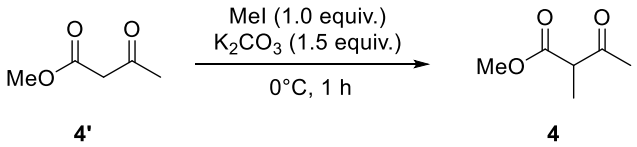

Scheme III-5: Formation of precursor methyl 2-methyl-3-oxobutanoate (**4**) by methylation.

Subsequently, intermediate **5** was stirred in hot formic acid for 20 hours, to form indole **6** by a Fischer indole synthesis in poor yield (36%) (Scheme III-6). A byproduct (**6'**) occurred in a ratio of 25% of the total yield, which was formed by an alternative ring-closing reaction. Unfortunately, it could not be separated from the main product by column chromatography and was therefore also converted in the next reaction steps.

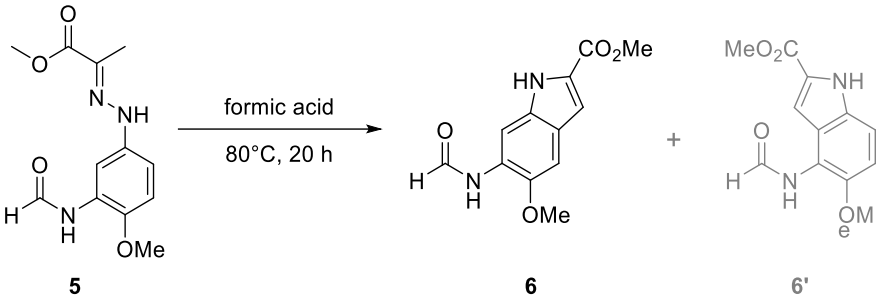

Scheme III-6: Formation of indole 6 by a Fischer indole synthesis.

Deprotection of the N-formyl group was carried out in refluxing hydrochloric acid (Scheme III-7), leading to compound **7** in good yield (91%).

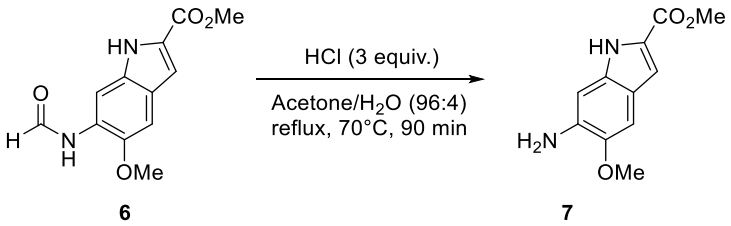

Scheme III-7: Deprotection of the N-formyl group.

Hydroxypiperidine **9** was generated in poor yield (41%) by the addition of dimethyl (E)-4-oxopent-2-enedioate (**8**) in a Doebner–Miller reaction. **9** was dehydrated by bubbling catalytic dry hydrogen chloride through a solution of **9** in DCM, leading to pyrroloquinoline **10** in 35% yield (Scheme III-8).

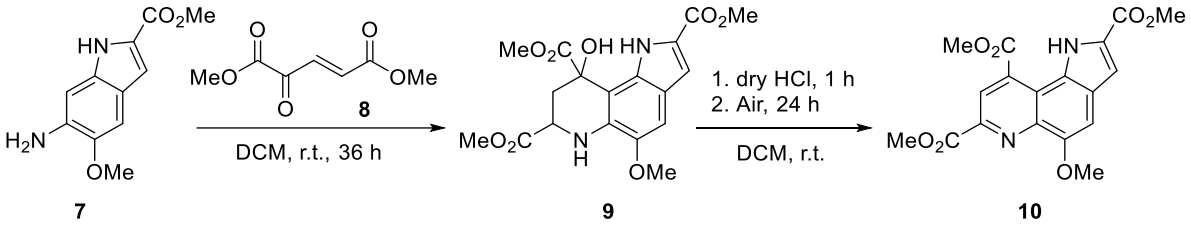

Scheme III-8: Doebner–Miller reaction and subsequent aromatization to pyrroloquinoline **10**.

The precursor **8** was synthesized in three steps, according to a procedure described by Carrigan *et al.*[153] α-Ketoglutaric acid (**8a**) was esterified by letting it stand in pure methanol for 5 days. Dimethyloxoglutarate (**8b**) was then treated with bromine to form **8c**, which was directly converted to **8** by deprotonation with triethylamine and elimination of triethylammonium

bromide. While esterification gave only 59% yield, bromination and following elimination proceeded almost quantitative.

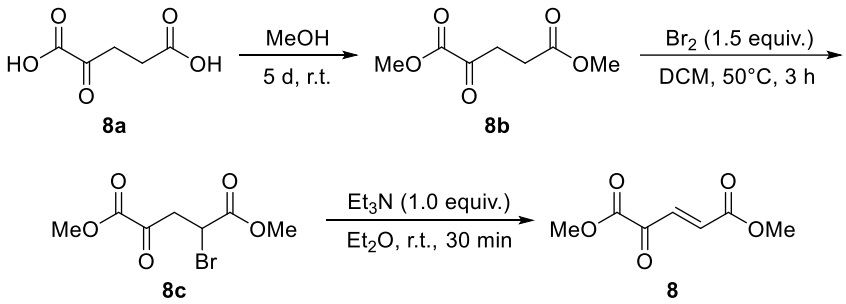

Scheme III-9: Reaction sequence towards dimethyl (E)-4-oxopent-2-enedioate (**8**), including esterification of α-ketoglutaric acid (**8a**), bromination in C2 position and following elimination.

The last step in the reaction sequence was the oxidation with ceric ammonium nitrate, which led to the $PQQMe_3$ (**11**) in 35% yield (Scheme III-10). The overall yield over seven steps (without precursor synthesis of **4** and **8**) was 0.8%.

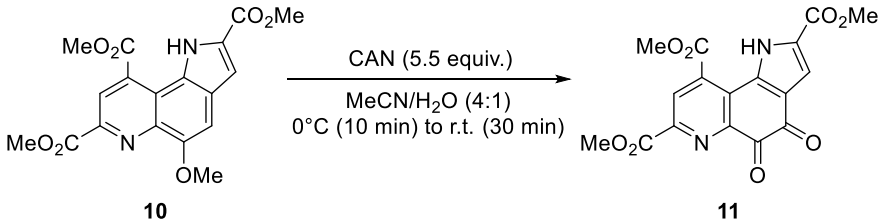

Scheme III-10: Oxidation with ceric ammonium nitrate.

3. Purification of Biological Produced PQQ

3.1. Introduction

The total synthesis described in subchapter **2** required three month of laboratory work and resulted in a few hundred milligrams of PQQ precursors **10** and **11** in total. In demand of larger amounts for further synthetic approaches and spectroscopic studies, alternative supply lines were evaluated. The standard chemical suppliers only sell PQQ for extraordinary high prices (~140€ per mg from Sigma Aldrich, as to the date of 02.09.2019) or do not sell it at all. One gram was purchased from the Fluorochem company, Hadfield, UK. On the other hand, a multitude of companies sell PQQ as food supplement for a fraction of the amount from chemical suppliers. One of those suppliers, Doctor's Best® Science-Based Nutrition™ was tested for an alternative (and cheap) source of pure PQQ. From a scientific standpoint, it is highly questionable to support companies in their marketing of PQQ based on at least questionable

health benefits, but the sheer amount of PQQ needed for this research project made compromises necessary.

3.2. Purification of Vitamin Capsule Derived PQQ

As nutritional supplement, PQQ is used as its disodium salt $PQQNa_2$ (**14**), which is sold in capsules together with cellulose as filler. Those capsules were emptied and the containing powder was given into water. While $PQQNa_2$ shows good solubility in water, the containing cellulose remained as a colorless solid and was filtered off. The water was subsequently removed under reduced pressure to give the monohydrated $PQQNa_2$ as a reddish brown powder. To convert the sodium salt into pure PQQ, a procedure was followed, described by Ikemoto *et al.*[154] $PQQNa_2$ was redissolved in water, heated to 70°C, acidified to pH 1.5 with HCl and further stirred for 24 h at 70°C to give pure PQQ as a bright red powder, which was filtered off and dried under high vacuum. Elemental analysis indicated a monohydrated $PQQ{\cdot}H_2O$ species in high purity which was further confirmed by NMR. The water equivalent could not be removed, even after drying the product for several hours at 100°C. However, ssNMR revealed pure PQQ (**13**) and not the covalently bound PQQ-water adduct (**15**) (see also Chapter IV for more details).

4. Synthesis of PQQ Derivatives

4.1. Synthesis of $PQQMe_3$

4.1.1 Introduction

In its protonated form, PQQ (**13**) is soluble in polar solvents like alcohols, DMF or DMSO. The solubility in water is limited to its (partially) deprotonated form. In MeCN, no solubility was observed. The trimethylester $PQQMe_3$ (**11**) shows good solubility in apolar media like DCM and TCM but also in MeCN. Besides the altered solubilty, **11** was also used as a precursor for the synthesis of biomimetic model complexes[152] and prevent alternative coordination sites in solution.[155] In order to have the trimethylester $PQQMe_3$ (**11**) available without the need of the time-consuming total synthesis described in subchapter III.2, possibilities were sought to directly esterify free PQQ.

4.1.2 Synthesis of $PQQMe_3$ by Methylation with CH_3I or by Steglich Esterification

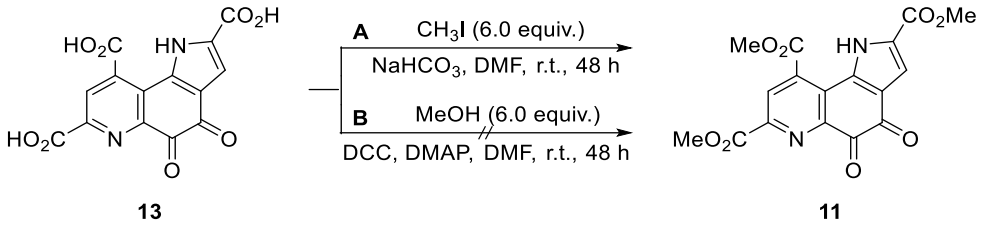

Scheme III-11: Synthetic approaches towards $PQQMe_3$ (**11**), including methylation with methyl iodide (A) and Steglich esterification with methanol (B).

The direct esterification with methyl iodide in DMF resulted in insufficient yields of 20% and large quantities of impurities were present, which could not be separated by column chromatography. The Steglich esterification with methanol, DCC and DMAP in DMF only gave unreacted starting material.

4.1.3 Synthesis of $PQQMe_3$ by Fischer Esterification

Fischer esterification was performed in a methanolic solution of PQQ, to which few drops of concentrated H_2SO_4 were added as catalyst (Scheme III-12). Itoh *et al.* described $PQQMe_3$ to precipitate as hemiketal **17** out of methanolic solutions[156] but the H_2SO_4 prevented such reaction.

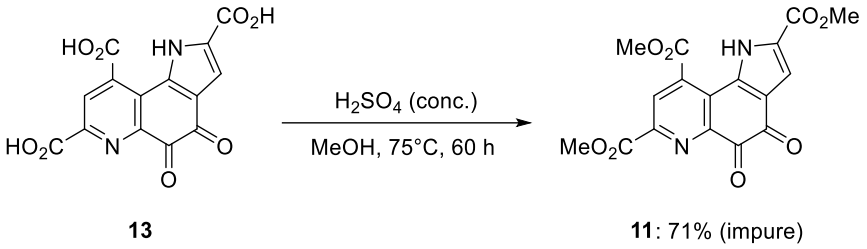

Scheme III-12: Fischer esterification of PQQ in methanol with catalytic amounts of concentrated H_2SO_4.

The mixture was refluxed overnight but TLC stated large amounts of unreacted starting material. More H_2SO_4 and longer reaction times finally gave the crude product after extraction with TCM in 71% yield, which was analysed by NMR to be a 90:10 mixture of $PQQMe_3$ (**11**) and a second $PQQMe_3$-derivative, most likely the hemiketal **17** or the water adduct **18** stemming from residues of water in both the methanol reaction solution and in the deuterated TCM. From the aqueous workup solution, small amounts (4%) of a $PQQMe_2$ (**19**) species could be isolated. Several attempts to further purify the crude $PQQMe_3$ mixture by column chromatography failed, regardless of the column material (normal or reversed phase) or the solvent system (mixtures of DCM or TCM with EtOAc, MeOH, EtOH or *i*-PrOH or *i*-hexane/EtOAc or H_2O/MeCN for reversed phase). The yield decreased after every column, without receiving pure

compounds. The quinone is known for its reactivity and likely interacted with the column material.

4.1.4 Synthesis of $PQQMe_3$ *via* an Oxazole Derivative

A different approach combined two literature procedures: van Kleef *et al.* described the reaction of PQQ with several amino acids resulting in oxazole formation.[157] By the use of glycine, the two C=O bonds of the quinone can be protected in a straightforward fahsion in nearly quantitative yields in buffered solution, giving PQQ-oxazole (**20**) (Scheme III-13):

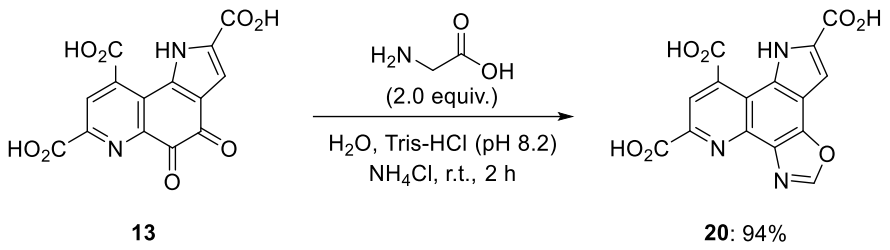

Scheme III-13: Oxazole formation of PQQ with glycine in buffered solution.

Itoh *et al.* used the oxazole derivative **20** to esterify the carboxyl groups with Me_2SO_4 in dry DMF under nitrogen, to give the product as an orange powder after acidification with HCl (yield: 85%).[158]

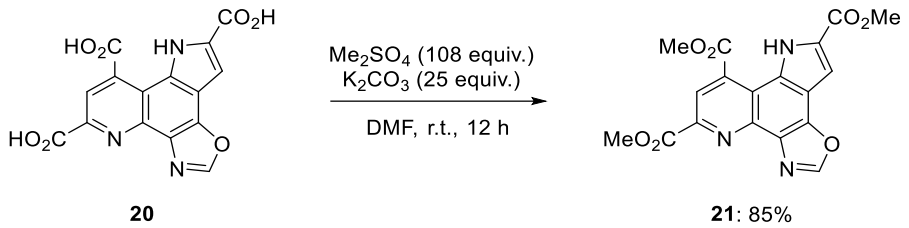

Scheme III-14: Esterification of the PQQ-oxazole derivative (**20**) by Me_2SO_4, with equivalents used and yields received by Itoh *et al.*[158]

The synthesis was tested in a small scale first (3 mg starting material), which gave the desired product **21** as an orange powder in 83% yield. For a bigger approach with 100 mg PQQ-oxazole, the assumingly unnecessary high amount of Me_2SO_4 was reduced to 25 equiv. Unfortunately, no precipitation occurred after acidification. Therefore, the reaction mixture was extracted with EtOAc instead, to give 30 mg of an orange red powder. NMR analysis showed a mixture of $PQQMe_3$-oxazole (**21**) and the deprotected $PQQMe_3$ (**11**) in a 13:87 ratio, which could not be further separated. Van Kleef described the deprotection of oxazole derivatives by acid hydrolysis in 2 M HCl at 100°C for 2 h.[157] The mixture was treated with these conditions to obtain $PQQMe_3$ (**11**). Unfortunately, the crude product still showed traces of the oxazole-

derivative **21**. Separation was then performed by column chromatography, to give both $PQQMe_3$-oxazole (**21**) (5%) and $PQQMe_3$ (**11**) (8%) in poor yields.

4.1.5 Synthesis of $PQQMe_3$ by Direct Methylation with Me_2SO_4

Duine *et al.* described direct methylation of PQQ by Me_2SO_4 and K_2CO_3 but used a very small scale of 0.5 mg PQQ starting material.[159] By applying a similar procedure as described for the PQQ-oxazole (**20**) (Scheme III-14), the method was tested on a 50 mg scale.

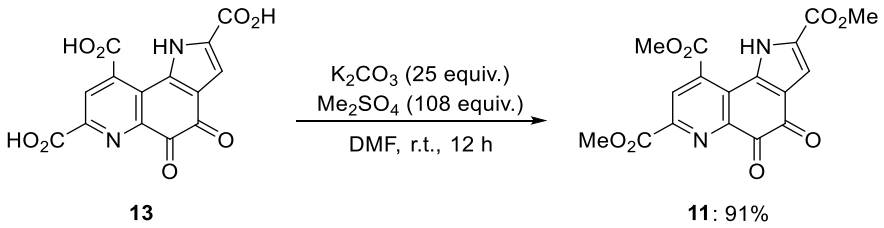

Scheme III-15: Direct esterification of PQQ by the use of Me_2SO_4.

After excess Me_2SO_4 and K_2CO_3 were quenched with HCl, the precipitated product was simply filtered off, to give clean $PQQMe_3$ as an orange powder in 91% yield. The aqueous solution was further extracted with $CHCl_3$ to give **11** with minor impurities and a combined almost quantitative conversion to the trimethylester. The scale was successively increased in further reactions and can easily be run in a 500 mg scale, with slightly decreased yield of 86%.

4.2. Synthesis of $PQQMe_2$

In order to use $PQQMe_3$ (**11**) for ligand-synthesis, the pre-oxidized pyrroloquinoline **10** from total synthesis was selectively saponified, using a literature known procedure (Scheme III-16).[129, 152]

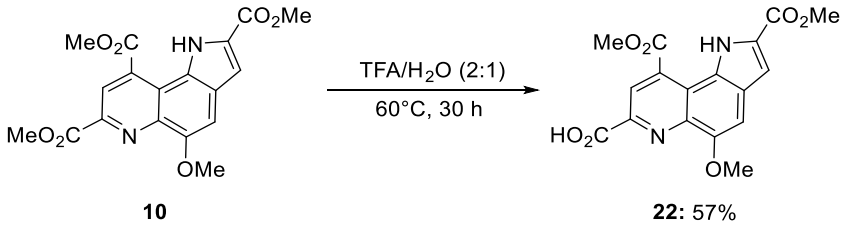

Scheme III-16: Selective saponification of pyrroloquinoline **10**.

Unfortunately, even after longer reaction times, a complete conversion was not possible and the yield could not increased over 57%.

Due to the good availability of PQQ (**13**) out of nutritional supplement capsules and the direct methylation of PQQ with Me_2SO_4 (Scheme III-15), the same acidic saponification as described above was tested on $PQQMe_3$ (**11**) (Scheme III-17).

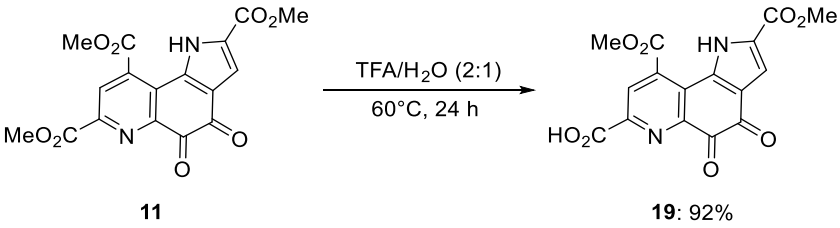

Scheme III-17: Acidic saponification of $PQQMe_3$ in position C7.

In comparison with $PQQMe_3$-OMe (**10**), the reaction proceeded smoothly with the quinone $PQQMe_3$ (**11**) since the product $PQQMe_2$ (**19**) precipitated after quenching with water and was easily filtered off with isolated yields over 90%. While NMR analysis of the product already indicated saponification at the preferred C7 position, X-ray analysis verified the shown structure (Figure III.1).

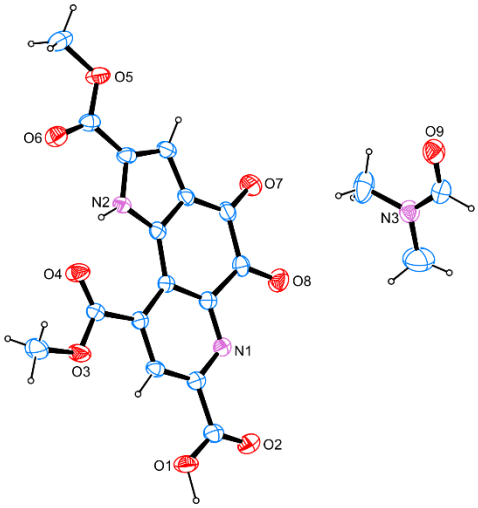

Figure III.1: Molecular structure of $PQQMe_2$·DMF in the crystal, ORTEP representation.[160] Thermal ellipsoids are drawn at 50 % probability level.

4.3. Synthesis of $PQQH_2$

To obtain the reduced PQQ species $PQQH_2$ (**24**) as a solid for reoxidation experiments, a literature known procedure was tested.[161] By reduction of PQQ with L-(+)-ascorbic acid in an acidic aqueous solution (Scheme III-18), followed by filtration of the precipitated solid, $PQQH_2$ (**24**) was synthesized in 95% yield. The received NMR spectra were in accordance with the literature.[161]

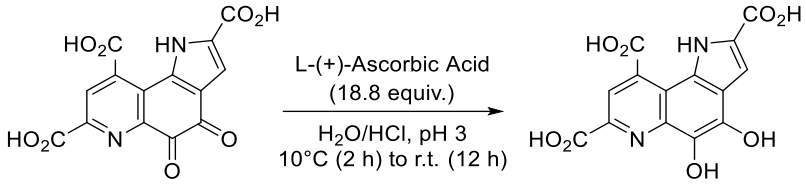

13 **24**: 95%

Scheme III-18: Reduction of PQQ with L-(+)-ascorbic acid giving the reduced $PQQH_2$ species.

While **24** is rapidly oxidized back in neutral or basic aqueous solution, it shows good stability in acidic aqueous solutions and and in oxygen-free DMSO (degassed with argon or nitrogen). In fact, an NMR solution of **24** in degassed DMSO-d_6 did not show any reoxidation after several weeks.

5. Conclusion

Several pathways for the synthesis and acquisition of PQQ (**13**) and its derivatives were presented, compared and evaluated throughout this chapter. The total synthesis described by Corey and Tramontano[129] was realised and slightly improved in several reaction steps. An alternative source of PQQ was successfully found in nutritional supplement capsules, and a purification procedure was implemented to give very pure **13** without the need of long reaction sequences.

Several methods for the synthesis of the trimethylester $PQQMe_3$ (**11**) were evaluated. Direct methylation of **13** with Me_2SO_4 led to **11** in high yield and purity without any by-products. No previous protection steps or further purification procedures were necessary. The reaction can be run on a 500 mg scale. The selective saponification of one of the methyl esters is literature known for the $PQQMe_3$ precursor **10**. The reaction was successfully adopted for the synthesis of $PQQMe_2$ (**19**) out of **11**, which allows coupling to ligand scaffolds to yield MDH active site biomimetics without the need of any precursors from time and resource consuming PQQ total synthesis. Methylated carboxyl groups of **11** increase the solubility in organic solvents and prevent complexation of unwanted coordination sites.[155] Both advantages could be enhanced by implementation of the bulkier trimethylsilyl groups, a well-established method of which even solvent-free methods are described.[162]

With L-(+)-ascorbic acid the reduced species $PQQH_2$ (**24**) was synthesized by a literature known procedure,[161] which allows elucidation of the redox properties of PQQ.

IV. COORDINATION CHEMISTRY OF PQQ

1. Interaction of PQQ with Lanthanides and Calcium

The following section is part of the publication:

Studies of the Redox Cofactor Pyrroloquinoline Quinone and its Interaction with Lanthanides(III) and Calcium(II)

Henning Lumpe and Lena J. Daumann

Published in: *Inorg. Chem.* **2019**, *58*, 8432-8441. DOI: 10.1021/acs.inorgchem.9b00568.
Reprinted with permission. Copyright (2019) American Chemical Society.

Abstract

Recently it was discovered that lanthanides are biologically relevant and found at the centers of many bacterial proteins. Poorly understood, however, is the evolutionary advantage that certain lanthanides might have over calcium at the center of methanol dehydrogenase enzymes bearing the redox cofactor PQQ. Here, we present a straightforward method to obtain clean PQQ from vitamin capsules. Further, we provide full NMR, IR and UV-Vis spectroscopic characterization of PQQ. We conducted NMR experiments with stepwise addition of diamagnetic and paramagnetic lanthanides to evaluate binding to PQQ in solution. This study provides a deeper understanding about PQQ chemistry and its interaction with lanthanides.

1.1. Introduction

Oxidoreductases are a group of enzymes which transfer redox equivalents from, or to, substrates.[163] While nicotinamide or flavin are commonly found cofactors in such enzymes,[164] in 1964 Anthony and Zatman discovered an enzyme with an alternative, non-covalently bound redox cofactor,[42-43] which was later determined to be pyrroloquinoline quinone (PQQ,

Methoxatin). PQQ-containing enzymes form the oxidoreductase subgroup of quinoproteins and are an essential part of the energy metabolism of many organisms.[164]

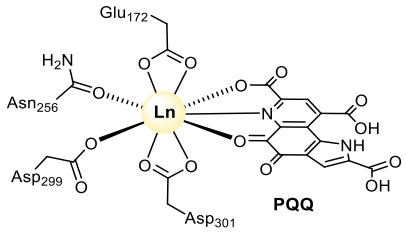

Figure IV.1: Active site visualization of Ln-MDH from strain SolV, including cofactor PQQ, central metal (Ln) and surrounding amino acid residues.[36]

The redox cofactor PQQ is activated by a Lewis acid.[165] For more than 30 years it was thought that calcium was the only metal ion that held this function in nature. However, many methanol-oxidising bacteria can in fact produce two types of MDH; the traditional one that has been studied intensively for more than 50 years uses calcium; and a second one, which has only recently been discovered, uses lanthanides instead of calcium. Lanthanides have long been thought to have no biological relevance but are now firmly established as the natural metal ion cofactors in MDH enzymes that are encoded by the *xoxF* gene.[36, 99] Phylogenetic analysis show that this lanthanide dependent class of MDH is, in fact, more widespread in nature and might be evolutionarily older than its calcium counterpart and perhaps the major pathway for methanol oxidation in methylotrophic bacteria growing on methane or methanol.[54] The first structure of a Ln-MDH was obtained from the XoxF-MDH isolated from strain *Methylacidiphilum fumariolicum* SolV and was reported by Pol *et al.*[36] The active site (Figure IV.1) contains a nine-coordinate lanthanide ion, surrounded by the cofactor PQQ, three carboxyl groups from Asp299, Asp301 (a residue that is lacking in Ca-MDH) and Glu172, as well as an amide from Asn256. This MDH X-ray structure was refined with Ce^{3+} (PDB 4MAE). Structures of a Eu-MDH (PDB 6FKW) from the same organism and a La-MDH (PDB 6DAM) from Methylomicrobium buryatense 5GB1C are now also available, showing similar active site arrangements.[39, 94, 98] In Ca-MDH, PQQ is coordinated in the same way by the Lewis acid (Site 1, Figure IV.2).[122, 166] Many bacteria possess genes for both MDH enzymes encoded by *mxaF* (Ca-MDH) and *xoxF* (Ln-MDH), respectively and can switch between them depending on Ln-availability; this has been termed the 'lanthanide switch'.[55-59] It has been shown that Methylobacterium extorquens AM1 preferentially expresses Ln-MDH even with only nanomolar concentrations of lanthanides and 20 µM concentrations of Ca in the cultivation medium.[63, 167] The trivalent lanthanides are better Lewis acids than calcium and it has been suggested that they pose an advantage in the redox cycling of PQQ.[76] Further, it has been

shown that not all lanthanides promote methanol oxidation in Ln-MDH equally.[36, 58, 62-64, 94, 168] For the native metalloenzyme isolated from SolV, it has been shown that the enzyme functions more efficiently with early lanthanides (La-Nd).[168]

Bacteria also prefer early lanthanides for growth and show improved uptake of these elements.[36, 62] The lanthanide switch, advantage over calcium, and why some Ln are better than others are currently not yet fully understood.

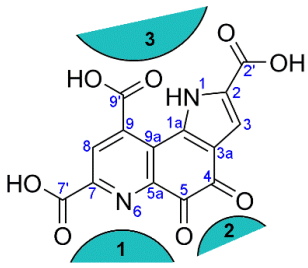

Figure IV.2: PQQ numbering scheme according to Unkefer *et al.*[169] and possible binding sites in solution, adapted from Nakamura *et al.*[155]

The cofactor PQQ was first isolated by Anthony *et al.*,[170] and was later determined to be a quinone by Duine *et al.*[171] Salisbury *et al.*[128] reported the first crystal structure of the acetone adduct and proposed the structure of PQQ, shown in Figure IV.2. The unusual orthoquinone structure of PQQ, detected in the EPR measurements of Duine *et al.*, led them to propose the name Pyrrolo-quinoline quinone for this new prosthetic group.[159]In the following years, PQQ was extensively studied regarding total synthesis,[129, 137, 142] adduct formation with nucleophiles,[156] redox behavior[172] or metal ion interaction (Ca^{2+})[173] with several reviews published.[95, 164, 174] PQQ has also been proposed to be a vitamin for humans, however, these claims remain doubtful.[149, 175] Previously, it was reported that PQQ without the surrounding enzyme pocket is capable of the coordination of metal ions at three positions (Figure IV.2). This is supported by several crystal structure determinations (site 1[176] (Cu), site 2[177] (Ru), site 3[155] (Cu)). For Ca^{2+}, no crystal structure exists with PQQ by itself, but studies of the trimethylester derivative $PQQMe_3$ (**11**) in MeCN suggest a coordination mode similar to MDH.[173] In light of the discovery of lanthanide dependent metalloenzymes, we have investigated the metal ion coordination behavior of PQQ in solution by NMR and UV-Vis spectroscopy, using lanthanides and calcium. Our studies suggest that in solution, the coordination of lanthanides occurs in the same position as in MDH (site 1) and that even if PQQ acts as a tridentate ligand (C_5=**O**, $\mathbf{N}_6$, C_7-C$\mathbf{O}_2$H), the Ln-PQQ complexes undergo fast exchange in solution. In this study we have investigated the diamagnetic trivalent lanthanides La and Lu, as well as calcium(II) and compared them with the paramagnetic lanthanides Ce, Pr, Sm, Eu, Tb, Er and Tm.

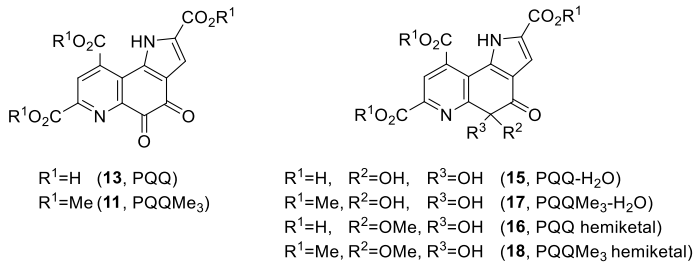

Figure IV.3: Structures of the different PQQ-species and -adducts referred to in this study.

1.2. Results and Discussion

1.2.1 Study of Metal Ion Interactions with PQQ in Water

After precipitation of PQQ the water equivalent present in the solid could not be removed by drying at 100°C or under high vacuum. To exclude the possibility that the solid could be the water adduct of PQQ (**15**, a geminal diol can result from the hydration of the quinone **13** at the C5 position, Figure IV.2 and Figure IV.3) solid state NMR was performed, which indicated pure PQQ (**13**) and can be found in the supporting information (Figure IX.16). IR spectra of disodium salt and purified fully protonated PQQ can be found in the supporting information (Figure IX.18, Table IX.12). The solubility of PQQ in water is limited to its (partly) deprotonated form (pK_a = 0.30 (N_6), 1.60 (C_7-CO_2H), 2.20 (C_9-CO_2H), 3.30 (C_2-CO_2H), 10.30 (N_1)).[178-180] In addition, PQQ will form the germinal diol **15** in a molar ratio of 2 (**13**) : 1 (**15**) in water, as observed by NMR by Duine *et al.*[181-182] In DMF PQQ will form **15** to some extend when traces of water are present or introduced by the addition of metal salts containing waters of crystallization (Figure IX.15A). Based on DFT calculations (Table IX.13) we propose this addition is taking place at the C5 carbon. The formation of a diol is evidenced by a new resonance at 91.7 ppm stemming from a diol moiety in position 5. Formation of **15** is also supported by ESI mass spectrometry in a H_2O/MeCN mixture where both PQQ (**13**, m/z = 329.0051, $[C_{14}H_5N_2O_8]^-$) and PQQ-H_2O (**15**, m/z = 347.0157 $[C_{14}H_7N_2O_9]^-$) are observed (Figure IX.15B). Previously, Zheng and Bruice also showed with calculations, that (methanol) adducts at C5 of PQQ are energetically favored.[47] When trivalent lanthanide ions or calcium(II) were added to an aqueous, concentrated solution of $PQQNa_2$ (**14**) (pH > 7), a 1:1 PQQ-metal complex precipitated. Elemental microanalysis of the solids revealed similar stoichiometries, regardless of the amount of added metal salt. Analysis suggested the formation of a PQQ·M·5H_2O complex (M=Ca^{2+}, La^{3+}, Eu^{3+}, Lu^{3+}), although the exact coordination mode in the solid state could so far not be

ascertained. TGA analysis of the solids (PQQ + Eu or La) did not give a clear indication whether the five water molecules were bound tightly to the metal ion in the complex or just were present as co-crystallized water molecules, or whether one of them was covalently bound to PQQ to form **15**. TGA analysis showed a continuous weight loss to 84% on heating to 100°C, which fits to the elimination of the five water molecules (Figure IX.27). The compound then gradually lost three CO_2 molecules until heating to 500°C (Figure IX.27). Numerous attempts to recrystallize the solid or obtain single crystals suitable for X-ray crystallography were unsuccessful. IR spectra of solid PQQ (**13**) showed seven bands between 1743 – 1583 cm^{-1} which can be attributed to the C=O stretching vibrations of the carboxyl and quinone groups (Figure IV.4).[183-184]

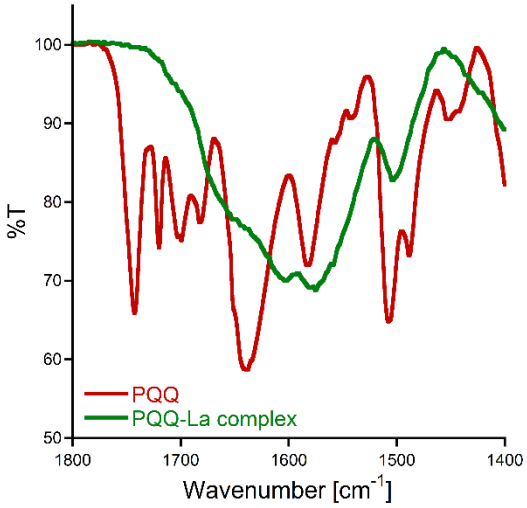

Figure IV.4: Overlayed IR spectra of PQQ (red) and the PQQ-La complex (green) between 1800 – 1400 cm^{-1}.

A complex of PQQ with Ti^{4+} in binding site 1, previously described by Dimitrijevic *et al.*[185] led to a splitting of the quinone signal into two features (1643 cm^{-1} to 1653 and 1636 cm^{-1}) and an intensity reduction of one of the carbonyl-stretches (1744 cm^{-1}) due to coordination to C_5=O and C_7-CO_2H while the other carbonyl signals remained unaffected. It is important to note that the affected carboxyl group was denoted by Dimitrijevic *et al.*[185] to be an ester, stemming from an impurity in their PQQ sample. However, their PQQ data match that obtained in the present work (from biological synthesis - fermentation, highly purified sample), making the previous ester assignment doubtful and the feature at 1744 cm^{-1} more likely to be a carboxylic acid stretch. In our study, the coordination with lanthanum(III) lead to a strong shift of all seven carboxyl and quinone absorption bands and appearance of a broad, poorly resolved feature between 1734 – 1521 cm^{-1} (Figure IV.4). In IR spectra of Fe^{2+} and Fe^{3+} complexes with structural PQQ-analogues, the bands associated with the coordinated carboxyl groups (C_7) are much more strongly shifted, or disappear completely, in comparison to non-coordinating carboxyl- or ester-groups (C_9).[186]

Hence, a clear statement about the coordination mode of lanthanides solely by IR-data remains difficult, but the data indicate a participation of all three carboxyl groups in a three-dimensional coordination network in the solid state with different coordination modes.

Analysis of the PQQ-lanthanide complexes in water was difficult as the precipitation of Ln-PQQ complexes limited the investigations to UV-Vis spectroscopy at low concentrations. Further, as mentioned above, PQQ forms at least two species (**13** and **15**) in aqueous solution. Upon metal ion addition, there are then at least four different species present: 1, 3 and M-1 and M-3. The UV-Vis spectra of PQQ with stepwise addition of lanthanum(III) or lutetium(III) in unbuffered water is shown in Figure IV.5. Both lanthanides induce a decrease of the 330 and 478 nm transitions of PQQ (mixture of **13** and **15**) and give rise to an additional absorption feature at 375 (La) or 380 (Lu) nm, respectively. With the same amount of calcium(II) the changes are less pronounced and the new feature is not as red shifted and appears at 357 nm. The absence of clear isosbestic points, overlapping transitions and the presence of more than two species complicates analysis of the stoichiometry in solution using Job's method (Figure IX.22).[187]

1.2.2 Study of Metal Ion Interactions with PQQ in Non-aqueous Solvents

The coordination chemistry of PQQ was previously examined with several transition metals as well as sodium ions both in solid state and in solution. Depending on the metal and the co-ligands, all three possible binding sites of PQQ can be occupied: With structural PQQ analogues (benzoquinolines) and Fe^{2+},[186] or with C9-decarboxy PQQ and Cd^{2+},[188] or Cu^{2+},[188] coordination was observed in site 1 (Figure IV.2). With Cu^{2+}, PQQ and 2,2'-bipyridine (bipy) or terpyridine (terpy) coordination also took place in site 1,[189] as well as with Cu^{2+}, PQQ and terpy,[155] and with Cu^{+}, $PQQMe_3$ and PPh_3 as co-ligand also in site 1.[176] With Cu^{+}, PQQ and terpy, however, coordination took place in site 1 and 3[155] and with Ru^{2+}, PQQ and bipy in site 2.[190] With Na^{+} coordination was observed in all three sites.[191]

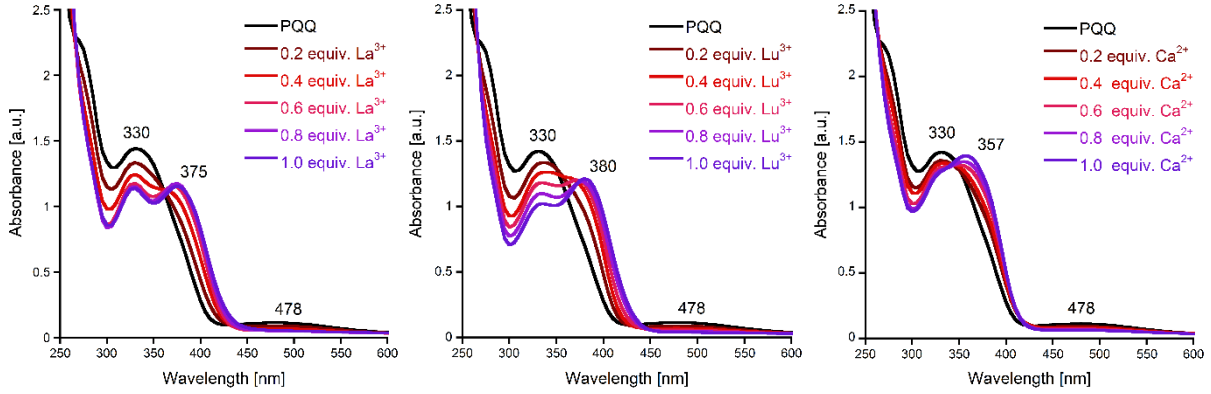

Figure IV.5: UV-Vis spectra of PQQ in H_2O (250 µM) with increasing equivalents of $LnCl_3 \cdot nH_2O$ (Ln = La, Lu) or $CaCl_2 \cdot 2H_2O$, directly measured after metal addition – for spectra of the complete Ln-series and data showing addition of up to five metal equivalents, see Figure IX.20 and Figure IX.21.

Itoh *et al.* described a Ca^{2+} coordination with the trimethyl ester $PQQMe_3$ (**11**) in MeCN solution, where shifts of the proton and carbon NMR resonances indicated coordination in site 1. [50, 173] However, not all PQQ signals were mentioned and no indication was given of the PQQ to metal ratio. An ESI mass spectrometry, UV-Vis spectroscopy and *in silico* study into the interaction of the uranyl ion and Ca^{2+} with PQQ suggested binding in site 1.[192] In 2018, Schelter described a La^{3+} coordination in site 1 with a MDH active site model-ligand, containing a structural PQQ-analogue (benzoquinoline quinone).[114] Here, we examine the interaction of PQQ (**13**) with lanthanides for the first time directly, without the help of structural analogues or the methylester species $PQQMe_3$ (**11**). As mentioned above, water proved to be problematic for metal coordination experiments due to precipitation of a poorly soluble complex in higher concentrations, limiting analysis in water to UV-Vis spectroscopy. PQQ shows good solubility in MeOH, DMF and DMSO and for the $PQQNa_2$ salt also in H_2O (UV-Vis spectra are included in the SI, Figure IX.19, Table IX.14). Since PQQ is known to form hemiketal adducts in methanol (**16**, **18**),[181] and water adducts (to yield **15**), additional coordination experiments were conducted in DMF. UV-Vis experiments with stepwise addition of lanthanides and calcium ions to PQQ are shown in Figure IV.6 and Figure IX.23-25. The UV-Vis spectrum of PQQ (**13**) in DMF is only slightly influenced by Ca^{2+}, leading to a decrease of the intraligand absorption bands at 334 and 447 nm. Throughout the lanthanide series, the absorption intensity is steadily reduced, upon addition of one equivalent of Ln (La^{3+} to Gd^{3+}), accompanied with a small but steady shift towards longer wavelengths. The effects of metal ions on PQQ in DMF are much weaker than in water.

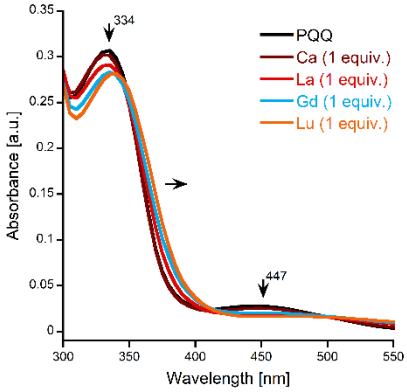

Figure IV.6: UV-Vis spectra of PQQ in DMF (40 µM) with 1 equiv. of $LnCl_3 \cdot nH_2O$ (Ln = La, Gd, Lu) or $CaCl_2 \cdot 2H_2O$, directly measured after metal addition – for spectra of the complete Ln-series, see Figure IX.24.

However, coordination to Ln in DMF clearly influences the electronic structure of PQQ. From Tb^{3+} onwards, the redshift is more pronounced with the maximum absorbance now being at 340 nm. However, the intensity change of the absorption (upon Tb^{3+} to Lu^{3+} addition) is less drastic as with the earlier lanthanide-series ions (Figure IX.24). We can only speculate why such a clear break between early and late lanthanides appears, but a decrease of the coordination number, caused by the lanthanide contraction, is common for lanthanide complexes and could also be of relevance here.[193] Kaim *et al.* had previously observed a shift from 364 and 434 nm to 378 and 488 nm upon binding of Cu^+ to the trimethylester derivative **11** in CH_2Cl_2.[176] Our experiment in DMF shows that the interaction of **13** with Ln follows a pattern that can be attributed to the different properties of the lanthanides (decrease of ionic radii; increase of Lewis acidity) caused by the lanthanide contraction. Spectra were recorded again after 15 minutes and with a total PQQ to metal ratio of 1:11 (Figure IX.24 and Figure IX.25), leading to a further increase of the observed effects: Redshift and absorption intensity change. The addition of water (10 µL – 5 vol%) to the DMF solution decreases the intraligand absorption bands even further, but only slightly causes a redshift (Figure IX.24 and Figure IX.25). Due to the up to 7 equivalents of water in the lanthanide salts, not only metal coordination but also water-adduct formation has to be taken into account. This is also further elaborated in the NMR section below. As lutetium generated the strongest shift in the UV-vis spectrum in DMF we attempted to analyze the binding of this lanthanide using the method of continuous variation (Job's plot)[194] in the absence (to avoid formation of **15**) and presence of traces of water.[187, 194] As the most pronounced change in the absorption spectrum of PQQ - without other overlapping transitions -was in the region of 435 nm, we used this wavelength for our analysis. As mentioned above, PQQ can add water and thus we have to assume the presence of multiple PQQ species before even adding metal ions. We thus collected the data in dry DMF and with anhydrous $LuCl_3$. The data collected directly after mixing PQQ with Lu^{3+} suggest a PQQ-Lu 1:1 complex (Mole

fraction ~ 0.5, Figure IX.23). Surprisingly, the absorbance changed slightly over time (within 15 minutes) shifting the maximum of the Job's plot to 0.6 which could indicate a different stoichiometry and/or the presence of a dynamic process/formation of another species. We want to emphasize here, that the complex nature of multiple species of PQQ in solution clearly hampers a straightforward analysis of stoichiometry in solution and that PQQ does add traces of water at C5 position, leading to the formation of water adduct **15**. When using $LuCl_3{\cdot}6H_2O$ instead of anhydrous lutetium salt the shift over time was stronger, clearly indicating an effect of water on PQQ. Furthermore, the curvature was stronger in DMF, indicating low binding affinity of PQQ (Figure IX.23). We have also explored the possibility to learn about the coordination of lanthanides using the hypersensitive transitions that some Ln exhibit.[195-196] As can be seen in Figure IX.26, the hypersensitive transitions of the Nd^{3+} ion are visible before and after PQQ addition. The transition at 578 nm gains some intensity, however, within this experimental setup no meaningful insight into the nature of the coordination sphere of Nd was obtained. To investigate the site of coordination in solution further, we conducted NMR experiments of **13** with stepwise addition of different lanthanides. Full NMR data of **13** in DMSO are included in the supporting information (Table IX.11), however, this solvent is known to be more strongly coordinating (to lanthanides)[123] and **13** is less soluble in DMSO, hence DMF was used to investigate the interaction with metal ions. Initial investigations included Ca^{2+} and diamagnetic Ln salts La^{3+} and Lu^{3+}, with chlorides and nitrates as counter ions with increasing amounts of added metal salts from 1 to 10 equivalents and with and without controlled ionic strength ($LiClO_4$). For all three metals and regardless of the counter ion employed, the resulting shift for both ^{1}H- and ^{13}C-NMR experiment was very small, with the exception of C_9 (Figure IV.2, para to N_{pyr}). In addition, new resonances appeared both in ^{1}H- and ^{13}C-NMR experiments, especially with increasing amounts of added metals. Due to the presence of up to seven waters of crystallization per added lanthanide equivalent, the formation of a water adduct is plausible. In fact, the addition of water itself (20 equiv.; 9.8 µL) to a solution of **13**, $CaCl_2$ (10 equiv.) and $LiClO_4$ in DMF further increased the intensity of the new signal sets, confirming the presence of the water adduct **15**. Even a sample of purified **13** showed minute traces of additional signals due to trace amounts of residual water. A recrystallized pure sample of **13**, which contained two equivalents of DMF crystal solvent but no traces of water, did not show such additional signals in the ^{1}H-NMR recorded in dry DMF (Figure IX.28). This demonstrates that PQQ readily adds water in non-aqueous solvents even when only minute traces are present, confirming our conclusions from UV-Vis spectroscopy. Based on DFT NMR-shift calculations this addition is proposed to take place at the C_5 carbon

(Table IX.13). In contrast to the experiments with $PQQMe_3$ (**11**) described by Itoh,[173] where one coordination site is blocked (site 3, see Figure IV.2), a clear conclusion solely based on resonance shifts as to where metal coordination takes place with the diamagnetic metal ions and PQQ (**13**), proved to be challenging. Interestingly, besides the discussed water-resonances, no new resonances which could be attributed to complex formation appeared. Thus temperature dependent NMR-experiments with $La(NO_3)_3$ (0.5 equiv.) were conducted at r.t., 0°C and -50°C (the lowest accessible temperature within our experimental setup), but regardless of the temperature, only one signal set was visible for PQQ, suggesting a fast exchange in solution even at low temperatures. However, all resonances were further shifted depending on the temperature (^{1}H- and ^{13}C-NMR - $C_{9'}$, $C_{7'}$, $C_{2'}$ and C_{5a} downfield, all other signals upfield).

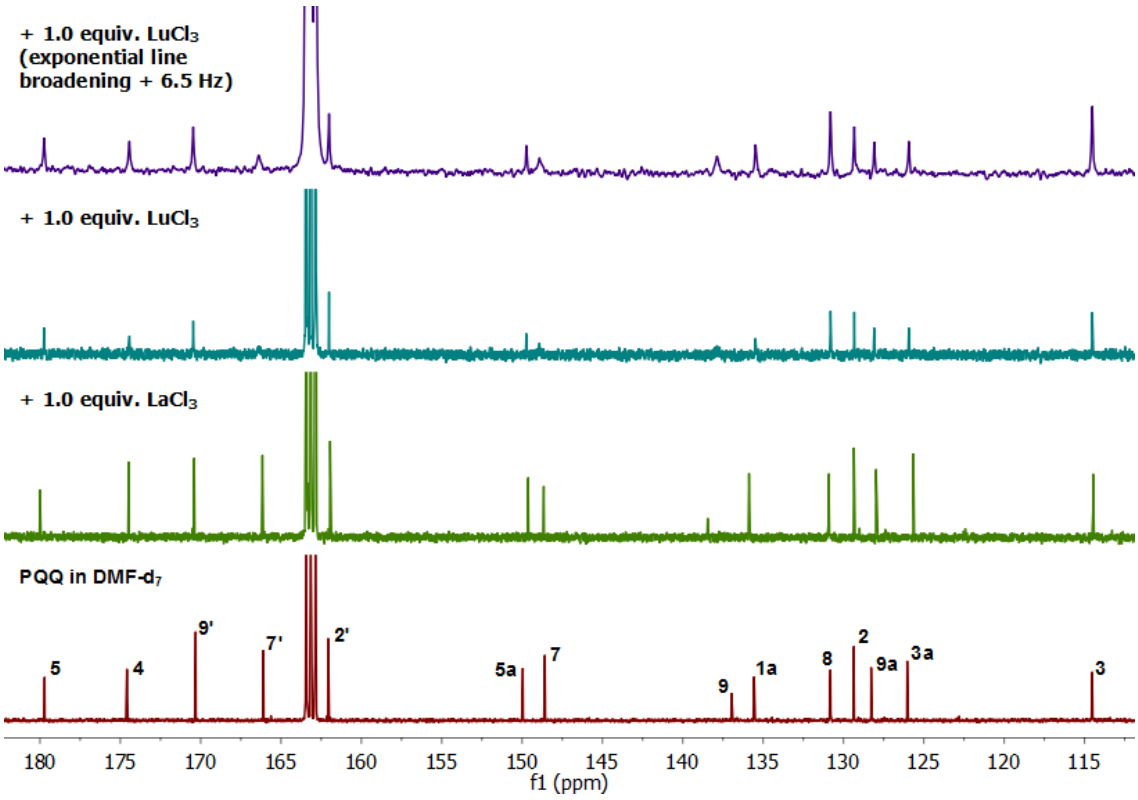

Figure IV.7: Stacked ^{13}C-NMR spectra of **13** in DMF-d_7 (27.2 µmol) with 1.0 equiv. of $LaCl_3 \cdot 7H_2O$ or $LuCl_3 \cdot 6H_2O$ showing the broadening of some resonances after addition of these diamagnetic metal ions.

Experiments reported with lanthanides and 2,6-dipicolinic acid (dpa) reported by Piguet and coworkers showed a similar phenomenon:[197] An excess of ligand, added to an already formed $[Lu(dpa)_3]$ complex in D_2O gave distinct NMR signals for free and bound ligands, which merged to one signal set at higher temperatures. Hence, -50°C is likely not low enough to affect a signal separation in our experiments. While no strong metal induced shifts could help with the assignment of the coordination position, we recognized a broadening of some resonances with increasing amounts of lanthanum and lutetium, but not with calcium.

Especially with lutetium, the addition of one equivalent led resonances $C_{7'}$, C_7 and C_9 almost disappear in the noise, and exponential line broadening (6.5 Hz) had to be used to make them visible (Figure IV.7). To further study the coordination mode of PQQ to biologically relevant metals in solution, paramagnetic lanthanides were used.[198-200] Shifts of the light paramagnetic Ln-chlorides (Ce, Pr, Sm, Eu) for ^{1}H-NMR experiments with 0.5 equiv. metal salt were as expected stronger than the ones from diamagnetic Ln (0.04 – 0.19 (H_1), 0.05 – 0.62 (H_8), 0.01 – 0.11 (H_3) and all signals became broadened, especially H8 (Eu > Pr > Ce > Sm, Table IX.8-10). With increasing amounts of metal salt (0.5 – 3.0 equiv.), all signals were further shifted and broadened (8 > 1 > 3). Shifts of ^{13}C-NMR experiments were in the same range as those from diamagnetic Ln, however resonances that decreased in intensity or completely disappeared due to strong broadening (especially C5, C7' and C7) were induced by lower metal ion concentrations. With 0.5 equivalents, certain resonances were already undetectable (Figure IV.8). With Pr and Eu, more resonances decreased in intensity or disappeared than with Ce and Sm (Table IX.10), probably stemming from differences in the electronic structure and the magnetic susceptibility tensor of the lanthanides.[198, 200-201] The resonances, which disappeared, were partly different (Table IX.10) and were affected by the amount of added metal.

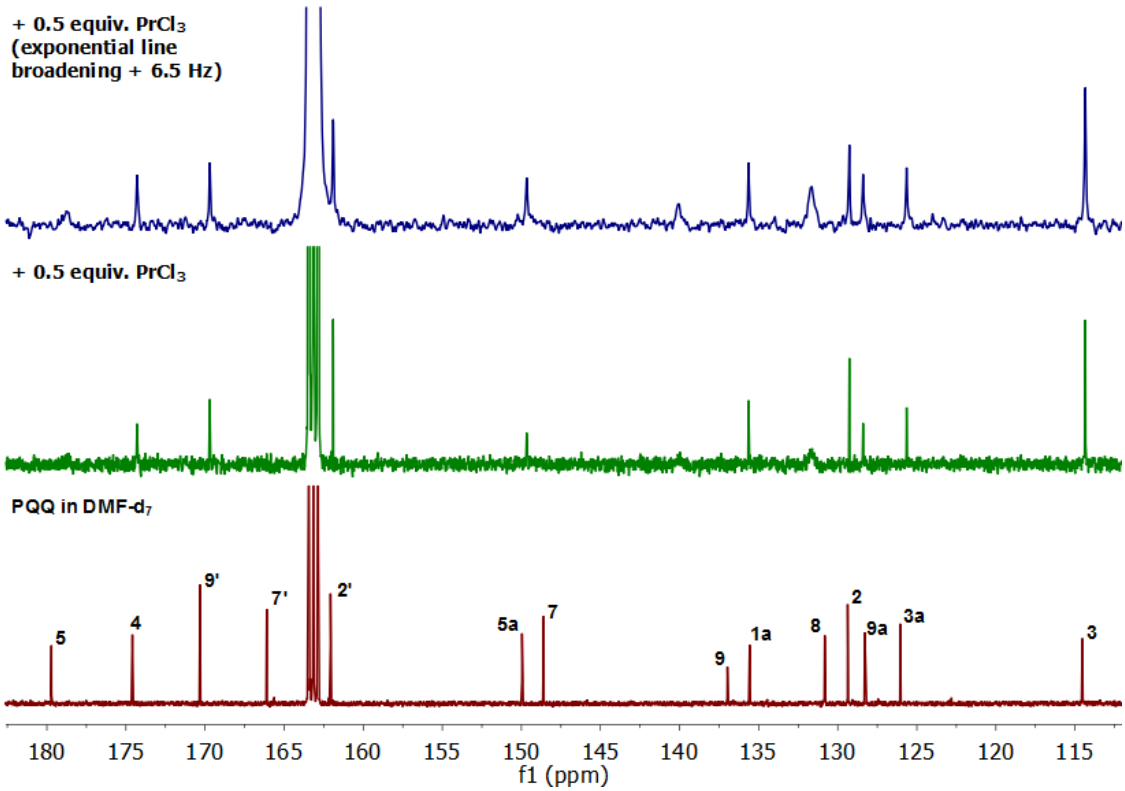

Figure IV.8: Stacked ^{13}C-NMR spectra of **13** in DMF-d_7 (27.2 µmol) with 0.5 equiv. of $PrCl_3 \cdot 6H_2O$, showing the disappearance of some resonances after metal addition.

The only resonances, which remained unaffected in these experiments, were C_{1a}, C_{3a} and C_3. With the heavier, paramagnetic Ln-chlorides of Tb, Er and Tm, already 0.01 equiv. of metal salt led to the above-mentioned changes. Due to the commonly known pseudocontact shift of paramagnetic compounds,[200, 202-203] the spectral width of ^{13}C-NMR experiments was increased to -300 – 600 ppm.[197] However, no additional resonances were detected in this range. It is still possible that, due to the paramagnetic induced broadening, the resonances were indeed shifted low- or highfield but were too broad to be observed. Experiments were also repeated with higher amounts of PQQ (50 mg, 143.2 µmol) with 1 equiv. of $CeCl_3$ or $PrCl_3$ but besides the now clearly visible resonances of the water adduct **15**, no additional resonances were observed. However, taking together the observation that certain ^{13}C-NMR resonances were unaffected (C_{1a}, C_{3a} and C_3) while others (especially C_5, $C_{7'}$ and C_7) decreased in intensity or completely disappeared due to broadening, our experiments support binding of lanthanides to PQQ in solution in the biological relevant coordination pocket (site 1, Figure IV.2) as was also proposed for the uranyl ion by Peyton and coworkers.[192]

1.3. Conclusion

While PQQ has been known and studied for over 50 years, many analytical details of species have only been sparingly reported and often relied on the use of the trimethyl ester. For the first time, we report full NMR, IR and UV-Vis characterization of PQQ and its water adduct. In addition, the interaction of PQQ in solution with biologically relevant metal ions (lanthanides and calcium) has been investigated and these studies suggest that the coordination of lanthanides in non-aqueous solvents takes place in the biologically relevant pocket (site 1).[36, 122, 166] We further show that even if lanthanides have similar chemical properties, the subtle differences in ionic radii across the series impact the electronic structure as evidenced in the UV-Vis spectrum of PQQ. These results will aid the development of PQQ-based model systems and further our understanding of lanthanide dependent enzymes.

2. Further Investigation of the PQQ Complexation

In the before mentioned publication, PQQ-metal complexes were reported with the trivalent lanthanides La^{3+}, Eu^{3+} and Lu^{3+} and with Ca^{2+}. Regardless of the excess of added metal salt, 1:1 complexes were identified by elemental analysis. A three-dimensional coordination network was presumed based on IR. Such networks are known for sodium complexes of PQQ, such as a literature known $PQQNa_2 \cdot 3H_2O$ structure from Ikemoto *et al.* [204] Here, two different sodium ions are coordinated by both quinone oxygens (C4-O and C5-O), N6 and the C7'- and C2'-carboxyl groups (Figure IV.9).

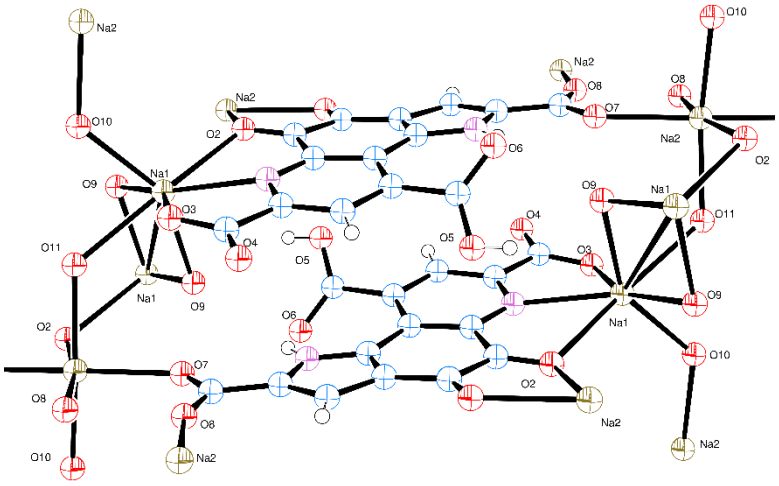

Figure IV.9: Crystal structure of a $PQQNa_2 \cdot 3H_2O$ complex, showing a 3-dimensional coordination network of PQQ spanned with two differently coordinated sodium atoms. CIF taken from Ikemoto *et al.*[204] ORTEP representation.[160] Thermal ellipsoids are drawn at 50 % probability level.

Comparison of the IR spectra of our $PQQNa_2$ (**14**) starting material with the precipitated 1:1 PQQ-La complex, revealed indeed large similarities (Figure IV.10). While the height of the large absorption bands between 3600 – 2600 cm^{-1} is a direct result of the different amounts of co-crystallized water, the overall large similarities between 1800 – 800 cm^{-1} indicate related coordination modes of PQQ in the solids. As already discussed for Figure IV.4, the PQQ C=O stretching vibrations of the carboxyl and quinone groups absorb between 1743 – 1583 cm^{-1}. Although showing large similarities, the peaks at 1743 cm^{-1} and 1707 cm^{-1} for $PQQNa_2$ which are not present for the PQQ-La complex, indicate slight differences in participation of the quinone and carboxyl groups in coordination.

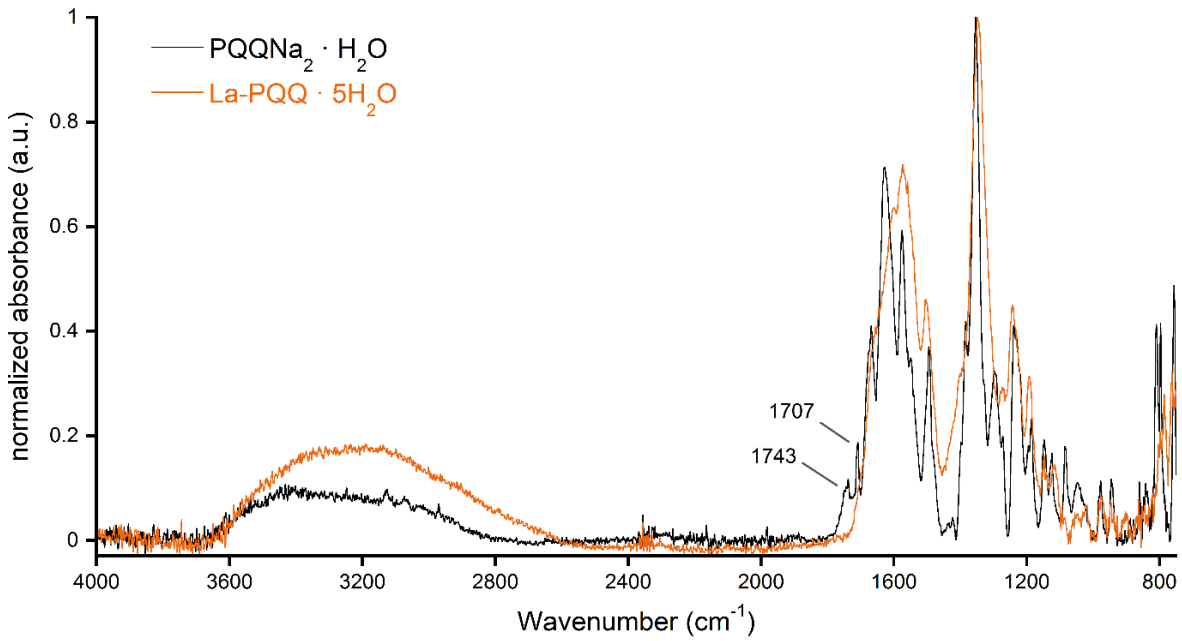

Figure IV.10: Normalized IR absorption spectra of the $PQQNa_2$ starting material and the 1:1 PQQ-La complex.

From the aqueous washing solution of the precipitate, which was formed after the addition of 2 equiv. $CaCl_2$ to $PQQNa_2$, crystals were grown over several months, suitable for X-ray analysis (Figure IV.11).

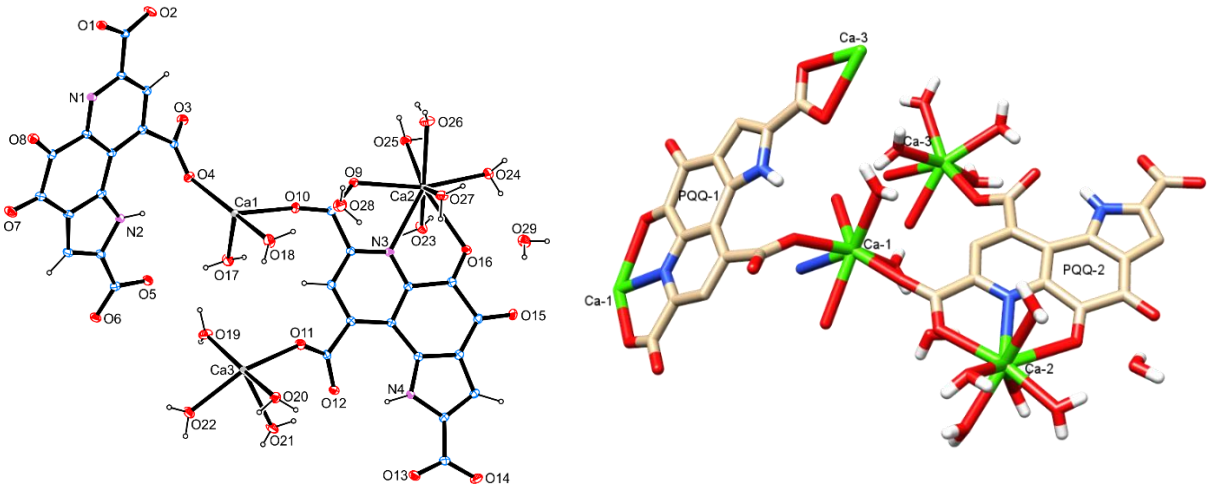

Figure IV.11: Crystal structure of $PQQ_2Ca_3{\cdot}13H_2O$ complex, showing a 3-dimensional coordination network of PQQ spanned with three differently coordinated calcium atoms. Left: ORTEP representation of the asymmetric unit with 50% thermal ellipsoid plots.[160] Right: Chimera representation for better visibility of the different coordination modes.[41]

The structure reveals three different Ca^{2+} ions and two differently coordinated PQQ equivalents. PQQ-1 coordinates calcium under participation of all three carboxyl groups and coordinates Ca-1 by 7'-O, 6-N, 5-O and 9'-O and Ca-3 by bidentate 2'-O. PQQ-2 coordinates with only two of the three carboxyl groups and coordinates Ca-1 by 7'-O; Ca-2 by 7'-O, 6-N and 5-O and Ca-3 by 9'-O. As a result, Ca-1 and Ca-3 show pentagonal bipyramidal geometries with coordination numbers of 7 and Ca-2 shows a distorted geometry with a coordination number of

8. Both Ca-1 and Ca-2 are distorted which is probably a result of the rigid PQQ ligand. Although dissolved in aqueous solution, the PQQ-water adduct (**15**) is not present in the complex, like all known crystal structures for PQQ to the best of our knowledge.

The IR spectrum reveal overall large similarities to both $PQQNa_2$ and the 1:1 PQQ-La complex (Figure IV.12). The absorption band between 3600 – 2600 cm^{-1} is increased due to the higher amounts of crystal water.

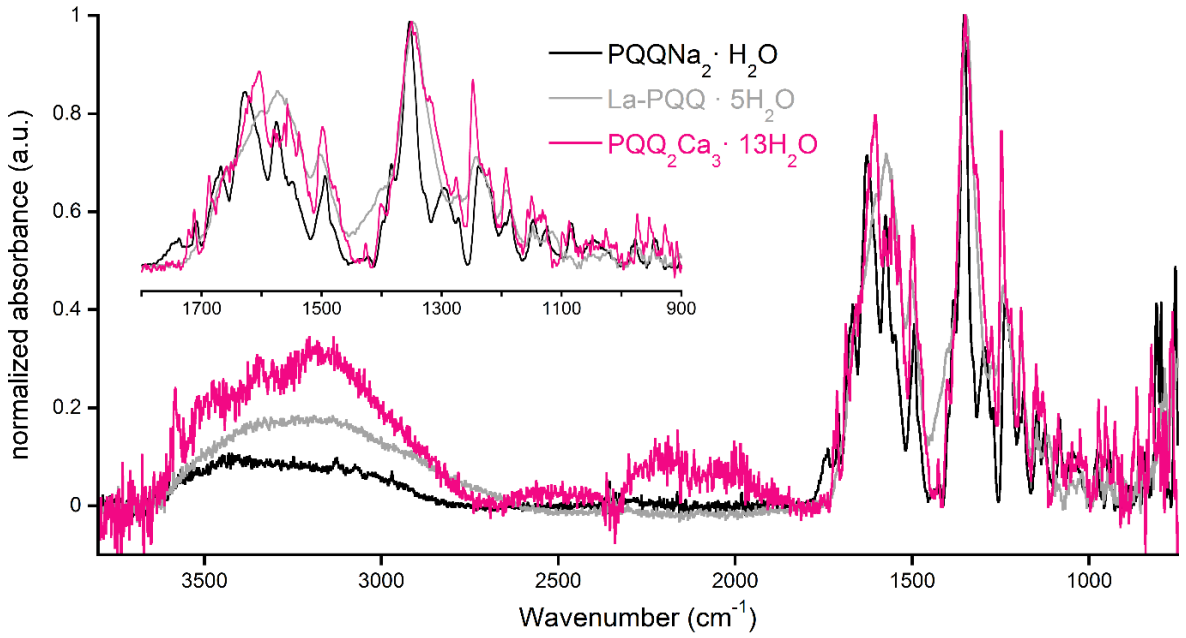

Figure IV.12: Normalized IR absorption spectra of the $PQQNa_2$ starting material in black, the 1:1 PQQ-La complex in grey and the PQQ_2Ca_3 crystal in pink.

In direct comparison to Figure IV.11 the peak at 1707 cm^{-1} is also present for the calcium structure but not the one at 1743 cm^{-1}, indicating distinct differences in participation of the quinone and carboxyl groups.

We were further interested in complexation of PQQ with mixed metal solutions in order to identify trends in coordination behavior throughout the lanthanide series. For this purpose, aqueous solutions of 3 equiv. $LaCl_3{\cdot}7H_2O$ and 3 equiv. of a different $LnCl_3$ or $CaCl_2$ were prepared and mixed with aqueous solutions containing 1 equiv. of $PQQNa_2$ (**14**). The received solids showed again largely similar IR absorption bands (Figure IV.13). The main difference over the series of coordinated lanthanides is the appearance of a small absorption band between 1775 – 1700 cm^{-1}, which increase in intensity from early to late lanthanides and calcium. ssNMR of the La-PQQ complex revealed a small band at 92.55 ppm. This shift is in the same range as C5 carbon shifts from the PQQ-water adduct (**15**) (91.07 ppm in MeOD-d_4, Table IX.11) and from the PQQ-hemiketal (**16**) (92.42 ppm, ssNMR - Figure IX.29). It is possible,

that small amounts of water adduct **15** are present in the precipitated solids, which cause the IR absorption band between 1775 – 1700 cm^{-1}, depending on the total amount of **15** present. To verify this concept, ssNMR from the Lu-PQQ complex was performed, however, no meaningful ^{13}C-NMR spectra could be recorded, possibly due to interference of the Lu nucleus.

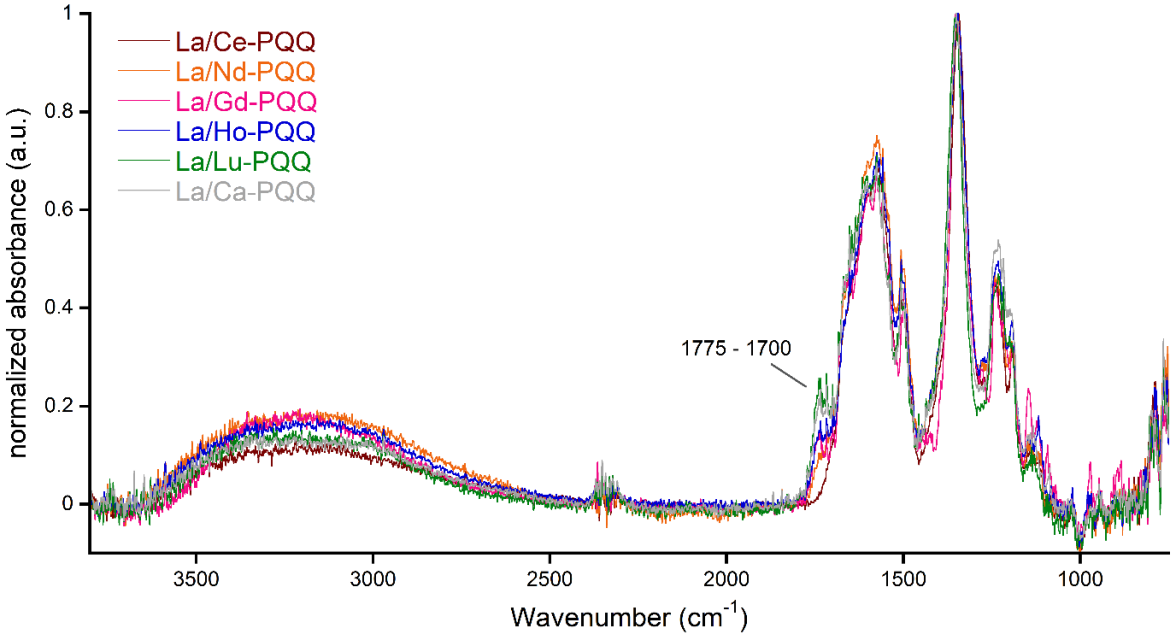

Figure IV.13: Normalized IR absorption spectra of the complexes formed from La/Ln or La/Ca mixtures and $PQQNa_2$. Ln = Ce, Nd, Gd, Ho and Lu, exemplary for the whole Ln series, excluding Pm.

ICP-MS revealed the composition of the La/Ln and La/Ca couple. The experiment was repeated three times and the results are given in Figure IV.14.

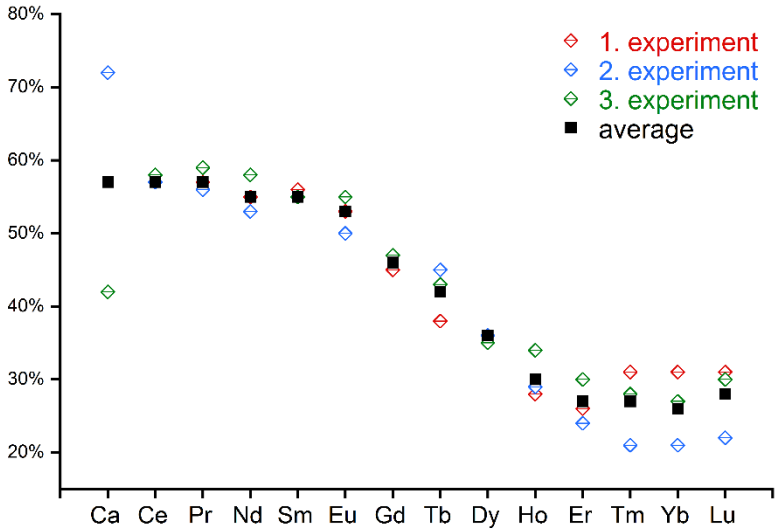

Figure IV.14: Percent amount of Ln and Ca *vs.* La in a 1:1 PQQ-metal complex, precipitated from aqueous $PQQNa_2$ (51 µM) solutions at room temperature. Values of three experiments are shown as bars, the averaged values of all three experiments are shown as squares.

The percent amount of lanthanides in the precipitated solid decreases throughout the series. The La/Ce couple shows 57% Ce over 43% La while the Yb amount is only 26% and then slightly reincreases to 28% for Lu. Ca shows a similar 57% to Ce, however, the variance is quite large from 42 – 72%.

Without more structural information, it is difficult to comment on what causes this distribution. In general, increasing Lewis acidities throughout the Ln series lead to higher complex stabilities and therefore to a preference of the late Ln.[92] This is for example the case for $[Ln\ EDTA]^-$ complexes, where the stability constants increase by four orders of magnitude across the lanthanide series,[205] and in the technical liquid extraction, where the used extractors (organophosphates or carboxylic acids) preferentially bind the late Ln.[11] Early Ln are only privileged in cases, where the small size of the late Ln is unfavorable, as reported for complexes with substituted diaza-18-crown-6[206-207] or diaza-15-crown-5[208-209] compounds or the tripodal hydroxylaminato ligand $TriNOx^{3-}$.[210]

The PQQ-metal complexes precipitate immediately after metal addition. Kinetic factors should therefore be considered as well. However, formation rates throughout the lanthanide series are somewhat more varied than the stability constants.

With the cyclic PCTA ligand, both formation and stability constants increase throughout the lanthanide series.[211] The related DOTA ligand shows a similar behavior in unbuffered media of pH 3 – 5,[212] while buffered solutions of pH 4.2 show increasing formation rates from Sm to Dy but then a decrease over Yb to Lu (1.44 *vs*. 5.20 *vs*. 4.56 *vs*. $4.54 \cdot 10^{-2}$ mM^{-1} min^{-1}).[213] The smaller sized cyclic NOTA ligand shows formation rates, independent of the ion size.[214] Coordination with EDTA or the related DTPA show increasing rate constants from La to Gd followed by decreasing rate constants to Lu, probably reflecting increased steric strain for the smaller Ln.[215] For the early Ln, the formation constants are higher for the larger DTPA which is explained by a reduced steric barrier for “wrapping-around” the central metal.[215]

The preferred coordination site of metals with PQQ is commonly site 1 (Figure IV.2), as seen for the Ca complex showing additional co-complexation of the carboxyl groups (Figure IV.11). The relative rigidity of the chelating PQQ molecule could be the reason for the preference of early lanthanides, contrary to the stability trends with increasing Lewis acidities. The distance between the two oxygen atoms of C5=O and C7-O is 4.4 Å in the $PQQ_2Ca_3 \cdot 13H_2O$ crystal structure and therefore possibly more favorable to the larger, early lanthanides.

However, crystal structures of the whole lanthanide series or at least more structural information are necessary for determination of such a size effect. Complexation experiments at different temperatures would help to evaluate, if the lanthanide preference of PQQ is based on enthalpy or formation kinetics.

V. REDOX-CHEMISTRY OF PQQ

1. Introduction

Quinones are vital as electron acceptors for many metabolic processes such as photosynthetic and respiratory electron transport chains.[216] This biological role has already been inspired materials for the harvest and storage of energy.[217] Also in MDH, the quinone PQQ (**13**) acts as electron acceptor and concurrent to methanol oxidation, both hemiketal- and hydride transfer mechanism include the formation of a reduced $PQQH_2$ (**24**) species. $PQQH_2$ is subsequently oxidized in two distinct one-electron steps *via* the $PQQ^{\bullet-}$ semiquinone with help of a cytochrome (Figure V.1).[218]

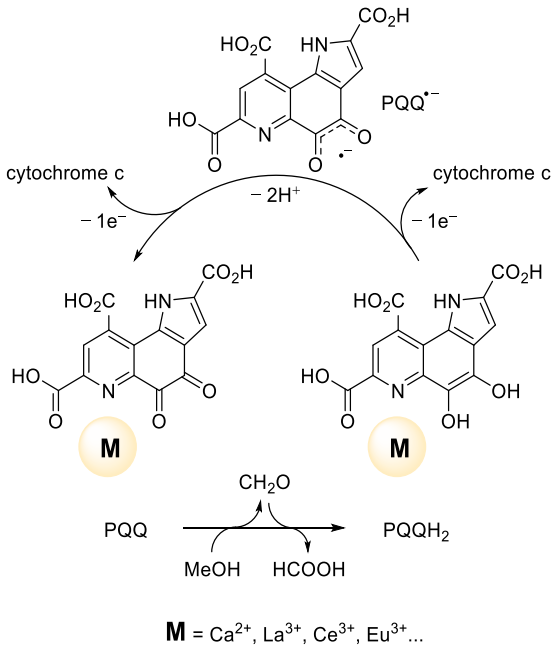

Figure V.1: Redox cycle of PQQ in MDH, adapted from our previous publication.[168]

Schelter *et al.* proposed, that Ln would result in lowered virtual orbitals and would therefore facilitate PQQ reduction and in turn methanol oxidation.[76] Whether Ln have an influence on the reduction of PQQ and reoxidation of $PQQH_2$ (**24**) is further examined in this chapter.

2. Reduction of PQQ with Ascorbic Acid

Mukai *et al.* described the reduction of PQQ (**13**) to $PQQH_2$ (**24**) with ascorbic acid in phosphate buffer (pH 7.4, 0.05 M) in a nitrogen atmosphere.[161] The reduction is described of radical nature, with four reactions taking place:

$$PQQ + AsH^- \rightarrow PQQH^\bullet + As^{\bullet-} \quad (1)$$

$$PQQH^\bullet + AsH^- \rightarrow PQQH_2 + As^{\bullet-} \quad (2)$$

$$PQQH^\bullet + PQQH^\bullet \rightarrow PQQ + PQQH_2 \quad (3)$$

$$As^{\bullet-} + As^{\bullet-} + 2H_2O \rightarrow AsH_2 + As + 2OH^- \quad (4)$$

PQQ (**13**) is converted by deprotonated L-(+)-ascorbic acid (AsH^-) in (1), forming the radical species $PQQH^\bullet$ which is further oxidized to $PQQH_2$ (**24**) in (2), releasing an $As^{\bullet-}$ radical in each step. Two $PQQH^\bullet$ radicals can also disproportionate to **13** and **24** (3), while the formed $As^{\bullet-}$ radicals react with water to protonated AsH_2 and deprotonated diketone As in (4).[161]

The used phosphate buffer in the work by Mukai *et al.* is known to form poorly soluble salts with lanthanides,[107] hence other buffers (TRIS-HCl and PIPES – pH 7.4) and DMSO were tested as media for PQQ reduction experiments (Figure V.2).

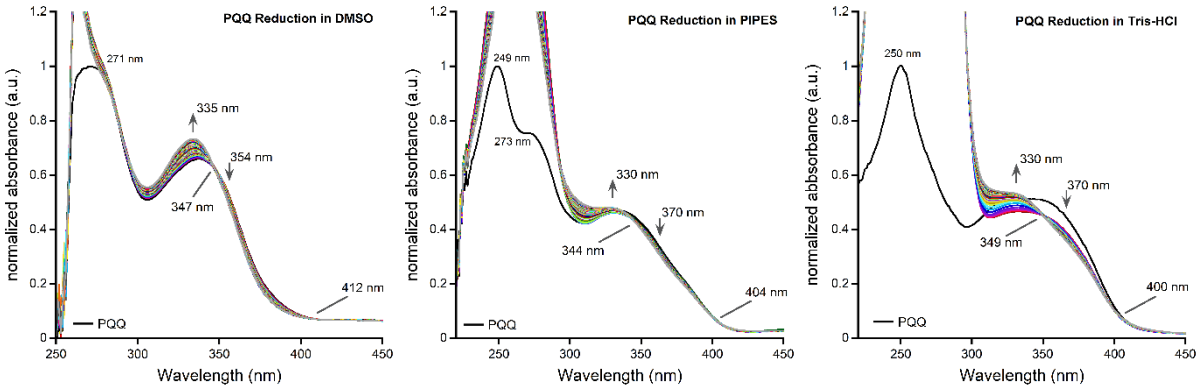

Figure V.2: Spectrophotometric analysis of the reduction of PQQ (**13**) (10 µM) in DMSO (left) or in aqueous PIPES (middle) or TRIS-HCl (right) buffer (pH 7.4, 50 mM) (0.96 mL) with L-(+)-ascorbic acid (120 µM) under nitrogen. Black lines indicate absorption of pure PQQ before the addition of ascorbic acid. The spectrum of pure PQQ is normalized to an absorbance of 1 at 271 nm in DMSO, 249 nm in PIPES buffer and 250 nm in TRIS-HCl buffer and the spectra with ascorbic acid addition are adjusted accordingly. Spectra recorded every 60 seconds for 90 minutes in total.

Upon addition of ascorbic acid, large absorption bands became visible between 250 – 300 nm (in DMSO) and 220 – 300 nm (in buffer) which partly overlayed PQQ absorption. Spectra for PQQ (black lines) shifted to some degree upon ascorbic acid addition (TRIS-HCl > PIPES > DMSO) and new maxima at 335 nm (in DMSO) and 330 nm (in buffer) appeared and increased absorption overtime, indicating the reduction of PQQ to $PQQH_2$. Several isosbestic points

further underline a conversion of two species. One of the distinct absorption maxima of $PQQH_2$, which is described by Mukai *et al.* at 304 nm in phosphate buffer,[161] was completely hidden under the strong absorption band of ascorbic acid.

As changes on the absorption spectra of PQQ (**13**) and $PQQH_2$ (**24**) were most pronounced in TRIS-HCl buffer, the influence of metal salts on PQQ reduction was analyzed in this solvent system. The same experimental set-up was used as described above, but with one equiv. of $CaCl_2 \cdot 2H_2O$ or $LaCl_3 \cdot 7H_2O$ (Figure V.3).

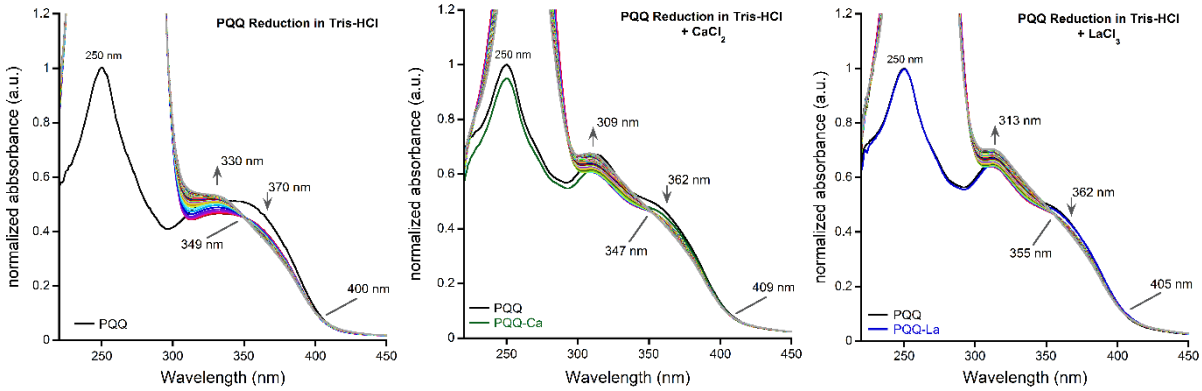

Figure V.3: Spectrophotometric analysis of the reduction of PQQ (10 µM) in aqueous TRIS-HCl buffer (pH 7.4, 50 mM) (0.96 mL) with L-(+)-ascorbic acid (120 µM) under nitrogen. Without metal addition (left) or with 1.0 equiv. (10.0 µM) $CaCl_2$ (middle) or $LaCl_3$ (right) added. Black lines indicate absorption of pure PQQ, green and blue lines PQQ absorption with 1.0 equiv. $CaCl_2$ (green) or $LaCl_3$ (blue) added, each before the addition of ascorbic acid. The spectrum of pure PQQ is normalized to an absorbance of 1 at 250 nm and the spectra with addition of metal salts and ascorbic acid are adjusted accordingly. Spectra recorded every 60 seconds for 90 minutes in total.

Interestingly, the PQQ spectrum remained almost identical after addition of 1 equiv. La^{3+} (blue line) and slightly decreased in intensity after the addition of Ca^{2+} (green line). After addition of ascorbic acid, differences were more pronounced, since the added metals caused a shift of the growing $PQQH_2$ absorption maximum from 330 nm without metal to 309 nm with Ca^{2+} and 313 nm upon La^{3+} addition. Reduction of PQQ to $PQQH_2$ was observed. However, ascorbic acid is known for its coordination chemistry,[219] and complexation with Ca^{2+} and Ln^{3+} has been reported.[220-223] An effect of metals on reduction of PQQ is therefore difficult to observe with the experimental setup, since both PQQ and ascorbic acid will compete for complexation. Also the absorption properties of ascorbic acid are problematic, as it absorbs in the same spectral region as PQQ.

Since the reduced $PQQH_2$ species is readily available as solid through bulk reduction with ascorbic acid, reoxidation of this species was further examined. $PQQH_2$ can be reoxidized with oxygen[161] and no further additives are needed which would possibly interfere with the obtained UV-Vis spectra .

3. Reoxidation of $PQQH_2$

3.1. Solvent Selection

The reduced $PQQH_2$ species (**24**) can be received as solid by bulk reduction with ascorbic acid (see Chapter III.4.3). With oxygen, $PQQH_2$ is reoxidized to PQQ (**13**).[161] Whether lanthanides or calcium have an influence on this reoxidation is discussed in this section. Several solvent mixtures were tested in preliminary experiments regarding observed reoxidation, metal binding and precipitation of a metal-ligand complex (Table V.1). The previously used TRIS-HCl buffer was omitted as it is suspected to show metal coordination itself. Ln complexes with the related Bis-TRIS buffer are reported.[224]

Table V.1: Solvent mixtures for $PQQH_2$ reoxidation experiments. Non-observable reoxidation or metal binding or occurred precipitation is indicated by a minus sign −. ✓ indicates observable reoxidation or metal binding or that no precipitation occurred. To each solvent mixture, $PQQH_2$ (50 µL, 2 mM) was added as DMSO solution in case of DMSO- or pure PIPES measurements or as DMF solution for DMF including measurements. 1.5 equiv. of $CaCl_2 \cdot 2H_2O$, $LaCl_3 \cdot 7H_2O$ or $EuCl_3 \cdot 6H_2O$ (7.5 µL, 20 mM) in either DMSO, DMF or H_2O were added and metal coordination was evaluated by observed UV-Vis shifts. For reoxidation, the cap of the cuvette was removed and the solution was stirred open to air.

Solvent	reoxidation	metal binding	no precipitation
DMSO	−	−	✓
DMF	−	✓	✓
PIPES (pH 7.2)	✓	✓	−
DMF + H_2O (2.8 / 0.3 mL)	✓	✓	✓
DMF + PIPES (pH 7.2, 100 mM NaCl) (2.65 mL / 0.3 mL)	✓	✓	−
DMF + H_2O (100 mM NaCl) (2.65 mL / 0.3 mL)	✓	✓	−
DMF + H_2O (100 mM $LiClO_4$) (2.65 / 0.1 mL)	✓	✓	La^{3+} and Ca^{2+} ✓ Eu^{3+} −
DMF (75 mM $LiClO_4$) + H_2O (2.99 mL / 0.01 mL)	✓	✓	✓

While no metal binding or reoxidation was observed for DMSO solutions, an aqueous PIPES solution of $PQQH_2$ led to precipitation of a PQQ-metal complex, similar to the complex formation described in Chapter IV. DMF solutions showed no such precipitation and the metal binding was well observable. Quinols are known to be prone to oxidation by oxygen, forming the respective quinone and water.[225] Itoh *et al.* described the formation of H_2O_2 during the reoxidation of $PQQH_2$ in an aqueous solution which was saturated with oxygen.[226] Unfortunately, in DMF alone, no reoxidation was observed, even after directly bubbling air through the $PQQH_2$ solution, unless water was added. Water is known to stabilize the intermediate semiquinone via hydrogen bonding,[227] which could also be of relevance in this approach. Without water, the oxidation potential of oxygen might not be high enough, explaining why $PQQH_2$ is stable in dry DMF and DMSO.

Attempts were made to exchange the added water with buffer. PIPES is used in metal ion containing essays and described as good substitute to TRIS.[228] PIPES buffer with an ionic strength of 100 mM NaCl was used and the pH was set to 7.2, which is the optimum of XoxF MDH from SolV.[36, 94] Unfortunately, precipitation occurred under these conditions. The addition of water (0.3 mL, 100 mM NaCl) to a DMF solution also led to precipitation. The reduction to 0.1 mL H_2O and the change from NaCl to $LiClO_4$ still accomplished reoxidation, while no precipitation was observed for La^{3+} and Ca^{2+}. However, the smaller Eu^{3+} ion still caused precipitation. The results of spectrophotometric measurements using this solvent mixture are given in the following section. A slightly higher metal concentration of 1.5 equiv. was used, to ensure complete PQQ complexation.

3.2. Spectrophotometric Measurements in DMF

3.2.1 Reoxidation of $PQQH_2$ in DMF with 1.5 Metal Equiv. and 3.4 vol% H_2O

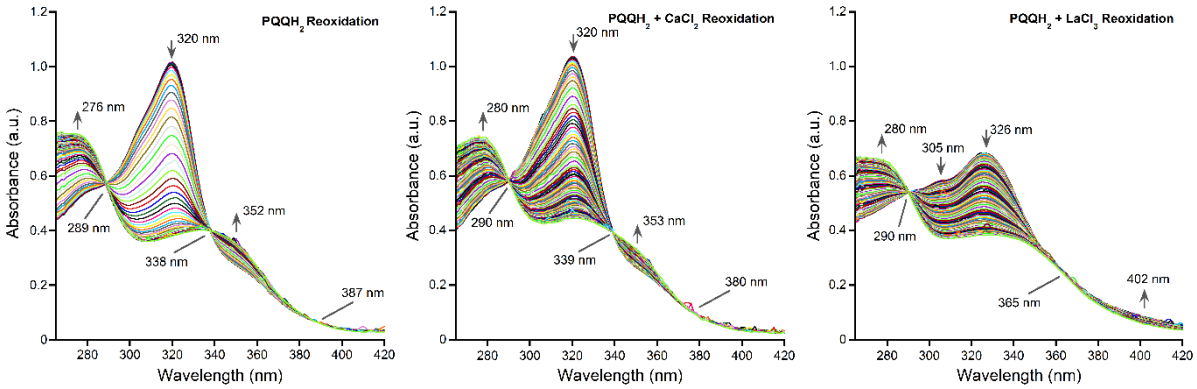

Figure V.4: Spectrophotometric analysis of the reoxidation of $PQQH_2$ (33.4 µM) in DMF (2.9 mL) and H_2O (100 µL, 1.83 M) with controlled ionic strength ($LiClO_4$, 3.34 mM) under air, without metal addition (left) or with 1.5 equiv. (50.0 µM) $CaCl_2$ (middle) or $LaCl_3$ (right) added. Spectra recorded every 30 seconds - first 100 spectra (50 minutes) are shown.

The spectra received from the $PQQH_2$ and $PQQH_2$ + $CaCl_2$ measurements appeared rather similar, with a maximum at 320 nm. Over reoxidation, the absorption of the maximum at 320 nm decreased, and a new absorption band emerged at 276 nm (280 nm for Ca^{2+}) as well as a shoulder at 352 nm (353 nm). Isobestic points at 289, 338 and 387 nm (290, 339, 380 nm) indicate a clear conversion back to PQQ (compare with Figure V.5). The addition of $LaCl_3$ to $PQQH_2$ led to a shift of the absorption maximum to 326 nm and a new maximum at 305 nm. In direct comparison, the maximum was reduced from 1.02 a.u. (1.04 a.u. for Ca^{2+}) to 0.69 a.u. with La^{3+}. Over reoxidation, the maximum at 305 nm disappeared, while the maximum at 326 nm slowly decreased its intensity and a new maximum appeared at 280 nm. Only two isosbestic points were visible at 290 nm and 365 nm, while the absorbance at 402 nm increased.

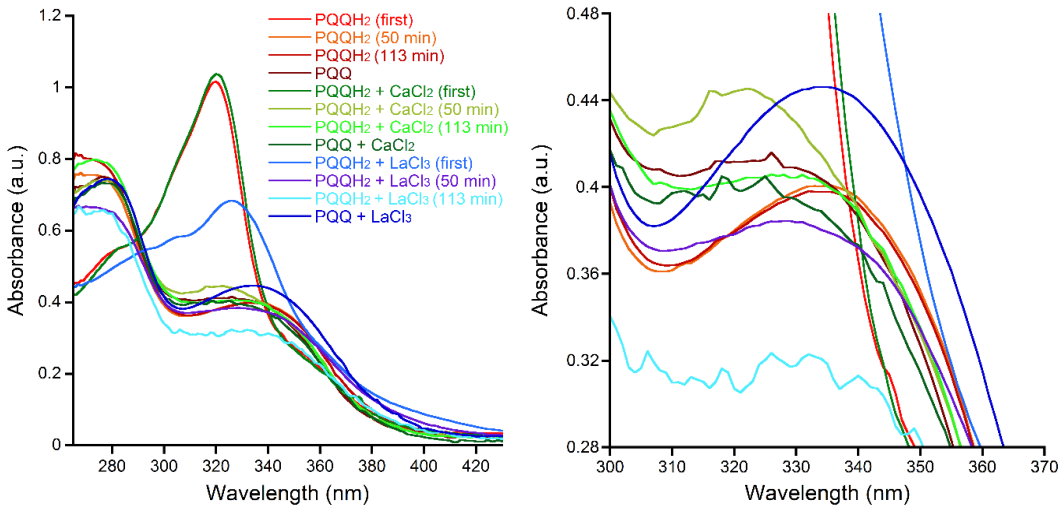

Figure V.5: Combined spectra of $PQQH_2$ (33.4 µM) in DMF (2.9 mL) and H_2O (100 µL, 1.83 M) with controlled ionic strength ($LiClO_4$, 3.34 mM) under air, with or without the addition of $LaCl_3$ or $CaCl_2$ (1.5 equiv.) at T = 0, 50 and 113 minutes, respectively. For comparison, additional spectra of PQQ in the same solvent mixture with or without metal addition are shown.

Figure V.5 shows the first and last spectrum received from the spectrophotometric measurements of $PQQH_2$ in DMF and H_2O, with or without the addition of metal salts. For comparison, a spectrum of PQQ was recorded in the same solvent mixture and concentration, with or without the addition of metal salts. In theory, the last spectrum of the measurements should only contain reoxidized PQQ and should therefore appear similar to the reference spectra. While this is the case for $PQQH_2$ + $CaCl_2$ (green lines) and to some extend for free PQQ (red lines), $PQQH_2$ + $LaCl_3$ differ quite strong compared to the reference spectrum (blue lines). The contents of the cuvette that contained $PQQH_2$ and $LaCl_3$ showed signs of precipitation after 1 h (see Figure V.6) likely causing this deviation.

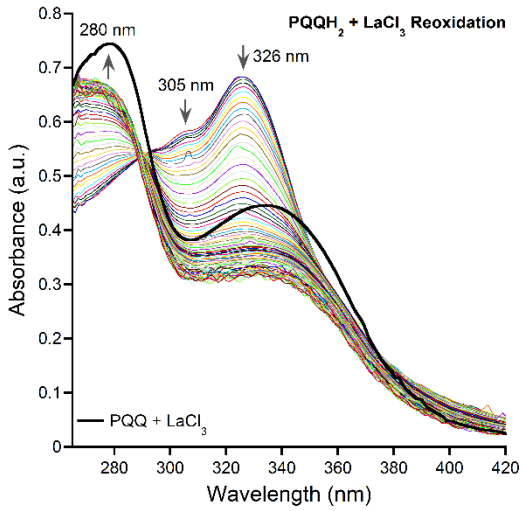

Figure V.6: Spectrophotometric analysis of the reoxidation of $PQQH_2$ (33.4 µM) and 1.5 equiv. $LaCl_3$ (50.0 µM) in DMF (2.9 mL) and H_2O (100 µL, 1.83 M) with controlled ionic strength ($LiClO_4$, 3.34 mM) under air. The black line is pure PQQ (33.4 µM) + 1.5 equiv. $LaCl_3$ (50.0 µM) under the same conditions. Spectra recorded every 30 seconds for 2 h in total – every third spectrum (= every 90 seconds) is shown. The noisy spectra indicate starting precipitation.

To compare the spectra received from $PQQH_2$ reoxidation experiments, the absorbance of the maximum at 320 nm (with Ca^{2+}: 320 nm; with La^{3+}: 326 nm) was normalized to values between 1 and 0 and plotted against the elapsed time (Figure V.7).

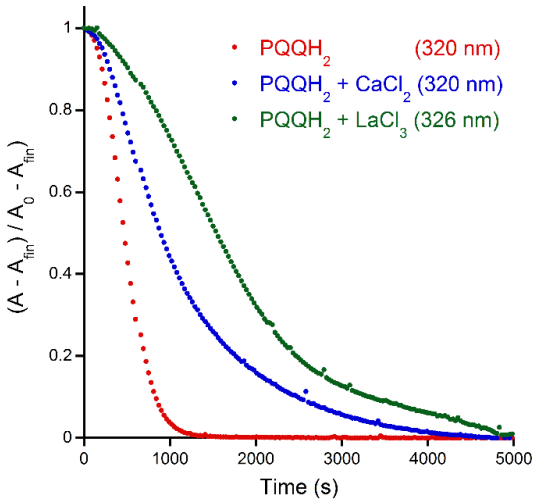

Figure V.7: Normalized absorbance of the maximum at 320 nm (PQQ; PQQ + $CaCl_2$) and 326 nm (PQQ + $LaCl_3$) *vs*. time (s) for measurements of $PQQH_2$ (33.4 µM) in DMF (2.9 mL) and H_2O (100 µL, 1.83 M) with controlled ionic strength ($LiClO_4$, 3.34 mM) under air, with or without the addition of $LaCl_3$ or $CaCl_2$ (1.5 equiv.). Spectra recorded every 30 seconds. A = absorbance, A_0 = starting absorbance, A_{fin} = final absorbance.

It is clearly visible that presence of the added metal salts does not enhance the reoxidation, since pure $PQQH_2$ (red curve) shows the fastest decrease of absorbance and therefore the fastest reoxidation to PQQ. The decrease of absorbance for PQQ + $CaCl_2$ (blue curve) is less steep, while PQQ + $LaCl_3$ (green curve) shows the slowest reoxidation and the appearance of the curve is distinctly different from pure PQQ. A closer look on how exactly metals interact with $PQQH_2$ during reoxidation is given in section V.3.3.

3.2.2 Reoxidation of $PQQH_2$ in DMF with 3.0 Metal Equiv. and 0.3 vol% H_2O

Since the approach mentioned above caused precipitation after the addition of $LaCl_3$, an alternative solvent mixture needed to be tested for reoxidation experiments. Therefore, only 10 µL (0.3 vol%) of water were added to a DMF solution of $PQQH_2$. Three equiv. of metal salts were added in these experiments to study the impact of higher metal concentrations. Furthermore, $EuCl_3$ was included, to study the impact of ion size (La^{3+} - 1.03 Å *vs*. Eu^{3+} - 0.95 Å in hexadentate complexes according to Shannon)[20] and Lewis acidity ($La^{3+} < Eu^{3+}$)[11] The ionic strength was now controlled by dissolving $LiClO_4$ directly in DMF (75 mM), resulting in the following spectra:

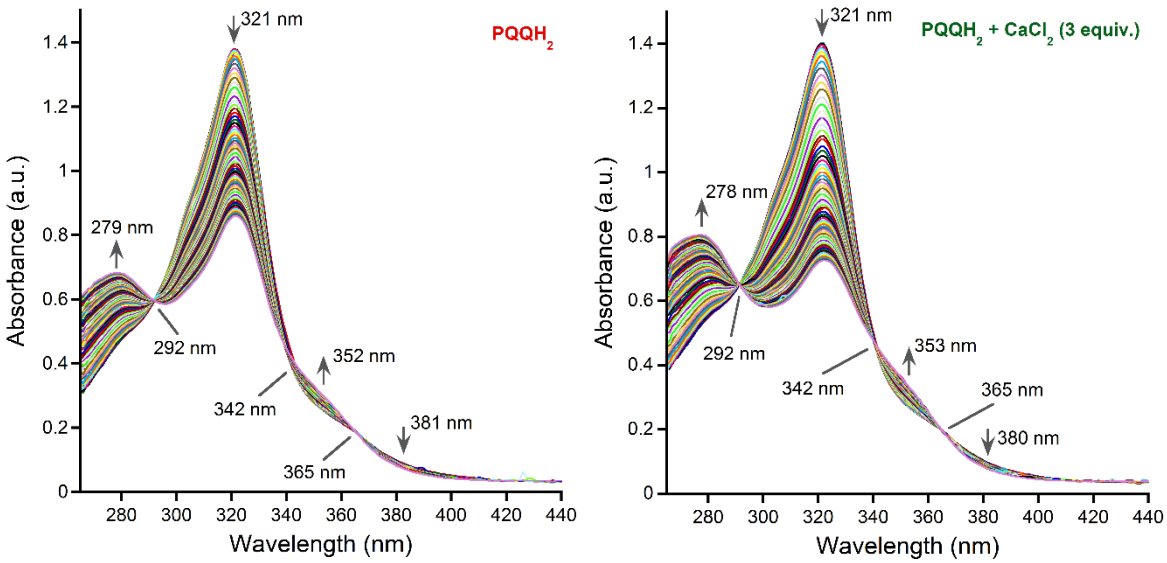

Figure V.8: Spectrophotometric analysis of the reoxidation of $PQQH_2$ (33.4 µM) in DMF (2.99 mL) and H_2O (10 µL, 183 mM) with controlled ionic strength ($LiClO_4$, 73.1 mM) under air. Left: $PQQH_2$ without metal addition. Right: $PQQH_2$ with 3.0 equiv. $CaCl_2$ added (100.2 µM). Spectra recorded every 30 seconds - first 100 spectra (50 minutes) are shown.

The spectra obtained from $PQQH_2$ reoxidation (left) and the ones with calcium addition (right) appeared similar, with decreased absorption maxima at 321 nm, and increased new maxima at 279 nm ($PQQH_2$) or 277 nm (with $CaCl_2$). The appearance of three isosbestic points indicate a conversion back to PQQ both in the presence and absence of calcium.

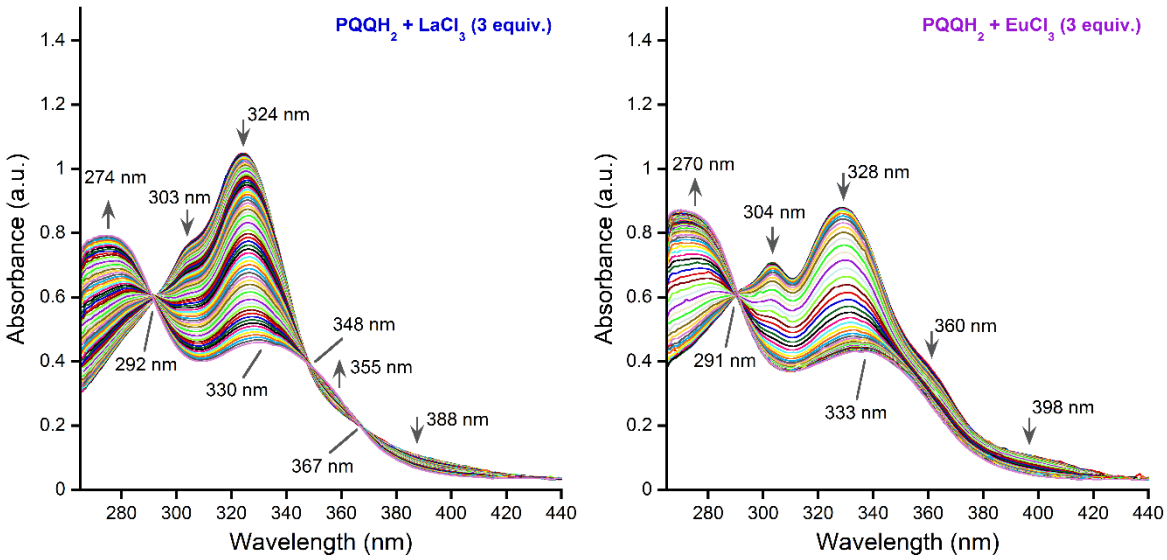

Figure V.9: Spectrophotometric analysis of the reoxidation of $PQQH_2$ (33.4 µM) in DMF (2.99 mL) and H_2O (10 µL, 183 mM) with controlled ionic strength ($LiClO_4$, 73.1 mM) under air with 3.0 equiv. (100.2 µM) $LaCl_3$ (left) or $EuCl_3$ (right) added. Spectra recorded every 30 seconds - first 100 spectra (50 minutes) are shown.

The addition of $LaCl_3$ led to a redshift of the absorption maximum from 321 to 324 nm, which was further redshifted throughout reoxidation. A second maximum was visible as a shoulder at 303 nm which slowly disappeared. Also in this case, a new maximum appeared at 274 nm and

all three isobestic points were clearly visible. In comparison, the addition of $EuCl_3$ led to a further shift of the absorption maximum to 328 nm, which in turn exposed a second local maximum at 304 nm. While an isosbestic point was clearly visible at 291 nm, the other two isosbestic points disappeared and the absorption continuously decreased between 350 nm and 430 nm.

3.2.3 Reoxidation of $PQQH_2$ in DMF with 10 Metal Equiv. and 0.3 vol% H_2O

In order to further examine influence of metals on $PQQH_2$ reoxidation, the experiments were repeated with 10 equiv. of metal salts under the same conditions receiving the following spectra:

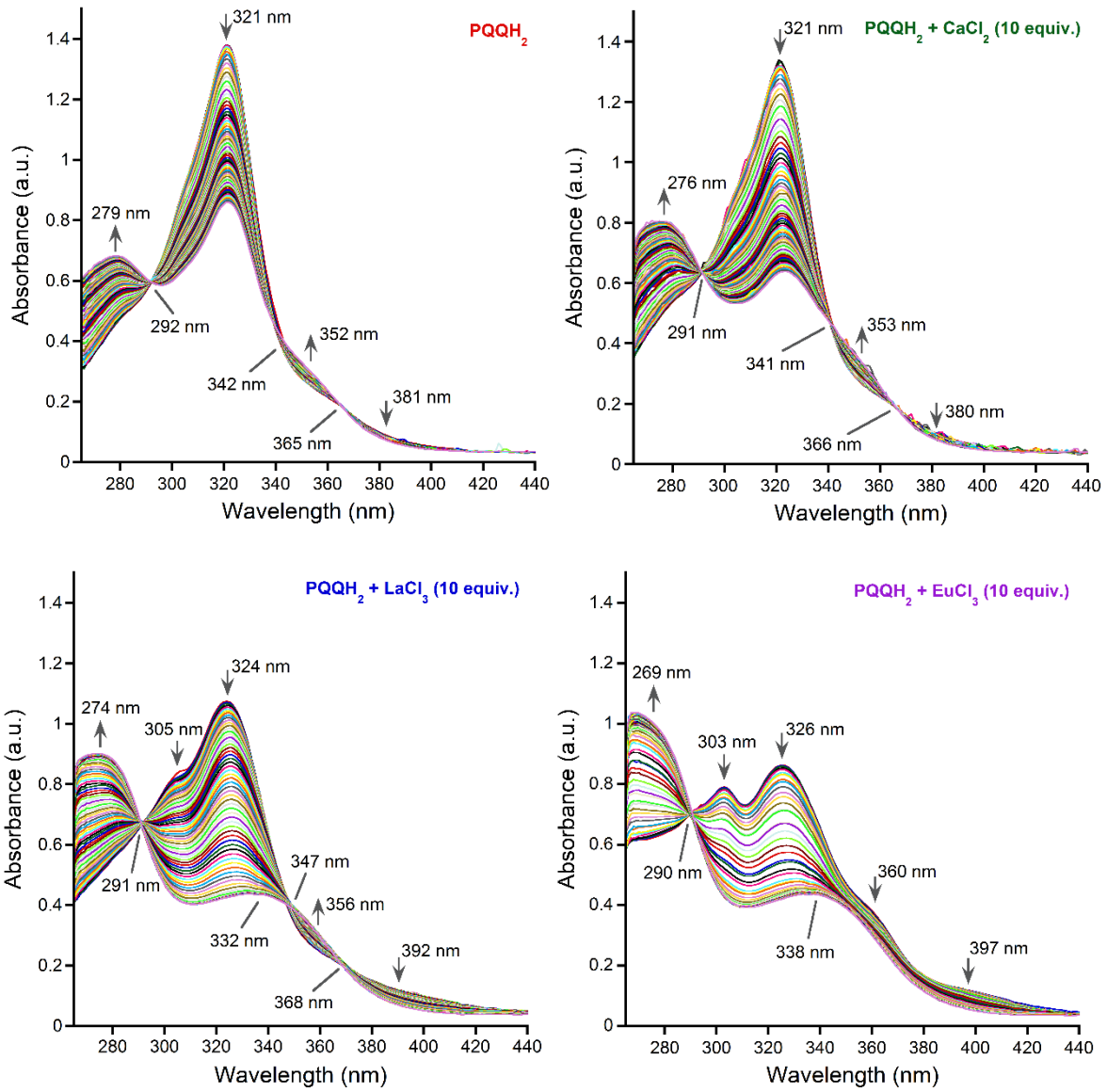

Figure V.10: Spectrophotometric analysis of the reoxidation of $PQQH_2$ (33.3 µM) in DMF (2.99 mL) and H_2O (10 µL, 183 mM) with controlled ionic strength ($LiClO_4$, 72.3 mM) under air without metal addition (top-left) or with 10.0 equiv. (333.3 µM) $CaCl_2$ (top-right), $LaCl_3$ (bottom-left) or $EuCl_3$ (bottom-right) added.

The obtained spectra appeared similar to the ones received from measurements with 3.0 equiv. of added metal salt (see Figure V.8 and Figure V.9) with values for maxima and isosbestic points changed only marginally by 1-2 nm. As an exception, the shift of the final maximum at 338 nm for 10 equiv. $EuCl_3$ was more pronounced compared to the original 333 nm for 3 equiv. $EuCl_3$.

3.3. Evaluation of the Reoxidation Kinetics

To compare the spectra received from the $PQQH_2$ reoxidation experiments with 3 or 10 metal equiv., the absorbance of the decreasing maximum around 321 nm was normalized to values between 1 (first measurement) and 0 (last measurement) and plotted versus the elapsed time (Figure V.11). Without metal addition (red line), absorption of $PQQH_2$ increased for the first 2.5 minutes before the maximum started to diminish. For better comparison, the increasing maximum around 270 nm was plotted additionally, where no such delay was observed. The overall appearance of the metal addition curves remained the same for both plots, but the curve for metal free $PQQH_2$ (red line) was now almost identical to the ones received from Ca^{2+} addition (green lines). An effect on the reoxidation of $PQQH_2$ is therefore questionable. The curves for 3 and 10 equiv. Ca^{2+} are in close proximity, especially for the maxima around 270 nm, while the small deviation is probably within the error of the experiment. This is also the case for Eu^{3+} addition (violet curves), where the raise to 10 equiv. is not reflected by a different curve progression. However, the addition of Eu^{3+} clearly accelerated $PQQH_2$ reoxidation, as the curves are steeper for both plots and stagnated already after 2500 s (maxima around 320 nm), indicating a shorter reaction time until $PQQH_2$ is completely oxidized back to PQQ. The curves for La^{3+} addition (blue curves) show a different progression and are therefore rather difficult to interpret. With 3 equiv. La^{3+}, the curve appears less steep than without metal addition. Unlike in the other experiments, the raise to 10 equiv. La^{3+} has a clear impact on the curve, now showing a faster acceleration and reaching stagnation after about 3200 s (maximum around 320 nm). In summary, Ca^{2+} shows no effect on $PQQH_2$ reoxidation, while Eu^{3+} clearly accelerates the reaction. La^{3+} accelerates the reaction only with 10 but not with 3 equiv.

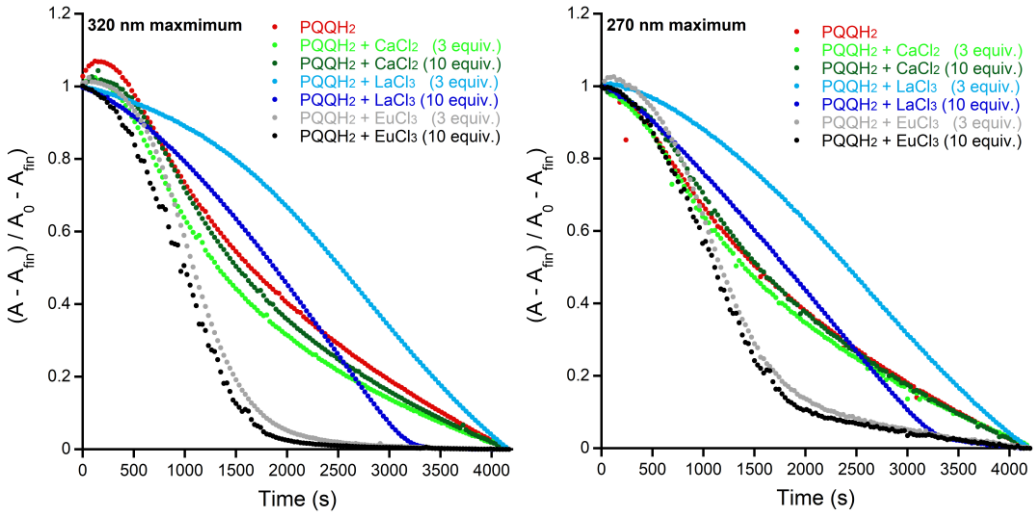

Figure V.11: Normalized absorbance of the maximum at left: 321 nm (PQQ; PQQ + $CaCl_2$), 324 nm (PQQ + $LaCl_3$) or 328 nm (PQQ + $EuCl_3$) or right: 279 nm (PQQ; PQQ + $CaCl_2$), 274 nm (PQQ + $LaCl_3$) or 270 nm (PQQ + $EuCl_3$) *vs.* time (s) for measurements of $PQQH_2$ (33.4 or 33.3 µM) in DMF (2.99 mL) and H_2O (100 µL, 1.83 M) with controlled ionic strength ($LiClO_4$, 73.1 or 72.3 mM) under air, with or without the addition of $CaCl_2$, $LaCl_3$ or $EuCl_3$ (3.0 equiv. - 100.2 µM or 10.0 equiv. - 333.3 µM). Spectra recorded every 30 seconds. A = absorbance, A_0 = starting absorbance, A_{fin} = final absorbance.

The findings are in contradiction to the ones received in V.3.2 - Figure V.7. The addition of 1.5 equiv. La^{3+} or Ca^{2+} led to a decelerated reoxidation in both cases. However, the experimental setup was different, with larger amounts of H_2O (3 vol% *vs.* 0.3 vol%) and less $LiClO_4$ (3.34 mM *vs.* 72-73 mM). Water was already mentioned to stabilize the intermediate semiquinone,[227] and is needed to reoxidize $PQQH_2$ in DMF. Redox cycling appears much more simplified in water than in organic solvents, as discussed in the following electrochemistry section (Chapter V.4). Having enough water present to accelerate reoxidation, the coordinating metals show a slowing effect. Vice versa, having only small amounts of water available, complexation leads to an acceleration, at least for Eu^{3+} and La^{3+} in higher concentrations.

But how is the reoxidation influenced by metals in detail? Kharisov *et al.* summarize the coordination chemistry of o-quinones in their review.[229] Coordinating metals are known to stabilize radical species.[230] As quinone redox processes normally proceed *via* $1e^-$ steps including semiquinone radicals,[229] this could also be of relevance here and depending on the coordinating metal, the transitional semiquinone $PQQ^{\bullet-}$ species could be stabilized differently well. Especially Yb can stabilize radical ligands,[231-232] however, the participation of the Yb^{2+} oxidation state is described, which is only accessible for few other lanthanides (Nd, Sm, Eu, Dy).[86] Stable complexes of Nd^{3+} with three different oxidation states of iminoquinones are known without changing the +3 neodymium oxidation state.[233] As seen in Chapter II.3.2.3, the different metal ions only had a small influence on the position of the LUMO and HOMO in calculations for the active side of XoxF

MDH with PQQ or $PQQ^{\bullet-}$. A complete complexation can be assumed when comparing the overall similar spectra in Figure V.4 (1.5 metal equiv.), Figure V.8 - Figure V.9 (3.0 metal equiv.) and Figure V.10 (10 metal equiv.) and the similar curve progressions of 3.0 and 10 metal equiv. for Ca^{2+} or Eu^{3+} in Figure V.11. On the other hand, the total amount of added H_2O accelerates the reoxidation rate, since H_2O_2 is generated throughout the reaction, as already determined by Itoh *et al.*[226] One could argue that the added crystal water of the metal salts also increase the total amount of water in the reaction. Although, even with 10 equiv. of $EuCl_3{\cdot}6H_2O$, the amount of water is only increased by 1% or 60 equiv. compared to the already added 10 µL (5541 equiv.). Differences of the added metal ions are apparently the more important factor. Lanthanide aqua complexes are prone to hydrolysis and thus commonly reduce the pH by proton abstraction from the hydration sphere.[234]

$$[Ln(H_2O)_8]^{3+} + H_2O \rightarrow [Ln(H_2O)_7(OH)]^{2+} + H_3O^+$$

This would fit to the received curves, which decrease faster the stronger the Lewis acidity of the added metal ion is (Eu > La > Ca), at least for the experiment with 10 equiv. of added metal salt. However, only 10 µL of water are present in solution and the solvation sphere is more likely saturated with DMF $[Ln(DMF)_8]^{3+}$.[123] Nevertheless, the influence of acids on the reoxidation of $PQQH_2$ should be tested in future experiments. In addition, possibilities should be evaluated to buffer the DMF/H_2O solvent mixture. However, it should be mentioned that $PQQH_2$ is described stable in acidic environments below pH 4, even in the presence of oxygen.[181] Coordinated metals to the $PQQH_2$ quinol could also lead to facilitated deprotonation, concurrent to stabilization of the then negatively charged oxygen intermediate (Scheme V.1).

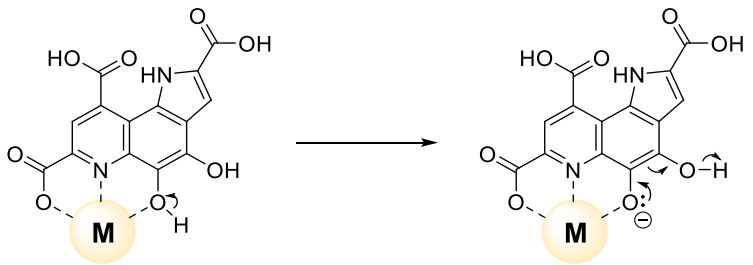

Scheme V.1: Possible reoxidation of $PQQH_2$, accelerated by coordinated metals. M = Ca^{2+}, Ln^{3+}.

Facilitated deprotonation and stabilization would be both positively influenced by increased Lewis acidities of the central metal through electron density reduction of the coordinating oxygen. Similarities in energy levels are important for shifts in charge distribution

between metal and ligand,[235] and orbital energies of the central metal need to be especially low for metal localization of electron-density.[236]

However, both theories do not explain the different shape of the La^{3+} curves in Figure V.11, a phenomenon which could not be ultimately clarified.

3.4. Conclusion

Reduction of PQQ with ascorbic acid and reoxidation of $PQQH_2$ with oxygen was studied throughout this chapter by UV-Vis measurements. The influence of added lanthanides and calcium was analyzed for both redox reactions in order to better understand the role of those metals in enzymatic MDH activity. While no acceleration was observed for the reduction from PQQ to $PQQH_2$, the reoxidation of $PQQH_2$ was accelerated with Eu^{3+} and 10 equiv. of La^{3+} but not with Ca^{2+}. The opposite effect – deceleration of the reoxidation was observed for Ca^{2+} and La^{3+} when larger amounts of water were available in the system. While the exact role of the different metals on reoxidation could not be clarified, also the changing Lewis acidity has to be taken into account, which has an influence on both pH and the proton abstraction of $PQQH_2$. While measurements in buffered aqueous solvents are not possible due to their precipitation, DMF can directly buffered instead to produce comparable kinetic reoxidation experiments with calcium and lanthanides. Literature shows that a pH value can also be determined for solvents other than water.[237-238] Since glass electrodes can even be used for measurements in DMF,[239] common buffer substances could be tested for usability in this solvent.

4. Electrochemistry of PQQ

4.1. Introduction

The electrochemistry of PQQ has already been extensively studied in the past, including cyclic voltammetry (CV) measurements of PQQ (**13**) and $PQQMe_3$ (**11**) in aqueous and organic solutions and with or without calcium addition. Table V.2 summarizes the literature available and reported potentials.

Table V.2: Oxidation, reduction and $E_{1/2}$ potentials of PQQ and related compounds, taken from the literature and standardized to SHE in Volt (V). *Used reference. Q for quinone, QH for quinol and Q•− for semiquinone. [a]0.1 M Na_2HPO_4 buffer, [b]2 M sodium salicylate buffer, [c]Na_2HPO_4+HNO_3 buffer, [d]0.5 M $HClO_4$ buffer, [e]0.5 M KH_2PO_4 buffer, [f]0.5 M NaOAc buffer, [g]0.1 M Et_4NClO_4, [h]0.1 M Bu_4NPF_6, [i]0.1 M nPr$_4$N][BAr$^F_4$]. Values referenced to Fc/Fc^+ were converted to SHE, according to Aranzaes *et al.*[240] and Pavlishchuk *et al.*[241]. The same electrolyte was used for [172] and the references [240] and [241] (0.10 M Bu_4NPF_6). [114] used a different electrolyte (0.10 M [nPr$_4$N][BAr$^F_4$]) so this conversion is not as accurate. Conversion factors are: +0.241 (SCE→SHE); 0 (NHE→SHE); +0.475 (DCM), +0.382 (MeCN) and +0.435 (DMSO), respectively for (Fc/Fc^+ →SCE).

Ref.	Compound	Solvent (pH)	*	Standardized to SHE [V]
[179, 181]	PQQ	H_2O (2)[a]	SHE	0.42 ($E_{1/2}$) (Q/QH)
[179, 181]	PQQ	H_2O (7)[a]	SHE	0.09 ($E_{1/2}$) (Q/QH)
[179, 181]	PQQ	H_2O (13)[b]	SHE	−0.22 ($E_{1/2}$) (Q/Q•−), −0.24 ($E_{1/2}$) (Q•−/QH)
[179]	PQQ	H_2O (7.2)[c]	SCE	0.51 ($E_{1/2}$) (Q/Q•−/QH), −0.87 (red) (Dihydroquinol)
[242]	PQQ	H_2O (0.3)[d]	NHE	0.51 ($E_{1/2}$) (Q/QH)
[242]	$PQQMe_3$	H_2O (0.3)[d]	NHE	0.53 ($E_{1/2}$) (Q/QH)
[242]	PQQ	H_2O (2.89)[e]	NHE	0.34 ($E_{1/2}$) (Q/QH)
[242]	PQQ+Zn(II)	H_2O (2.89)[e]	NHE	0.34 ($E_{1/2}$) (Q/QH)
[242]	$PQQMe_3$	H_2O (3.01)[e]	NHE	0.38 ($E_{1/2}$) (Q/QH)
[242]	$PQQMe_3$+Zn(II)	H_2O (3.01)[e]	NHE	0.38 ($E_{1/2}$) (Q/QH)
[242]	PQQ	H_2O (5.6)[f]	NHE	0.15 ($E_{1/2}$) (Q/QH)
[242]	PQQ+Zn(II)	H_2O (5.6)[f]	NHE	0.23 ($E_{1/2}$), 0.17 ($E_{1/2}$)
[242]	PQQ	DMF[g]	NHE	−0.05(0.8) (red) ([QQ•−]), −0.71 (red) ([(Q•−)$_2$]), −0.94 (red) (QH), −1.53 (red) ([(Q•−)$_2$]) ⟶ Q•− + QH)*
[242]	PQQ+DBN	DMF[g]	NHE	−1.09 (red) (Q ⟶ QH)
[242]	$PQQMe_3$	MeCN[g]	NHE	0.05 (red) ([QQ•−]), −0.69 (red) ([(Q•−)$_2$]), −0.97 (red) (QH)*
[242]	$PQQMe_3$+DBN	MeCN[g]	NHE	no effect – same as above
[172]	$PQQMe_3$	DCM[h]	Fc/Fc^+	−0.22 (red), −0.66 (red), −0.76 (red), −0.64 (ox), −0.42 (ox), 0.29 (ox), 0.54 (ox)*
[172]	$PQQMe_3$	MeCN[h]	Fc/Fc^+	−0.13 (red), −0.63 (red), −0.77 (red), −0.67 (ox), −0.44 (ox), 0.44 (ox)*
[172]	$PQQMe_3$	DMSO[h]	Fc/Fc^+	−0.12 (red), −0.55 (red), −0.66 (red), −0.57 (ox), −0.39 (ox), 0.07 (ox), 0.48 (ox)*
[172]	PQQ-Me_4	DCM[h]	Fc/Fc^+	−0.18 ($E_{1/2}$) (Q/Q•−)
[172]	PQQ-Me_4 +HOAc	DCM[h]	Fc/Fc^+	~ −0.18 (red) , 0.38 (ox) protonation and disproportionation of Q•−, followed by reoxidation
[172]	PQQ-Me_4 +$Ca(ClO_4)_2$	MeCN[h]	Fc/Fc^+	0.29 ($E_{1/2}$) (Q/Q•−), 1.06 (ox) (protonation, disprotportionation and reoxidation as above)
[114]	L_{QQ}	DCM[i]	Fc/Fc^+	−0.23 ($E_{1/2}$) (Q/Q•−), −1.04 (red) (Q•−/QH)
[114]	[La(L_{QQ})(NO_3)$_3$]	DCM[i]	Fc/Fc^+	0.38 ($E_{1/2}$) (Q/Q•−), 0.04 (red), −0.05 (red), 0.06 (ox), 0.20 (ox) → dimerization equilibria and loss of NO_3^-

In 1990, Kano *et al*. published CV measurements of PQQ in buffered aqueous solution, showing a redox process at a midpoint potential of −0.19 V and an irreversible cathodic wave at a peak potential of −1.11 V *vs*. SCE.[179] By comparison with simulations, the redox couple was assigned by the authors to a two-step one-electron mechanism via the semiquinone $PQQ^{\bullet-}$ (Figure V.12). The irreversible wave was assigned to the reduction of reduced $PQQH_2$ to PQQ 4,5 dihydroquinole. As described by the authors, PQQ forms several acid-base and redox equilibria in aqueous solutions (Figure V.12).

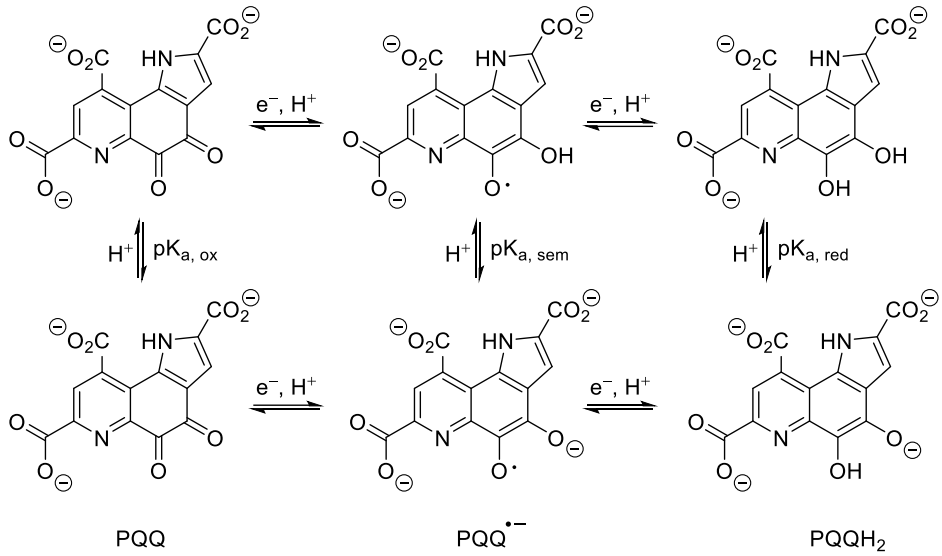

Figure V.12: Acid-base and redox equilibria of PQQ, $PQQ^{\bullet-}$ and $PQQH_2$. Reported from Kano *et al.*[179]

In 1982, Eckert el at. published CV measurements of PQQ, $PQQMe_3$ and structural analoga in aqueous media, in DMF and in MeCN.[242] Unfortunately, insufficient experimental details without PQQ concentrations were given and no CVs were shown. However, several midwave redox potentials were given for aqueous solutions at different pH values, which are described as single $2e^-$ steps. CV measurements in non-aqueous solvents were described to be more complicated with several reversible reduction steps.[242] While the number of transferred e^- was described to be difficult to measure, the authors mentioned, that reduction would not occur through single $PQQ \rightarrow PQQ^{\bullet-} \rightarrow PQQH_2$ $1e^-$ steps. Instead, four reduction potentials are given, which are explained by the authors with following scheme:

Couple I	$PQQ + e^-$	$\rightleftharpoons$	$PQQ^{\bullet-}$
	$PQQ + PQQ^{\bullet-}$	$\rightleftharpoons$	$[(PQQ)(PQQ^{\bullet-})]$
Couple II	$[(PQQ)(PQQ^{\bullet-})] + e^-$	$\rightleftharpoons$	$[(PQQ^{\bullet-})_2]$
	$[(PQQ^{\bullet-})_2]$	$\rightleftharpoons$	$2\ PQQ^{\bullet-}$
Couple III	$PQQ^{\bullet-} + e^-$	$\rightleftharpoons$	$PQQH^-$
Couple IV	$[(PQQ^{\bullet-})_2]\ e^-$	$\rightleftharpoons$	$PQQ^{\bullet-} + PQQH^-$

Scheme V.2: Proposed reduction steps of PQQ quinone to quinol in non-aqueous media. Reported from Eckert *et al.*[242]

By addition of the non-nucleophilic base 1,5-diazabicyclo[4,3,0]non-5-ene (DBN), the reduction potential of PQQ was simplified to a $2e^-$ transfer, while the addition of DBN to $PQQMe_3$ showed no effect. The authors explained this with electrostatic repulsive forces of the now deprotonated carboxyl groups, which prevented association of radical species as described in Scheme V.2.

In 1998 Itoh *et al.* published CV measurements of $PQQMe_3$ in DCM, MeCN and DMSO.[172] The recorded CVs showed several isolated reduction and oxidation processes as it was also described by Eckert *et al.*[242] The authors described the occurrence of those isolated reduction and oxidation processes with several radical species, which can interact with each other and which are subject to acid-base equilibria as well.[172]

reduction

$$1_{ox}H + e^- \rightarrow 1_{rad}H^-$$
$$1_{rad}H^- + e^- \rightarrow 1_{red}H^{2-}$$
$$1_{ox}^- + e^- \rightarrow 1_{rad}^{2-}$$

oxidation

$$1_{rad}^{2-} \rightarrow 1_{ox}H + e^-$$
$$1_{red}H^{2-} \rightarrow 1_{rad}H^- + e^-$$
$$1_{red}H^{2-} \rightarrow 1_{rad}H_2 + e^-$$
$$1_{red}H_3 \rightarrow 1_{rad}H_3 + e^-$$

acid-base equilibrium

$$1_{rad}H^- + 1_{ox}H \rightleftharpoons 1_{rad}H_2 + 1_{ox}^-$$
$$1_{red}H^{2-} + 1_{ox}H \rightleftharpoons 1_{red}H^{2-} + 1_{ox}^-$$

disproportionation

$$1_{rad}H_2 \rightarrow ½\ 1_{ox}H + ½\ 1_{red}H_3$$

Scheme V.3: Proposed reduction and reoxidation processes of $PQQMe_3$ ($1_{ox}H$), as well as acid-base equilibria and disproportionation reactions. Reported from Itoh *et al.*[172]

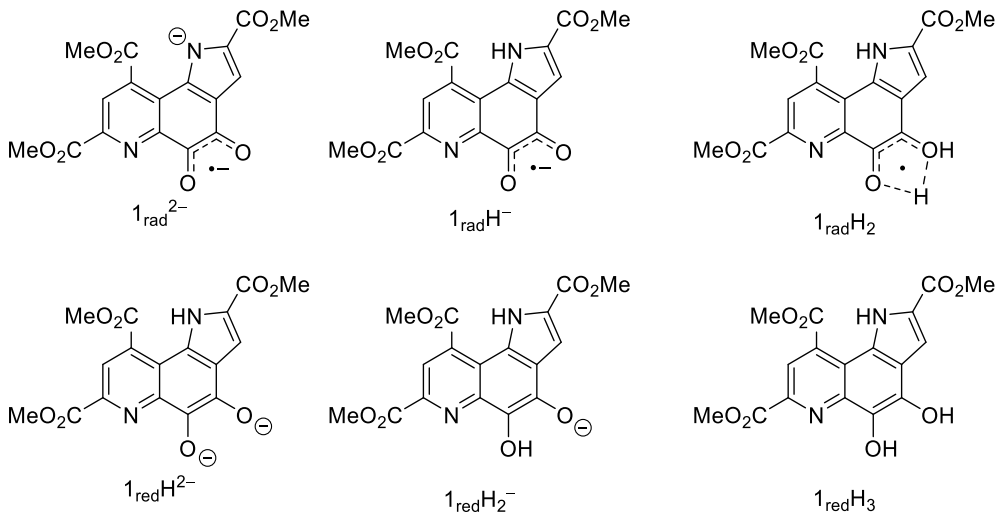

Scheme V.4: Structures and nomenclature of several proposed intermediate states during the reduction of $PQQMe_3$ ($1_{ox}H$).[172]

By using a fully methylated species $PQQ\text{-}Me_4$ ($1_{ox}Me$ – methylated pyrrol-N), the CV simplified to a reversible $1e^-$ redox couple at $E_{1/2} = -0.90$ V *vs.* Fc/Fc^+, corresponding to $1_{ox}Me/1_{rad}Me^-$. By the addition of equimolar amounts of acetic acid, the oxidation peak current

at −0.84 V disappeared while a new oxidation peak appeared at −0.34 V. The now irreversible redox process is explained by protonation of the generated $1_{rad}Me^-$ to $1_{rad}MeH$, which disproportionates into ½ $1_{ox}Me$ and ½ $1_{red}MeH_2$ of which the latter is then oxidized at −0.34 V. The authors also examined the influence of calcium on the redox behavior of $1_{ox}Me$ in MeCN. After the addition of one equivalent of $Ca(ClO_4)_2 \cdot nH_2O$, the $1e^-$ redox couple was positively shifted by 0.57 V. Due to protonation by the now present water and disproportionation of the reduced $1_{rad}Me^-$ species (as described above) the oxidation peak was again shifted to higher voltage (0.44 V). Due to the positive redox shift caused by calcium, the authors postulated a significant enhancement of PQQs oxidation power in MDH when coordinated to calcium.

After the discovery of lanthanide dependent methanol dehydrogenases, the question arose, in which way those metals would influence the electrochemistry of PQQ and if they would be superior over calcium in activating the cofactor for methanol oxidation.

Schelter *et al.* synthesized the model ligand L_{QQ} and were able to show lanthanum coordination as $[La(L_{QQ})(NO_3)_3]$.[114]

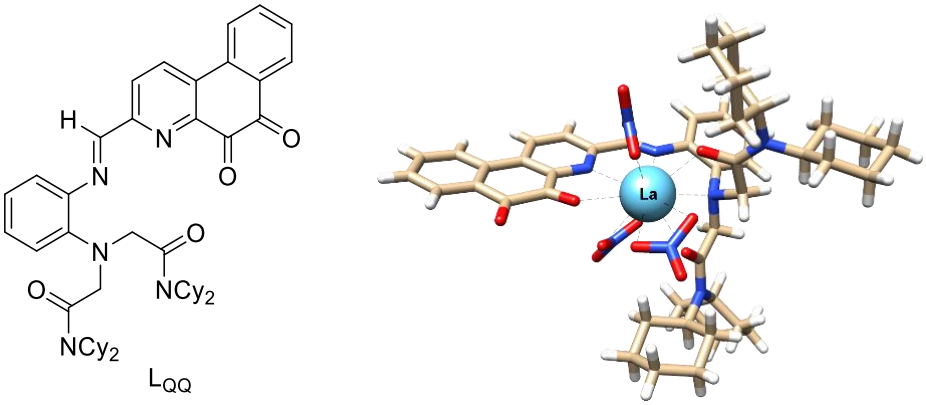

Figure V.13: Left: Model ligand L_{QQ}, containing a benzoquinoline quinone as structural analogon to PQQ. Right: Crystal structure of $[La(L_{QQ})(NO_3)_3]$. Reported from Schelter *et al.*[114]

CV of L_{QQ} gave a reversible redox process at $E_{1/2} = -0.95$ V, which was assigned by the authors as the quinone-semiquinone ($QQ/QQ^{\bullet-}$) couple. An irreversible reduction wave at E = −1.76 was assigned as formation of the catecholate dianion (Q^{2-}).

When coordinated to lanthanum ($[La(L_{QQ})(NO_3)_3]$), the $QQ/QQ^{\bullet-}$ redox couple was shifted towards more positive potentials at $E_{1/2} = -0.34$ V, explained by stabilization of the $QQ^{\bullet-}$ anion by the coordinated metal ion. Further, poorly reversible reductions were visible, which are explained as loss of NO_3^- ligands and dimerization equilibria. Related to the positive redox shift upon lanthanum coordination, the authors could further show that $[La(L_{QQ})(NO_3)_3]$ was able to oxidize $^{4Me}BnOH$ to $^{4Me}PhCHO$ in DCM, which was not possible by the free ligand L_{QQ} alone.

4.2. Measurements of $PQQMe_3$ in Non-aqueous Solvents

Investigation began with the reproduction of literature known CV measurements. Itoh *et al.* showed cyclovoltammograms of $PQQMe_3$ in DCM and MeCN with corresponding reduction and oxidation potentials (Figure V.14).[172]

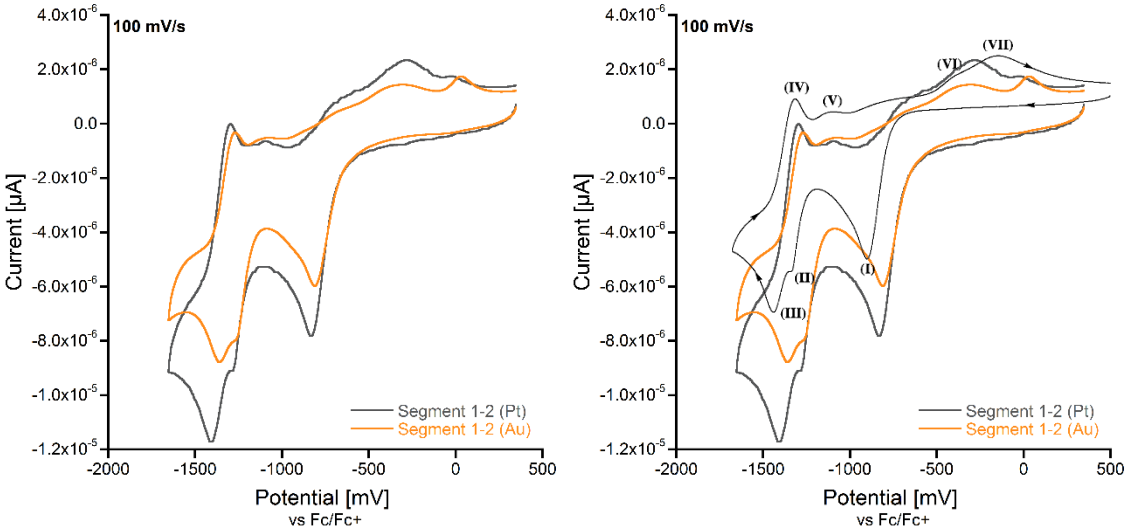

Figure V.14: Left: $PQQMe_3$ (0.001 M) + Bu_4NPF_6 (0.1 M) in DCM. WE: Pt/Au, CE: Pt-wire, RE: Ag-wire pseudo. Right: Superposition of experimental CVs and the literature known one from Itoh *et al.*[172] Reprinted with permission from Itoh *et al.*[172] Copyright (1998) American Chemical Society.

The experimental procedures were reproduced as closely to the experimental description as possible, but although the general shape of the received CVs was quite similar to the literature ones, the potentials of the oxidation and reduction waves differed up to 100 mV (Table V.3).

Table V.3: Reduction and oxidation peak potentials of $PQQMe_3$ in anhydrous DCM (mV *vs.* Fc/Fc^+). Sweep rate = 100 mV s^{-1}.

	Reduction (mV)			Oxidation (mV)			
	I	II	III	IV	V	VI	VII
Pt	−833	−1285	−1403	−1299	−1097	−285	−14
Au	−807	−1257	−1354	−1271	−1104	−340	35
Lit.(Au)[172]	−940	−1380	−1480	−1360	−1140	−430	−180

The experiment was repeated in MeCN, yielding a similar shaped CV as for the DCM measurement (Figure V.15).

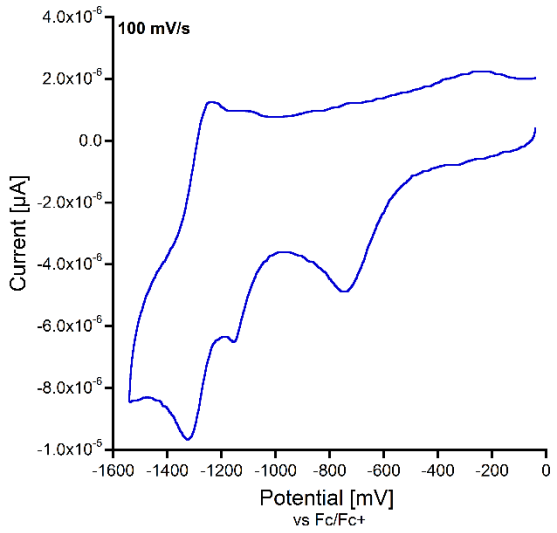

Figure V.15: $PQQMe_3$ (0.001 M) + Et_4NClO_4 (0.1 M) in MeCN. WE: Pt, CE: Pt-wire, RE: Ag-wire pseudo.

In this case, the literature values for the reduction and oxidation waves fitted better to the experimental ones, taking the different electrode materials (Pt *vs*. Au) into account (Table V.4).

Table V.4: Reduction and oxidation peak potentials of PQQMe3 in anhydrous MeCN (mV *vs*. Fc/Fc+). Sweep rate = 100 mV s-1.

	Reduction (mV)			Oxidation (mV)			
	I	II	III	IV	V	VI	VII
Pt	−833	−1285	−1403	−1299	−1097	−285	−14
Lit. (Au)[172]	−807	−1257	−1354	−1271	−1104	−340	35

While the available lanthanide salts (chlorides and nitrates) were not soluble in DCM, metal titration with $La(NO_3)_3$ was performed with $PQQMe_3$ in MeCN (Figure V.16).

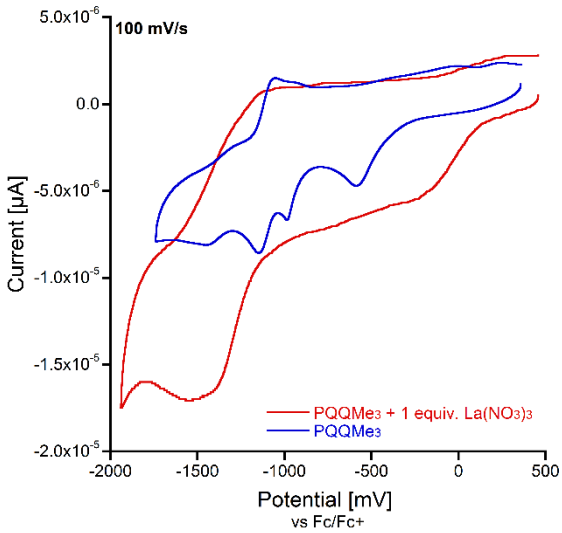

Figure V.16: $PQQMe_3$ (0.001 M) + Et_4NClO_4 (0.1 M) in MeCN (led line) + 1.0 equiv. of $La(NO_3)_3{\cdot}6H_2O$ (blue line) at 100mV/s. WE: Pt, CE: Pt-wire, RE: Ag-wire pseudo. Voltammograms are not reproducible and change every measurement.

Unfortunately, the voltammogram changed completely upon metal addition with very broad reduction and oxidation waves, making an interpretation unfeasible. In addition, the received voltammograms were non-reproducible and changed their appearance and position of the reduction and oxidation waves after every measurement. Therefore, the solvent system was switched to DMF.

In DMF, the CVs of $PQQMe_3$ were even more complex, and multiple isolated reduction and oxidation processes were visible especially with decreased scan rates (Figure V.17).

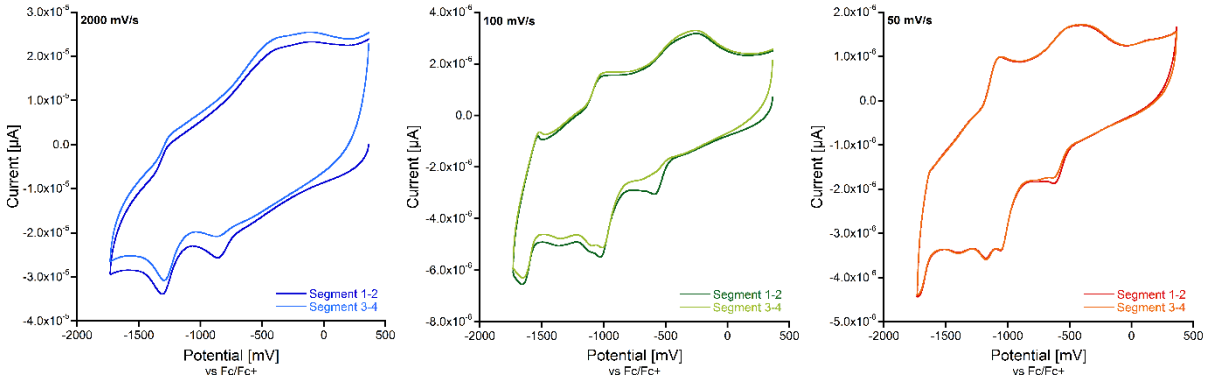

Figure V.17: $PQQMe_3$ (0.001 M) + Et_4NClO_4 (0.1 M) in DMF. WE: Pt, CE: Pt-wire, RE: Ag-wire pseudo.

Keeping the complex redox processes of PQQ species in non-aqueous media in mind as described by Eckert[242] and Itoh[172], the correct assignment of the visible reduction and oxidation processes is nontrivial and requires supporting simulated voltammograms.

The influence of lanthanum on the CVs of $PQQMe_3$ in DMF was tested as well (Figure V.18).

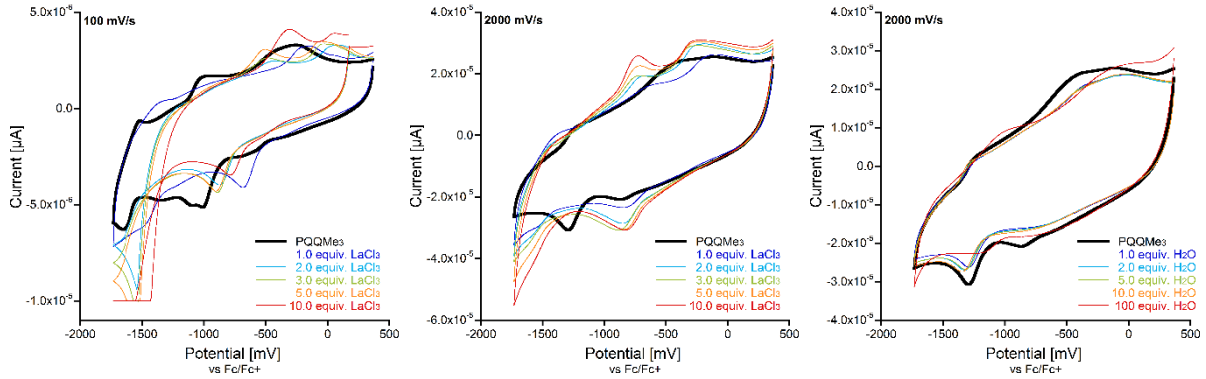

Figure V.18: $PQQMe_3$ (0.001 M) + Et_4NClO_4 (0.1 M) in DMF. Left and middle: Addition of $LaCl_3 \cdot 7H_2O$ in DMF (0.1 M – 10 µL per equiv.) Right: Addition of water. WE: Pt, CE: Pt-wire, RE: Ag-wire pseudo. Segments 3-4 are shown.

Already with 1.0 equiv. $LaCl_3 \cdot 7H_2O$, the potentials of the reduction processes were shifted to more positive values and simplified to a single peak. While the position of the peak varied with more equiv. of lanthanum at 100 mV/s, it remained constant with an increased scan rate of 2000 mV/s and only the current increased likely due to an increased conductivity with more ions in

solution. Due to the present crystal water in $LaCl_3 \cdot 7H_2O$, the sole influence of water was tested as well. Here, only larger amounts of water (100 equiv.) caused a change in the voltammogram.

4.3. Measurements of PQQ in Non-aqueous Solvents

In the next step, voltammograms of free PQQ were recorded and the influence of lanthanum, water and HCl was tested (Figure V.19). Similar to $PQQMe_3$, several reductions were visible (−1142 mV, −1242 mV, −1675 mV), as well as one oxidation (−775 mV). With 1.0 equiv. $LaCl_3 \cdot 7H_2O$ the received voltammogram changed drastically, with two reduction peaks at −642 mV and −1633 mV and two oxidation peaks at −1200 mV and −608 mV. With more lanthanum equiv., only one reduction peak was visible at −1375 mV to −1425 mV and one oxidation peak at −1333 mV to −1117 mV. With 10 equiv. of $LaCl_3 \cdot 7H_2O$ present, redox processes could no longer be observed.

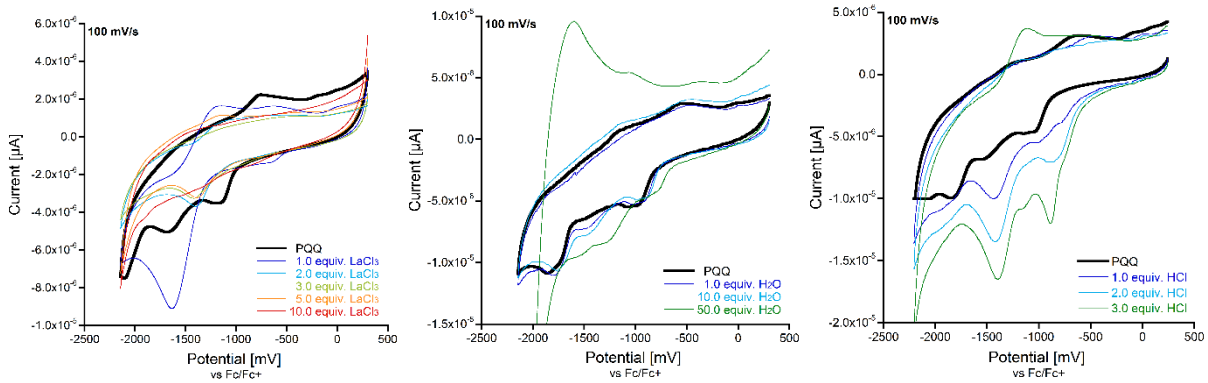

Figure V.19: PQQ (0.001 M) + Et_4NClO_4 (0.1 M) in DMF. Left: Addition of $LaCl_3 \cdot 7H_2O$ in DMF (0.1 M – 10 µL per equiv.) Middle: addition of water. Right: Addition of HCl (1 M). WE: Pt, CE: Pt-wire, RE: Ag-wire pseudo. Segments 1-2 are shown.

As a control, small amounts of water were added to the DMF solution of PQQ and no change of the voltammogram could be observed. Higher amounts of water (50 equiv.) led to a completely different voltammogram, though. Since protons are needed for the complete conversion of PQQ (quinone) to $PQQH_2$ (quinol), the influence of small amounts of added HCl was tested, which caused shifted reduction and oxidation peaks with growing currents.

With larger amounts of HCl (55 equiv.), the obtained voltammogram changed (Figure V.20). Two redox processes were now well observable, with the high current one at -965_{red} mV to -590_{ox} mV ($E_{½}$ = −777.5 mV) and a lower current one at -1430_{red} mV to -1236_{ox} mV ($E_{½}$ = −1333 mV).

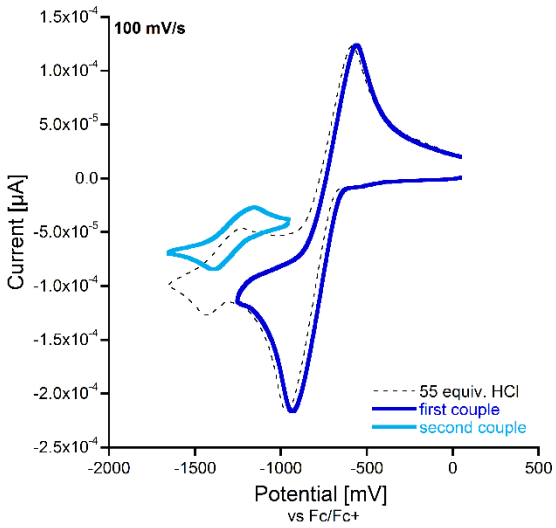

Figure V.20: PQQ (0.001M) + Et_4NClO_4 (0.1M) in DMF with 55 equiv. of HCl (1M). WE: Pt, CE: Pt-wire, RE: Ag-wire pseudo. Segments 1-2 are shown. Both redox processes can also be measured independently (blue lines).

The voltammogram could be drastically simplified with HCl, but the excess of acid would protonate all carboxyl groups of PQQ, making complexation with lanthanides unfavorable. Therefore, other solvent systems were required, which would allow complexation while limiting the number of different species.

4.4. Measurements of PQQ in H_2O/DMF Solvent Mixtures

The CV of PQQ in water shows a single two-step one-electron redox process for the quinone/quinol couple. In comparison, voltammograms recorded in non-aqueous media show multiple isolated reduction and oxidation processes, making interpretation challenging. Therefore, measurements in water would be preferable for investigations of the lanthanide-influence on redox processes of PQQ, but in this medium, lanthanide coordination always lead to precipitation. Therefore, solvent mixtures of DMF and water were tested. While large ratios of water still led to complex precipitation of PQQ with lanthanides, a 70:30 mixture of water and DMF still indicated complex formation as observed by a distinct color change, but precipitation was delayed and occurred not earlier than 15 minutes after metal addition. The CV of PQQ in this mixture showed two redox couples (Figure V.21).

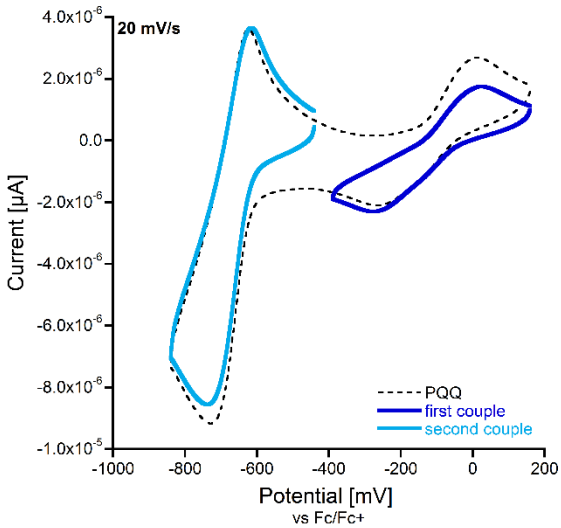

Figure V.21: PQQ (0.001 M) + Et_4NClO_4 (0.1 M) in a 70:30 H_2O/DMF mixture. WE: Pt, CE: Pt-wire, RE: Ag-wire pseudo. Segments 3-4 are shown. Both redox processes can also be measured independently (blue lines).

One couple appeared between -263_{red} mV and 10_{ox} mV ($E_{½}$ = −126.5 mV) and one couple between -730_{red} and -627_{ox} ($E_{½}$ = −678.5 mV).

4.5. Spectroelectrochemistry of PQQ in H_2O/DMF Solvent Mixtures

In order to assign the two redox processes of PQQ in 70:30 H_2O/DMF mixtures, bulk electrochemical reduction/oxidation of the sample was performed in combination with UV-Vis measurements (spectroelectrochemistry). Following spectra were received:

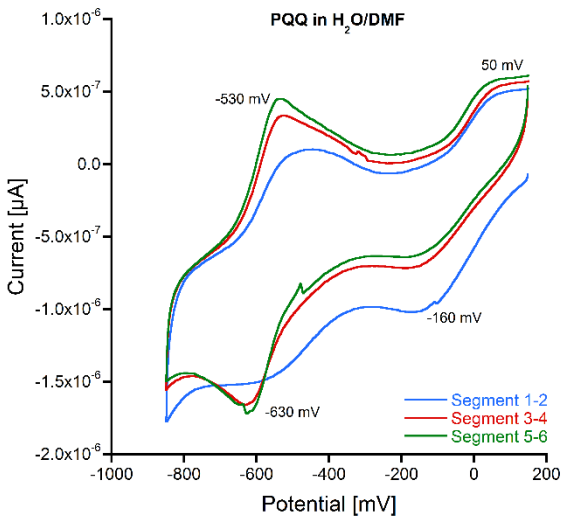

Figure V.22: PQQ (0.8 mM) + Et_4NClO_4 (0.1 M) in a 70:30 H_2O/DMF mixture. WE: Pt, CE: Pt-wire, RE: Ag-wire pseudo. Potentials are not referenced *vs*. the Fc/Fc^+ couple, as this voltammogram is used as overview over the different potentials at which UV-Vis measurements were performed.

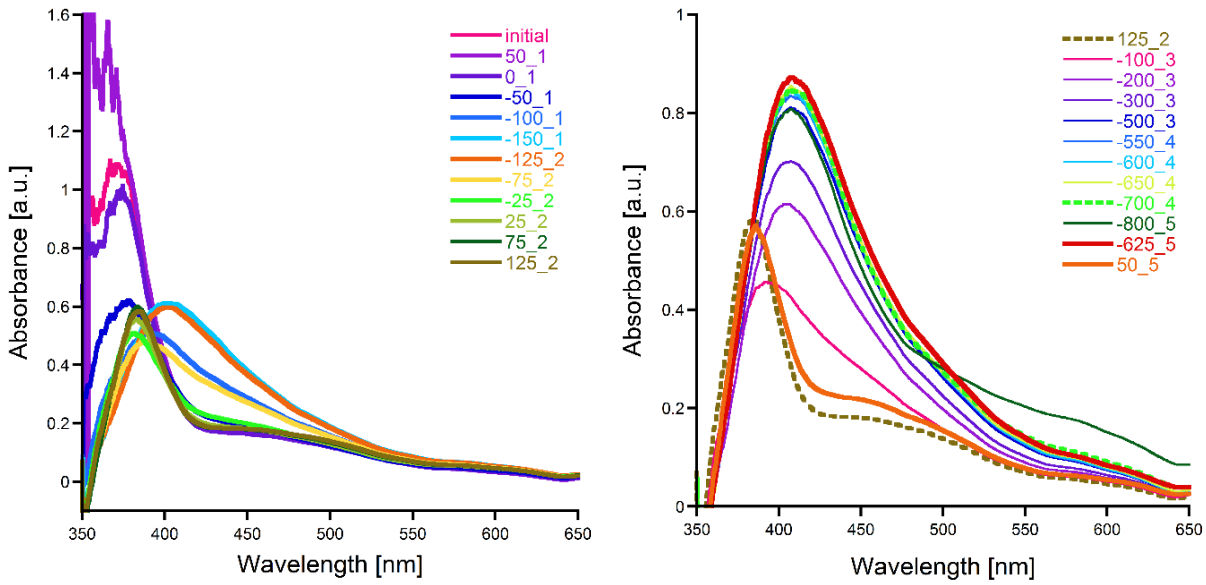

Figure V.23: UV-Vis spectra of PQQ (0.8 mM) + Et_4NClO_4 (0.1 M) in a 70:30 H_2O/DMF mixture at different potentials. Potentials are given in the legend, while the second number indicates a change in the direction of potential adjustment (cycle).

The first cycle went from 50 to −150 mV, in order to go through the first reduction peak. This led to a decrease of the absorbance maximum at 378 nm and finally to a shift of the maximum to 402 nm (light blue line - −150_1). By reincreasing the potential to 125 mV, the process was reversed and the absorbance maximum changed back to 383 nm, however, without reaching the initial high absorbance. In order to go through the second reduction peak, the potential was stepwise decreased to −700 mV (3-4 cycle). This led the absorbance maximum shift to 409 nm, accompanied with an increase of the absorbance. This spectrum, as well as the transformation through the different potentials appeared rather similar to spectra received from the reoxidation of $PQQH_2$ in a DMF/H_2O mixture (Figure V.4).

Although the maxima are shifted, the solvent systems are different – 70:30 H_2O/DMF for the spectroelectrochemical measurements compared to a 04:96 H_2O/DMF mixture for the $PQQH_2$ spectra. If both species are the same, then the second redox couple at $E_{½}$ = −678.5 mV would be the PQQ/$PQQH_2$ (quinone/quinol) pair, while the first couple at $E_{½}$ = −126.5 mV would still be unknown. It is feasible that the first redox couple is the PQQ/$PQQ^{\bullet-}$ while the second redox couple is the $PQQ^{\bullet-}$/$PQQH_2$ pair.

However contradicting this theory, the potential in the fifth cycle of the spectroelectrochemical measurement is reincreased from −700 mV. The conversion seems to be irreversible since the potential had to be set back to 50 mV (intermediate steps not shown),

to finally change the PQQ species back to the original one, skipping the species with a maximum at 402 nm (light blue line - −150_1).

4.6. Influence of Lanthanides and Calcium on the CV of PQQ in H_2O/DMF Mixtures

In a 70:30 H_2O/DMF mixture, complexes of PQQ with lanthanides remained in solution, hence it was possible to investigate the influence of lanthanides on the electrochemistry of PQQ. PQQ in DMF (0.1 M, 10 µL) was added to a solution of H_2O (700 µL, 0.1 M Et_4NClO_4) and DMF (280 µL, 0.1 M Et_4NClO_4) and a CV was recorded at 20 mV/s. Increasing amounts of metal chlorides in DMF (0.1 M, 10 µL per equiv.) were added to the solution and CV were measured. Used metal chlorides were $LaCl_3{\cdot}7H_2O$, $PrCl_3{\cdot}6H_2O$, $EuCl_3{\cdot}6H_2O$, $YbCl_3{\cdot}6H_2O$, $LuCl_3{\cdot}6H_2O$ and $CaCl_2{\cdot}2H_2O$.

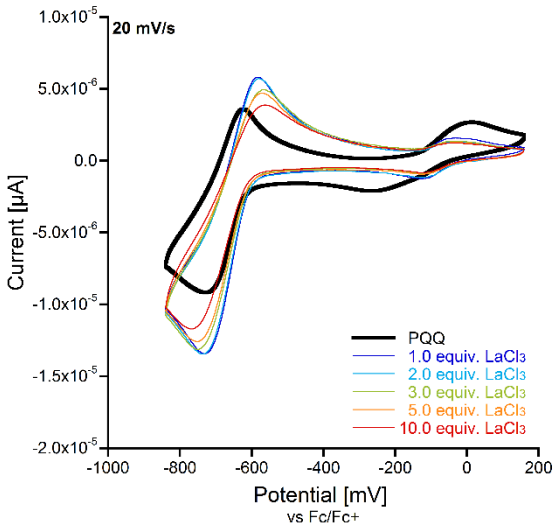

Figure V.24: CV's of PQQ (0.001 M) + Et_4NClO_4 (0.1 M) in a 70:30 H_2O/DMF mixture with increasing amounts of $LaCl_3{\cdot}7H_2O$ (0.1 M in DMF, 10 µL per equiv.). WE: Pt, CE: Pt-wire, RE: Ag-wire pseudo. Segments 3-4 are shown.

Upon addition of one equiv. of lanthanum, the $E_{1/2}$ value of the first redox pair shifted to more positive values and the distance of the positive and negative maximum decreased. With more metal equiv., the observed current slightly decreased, possibly caused by beginning precipitation, but the $E_{1/2}$ position stayed constant. The $E_{1/2}$ value for the second redox couple was shifted to more positive potentials upon lanthanum addition as well and further shifted with more metal equiv. Also in this case, the current decreased with more metal equiv., but stronger than for the first redox couple. Additional CVs were recorded with different lanthanides and calcium (Figure V.25).

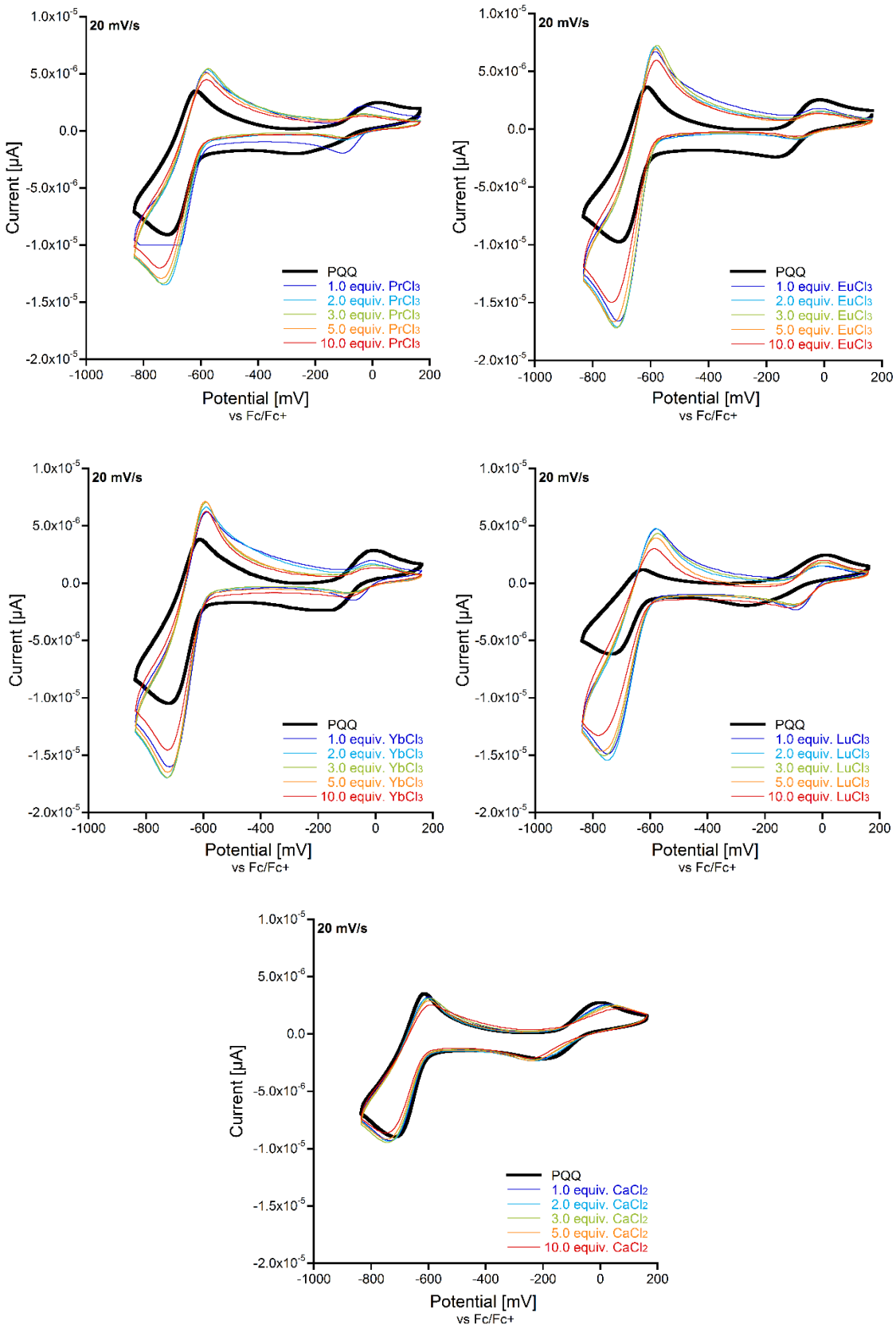

Figure V.25: CV's of PQQ (0.001 M) + Et_4NClO_4 (0.1 M) in a 70:30 H_2O/DMF mixture with increasing amounts of metal chlorides (0.1 M in DMF, 10 µL per equiv.). WE: Pt, CE: Pt-wire, RE: Ag-wire pseudo. Segments 3-4 are shown. Upper left: $PrCl_3 \cdot 6H_2O$; upper right: $EuCl_3 \cdot 6H_2O$; left: $YbCl_3 \cdot 6H_2O$; right: $LuCl_3 \cdot 6H_2O$; bottom: $CaCl_2 \cdot 2H_2O$.

Regardless of the added lanthanide, voltammograms appeared similar with only slight differences in the current and position of the maxima and minima. The CV obtained from PQQ with added calcium differed, since influence of calcium on the elecotrochemistry of PQQ was only minimal (Figure V.25). Table V.5 gives an overview over the maxima and minima and the corresponding $E_{1/2}$ values of the different CVs from Figure V.24 and Figure V.25.

Table V.5: Potentials of maxima, minima and corresponding $E_{1/2}$ values of PQQ (0.001 M) + Et_4NClO_4 (0.1 M) in 70:30 H_2O/DMF with one equiv. of metal chlorides (0.1 M in DMF, 10 µL per equiv.). Due to the varying values of the PQQ measurements (without metal), the maxima of the first couple were all set to 14 and the CV were shifted accordingly – those new values are given in additional column with grey backgrounds.

1.0 equiv.	first couple (mV)						second couple (mV)					
Lanthan	Maxima		Minima		$E_{1/2}$		Maxima		Minima		$E_{1/2}$	
PQQ	14	14	-262	-262	-124	-124	-623	-623	-728	-728	-676	-676
$LaCl_3$	-34	-34	-123	-123	-78.5	-79	-583	-583	-728	-728	-656	-656
Praseodym												
PQQ	18	14	-271	-275	-127	-131	-617	-621	-716	-720	-667	-671
$PrCl_3$	-30	-34	-103	-107	-67	-71	-579	-583	-719	-723	-649	-653
Europium												
PQQ	-16	14	-167	-137	-92	-62	-612	-582	-710	-680	-661	-631
$EuCl_3$	-19	11	-95	-65	-57	-27	-584	-554	-711	-681	-647.5	-618
Ytterbium												
PQQ	-8	14	-169	-147	-89	-67	-614	-592	-718	-696	-666	-644
$YbCl_3$	-16	6	-78	-56	-47	-25	-587	-565	-718	-696	-653	-631
Lutetium												
PQQ	11	14	-262	-259	-126	-123	-627	-624	-734	-731	-681	-678
$LuCl_3$	-3	0	-92	-89	-48	-45	-579	-576	-743	-740	-661	-658
Calcium												
PQQ	0	14	-199	-185	-100	-86	-614	-600	-716	-702	-665	-651
$CaCl_2$	29	43	-231	-217	-101	-87	-600	-586	-732	-718	-666	-652

For better comparison, only the values for one equiv. of metal are given in Table V.5. The values for PQQ alone (without metal) vary from experiment to experiment, even with ferrocene reference. On the one hand, those variations could occur due to self-made pseudo-reference electrodes used in the experiments (silver-wire in 70:30 H_2O/DMF + Et_4NClO_4 (0.1 M)), were the depth of immersion could already cause differences. On the other hand, the ferrocene measurements were always taken isolated under the same conditions after the experimental measurements (external standart). An internal standard (small amounts of ferrocene in every measurement) would give more accurate data, but the redox potential of ferrocene overlaps with the first redox couple of PQQ. Other standards could be used, as cobaltocene or

decamethylferrocene, but experiments, where small amounts of ferrocene or cobaltocene were added to solutions of PQQ and lanthanide chlorides failed. Immediate color change to black was observed, together with precipitation of a black solid and complete change of the received CV. A chemical interaction of the internal standard with PQQ or the lanthanides seemed to occur, which excluded this method.

In order to better compare the data in Table V.5, the maxima of the first couple for the PQQ measurements were all set to 14 mV and all CV were shifted accordingly. By comparison of the $E_{1/2}$ values before and after lanthanide addition, all $E_{1/2}$ values for both first and second redox couple are shifted to more positive values. Therefore, those metals seem to enhance the reduction ability of PQQ and its oxidation power towards substrates like methanol. Due to the described variations in the redox potentials between experiments, direct comparison between the different lanthanides should be treated with caution. Table V.6 gives the differences between PQQ potentials before and after metal addition. While the second couple is influenced in a similar fashion, the differences for the first couple are larger, but no clear pattern can be observed, such as increasing shifts throughout the lanthanide series.

Table V.6: $E_{1/2}$ values of for the redox couple of PQQ (0.001 M) in 70:30 H_2O/DMF + Et_4NClO_4 (0.1 M) with one equiv. of metal chlorides (0.1 M in DMF, 10 µL per equiv.) and the differences of both measurements.

1.0 equiv.	first couple (mV)		second couple (mV)	
Lanthan	$E_{1/2}$	Difference	$E_{1/2}$	Difference
PQQ	-124	45	-676	20
$LaCl_3$	-79		-656	
Praseodym				
PQQ	-131	60	-671	18
$PrCl_3$	-71		-653	
Europium				
PQQ	-62	35	-631	13
$EuCl_3$	-27		-618	
Ytterbium				
PQQ	-67	42	-644	13
$YbCl_3$	-25		-631	
Lutetium				
PQQ	-123	78	-678	20
$LuCl_3$	-45		-658	
Calcium				
PQQ	-86	1	-651	1
$CaCl_2$	-87		-652	

As already seen in Figure V.25, the addition of calcium leads to small shifts of the maxima and minima, whereas the $E_{1/2}$ values stay constant.

4.7. Influence of Acids and Bases on the CV of PQQ in H_2O/DMF Solvent Mixtures

In order to examine the influence of pH variations on the electrochemistry of PQQ, small amounts of acid (HCl) or base (NEt_3) were added to PQQ in a 70:30 H_2O/DMF solution. The addition of HCl (1 M in H_2O, 1 µL per equiv., Figure V.26) did not change the overall shape of the received voltammograms, but largely increased the current, especially for the second redox couple. In addition, small shifts towards more positive potentials could be observed. Protons are required for the complete conversion from quinone to quinol, which could explain the enhanced redox processes, especially for the largely increased reduction.

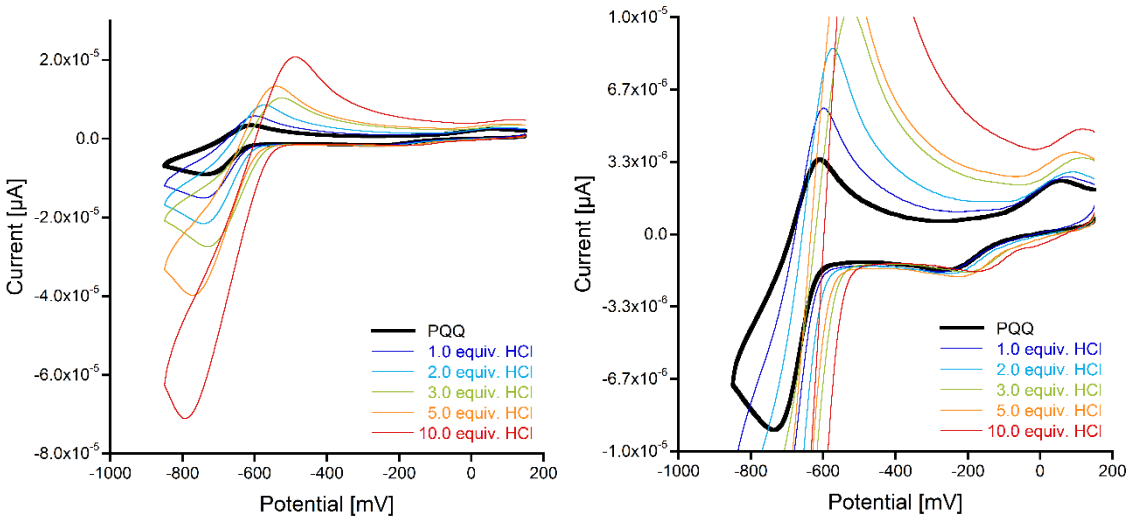

Figure V.26: Left: CV's of PQQ (0.001 M) + Et_4NClO_4 (0.1 M) in a 70:30 H_2O/DMF mixture with increasing amounts of HCl (1 M in H_2O, 1 µL per equiv.). WE: Pt, CE: Pt-wire, RE: Ag-wire pseudo. Segments 3-4 are shown. Right: Closeup of the CV's.

The addition of NEt_3 (0.14 µL per equiv.) caused similar changes (Figure V.27). The voltammograms were shifted towards more positive potentials and the current largely increased. Interestingly, addition of 5 equiv. and more caused the opposite effects: The voltammogram shifted back to more negative potentials and the current decreased as well. With 10 equiv., only two isolated broad reduction and oxidation peaks were visible, which disappeared with 50 equiv.

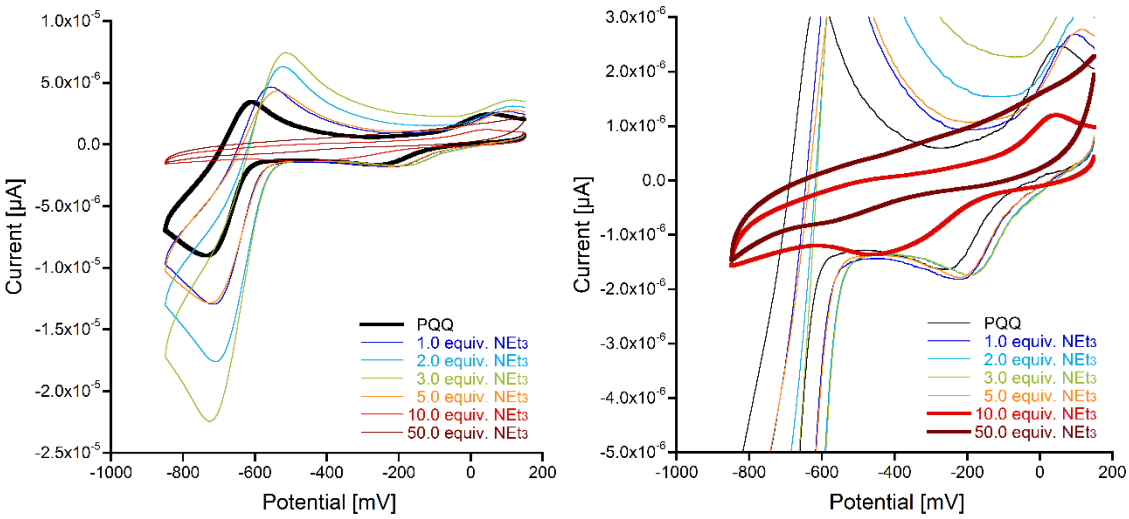

Figure V.27: Left: CV's of PQQ (0.001 M) + Et_4NClO_4 (0.1 M) in a 70:30 H_2O/DMF mixture with increasing amounts of NEt_3 (0.14 µL per equiv.). WE: Pt, CE: Pt-wire, RE: Ag-wire pseudo. Segments 3-4 are shown. Right: Close-up of the CV's.

Itoh *et al.*[172] and Schelter *et al.*[114] already demonstrated, that upon addition of the base DBU (1,8-diazabicyclo[5,4,0]undec-7-ene) (29 equiv. to PQQ-aza-crown-5 – Itoh and 2.2 equiv. to L_{QQ} – Schelter) the oxidation of alcohols by quinone-containing model compounds was accelerated. Et_3N could have the same effect in this experiment, enhancing the redox processes of PQQ. On the other hand, a large excess of this base seem to inhibit redox reactions almost completely.

4.8. Measurements of $PQQMe_3$ in H_2O/DMF Solvent Mixtures

CV's were further recorded for $PQQMe_3$ in the 70:30 H_2O/DMF mixture in addition with increasing amounts of $LaCl_3{\cdot}H_2O$, $EuCl_3{\cdot}H_2O$ or $YbCl_3{\cdot}H_2O$ (Figure V.28). In comparison with the two redox couples of PQQ, $PQQMe_3$ exhibits only two isolated broad reduction and oxidation peaks around -450_{red} mV and -260_{ox} mV, with a shoulder at −410ox mV. Addition of lanthanides caused a positive shift of both peaks, which is smaller for reduction and larger for oxidation. In case of Eu and Yb, the oxidation peak is more pronounced. As already described in V.4.6, problems with the used pseudo-reference electrode and the external ferrocene standart make the obtained data challenging to compare, which appears escpecially pronounced for the voltammograms of $PQQMe_3$ before metal addition (thick black and grey lines). However, the addition of lanthanides seem to facilitate reduction also in the case of $PQQMe_3$ and therefore enhance its oxidation capacity.

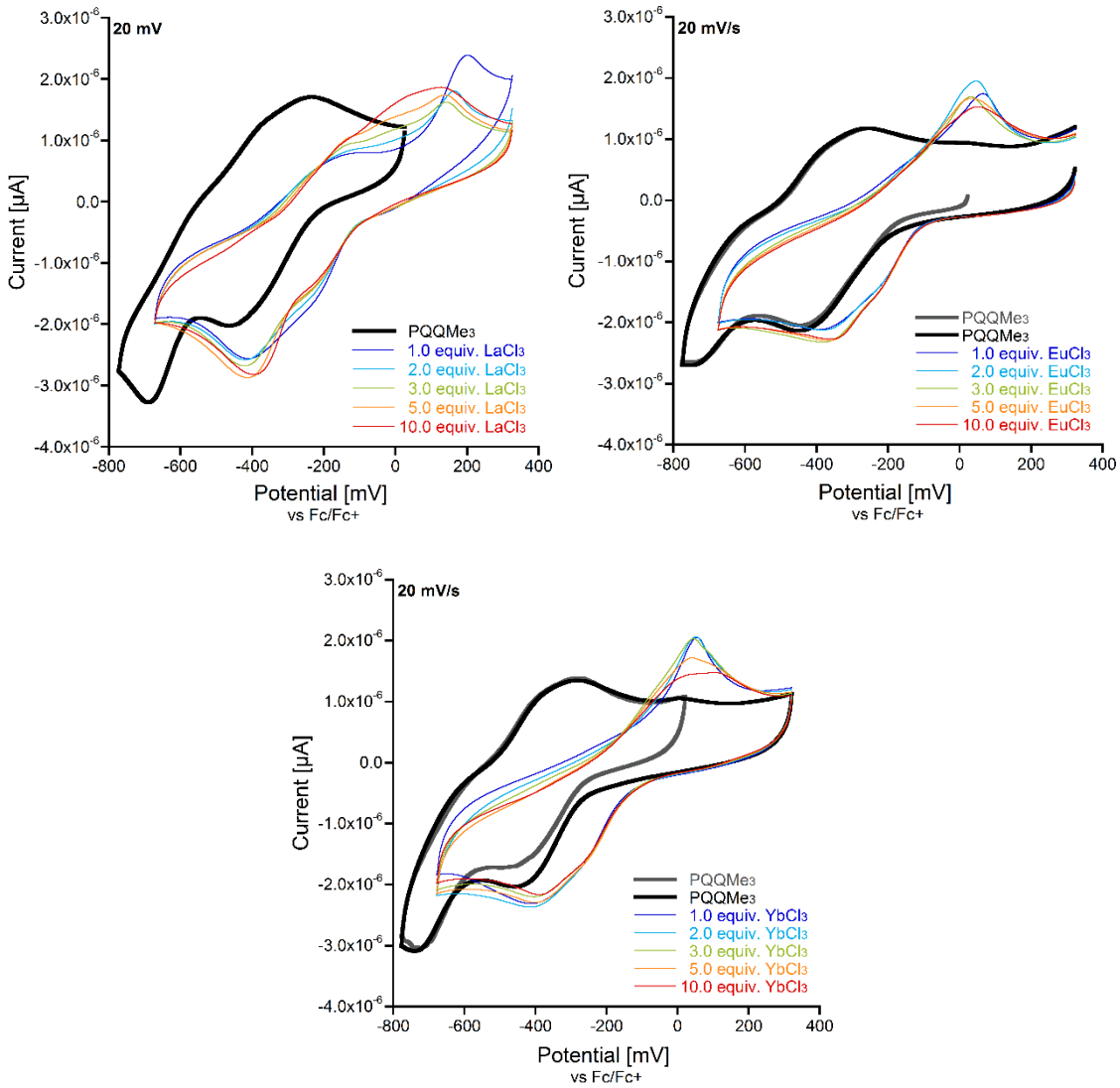

Figure V.28: CV's of $PQQMe_3$ (0.001 M) + Et_4NClO_4 (0.1 M) in a 70:30 H_2O/DMF mixture with increasing amounts of metal chlorides (0.1 M in DMF, 10 µL per equiv.). WE: Pt, CE: Pt-wire, RE: Ag-wire pseudo. Segments 3-4 are shown. Upper left: $LaCl_3 \cdot 7H_2O$; Upper right: $EuCl_3 \cdot 6H_2O$; bottom: $YbCl_3 \cdot 6H_2O$.

4.9. Additional Measurements on a Metrohm Device

Measurements of PQQ in the H_2O/DMF mixture were repeated on a Metrohm device (Autolab PGSTAT101). With this device, only staircase measurements could be performed, implying that the potential is scanned stepwise with small increments, rather than linearly. While this method shows CVs in good quality with slow scan rates, faster scan rates tend to give more noise. Due to larger electrodes and electrochemical cells, volumina had to be adjusted accordingly.

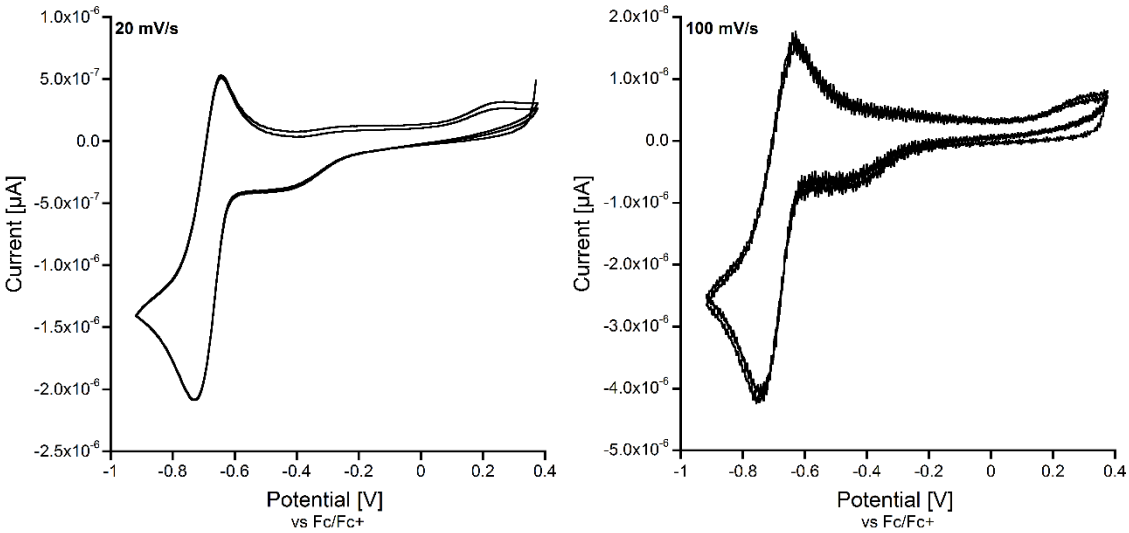

Figure V.29: CV's of PQQ (0.001 M) + Et_4NClO_4 (0.1 M) in a 70:30 H_2O/DMF mixture (25 mL in total). WE: Pt, CE: Pt-wire, RE: Ag-wire pseudo. Segments 1-4 are shown.

While the second redox couple is well reproduced (-732_{red} mV, -642_{ox} mV), the first redox couple is only visible to some degree. In addition, a broad reduction process is now visible at −405 mV. This reduction is not visible with 1.0 equiv. of $LaCl_3{\cdot}7H_2O$ (Figure V.31 - no ferrocene standart), but reappears with faster scan rates, also revealing the first redox couple with -80_{red} mV, -31_{ox} mV, $E_{1/2}$ = −55 mV which is shifted to more negative potentials in comparison with the experiments described above. The second redox couple (PQQ: -675_{red} mV; -587_{ox} mV; $E_{1/2}$ = −631 mV) is again slightly shifted towards more positive potentials upon lanthanum addition (-662_{red} mV, -569_{ox} mV, $E_{1/2}$ = −616 mV) and the current showed a strong increase.

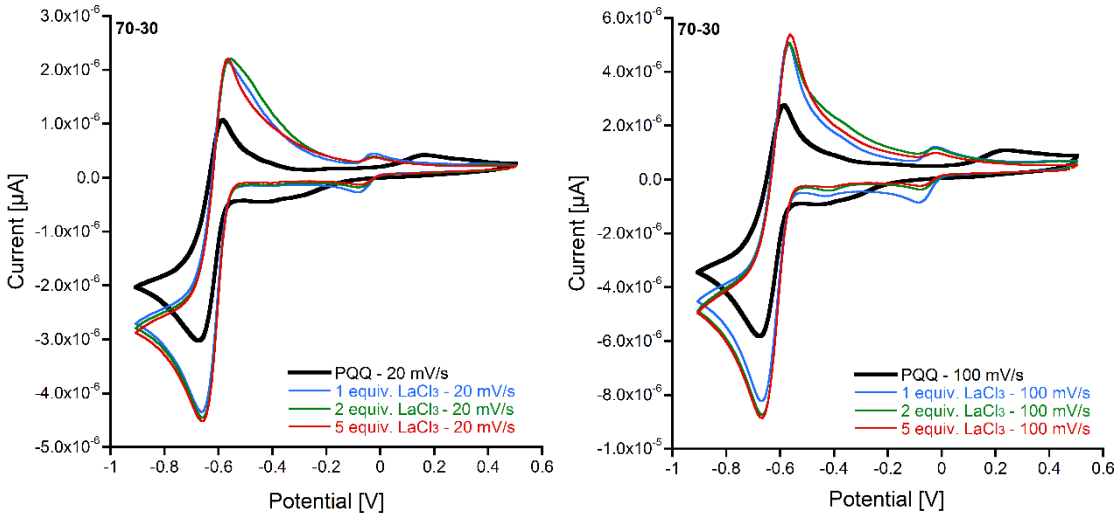

Figure V.30: CV's of PQQ (0.001 M) + Et_4NClO_4 (0.1 M) in a 70:30 H_2O/DMF mixture (25 mL in total) with increasing amounts of $LaCl_3{\cdot}7H_2O$ (0.2 M in H_2O, 125 µL per equiv.) and with different scan rates (20 – 100 mV/s). WE: Pt, CE: Pt-wire, RE: Ag-wire pseudo. Segments 1-2 are shown.

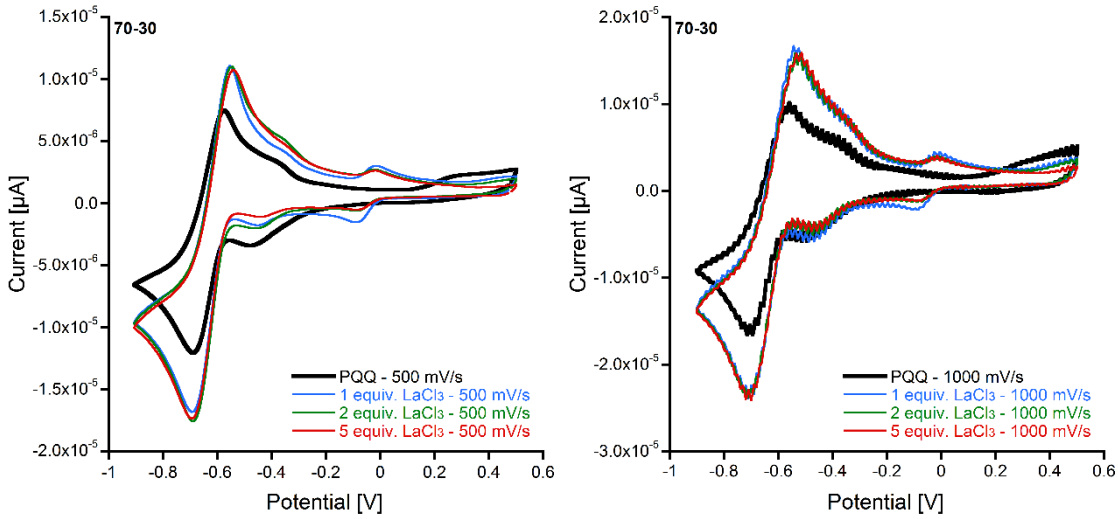

Figure V.31: CV's of PQQ (0.001 M) + Et_4NClO_4 (0.1 M) in a 70:30 H_2O/DMF mixture (25 mL in total) with increasing amounts of $LaCl_3 \cdot 7H_2O$ (0.2 M in H_2O, 125 µL per equiv.) and with different scan rates (100 – 1000 mV/s). WE: Pt, CE: Pt-wire, RE: Ag-wire pseudo. Segments 1-2 are shown.

4.10. Conclusion

The electrochemistry of PQQ has already been analyzed extensively in the past by cyclic voltammetry. While voltammograms in water remain easy to interpret, non-aqueous solvents complicate the voltammograms with a number of separated reduction and oxidation peaks. Metal addition is described in the literature for PQQ and Zn(II) in water (pH 5.6) and for PQQ-4Me and Ca^{2+} in MeCN – both lead to a shift to higher potentials and therefore to an increased oxidation power of PQQ. Here for the first time PQQ was analyzed in the presence of lanthanides. As addition of lanthanides lead to precipitation of PQQ-lanthanide complexes from water, other solvents had to be explored. In DMF, shifts are observable after lanthanide addition, but the voltammograms are difficult to interpret. In a 70:30 H_2O/DMF mixture, only two redox couples are visible, which appears to be the PQQ/$PQQ^{\bullet-}$ and $PQQ^{\bullet-}$/$PQQH_2$ couple by comparison with spectroelectro measurements. UV-Vis data of the $PQQH_2$ reoxidation appears similar, but not identical. Upon lanthanide addition, both redox couples are shifted towards higher potentials, but no clear trend throughout the lanthanide series can be determined. Also referencing to the same ferrocene standard remains challenging. With an alternative cyclic voltammetry device, the data was not completely reproducible. The second redox couple is slightly shifted and the first redox couple is missing completely without metal addition. Also an unknown reduction process appears with faster scan rates.

In summary, it was demonstrated that lanthanides indeed have an influence on the electrochemistry of PQQ and that differences occur throughout the series. However, several

questions remain to be solved. The voltammograms have to be better understood in order to be able to explain the influence of coordinated lanthanides. Simulated voltammograms would aid in this task. Measurements with water-free solvents, metal salts and PQQ would be preferable to exclude the formation of the water-adduct **15**, since the influence of this species remains to be elucidated as well. Finally, the synthesis of PQQ-4Me would help in interpretation, as voltammograms with this species are known to be simplified. Also other synthetic approaches are conceivable, like the implementation of silyl- instead of methyl groups, which are bulkier and further hinder complexation in unwanted coordination sites of PQQ. Presented work in this chapter therefore forms the foundation for further studies about the electrochemistry of PQQ. However, for the completion of such a project, work of several months would be needed and likely involve the need for a glovebox for strict water-free conditions, which is beyond the scope of this thesis and the equipment currently available.

VI. SMALL MOLECULE INTERACTION

1. Introduction

A feature, which was recognized early in PQQ research is the ability, to form adducts with nucleophiles.[128] Over the years, a wide range of small molecules was tested upon this feature,[95, 164] including acetone,[128] water[181-182] and methanol[156, 181], but also cyanide,[243] ammonia,[182, 244-245] urea[182] and even benzylamine[246] or dinitrophenylhydrazine.[247] Usually, nucleophilic attack occurs in C5 position of the quinone, but also the C4 position is affected in some cases. For example a dimethyl ketal species in C4 was afforded under acidic conditions with methanol.[156] The addition of amino acids to PQQ yield the formation of oxazole derivatives, involving both C4 and C5.[158]

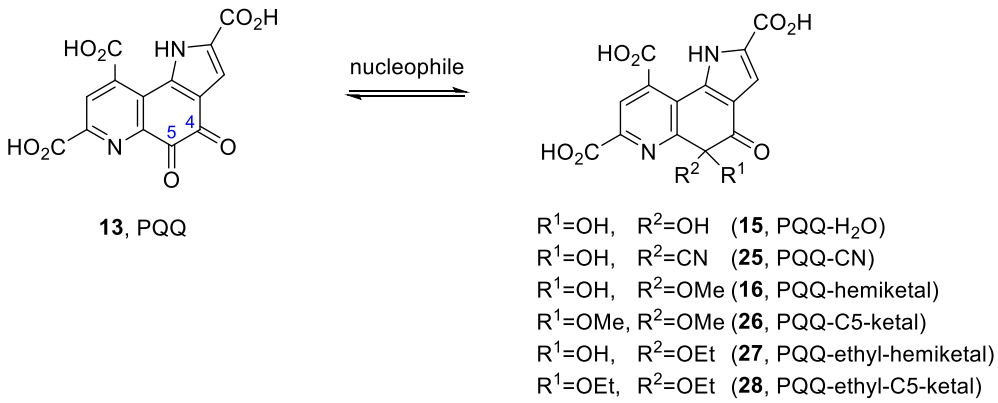

Figure VI.1: Equilibrium reaction between PQQ and nucleophiles, forming C5 adducts. Some examples are given, which will be further discussed in this chapter.

Although being described in literature, analysis was often incomplete and no metal influence on adduct formation was analyzed. In MDH, a Lewis acid is needed for activation of the C5 C=O bond.[44-45] Lanthanides have been proposed to activate C5 better than calcium, due to their higher Lewis acidity.[76, 168] To test this, we first investigated the C5 reactivity with nucleophiles in the absence and then in the presence of lanthanides and calcium. While water adduct formation in aprotic solvents (DMSO, DMF) was already described in Chapter IV and in the literature,[248] this chapter further elucidates interaction of PQQ with cyanide and methanol. Cyanide plays an important role in biochemical assays of methanol dehydrogenases by suppressing proteinogenic side reactions and alleviating effects from artificial electron acceptor

inhibition.[71, 109] How cyanide acts, is not well understood. An interaction with PQQ has been proposed.[249] To better understand the interaction of PQQ with cyanide, we investigated cyanide adduct formation by NMR.

Methanol is the natural substrate of MDH enzymes. Currently there is no consensus on the mechanism of enzymatic action and different mechanisms have been discussed.[45, 70, 72, 77] This chapter investigates the reactivity of methanol with PQQ and elucidates the influence of coordinating lanthanides and calcium on nucleophilic methanol addition.

Finally, the aim of this chapter is to gain a fundamental understanding of the (coordination) chemistry of PQQ with biologically relevant metal ions and nucleophiles. This is important for the development of MDH biomimetics.

2. Cyanide Adduct Formation

2.1. Introduction

Unkefer *et al.* reported the addition of cyanide to C5 of PQQ by ^{13}C-NMR in DMSO but did only report three NMR shifts (C5, 74.8 ppm; C9a, 119.6 ppm; -CN, 117.9 ppm).[243] The aim of this section was to better characterize this species in polar protic and aprotic media by NMR spectroscopy to shed light on this nucleophile in the context of MDH reactivity.

2.2. Elucidation of PQQ Cyanide Adduct Formation

By adding 1.0 equiv. of solid KCN to a PQQ solution in DMF-d_7 (54.5 mM), a cyanide-adduct readily formed in a 2:1 ratio to free PQQ, as indicated by NMR (Figure VI.2).

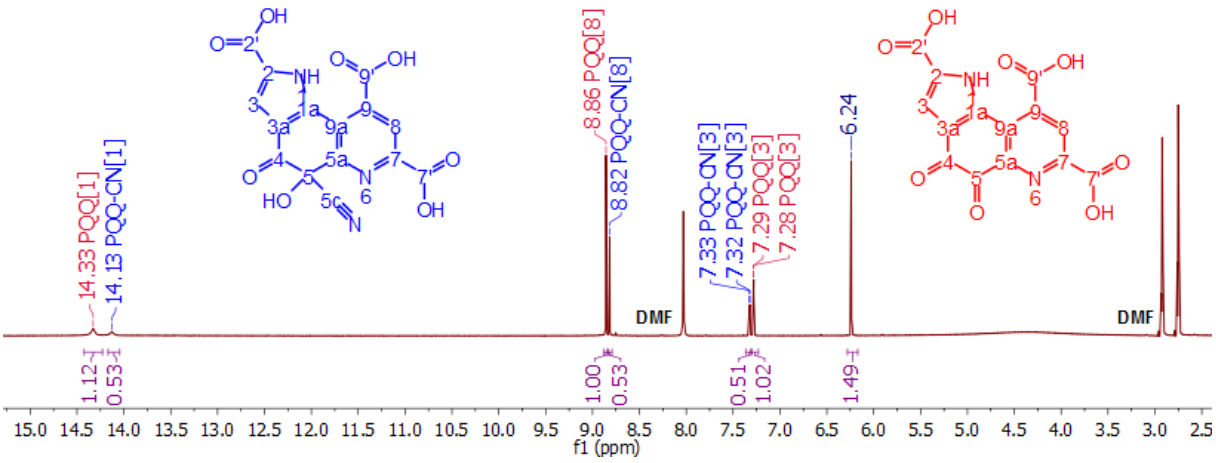

Figure VI.2: ^{1}H-NMR spectrum of PQQ (9 mg, 27.2 µmol) in DMF-d_7 (0.5 mL) with KCN (1.0 equiv., 1.8 mg, 27.2 µmol).

Cyanide-adduct formation was now elucidated in D_2O, for better comparison with described biochemical assays. While PQQ is almost insoluble in water in its fully protonated form, $PQQNa_2$ shows higher solublities, yet still not high enough for concentrations needed for ^{13}C-NMR measurements. Therefore, 2.15 equiv. of ND_4OD in D_2O were added for a complete dissolution of PQQ. Even without KCN, NMR indicated two species in a 1:0.67 ratio: Free PQQ (**13**) and a PQQ-C5 adduct, probably being the water adduct of PQQ. Due to the added ammonia, the second species could also be the ND_3-adduct, which remains elusive by NMR methods alone. After 1.0 equiv. of solid KCN was added to the aqueous PQQ solution, causing a color change from dark- to light red, NMR indicated only one PQQ species, with some additional trace-signals visible in the proton spectrum (Figure VI.3). The C5 resonance in ^{13}C-NMR was shifted upfield to 60.76 ppm in comparison to 89.38 ppm for the water/ammonia adduct. A new carbon resonance was now visible at 119.88 ppm, indicating the species as the PQQ-CN adduct (**25**).

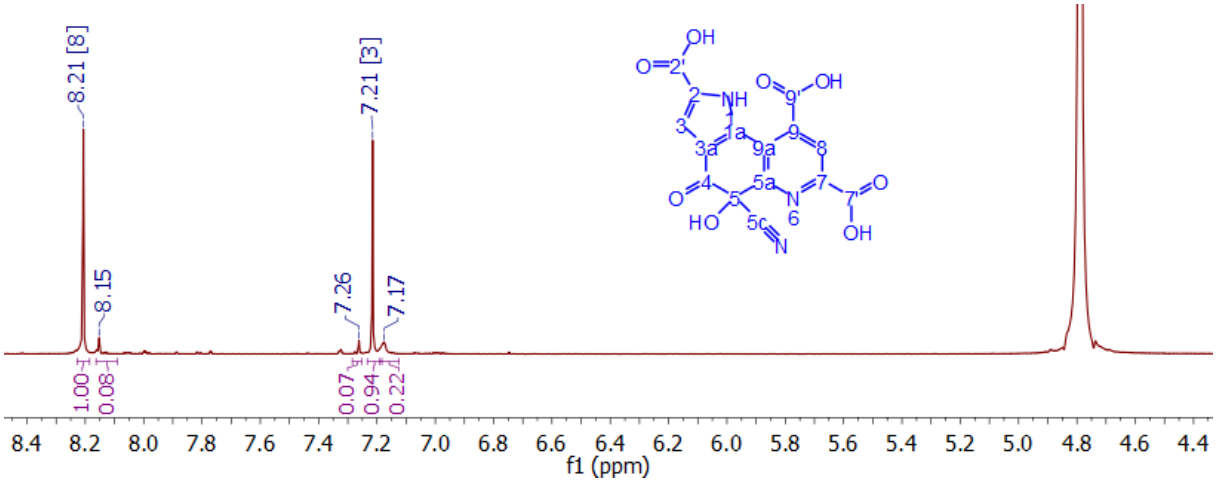

Figure VI.3: ^1H-NMR spectrum of PQQ (9 mg, 27.2 µmol) and ND_4OD in D_2O (26 wt.%; 3.3 mg; 58.7 µmol, 12 µL, 2.15 equiv.) in D_2O (0.5 mL) with KCN (1.0 equiv., 1.8 mg, 27.2 µmol).Carboxyl groups of the shown structure are (partially) deprotonated due to the added ND4OD.

The pK_a values of the PQQ carboxyl groups are between 1.60 (C_7-CO_2H), 2.20 (C_9-CO_2H) and 3.30 (C_2-CO_2H),[178-179] and are therefore all capable of protonating the cyanide CN^- ion. HCN is considered a weak acid with a pK_a of 9.0 in both H_2O and D_2O.[250] This might be the reason for the incomplete formation of a cyanide-adduct in DMF-d_7 (Figure VI.2), since hydrogen cyanide is a much weaker nucleophile than the corresponding cyanide ion.[251]

In D_2O, the added ND_4OD should lead to an increased ratio of deprotonated cyanide, explaining the larger amounts of PQQ-CN adduct in solution. The cyanide also has a higher affinity to PQQ than OH^-, since no water-adduct, or only a trace of it is visible with cyanide present. The following table gives an overview over the discussed species and the assignment of their NMR resonances.

Table VI.1: ^{1}H- and ^{13}C-NMR shifts of PQQ (9 mg, 27.2 µmol) in DMF-d_7 (0.5 mL) or in D_2O (0.5 mL) by the addition of ND_4OD in D_2O (26 wt.%; 3.3 mg; 58.7 µmol, 12 µL, 2.15 equiv.), with or without KCN (1.0 equiv., 1.8 mg, 27.2 µmol). Shifts in ppm relative to the respective solvent signals (see VIII.2.1). Signal assignments based on 2D HMQC and HMBC experiments, DFT calculations and comparison with data from the literature.[169, 243] DFT based on Structure optimization of PQQ-CN with B3LYP; 6-31g(d); CPCM=DMF and NMR calculation by the GIAO-method at the same level of theory. Calculated shifts relative to TMS, calculated the same way.

#	DMF + KCN				DMF calc.	D_2O				D_2O + KCN		#
	PQQ (**13**)		PQQ-CN (**25**)		PQQ-CN	PQQ (**13**)		PQQ-H_2O (**15**)		PQQ-CN (**25**)		
^{13}C	**^{13}C**	**^{1}H**	**^{13}C**	**^{1}H**	**^{13}C**	**^{13}C**	**^{1}H**	**^{13}C**	**^{1}H**	**^{13}C**	**^{1}H**	**^{1}H**
5	180.18	14.33 (s)	76.16	14.13 (s)	73.30	181.98		89.38		60.76		1
4	174.68	8.86 (s)	184.00	8.82 (s)	178.82	175.11	8.27 (s)	190.07	8.18 (s)	185.44	8.21 (s)	8
9‘	169.88	7.28 (d) J = 2.1Hz	169.81	7.32 (d) J = 2.2Hz	160.29	173.23	7.15 (s)	174.08	7.19 (s)	173.88	7.21 (s)	3
7‘	166.33		166.02		155.12	170.75		171.31		171.29		
2‘	162.26		162.16		151.50	166.75		167.03		167.21		
5a	149.85		157.77		150.02	152.41		156.65		153.51		
7	148.52		147.58		138.70	150.82		146.05		152.27		
9	136.46		139.01		130.62	143.22		142.68		143.11		
1a	136.01		129.90		130.48	136.41		135.57		136.24		
8	131.18		129.13		124.31	128.01		124.32		124.46		
2	129.46		120.77		123.61	133.14		132.69		133.84		
9a	128.29		123.18		121.94	123.92		117.02		117.10		
3a	125.75		119.09		116.19	122.39		118.34		117.68		
3	114.67		113.74		111.55	112.33		110.88		110.60		
-CN			114.00		108.92					119.88		

The presented experiments indicate formation of the PQQ-CN adduct (**25**) in both polar protic and aprotic solvents. Especially basic pH is advantageous for keeping CN^- deprotonated, which is the better nucleophile than HCN. Essays of MxaF Ca-MDH are performed by default at buffered pH 9. Formation of the cyanide adduct with MDH containing PQQ is feasable. However, such formation does not explain the inhibition of side reactions in the assay, since cyanide would compete with methanol for PQQ.

Further experiments are necessary, especially spectrophotometric measurements of MDH with cyanide in comparison with isolated PQQ and cyanide, in order to evaluate possible cyanide adduct formation in the enzyme itself. Competing experiments between methanol and cyanide for PQQ would be of interest as well, to rule out inhibitory effects, when the cyanide adduct is formed.

Fluorescence titrations would help in this task and were already performed for investigations on the PQQ water- (**15**) and methanol adduct formation (**16**),[182, 252] and for tracking reduction rates to $PQQH_2$ (**24**) in a related glucose dehydrogenase enzyme.[253]

3. Methanol Adduct Formation

3.1. Introduction

Duine *et al.* observed methanol addition to $PQQMe_3$ (**11**) in $CDCl_3$ via ^{1}H-NMR and first suggested a hemiketal formation in position C5.[181] Itoh *et al.* confirmed this and reported a crystal structure of the C5-hemiketal, from crystals grown out of a $PQQMe_3$ methanol solution.[156] Surprisingly, by treating **11** in refluxing methanol with catalytic amounts of pTSA, a ketal derivative was received instead, containing two methoxy groups in position C4 (**29**), which was confirmed by X-ray analysis and NMR.[156] Unlike hemiketal **16** or **18**, this ketal species is described stable in solution and does not convert back to free PQQ.[156] To this point, ketal formation was believed to occur in position 5, as described by van der Meer *et al.* on a PQQ-dihexyl ketal, derived from a PQQ solution in a 3:1 mixture of refluxing 3M HCl and n-hexanol.[254] Methanol addition to underivatized PQQ (**13**) had not been fully investigated previously thus, NMR and UV-Vis studies of **13** in methanol were conducted and the influence of metals on hemiketal formation was studied.

3.2. PQQ Adduct Formation in MeOD-d_4

As described above, dissolution of PQQ in pure methanol lead to precipitation of yellow colored hemiketal (**15**) within hours.[156] When dissolved in deuterated MeOD-d_4 and directly analyzed via NMR, three species are visible both in ^{1}H- and ^{13}C-NMR spectra in a 9:81:9 ratio (Figure VI.4), and assigned to free PQQ (**13**, red), PQQ-hemiketal (**16**, green) and a second PQQ-adduct of unknown structure in blue.

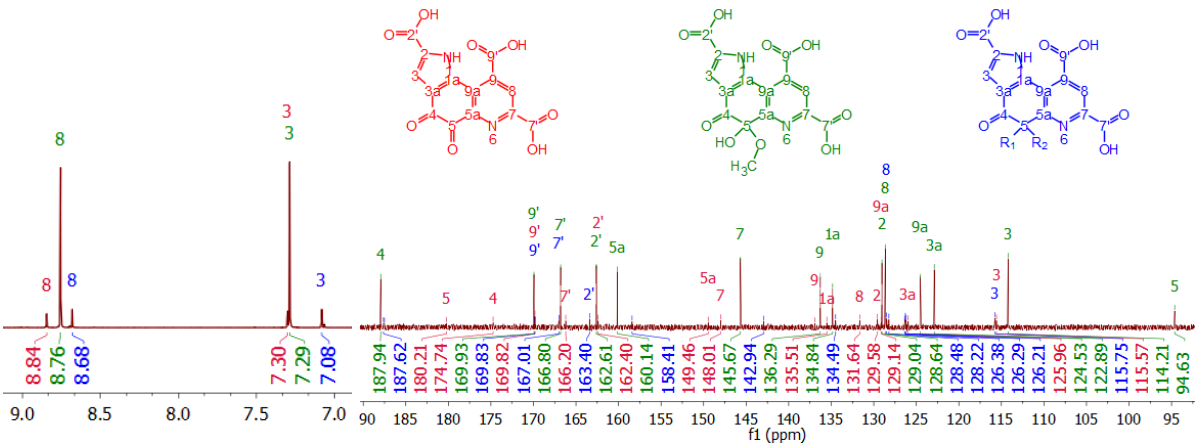

Figure VI.4: ^{1}H- and ^{13}C-NMR spectra of PQQ in MeOD-d_4 (0.6 mL, 22.7 mM), showing resonances of three different species, beeing most likely PQQ (**13**, red), the literature known hemiketal (**16**, green) and an unknown PQQ adduct in blue (For simplification, only position C5 is shown, which could also be the C4 adduct).

Following table provides an overview over all described species in this section and the assignment of their NMR resonances.

Table VI.2: ^{1}H- and ^{13}C-NMR shifts of PQQ (4.5 mg, 13.6 µmol) in either MeOD-d_4 (0.6 mL) or EtOD-d_6 (0.6 mL). Shifts in ppm relative to the respective solvent signals (see VIII.2.1). Signal assignments based on 2D HMQC and HMBC experiments. Red numbers indicate that no assignment was possible by 2D NMR, since no proton correlation could be observed. Additional proton resonances for PQQ in EtOD-d_6 given in the text. DFT based on Structure optimizations of PQQ-hemiketal (**16**) and PQQ-ketal (**26**) with B3LYP; 6-31G++(d,p); CPCM (DMSO / MeOH) and NMR calculation by the GIAO-method at the same level of theory. Calculated shifts relative to tetramethylsilane (TMS). Only bold written ^{13}C-NMR resonances for C4-PQQMe$_3$-ketal (**29**) were assigned by Itoh *et al.*[156] – the three methyl ester signals are not shown.

#	MeOD-d_4						EtOD-d_6		Calculated in Methanol				CDCl$_3$ (^{1}H) DMSO-d_6 (^{13}C)		#
	PQQ (**13**)		PQQ-hemiketal (**16**)		PQQ-ketal (**26**)		PQQ-ethoxy hemiketal (**27**)		**16** (C5)	**26** (C5)	**30** (C4)	**15** (C5)	**29** (C4) by Itoh *et al.*[156]		
^{13}C	**^{13}C**	**^{1}H**	**^{13}C**	**^{1}H**	**^{13}C**	**^{1}H**	**^{13}C**	**^{1}H**	**^{13}C**	**^{13}C**	**^{13}C**	**^{13}C**	**^{1}H**	**^{13}C**	**^{1}H**
5	180.21	-	94.63	-	-	-	94.54	-	95.47	99.21	191.10	92.71	12.22 (brs)	**193.1**	**1**
4	174.75	8.84 (s)	187.94	8.76 (s)	187.62	8.68 (s)	187.82	8.78 (s)	186.55	186.81	98.51	184.22	8.71 (s)	**96.8**	**8**
9‘	169.83	7.30 (s)	169.93	7.29 (s)	169.83	7.08 (s)	169.54	7.29 (s)	165.98	166.47	166.16	165.70	7.13 (d)	165.8	**3**
7‘	166.21		166.80		167.01		166.29		160.82	160.96	160.49	160.49		163.8	
2‘	162.40		162.60		163.41		162.06		157.96	158.09	158.36	157.94		160.2	
5a	149.47		160.14		158.41		160.4		157.85	160.76	148.41	160.64		149.5	
7	148.01		145.67		142.94		145.39		140.56	143.12	141.76	141.63		145.7	
9	136.93		136.29		-		135.79		130.66	130.48	130.11	131.14		132.9	
1a	135.52		134.84		134.49		134.19		133.69	133.94	127.65	134.02		128.8	
8	131.64		128.64		128.48		128.21		129.27	129.31	131.37	128.96		126.3	
2	129.58		129.04		128.23		128.95		126.41	126.18	125.49	125.78		125.3	
9a	129.14		124.53		126.22		124.23		127.04	125.93	131.08	124.33		125.2	
3a	125.96		122.89		126.29		122.88		123.83	122.54	127.41	123.48		122.3	
3	115.57		114.21		115.76		113.99		115.01	115.33	115.04	115.48		114.6	
$\underline{C}H_3$			-		-				51.47	57.95	55.60		3.41	**51.4**	
$\underline{C}H_3$					-					54.63	51.72		3.41	**51.4**	

Resonances for hemiketal or ketal methoxy- or ethoxy groups are most likely hidden under solvent signals.

The PQQ-hemiketal (**16** – green peaks Figure VI.4) is the main species, with free PQQ (**13**- red peaks) being a minor component. Interestingly, a peak set of an additional PQQ-species is visible (blue peaks). With NMR spectroscopy alone, this additional species cannot be assigned properly due to its low concentration. However the ESI mass-spectrum of **13** dissolved in methanol, shows peaks for a ketal species (**26/30**), besides free PQQ (**13**, red) and the hemiketal (**16**, green) (Figure VI.5).

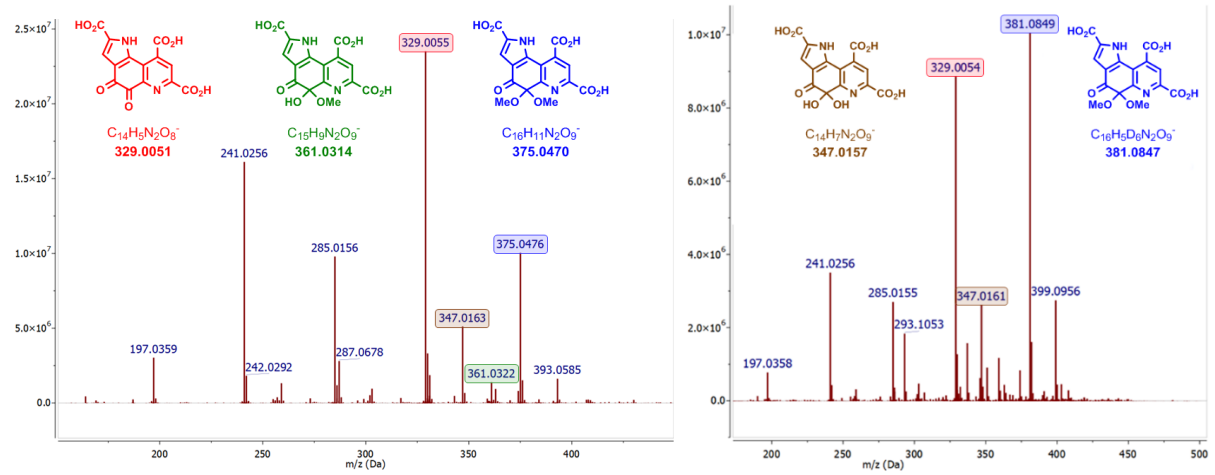

Figure VI.5: Left: ESI (−) mass spectrum of PQQ dissolved in MeOH (9 mM). Right: ESI (−) mass spectrum of PQQ in MeOD-d_4 (9 mM). Both spectra recorded in a water/acetonitrile mixture. For simplification, only position C5 ketal (**26**) is shown, which could also be the C4 ketal (**30**), based on mass spectrometric assignments alone.

In a similar experiment, using deuterated MeOD-d_4, a species with six mass units higher was now visible, supporting the formation of a ketal species (Figure VI.5). It cannot be clearly stated if the compound is a similar C4 PQQ-ketal which is described by Itoh *et al.*[156] (**29**) or if ketal formation in methanol without acid-catalysis occurs in position C5. ^{13}C-NMR shifts of **29** are 149.5 ppm (5a) and 145.7 ppm (7). Comparison with DFT calculated shifts in methanol (Table VI.2) reveal shifts of 160.76 ppm (5a) and 143.12 ppm (7) for the C5 ketal (**26**) and 148.41 ppm (5a) and 141.76 ppm (7) for the C4 ketal (**30**), respectively. Large downfield shifts for 5a are also visible for the water- (**15** - 156.65 ppm) and the cyanide adduct (**25** - 157.77 ppm) (Table VI.1) and seem to be common for C5 adduct formation in general. While free PQQ (**13**) in MeOD-d_4 show 149.47 ppm (5a), both PQQ-hemiketal (**16**) (5a: 160.14 ppm) and the unknown species (**26**/**30**) (5a: 158.41 ppm) are further shifted upfield determining the unknown species as a probable C5 adduct. Since trace amounts of water can already lead to water-adduct formation in DMF (Chapter IV), it is also possible, that the unknown species is the water-adduct in methanol. DFT calculations of the ketal species **26**/**30** and the water adduct **15** give no additional information, as the generated NMR spectra of both species are very similar (Table VI.2). Both mass experiments show signals at 347.016 mass units, which can be indeed assigned to the negatively charged water adduct **15** (*m/z* 347.0157). But since both mass spectra were recorded in a water/acetonitrile mixture, the water-adduct could have also been formed through the conditions of this particular experiment.

To exclude the unknown species to be the water adduct **15**, small amounts of undeuterated water were added to a methanolic solution of PQQ and ^{1}H-NMR spectra

were recorded immediately after (Figure VI.6). The pure methanolic solution of PQQ gave the PQQ (**13**), PQQ-hemiketal (**16**) and unknown-species (**26**/**30**) in a 9:90:1 ratio. Upon addition of water, a new signal set with similar integral values appeared at 8.72 and 7.36 ppm and the ratio was now 9.6 (**13**) : 88.9 (**16**) : 0.6 (**15**) : 0.9 (**26**/**30**).

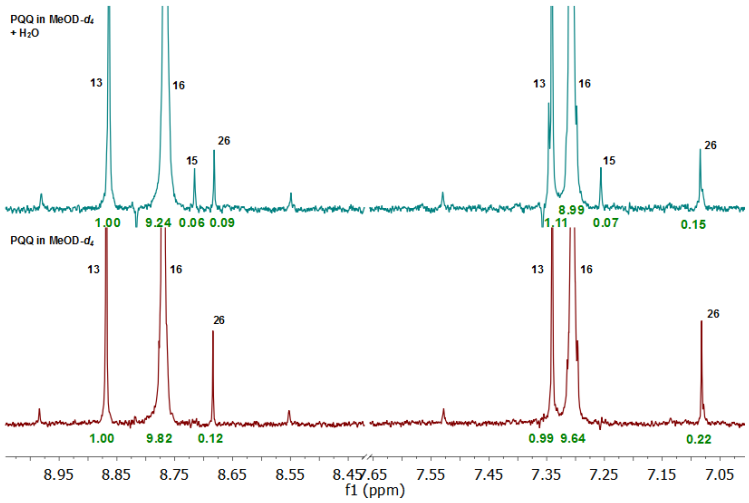

Figure VI.6: Stacked ^{1}H- spectra PQQ in MeOD-d_4 (0.6 mL, 22.7 mM) and PQQ in MeOD-d_4 (0.6 mL, 22.7 mM) + 10µL H_2O. All spectra relative to the solvent quintet (3.310 ppm). Integral values in green.

This experiment confirms the third species as the PQQ-ketal and in combination with the DFT calculations, we propose this species to be the C5 PQQ-ketal (**26**).

For both hemiketal and ketal species, the resonances stemming from the methyl groups were mainly hidden by the solvent signal in the ^{13}C-NMR (Figure VI.7).

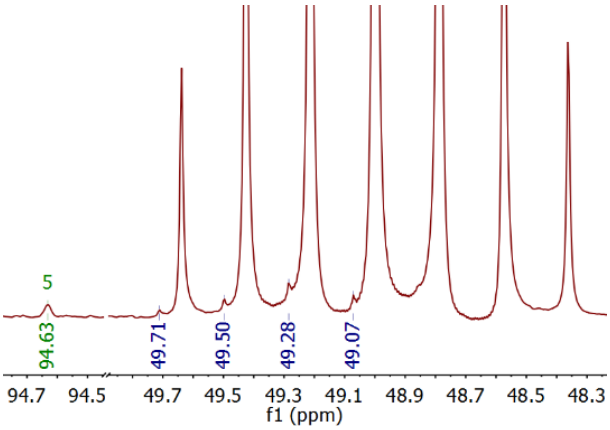

Figure VI.7: Zoom into the solvent residual area of the ^{13}C-NMR spectrum of PQQ in MeOD-d_4 (0.6 mL, 22.7 mM), showing additional small side peaks possibly from methoxy groups of **16** and **26**. C5 Resonance of the PQQ-hemiketal (**16**) species is shown for size comparison.

In order to detect the missing methoxy resonances, PQQ-NMR spectra were also recorded in additional solvents. In deuterated ethanol, three species are visible in the proton spectrum in a ratio of 8:91:1,

probably being free PQQ (**13**) (8.90, 7.32 ppm), PQQ-ethyl-hemiketal (**27**) (8.78, 7.29 ppm) and PQQ-ethyl-ketal (**28**) (8.66, 7.09 ppm). In ^{13}C-NMR, only the main species (**27**) is visible (Table VI.2). Neither in ^{1}H-, nor in ^{13}C-NMR spectra could additional ethoxy- resonances be observed. In ^{13}C-enriched methanol, no additional resonance is visible which can be assigned to the missing methoxy-group. An additional resonance appears at 49.85 ppm, close to the solvent septet, however, this resonance appears as well in the same solvent distribution without PQQ (0.5 mL MeOD-*d4* and 0.5 µL ^{13}C-MeOH only) and is therefore related to free ^{13}C-MeOH in solution.

3.3. Isolation Attempts of the PQQ-ketal Species of unknown Structure

To further characterize the PQQ-ketal, it was attempted to isolate this species. One equiv. of water is released from the hemiketal during ketal formation (Figure VI.8). Hence, removal of water should shift the equilibrium to the latter species.

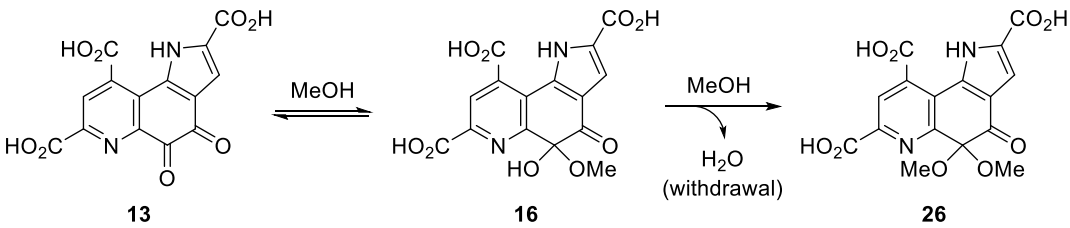

Figure VI.8: PQQ-ketal (**26**) formation by withdrawal of water, which is formed during reaction.

Activated molecular sieve (3Å) was added to solutions of PQQ (30 mg, 90.8 µmol) in 5 mL of A: MeOH, B: MeOD-*d4* or C: EtOH, under nitrogen. PQQ showed only poor solubility in EtOH, resulting in a light red suspension. A and B yielded yellow solutions, from which brown-red solids precipitated within one day. All three suspensions were stored under nitrogen for one week, followed by careful separation of the precipitates from the molecular sieve, using Pasteur pipettes. The precipitates were filtered and dried under high vacuum overnight to give light-brown powders for A (14.4 mg) and B (16.3 mg) and light-orange powder for C (11.2 mg). The filtrate was colored light-yellow in case of A & B and completely colorless in case of C. A ^{1}H-NMR was recorded from filtrate B (MeOD-*d4*) which is given below:

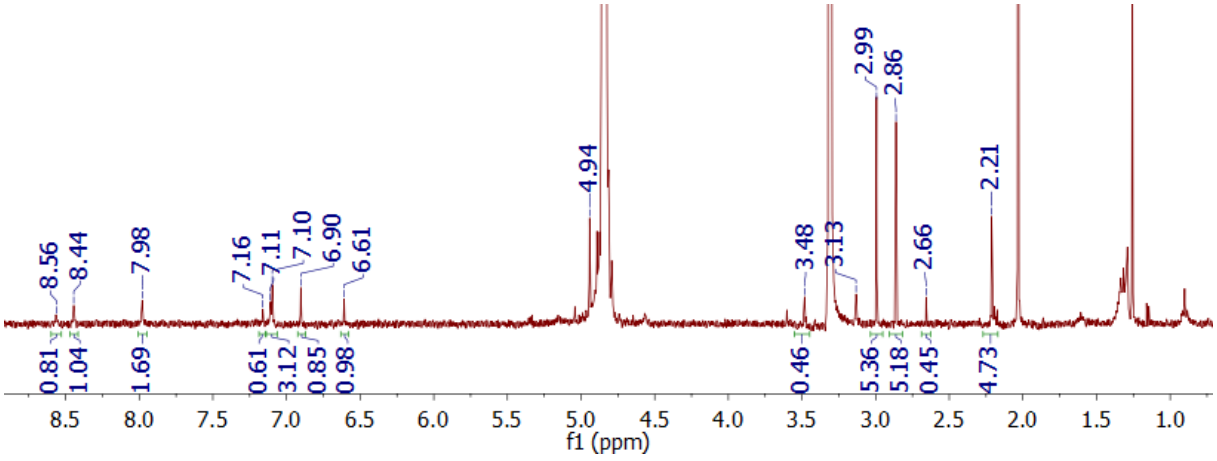

Figure VI.9: ^{1}H-NMR spectrum of the filtrate from approach B (PQQ in MeOD-d_4).

The filtrate was very diluted, due to the weak resonances received (Figure VI.9). None of the resonances matches the ones received from PQQ (**13**) in MeOH or a PQQ-hemiketal (**16**) or –ketal (**26**) species. However, the resonances in the area around 8.5 and 7 ppm are generally in the range for 8H and 3H protons from PQQ-species. The shift of the two doublets (3.00 and 2.86 ppm) would fit to a methoxy group, but the integrals are too high, compared to the other signals.

The received powders showed no solubility in MeOH and were partly soluble in DMF or DMSO. Since DMSO showed the best results, the powders (~ 9 mg each) were suspended into DMSO-d_6 (0.6 mL). Even after vortexing, sonicating or letting the suspension stay for one day, the powders could only be partly dissolved. The supernatant was filtered and ^{1}H-NMR spectra were recorded (Figure VI.10) whereas concentration was too low for ^{13}C-NMR.

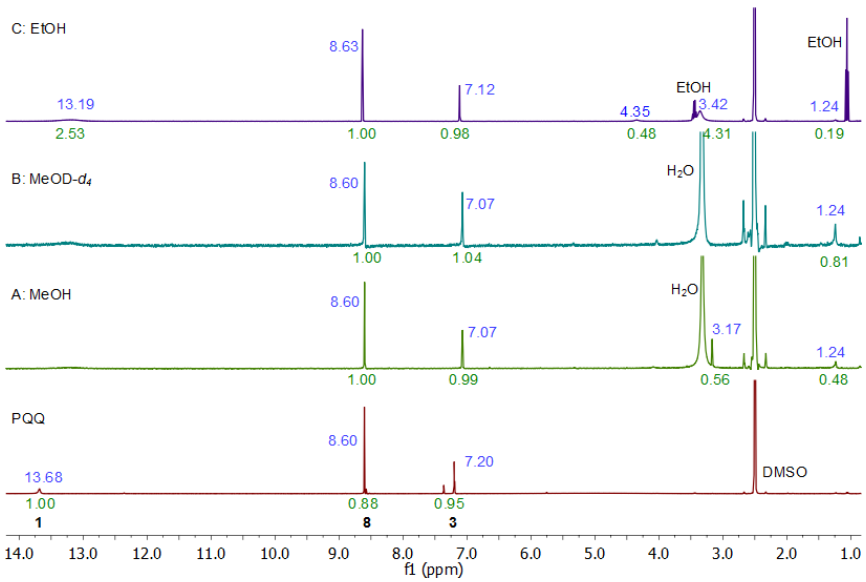

Figure VI.10: Stacked ^{1}H-NMR spectra of PQQ in DMSO-d_6 (22.7 µM) and the powders received from experiments with molecular sieves, dissolved in DMSO-d_6 (~9 mg in 0.6 mL).

All three spectra show the two typical aromatic resonances around 8 and 7 ppm. While A and B show the same 8H shift as the comparative PQQ spectrum (8.60 ppm), the resonance for 3H is shifted upfield to 7.07 ppm, indicating a different species to pure PQQ. Both A and B show in addition a large resonance at 3.32 ppm, which would be water, according to Gottlieb *et al.* (3.33 ppm).[255] Since dry DMSO-d_6 was used out of a flask under inert gas with septum and approach C does not show such a resonance, remaining methanol seems to be more likely which would rise at 3.16 ppm, however. Two more resonances are visible at 3.17 and 1.24 ppm, likely being impurities. The aromatic resonances of approach C are shifted both for 8H (8.63 ppm) and 3H (7.12 ppm). Ethanol resonances are clearly visible at 3.44 and 1.06 ppm. Since both resonances are in accordance to Gottlieb *et al.* (1.06 & 3.44 ppm)[255] and the integral values do not fit to the aromatic resonances, the ethanol seems to be free in solution and not bound to PQQ. Also in this case, several minor resonances appear at 13.1 (probably the N-H resonance), 4.35, 3.42 and 1.24 ppm, which all do not match to the aromatic integrals. To summarize, due to the large shift of the 3H proton, the generation of a new PQQ-species seems to be likely. On the other hand, no resonance can be found for a methoxy or ethoxy group, which would indicate a potential PQQ-ketal. To get analyzable ^{13}C-NMR data, solid state NMR was performed for B, showing eight broadened resonances in total (Figure VI.11).

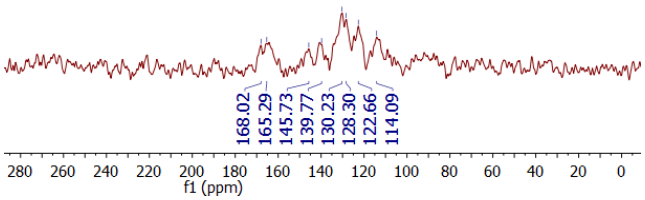

Figure VI.11: Solid-state ^{13}C-NMR spectrum of the powder received from approach B (PQQ in MeOD-d_4 with molecular sieve), showing 8 resonances.

Even though the spectrum was recorded over two days, not all PQQ carbon resonances could be visualized (quinone C4 or C5 between 170-190 ppm) and no additional resonances in the area for potential methoxy groups (between 40 – 60 ppm) are visible.

To get additional information of the received solids, IR spectra were recorded for all three species and compared to reference spectra from authentic samples of PQQ (**13**) (Figure VI.13) and PQQ-hemiketal (**16**) (Figure VI.14).

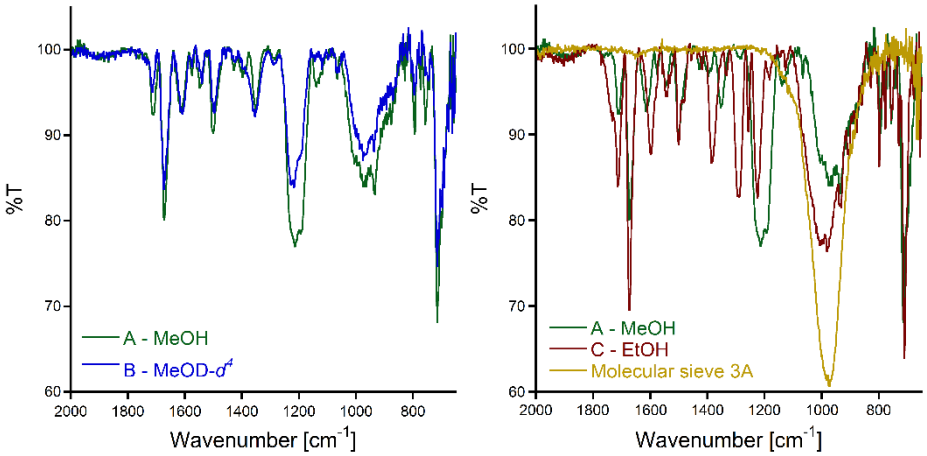

Figure VI.12: IR-Spectra (close-up) for A: PQQ in MeOH with molecular sieve (green) and B: PQQ in MeOD-d_4 with molecular sieve (blue), C: PQQ in EtOH with molecular sieve (dark-red) and molecular sieve 3Å (yellow).

The received spectra from A and B only differ marginally (Figure VI.12), indicating the formation of similar species (the deuterated methanol-d_4 does not have a strong impact on the received IR vibrations). Spectrum C looks similar to A, especially in the area around 1750 – 1500 cm^{-1}. The remaining signals between 1500 – 1100 cm^{-1} appear similar as well, but are shifted to higher energies. The broad signal between 1080 – 820 cm^{-1} is related to residues of molecular sieve, as shown by the yellow reference spectrum.

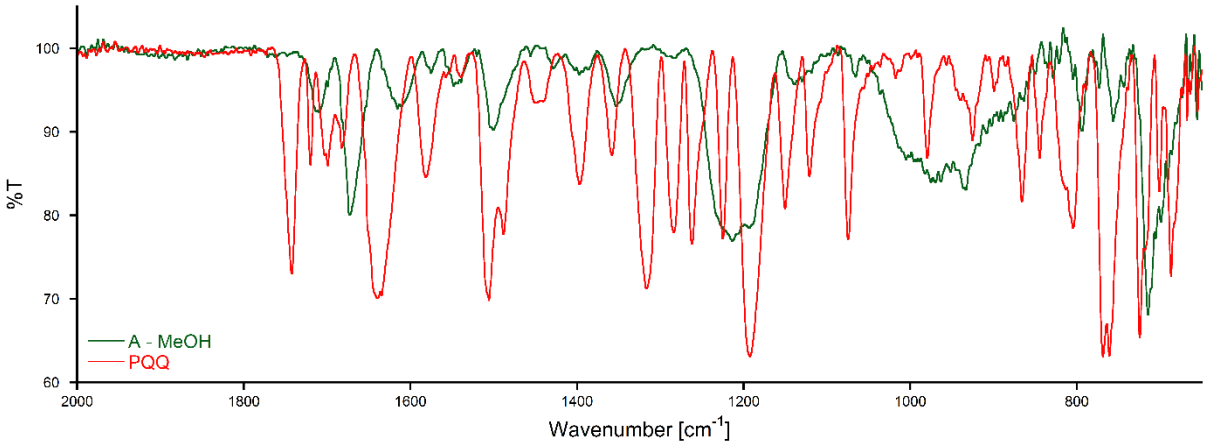

Figure VI.13: IR-Spectra (close-up) for A: PQQ in MeOH with molecular sieve (green) and PQQ (red).

As described in Chapter IV and in the literature,[248] the four signals between 1742 – 1682 cm^{-1} of the PQQ spectrum are related to carboxyl- and quinone C=O stretching vibrations. In the green spectrum A, only two broad peaks are visible in this area (Figure VI.13). This could be a hint for a formed ketal species, which would remove the C5 quinone vibration. Most of the following signals of spectrum A, starting from the strong signal at 1673 cm^{-1} to 1353 cm^{-1} are present in the PQQ spectrum as well, but are either shifted to higher or lower wavenumbers.

The broad signal between 1213 – 1190 cm^{-1} is probably an overlap of the symmetric stretching vibration of the three carboxylic ions.[183]

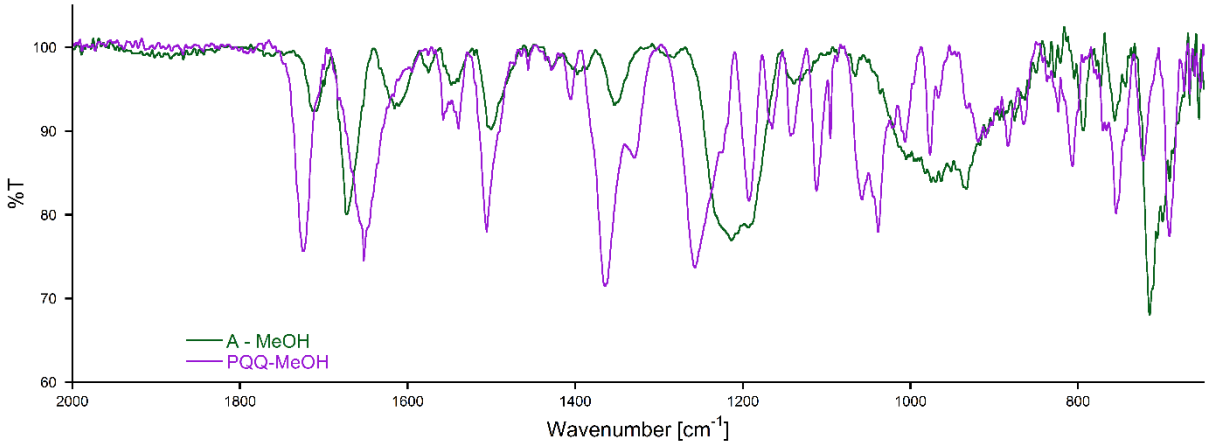

Figure VI.14: IR-Spectra (close-up) for A: PQQ in MeOH with molecular sieve (green) and PQQ-Hemiketal (**16**) (purple).

Comparison of spectrum A with the IR spectrum of isolated PQQ-hemiketal (**16**) (Figure VI.14) reveal a much closer similarity of those two species than to free PQQ, which would further support a potential PQQ-ketal formation.

To summarize, solids were received by letting alcoholic PQQ solutions stand over molecular sieve to shift the equilibrium to a potential PQQ-ketal. NMR indicate the formation of PQQ-adducts when (deuterated-) methanol was used, but no direct evidence can be given due to missing methoxy-resonances. No ethanol-adduct formation could be observed. Also IR indicate the formation of a species, different to PQQ (**13**) and PQQ-hemiketal (**16**) but whether this species is the desired ketal **26** remains to be elusive.

3.4. Influence of Metals on Hemiketal Formation

3.4.1 Hemiketal Formation in Solvent Mixtures

To investigate, whether methanol addition to the C5 carbon of PQQ is influenced by the presence of biological relevant lanthanides and calcium, different solvent mixtures of DMSO/MeOH were prepared. By the addition of MeOD-d_4 (30 mol%) to a solution of PQQ (**13**) in DMSO-d_6, nearly equimolar ratios of PQQ (**13**) and the hemiketal **16** emerge (Figure VI.15)

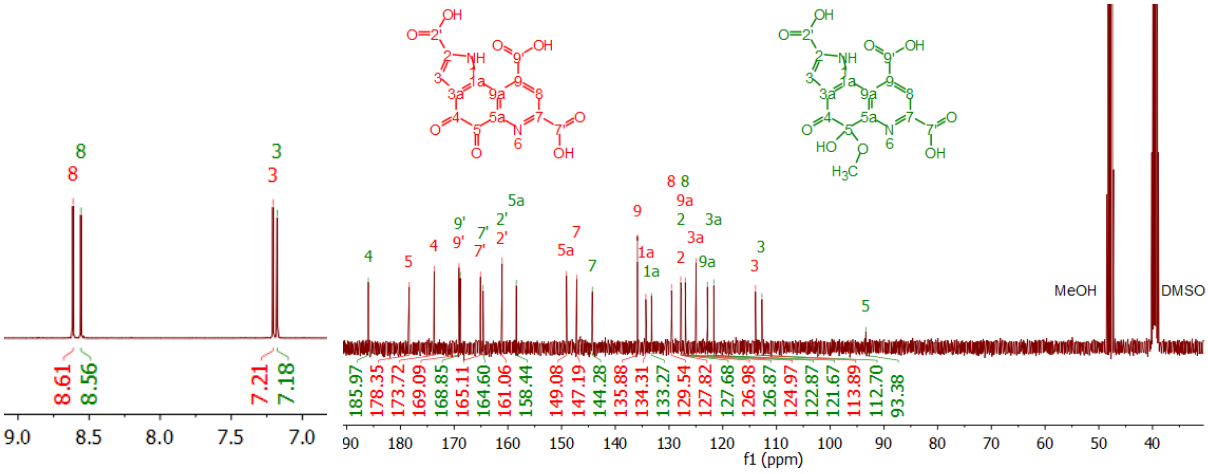

Figure VI.15: ^{1}H- and ^{13}C-NMR spectra of PQQ (9 mg, 27.2 µmol), dissolved in DMSO-d_6 (0.48 mL) and MeOD-d_4 (0.12 mL, 30 mol%). All signals were assigned by 2D-HMBC and HMQC experiments and are in accordance with reported shifts in case of PQQ (no literature data available for PQQ-MeOH in DMSO).[67] The resonance at 161.06 ppm can be assigned both to PQQ and PQQ-MeOH. A signal for hemiketal C9 is not visible or is hidden under another signal which cannot be clearly stated by the HMBC experiment.

Also in this case, no resonance was visible, which could be assigned to the hemiketal methoxy-group, so the experiment was repeated with unlabeled MeOH, giving the same distribution of signals (Figure VI.16). Here, the observed resonances for the PQQ-hemiketal are less intense as a result of less methanol being added (16 mol%).

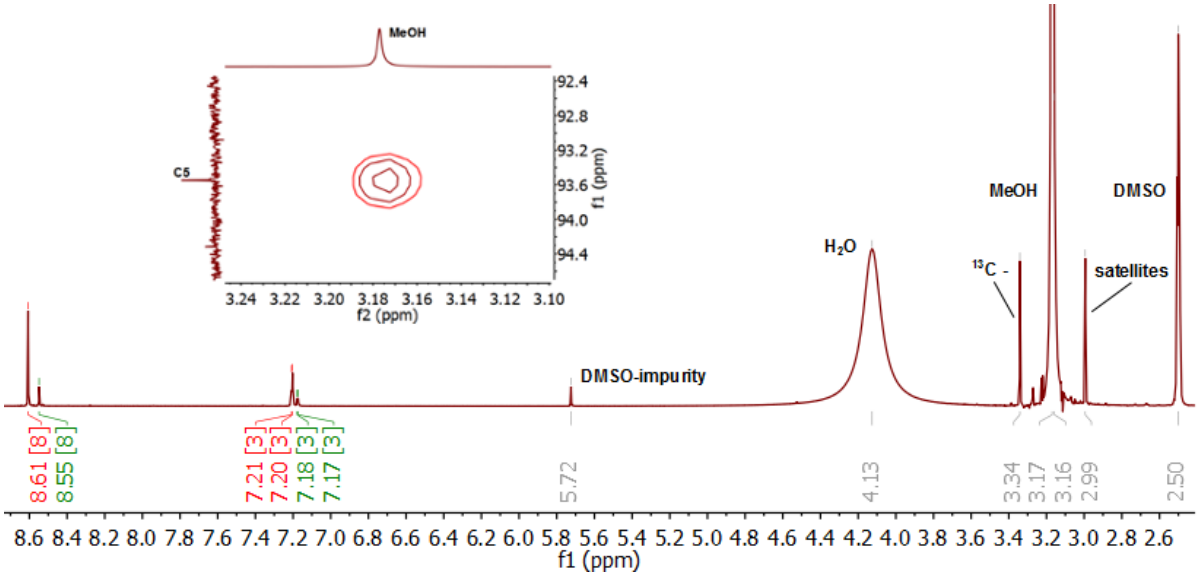

Figure VI.16: ^{1}H-NMR spectrum of PQQ (4.5 mg), dissolved in DMSO-d_6 (0.38 mL) and MeOH (0.042 mL, 16 mol%). The two signals left and right of the MeOH signal (3.34 & 2.99 ppm) are ^{13}C-satellites, which appear as well in the same solvent distribution without PQQ. Inset: HMBC spectrum, showing interaction between the C5 carbon of the hemiketal species and the methanol solvent peak, speaking for an overlap of the solvent with the hemiketal methoxy-group.

Interestingly, the HMBC spectrum of the solution (Inset Figure VI.16) shows a C5 carbon correlation of the hemiketal **16** with a signal hidden under the solvent peak (MeOH), indicating an overlap of the solvent with the hemiketal methoxy-group.

The hemiketal can also be observed in DMF-d_7 by formation of a new signal set, after methanol-d_4 (30 mol%) is added (Table VI.3). Following table gives an overview over all described species in this section and the assignment of their NMR resonances.

Table VI.3: ^{1}H- and ^{13}C-NMR spectra of PQQ (9 mg, 27.2 µmol), dissolved in DMSO-d_6 (0.48 mL) and MeOD-d_4 (0.12 mL, 30 mol%); of PQQ (4.5 mg), dissolved in DMSO-d_6 (0.38 mL) and MeOH (0.042 mL, 16 mol%) and of PQQ (9.0 mg, 27.2 µmol) dissolved in DMF-d_7 (0.48 mL) and MeOD-d_4 (0.12 mL, 32 mol%). Shifts in ppm relative to the respective solvent signals (see VIII.2.1). Signal assignments based on 2D HMQC and HMBC experiments and comparison with data from the literature.[169, 243]

#	DMSO/MeOD-d_4 (80:20)				DMSO/MeOH (90:10)				DMF/ MeOD-d_4 (80:20)				#
	13		**16**		**13**		**16**		**13**		**16**		
^{13}C	**^{13}C**	**^{1}H**	**^{13}C**	**^{1}H**	**^{13}C**	**^{1}H**	**^{13}C**	**^{1}H**	**^{13}C**	**^{1}H**	**^{13}C**	**^{1}H**	**^{1}H**
5	178.35	13.17 (s)	93.38	12.88 (s)	178.10	13.29 (s)	93.23	12.95 (s)	179.60	13.89 (s)	94.04	13.31 (s)	1
4	173.72	8.61 (s)	185.97	8.56 (s)	173.49	8.61 (s)	185.8	8.55 (s)	174.28	8.83 (s)	186.42	8.77 (s)	8
9‘	169.09	7.21 (s)	168.85	7.18 (s)	168.94	7.21 (d) J = 2.2 Hz	168.75	7.18 (d) J = 2.3 Hz	169.65	7.29 (s)	169.57	7.28 (s)	3
7‘	165.11		164.60		165.06		164.42		165.70		165.29		
2‘	161.06		161.06		161.01		160.97		161.66		161.65		
5a	149.08		158.44		148.85		158.09		149.45		159.44		
7	147.19		144.28		146.99		144.11		147.97		145.04		
9	135.88		-		136.15		136.04		137.03		137.76		
1a	134.31		133.27		134.35		133.24		135.46		134.13		
8	129.54		126.87		129.28		126.61		130.65		127.78		
2	127.82		127.68		127.76		127.65		128.74		128.45		
9a	126.98		122.87		126.61		122.52		127.90		123.67		
3a	124.97		121.67		124.66		121.32		125.50		122.45		
3	113.89		112.70		113.63		112.42		114.34		113.14		
-$\underline{C}H_3$			-	3.17			-	-			-	-	

3.4.2 NMR Titration with Methanol and Investigation of the Influence of La and Ca

Hemiketal-distribution was now analyzed for different ratios of MeOD-d_4 and DMSO-d_6 mixtures. The NMR titration was performed with a constant total volume (0.5 mL) with or without $LaCl_3$ or $CaCl_2$ (see VIII.8.2.1). Metals were added in excess to ensure PQQ complexation.

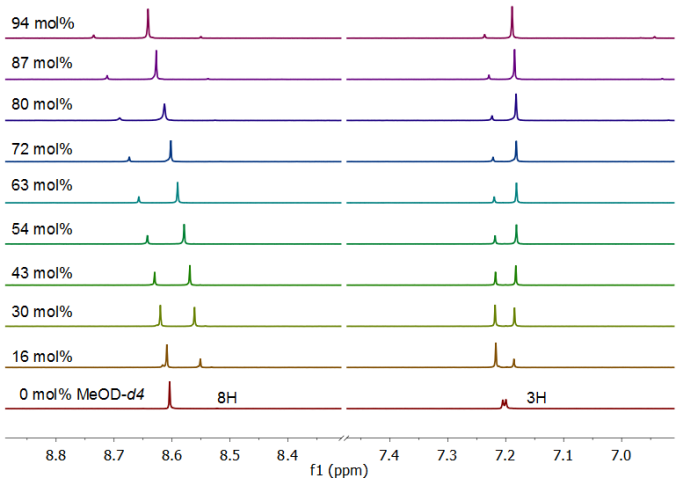

Figure VI.17: Stacked ^{1}H-NMR spectra of PQQ (8 mM) in DMSO-d_6 with increasing amounts of MeOD-d_4 but a constant total volume of 0.5 mL. All spectra were referenced to the DMSO (δH = 2.50) signal.

Starting with 16 mol% MeOD-d_4, resonances for **16** were visible, which grew in intensity with higher amounts of MeOD-d_4, while the signals for free PQQ (**13**) decreased. At 80 mol% MeOD-d_4, a third signal set for the PQQ-ketal species (**26**) was visible as well (Figure VI.17). Interestingly, the resonances for the 8H-proton were shifted low field, while the resonances for the 3H-proton stayed in their position. By comparison of the integrals for the 8H proton, the total hemiketal amount (**16**) was determined. The 8H-resonance for **13** was set to 1.0. The following equation was used:

$$\text{PQQ-hemiketal (\%)} = \frac{\mathrm{I}(\mathbf{16})}{(\mathrm{I}(\mathbf{13})+\mathrm{I}(\mathbf{16})+\mathrm{I}(\mathbf{26}))} \quad (1)$$

I = Integral value of the ^{1}H-NMR experiments.

By calculating the hemiketal amount for each experiment, using the integral values given in Table VI.4, and plotting those amounts versus the molar fractions of methanol, following graph was generated:

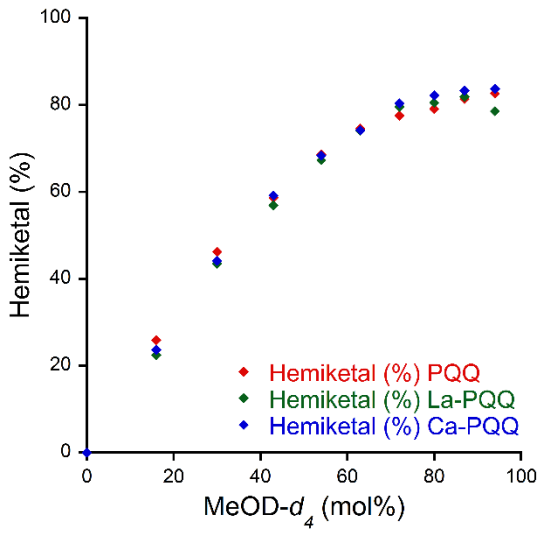

Figure VI.18: Plot of the molar fraction of deuterated methanol (increasing) *vs*. the percent amount of hemiketal species of PQQ (red), La-PQQ (green) and Ca-PQQ (blue), showing, that adding metal ions (Ca, La) did not significantly influence the distribution of **13** and **16**.

Table VI.4: Integral values of the three PQQ species and the calculated percent amounts of the hemiketal **16**.

		PQQ			PQQ + 3 equiv. $LaCl_3 \cdot 7H_2O$			PQQ + 3 equiv. $CaCl_2 \cdot 2H_2O$		
MeOD-d_4 *(mol%)*	**13**	**16**	**26**	**16** (%)	**16**	**26**	**16** (%)	**16**	**26**	**16** (%)
16	1.00	0.35	0	0.26	0.29	0	0.22	0.31	0	0.24
30	1.00	0.86	0	0.46	0.77	0	0.44	0.79	0	0.44
43	1.00	1.42	0	0.59	1.32	0	0.57	1.45	0	0.59
54	1.00	2.19	0	0.69	2.06	0	0.67	2.16	0	0.68
63	1.00	3.08	0.05	0.75	2.87	0	0.74	2.91	0.01	0.74
72	1.00	3.84	0.11	0.78	3.94	0.01	0.80	4.3	0.05	0.80
80	1.00	4.43	0.17	0.79	4.43	0.07	0.81	5.18	0.12	0.82
87	1.00	5.43	0.24	0.81	5.15	0.14	0.82	6.34	0.27	0.83
94	1.00	6.67	0.4	0.83	4.3	0.17	0.79	7.77	0.51	0.84

One would expect, that due to the Lewis-acidity of the metals (La > Ca), hemiketal formation would be enhanced through activation of PQQ C5, similar to the described addition-elimination mechanism in Chapter I.3 and II.3. The hemiketal amount would therefore be highest with lanthanum, followed by calcium and then uncoordinated PQQ. However, comparison of the percent amounts of hemiketal species of free PQQ (red diamonds) with its lanthanum- (blue diamonds) and calcium- (green diamonds) equivalents (Figure VI.18 and Table VI.4) revealed, that metal ion addition does not strongly influence the distribution of hemiketal (**16**) to free PQQ (**13**). At lower MeOH concentrations (< 63 mol%), the percent amount of hemiketal species is higher without a metal coordination and vice versa with increasing amounts of methanol (> 63 mol%). At 63 mol% MeOH, the percentage of hemiketal species is nearly the same for all three curves. Interestingly, the amount of hemiketal species for La-PQQ decreases at 94 mol% methanol. It is important to note, that with this method it is not possible to determine the influence on the rate of hemiketal formation nor to evaluate the impact on the rate of addition of nucleophiles to PQQ in the presence of biologically relevant metal ions. Equilibria between hemiketal and free PQQ can develop over the time course of the experiment and seem to be much more influenced by the mole fraction of methanol rather than by coordinated metals.

3.4.3 NMR Titration with decreasing Methanol Concentrations and Influence of La and Ca

In order to confirm the reversibility of the hemiketal formation, a backwards titration was conducted with PQQ in MeOD-d_4 and increasing amounts of DMSO-d_6. In the literature, crystalline samples of PQQ-hemiketal (**16**) were already described unstable in solution.[156] Through addition of lanthanum or calcium, the effect of coordinating metals on hemiketal decay was observed (see VIII.8.2.2).

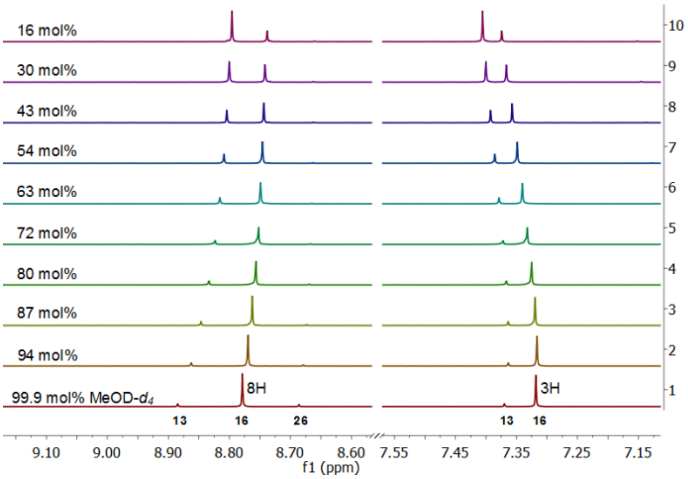

Figure VI.19: Stacked ^{1}H-NMR spectra of PQQ (8mM) in MeOD-d_4 with increasing amounts of DMSO-d_6 but a constant total volume of 0.5 mL. All spectra were referenced to the MeOH (δH = 3.33) signal.

Starting with 100 vol% MeOD-d_4 (99.99 mol%), the hemiketal **16** is the predominant species with additional signals for PQQ (**13**) and the PQQ-ketal (**26**) (Figure VI.19). With increasing amounts of DMSO-d_6 (decreasing amounts of MeOD-d_4), the resonances of the hemiketal (and the one for **26**) loose intensity while the intensity of PQQ increases, speaking for a release of methanol and decomposition of the hemiketal. Compared to the first titration experiment (Figure VI.17) the resonances for the 8H-proton are now shifted upfield, since titrations are performed in the reversed order. Interestingly, the resonances for the 3H proton do not stay in their position in this case, but are shifted lowfield as well. For determination of the total amount of hemiketal species, the integral of free PQQ was always set to 1.0 and equation (1) was used again with integral values given in Table VI.5.

Table VI.5: Integral values of the three PQQ species and the calculated percent amounts of the hemiketal **16**.

		PQQ			PQQ + 3 equiv. $LaCl_3 \cdot 7H_2O$			PQQ + 3 equiv. $CaCl_2 \cdot 2H_2O$		
MeOD-d_4 *(mol%)*	**13**	**16**	**26**	**16** (%)	**16**	**26**	**16** (%)	**16**	**26**	**16** (%)
99	1.00	11.38	0.72	0.87	-	-	-	5.99	0.39	0.81
94	1.00	8.4	0.31	0.87	4.72	0.22	0.79	6.52	0.34	0.83
87	1.00	6.81	0.23	0.85	4.9	0.11	0.82	6.05	0.14	0.84
80	1.00	5.73	0.13	0.84	4.52	0.04	0.81	5.01	0.05	0.83
72	1.00	4.62	0.11	0.81	3.91	0.01	0.79	3.99	0.01	0.80
63	1.00	3.05	0.06	0.74	2.92	0	0.74	3.09	0.01	0.75
54	1.00	2.28	0.03	0.69	1.99	0	0.67	2.23	0.01	0.69
43	1.00	1.57	0.03	0.60	1.26	0	0.56	1.35	0	0.57
30	1.00	0.85	0.02	0.45	0.73	0	0.42	0.81	0	0.45
16	1.00	0.37	0.01	0.27	0.32	0	0.24	0.31	0	0.24

The hemiketal amount was calculated for each experiment and was plotted versus the molar fractions of methanol, together with the data received from the forward titration experiment (Figure VI.20).

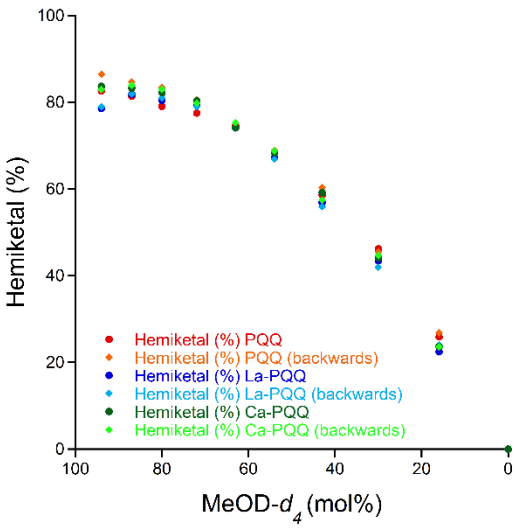

Figure VI.20: Plot of the mole fraction of methanol *vs.* the percent amount of hemiketal species of PQQ (orange), La-PQQ (light-blue) and Ca-PQQ (light-green), given as diamonds. The values of the forward titration are given as well as dots for PQQ (red), La-PQQ (blue) and Ca-PQQ (green).

Hemiketal values of the forward and backwards titrations are relatively similar for La- (blue) and Ca-PQQ (green) plots and to some extend (≤63 mol% MeOD-d_4) also for free PQQ (orange/red), taking errors for pipetting and weighting into account. Hemiketal formation is reversible and the distribution of **13** and **16** dependent on the mole fraction of methanol present in the solvent mixture. Both lanthanum and calcium do not have a large impact on this distribution, however, those metals enhance methanol elimination to some extent. Since backwards titration starts with pure methanol solutions of PQQ, containing almost exclusively hemiketal **16**, the added DMSO shifts equilibria back to **13**. While forward and backward titration lead to similar hemiketal amounts for both metal-containing plots, the hemiketal amount is 4-5% higher at high methanol amounts for the backwards titration with uncoordinated PQQ. This would mean that higher amounts of DMSO are needed to convert **16** back to **13**. However, the difference is only small and most likely within the error of the experiment.

3.4.4 Hemiketal UV-Vis Experiments in the Literature

In order to corroborate the results received from NMR spectroscopy, UV-Vis titrations were performed. In the literature, Dekker *et al.* described the UV-Vis spectroscopic investigation of PQQ in methanol and showed a temperature dependency of the hemiketal formation (Figure VI.21).[182]

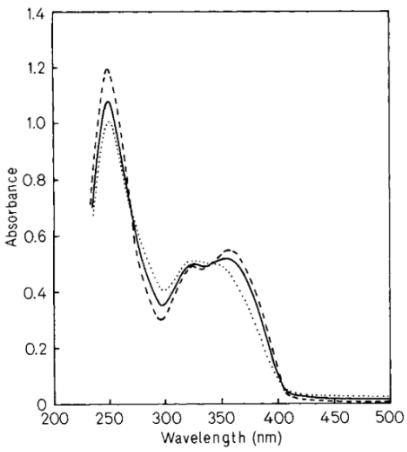

Figure VI.21: Spectral changes on a methanolic solution of PQQ, measured at 0°C (- - -), 30°C (—) and 55°C (· · ·), indicating higher amounts of hemiketal-species (maximum at ~358 nm) at lower temperatures and higher amounts of free PQQ (maximum at ~325 nm) at higher temperatures. Reprinted with permission from Dekker *et al.*[182] Copyright John Wiley and Sons (2005).

With $PQQMe_3$ (**11**), UV-Vis titration experiments with methanol in MeCN were conducted by Itoh *et al.*[156] To monitor the formation of hemiketal **18**, $PQQMe_3$ (**11**) (0.484 mM) was titrated by the authors with large excess of methanol (0 – 12 M) in MeCN (Figure VI.22), resulting in an increase of absorption at 371 nm, while the shoulders at 275 nm and 440 nm decreased. Isosbestic points were visible at 252 nm, 354 nm and 413 nm.

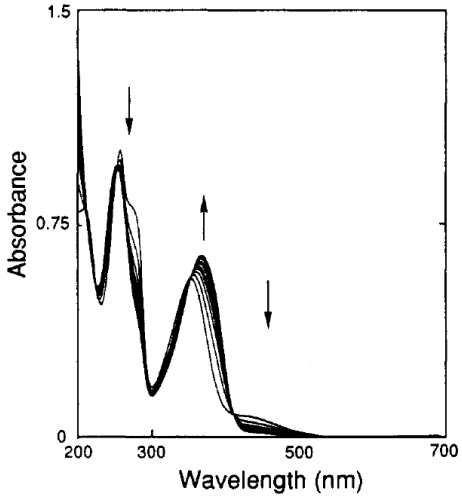

Figure VI.22: Spectral changes in the titration of $PQQMe_3$ (**11**) (0.484mM) with methanol (0 - 12 M) in MeCN. Reprinted with permission from Itoh *et al.*[156] Copyright (1993) American Chemical Society.

In a subsequent publication, Itoh *et al.* examined the effect of Ca^{2+} ions on the hemiketal formation of $PQQMe_3$ (**11**).[173] First step was the titration of $PQQMe_3$ (**11** - 0.025 mM) with $Ca(ClO_4)_2$ (0 - 6.5 mM) in MeCN (Figure VI.23), resulting in a red shift of the absorption maximum at 354 nm to 368 nm, while the shoulder at 280 nm decreased. Isosbestic points were visible at 268 nm, 289 nm, 303 nm, 361 nm and 422 nm, respectively.

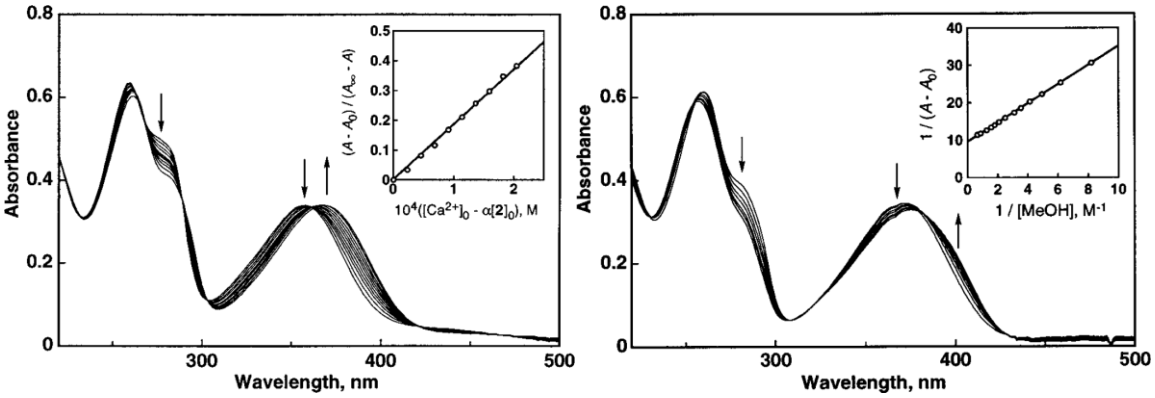

Figure VI.23: Left: Spectral change in the titration of $PQQMe_3$ (0.025 mM) with $Ca(ClO_4)_2$ (0 - 6.5 mM) in MeCN. Right: Spectral change in the titration of $PQQMe_3$ (0.025 mM) with MeOH (0 - 1.1 M) in the presence of $Ca(ClO_4)_2$ (15 mM) in MeCN. Reprinted with permission from Itoh *et al.*[156] Copyright (1993) American Chemical Society.

After the effect of coordinating Ca^{2+} ions to the absorption of $PQQMe_3$ (**11**) was shown, Itoh *et al.* further examined the hemiketal (**18**) formation of Ca-coordinated $PQQMe_3$. Therefore, $PQQMe_3$ (**11**) (0.025 mM) was titrated with MeOH (0 - 1.1 M) in the presence of large excess of $Ca(ClO_4)_2$ (15 mM) in MeCN (Figure VI.23). By determination of the hemiketal formation constant (slope of the linear plot in the inset of Figure VI.23), it could be shown, that the constant was nearly six times higher in the presence of Ca^{2+} (3.6 M^{-1}) than without a metal (0.63 M^{-1}).

3.4.5 Calculated UV-Vis Spectra of PQQ and its Methanol Adducts

UV-Vis spectra for PQQ (**13**), PQQ-hemiketal (**16**) and PQQ-ketal (**26**) were calculated using DFT methods (Figure VI.24).

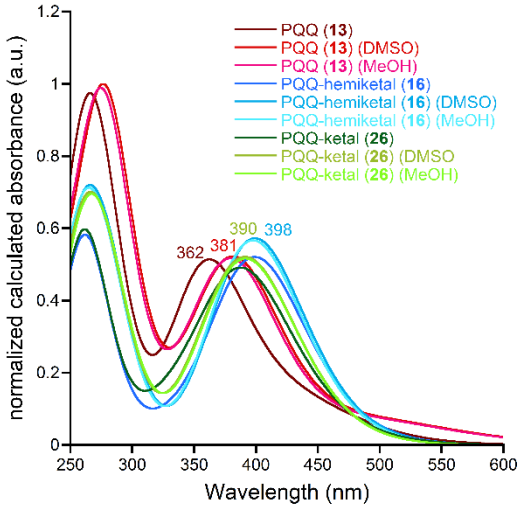

Figure VI.24: Calculated UV-Vis spectra for PQQ (**13**) (red), PQQ-hemiketal (**16**) (blue) and PQQ-ketal (**26**) (green), each in gas phase, DMSO and methanol, received by DFT calculations: Gaussian 09, TD-DFT, 100 states, restricted, B3LYP, 6-31G++(d,p), CPCM (DMSO / MeOH).

The optimized structures used for the calculations are listed below:

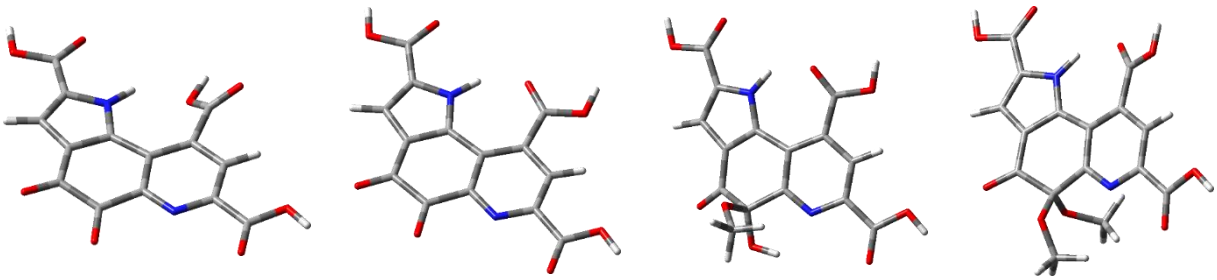

13 (gas phase) **13 (DMSO)** **16 (gas phase)** **26 (gas phase)**

Figure VI.25: Optimized structures for PQQ in gas phase (far left), PQQ in DMSO (left) PQQMeOH in gas phase (right) and PQQ(MeOH)$_2$ in gas phase (far right). Not shown: Optimized strucutres in methanol and DMSO.

In general, calculations in DMSO differed only slightly to the ones calculated in methanol. Calculations in gas phase differed stronger, especially in case of free PQQ. Here, the C9-carboxyl group is slightly twisted out of plane (Figure VI.25), compared to the calculations in solution, which could cause the blue shift of the absorption maximum at 381 nm (red lines). The same absorption maximum is slightly red-shifted in case of **26** (green lines) and stronger red-shifted in case of **16** (blue lines), which is in good agreement with the UV-Vis titrations described in the following section.

3.4.6 UV-Vis Titration with Increasing Methanol Concentrations and Influence of La and Ca

In order to further elucidate the influence of La or Ca on the PQQ-hemiketal formation with changing ratios of methanol, UV-Vis titrations were performed (Figure VI.26). Due to the experimental setup, higher dilutions were necessary compared to NMR (NMR: 8 mM; UV-Vis: 0.04 mM – see VIII.8.2.4).

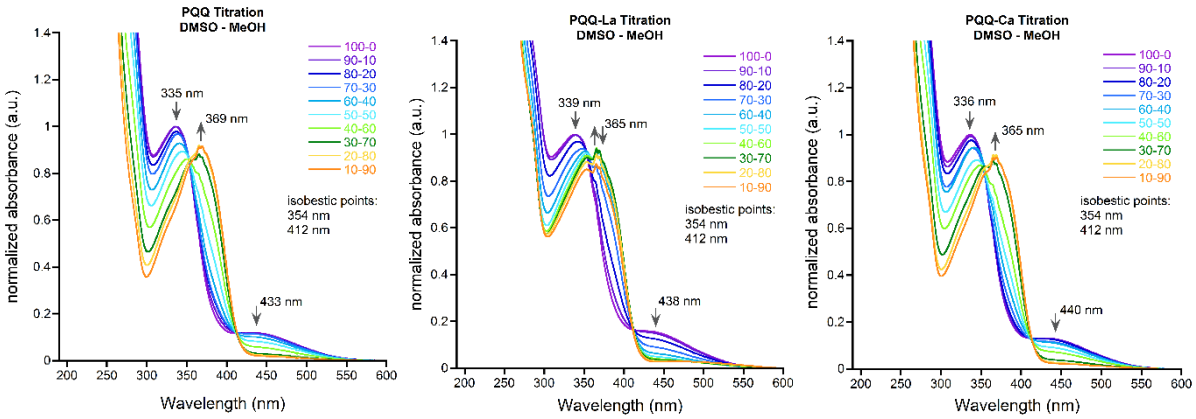

Figure VI.26: Titration of PQQ (left), La-PQQ (middle) and Ca-PQQ (right) in DMSO with increasing amounts of MeOH but a constant total volume of 1 mL (0.04 mM PQQ, 0.12 mM metal chloride). 100-0 for a pure DMSO solution, 10-90 for a mixture of 10 vol% DMSO and 90 vol% MeOH. Blank measurement performed with empty cuvette, solvent blank measurement was not exercised due to the changing ratios of solvent. Baseline was corrected to an absorbance of 0 at 600 nm. Since absorbance maxima were influenced by metal coordination, the spectra in pure DMSO (100-0) are normalized to an absorbance of 1 at 335 nm (PQQ), 339 nm (PQQ-La) and 336 nm (PQQ-Ca) and the spectra with increasing methanol amounts are adjusted accordingly.

The UV-Vis absorption spectrum of PQQ in DMSO showed two maxima at 335 and 433 nm, which were slightly shifted in presence of metals (La-PQQ: 339, 438 nm; Ca-PQQ: 336, 440 nm), due to complex formation, as described in Chapter IV. This redshift can also be observed in MDH, as Ln-MDH from the XoxF type shows a maximum at 355 nm, while the maximum from the related Ca-MDH (MxaF) is at 345 nm.[94] Upon raising the methanol concentrations, the absorption maxima decreased and a new maximum appeared (PQQ: 369 nm, La-PQQ: 365 nm, Ca-PQQ: 365 nm). By comparison with literature values (shift from 325 to 358 nm -Figure VI.21) and DFT calculations (381 to 398 nm - Figure VI.24) this new maximum can be assigned to the hemiketal-form. With the exception of La-PQQ, two isosbestic points can be observed in each spectrum (PQQ: 354, 412 nm; La-PQQ: 412 nm; Ca-PQQ: 354, 412 nm), underlining the conversion of species. While the PQQ and Ca-PQQ hemiketal-form constantly increase the intensity up to 94 mol% MeOH, the La-PQQ hemiketal reach maximum at 72 mol% MeOH and loose intensity again at higher MeOH amounts. In addition, the first isosbestic point is not as clear as in the other spectra, speaking for more species than just the PQQ – PQQ-hemiketal conversion. Both PQQ-ketal (**26**), non-coordinated PQQ or even the PQQ-water adduct (**15**) (through added crystal water) could all have an influence here.

For better comparability with the NMR experiments, the percent amount of hemiketal **16** was plotted *vs*. the mole fraction of methanol. For the percent amount of hemiketal-species, following equation was used:

$$\text{PQQ-hemiketal (\%)} = \frac{A(H)-A_0(H)}{[A(H)-A_0(H)]-A(P)} \quad (2)$$

A(H) = Absorption at the hemiketal-maximum (PQQ: 369 nm; PQQ-La: 365 nm; PQQ-Ca: 365 nm). A_0(H) = Starting value (MeOH = 0 vol%) of the absorption at the hemiketal-maximum (PQQ: 369 nm; La-PQQ: 365 nm; Ca-PQQ: 365 nm). A(P) = Absorption at the second PQQ-maximum (PQQ: 433 nm; La-PQQ: 438 nm; Ca-PQQ: 440 nm).

Since the absorption of both species overlap to some extent, the absorption of the hemiketal **16** was subtracted by the starting absorption value of this wavelength. For the same reason, the second absorption maximum of PQQ (**13**) (433 nm) (La-PQQ: 438 nm; Ca-PQQ: 440 nm) was used which does not overlap with the absorption of the hemiketal-species.

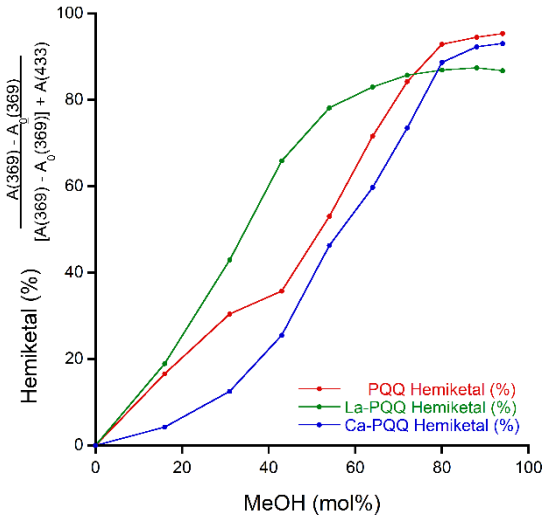

Figure VI.27: Combined plots of the percentage of hemiketal-species versus the mole fraction of methanol. Measuring points were connected for better visibility of the progression. A curve fit was not possible.

Without metal, the concentration of hemiketal **16** rapidly increases with increasing methanol concentrations but then flattens beginning with 80 mol% MeOH (Figure VI.27). With La, the curve is steeper, but shows a lower hemiketal maximum concentration. The graph of Ca-PQQ is "S"-like with a slower growth in the beginning and a maximum concentration between PQQ and La-PQQ. In comparison with the NMR experiments, where all three graphs look very similar, regardless of the added metal-ions, the graphs received by UV-Vis titrations differ in a greater value. A direct comparison should be made with caution, since the UV-Vis measurements are 200-times more diluted than the NMR ones. In addition, absorption is much more influenced by coordinated metals than NMR shifts and additional PQQ species (ketal **26**, water-adduct **15**) could influence the received spectra. On the basis of the received data, La^{3+}

shifts equilibria to higher hemiketal concentrations, which is in line with the proposed MDH mechanism, where the central metal acts as a Lewis acid and activates the PQQ-C5 C=O bond for nucleophilic attack.[44-45] However, coordinating Ca^{2+} should have the same effect but shows reduced hemiketal concentrations in Figure VI.27. This experiment shows the limitations of UV-Vis spectroscopy. The hemiketal concentration can only be determined *via* absorption maxima and not directly *via* integral values in NMR. This makes UV-Vis much more prone to errors, especially in combination with the complicated distribution of PQQ species in solution. PQQ (**13**), PQQ-hemiketal (**16**), -ketal (**26**) or the water adduct (**15**), either coordinated or non-coordinated with metals are all in equilibrium and contribute to the received UV-Vis spectra.

3.4.7 UV-Vis Titration with decreasing Methanol Concentrations and Influence of La and Ca

Similar to the NMR experiments, a backwards titration was conducted, starting with a 100 vol% solution of PQQ (0.04 mM) in MeOH and increasing amounts of DMSO with or without 3 equiv. of $LaCl_3 \cdot 7H_2O$ or $CaCl_2 \cdot 2H_2O$ with a constant total volume of 1 mL (see VIII.8.2.5).

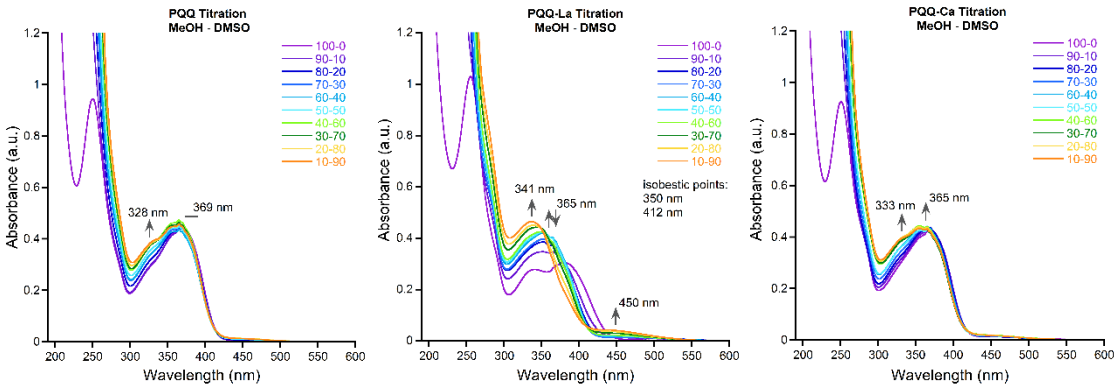

Figure VI.28: Titration of PQQ (left), La-PQQ (middle) and Ca-PQQ (right) in MeOH with increasing amounts of DMSO but a constant total volume of 1 mL (0.04 mM PQQ, 0.12 mM metal chloride). 100-0 for a pure MeOH solution, 10-90 for a mixture of 10 vol% MeOH and 90 vol% DMSO. Blank measurement performed with empty cuvette, solvent blank measurement was not exercised due to the changing ratios of solvent. Baseline was corrected to an absorbance of 0 at 600 nm.

Interestingly, the received spectra look very different to the ones received from the forward titration (Figure VI.28). In the PQQ and Ca-PQQ spectra, an increase of absorption can be observed at 335 nm (Ca-PPQ: 333 nm) which is the absorption maximum of the free PQQ-species, in accordance to the forward titration (VI.3.4.6) and the literature (Figure VI.21). It is interesting that the absorption maximum at 369 nm (Ca-PQQ: 365 nm) for the hemiketal-species **16** remains in its position. It seems, that the hemiketal-species is not changed back to PQQ (**13**) and is not affected by increasing amounts of DMSO. This contradicts the NMR-experiments, where the amount of hemiketal-species was reduced, after the MeOH/DMSO ratio

was changed back to higher DMSO amounts. Due to the 200 times higher PQQ concentration in the NMR-experiments, it is possible, that the concentration of PQQ and therefore the total amount of MeOH is important for the equilibrium of **13** and **16**. Another difference is the time scale. The UV-Vis measurements were performed immediately after the mixtures were prepared, while the mixtures for the NMR experiments were all prepared at the same time and then successively measured *via* autosampling. It is therefore possible, that equilibrium had not been reached in the UV-Vis measurements.On the other hand, the spectrum of La-PQQ is similar to the one received from the methanol titration (VI.3.4.9). By splitting the received spectra into two parts (Figure VI.29), it is apparent, that two different conversions occur:

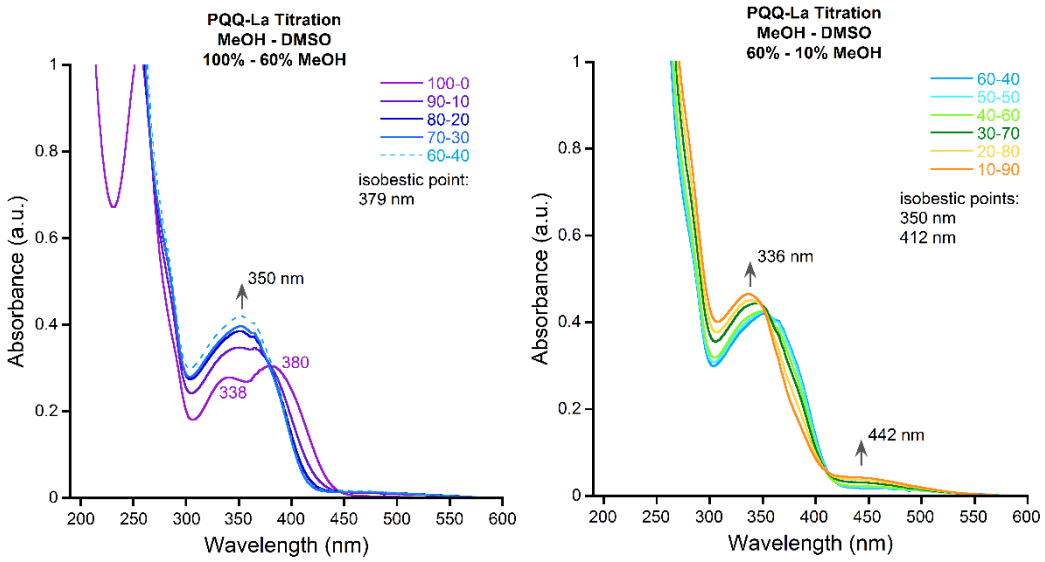

Figure VI.29: Titration of La-PQQ in MeOH with increasing amounts of DMSO. Left: From 100 vol% - 60 vol% MeOH, right: from 60 vol% - 10 vol% MeOH.

In 100 vol% MeOH, PQQ possesses two absorption maxima at 339 nm and 379 nm. By decreasing the amount of MeOH, a single maximum at 350 nm appears which increases its intensity until 60 vol% MeOH. In addition, a clear isosbestic point is visible at 379 nm. When the amount of MeOH is further decreased to 10 vol%, new absorption maxima appear at 336 nm and 442 nm, with clear isosbestic points at 350 nm and 412 nm. By comparison of the spectra received from titrations with increasing methanol concentrations (see VI.3.4.6) and lanthanum titrations in MeOH (see VI.3.4.9), it is possible that the lanthanum-PQQ-hemiketal complex disintegrates first with increasing concentrations of DMSO, releasing free PQQ-hemiketal (**16**) until 60% MeOH. Subsequently **16** is converted back to PQQ (**13**). On the other hand, it is not clear, why free PQQ and Ca-PQQ hemiketal species are not converted back as well. Due to the higher water contents of $LaCl_3 \cdot 7H_2O$, the formation of PQQ-water adduct (**15**), could also be of relevance here.

3.4.8 UV-Vis Titration with Controlled Ionic Strength

In order to exclude the influence of the total ion content (3 Cl^- for lanthanum *vs*. 2 Cl^- for calcium), the experiments were repeated with an excess of NaCl in solution (3 equiv. and 100 equiv. – see Figure VI.30 and Figure VI.31 and the experimental procedure in VIII.8.2.6).

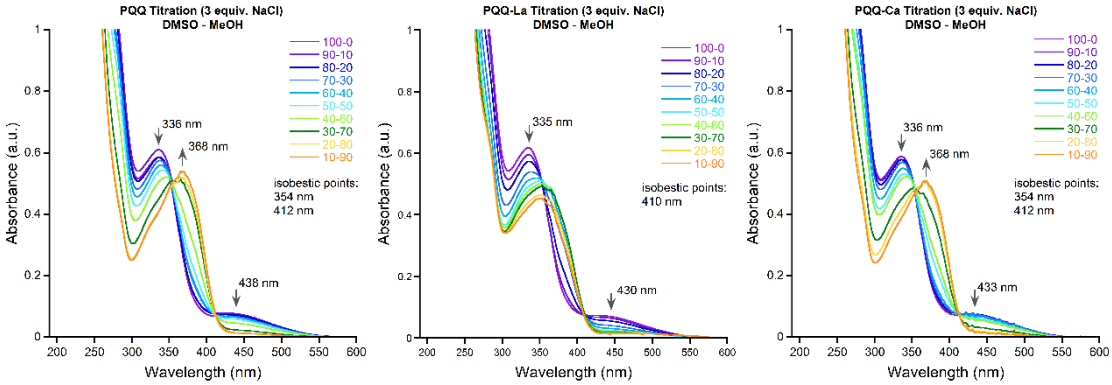

Figure VI.30: Titration of PQQ (left), La-PQQ (middle) and Ca-PQQ (right) in DMSO with 3 equiv. of NaCl and increasing amounts of MeOH but a constant total volume of 1 mL (0.04 mM PQQ, 0.12 mM NaCl, 0.12 mM metal chloride). 100-0 for a pure DMSO solution, 10-90 for a mixture of 10 vol% DMSO and 90 vol% MeOH. Blank measurement performed with empty cuvette, solvent blank measurement was not exercised due to the changing ratios of solvent. Baseline was corrected to an absorbance of 0 at 600 nm.

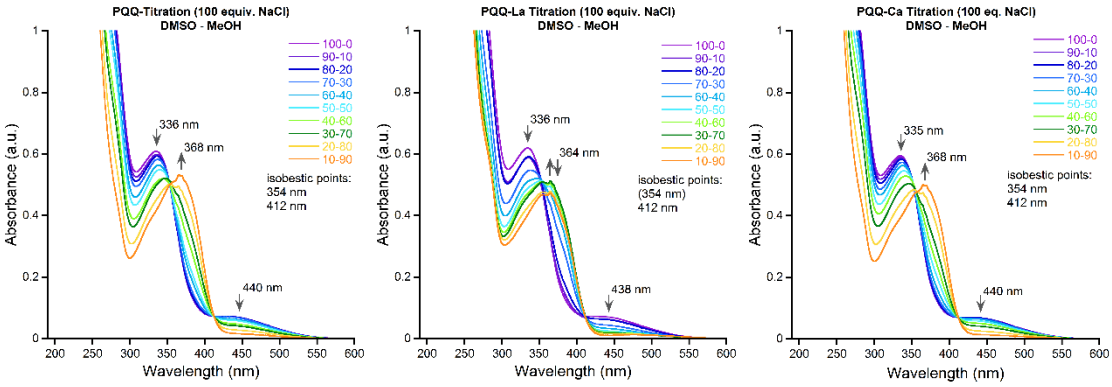

Figure VI.31: Titration of PQQ (left), La-PQQ (middle) and Ca-PQQ (right) in DMSO with 100 equiv. of NaCl and increasing amounts of MeOH but a constant total volume of 1 mL (0.04 mM PQQ, 4 mM NaCl, 0.12 mM metal chloride). 100-0 for a pure DMSO solution, 10-90 for a mixture of 10 vol% DMSO and 90 vol% MeOH. Blank measurement performed with empty cuvette, solvent blank measurement was not exercised due to the changing ratios of solvent. Baseline was corrected to an absorbance of 0 at 600 nm.

The spectra received by titrations with PQQ and Ca-PQQ solutions looked similar to the ones received without the addition of NaCl. The high ion concentrations seemed to have a higher impact to the titrations with La-PQQ, since no absorption maximum at 368 nm could be observed and therefore, no formation of hemiketal-species seemed to occur. For a detailed examination of the ion influence, the percent amount of hemiketal **16** was plotted *vs*. the mole fraction of methanol in case of PQQ and Ca-PQQ (Figure VI.32). For calculation of the amount of **16**, equation (2) was used again.

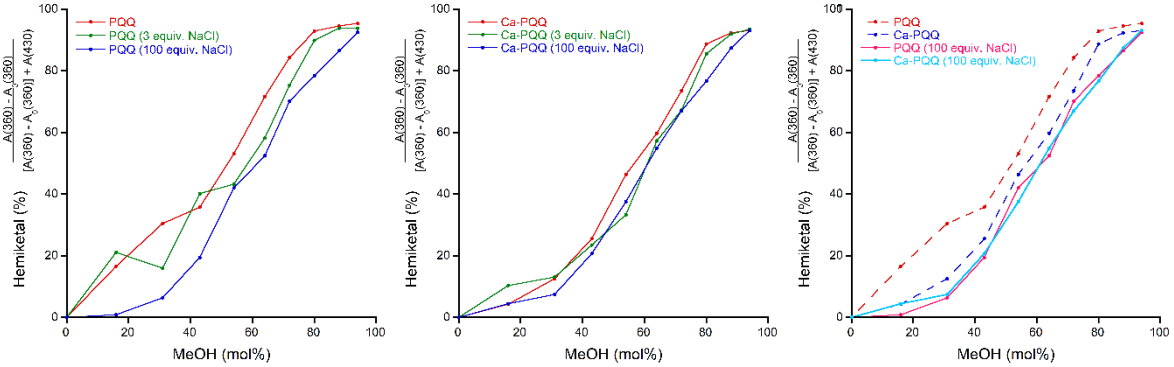

Figure VI.32: Combined plots of the percent amount of hemiketal-species *vs*. the percent amount of methanol under influence of 3 or 100 equiv. of NaCl. Left: PQQ, middle: Ca-PQQ, right: Combined PQQ & Ca-PQQ plots with and without NaCl. Measuring points were connected for better visibility of the progression. A curve fit was not possible.

By comparison of the percentages of hemiketal species, high NaCl concentrations have a higher impact than expected. In both cases (PQQ and Ca-PQQ), the addition of NaCl lead to decreased hemiketal concentrations, given by weaker slopes of the green (3 equiv. NaCl) and blue (100 equiv. NaCl) curves. This effect is stronger for free PQQ, while the curves for Ca-PQQ do not change drastically. On the other hand, the final concentrations of hemiketal **16** at 90 vol% MeOH concentration do not differ strongly and are almost the same for Ca-PQQ. The reason for the zigzag progression of the green (PQQ) curve could be the result of a pipetting error. Time could also be a factor here. All mixtures were prepared successively and each immediately before measurements. However, equilibria could take longer (or shorter) times to adjust when metal ions are present. A possibility, which has to be investigated in future experiments.

Interestingly, by direct comparison of the curves for PQQ (pink) and Ca-PQQ (light blue) under influence of 100 equiv. of NaCl in the right spectrum, the curve progression is almost identical. This raises the question, whether high amounts of NaCl inhibit a metal effect to the hemiketal formation or if the high ion concentration prevent a Ca^{2+}-coordination to PQQ in the first place. It should be noted here, that Na^{+} can coordinate to PQQ as well, illustrated by a number of crystal structures.[191, 204, 256]

3.4.9 PQQ Metal Titrations in Methanol

In order to better understand the hemiketal experiments (vide supra) and the influence of coordinating metals on the equilibrium between PQQ (**13**) and PQQ-hemiketal (**16**), metal titrations were conducted in methanol with the same PQQ concentrations as for the previous experiments and up to 5 equiv. of Ca^{2+}, La^{3+} or Eu^{3+} (Figure VI.33). Europium is the stronger Lewis acid in comparison to lanthanum and should therefore show a better activation of the C5

C=O bond for nucleophilic attack.[44-45, 76, 168] Eu^{3+} ions were already successfully implemented as central metals in the XoxF active site.[94]

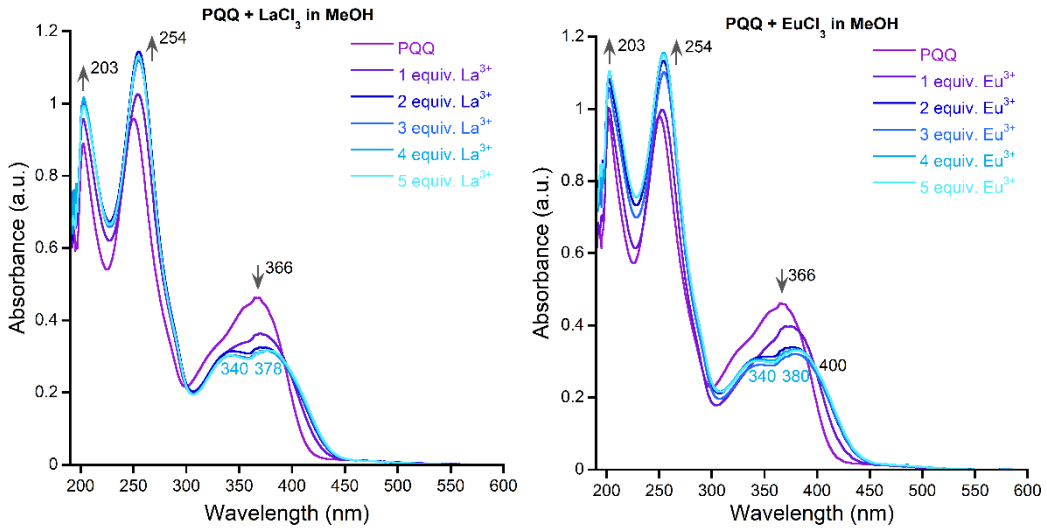

Figure VI.33: Titration of PQQ with increasing amounts of $LaCl_3$ (left), $EuCl_3$ (middle) and $CaCl_2$ (right) in MeOH, but a constant total volume of 1 mL (0.04 mM PQQ, 0.04 - 0.20 mM metal chloride). Blank measurement was performed in pure methanol and the baseline was corrected to an absorbance of 0 at 600 nm.

In methanol, PQQ shows three absorption maxima, at 203, 254 and 366 nm. Upon addition of trivalent lanthanum or europium, an increase of absorption at 203 and 254 nm was observed, while the maximum at 366 nm decreased. Interestingly, higher amounts of metal salts led to a formation of two new absorption maxima at 340 and 378 nm (Eu: 340 and 380 nm) with a clear isosbestic point at 391 nm (Eu: 400 nm). It was not possible to record meaningful spectra with $CaCl_2$. The maxima of absorbance varied strongly, regardless of the amount of metal salt added, which could indicate weak binding or exchange processes. The general appearance and change of absorbance after addition of $CaCl_2$ was however in accordance with the two spectra received from titration with the lanthanide salts.

3.5. Kinetics of the Formation and Decay of PQQ-hemiketal

3.5.1 Reversibility of the C5-hemiketal Formation

Upon standing in methanol, the formed PQQ-hemiketal (**16**) starts to precipitate as a pale-yellow solid.[182] By re-dissolving this precipitate in DMF, a color-change was observed from bright yellow to dark red within minutes, indicating a conversion from **16** back to free PQQ (**13**). Itoh *et al.* described a similar conversion of the $PQQMe_3$-hemiketal (**18**) back to the quinone (**11**) in MeCN within minutes.[156]

To understand the time dependence of the PQQ-hemiketal (**16**) decay to free PQQ (**13**), hemiketal **16** was dissolved in DMF-d_7 and ^{1}H-NMR spectra were immediately recorded at low temperature (4°C, to slow down the conversion).

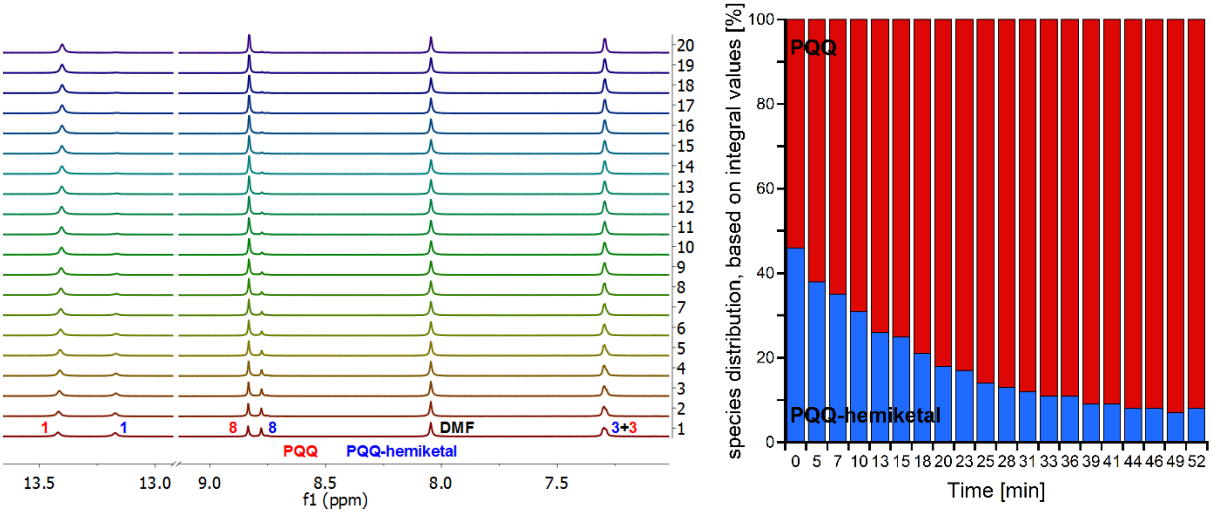

Figure VI.34: Left: Stacked ^{1}H-NMR spectra of PQQ-hemiketal (**16**) (9 mg, 24.8 µmol) in DMF-d_7 (0.6 mL). For each measurement, four spectra were recorded and averaged afterwards. Right: Bar diagram of the amount of PQQ (**13**) and PQQ-hemiketal (**16**) at a certain time.

As it is clearly visible, two signal sets are present for protons H1, H8 and H3, one for PQQ (**13**) (red) and one for the PQQ-hemiketal (**16**) (blue). Within one hour the resonances for **16** decreased until equilibrium was reached at around 8%, while the ones for PQQ (**13**) increased (Figure VI.34). The conversion back to **13** can also be visualized by plotting the time after addition of the solvent in minutes, versus the integral value of the two PQQ species (Table VIII.9, Figure VI.34). This experiment demonstrates the conversion of PQQ-hemiketal (**16**) and its instability in other media than methanol. It also highlights the importance to consider the time frame when studying PQQ addition/elimination reactions.

3.5.2 Kinetics of the PQQ-methanol Adduct Formation

Hemiketal formation equilibria in different methanol ratios with or without the influence of coordinating metals were determined in VI.3.4. A valuable addition would be the determination of the hemiketal formation kinetics. NMR was used for this study, starting with a solution of PQQ (9 mg, 27.2 µmol) in DMF-d_7 (0.45 mL). After the first ^{1}H-NMR measurement, 50 µL MeOD-d_4 (10 vol%) were added to the PQQ solution and additional spectra were recorded at 0°C, to slow down hemiketal formation. Unfortunately, the experimental setup was too slow (first ^{1}H-NMR spectrum ~5 min after metal addition due to locking process) and all spectra only showed the same PQQ to hemiketal distribution (Figure VI.35).

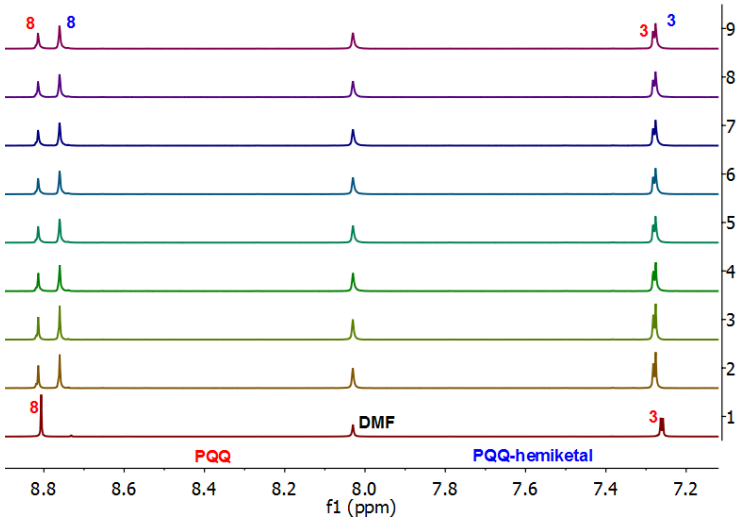

Figure VI.35: Stacked ^{1}H-NMR spectra of PQQ (9 mg, 27.2 µmol) in DMF-d_7 (0.45 mL) [first spectrum] + MeOD-d_4 (0.05 mL – 10 mol%), measured roughly every 90 seconds (4 scans per measurement).

To slow down the conversion, solid PQQ (9 mg, 27.2 µmol) was used in a second approach, to which MeOD-d_4 (0.5 mL) was added. The NMR tube was shaken and ^{1}H-NMR spectra were measured immediately after at 0°C. Also in this case, the first spectrum could only be recorded 5 minutes after methanol addition, but due to the slow dissolution of PQQ at 0°C, differences in the ^{1}H-NMR spectra were observable (Figure VI.36).

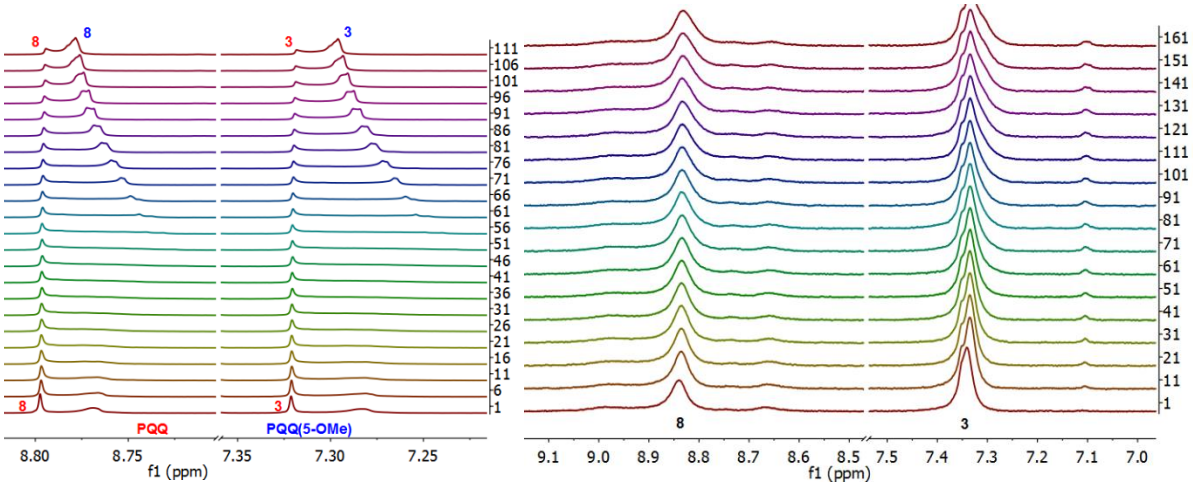

Figure VI.36: Left: Stacked ^{1}H-NMR spectra of solid PQQ (9 mg, 27.2 µmol) to which 0.5 mL of MeOD-d_4 were added. Every 5th spectrum (~ every 7.5 min) is shown. Right: Stacked ^{1}H-NMR spectra of solid PQQ (9 mg, 27.2 µmol) + solid $LaCl_3 \cdot 7H_2O$ (9.6 mg, 27.2 µmol) to which 0.5 mL of MeOD-d_4 were added. Every 10th spectrum (~ every 15 min) is shown. ^{1}H-NMR spectra recorded roughly every 90 seconds (4 scans per measurement).

In the beginning, large resonances for PQQ-8H and -3H are visible, while the corresponding hemiketal resonances are very small and broad and further broaden in the course of the experiment. Beginning with spectrum 61 (after ~ 91.5 min) the resonances sharpen again and

grow in intensity, while the ones for PQQ decrease. It is therefore quite likely, that PQQ is dissolved in MeOD-d_4 first, while hemiketal formation proceeds over time.

In order to study the influence of coordinating metals to the hemiketal formation, the same setup was used, including solid PQQ (9 mg, 27.2 µmol), but this time, 1.0 equiv. of solid $LaCl_3 \cdot 7H_2O$ (9.6 mg, 27.2 µmol) was added before MeOD-d_4 (0.5 mL) was introduced to the solids and ^{1}H-NMR spectra were recorded at 0°C (Figure VI.36). In comparison with the spectra received without $LaCl_3$, all spectra here look very similar and only get broadened over time. This suggests, that hemiketal formation is much faster with lanthanum, since no conversion of species can be observed. Additional resonances are visible around 8.68 and 7.10 ppm. By comparison with Table VI.2 (PQQ in methanol-d_4), these resonances can be assigned to PQQ-ketal (**26**) (8.68, 7.08 ppm) which grows in intensity throughout the experiment.

To summarize, hemiketal (**16**) formation occurs rapidly after methanol-d_4 is added to DMF-d_7 solutions of PQQ in NMR experiments. Solid PQQ is dissolved by methanol first, while hemiketal formation takes time to proceed. Formation of ketal (**26**) can be observed as well. The data suggests an enhanced hemiketal formation through addition of lanthanum. This is in line with the proposed purpose of lanthanides as cofactors in MDH, namely the activation of the PQQ-C5 C=O bond for nucleophilic attack.

4. Conclusion

A range of PQQ derivatives was fully characterized by NMR in solution and to some extend by mass spectrometry, UV-Vis and DFT.

PQQ cyanide adduct formation is pH dependent and favors basic pH, since CN^- is the better nucleophile than HCN. As a result, a 2:1 ratio of PQQ-CN to free PQQ was observed in DMF-d_7, while almost full conversion to the cyanide adduct was observed in basic D_2O solution. No water adduct was observed in the aqueous, cyanide containing PQQ solution, indicating CN^- as the better nucleophile than OH^-.

In pure MeOD-d_4, a new PQQ-adduct was observed and characterized as the PQQ-ketal (**26**) by NMR, mass spectrometry, IR and DFT. It is a side product which is formed in methanolic PQQ solutions in addition to the literature known PQQ-hemiketal (**16**). In EtOD-d_6, the same distribution of PQQ derivatives was observed, underlining the complex nature of PQQ chemistry in solution.

The hemiketal species **16** is in equilibrium with PQQ (**13**), its concentration is dependent on the total amount of methanol in solution and the formation reversible by reincreasing the amount of DMF or DMSO.

The effect of coordinating metals (Ca^{2+}, La^{3+}) on the hemiketal equilibrium was examined by NMR, but no major differences were observed in comparison to uncoordinated PQQ. The impact of metals was more facile to be observed with UV-Vis titrations, and especially La^{3+} coordination caused enhanced hemiketal formation and decay. However, the presence of multiple PQQ species in solution made UV-Vis spectra difficult to interpret and prone to errors.

NMR measurements of the hemiketal formation kinetics revealed, that the PQQ-hemiketal forms rapidly after methanol addition in solution. By methanol addition to solid PQQ, NMR data indicate initial dissolution of PQQ followed by slow conversion to the hemiketal afterwards. Through addition of trivalent lanthanum, this hemiketal formation was accelerated.

The MDH mechanism of action is still subject of debate in the literature.[13] The immediate formation of the hemiketal adduct in solution, observed throughout this chapter, could at first glance support the addition-elimination mechanism. However, the rapid reaction of PQQ with different nucleophiles outside of the active site of MDH does not necessarily proove that the addition-elimination mechanism is the one favored in the enzyme. The conducted experiments gave some indication for the enhancing effect of coordinated lanthanum on nucleophilic attack on PQQ. However, this effect could only be shown in experiments, where PQQ was used as a solid since conversion to the hemiketal was too rapid for the available experimental setup.

Since UV-Vis spectroscopy turned out to be cumbersome due to overlapping species, future experimentation should concentrate on alternative techniques. Fluorescence spectroscopy was already performed with PQQ,[182, 252] however, this method has the same problems with different PQQ species, which superimpose and interact with each other.

NMR proved useful, as different PQQ species can be directly distinguished from each other. In the future, kinetics should be recorded at low temperatures to finally measure the rate of the very fast conversion from PQQ to PQQ-hemiketal in solution and to elucidate the influence of Ca^{2+} and especially of different lanthanides on this conversion. By comparing the rate of conversion with different lanthanides, the role of Lewis acidity and ion size on PQQ activation will be better understood.

VII. BIOMIMETIC COMPLEXES

1. Introduction

In order to broaden the knowledge of XoxF- and MxaF-type MDH enzymes, the synthesis of several model complexes was described in the literature, mimicking the structure of the active sites. Itoh *et al.* investigated the Ca-dependent MxaF-type MDH by synthesizing **31** through coupling of the total synthesis PQQ precursor **22** ($PQQMe_2$-OMe) with an aza-crown ether (Scheme VII-1).[152]

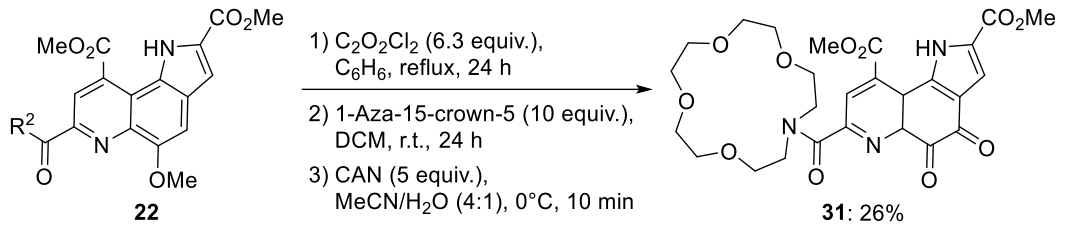

Scheme VII-1: Coupling of 1-aza-15-crow-5 with $PQQMe_2$-OMe (**22**), as described by Itoh *et al.*[152] **31** is generated in a three-step synthesis, starting with acid chlorination, amide coupling of the acyl chloride with the secondary amine and oxidation to the quinone with CAN.

The crown ether oxygen atoms mimic the enzymatic amino acid ones and coordinate Ca^{2+} in addition to PQQ. The authors could show enhanced binding constants with alkaline earth elements (210 000 M^{-1} for Ca^{2+}) in comparison to $PQQMe_3$ (**11**) (1900 M^{-1} for Ca^{2+}). Coordinated Ca^{2+} enhances EtOH addition to **31**, as the equilibrium constant is six times higher (1.2 M^{-1}) than without Ca^{2+} (0.2 M^{-1}). By addition of the strong base DBU to an ethanol containing solution of $[Ca(\mathbf{31})]^{2+}$, the quinone is reduced to the corresponding quinol, concurrent to acetaldehyde formation by oxidation of ethanol. The rate constant of the ethanol oxidation is almost the same for $[Ca(\mathbf{31})]^{2+}$ (1.7 $M^{-1}\,s^{-1}$) in comparison to $[Ca(\mathbf{11})]^{2+}$ (2.1 $M^{-1}\,s^{-1}$). The authors propose the addition-elimination mechanism for the enzymatic alcohol oxidation based on their spectroscopic and kinetic investigations. The larger alkaline earth elements revealed slightly reduced alcohol addition for Ba^{2+} but enhanced oxidation rates.

Table VII.1: Ethanol binding constants and oxidation rates of **31**, coordinated with alkaline earth elements.

	ethanol addition (M^{-1})	oxidation rate ($M^{-1}\,s^{-1}$)
Ca^{2+}	1.2	1.7
Sr^{2+}	1.5	58
Ba^{2+}	0.38	2800

The first model complex for Ln-dependent XoxF-type MDH was synthesized by Schelter *et al.* in an 11-step synthesis,[114] by coupling the PQQ related quinone **B** with tetracyclohexyl-3-(2-aminophenyl)pentanediamide **A** in the final step (Scheme VII-2).

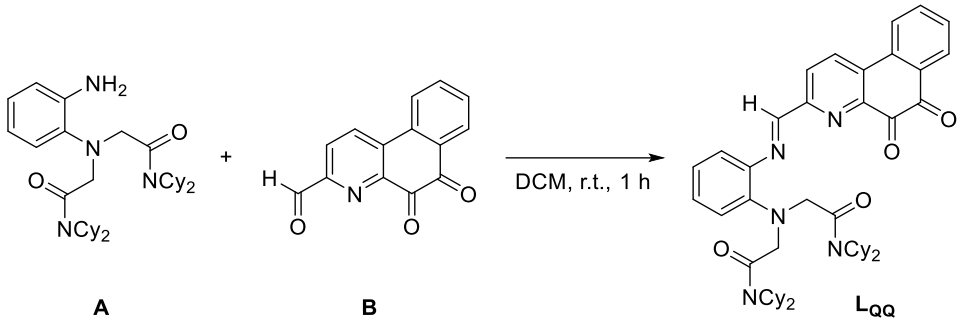

Scheme VII-2: Final step in the synthesis of model ligand $\mathbf{L_{QQ}}$, by imine coupling of the structural PQQ analog **B** with tetracyclohexyl-3-(2-aminophenyl)pentanediamide **A**.

The authors demonstrated La^{3+} coordination to L_{QQ} and provided a crystal structure with three nitrate equivalents as counter ions. Cyclic voltammograms revealed the quinone/semiquinone reversible couple at $E_{1/2} = -0.95$ V for L_{QQ}, which was shifted to higher potentials upon La^{3+} coordination ($E_{1/2} = -0.34$ V) by stabilizing the semiquinone state. Through La^{3+} coordination, oxidation of 4-methylphenol to the respective aldehyde was demonstrated, and this process was accelerated by addition of DBU. With the uncoordinated ligand alone, oxidation was observed in small traces only. Using DFT, the authors calculated both, the hemiketal and hydride transfer mechanism for the methylphenol oxidation. Hydride transfer was clearly favored with either a weak base (2,6-lutidine) or without a base. Addition of DBU drastically reduced the energy barrier for the hemiketal aldehyde elimination from 32.7 to 14.8 kcal mol^{-1} making this mechanism energetically possible. However, the barrier was still slightly higher than for the hydride transfer (9 kcal mol^{-1}).

As a starting point for the synthesis of new Ln related model compounds, which are presented throughout this chapter, work from the Raymond group was evaluated, about the synthesis of Ln complexes for new MRI contrast agents.[257-259] The literature-known ligand TREN-(1,2-HOPO)$_3$ (**32 -** Figure VII.1) was chosen as a candidate for its facile synthesis and excellent lanthanide coordination properties.[260] Studies with Gd^{3+} revealed high complex stabilities (**32**: pGd = 19.3 compared to chelating agent diethylene-triaminepentaacetic acid DTPA – pGd = 19.1)[261] and high lanthanide selectivities, as other metals like Zn (pZn = 15.2) and Ca (pCa = 8.8) showed lower stabilities.[261] In addition, **32** has the same number of coordinating oxygen atoms as the amino acids in the XoxF active site (6) and, being deprotonated, further exhibits the same charge of −3.

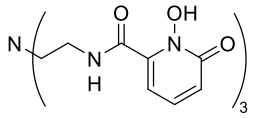

32

Figure VII.1: Structure of the literature-known TREN-(1,2-HOPO)$_3$ ligand (**32**).[260]

As a second project, the PQQ-crown ether ligand synthesized by Itoh *et al.* was evaluated for the coordination with lanthanides to model the XoxF active site. For this purpose, the original ligand was synthesized in addition to a modified ligand carrying a larger crown ether, to account for the higher coordination number preferrence of lanthanides in comparison to calcium.

2. Synthesis and Investigation of TREN-(1,2-HOPO)$_3$

2.1. Precursor Synthesis

First step of the ligand synthesis was the preparation of the precursor 1,2-HOPOBn (**36**), following a literature procedure (Scheme VII-3):[262]

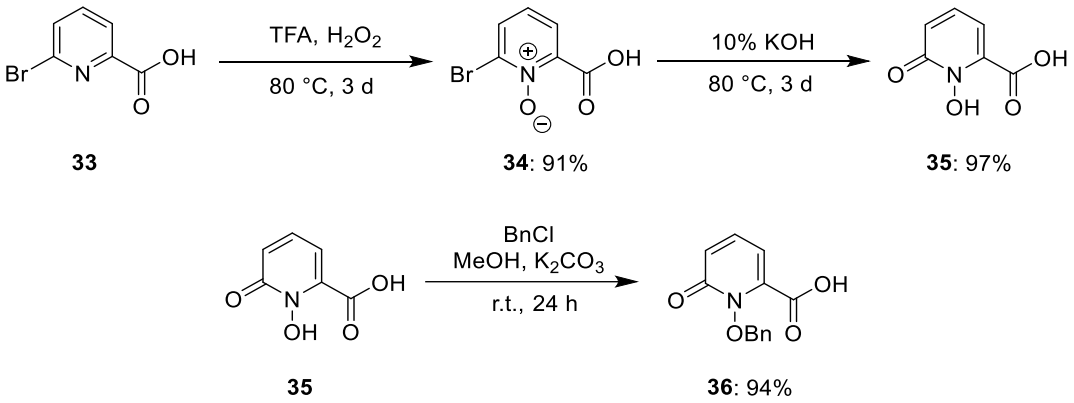

Scheme VII-3: Synthesis of 1,2-HOPOBn (**36)** and subsequent benzyl protection.

Starting with commercially available 6-bromopicolinic acid (**33**), oxidation with hydrogen peroxide in trifluoroacetic acid led to 2-bromo-6-carboxypyridine 1-oxide (**34**) in 91% yield. Subsequent dehalogenation with potassium hydroxide provided 1-hydroxy-pyridin-2-one (1,2-HOPO) (**35**) in 97% yield. Afterwards, the free alcohol was protected using benzylchloride, to afford 1,2-HOPO(Bn) (**36**) in 94% yield.

After synthesis of the benzyl-protected 1,2-HOPO acid (**36**), the precursor was activated for subsequent coupling with primary amines, according to a literature procedure.[263] As shown in Scheme VII-4, 1,2-HOPO-thiaz (**20**) was prepared in two steps from the carboxylic acid by treatment with oxalyl chloride and catalytic amounts of DMF, followed by reaction with 2-mercaptothiazoline.

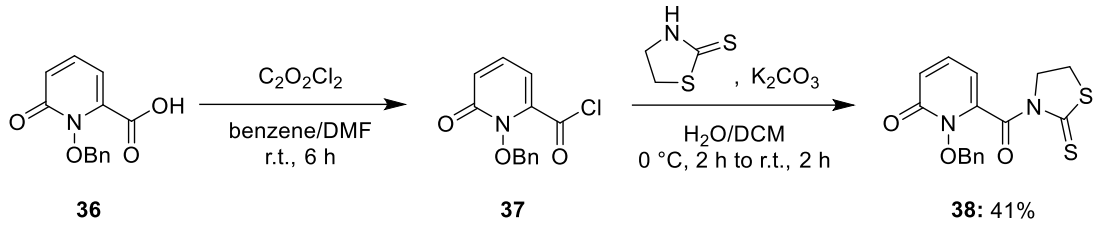

Scheme VII-4: Two-step activation of the carboxyl group from 1,2-HOPO(Bn) (**36**) by using oxalyl chloride and 2-mercaptothiazoline.

2.2. Synthesis of TREN-(1,2-HOPO)$_3$

With 1,2-HOPO-thiaz (**38**), the synthesis of TREN-(1,2-HOPO)$_3$ (**30**) was performed using a literature procedure.[260] First step was a threefold amide coupling with tris(2-aminoethyl)amine (TREN), leading to compound **39** in 81% yield (Scheme VII-5).

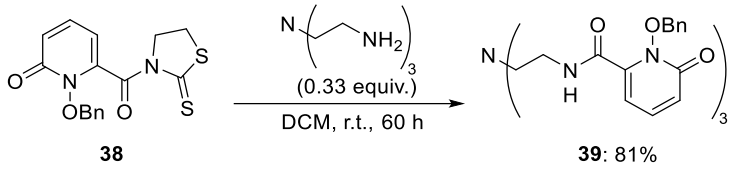

Scheme VII-5: Amide coupling of 1-2-HOPO-thiaz (**38**) with threefold amine TREN.

Deprotection of the benzyl group using a mixture of concentrated acetic acid and hydrochloric acid led to the desired ligand TREN-(1,2-HOPO)$_3$ (**32**) in quantitative yield (Scheme VII-6) with an overall yield of 27.5% over seven reaction steps.

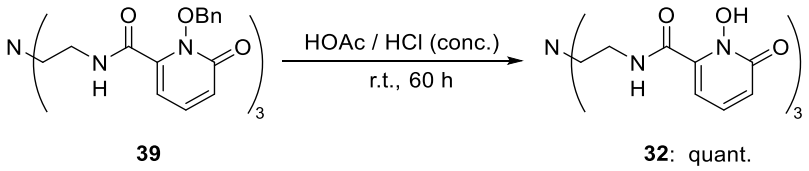

Scheme VII-6: Acidic deprotection of the benzyl group.

2.3. Complex Formation

TREN-(1,2-HOPO)$_3$ (**32**) was now tested for its complexation with lanthanides and possible co-complexation capabilities with PQQ or the structural analog 6-methoxycarbonyl picolinic acid (PDC) (**40**). Mass spectrometry, NMR and UV-Vis were used and the results discussed below.

2.3.1 Mass Spectrometry

ESI-mass spectra were measured from solutions of *in situ* generated complexes of TREN-(1,2-HOPO)$_3$ (**32**) with lanthanum or calcium in methanol (3 mM). Pyridine was added to deprotonate the HOPO hydroxyl groups and promote complexation. Moreover, PQQ (**13**) or the structural analogue pyridinedicarboxylic acid monomethyl ester (PDC) (**40**) were added to show a possible co-complexation. Initially, all compounds were dissolved in appropriate solvents (0.1 mg per µL) and combined subsequently (see VIII.9.2.3). A [La (**32**) (**40**)] complex was observed in the positive and negative ionization mode, underlining the formation of a biomimetic compound. The formation of a [Ca (**32**) (**40**)] complex was not confirmed. With the preferred coordination number of Ca^{2+} being between 6-8,[264] the coordination of both TREN-(1,2-HOPO)$_3$ and PDC, resulting in a CN of 9, could be unfavorable. No peak could be assigned to a complex with an incorporation of PQQ (**13**). Instead, the spectrum showed the TREN-(1,2-HOPO)$_3$ – La complex. However, it should be mentioned that limitations of the method or the instrument could have led to the missing formation of the [La (**32**) (**13**)] complex, which was already measured on a different instrument in the past.

2.3.2 NMR Experiments

To further study the binding mode and species distribution of TREN-(1,2-HOPO)$_3$ with La^{3+} and PDC, NMR spectroscopy was conducted. Piguet *et al.* reported ^{1}H- and ^{13}C-NMR shifts of lanthanide complexes with dipicolinic acid in D_2O.[197] The chemical shift upon La^{3+} coordination appeared between 0.16 and 0.24 ppm downfield for the aromatic protons and 0.92 – 14.02 ppm up- and downfield for the carbon resonances. The strongest shift was observed for the carboxylic carbons (downfield).[197] In DMSO-d_6, both ^{1}H- and ^{13}C-NMR spectra of TREN-(1,2-HOPO)$_3$ (**32**) show resonance shifts after the addition of pyridine and La^{3+} (Figure VII.2 – red and green spectra). Especially the stronger shift of 10H in comparison to 8H of the HOPO unit, which is closer to the potential coordinating C=O group, as well as the overall large shift of all carbon resonances indicates complex formation. The added PDC (**40**) shows very weak to no shifts in relation to a comparative sample (turquoise and violet spectra), making a co-complexation of the ligand doubtful. In an experiment using La(AcO)$_3$ instead of $LaCl_3$ and pyridine, similar shifts of the TREN-(1,2-HOPO)$_3$ resonances were observed, while the PDC resonances remained unaffected again (see Figure IX.32).

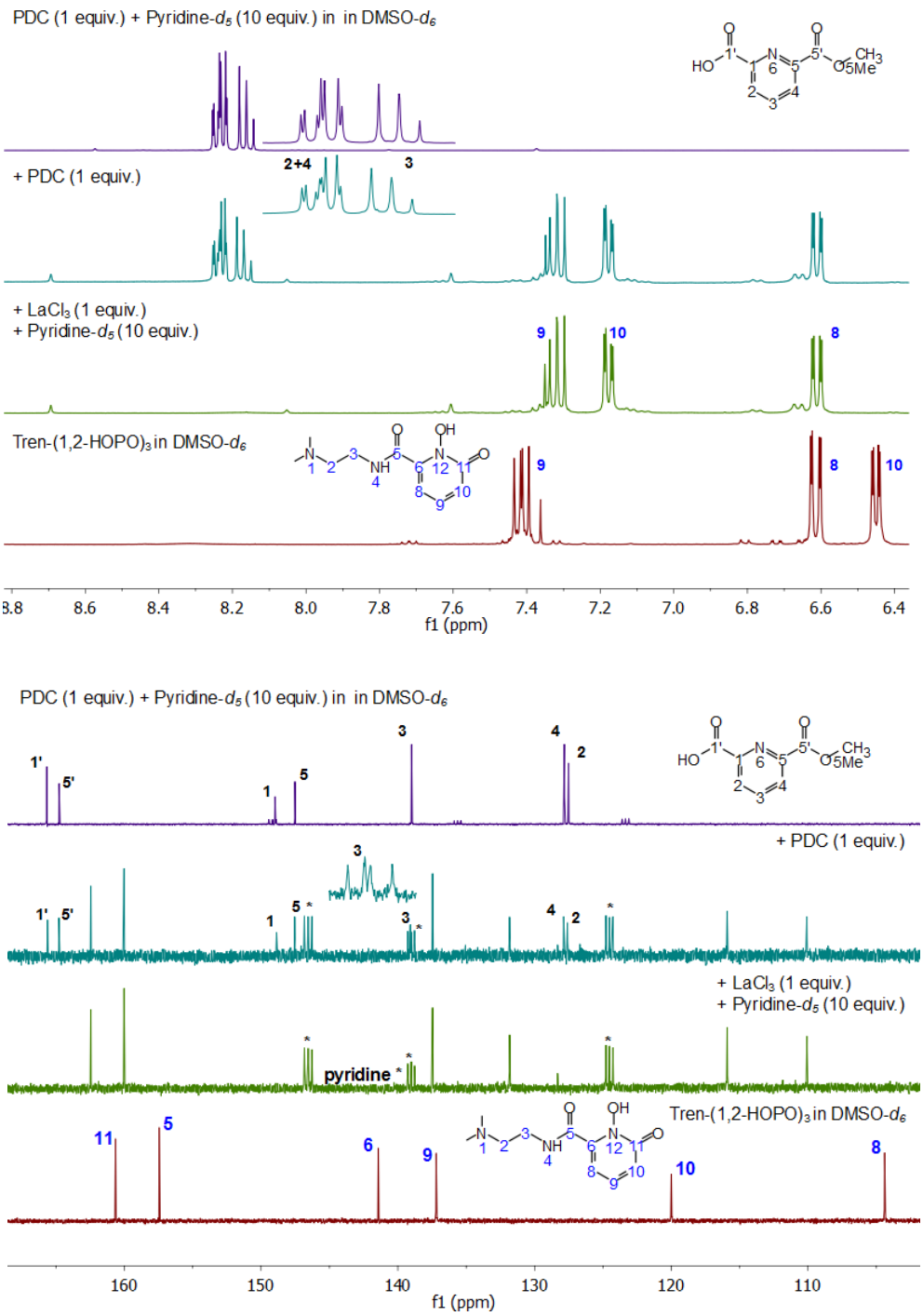

Figure VII.2: Stacked ^{1}H- and ^{13}C-NMR spectra with selected resonances of TREN-(1,2-(HOPO)$_3$ (**32**, 10 mg, 17.9 µmol) in the presence of $LaCl_3 \cdot 7H_2O$ (6.6 mg, 17.9 µmol), pyridine-d_5 (15 µL, 186 µmol) and PDC (**40**, 3.2 mg, 17.9 µmol) in DMSO-d_6 (5.5 µL). Upper spectrum (violet) shows PDC (**40**, 3.2 mg, 17.9 µmol) and pyridine-d_5 (15 µL, 186 µmol) as comparison. Assignments are based on spectra, calculated by MestReNova 11.0.4 and by 2D-NMR experiments.

As mass experiments conducted in methanol showed co-complexation of PDC, additional NMR spectra were recorded in MeOD-d_4 and DMF-d_7. Furthermore, PDC was replaced with PQQ in order to directly examine possible complexation of the cofactor. Instead of diamagnetic $LaCl_3 \cdot 7H_2O$, paramagnetic $PrCl_3 \cdot 6H_2O$ was used which already showed strong interaction with

PQQ alone (Chapter IV). Equimolar PQQ – metal solutions (0.5 mL, 54.4 mM) were prepared in MeOD-d_4 or DMF-d_7, to which equimolar solutions of TREN-(1,2-HOPO)$_3$ (**32**) (0.1 mL, 272 mM) were added. Immediately after addition a white/light yellow solid precipitated in both MeOD-d_4 and DMF-d_7, which was analyzed as the [Pr (**32**)] complex. PQQ stayed in solution as confirmed by NMR.

3. Synthesis and Investigation of TREN-(1,2-HOPO)$_2$-TAM-N1-PDA

3.1. Introduction

To further model the sterics imposed by the protein structure and to preorganize the redox cofactor for metal coordination, a ligand precursor was designed that allows connection of PQQ (**13**) and structural mimics of this cofactor directly to the ligand.

The framework is based on the previously described TREN-(1,2-HOPO)$_3$ (**32**). Raymond *et al.* reported on a similar ligand TREN-(1,2-HOPO)$_2$-TAM-N1 (**41**), where of one of the three HOPO subunits is replaced with a dihydroxy-terephthalamide (TAM), connected with an ethyl-amine (Figure VII.3).[265]

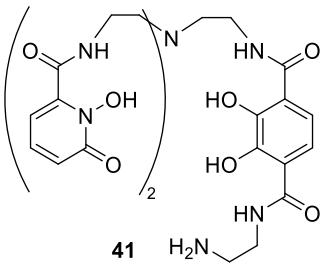

Figure VII.3: Structure of the literature-known TREN-(1,2-HOPO)$_2$-TAM-N1 (**41**) ligand.[265]

The primary amine of **41** allows amide coupling with the carboxylic acid of partly protected PQQMe$_2$ (**19**), leading to the final TREN-(1,2-HOPO)$_2$-TAM-N1-PQQ ligand (**42**) (Figure VII.4). The length of the connecting alkyl chain between the PQQ and TAM moieties was adjusted to a propyl, as preliminary DFT calculations with the original ethyl group showed too much strain.

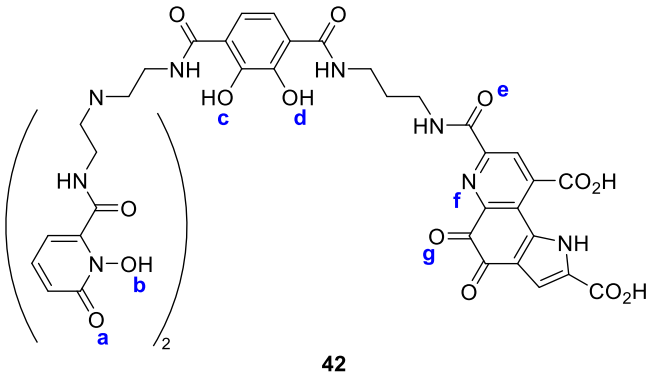

42

Figure VII.4: Structure of the designed PQQ-ligand framework **42** with possible coordination sites a-h.

As described for TREN-(1,2-HOPO)$_3$ (**32**), also the new ligand **42** has the same number of coordinating oxygen atoms as the amino acids in the XoxF active site (6). The TAM moiety allows to keep the overall charge of −4 as the deprotonated PQQ carboxyl group in the active site is part of the amide group in **42**. In the active site, a charge of −3 is build up from the surrounding amino acids in addition to the deprotonated carboxylic acid from PQQ.

3.2. DFT Calculation

DFT calculations were performed for an initial estimation of the coordination mode of **42** with lanthanides (Figure VII.5). The nonadentate ligand wraps around the central metal and allows the cofactor PQQ to come in close proximity. The oxygen of the connecting amide group (Figure VII.4 - e) is slightly out of plane, but the enzymatic coordination, mode is preserved, with complex bond lengths of 2.89 Å (-N-C=O$_e$), 3.02 Å (N$_f$) and 2.67 Å (C=O$_g$). The HOPO and TAM units (a-d) tightly enclosed the central metal with complex bond lengths between 2.48 and 2.56 Å. Comparison of the calculated bond lengths with the enzymatic ones is given in table Table VII.2

Table VII.2: Bond lengths of the primary metal-coordination sphere of calculated [La **42**]$^-$ complex and the active site of XoxF MDH.

coordination sites		Ln – ligand bond lengths [Å]	
[La **42**]$^-$	XoxF (Ce)[36]	[La **42**]$^-$	XoxF (Ce)[36]
-N-C=O$_e$	PQQ-7CO$_2^-$	2.89	2.7
N$_f$	PQQ-6N	3.02	2.8
C=O$_g$	PQQ-5C=O	2.67	2.6
a-d	amino acids	2.48 – 2.56	2.5 – 2.9

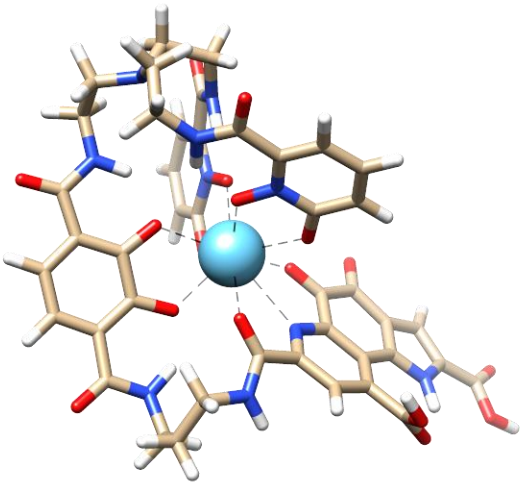

Figure VII.5: DFT optimized structure of La^{3+} coordinated TREN-(1,2-HOPO)$_2$-TAM-N1-PQQ (**42**). Gaussian 09, rB3LYP, 6-31G(d), La-ECP:28 MWB. Image generated with the UCSF Chimera package 1.12.[41]

3.3. Ligand Synthesis

For initial synthetic efforts, PQQ (**13**) was substituted with the commercially available pyridinedicarboxylic acid (PDA) (**44**) as a structural analogue, leading to the PDA-ligand framework **43** as a target molecule (Figure VII.6).

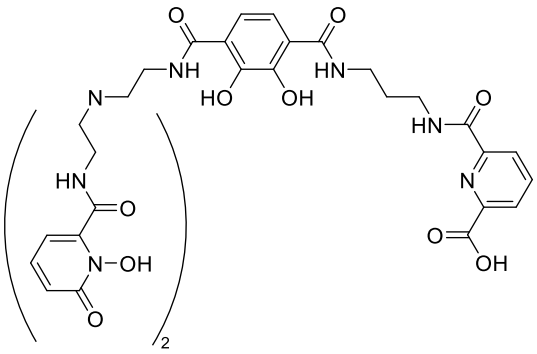

43

Figure VII.6: Structure of PDA-ligand framework **43** as a target molecule.

Synthesis started towards the literature-known TREN-(1,2-HOPO)$_2$-TAM-N1 (**41**) (now with a propyl chain (see VII.3.1) and was in accordance to the described procedures unless otherwise stated.[265] The first step was similar as for the synthesis of TREN-1,2-HOPO$_3$ (**32**), but with just two equivalents of 1,2-HOPO-thiaz (**38**), which were added by slow addition and in high dilution to the threefold amine TREN. A crude mixture of bis- and tris-substituted derivatives was obtained, which were separated by column chromatography. Precursor **36** was obtained in 71% yield as well as TREN-1,2-HOPO$_3$ (**30**) as a side product (Scheme VII-7), whereas the literature described yield was only 46%.[265]

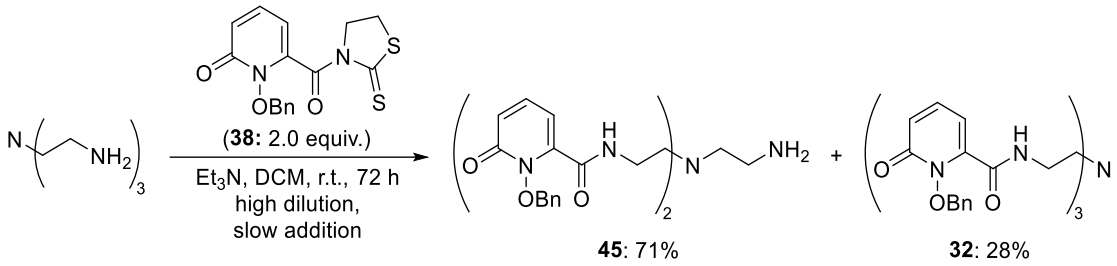

Scheme VII-7: Synthesis of TREN-[1,2-HOPO(Bn)]$_2$ (**45**).

In an independent reaction, *N*-Boc-1,3-propanediamine (**N1**) was coupled to the benzyl-protected terephthalamide moiety (TAM – **46)** (Scheme VII-8). Literature described an alternative route, including the coupling of **45** with **46** first, followed by coupling with mono-BOC-protected ethylene diamine.[265] However, described yield over the two reaction steps was quite low (34%). To avoid reaction of both thiazolide groups of the TAM unit, the reaction was performed in the presence of large excess of **46** and the amine solution was added by slow addition and in high dilution over a period of two days to the reaction mixture. That afforded coupling of the amine to the one side of the TAM unit while preserving the second thiazolide group for later reactions. The reaction provided the desired product **47** in 82% yield.

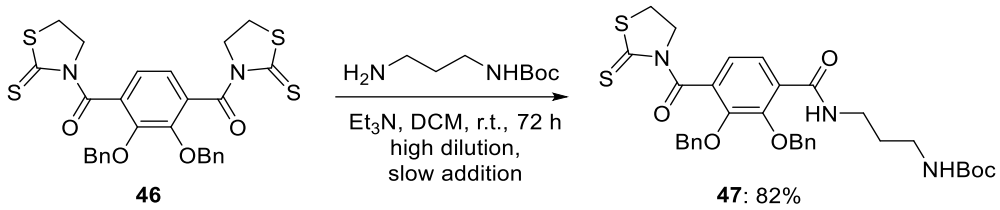

Scheme VII-8: Preparation of thiazolide-activated TAM-N1 intermediate **47**.

With the thiazolide-activated TAM-N1 unit **47**, coupling reaction with **45** was performed in 80% yield (Scheme VII-9). In comparison to the literature route described above (34% yield), the yield over two reaction steps was now almost doubled (66%).

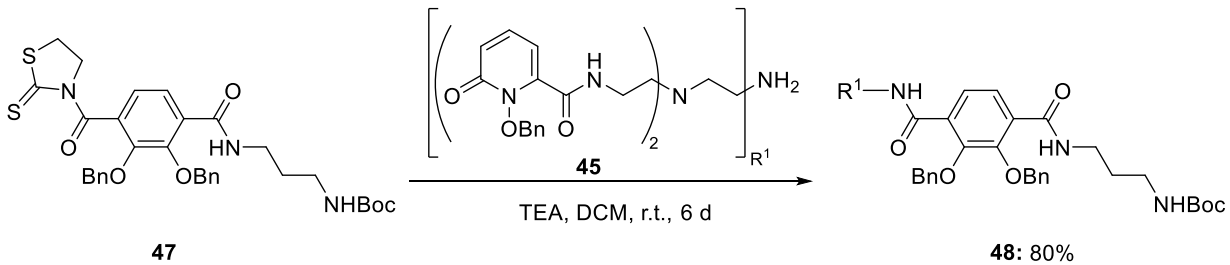

Scheme VII-9: Coupling of the TAM-N1 unit (**47**) with TREN-(1,2-HOPOBn)$_2$ (**45**).

The final step in the ligand synthesis was the Boc-deprotection of **48** by hydrochloric acid (Scheme VII-10), followed by reaction of the primary amine with the carboxyl group of PDC (**40**). Deprotection was monitored by TLC and the crude product was directly used for the next

reaction step. Additional deprotection of the benzyl groups was not observed, as those groups are removed in a concentrated HCl / glacial acetic acid mixture.

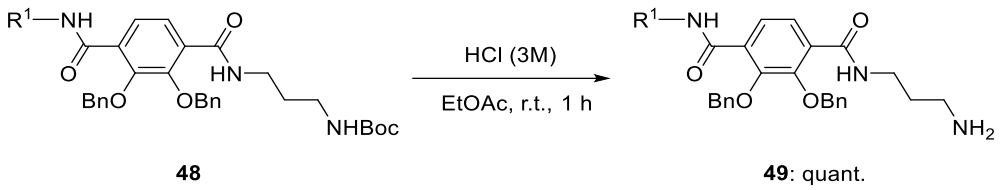

Scheme VII-10:Boc-deprotection of compound **48** by hydrochloric acid.

Oxalyl chloride with catalytic amounts of DMF was used for activation of the PDC carboxyl group by formation of an acyl chloride, following the same procedure as described above (Scheme VII-11).

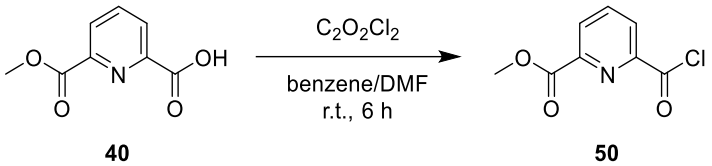

Scheme VII-11: Carboxyl group activation of PDC by the use of oxalyl chloride.

Formation of an amide bond between compounds **49** and **50** was unsuccessful (Scheme VII-12), most likely due to insufficient activation of the PDC unit **40**. An attempt with catalytic amounts of TEA was unsuccessful as well.

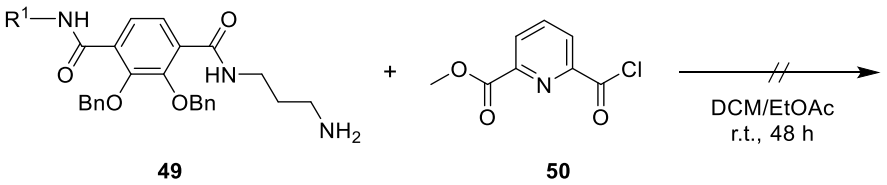

Scheme VII-12: Amidation attempt between compound **49** and activated PDC (**50**).

For an alternative amide bond formation, the previously synthesized PDC-thiazolide (**24**) was used (Scheme VII-13).

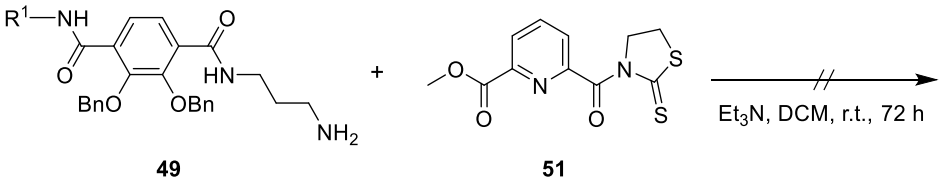

Scheme VII-13: Amidation attempt between compound **49** and activated PDC (**51**).

The reaction progress was monitored using TLC and a new spot indicated the presence of free 2-mercaptothiazoline. However, the desired coupling product could not be isolated and its formation was not verified. Furthermore, an alternative procedure to build an amide bond was attempted, using PyBOP and *N*-methylmorpholine (NMM) as activation reagents.[266] However,

the effort to couple TREN-(1,2-HOPO(Bn)$_2$-TAM-N1 (**49**) and PDC using different reaction conditions was unsuccessful (Scheme VII-14).

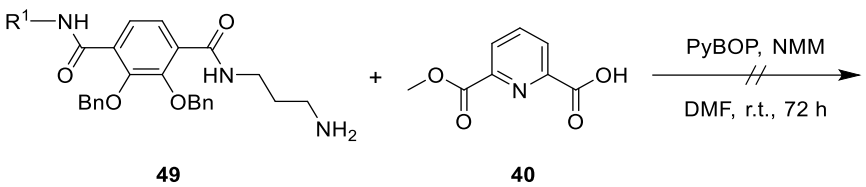

Scheme VII-14: Amidation attempt between compound **49** and PDC (**40**), using PyBOP as coupling reagent.

Since the last step of the ligand synthesis, involving the coupling of TREN-(1,2-HOPOBn)$_2$-TAM-N1 (**49**) and PDC (**40**) failed to accomplish, an alternative attempt towards the ligand preparation was performed. The new strategy involved the construction of the ligand following the "reversed" route, starting with the amide coupling of PDC-thiazolide (**51**) and *N*-Boc-1,3-propanediamine (**N1**) (Scheme VII-15). The synthesis of PDC-N1 (**52**) proceeded exceptionally well, with an overall yield of 90%.

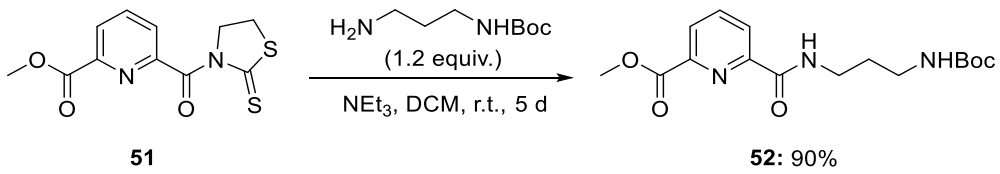

Scheme VII-15: Synthesis of PDC-N1 (**52**) from PDC-thiazolide (**51**) and N-Boc-1,3-propanediamine (**N1**).

Subsequently the Boc-protecting group was removed from PDC-N1 (**52**) under acidic conditions and the resulting primary amine **53** was coupled to the benzyl-protected terephthalamide (TAM) moiety **46** (Scheme VII-16). Once again, the coupling reaction involved a slow addition of highly diluted **53** to an excess of **46** to yield the monoactivated intermediate PDC-N1-TAM (**47**).

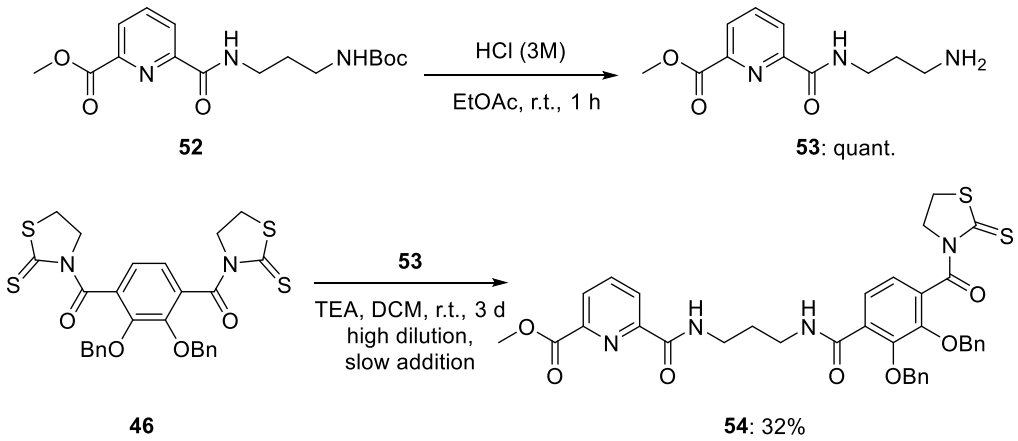

Scheme VII-16: Boc-deprotection of **52** and following synthesis of thiazolide-activated PDC-N1-TAM (**54**) intermediate.

Finally, TREN-[1,2-HOPO(Bn)]$_2$ (**45**) was coupled to the thiazolide-activated PDC-N1-TAM (**54**) intermediate to obtain the benzyl-protected TREN-(1,2-HOPOBn)$_2$-TAM-N1-PDC-ligand (**55**) in 61% yield (Scheme VII-17).

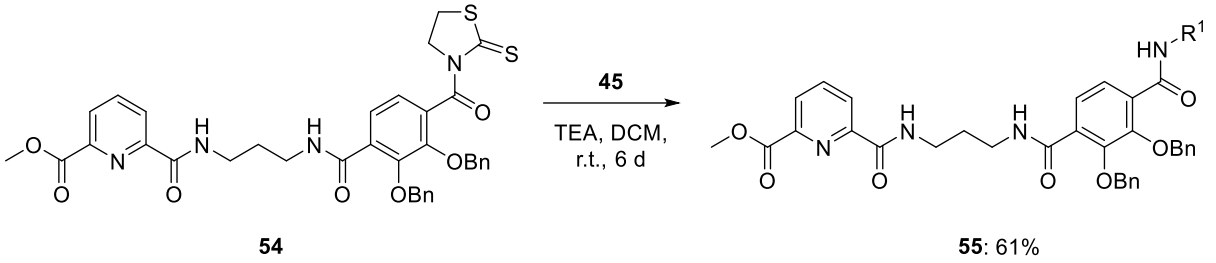

Scheme VII-17: Synthesis of benzyl-protected TREN-[1,2-HOPO(Bn)]$_2$-TAM-N1-PDC-ligand (**55**).

The final step in the ligand synthesis included deprotection of the benzyl groups and the PDC methyl ester, using the same procedure as for the TREN-(1,2-HOPO)$_3$ (**32**) ligand.

The reaction proceeded smoothly and led to the desired target molecule **43** in quantitative amounts (Scheme VII-18). However, traces of **43** with the PDC moiety still esterified were detected by mass spectrometry (**43a**).

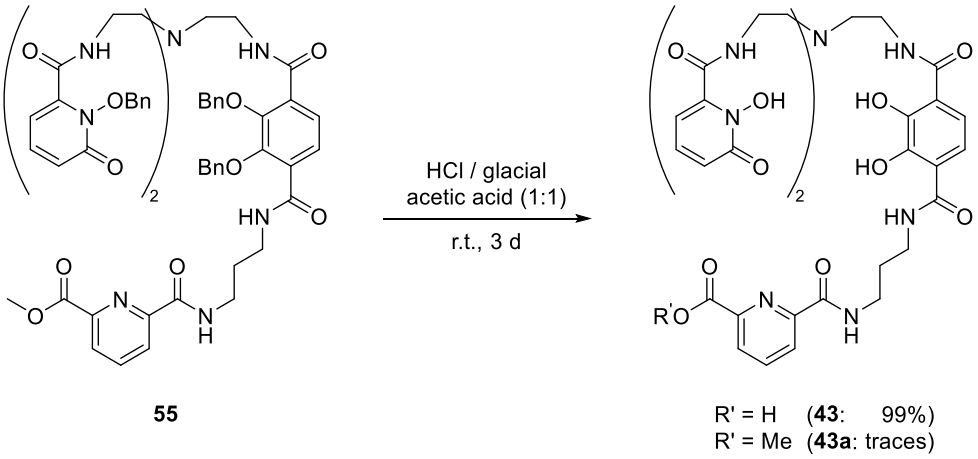

Scheme VII-18: Formation of target ligand **43** by deprotection of the benzyl groups and saponification of the PDC methyl ester from TREN-(1,2-HOPOBn)$_2$-TAM-N1-PDC (**55**).

3.4. Complex Formation

3.4.3 Mass Spectrometry

In order to verify complex formation of the synthesized ligand with lanthanides, ESI-mass spectra were measured from equimolar solutions of TREN-(1,2-HOPO)$_2$-TAM-N1-PDA (**43**) with lanthanum- or europium chloride in methanol (2 mM). Both experiments led to the desired complexes. The isotope pattern of the ESI-mass spectra is in accordance with the calculated values (Table VII.3). In both cases, two different complexes are visible, which differ in the mass of one methyl group, stemming from coordinated **43** or **43a**. Several peaks with higher m/z values are visible especially for the europium complexation experiment (see Figure IX.30 and Figure IX.31). While not all peaks can be assigned, the mass of 1104.0737 (ESI +) corresponds to a species with two coordinated Eu^{3+} ions (calc. for [$C_{36}H_{34}Eu_2N_9O_{13}^+$]: 1104.0681). The mass for a twofold positively charged complex is visible as well and the isotope pattern is in line with the calculated value, indicating the ability of **43**, to coordinate more than one lanthanide ion.

Table VII.3: Calculated and found masses of [Ln (**43**)] and [Ln_2 (**43**)]$^+$ complexes from ESI mass experiments of TREN-(1,2-HOPO)$_2$-TAM-N1-PDA (1.3 mg, 1.6 µmol) and pyridine (0.4 mg, 0.4 µL, 5.1 µmol) in methanol (600 µL) with $LaCl_3 \cdot 7H_2O$ (0.6 mg, 1.6 µmol) or $EuCl_3 \cdot 6H_2O$ (0.6 mg, 1.7 µmol). All compounds were initially dissolved in small amounts of methanol before combination. Relatively low abundancies are omitted.

[La (**43**)]	[La (**43**)]	[La (**43a**)]	[La (**43a**)]	[Eu (**43**)]	[Eu (**43**)]	[Eu (**43a**)]	[Eu (**43a**)]	[Eu_2 (**43**)]$^+$	[Eu_2 (**43**)]$^+$	[Eu_2 (**43**)]$^+$	[Eu_2 (**43**)]$^+$
(ESI +)	(ESI +)	(ESI +)	(ESI +)	(ESI –)	(ESI –)	(ESI –)	(ESI –)	(ESI +)	(ESI +)	(ESI +)	(ESI +)
calc.	found	calc.	found	calc.	found	calc.	found	calc.	found	calc.	found
$C_{36}H_{37}LaN_9O_{13}^+$	$C_{36}H_{37}LaN_9O_{13}^+$	$C_{37}H_{39}LaN_9O_{13}^+$	$C_{37}H_{39}LaN_9O_{13}^+$	$C_{36}H_{35}EuN_9O_{13}^-$	$C_{36}H_{35}EuN_9O_{13}^-$	$C_{37}H_{37}EuN_9O_{13}^-$	$C_{37}H_{37}EuN_9O_{13}^-$	$C_{36}H_{34}Eu_2N_9O_{13}^+$	$C_{36}H_{34}Eu_2N_9O_{13}^+$	$C_{36}H_{35}Eu_2N_9O_{13}^{2+}$	$C_{36}H_{35}Eu_2N_9O_{13}^{2+}$
942.1569 (100.0%)	942.1581 (100.0%)	956.1725 (100.0%)	956.1737 (100%)	954.1572 (100.0%)	954.1579 (100.0%)	968.1729 (100.0%)	968.1746 (100.0%)	1104.0681 (100.0%)	1104.0737 (100.0%)	552.5377 (100.0%)	552.5391 (100.0%)
943.1602 (38.9%)	943.1617 (41.6%)	957.1759 (40.0%)	957.1773 (39.3%)	952.1558 (91.6%)	952.1566 (88.9%)	966.1715 (91.6%)	966.1731 (90.6%)	1106.0695 (54.6%)	1106.0753 (48.9%)	553.5384 (54.6%)	553.5397 (53.9%)
944.1636 (7.4%)	944.1652 (8.6%)	958.1792 (7.8%)	958.1806 (8.0%)	955.1606 (38.9%)	955.1615 (37.9%)	969.1762 (40.0%)	969.1784 (33.9%)	1102.0668 (45.8%)	1102.0719 (40.1%)	551.5370 (45.8%)	551.5384 (46.1%)
943.1539 (3.3%)	-	957.169 6 (3.3%)	959.1825 (1.3%)	953.1592 (35.7%)	953.1601 (28.7%)	967.1748 (36.7%)	967.1770 (30.7%)	1105.0715 (38.9%)	1105.0761 (50.0%)	553.0394 (38.9%)	553.0410 (35.2%)
944.1611 (2.7%)	-	958.1768 (2.7%)	-	954.1625 (6.8%)	-	968.1782 (7.1%)	-	1107.0729 (21.3%)	1107.0781 (18.3%)	554.0401 (21.3%)	554.0114 (19.1%)
944.1573 (1.3%)	-	958.1729 (1.3%)	-	956.1639 (4.7%)	956.1655 (7.1%).	970.1796 (5.1%)	970.1816 (7.3%)	1103.0701 (17.8%)	1103.0737 (28.9%)	552.0387 (17.8%)	552.0404 (10.4%)
945.1645 (1.0%)	-	959.1801 (1.1%)	-	955.1542 (3.3%)	-	-	966.1522 (5.3%).	1106.0748 (7.4%)	1104.5751 (15.3%)	553.5411 (6.0%)	-

3.4.1 UV-Vis

To further elucidate the coordination of TREN-(1,2-HOPO)$_2$-TAM-N1-PDA (**43**) with lanthanides and to determine the total amount of metals which can be coordinated by the ligand, UV-Vis spectroscopy was performed. Spectrophotometric titrations were conducted in the presence of lanthanum- or europium chloride in methanol for both **43** and the PDC lacking ligand TREN-(1,2-HOPO)$_3$ (**32**). Experimental details are given in VIII.9.3.11.

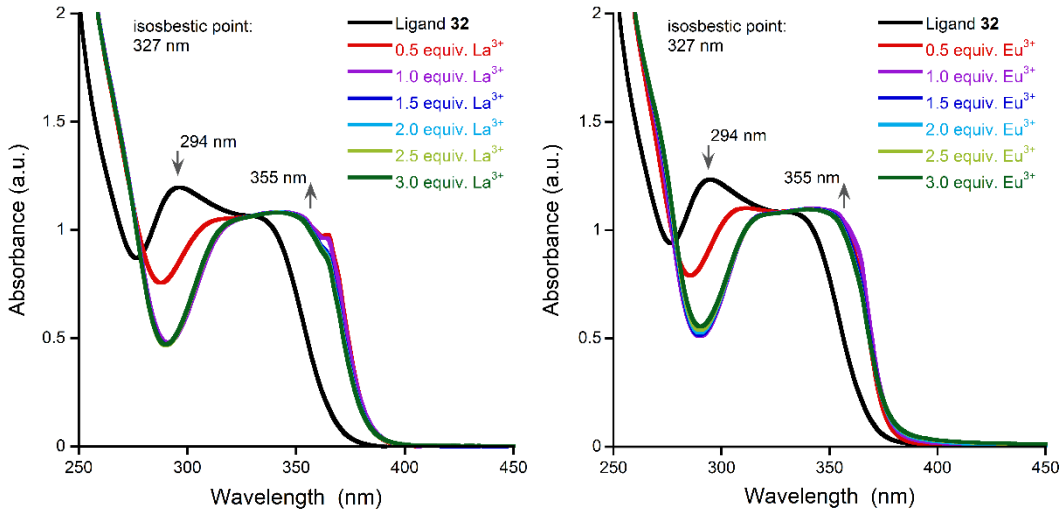

Figure VII.7: Titration of TREN-(1,2-HOPO)$_3$ (**32**) with increasing amounts of $LaCl_3$ (left) or $EuCl_3$ (right) in methanol, but a constant total volume of 1 mL (0.292 mM **32**, 0.146 - 0.875 mM metal chloride). Blank measurement was performed in pure methanol.

Figure VII.7 shows the resulting spectra of TREN-(1,2-HOPO)$_3$ (**32**) with increasing amounts of La^{3+} or Eu^{3+} (= Ln^{3+}). Both titrations are very similar, indicating no major change in the coordination mode from the larger La^{3+} (1.22 Å) to the smaller Eu^{3+} (1.12 Å – ionic radii in nonadentate complexes according to Shannon[20]). A local minimum at 290 nm appeared upon addition of 0.5 equiv. Ln^{3+} concurrent to a shift of the absorption maximum at 340 nm towards lower energies. An isosbestic point at 330 nm clearly indicated the conversion of uncoordinated to coordinated **32**. Stagnation after the addition of one equivalent of Ln^{3+} further indicated a Ln_1**32**$_1$ species. In direct comparison, a small shoulder at 365 nm appeared after the addition of La^{3+}, which is not or only marginally present in the Eu^{3+} titration.

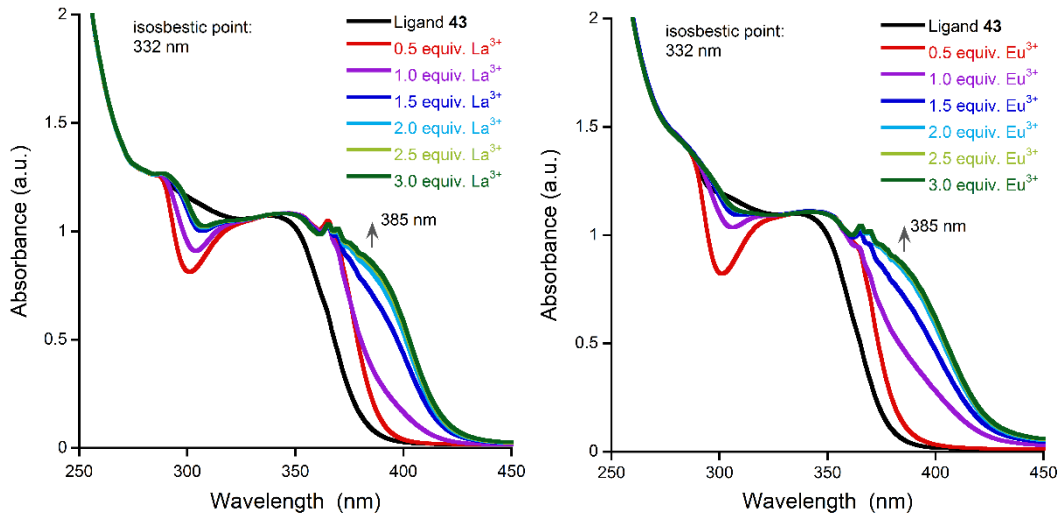

Figure VII.8: Titration of TREN-(1,2-HOPO)$_2$-TAM-N1-PDA (**43**) with increasing amounts of $LaCl_3$ (left) or $EuCl_3$ (right) in methanol, but a constant total volume of 1 mL (0.292 mM **43**, 0.146 - 0.875 mM metal chloride). Blank measurement was performed in pure methanol.

Figure VII.8 shows a similar titration with the TREN-(1,2-HOPO)$_2$-TAM-N1-PDA (**43**) ligand. Again, both titrations are very similar, indicating the same coordination mode for the larger La^{3+} and the smaller Eu^{3+}. Also with this ligand, a local minimum appeared at 300 nm upon addition of 0.5 equiv. Ln^{3+} (not as pronounced as with **32**) while the absorption maximum at 355 nm shifted towards lower energies (stronger shift than with **32**). Again, an isosbestic point at 332 nm indicated the direct conversion of uncoordinated to coordinated **43**. However, the absorption spectra did not stagnate until two equiv. of Ln^{3+} were added, indicating the formation of a Ln_2**43**$_1$ species.

No such bimetallic species was reported for the TREN-(1,2-HOPO)$_2$-TAM-N1 (**41**)[265] or related ligands.[260-261, 267] Even a similar ligand to **41**, where the ethylamine was replaced with a polyethylenglycol chain of 122 repeating units and therefore multiple alternative coordination sites,[268] still showed monometallic complexation.[267] However, metal addition was kept equimolar in all cases and no information are available about complex formation with more metal equiv. added. Gd complexes of TREN-(1,2-HOPO)$_3$ (**32**) and related ligands show two additional water molecules coordinated to the central metal.[267] The preferred CN in such complexes should therefore be high enough to coordinate both PDA and the HOPO and TAM moieties at the same time. Coordination numbers of nine are common for lanthanide complexes.[193]

However, the concept of a nonadentate ligand **43**, which coordinates just one Ln similar to the XoxF MDH active site was not confirmed with this experiment.

3.4.4 NMR

To further investigate the binding mode of TREN-(1,2-HOPO)$_2$-TAM-N1-PDA (**43**) with Ln, NMR spectroscopy was conducted. ^{1}H- and ^{13}C-NMR spectra of the ligand in MeOD-d_4 with assigned signals can be found in the experimental part (VIII.9.3.9) and in the Appendix (Figure IX.33). Since higher concentrations of TREN-(1,2-HOPO)$_3$ (**32**) led to precipitation with Pr^{3+} in methanol (VII.2.3.2), TREN-(1,2-HOPO)$_2$-TAM-N1-PDA (**43**) was dissolved in DMSO-d_6 for NMR titration experiments with $Lu(AcO)_3 \cdot 1H_2O$.

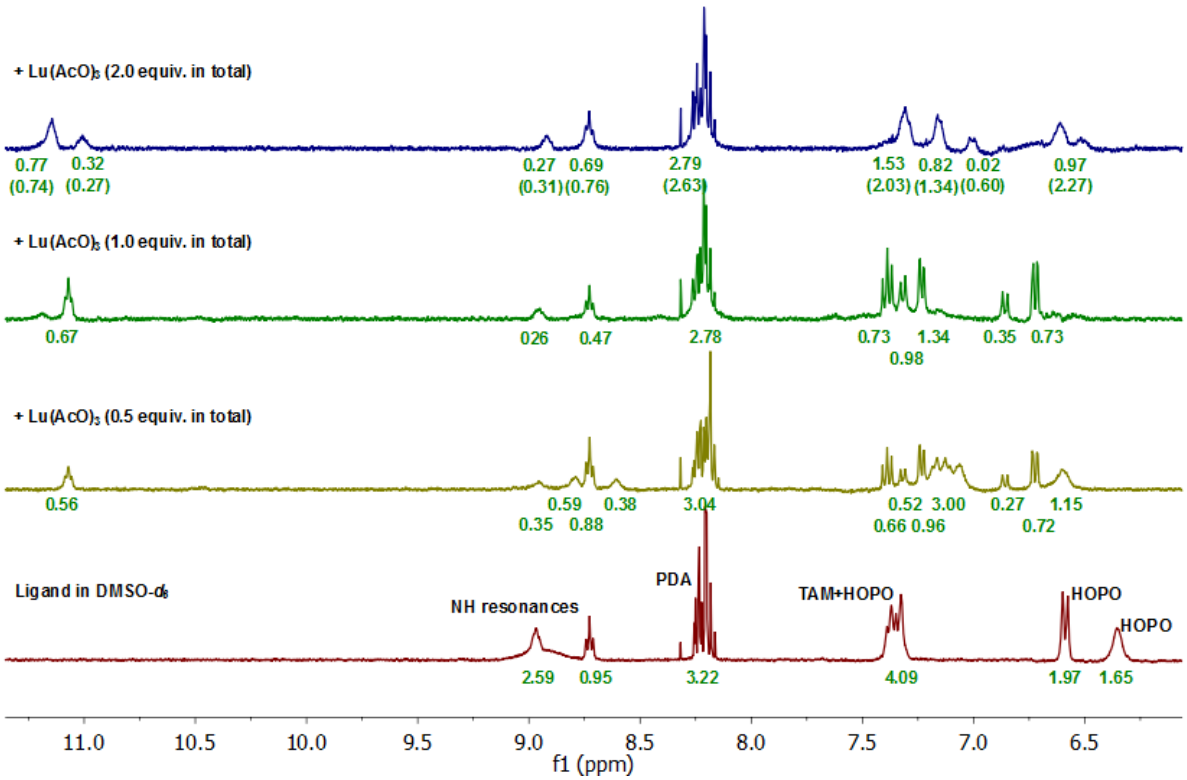

Figure VII.9: Stacked ^{1}H-NMR spectra with aromatic signals of TREN-(1,2-HOPO)$_2$-TAM-N1-PDA (**43**, 5 µmol) in DMSO-d_6 (0.6 mL) and increasing amounts of Lu(AcO)$_3$. Green numbers indicate integral values of the resonances with a set integral value of 100 for the solvent residual signal (DMSO) as an internal standart. Phasing problems occurred for the blue spectrum (2 equiv. Lu(AcO)$_3$), which hindered correct integral estimation. Numbers in brackets indicate integral values, after the NMR tube was heated for 3 h at 65°C.

The red spectrum (Figure VII.9) shows ligand **43** before metal addition with proton resonances for PDA, the HOPO units which partly overlap with TAM and several NH resonances. Upon addition of 0.5 equiv. Lu(AcO)$_3$ (yellow spectrum), a metal induced shift is visible for the proton resonances of the HOPO and TAM units and several new signals appear, indicating beginning complex formation. The PDA resonances show a very small metal induced shift, yet also here, the appearance of new signals is visible after 0.5 equiv. Lu^{3+} were added, indicating participation of PDA in coordination. After the addition of another 0.5 equiv. Lu(AcO)$_3$ (green spectrum), the additional resonances disappeared, indicating the presence of just one complex with chemically equivalent HOPO units. A large singlet at 11.95 ppm additionally appeared after the addition of 1.0 equiv. Lu(AcO)$_3$ with an integral value of 4.30 (see Figure IX.34 for full spectrum). The signal could not be assigned, as none of the HOPO or TAM resonances would show such a large shift. To drive complex formation, the NMR tube was heated at 65°C for 4.5 h. However, the obtained spectrum and the integrals remained unchanged.

The addition of another equiv. Lu(AcO)$_3$ (blue spectrum) caused a broadening and shift of most aromatic resonances with an exception of the PDA ones, which largely remained unaffected (Figure VII.10).

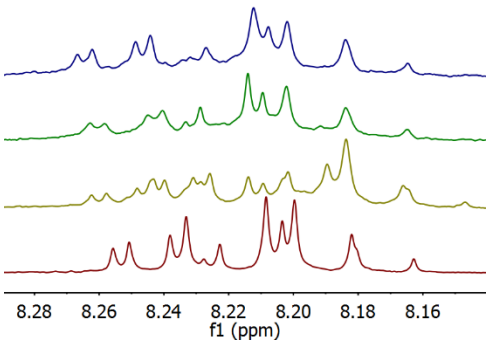

Figure VII.10: Zoom in the aromatic PDA signals of **43**. Strong variations are visible between the spectra of **43** (red) upon addition of 0.5 equiv. (yellow) and 1.0 equiv. (green) $Lu(AcO)_3$, while the resonances remain largely unaffected upon addition of 2.0 equiv. $Lu(AcO)_3$ (blue).

The large singlet at 11.95 ppm completely disappeared. Heating of the NMR tube at 65°C for 3 h had no effect on the spectrum.

Previous mass and UV-Vis experiments stated the coordination of more than one metal equivalent by **43**. With NMR, exact elucidation of the coordination mode is difficult. With 2.0 equiv. Lu^{3+} the HOPO and TAM resonances further shifted and broadened. This could indicate additional coordination with those groups. However, no bimetallic species are reported for the related TREN-(1,2-HOPO)$_3$ (**32**) ligand. The observed resonance shifts could also be caused by further deprotonation of the ligand after $Lu(AcO)_3$ addition. Participation of the PDA unit in additional coordination is rather unlikely, as PDA resonances largely remain unaffected, visualized in Figure VII.10. which shows no difference between the green spectrum (1.0 equiv. Lu^{3+}) and the blue spectrum (2.0 equiv. Lu^{3+})

3.5. Conclusion

TREN-(1,2-HOPO)$_2$-TAM-N1-PDA (**43**) was synthesized to align the PQQ analogue PDC (**40**) for metal coordination by a direct connection of PDC with the ligand framework. However, complexation experiments followed by mass spectrometry, UV-Vis and NMR all indicated coordination of an additional lanthanide ion. Such a Ln_2**43**$_1$ species largely differs from the MDH active site with only one coordinated Ln. Therefore, no additional synthetic approaches towards the PQQ analogue TREN-(1,2-HOPO)$_2$-TAM-N1-PQQ (**42**) were made and the focus was directed on other model ligands instead.

4. Synthesis and Investigation of PQQ-Aza-Crown Ether Complexes

4.1. Synthetic Approaches

Based on the work of Itoh *et al.*[152] two aza-crown ethers of different sizes were attached to the PQQ scaffold. Starting with the selectively saponified pyrroloquinoline **22** from Corey's total synthesis,[129] the free carboxyl group needed to be activated for amide coupling. Acyl chloride formation with oxalyl chloride was performed (Scheme VII-19), following the same procedure as described above (Scheme VII-4).

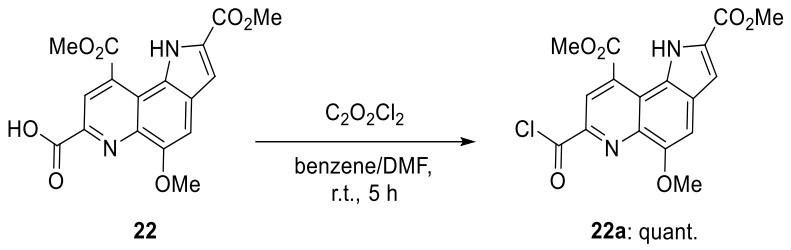

Scheme VII-19: Carboxyl group activation of **22** by the use of oxalyl chloride.

While Itoh described the acyl chlorination in pure benzene at refluxing temperature (~ 80°C), the reaction temperature was decreased to room temperature by the use of small amounts of DMF as catalyst. Due to its low stability, the formed acyl chloride was directly used for the following aza-crown ether coupling in DCM (Scheme VII-20). Two different aza-crown ethers were used, leading to the 1-aza-15-crown-5 compound **56** in 27% yield and the 1-aza-18-crown-6 compound **57** in 46% yield. Itoh *et al.* described the synthesis with 10 equiv. of 1-aza-15-crown-5, but also received a relatively low yield of 43% for **56**.

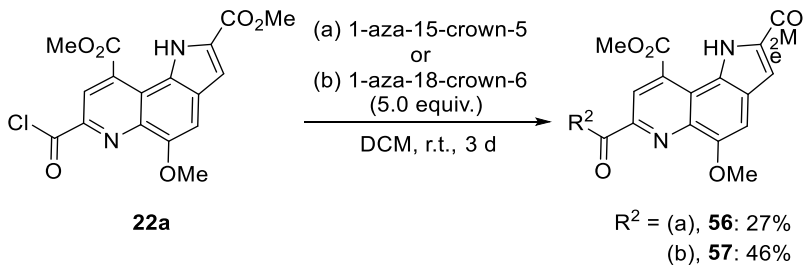

Scheme VII-20: Amide coupling of activated pyrroloquinoline **22a** with 1-aza-15-crown-5 (a) or 1-aza-18-crown-6 (b).

Next step was oxidation with CAN, to receive PQQ in its quinone form. Reactions were performed with both crown ether compounds **56** and **57** (Scheme VII-21).

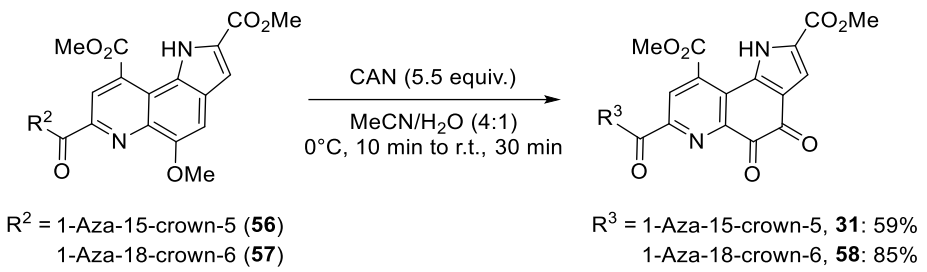

Scheme VII-21: Oxidation with ceric ammonium nitrate, according to Itoh *et al.*[152] Given yields related to unpurified compounds.

ESI-mass analysis and ^{1}H-NMR stated the successful conversion to both compounds **31** and **58**, but no sufficient purification procedure was found. Itoh *et al.* described column chromatography with silica and a 80:290 EtOAc/EtOH mixture as eluent.[152] However, implementation of this method led to degradation of the product and thus largely reduced the yield.

As precursor pyrroloquinoline **22** is only available in low yields *via* 8-step synthesis (see Chapter III), the usage of methylated and selectively saponified $PQQMe_2$ (**19**) as a precursor was evaluated. The advantage of **19** is that the quinone moiety is already formed, making the oxidation with CAN unnecessary.

In order to couple 1-aza-15-crown-5 to **19**, the same reaction sequence was used (Scheme VII-22) as described above, but with higher amounts of aza-crown ether (10 equiv.).

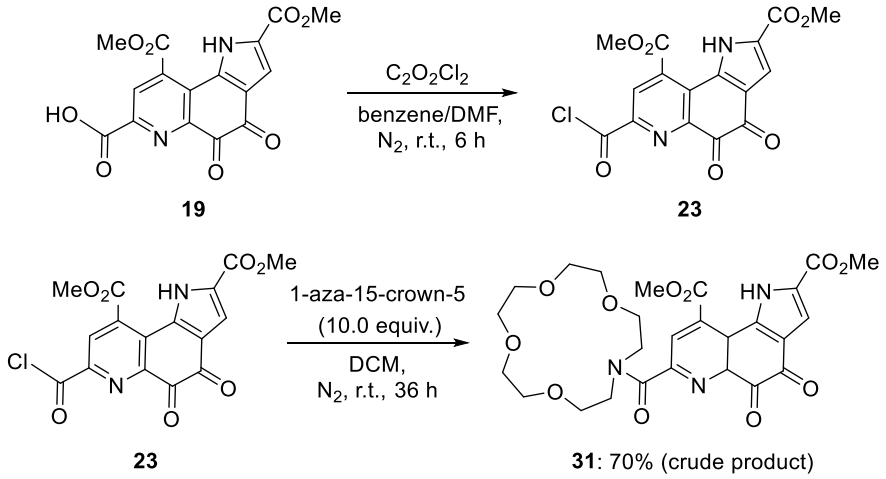

Scheme VII-22: Reactions sequence for the amide coupling of 1-aza-15-crown-5 with $PQQMe_2$ (**19**) *via* an activated acyl chloride.

While analysis of the crude product clearly indicated the formation of the preferred $PQQMe_2$-crown ether compound **31** (by NMR and ESI), purification attempts were unsuccessful again (column chromatography with EtOAc/EtOH as described by Itoh or DCM/MeOH and DCM/EtOH).

For a screening towards effective purification procedures, larger amounts of the PQQMe$_2$-crown ether product were necessary. Since the reaction sequence shown in Scheme VII-22 is time consuming, needs large amounts of expensive aza-crown ether and only gives insufficient yields, an alternative procedure was tested including the peptide coupling reagent PyBOP (Scheme VII-23).[269]

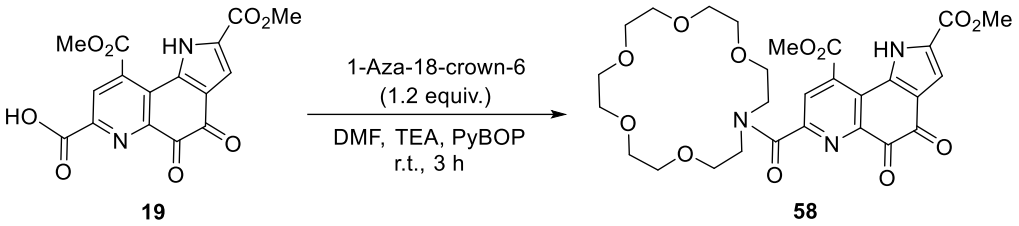

Scheme VII-23: Amide coupling between PQQMe$_2$ (**19**) and 1-aza-18-crown-6 by using PyBOP.

The reaction proceeded successfully and TLC indicated a complete conversion of the starting materials. Both NMR and ESI indicated the formation of the preferred PQQMe$_2$-crown ether product (see VIII.9.4.1). Since equimolar amounts of pyrrolidinphosphine oxide are generated in reactions with PyBOP, purification by column chromatography was necessary. A wide range of different column conditions was tested by TLC, including reversed phase and aluminum oxide or silica with basic or acidic additives (TEA or HCl). No clear separation of fractions was observed in almost all cases. The reactivity of the quinone with all kind of nucleophiles like alcohols or water further complicates chromatographic purification.

The most promising method was a 99:1 DCM/EtOH mixture. Column chromatography gave one clean fraction, while the majority of the crude product remained on the column (even with 15% EtOH) and needed to be recovered by partly dissolving the silica in water and extraction with DCM. The isolated fraction, however, resulted in a different NMR spectrum compared to the crude and no product peak could be found in the ESI mass analysis anymore. Instead a related compound was identified, showing an ethyl ester in C9 position (VIII.9.4.1 and Figure IX.35). Most likely, a transesterification had occurred on the column.

In order to achieve the PQQ-crown ether without pyrrolidinphosphine residues from the PyBOP coupling reagent, an alternative coupling procedure was evaluated. Together with TEA, 1,1'-carbonyldiimidazole (CDI) was used, as it has the advantage over PyBOP to only produce CO_2 and imidazole as byproducts (Scheme VII-24).[270]

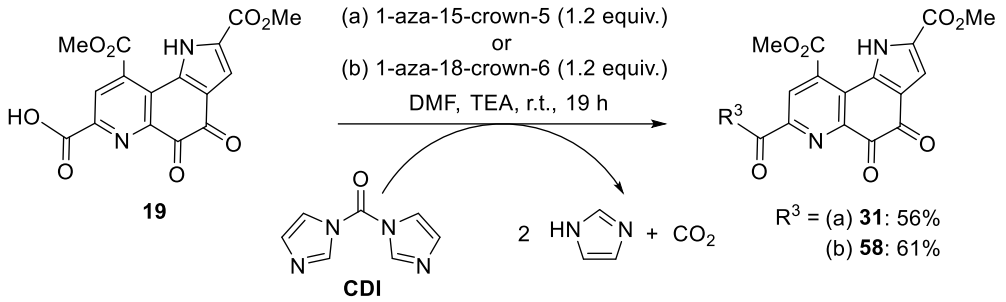

Scheme VII-24: Amide coupling between $PQQMe_2$ (**19**) and 1-aza-15-crown-5 (a) or 1-aza-18-crown-6 (b) using CDI.

A routinely used procedure from our lab was implemented, which proceeded successfully and resulted in both crown-ether products **31** and **58** in average yields. Attempts to purify the compounds by reversed-phase column-chromatography or by HPLC failed. However, the NMR spectra of the crude product showed no major impurities (Figure IX.36 and Figure IX.37) and the EA was in good agreement with the calculated values and with Itoh *et al.*[152], with small deviations caused by residual H_2O, DMF and unreacted aza-crown ether.

4.2. Coordination with Ca and La

LC/MS of equimolar solutions of **31** or **58** and $La(NO_3)_3{\cdot}6H_2O$ in acetonitrile revealed signals for ligand+La^{3+}+$2NO_3^-$ complexes in the positive ionization mode, both for the smaller **31** (m/z 822.1 – $[La(\mathbf{31})(NO_3)_2]^+$) and the larger **58** (m/z 866.1 - $[La(\mathbf{58})(NO_3)_2]^+$) aza-crown ether ligand. Also with $Ca(NO_3)_2{\cdot}2H_2O$, signals for ligand+Ca^{2+}+NO_3^- were detected for **31** (m/z 661.5 - $[Ca(\mathbf{31})(NO_3)]^+$) and **58** (m/z 705.3 - $[Ca(\mathbf{58})(NO_3)]^+$), clearly indicating the ability of the synthesized ligands, to readily form complexes with biologically relevant metals. Complexes of **31** and **58** with lanthanum were further confirmed with direct infusion analysis high-resolution ESI measurements (see Figure IX.38 and Figure IX.39 in the Appendix). The unusual mass peaks with nitrate incorporation can be explained with $La(NO_3)_3$ being a non-electrolyte in acetonitrile.[271] Nitrate ions coordinate in solution, increasing the probability of their co-complexation with ligands **31** and **58**.

To further elucidate coordination behavior of aza-crown ether ligands **31** and **58**, UV-Vis spectroscopy was performed. As described by Itoh *et al.*,[152] spectrophotometric titrations were conducted with **31** and **58** in the presence of increasing amounts of lanthanum and calcium perchlorate in dry and deaerated acetonitrile (see VIII.9.5). Figure VII.11 shows the received spectra of **31** with increasing amounts of Ca^{2+} or La^{3+}. The maximum at 279 nm decreases concurrent to an increase of absorption at 260 (256) nm and a shift of the second maximum at

353 nm towards longer wavelengths. Those shifts are in good agreement with the observations described by Itoh *et al.*[152] (Table VII.4). Comparison with maxima of $PQQMe_3$ (**11**) (Table VII.4) further reveal large similarities. Absorbance is related to the PQQ residue and less affected by the coupled crown ethers. This is especially visible when comparing non-coordinated **31** and **58**, which show almost identical spectra. Larger differences are observed between complexes with the different metal ions. In direct comparison, changes are more pronounced with La^{3+} with larger shifts of the maxima and more distinct isosbestic points (Figure VII.11).

Table VII.4: Absorbance maxima of aza-crown ether ligands **31** and **58** as free ligands or as lanthanum or calcium complexes in dry acetonitrile. Literature values of **31,** [Ca (**31**)]$^{2+}$ and $PQQMe_3$ (**11**) in acetonitrile are given for comparison. * estimated from the shown figure.

	first maximum [nm]	second maximum [nm]
31	279	353
31[152]	278	352
[Ca (**31**)]$^{2+}$	260	364
[Ca (**31**)]$^{2+}$ [152]	260	360
[La (**31**)]$^{3+}$	256	386
58	279	352
[Ca (**58**)]$^{2+}$	258	354
[La (**58**)]$^{3+}$	256	383
$PQQMe_3$ (**11**)[173]	280	354
[Ca (**11**)]$^{2+}$ [173]	~258*	368

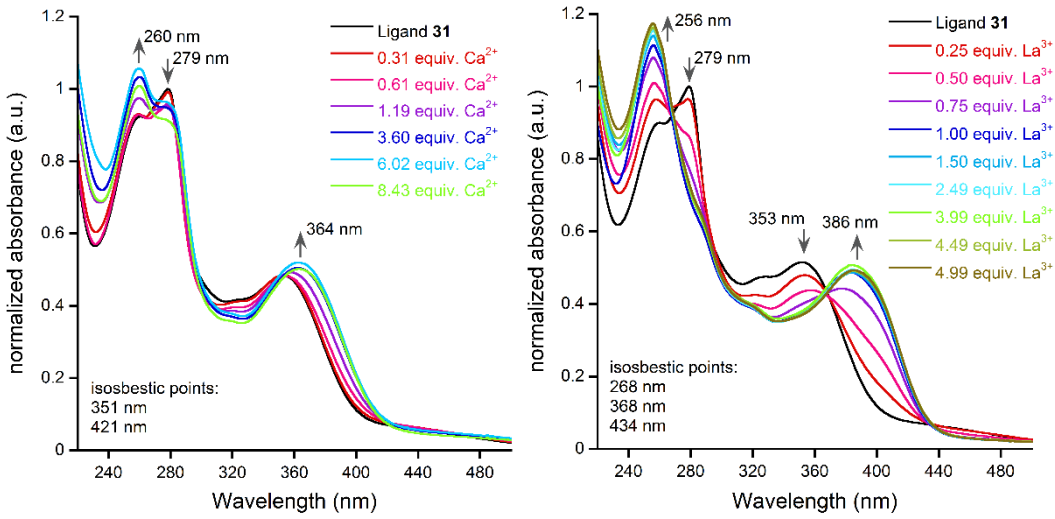

Figure VII.11: Titration of $PQQMe_2$-aza-15-crown-5 (**31**) with increasing amounts of $Ca(ClO_4)_2$ (left) or $La(ClO_4)_3$ (right) in dry and deaerated acetonitrile, but a constant total volume of 3 mL (25 µM **31**). Blank measurement was performed in pure deaerated acetonitrile. Spectra are baseline corrected to a set value of 0 at 800 nm. The spectrum of the free ligand is normalized to an absorbance of 1 at 279 nm and the spectra with metal addition are adjusted accordingly.

With the larger PQQMe$_2$-aza-18-crown-6 (**58**), similar spectra are received upon metal titration (Figure VII.12). While the titration with La^{3+} leads to almost identical spectra as in Figure VII.11, the addition of Ca^{2+} is less pronounced in direct comparison to titration with the smaller **31**. Especially the maximum at 354 nm only slightly shifts upon Ca^{2+} addition and also the raise in absorbance of the 258 nm maximum is weaker.

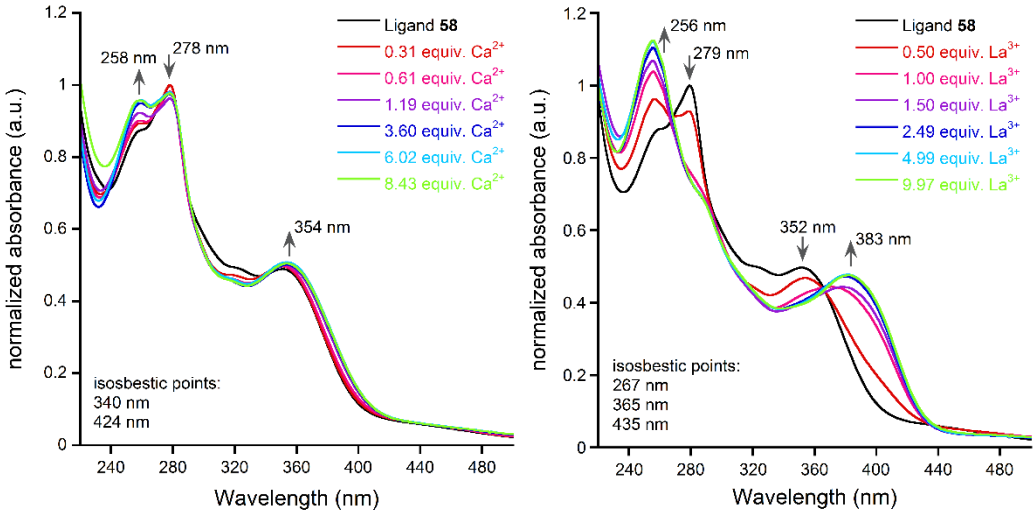

Figure VII.12: Titration of PQQMe$_2$-aza-18-crown-6 (**58**) with increasing amounts of $Ca(ClO_4)_2$ (left) or $La(ClO_4)_3$ (right) in dry and deaerated acetonitrile, but a constant total volume of 3 mL (25 µM **58**). Blank measurement was performed in pure deaerated acetonitrile. Spectra are baseline corrected to a set value of 0 at 800 nm. The spectrum of the free ligand is normalized to an absorbance of 1 at 279 nm and the spectra with metal addition are adjusted accordingly.

When plotting the added equiv. versus the absorbance of one of the two increasing maxima, a sigmoidal curve progression is in very good agreement with all titrations.

$$y = A1 + \frac{(A2 - A1)}{(1 + (\frac{x}{x_0})^p)} \tag{3}$$

Generalized logistic function (3), preset in KaleidaGraph software package 4.5.2 with A1 (maximum value), A2 (minimum value), x_0 (x-value of the sigmoid's midpoint) and p (logistic growth rate / steepness).

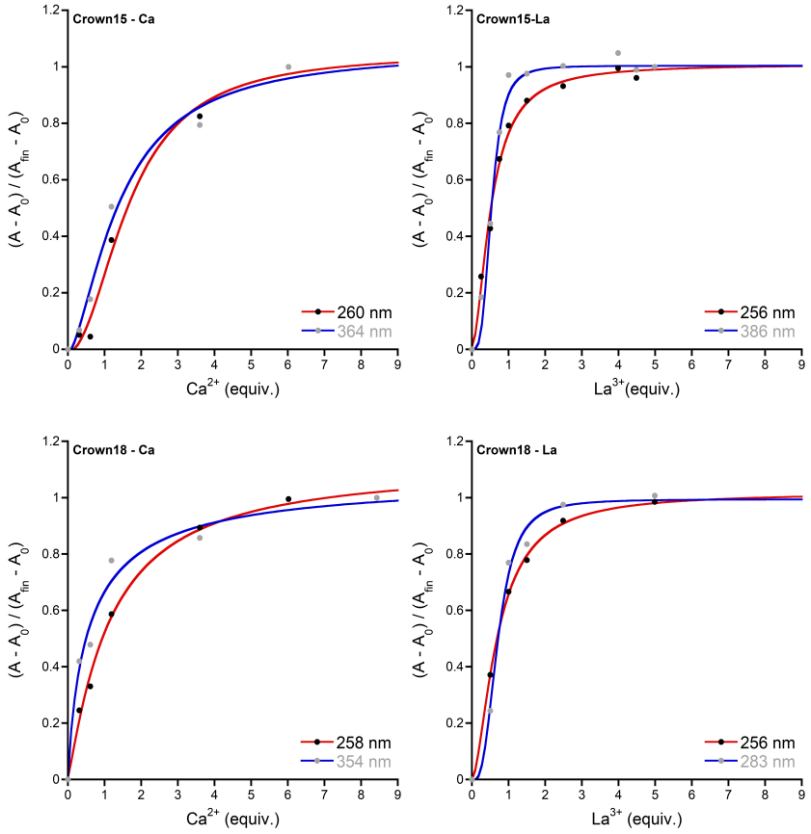

Figure VII.13: Plot of the added metal equiv. (Ca^{2+} or La^{3+}) versus the normalized absorbance at the first (black) or second (grey) maximum. Normalization by $(A-A_0)/(A_{fin}-A_0)$ with starting absorbance A_0, final absorbance A_{fin} and altering absorbance A. Upper left: **31** with Ca^{2+}; upper right: **31** with La^{3+}; bottom left: **58** with Ca^{2+}; bottom right: **58** with La^{3+}. Red lines represent sigmoidal curve fits for the absorbance at the first maximum, blue lines for the second maximum. Plots and curve fits executed with the KaleidaGraph software package 4.5.2 with preset function (3). The curve fit of **31** with La^{3+} (top-right – blue line) caused program errors unless three values were ignored for the calculation.

Based on the curve fits, the ligands show a much higher affinity to La^{3+}, as the added metal gets directly coordinated upon addition, indicated by the almost linear increase of $(A-A_0)/(A_{fin}-A_0)$ and the fast saturation, after 1.0 equiv. of the metal salt are added. No major differences between **31** and **58** can be observed. However, the steepness of **31** is slightly higher, indicating a larger La^{3+} affinity. The curves for both Ca^{2+} titrations are less steep and more equivalents are needed to reach saturation. In direct comparison between both aza-crown ethers, **58** shows a steeper slope and therefore the higher affinity to Ca^{2+}.

The curve fit data (Table VII.5) support this observation. The La^{3+} titrations show overall larger values for p and reach the midpoint of the progression (indicated by x_0) faster than Ca^{2+}. Counterintuitively and deviating from the original ligand design concept, the smaller PQQMe$_2$-aza-15-crown-5 (**31**) shows higher affinities for La^{3+} than the larger PQQMe$_2$-aza-18-crown-6 (**58**) and vice versa Ca^{2+} shows higher affinities for the larger **58**.

Table VII.5: Determined parameters and determination coefficients R^2 for each curve fit, using equation (3). Curve fit executed with the KaleidaGraph 4.5.2 software package. R^2 value for Crown15-La (386 nm) in brackets, as three data points had to be ignored for the calculation which would have caused program errors otherwise.

Plot	Abs(nm)	A1	A2	x_0	p	R^2
Crown15-Ca	260	1.05	-0.01	1.68	2.02	0.990
Crown15-Ca	364	1.06	-0.02	1.41	1.55	0.988
Crown15-La	256	1.01	0.01	0.53	1.77	0.994
Crown15-La	386	1.00	0.00	0.53	3.48	(0.999)
Crown18-Ca	258	1.12	0.01	1.14	1.16	0.996
Crown18-Ca	354	1.08	0.00	0.58	0.89	0.980
Crown18-La	256	1.02	0.00	0.70	1.66	0.999
Crown18-La	383	0.99	-0.01	0.71	2.94	0.994

In order to verify those observations, binding constants K were calculated. Itoh *et al.* used equation (4) for binding constant determination, where [M] and [Q] are the concentrations of Ca^{2+} and ligand **31** respectively and K can be determined as the slope of the straight line of the plot $(A-A_0)/(A_{fin}-A)$ versus $10^5[Ca^{2+}]_0-((A-A_0)/(A_{fin}-A)[\mathbf{31}]_0)$.[152]

$$\frac{A-A_0}{A_{fin}-A_0} = K\left([M]_0 - \frac{A-A_0}{A_{fin}-A_0}[Q]_0\right) \tag{4}$$

However, no further information are given for the equation and it remains elusive, why the 10^5 potency was added and which concentrations should be used for [M] and [Q] as the "0" subscripts are also not further explained. In addition, the last measurement value is undefined due to the $(A-A_0)/(A_{fin}-A)$ term which leads to division by 0. The binding constant provided by Itoh *et al.* for Crown15-Ca is 210 000 M^{-1} or 5.32 K_{log}.[152] Figure IX.41 (Appendix) gives the plot of our own Crown15-Ca titration data for the absorbance maximum at 364 nm. The plot results in a straight line as well but the received K value is only 44 960 M^{-1} or 4.69 K_{log}. Similar plots for the other titrations failed to accomplish as no linear relationship was observed.

Since no further explanation or utilization of equation (4) was found in the literature, the Benesi–Hildebrand equation was used instead for binding constant determination, assuming 1:1 complex formation.[272]

$$\frac{1}{A-A_0} = \frac{1}{K(A_{fin}-A_0)[M]} + \frac{1}{A_{fin}-A_0} \tag{5}$$

K can be graphically determined from the slope of the straight line of the plot $1/A-A_0$ versus 1/[M],[273] where M is the concentration of either Ca^{2+} or La^{3+}. Linear curve fits are given in the Appendix (Figure IX.40) while determined parameters for K are given in Table VII.6.

Table VII.6: Determined parameters and determination coefficients R^2 for curve fits of $1/A-A_0$ versus 1/[M] (given in Figure IX.40) from titration experiments of **31** (Crown15) and **58** (Crown18) with lanthanum or calcium.

	first maximum (256 – 260 nm)			second maximum (354 – 386 nm)		
Plot	K (M^{-1})	K_{log}	R^2	K (M^{-1})	K_{log}	R^2
Crown15-Ca	872	2.94	0.984	695	2.84	0.970
Crown18-Ca	3327	3.52	0.965	1425	3.15	0.883
Crown15-La	13127	4.12	0.990	7217	3.86	0.996
Crown18-La	11488	4.06	0.985	4336	3.64	0.989

It has to be noted that due to the $1/A-A_0$ term, the first value is undefined. Values received for titration over the saturation point (≥ 1.32 equiv. La^{3+} for Crown15-La, and ≥ 4.4 equiv. La^{3+} for Crown18-La) showed no more linear correlation and were ignored for the determination of K.

Determined binding constants K vary depending on the absorbance maximum used and show higher values for the first maximum in all cases. This can be explained by the overall larger absorbance growth of the first maximum and demonstrate the limitations of the method used for binding constant determination. However, the binding constants show the same trend as described above and shown in Figure VII.13. For Ca^{2+} higher K values are determined for the larger crown18 ligand **58**, while La^{3+} has the larger binding constant with the smaller crown15 ligand **31**.

Cavity sizes of related crown ether compounds without nitrogen are 1.7 - 2.2 Å for 15-crown-5 (15C5) and 2.6 - 3.2 Å for 18-crown-6 (18C6).[274] Ionic radii for the coordinated metals are similar, with 1.03 Å for La^{3+} and 1.00 Å for Ca^{2+}.[20] Both metals should therefore prefer the smaller crown15 ligand **31**, when a fitting cavity size would be the only criterion. However, similar trends are described in the literature. Gokel *et al.* obtained K_{log} values of 2.36 for $[Ca(15C5)]^{2+}$ and 3.90 for $[Ca(18C6)]^{2+}$.[275]

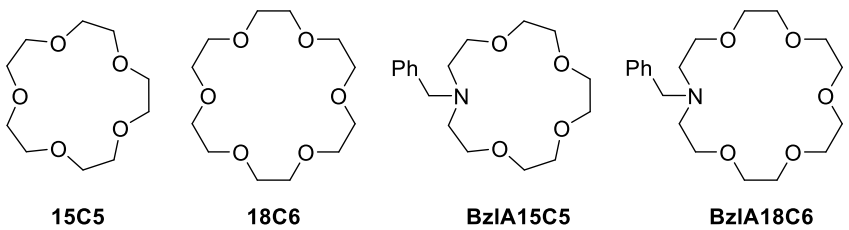

Figure VII.14: Different crown ether compounds discussed in this section.

While not explaining this phenomenon the authors gave additional criteria for complex stabilities besides the size-relationship, namely solvation enthalpies and entropies, the number of participating donor atoms and the conformation of the crown ether rings.[275] Liu, Han and Chen provide a summary of crown ether and aza-crown ether complexes with LRE in their

review.[276] La^{3+} shows higher K_{log} values for 15C5 (5.17)[277] and BzlA15C5 (see Figure VII.14) (4.55)[278] in direct comparison to values obtained from 18C6 (4.40)[279-280] and BzlA18C6 (3.77)[281] complexes. It is interesting to note, that K_{log} values decrease from La^{3+} to Gd^{3+} in case of 15C5, BzlA15C5 and 18C6 complexes as decreasing ionic radii[20] from 1.03 Å to 0.94 Å throughout the series become less favored.[276] In case of BzlA18C6, K_{log} values increase from La^{3+} to Gd^{3+} explained by efficient nitrogen participation in complex formation. Gatto and Gokel further demonstrated increased K_{log} values of Ca^{2+} complexes with diaza-18-crown-6 derivatives, when additional coordinating groups were integrated (Figure VII.15).[282]

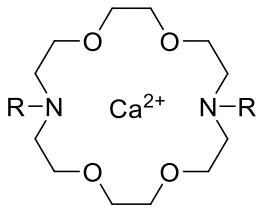

R =

$PhCH_2$-	(2.79)	CH_3-OCH_2CH_2-	(4.48)
2-MeO-$C_6H_4CH_2$-	(3.27)	$EtOCOCH_2$-	(6.78)
$HOCH_2CH_2$-	(6.02)	2-HO-$C_6H_4CH_2$-	(2.95)

Figure VII.15: Ca^{2+} complexes with diaza-18-crown-6 derivatives, reported by Gatto and Gokel.[282] Parenthesized numbers indicate K_{log} values of the Ca^{2+} complexes.

To summarize, although showing similar ionic radii, La^{3+} and Ca^{2+} prefer different sized aza-crown ether ligands as a result of differences in additional factors like charge, preferred coordination numbers and solvation entropies and enthalpies. The assumption, La^{3+} would prefer the larger ligand **58** due to the provided higher denticity was not confirmed.

5. Conclusion

Aim of this chapter was the synthesis and subsequent evaluation of a structural mimic for the active site of XoxF-type MDH, to gain deeper understanding of the enzymatic activity and the mechanism of action. The literature-known ligand TREN-(1,2-HOPO)$_3$ (**32**) was synthesized for mimicking the amino acid residues in co-complexation experiments with the cofactor PQQ. Mass experiments indicated co-complexation of the structural analog PDC, but not PQQ. Increased concentrations led to precipitation of a [Ln (**32**)] complex while PQQ remained in solution. To overcome this problem, PDC was directly connected to a structural similar TREN-(1,2-HOPO)$_2$-TAM ligand through amide linkage. The new ligand **43** performed well in DFT calculations and indeed, a [Ln (**43**)] complex was verified by mass spectrometry,

UV-Vis and NMR. However, a second Ln equiv. was coordinated by the ligand, making it unsuitable for a structural MDH mimic.

The coupling of aza-crown ethers to PQQ as alternative structural models was challenging. The literature procedure included a PQQ precursor from Corey's total synthesis. This precursor was successfully exchanged with PQQ from nutritional supplement capsules, saving time and reducing the number of synthesis steps. Problematic product purification could be overcome by introducing an alternative coupling procedure with CDI, which gave PQQ-crown15 (**31**) and PQQ-crown18 (**58**) in sufficient purity without the need of column chromatography. Preliminary UV-Vis titrations indicated overall higher affinities for La^{3+} over Ca^{2+} and a La^{3+} preference for **31** and Ca^{2+} preference for **58**. However, presence of water is very problematic, as it competes with alcohols for PQQ. Production of water-free metal-salt solutions was challenging and water-free UV-Vis titration prone to errors. For reproducible and comparable determination of binding constants, methanol addition constants and rate constants for the oxidation of methanol, strictly water-free conditions are necessary. This could be achieved in a glovebox, using water-free metal salts, ligands and solutions right from the beginning.

To summarize, a convenient way to produce aza-crown ether coupled PQQ ligands **31** and **58** in sufficient quality was successfully implemented and could be easily scaled up to 100 mg. Those ligands readily form complexes with Ca^{2+} and La^{3+} but for precise constant determinations (especially for the whole series of lanthanides), a collaboration partner with a glovebox UV-Vis setup and additional work of several months is needed which is beyond the scope of this thesis.

VIII. EXPERIMENTAL PART

1. General Considerations

Measurements and Reactions under nitrogen atmosphere were performed as followed: Glassware was dried by using a heat-gun (400°C) under high-vacuum (three times, in between flushed with nitrogen). Syringes to transfer liquids and solutions were flushed with nitrogen three times prior to use. Solids were added under nitrogen counter flow. A rotary evaporator with an attached membrane pump, followed by drying under high-vacuum was used to remove solvents. For oxygen-sensitive reactions or measurements, the used solvents were stored in Schlenk-flasks and nitrogen was passed through them for 10 minutes to remove residual oxygen.

For water sensitive reactions, DMF was purchased from Merck, which was dried by SeccoSolv® (max. 0.003% H_2O) and stored under N_2.

DCM, TCM and *i*-hexane were distilled by using the rotary evaporator prior to use. All other solvents were used without further purification, unless otherwise stated.

2. Analytical Methods

2.1. Nuclear Magnetic Resonance (NMR)

^{1}H-NMR and ^{13}C-NMR spectra were recorded by Brigitte Breitenstein or Christine Neumann. Unless otherwise stated, measurements were performed at room temperature on Jeol ECP 270 (400 MHz), Jeol ECX 400 (400 MHz) and Bruker Avance III (400 MHz) operating at 400 MHz for proton nuclei and 100 MHz for carbon nuclei. ^{1}H-NMR chemical shifts are reported in ppm relative to $CDCl_3$ (δ_H = 7.26), D_2O (δ_C = 4.79), MeOD-d_4 (central line of quintet: δ_H = 3.30), DMSO-d_6 (central line of quintet: δ_H = 2.50) or DMF-d_7 (δ_H = 8.03). ^{13}C-NMR chemical shifts are given in ppm relative to $CDCl_3$ (central line of triplet: δ_C = 77.16), MeOD-d_4 (central line of septet: δ_C = 49.00), DMSO-d_6 (central line of septet: δ_C = 39.52), DMF-d_7 (central line of triplet: δ_C = 163.15) or D_2O with 5% dioxane (δ_C = 67.20). The following abbreviations were used: s =

singlet, d = doublet, t = triplet, q = quartet, p = quintet, dd = doublet of doublet, dt = doublet of triplet, m = multiplet. Coupling constants are given in Hertz. The software used for data processing was MestReNova Version 12.02. Two-dimensional correlation spectroscopy (COSY), heteronuclear single quantum coherence (HSQC) and heterobinuclear multiple bond correlation (HMBC) experiments were used for signal assignment. Experiments were performed by default with 16 scans for ^{1}H-NMR and 2000 scans for ^{13}C-NMR experiments and were increased to up to 64 scans for ^{1}H-NMR and 10000 scans for ^{13}C-NMR for correct assignments and side-product analysis. Solid state NMR was performed at room temperature with a Bruker Avance III (500 MHz, 11,74 T) with Magic-Angle-Spinning (MAS) in 4 mm rotors by Christian Minke. ^{1}H-NMR performed with single pulse excitation, ^{13}C-NMR with cross-polarization over ^{1}H. Scan delays (d1): ^{13}C: 16 s; ^{1}H: 128 s. Chemical shifts are reported in units of ppm relative to TMS, indirectly measured with 0.1% TMS in $CDCl_3$.

2.2. FT-Infrared Spectroscopy

IR was carried out with a *Jasco* FT/IR-460Plus with an ATR Diamond Plate. Spectra Manager Version 2 from JASCO was used for Data processing.

2.3. UV-Vis Spectroscopy

Measurements were either conducted with an Agilent Cary 60 UV-Vis with Peltier Element, with an Agilent 8453 Diode Array Spectrophotometer with stirred, thermostatted cuvette holder or with an Epoch 2 Plate Reader from Biotek. 10 mm quartz suprasil cuvettes or a 96 well quartz microplate from Hellma were used unless noted otherwise. Measurements under an inert atmosphere were conducted in a screw top cuvette equipped with a septum.

2.4. Mass Spectrometry

EI was recorded with a Thermo Q Exactive GC, a Thermo Finnigan MAT 95 or a Jeol MStation mass spectrometers. ESI spectra were recorded with a Thermo Finnigan LTQ FT Ultra Fourier Transform Ion Cyclotron Resonance mass spectrometer with $MeCN/H_2O$ as carrier solvents. In both cases, measurements were performed by Dr. Werner Spahl.

2.5. Elemental Microanalyses

Elemental Microanalyses (C, H, N, S) were performed with an Elementar vario EL by Susanne Ebert or Robert Eicher. JASPER v1.0 - JavaScript Percentage Elemental Results Calculator was used for calculations (http://phoenix.tuwien.ac.at/jasper/ANALYSE2.HTM).

2.6. Inductively Coupled Plasma Optical Emission Spectroscopy

ICP-OES was conducted with a VARIAN-VISTA instrument with autosampler by Jarka Obel. Samples were digested in hot nitric acid and then diluted with Millipore water to a final HNO_3 concentration of 3%.

2.7. Inductively Coupled Plasma Mass Spectrometry

ICP-MS was performed on a Nexion 350D from Perkin Elmer, measurements were performed in kinetic energy discrimination (KED) cell mode by Christine Benning. An ICP reference standard from VWR was used for calibration, including 14 lanthanides (La-Lu, except Pm), Sc, Y and Th, each in 10 µg/mL concentration. Samples (~5-10 mg) were given in defined amounts of nitric acid (65%, Suprapur from Merck) and were diluted with water to a concentration of 3% HNO_3, which gave a sample concentration of 1.0256 mg/mL. In two additional dilution steps, concentration was set to 50.54 ppb. Addition of HNO_3 caused precipitation of protonated PQQ as red solid, while the no longer coordinated metal ions stayed in solution. Two additional samples were completely digested in hot nitric acid (65%, Suprapur from Merck) at 125°C under addition of a few drops of concentrated hydrochloric acid, and then diluted to a concentration of 50.54 ppb. ICP-MS gave similar results for both methods (Table IX.15) and therefore, the simplified work-up was used for all samples.

2.8. Electrochemistry

Cyclic voltammetry was performed on a BAS100B/W potentiostat employing either a gold or platinum working electrode, platinum auxiliary electrode and a Ag/Ag^+ pseudo reference electrode in dry DMF, DCM, MeCN or a 70:30 H_2O/DMF mixture for measurements in non-aqueous systems. All solutions were 1 mL total volume and were purged with nitrogen prior to measurements. Measurements were performed at the University of Queensland, Australia. Measurements shown in Figure V.29 and Figure V.31 were performed on an Autolab PGSTAT101 potentiostat from Metrohm, employing a platinum working electrode, platinum auxiliary electrode and a Ag/Ag^+ pseudo reference electrode in a 70:30 H_2O/DMF mixture. The supporting electrolyte was either Et_4NClO_4 or Bu_4NClO_4. Ferrocene (Fc) was used as external standart and all potentials are cited as versus $Fc^{+/0}$. All solutions were purged with N_2 before measurements. All solutions were 1 mL total volume for the BAS100B/W potentiostat or 25 mL for the Autolab PGSTAT101 potentiostat.

2.8.1 Measurements on a Metrohm Device

Voluma were adjusted due to larger electrodes and electrochemical cells. PQQ stock solution (0.1 M) in DMF – 250 µL in 25 mL for a 0.001 M solution. 7.25 mL DMF (0.1 M Et_4NClO_4). 17.5 mL H_2O (0.1 M Et_4NClO_4). Fc in DMF (0.1 M) for external standart – 250 µL in 25 mL for a 0.001 M solution.

2.9. Spectroelectrochemistry

The UV-Vis spectrum was recorded *in situ* at each potential step in a thin-layer spectroelectrochemical cell (0.5 mm pathlength) by an Ocean Optics PX-2 spectrophotometer. A transparent gold minigrid working electrode was used in this experiment. Measurements were performed in a glovebox under inert gas atmosphere at the University of Queensland, Australia.

2.10. X-Ray Crystallography

Data collection and structure elucidation was performed by Dr. Peter Mayer at the Chemistry Department of the Ludwig-Maximilians University Munich. The X-ray intensity data were collected on a Bruker D8 Venture TXS system equipped with a multilayer mirror optics monochromator and a Mo Kα rotating-anode X-ray tube (l mbda = 0.71073 Å). The frames were integrated with the Bruker SAINT software package usinga narrow-frame algorithm.[283] Data were corrected for absorption effects using the Multi-Scan method (SADABS).[284] The structure was solved and refined using the Bruker SHELXTL Software Package.[285]

2.11. DFT Calculations

Gaussian 09, Revision D.01 was used in electronic-structure calculations.[79] All calculations were performed by using the B3LYP DFT method.[80-83] Electron core pseudopotentials and a segmented basis set incorporating quasi-relativistic effects were used for heavy atoms and the 6–31g basis set was used for C, H, N, and O unless otherwise stated.[286-287] Solvent effects were modeled by using the conductor-like polarizable continuum model (CPCM) with the default universal force field (UFF) radii.[288-289] Magnetic properties (e.g. NMR-shifts) were calculated by the gauge-independent atomic orbital (GIAO) method.[290-291] Excited state calculations were performed by the time-dependent self-consistent field (TD-SCF) approximation.[292-293]

3. General Procedures

3.1. GP I: Benzyl Deprotection

All glassware was given in an aqueous, EDTA containing bath overnight, to remove remaining metal ions from the surface, which could otherwise coordinate to the deprotected ligand.

According to literature procedures,[294] in a metal-free round-bottom flask, the protected ligand was dissolved in a mixture of glacial acetic acid and concentrated hydrochloric acid (1:1, 6 mL per 100 mg Ligand) and was stirred at room temperature for 3 days. After removal of the acids under reduced pressure using H_2O and MeOH, the residue was dried *in vacuo* to give the deprotected ligand.

3.2. GP II: Acyl Chloride Formation

According to literature procedures,[263] in a dry and nitrogen flushed Schlenk-flask, equipped with a magnetic stirring bar and a septum, the respective acetic acid (1.0 equiv.) was dissolved or suspended in a small amount of dry benzene and oxalyl chloride (1.9 equiv.) was added. The reaction was catalyzed by the addition of small drops of dry DMF, which were added roughly every 30 minutes to the reaction mixture, until no more gas evolution could be observed (~6 h in total). The solvents were removed under reduced pressure and the crude product was further dried under high vacuum overnight.

3.3. GP III: Formation of Acyl Thiazolidine-2-thione

According to literature procedures,[263] in a first step, the respective acetic acid (1.0 equiv.) was transformed to its acyl chloride, following GP II. Under nitrogen atmosphere, the dry acyl chloride was dissolved in a small amount of dry DCM and was added dropwise over 3 h to a suspension of thiazolidine-2-thione (1.2 equiv.) and potassium carbonate (5.05 equiv.) in water at 0°C. After the reaction mixture was allowed to warm up to room temperature, the organic phase was separated and the hydrous phase was extracted three times with DCM. The combined organic phases were first washed with KOH (1 M), then with HCl (1 M) and finally with brine. The organic phase was dried with sodium sulfate, evaporated to dryness and further dried under high vacuum. The crude product was further purified via flash column chromatography.

4. Experimental Procedures for Chapter II

Experimental procedures and supporting information for the two subchapters II.2 - *Impact of Different Lanthanides on the Structure of XoxF* and II.3 - *Impact of the Lanthanide Contraction* are provided in IX.1.1 and IX.1.2.

5. Experimental Procedures for Chapter III

5.1. Precursor Synthesis

5.1.1 Synthesis of Methyl 2-methyl-3-oxobutanoate (**4**)

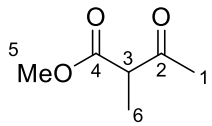

According to a literature procedure,[295] methyl iodide (35.5 g, 0.25 mol, 1.0 equiv.) was added to methyl 3-oxobutanoate (29 g, 0.25 mol, 1.0 equiv.) and the mixture was cooled down to 0°C. Under stirring, potassium carbonate (52 g, 0.375 mol, 1.5 equiv.) was added in four equal portions over the course of 1 hour. The mixture was allowed to warm up to room temperature and was further stirred overnight. After dilution with Et_2O (50 mL), the mixture was filtered and washed with Et_2O. After the solvent was removed under reduced pressure, the remaining liquid was purified by distillation (oil bath: 41°C, thermometer: 22°C, 0.05 mbar) to give the title compound (**4**) (31.32 g, 0.24 mol, 96%) as a colorless liquid.

^{1}H-NMR (400 MHz, $CDCl_3$): δ / ppm = 3.72 (s, 3H, 5), 3.50 (q, *J* = 7.2 Hz, 1H, 3), 2.22 (s, 3H, 1), 1.32 (d, *J* = 7.2 Hz, 3H, 6).

^{13}C-NMR (100 MHz, $CDCl_3$): δ / ppm = 203.7 (2), 171.1 (4), 53.5 (3), 52.5 (5), 28.5 (1), 12.9 (6).

IR (Diamond-ATR, neat): $\tilde{\nu}$ / cm^{-1} = 2992 (w), 2955 (w), 1742 (s), 1713 (s), 1454 (m), 1435 (m), 1359 (m), 1329 (m), 1244 (m), 1206 (m), 1152 (m), 1101 (m), 1077 (m), 1051 (m), 988 (w), 956 (w), 859 (m).

Analytical data were consistent with those reported in the literature.[295]

5.1.2 Synthesis of Dimethyl 2-oxopentanedioate (**8b**)

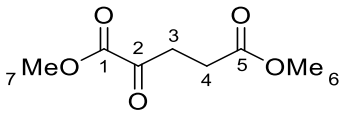

According to a literature procedure,[153] 2-oxopentanedioic acid (**8a**) (50 g, 0.34 mol, 1.0 equiv.) was dissolved in MeOH (200 mL) and was left for 5 days. 2,2-Dimethoxypropane (71 g, 0.68 mol, 2.0 equiv.) was added and the reaction mixture was left for another 24 h. The solvent was removed under reduced pressure and the remaining yellowish liquid was purified by distillation (oil bath: 165°C, thermometer: 112-115°C, 2.1 mbar) to give the title compound (**8b**) (34.78 g, 0.20 mol, 59%) as a clear liquid.

^{1}H-NMR (400 MHz, $CDCl_3$): δ / ppm = 3.87 (s, 3H, 7), 3.67 (s, 3H, 6), 3.15 (dd, *J* = 6.8, 6.2 Hz, 2H, 3), 2.67 (t, *J* = 6.5 Hz, 2H, 4).

Analytical data were consistent with those reported in the literature.[153]

5.1.3 Synthesis of Dimethyl 2-bromo-4-oxopentanedioate (**8c**)

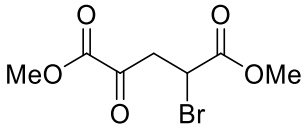

According to a literature procedure,[153] dimethyl 2-oxopentanedioate (**8b**) (10 g, 57,42 mmol, 1.0 equiv.) was dissolved in DCM (300 mL) and a solution of bromine (13.76 g, 86.13 mmol, 1.5 equiv.) in DCM (50 mL) was added dropwise over 10 minutes. The reaction mixture was heated to 50°C and was stirred for 3 hours at this temperature. The mixture was left open overnight at room temperature, to let remaining traces of bromine evaporate. The solvent was removed under reduced pressure and the remaining yellowish oil was further dried under high vacuum. The crude product (14.91 g) was not further purified and was directly used in the next reaction step.

5.1.4 Synthesis of Dimethyl (E)-4-oxopent-2-enedioate (**8**)

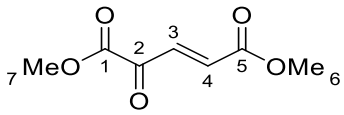

According to a literature procedure,[153] the crude product from the synthesis of dimethyl 2-bromo-4-oxopentanedioate (**8c**) (14.91 g, ~57.42 mmol) was dissolved in Et_2O (250 mL) and triethylamine (5.81 g, 7.96 mL, 57.42 mmol) was added (formation of a precipitate). The mixture was stirred for another 30 minutes at room temperature, was filtered over a pad of silica gel on a glass frit and washed with further Et_2O. The filtrate was evaporated under reduced pressure and the residue was further dried under high vacuum to afford the title compound (**8**) (9.84 g, 57.16 mmol, 99%) as a yellow, crystalline solid.

^{1}H-NMR (400 MHz, $CDCl_3$): δ / ppm = 7.60 (d, *J* = 16.0 Hz, 1H, 3), 6.96 (d, *J* = 16.0 Hz, 1H, 4), 3.92 (s, 3H, 6), 3.83 (s, 3H, 7).

^{13}C-NMR (100 MHz, $CDCl_3$): δ / ppm = 182.28, 165.28, 161.06, 135.54, 134.23, 53.52, 52.76.

IR (Diamond-ATR, neat): $\tilde{\nu}$ / cm^{-1} = 2961 (w), 1731 (s), 1712 (s), 1699 (s), 1639 (w), 1435 (m), 1307 (s), 1254 (s), 1207 (m), 1174 (m), 1077 (s), 998 (s), 953 (m), 929 (m), 827 (m), 778 (m), 684 (m), 672 (m).

HRMS (ESI –): *m/z* calc. for [2 x **8** $C_{14}H_{15}O_{10}]^-$: 343.0671; found: 343.0674.

Analytical data were consistent with those reported in the literature.[153]

5.2. Total Synthesis of PQQ

5.2.1 Synthesis of N-(2-methoxy-5-nitrophenyl)formamide (**2**)

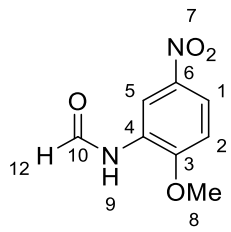

According to a literature procedure,[296-297] acetic formic anhydride was generated *in situ* by dropwise addition of formic acid (14.73 g, 320 mmol, 3.2 equiv.) to acetic anhydride (26.54 g, 260 mmol, 2.6 equiv.) over 5 min at 0°C. The mixture was diluted with THF (20 mL) and a

suspension of 2-methoxy-5-nitroaniline (16.81 g, 100 mmol, 1.0 equiv.) in THF (40 mL) was added dropwise at 0°C. The reaction mixture was allowed to warm up to room temperature and was stirred for 10 min, before it was heated to 60°C and was stirred for another 10 min. After cooling down to room temperature, the mixture was poured into water (150 mL). The precipitate was filtered off and washed with water, until the filtrate was pH-neutral. The filter residue was dried under high vacuum, to afford the title compound (**2**) (18.10 g, 92 mmol, 92%) as a brown-yellow powder.

^{1}H-NMR (400 MHz, $CDCl_3$): δ / ppm = 10.09 (s, 1H, 9), 9.11 (d, *J* = 2.9 Hz, 1H, 5), 8.38 (d, *J* = 1.8 Hz, 1H, 12), 8.01 (dd, *J* = 9.1, 2.9 Hz, 1H, 1), 7.25 (d, *J* = 9.1 Hz, 1H, 3), 4.00 (s, 3H, 8).

Analytical data were consistent with those reported in the literature.[297]

5.2.2 Synthesis of N-(5-Amino-2-methoxyphenyl)formamide (**3**)

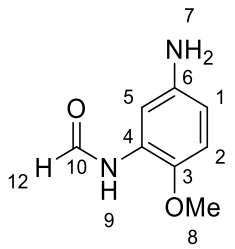

Based on literature procedures,[129, 297] N-(2-methoxy-5-nitrophenyl)formamide (**2**) (11.05 g, 56.33 mmol) was dissolved in ethanol (80 mL) and Pd/C (0.5 g, 0.84 mmol, 1.5mol%) was added. The mixture was given in an autoclave and was stirred for four hours under a hydrogen atmosphere (7 bar) at 65°C. After cooling down to room temperature, Pd/C was filtered off from the reaction mixture and the solvent was removed in vacuo. A crystalline solid remained in the reaction vessel, which was dissolved in DMF. The suspension was filtered and the solvent was removed *in vacuo* by the addition of toluene. The obtained solids were given into TCM, filtered off on a glass frit and washed with TCM to afford the title compound (**3**) (6.23 g, 37.45 mmol, 66%) as a light grey powder. Unreacted starting material remained in the TCM phase and could be recycled.

^{1}H-NMR (400 MHz, DMSO-d_6): δ / ppm = 9.38 (s, 1H, 9), 8.24 (d, *J* = 2.0 Hz, 1H, 12), 7.54 (d, *J* = 2.7 Hz, 1H, 5), 6.73 (d, *J* = 8.6 Hz, 1H, arH (2), 6.25 (dd, *J* = 8.6, 2.7 Hz, 1H, 1), 4.69 (s, 2H, 7), 3.70 (s, 3H, 8).

Analytical data were consistent with those reported in the literature.[297]

5.2.3 Synthesis of Methyl (E)-2-(2-(3-formamido-4-methoxyphenyl)hydrazineylidene)-propanoate (**5**)

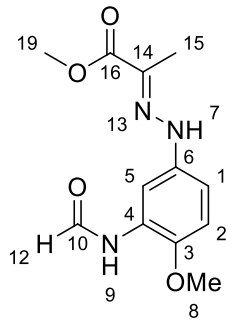

According to literature procedures,[129, 297] N-(5-amino-2-methoxyphenyl)formamide (**3**) (6.0 g, 36.10 mmol, 1.0 equiv.) was dissolved in HCl (0.3 M, 250 mL) and was cooled to 0°C. $NaNO_2$ (2.49 g, 36.10 mmol, 1.0 equiv.) was added, which caused a color change to dark brown and the viscous mixture was stirred for 15 min at 0°C. The produced diazonium salt was then poured into a stirring solution of methyl 2-methyl-3-oxobutanoate (5.64 g, 43.33 mmol, 1.2 equiv.) and KOH (2.43 g, 43.33 mmol, 1.2 equiv.) in a 1:1 H_2O/MeOH mixture, which was previously cooled down to -10°C. A dark red solid precipitated and the suspension was further stirred overnight and slowly warmed up to 0°C. The suspension was filtered on a glass-frit and washed several times with ice-cold EtOH/H_2O (1:1). The residue was dried under high vacuum, to afford the title compound (**5**) (7.75 g, 29.21 mmol, 81%) as a dark red solid.

^{1}H-NMR (400 MHz, DMSO-*d*$_6$): δ / ppm = 9.95 (s, 1H, 9), 9.63 (s, 1H, 12), 8.35 (d, *J* = 2.5 Hz, 1H, 5), 8.32 (d, *J* = 2.0 Hz, 1H, 2), 6.99 (d, *J* = 2.0 Hz, 1H, 1), 3.81 (s, 3H, 8), 3.75 (d, *J* = 34.8 Hz, 3H, 19), 2.34 (s, 3H, 15).

Analytical data were consistent with those reported in the literature.[297]

5.2.4 Synthesis of Methyl 6-formamido-5-methoxy-1H-indole-2-carboxylate (**6**)

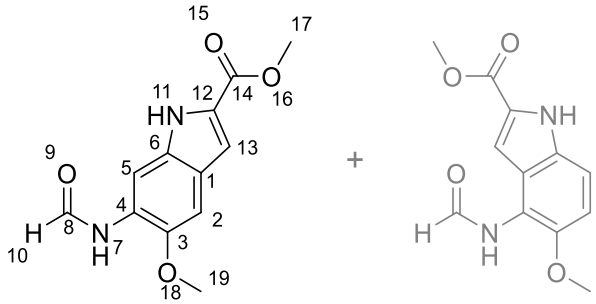

According to literature procedures,[129, 297], compound **5** (7.85 g, 32.04 mmol) was dissolved in formic acid (150 mL) and the reaction mixture was stirred at 80°C for 21 h. After cooling down

to room temperature, the solvent was removed under reduced pressure and the remaining brown solid was further dried *in vacuo*. The crude product was purified by flash column chromatography (*i*-hexane/EtOAc = 50:50) to give a mixture of the title compound (**6**) and the alternative ring closure product (2.86 g, 11.52 mmol, 36%) as a brown-yellow solid.

^{1}H-NMR (400 MHz, DMSO-*d*$_6$): δ / ppm = 11.72 (s, 1H, 11), 9.71 (s, 1H, 7), 8.43 (s, 1H, 5), 8.37 (d, *J* = 1.9 Hz, 1H, 10), 7.18 (s, 1H, 2), 7.04 (d, *J* = 1.3 Hz, 1H, 13), 3.87 (s, 3H, 19), 3.84 (s, 3H, 17), 3.74 (s, 1H).

^{13}C-NMR (100 MHz, DMSO-*d*$_6$): δ / ppm = 161.51 (14), 160.12 (8), 144.65 (3), 132.23 (arC), 126.54 (arC), 126.43 (arC), 122.14 (arC), 107.68 (13), 103.36 (5), 101.56 (2), 55.94 (19), 51.57 (17).

HRMS (ESI –): *m/z* calc. for $[C_{12}H_{11}N_2O_4]^-$: 247.0724; found: 247.0724.

Analytical data were consistent with those reported in the literature.[297]

5.2.5 Synthesis of Methyl 6-amino-5-methoxy-1H-indole-2-carboxylate (**7**)

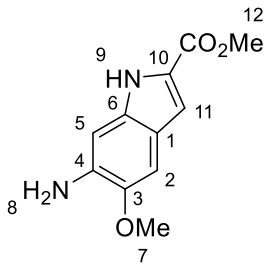

According to literature procedures,[129, 297], the outcome of VIII.5.2.4 (2.86 g, 11.52 mmol, 1.0 equiv.) was dissolved in a solution of conc. HCl (2.88 mL, 3.0 equiv.) in a 96:4 acetone/H_2O mixture (77 mL) and the reaction mixture was refluxed at 70°C for 90 min. After cooling down to room temperature, the solvents were removed under reduced pressure and the residue was ultrasonically redissolved in a mixture of NaOH (2 *M*, 30 mL) and DCM (30 mL). The organic phase was separated and the aqueous phase was extracted with DCM (4 x 20 mL). The combined organic phases were washed with brine and dried over sodium sulfate. After filtration, the solvent was evaporated *in vacuo* to afford the title compound (**7**) (2.30 g, 10.44 mmol, 91%) as a light brown solid. The product was directly used for the next reaction step and was not further purified.

^{1}H-NMR (400 MHz, $CDCl_3$): δ / ppm = 8.75 (s, 1H, 9), 7.07 (dd, *J* = 2.2, 0.9 Hz, 1H, 2), 6.94 (s, 1H, 11), 6.63 (d, *J* = 0.9 Hz, 1H, 5), 3.90 (s, 3H, 7), 3.88 (s, 3H, 12).

Analytical data were consistent with those reported in the literature.[297]

5.2.6 Synthesis of Trimethyl 9-hydroxy-5-methoxy-6,7,8,9-tetrahydro-1H-pyrrolo[2,3-f]quinoline-2,7,9-tricarboxylate (**9**)

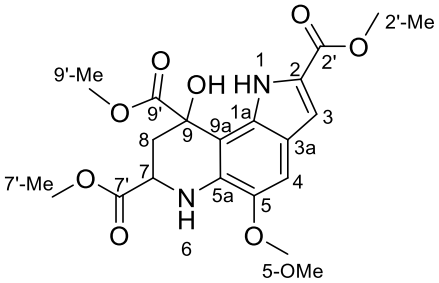

According to literature procedures,[129, 297] compound **7** (2.68 g, 12.17 mmol, 1.0 equiv.), was dissolved in DCM (50 mL). A solution of dimethyl (E)-4-oxopent-2-enedioate (**8**) (2.51 g, 14.60 mmol, 1.2 equiv.) in DCM (10 mL) was added and the mixture was stirred at room temperature for 36 h. The dark brown solution was concentrated under reduced pressure to about half of the original volume and the precipitated solid was filtered on a glass frit, washed with DCM / *i*-hexane (1:5) and dried under reduced pressure, to afford the title compound (**9**) (1.95 g, 4.97 mmol, 41%) as a brown powder.

^{1}H-NMR (400 MHz, DMSO-*d_6*): δ / ppm = 9.34 (d, *J* = 2.2 Hz, 1H, 1), 7.02 (s, 1H, 3), 7.02 (s, 1H, 4), 5.68 (s, 1H, OH), 4.10 (dd, *J* = 9.0, 4.7 Hz, 1H, 7), 3.84 (s, 3H, 2’-Me), 3.82 (s, 3H, 5-OMe), 3.69 (s, 3H, 9’-Me), 3.56 (s, 3H, 7’-Me), 2.56 – 2.46 (m, 1H, 8''), 2.32 (dd, *J* = 13.3, 4.3 Hz, 1H, 8').

^{13}C-NMR (100 MHz, DMSO-*d_6*): δ / ppm = 174.69 (9’), 172.30 (7’), 161.27 (2’), 143.66 (5), 134.11 (5a), 130.87 (1a), 123.23 (2), 117.76 (3a), 108.93 (3), 102.89 (9a), 101.29 (4), 70.84 (9), 55.72 (5-OMe), 52.56 (9’-Me), 52.08 (7’-Me), 51.47 (2’-Me), 50.29 (7), 36.76 (8).

HRMS (ESI +): *m/z* calc. for $[C_{18}H_{21}N_2O_8]^+$: 393.1292; found: 393.1297.

Analytical data were consistent with those reported in the literature.[297]

5.2.7 Synthesis of PQQMe$_3$-OMe (**10**)

Trimethyl 5-methoxy-1H-pyrrolo[2,3-f]quinoline-2,7,9-tricarboxylate

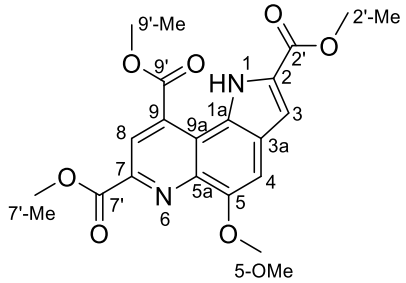

According to literature procedures,[129, 297] compound **9** (1.95 g, 4.97 mmol) was dissolved in DCM (100 mL) and *in situ* generated HCl (conc. H_2SO_4 added dropwise to NaCl) was bubbled through the stirring mixture for 30 minutes at room temperature. Subsequently, synthetic air was bubbled through the mixture for 10 minutes which was further stirred overnight at room temperature (color change from brown to yellow). Sat. aqueous Na_2CO_3 (80 mL) was added and the mixture was stirred for 10 minutes. The organic layer was separated and the aqueous layer was extracted with DCM (3 x 50 mL). The combined organic phases were washed with brine and dried over sodium sulfate. After filtration, the solvent was evaporated *in vacuo* and the crude product was purified by flash column chromatography (*i*-hexane/EtOAc 50:50 → 0:100 to remove the impurities; EtOAc/MeOH 97:03 → 94:06 for the product) to give the title compound (**10**) (0.65 g, 1.75 mmol, 35%) as a yellow solid.

R$_f$ = 0.46 in EtOAc

^{1}H-NMR (400 MHz, CDCl$_3$): δ / ppm = 12.20 (s, 1H, 1), 8.96 (s, 1H, 8), 7.34 (s, 1H, 4), 7.28 (d, *J* = 2.3 Hz, 1H, 3), 4.17 (s, 3H, 9’-Me), 4.12 (s, 3H, 5-OMe), 4.09 (s, 3H, 7’-Me), 4.00 (s, 3H, 2’-Me).

^{13}C-NMR (100 MHz, CDCl$_3$): δ / ppm = 168.78 (9’), 165.54 (7’), 161.65 (2’), 150.80 (5), 143.90 (3a), 142.27 (5a), 132.36 (7), 128.06 (9), 127.72 (2), 124.32 (1a), 124.23 (8), 117.53 (9a), 109.01 (3), 103.14 (4), 56.52 (5-OMe), 54.12 (9’-Me), 53.41 (7’-Me), 52.31 (2’-Me).

HRMS (ESI +): *m/z* calc. for $[C_{18}H_{17}N_2O_7]^+$: 373.1030; found: 373.1033.

IR (Diamond-ATR, neat): $\tilde{\nu}$ / cm^{-1} = 3344 (w), 3255 (w), 2952 (w), 2841 (w), 1714 (s), 1705 (s), 1656 (w), 1613 (m), 1435 (m), 1238 (s), 1224 (s), 1199 (m), 1015 (m), 1004 (m), 836 (w), 764 (s), 735 (m).

5.2.8 Synthesis of $PQQMe_3$ (**11**)

Trimethyl 4,5-dioxo-4,5-dihydro-1H-pyrrolo[2,3-f]quinoline-2,7,9-tricarboxylate

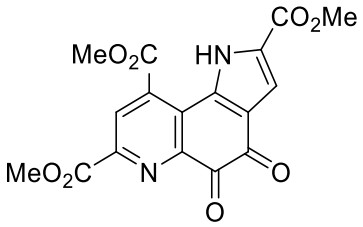

Compound **10** (0.4 g, 1.07 mmol, 1.0 equiv.) was dissolved in a 4:1 MeCN/H_2O mixture (20 mL) and the mixture was cooled down to 0°C. A solution of ceric ammonium nitrate (3.24 g, 5.91 mmol, 5.5 equiv.) in H_2O (2 mL) was added dropwise which caused a brown precipitate which redissolved to an orange solution. The reaction mixture was allowed to warm up to room temperature and was further stirred for 30 minutes. The mixture was extracted with EtOAc/DCM (4:1, 3 x 10 mL) and the combined organic phases were washed with brine and dried over sodium sulfate. The crude product was recrystallized from MeCN, filtered and washed with *i*-hexane to afford the title compound $PQQMe_3$ (**11**) (0.14 g, 0.38 mmol, 35%) as an orange powder.

^{1}H-NMR (400 MHz, DMSO-*d*$_6$): δ / ppm = 12.51 (s, 1H, 1), 8.56 (s, 1H, 8), 7.29 (d, *J* = 2.1 Hz, 1H, 3), 4.05 (s, 3H, 9'-Me), 3.97 (s, 3H, 7'-Me), 3.89 (s, 3H, 2'-Me).

^{13}C-NMR (100 MHz, DMSO-*d*$_6$): δ / ppm = 177.58 (5), 173.85 (4), 167.12 (9'), 164.36 (7'), 160.40 (2'), 149.49 (5a), 146.30 (7), 134.71 (9), 134.10 (1a), 129.04 (8), 127.14 (9a), 127.05 (2), 125.52 (3a), 114.40 (3), 54.76 (9'-Me), 53.51 (7'-Me), 52.92 (2'-Me).
Same numbering scheme as PQQ (**13**)

HRMS (ESI +): *m/z* calc. for $[C_{17}H_{13}N_2O_8]^+$: 373.0666; found: 373.0667.

IR (Diamond-ATR, neat): $\tilde{\nu}$ / cm^{-1} = 3126 (w, H_2O), 1717 (s, COOMe), 1679 (s, C=O), 1552 (w), 1495 (m), 1429 (s), 1345 (w), 1266 (s), 1200 (s), 1171 (s), 1115 (s), 1075 (s), 995 (s), 953 (s), 923 (s), 900 (s), 834 (s), 807 (s), 783 (s), 769 (s), 754 (s), 733 (s), 720 (s), 689 (m), 672 (m).

5.3. Isolation and Purification of PQQ

5.3.1 Isolation of $PQQNa_2$ (**14**)

Sodium 2-carboxy-4,5-dioxo-4,5-dihydro-1H-pyrrolo[2,3-f]quinoline-7,9-dicarboxylate

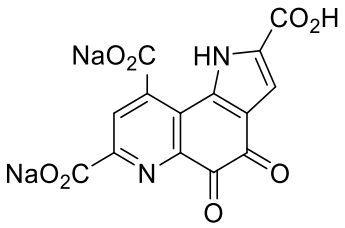

$PQQNa_2$ (**14**) was extracted from capsules from Doctor's Best® Science-Based Nutrition™ containing $PQQNa_2$ (**14**), cellulose and modified cellulose. The capsules (60 x 20 mg $PQQNa_2$ (**14**) = 1.20 g, 3.21 mmol) were emptied and the containing powder was given into water (250 mL). While PQQ was soluble in water, the containing cellulose remained as a solid, was filtered off and washed several times with water, until no red residues were visible. The water was subsequently removed under reduced pressure to give $PQQNa_2$ (**14**) as dark red powder (1.12 g, 2.99 mmol, 93 %).

^{1}H-NMR (400 MHz, DMSO-*d*$_6$): δ / ppm = 8.61 (s, 1H, 8), 7.08 (d, *J* = 1.4 Hz, 1H, 3).

^{13}C-ssNMR (500 MHz, CP–MAS): δ / ppm = 181.77, 173.64, 169.16, 167.42, 164.48, 151.06, 147.82, 143.52, 141.04, 133.99, 132.85, 129.20, 122.62, 113.66.

IR (Diamond-ATR, neat): $\tilde{\nu}$ / cm^{-1} = 1715 (m), 1673 (s), 1614 (s), 1540 (m), 1497 (m), 1354 (m), 1218 (s), 1144 (m), 1083 (m), 941 (m), 866 (m), 803 (m), 753 (m), 716 (m).

Elemental Analysis (CHN): Found C 42.72; H 1.56; N 7.19. Calc. for [$C_{14}H_4N_2Na_2O_8 \cdot 1H_2O$]: C 42.88; H 1.54; N 7.14.

5.3.2 Purification of PQQ (**13**)

4,5-Dioxo-4,5-dihydro-1H-pyrrolo[2,3-f]quinoline-2,7,9-tricarboxylic acid

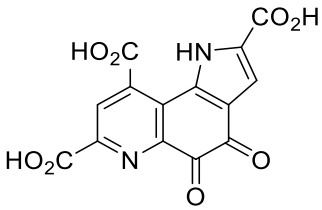

The isolated $PQQNa_2$ (**14**) was purified according to a literature procedure.[154] The crude $PQQNa_2$ (**14**) (1.12 g, 2.99 mmol) was dissolved in water (500 mL) and heated up to 70°C. Concentrated HCl (2.3 mL) was added and the reaction was stirred at 70°C for 24 h. The precipitate was filtered, washed with 2 M HCl and dried *in vacuo*. PQQ·H_2O (1.02 g,

2.93 mmol, 98 %) was isolated as a bright red solid. Total yield over two purification steps: 91%.

^{1}H-NMR (400 MHz, DMSO-*d*$_6$): δ / ppm = 13.22 (s, 1H, 1), 8.60 (s, 1H, 8), 7.20 (d, J = 2.2 Hz, 1H, 3).

^{13}C-NMR (100 MHz, DMSO-*d*$_6$): δ / ppm = 177.89 (5), 173.37 (4), 168.81 (9'), 164.94 (7'), 160.88 (2'), 148.77 (5a), 146.86 (7), 135.91 (9), 134.15 (1a), 129.10 (8), 127.62 (2), 126.45 (9a), 124.58 (3a), 113.51 (3).

^{13}C-ssNMR (500 MHz, CP–MAS): δ / ppm = 177.85, 173.43, 167.92, 164.12, 162.14, 146.25, 145.31, 139.30, 135.48, 131.47, 127.59, 123.10, 116.25.

IR (Diamond-ATR, neat): $\tilde{\nu}$ / cm^{-1} = 1743 (m, COOH), 1720 (m, COOH), 1702 (m), 1680 (m, C=O), 1652 (s, COO$^-$), 1640 (m, C=O), 1583 (m, C=C), 1507 (s, C=C), 1489 (s), 1449 (w), 1398 (m), 1358 (m, COO$^-$), 1315 (s), 1284 (s), 1262 (s), 1224 (s), 1195 (s), 1150 (m), 1121 (m), 1075 (m), 1045 (w), 1015 (w), 980(m), 925(m), 895(m), 867(m), 842(m), 815(m), 768(m), 760 (s), 725 (s), 699 (m), 685 (s), 657 (m).

HRMS (ESI −): *m/z* calc. for $[C_{14}H_5N_2O_8]^-$: 329.0051; found: 329.0054.

Elemental Analysis (CHN): Found: C, 48.04; H, 2.50; N, 7.93. Calc. for $[C_{14}H_6N_2O_8 \cdot 1.15H_2O]$: C, 47.92; H, 2.38; N, 7.98.

5.4. Synthesis of PQQ Derivatives

5.4.1 Synthesis of PQQMe$_3$ (**11**) by Fischer Esterification

Trimethyl 4,5-dioxo-4,5-dihydro-1H-pyrrolo[2,3-f]quinoline-2,7,9-tricarboxylate

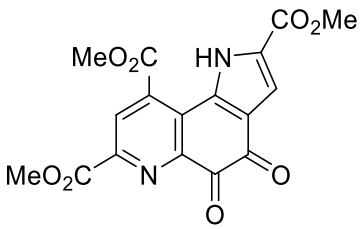

PQQ (**13**) (50 mg, 0.151 mmol) was dissolved in MeOH (10 mL), concentrated H_2SO_4 was added (10 drops) and the solution was refluxed at 75°C overnight. TLC (DCM/EtOAc 50:50) showed only a small product spot (R_f = 0.35) and an excess of unreacted starting material, so additional 20 drops H_2SO_4 were added and the solution was further refluxed for 24h. TLC

showed still an excess of starting material, so another 20 drops H_2SO_4 were added and the solution was again refluxed for 24h. The solvent was removed under reduced pressure and the viscous orange-red residue was given into H_2O (30 mL). The aqueous phase was extracted with $CHCl_3$ (3 x 20 mL) and the combined organic phases were washed with brine and dried over Na_2SO_4. After filtration, the solvent was evaporated *in vacuo* and the residue was further dried under high vacuum, to give 40 mg of an orange solid, which was analyzed by NMR to be a 90:10 mixture of $PQQMe_3$ (**11**) (~36 mg, 0.097 mmol, 64%) and a $PQQMe_3$-derivative, most likely the $PQQMe_3$-hemiketal (**18**) (~4 mg, 0.010 mmol, 6%). Through extraction, a red solid precipitated in the aqueous phase, which was filtered off and dried under reduced pressure to give $PQQMe_2$ (**19**) (2 mg, 0.005 mmol, 4%).

Orange solid - $PQQMe_3$ (**11**) + $PQQMe_3$-hemiketal (**18**)

^{1}H-NMR (400 MHz, $CDCl_3$): δ / ppm = 12.95 (1, 1H, 1), 12.62 (s, 1H, 1), 8.88 (s, 1H, 8), 8.70 (s, 1H, 8), 7.47 (d, *J* = 2.3 Hz, 1H, 3), 7.41 (d, *J* = 2.4 Hz, 1H, 3), 4.18 (s, 3H, 9'-Me), 4.13 (s, 3H, 9'-Me), 4.07 (s, 3H, 7'-Me), 4.03 (s, 3H, 7'-Me), 3.98 (s, 3H, 2'-Me), 3.95 (s, 3H, 2'-Me). (Integral values of the byproduct are 10% of the ones from the main species)

Filter-residue from aqueous phase - $PQQMe_2$ (**19**)

^{1}H-NMR (400 MHz, DMSO-*d*$_6$): δ / ppm = 13.88 (s, 1H), 8.62 (s, 1H), 7.27 (d, *J* = 2.2 Hz, 1H), 3.96 (s, 3H), 3.88 (s, 3H).

5.4.2 Synthesis of PQQ-oxazole (**20**)

8H-Oxazolo[5,4-h]pyrrolo[2,3-f]quinoline-5,7,9-tricarboxylic acid

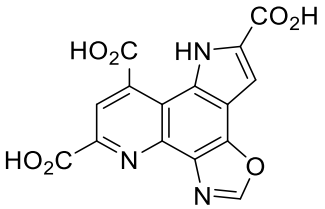

The compound was synthesized following a literature known procedure.[157] Ammonium chloride (3210 mg, 60.0 mmol) was dissolved in TRIS-HCl buffer (0.033 M, pH 8.2, 200 mL). PQQ (**13**) (190 mg, 0.57 mmol, 1.00 equiv.) and glycine (86.4 mg, 1.15 mmol, 2.00 equiv.) were added to the solution. The mixture was stirred at room temperature for 2 h. During the reaction, the pH was kept at 8.2 with 0.1 M NaOH. Afterwards the pH was brought to 1.5 with 2 M HCl and the solution was stored overnight at 4°C. The precipitate was filtered, washed

with 0.1 M HCl and dissolved in water (20 mL). The solution was stirred for 10 minutes at 90°C and then acidified to pH 1.5 and stored at 4°C overnight. The precipitate was filtered and washed again with 0.1 M HCl (20 mL). The product (**20**) (205 mg, quant.) was dried *in vacuo* and isolated as a light brown solid.

TRIS-HCl buffer was prepared by dissolving TRIS (799 mg, 6.60 mmol) in 200 mL H_2O and adjusting the pH to pH 8.2 with HCl.

^{1}H-NMR (400 MHz, DMSO-*d*$_6$): δ / ppm = 12.96 (s, 1H, 1), 9.28 (s, 1H, 10), 8.30 (s, 1H, 8), 7.28 (s, 1H, 3).

^{13}C-NMR (100 MHz, DMSO-*d*$_6$): δ / ppm = 173.44, 167.41, 162.17, 161.03, 134.35 (10), 133.00, 131.04, 129.04, 127.87, 127.55, 124.49, 121.50 (8), 121.29, 121.17, 111.99 (3).
Same numbering scheme as PQQ (**13**), with 10 for the oxazole N=<u>CH</u>-O.

HRMS (ESI +): *m/z* calc. for [$C_{14}H_7N_3O_5^{\bullet+}$ (-CO_2)]: 297.0380; found: 297.0826.

IR (Diamond-ATR, neat): $\tilde{\nu}$ / cm^{-1} = 1668 (m), 1544 (m), 1488 (m), 1375, (m), 1356 (m), 1182 (s), 998 (m), 934 (m), 870 (m).

Elemental Analysis (CHN): Found: C, 44.12; H, 3.08; N, 10.55. Calc. for [$C_{15}H_7N_3O_7 \cdot 2.1H_2O \cdot 0.75HCl$]: C, 44.33; H, 2.96; N, 10.34.

5.4.3 Synthesis of PQQMe$_3$-oxazole (**21**)

Trimethyl 8H-oxazolo[5,4-h]pyrrolo[2,3-f]quinoline-5,7,9-tricarboxylate

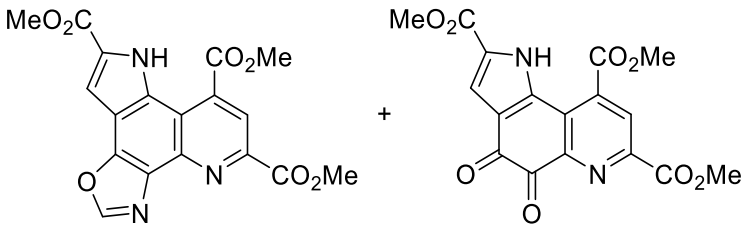

According to a literature procedure,[157] under nitrogen atmosphere, PQQ-Oxazole (**20**) (0.1 g, 0.30 mmol) was dissolved in dry DMF (10 mL). K_2CO_3 (1.04 g, 7.50 mmol, 25 equiv.) and Me_2SO_4 (0.95 g, 0.72 mL, 25 equiv.) were added and the mixture was stirred at room temperature overnight. With 2 M HCl, the pH of the mixture was set to 2. Unfortunately, no precipitation was observed, even after cooling the mixture down to 4°C overnight. Since Me_2SO_4 is completely hydrolyzed in acidic environment after 24h,[298] the following workup

can be performed without danger. The mixture was diluted with water (50 mL) and extracted with EtOAc (4 x 50 mL). The combined organic phases were washed with brine, dried with Na_2SO_4 and evaporated to dryness. The crude product was purified by column chromatography (DCM/MeOH 95:05 → 80:20) to give 30 mg of an orange-red powder. NMR analysis showed a mixture of PQQMe_3-Oxazole (**21**) (13%) and PQQMe_3 (**11**) (87%) which could not be further separated.

To deprotect the oxazole residue of PQQMe_3-oxazole (**21**), the mixture of **21** and **11** was dissolved in HCl (2 M, 10 mL), heated up to 100°C and was stirred at that temperature for 2h. After cooling down, the acid was removed *in vacuo* to give a brown powder (27 mg). NMR analysis stated, that there was still a mixture of free PQQMe_3 (**11**) and the oxazole species (**21**).

The mixture was dissolved completely in a small amount of a 95:05 DCM/MeOH mixture, was taken on silica gel and the solvent was removed completely (dry load). Separation was performed by column chromatography. EtOAc/*i*-hexane 90:10 gave the oxazole species (**21**) first (6 mg, 0.016 mmol, 6%), while solvent change to EtOAc/MeOH 85:15 gave the PQQMe_3 (**11**) species (9 mg, 0.024 mmol, 8%).

PQQMe_3-Oxazole (**21**): (orange solid)

R_f: 0.42 (EtOAc/*i*-hexane – 90:10).

^{1}H-NMR (400 MHz, $CDCl_3$): δ / ppm = 12.82 (s, 1H, 1), 9.39 (s, 1H, 10), 8.50 (s, 1H, 8), 7.65 (d, *J* = 2.4 Hz, 1H, 3), 4.17 (s, 3H, 9'-Me), 4.14 (s, 3H, 7'-Me), 3.99 (s, 3H, 2'-Me). Same numbering scheme as PQQ (**13**), with 10 for the oxazole N=<u>CH</u>-O.

PQQMe_3 (**11**): (orange solid)

R_f: 0.51 (EtOAc/*i*-hexane – 90:10)

^{1}H-NMR (400 MHz, $CDCl_3$): δ / ppm = 12.95 (s, 1H, 1), 8.89 (s, 1H, 8), 7.48 (d, *J* = 2.3 Hz, 1H, 3), 4.18 (s, 3H, 9'-Me), 4.07 (s, 3H, 7'-Me), 3.98 (s, 3H, 2'-Me).

5.4.4 Synthesis of $PQQMe_3$ (**11**) by Esterification with Me_2SO_4

Trimethyl 4,5-dioxo-4,5-dihydro-1H-pyrrolo[2,3-f]quinoline-2,7,9-tricarboxylate

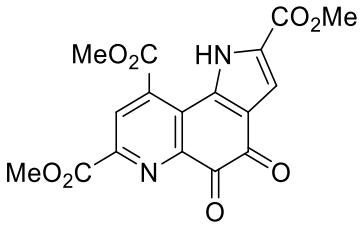

Based on procedures, described by Duine *et al.*[159] and Urakami *et al.*[299] in a dry and nitrogen flushed Schlenk flask, PQQ (**13**) (50 mg, 0.151 mmol) was dissolved in dry DMF (2 mL). K_2CO_3 (0.523 mg, 3.785 mmol, 25 equiv.), which was previously dried under high vacuum at 650°C (heat-gun), was given to the PQQ solution under nitrogen counter-flow. Me_2SO_4 (2063 mg, 1.55 mL, 108 equiv.) was added and the mixture was stirred at room temperature and under nitrogen overnight, to give a bright orange suspension the next day. In order to completely remove K_2CO_3 residues and to quench the excess of Me_2SO_4, HCl (8 mL 2M and 1 mL conc.) was added and the mixture was further stirred for 5h. The orange precipitate was filtered-off, and the residue was washed with water and dried under high vacuum to give pure $PQQMe_3$ (**11**) (51 mg, 0.137 mmol, 91%). The filtrate was also extracted with $CHCl_3$ (3 x 20 mL) and the combined organic phases were washed with brine and dried over Na_2SO_4. After filtration, the solvent was evaporated *in vacuo* and the residue was further dried under high vacuum, to give 9 mg of the crude product as a dark-orange solid, which could be further purified by column chromatography (DCM/EtOAc 100:0 – 90:10 – 50:50) [was done with the combined crude products of multiple methylation reactions].

^{1}H-NMR (400 MHz, DMSO-*d*$_6$): δ / ppm = 12.51 (s, 1H, 1), 8.56 (s, 1H, 8), 7.29 (d, *J* = 2.1 Hz, 1H, 3), 4.05 (s, 3H, 9'-Me), 3.96 (s, 3H, 7'-Me), 3.89 (s, 3H, 2'-Me).

^{13}C-NMR (100 MHz, DMSO-*d*$_6$): δ / ppm = 177.02 (5), 173.30 (4), 166.55 (9'), 163.80 (7'), 159.84 (2'), 148.94 (5a), 145.73 (7), 134.16 (9), 133.54 (1a), 128.48 (8), 126.58 (9a), 126.49 (2/3a), 124.96 (2/3a), 113.84 (3), 54.20 (9'-Me), 52.95 (7'-Me), 52.36 (2'-Me).

Elemental Analysis (CHN): Found: C, 54.59; H, 3.36; N, 7.48. Calc. for $PQQMe_3$ [$C_{17}H_{12}N_2O_{13}$]: C, 54.85; H, 3.25; N, 7.52.

HRMS (ESI +): *m/z* calc. for $[C_{17}H_{13}N_2O_8]^+$: 373.0666; found: 373.0665.

IR (Diamond-ATR, neat): $\tilde{\nu}$ / cm^{-1} = 3126 (w, H_2O), 1717 (s, COOMe), 1679 (s, C=O), 1552 (w), 1495 (m), 1429 (s), 1345 (w), 1266 (s), 1200 (s), 1171 (s), 1115 (s), 1075 (s), 995 (s), 953 (s), 923 (s), 900 (s), 834 (s), 807 (s), 783 (s), 769 (s), 754 (s), 733 (s), 720 (s), 689 (m), 672 (m).

5.5. Synthesis of PQQMe$_2$

5.5.1 Synthesis of PQQMe$_2$-OMe (**22**)

5-Methoxy-2,9-bis(methoxycarbonyl)-1H-pyrrolo[2,3-f]quinoline-7-carboxylic acid

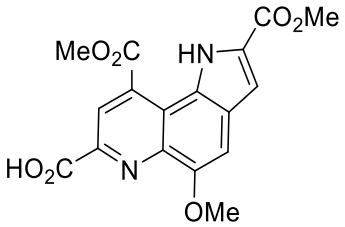

According to literature procedures,[152] PQQMe$_3$-OMe (**10**) (200 mg, 0.54 mmol) was solved in a mixture of TFA (1.33 mL) and H_2O (0.67 mL) and the dark solution was stirred at 60°C for 30 h. The reaction mixture was diluted with water (50 mL) and then extracted with trichloromethane (3 x 30 mL). A brown solid precipitated after the addition of TCM, which was filtered off and partly dissolved in TCM ultrasonifically. The combined trichloromethane phases of the extraction and the solid-solution were washed with water, then with brine and dried over sodium sulfate. After filtration, the solvent was evaporated *in vacuo* and the crude product was purified by flash column chromatography (DCM/MeOH 100:0 → 80:20) to give the title compound (**22**) (0.11 g, 0.31 mmol, 57%) as a yellow solid.

^{1}H-NMR (400 MHz, DMSO-*d*$_6$): δ / ppm = 11.89 (s, 1H, 1), 8.72 (s, 1H, 8), 7.63 (s, 1H, 4), 7.33 (s, 1H, 3), 4.13 (s, 3H, 9'-Me), 4.10 (s, 3H, 7'-Me), 3.94 (s, 3H, 2'-Me).
Same numbering scheme as PQQ (**13**).

Analytical data were consistent with those reported in the literature.[152]

5.5.2 Synthesis of $PQQMe_2$ (**19**)

2,9-Bis(methoxycarbonyl)-4,5-dioxo-4,5-dihydro-1H-pyrrolo[2,3-f]quinoline-7-carboxylic acid

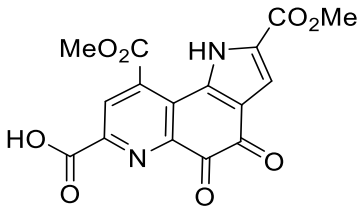

$PQQMe_3$ (**11**) (50 mg, 0.134 mmol) was given in a 10 mL round bottom flask and a 1:2 mixture of H_2O/TFA (2 mL) was added. The dark red solution was stirred at 60°C for 36 h. After cooling down to room temperature, H_2O (5 mL) was added, which caused immediate precipitation of a dark red solid. The precipitate was filtered off (glass frit, pore 4), washed with water, dried first at 100°C for several hours and then under high vacuum overnight, to afford 44 mg (0.123 mmol, 92%) of a light brown powder.

^{1}H-NMR (400 MHz, DMSO-*d*$_6$): δ / ppm = 12.52 (s, 1H, 1), 8.56 (s, 1H, 8), 7.28 (d, *J* = 1.4 Hz, 1H, 3), 4.05 (s, 3H, 9'-Me), 3.89 (s, 3H, 2'-Me).

^{13}C-NMR (100 MHz, DMSO-*d*$_6$): δ / ppm = 177.26 (5), 173.33 (4), 166.73 (9'), 164.78 (7'), 159.85 (2'), 148.87 (5a), 147.00 (7), 134.07 (9), 133.74 (1a), 128.49 (8), 126.38 (2/3a), 126.29 (9a), 124.82 (2/3a), 113.84 (3), 54.19 (9'-Me), 52.36 (2'-Me).
Same numbering scheme as PQQ (**13**). Assignments of 5, 4, 5a and 7 based on literature-known PQQ-shifts.

HRMS (ESI +): *m/z* calc. for $[C_{16}H_{11}N_2O_8]^+$: 359.05126; found: 359.0510.

IR (Diamond-ATR, neat): $\tilde{\nu}$ / cm^{-1} = 3443 (w), 3101 (w), 1762 (w), 1706 (s), 1675 (s), 1551 (w), 1495 (m), 1435 (m), 1362 (w), 1287 (s), 1240 (s), 1209 (s), 1156 (s), 1133 (s), 1058 (w), 994 (m), 960 (m), 921 (m), 870 (m), 768 (m), 692 (m).

Elemental Analysis (CHN): Found: C, 50.54; H, 3.21; N, 7.53. Calc. for $[C_{16}H_{10}N_2O_8 \cdot 1.2H_2O]$: C, 50.59; H, 3.29; N, 7.37.

Single Crystal X-Ray Diffraction Studies: See Table VIII.1.

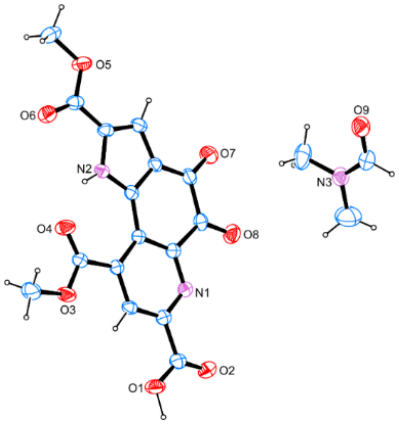

Figure VIII.1: Molecular structure of PQQMe$_2$·DMF in the crystal, ORTEP representation.[160] Thermal ellipsoids are drawn at 50 % probability level.

Table VIII.1**:** Details for X-ray data collection and structure refinement for PQQMe$_2$ (**19**).

PQQMe$_2$ (**19**)	
net formula	$C_{19}H_{17}N_3O_9$
M_r/g mol^{-1}	431.35
crystal size/mm	0.050 × 0.040 × 0.020
T/K	108.(2)
radiation	MoKα
diffractometer	'Bruker D8 Venture TXS'
crystal system	orthorhombic
space group	'P b c a'
a/Å	18.3353(6)
b/Å	8.3203(3)
c/Å	24.9988(9)
α/°	90
β/°	90
γ/°	90
V/Å^3	3813.7(2)
Z	8
calc. density/g cm^{-3}	1.503
μ/mm^{-1}	0.122
absorption correction	Multi-Scan
transmission factor range	0.94–1.00
refls. measured	57774
R_{int}	0.0556
mean σ(I)/I	0.0193
θ range	3.144–25.347
observed refls.	2957
x, y (weighting scheme)	0.0492, 4.2835
hydrogen refinement	H(C) constr, H(N,O) refall
refls in refinement	3474
parameters	292
restraints	0
$R(F_{obs})$	0.0531
$R_w(F^2)$	0.1318
S	1.123
shift/error$_{max}$	0.001
max electron density/e Å^{-3}	0.303
min electron density/e Å^{-3}	−0.278

5.5.3 Synthesis of $PQQH_2$ (**24**)

4,5-Dihydroxy-1H-pyrrolo[2,3-f]quinoline-2,7,9-tricarboxylic acid

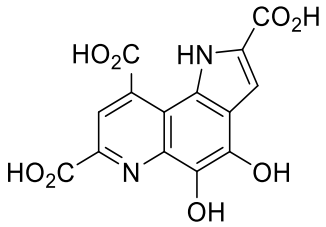

According to a literature procedure,[154] L-(+)-Ascorbic acid (400 mg, 2.27 mmol, 18.8 equiv.) was dissolved in H_2O (1.6 mL). With HCl (2 *M*), the pH of the solution was set to 3. PQQ (**13**) (40 mg, 0.12 mmol, 1.0 equiv.) was dissolved in H_2O (16 mL) and was added over 2 h to the solution of L-(+)-Ascorbic acid at 10°C. The mixture was allowed to warm up to room temperature and was further stirred overnight. The precipitated solid was filtered and washed with HCl (0.1 *M*). The product was further dried under high vacuum for 12 h to give the title compound (**24**) (38 mg, 0.10 mmol, 95%) as a dark brown powder. For NMR-analysis, the DMSO-d_6 was degassed with argon to prevent reoxidation.

^{1}H-NMR (400 MHz, DMSO-d_6): δ / ppm = 13.19 (s, 2H, -CO_2H), 12.37 (d, J = 2.1 Hz, 1H, 1), 10.14 (s, 1H, -OH), 9.22 (s, 1H, -OH), 8.58 (s, 1H, 8), 7.38 (d, J = 2.4 Hz, 1H, 3).

^{13}C-NMR (100 MHz, DMSO-d_6): δ / ppm = 169.79 (9'), 164.94 (7'), 161.84 (2'), 142.16 (7), 140.51 (5a), 137.62 (4), 133.99 (9), 130.91 (5), 127.83 (2), 123.31 (1a), 122.66 (3a), 118.95 (8), 110.71 (9a), 105.37 (3). (2, 1a, 3a and 9a possibly in another order, 7, 5a, 4, 9, 5 assigned by calculations. Same numbering scheme as PQQ (**13**)

HRMS (ESI +/-): Only signals for reoxidized PQQ visible.

IR (Diamond-ATR, neat): $\tilde{\nu}$ / cm^{-1} = 3655-2167 (m, broad), 1869 (m), 1720 (m), 1683 (m), 1553 (m), 1515 (m), 1385 (m), 1264 (m), 1199 (s), 1106 (m), 957 (m), 845 (m), 826 (m), 752 (m), 678 (m).

6. Experimental Procedures for Chapter IV

Experimental procedures and supporting information for the subchapter IV.1 - *Interaction of PQQ with Lanthanides and Calcium* are provided in IX.1.3.

Experimental procedures for the subchapter IV.2 - *Further Investigation of the PQQ Complexation* are provided below.

6.1. Complex Formation of $PQQNa_2$ With La/Ln or La/Ca Couple

$PQQNa_2 \cdot H_2O$ (**14**) (20 mg, 51.0 µmol, 1.0 equiv. as received from Doctor's Best® Science-Based Nutrition™ BioPQQ® capsules was completely dissolved in H_2O (8 mL) in 45 mL centrifuge tubes, resulting in a pH decrease to pH 3.5. Stock solutions of $LnCl_3 \cdot nH_2O$ in H_2O (100 µL / equiv. $PQQNa_2$) were prepared. For mixed samples, 300 µL (3 equiv.) $LaCl_3 \cdot 7H_2O$ and 300 µL (3 equiv.) of an additional $LnCl_3 \cdot nH_2O$ were mixed together and then added to the $PQQNa_2$ solution. To work-up the formed precipitate, the suspension was centrifuged (5 min at 4500 rpm in a Heraeus Megafuge 8R benchtop centrifuge with a swinging bucket), and the colorless supernatant was removed. To wash the resulting pellet, water was added (25 mL), and the suspension was first vortex mixed and then centrifuged (same configuration as above), followed by the removal of the supernatant. This washing step was repeated twice. The pellet was then lyophilized overnight (Christ Alpha) to afford a brown powder. Elemental analysis gave 1:1 PQQ-Ln complexes with different amounts of water (see Table IX.15).

6.1.1 Crystal Growth of $PQQ_2Ca_3 \cdot 13H_2O$

Experimental details are described in the Appendix (IX.1.3.3 - Coordination with Calcium). From the aqueous washing solution of experiment **C**: $PQQNa_2 \cdot H_2O$ (**14**) (30 mg, 0.08 mmol) in H_2O (12 mL) plus $CaCl_2 \cdot 2H_2O$ (2.0 equiv., 23.6 mg, 0.16 mmol), crystals were grown over several months.

IR (Diamond-ATR, neat): $\tilde{\nu}$ / cm^{-1} = 3643-2746 (w, broad), 1923-1714 (w, broad), 1686 (w), 1658 (w), 1605 (s), 1577 (m), 1553 (m), 1536 (m), 1498 (m), 1426 (w), 1400 (m), 1348 (s), 1277 (m), 1246 (m), 1191 (m), 1151 (m), 1132 (w), 1086 (w), 1027 (w), 972 (w), 951 (w), 926 (w), 868 (w), 824 (w), 767 (w), 719 (w), 700 (w), 669 (w).

Single Crystal X-Ray Diffraction Studies: See Table VIII.2

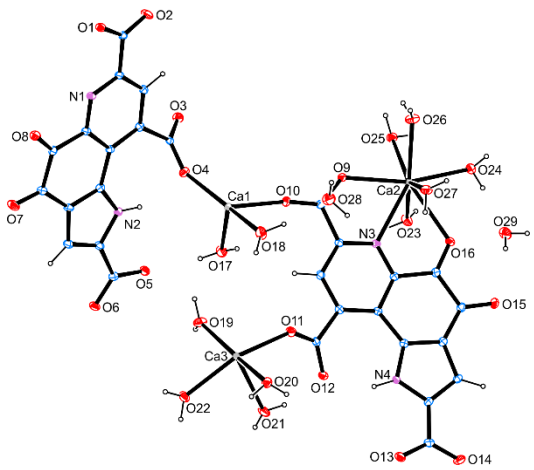

Figure VIII.2: Molecular structure of $PQQ_2Ca_3 \cdot 13H_2O$ in the crystal, ORTEP representation.[160] Thermal ellipsoids are drawn at 50 % probability level.

Table VIII.2: Details for X-ray data collection and structure refinement for $PQQ_2Ca_3 \cdot 13H_2O$.

$PQQ_2Ca_3 \cdot 13H_2O$	
net formula	$C_{28}H_{32}Ca_3N_4O_{29}$
M_r/g mol^{-1}	1008.81
crystal size/mm	0.100 × 0.020 × 0.010
T/K	109.(2)
radiation	MoKα
diffractometer	'Bruker D8 Venture TXS'
crystal system	triclinic
space group	'P -1'
a/Å	6.9363(3)
b/Å	15.9791(7)
c/Å	16.9786(7)
α/°	90.8440(10)
β/°	93.1060(10)
γ/°	98.296(2)
V/Å^3	1858.93(14)
Z	2
calc. density/g cm^{-3}	1.802
μ/mm^{-1}	0.563
absorption correction	Multi-Scan
transmission factor range	0.88–0.99
refls. measured	33048
R_{int}	0.0433
mean σ(I)/I	0.0383
θ range	2.868–27.102
observed refls.	7023
x, y (weighting scheme)	0.0197, 1.5570
hydrogen refinement	H(C) constr, H(N,O) refall
refls in refinement	8166
parameters	687
restraints	0
$R(F_{obs})$	0.0306
$R_w(F^2)$	0.0717
S	1.039
shift/error$_{max}$	0.001
max electron density/e Å^{-3}	0.390
min electron density/e Å^{-3}	−0.278

7. Experimental Procedures for Chapter V

Experimental procedures for the subchapters V.2 - *Reduction of PQQ with Ascorbic Acid* and V.3 - *Reoxidation of PQQH2* are provided below. Experimental procedures for subchapter V.4 - *Electrochemistry of PQQ* are summarized in the analytical methods VIII.2.8 and VIII.2.9 and in the respective figure captions.

7.1. General Working Methods

All solvents were rigorously degassed with nitrogen prior to use and stored under inert gas atmosphere. Quarz suprasil cuvettes (d = 1 cm), equipped with a screw top with rubber septum and a magnetic stirring bar were used for all experiments. For reduction experiments, a total volume of 1 mL was used and for oxidation experiments a total volume of 3 mL. A Cary60 UV-Vis spectrophotometer from Agilent was used for all experiments.

The cuvette was filled with the lid open and then degassed with nitrogen for another 5 minutes using cannulas. The cuvette was kept at a constant temperature of 25°C, using a Peltier Element. Before measurement, a blank was recorded in the respective solvent mixture. In case of reduction experiments, the cuvette was kept closed and was equipped with a nitrogen filled balloon, to keep the nitrogen atmosphere. In case of reoxidation experiments, the screw top of the cuvette was removed, so oxygen could slowly diffuse into the mixture and oxidize the $PQQH_2$-species. Metal salts with following amouts of crystal water were used in all experiments: $LaCl_3 \cdot 7H_2O$/$EuCl_3 \cdot 6H_2O$/$CaCl_2 \cdot 2H_2O$. All buffers were prepared with *Milli*-Q H_2O. The pH-value was adjusted with a FiveEasy pH-meter system from Mettler Toledo which was calibrated with calibration solutions prior to use.

7.2. Reduction of PQQ With Ascorbic Acid

7.2.1 Without Metal Addition

Experiments were either carried out in aqueous TRIS-HCl or PIPES buffer (pH 7.4, 50 mM) or in DMSO. Stock solutions of PQQ (1 mM) and L-(+)-ascorbic acid (4 mM) were prepared in each solvent. The cuvette was filled with 960 µL buffer or DMSO and a blank was recorded. 10 µL PQQ stock solution (1 mM) was added and the first spectrum was recorded. After the first measurement, 30 µL ascorbic acid (4 mM) stock solutions were added and spectra were

recorded every minute for 90 minutes from 200 – 800 nm with a scan rate of 4800 nm/min and a data interval of 1 nm.

7.2.2 With Metal Addition

The cuvette was filled with 950 µL aqueous TRIS-HCl buffer (pH 7.4, 50 mM) and a blank was recorded. 10 µL PQQ stock solution (1 mM) was added and the first spectrum was recorded. 10 µL metal salt stock solution ($LaCl_3$/$CaCl_2$ in H_2O, 1 mM, 1.0 equiv.) was added and the second spectrum was recorded. After the first two measurement, 30 µL ascorbic acid (4 mM) stock solution was added and spectra were recorded every minute for 90 minutes from 200 – 800 nm with a scan rate of 4800 nm/min and a data interval of 1 nm.

7.3. Spectrophotometric Measurement in DMF

7.3.1 100 µL H_2O (100 mM $LiClO_4$)

The cuvette was filled with 2.84 mL DMF, 0.1 mL H_2O (100 mM $LiClO_4$) and 7.5 µL metal salt ($LaCl_3$/$CaCl_2$ in DMF, 20 mM, 1.5 equiv.). In case of measurement of pure $PQQH_2$ without metal addition, pure DMF (7.5 µL) was added instead of the metal solutions. $PQQH_2$ in DMF (0.05 mL, 2 mM) was added via micro syringe and the cuvette was inverted for 20 seconds prior to measurement to receive a homogenous solution. After the first measurement, the screw top of the cuvette was removed, so oxygen could slowly diffuse into the mixture and oxidize the $PQQH_2$-species. Spectra were recorded for 2 h every 30 seconds from 260 – 500 nm with a scan rate of 600 nm/min and a data interval of 1 nm.

7.3.2 DMF (75 mM LiClO4) + 10 µL H_2O and 3.0 Equiv. Metal Salt

The cuvette was filled with 2.92 mL DMF (75 mM $LiClO_4$), 10 µL H_2O and 15 µL metal salt ($LaCl_3$/$EuCl_3$/$CaCl_2$ in DMF, 20 mM, 3.0 equiv.). In case of measurement of pure $PQQH_2$ without metal addition, pure DMF (15 µL) was added instead of the metal solutions. $PQQH_2$ in DMF (0.05 mL, 2 mM) was added via micro syringe and the cuvette was inverted for 20 seconds prior to measurement to receive a homogenous solution. After the first measurement, the screw top of the cuvette was removed, so oxygen could slowly diffuse into the mixture and oxidize the $PQQH_2$-species. Spectra were recorded for 70 minutes, every 30 seconds from 220 – 500 nm with a scan rate of 600 nm/min and a data interval of 1 nm.

7.3.3 DMF (75 mM LiClO4) + 10 µL H_2O and 10.0 Equiv. Metal Salt

The cuvette was filled with 2.89 mL DMF (75 mM $LiClO_4$), 10 µL H_2O and 50 µL metal salt ($LaCl_3$/ $EuCl_3$/$CaCl_2$ in DMF, 20 mM, 10.0 equiv.). In case of measurement of pure $PQQH_2$ without metal addition, pure DMF (50 µL) was added instead of the metal solutions. $PQQH_2$ in DMF (0.05 mL, 2 mM) was added via micro syringe and the cuvette was inverted for 20 seconds prior to measurement to receive a homogenous solution. After the first measurement, the screw top of the cuvette was removed, so oxygen could slowly diffuse into the mixture and oxidize the $PQQH_2$-species. Spectra were recorded for 70 minutes, every 30 seconds from 220 – 500 nm with a scan rate of 600 nm/min and a data interval of 1 nm.

8. Experimental Procedures for Chapter VI

8.1. General Considerations

Unless otherwise stated, all NMR experiments were conducted on a Bruker Avance III. PQQ was given in the NMR tube as solid and was dissolved in the respective solvent in an ultrasonic bath at 50°C. Metal salts were added as solids and were also dissolved in an ultrasonic bath at 50°C. In case of small amounts of added metal salts, stock solutions in deuterated solvents were prepared instead and added to the PQQ solution.

8.2. Influence of Metals on Hemiketal Formation

8.2.1 NMR-Titration with Methanol and Investigation of the Influence of La and Ca

Following stock solutions were prepared: PQQ (80 mM): 14.5 mg, 43.9 µmol in DMSO-d_6 (0.55 mL). La-/Ca- (240 mM) PQQ 80 mM): PQQ (31.7 mg, 96.0 mmol, 80 mM) in DMSO-d_6 (1.2 mL). In additional flasks, $LaCl_3 \cdot 7H_2O$ (49.0 mg, 132 µmol) and $CaCl_2 \cdot 2H_2O$ (19.4 mg, 132 µmol) were weighed and each dissolved in the PQQ-stock solution (0.55 mL, 80 mM PQQ). The stock solutions were then given in NMR tubes and diluted in DMSO-d_6 and MeOD-d_4 according to Table VIII.3.

Table VIII.3: NMR-Titration of PQQ in DMSO-d_6 (80 mM) with or without $LaCl_3 \cdot 7H_2O$ or $CaCl_2 \cdot 2H_2O$ (240 mM) and increasing amounts of MeOD-d_4. Constant total volume of 0.5 mL (8 mM PQQ) in each NMR experiment. The (La-/Ca-) PQQ-Stock solution was always added first, followed by DMSO-d_6 and then MeOD-d_4. Each NMR tube was shaked well and submitted for analysis. Measurements were conducted in a row by auto sampling and lasted approx. 3h in total.

Ratio – DMSO-d_6-MeOD-d_4 (vol%)	MeOD-d_4 (mol%)	(La-/Ca-) PQQ Stock, 80 mM, DMSO-d_6 (µL)	MeOD-d_4 (µL)	DMSO-d_6 (µL)
100-0	0	50	0	450
90-10	16	50	50	400
80-20	30	50	100	350
70-30	43	50	150	300
60-40	54	50	200	250
50-50	63	50	250	200
40-60	72	50	300	150
30-70	80	50	350	100
20-80	87	50	400	50
10-90	94	50	450	0

8.2.2 NMR-Titration with decreasing Methanol Concentrations and Influence of La and Ca

Following stock solutions were prepared: PQQ (80 mM): 46.0 mg, 139 µmol in MeOD-d_4 (1.741 mL). La-/Ca- (240 mM) PQQ 80 mM): $LaCl_3 \cdot 7H_2O$ (49.0 mg, 132 µmol) and $CaCl_2 \cdot 2H_2O$ (19.4 mg, 132 µmol) were each dissolved in the PQQ-stock solution (0.55 mL, 80 mM PQQ). The stock solutions were then given in NMR tubes and diluted in MeOD-d_4 and DMSO-d_6 according to Table VIII.4.

Table VIII.4**:** NMR-Titration of PQQ in MeOD-d_4 (80 mM) with or without $LaCl_3 \cdot 7H_2O$ or $CaCl_2 \cdot 2H_2O$ (240 mM) and increasing amounts of DMSO-d_6. Constant total volume of 0.5 mL (8 mM PQQ) in each NMR experiment. The (La-/Ca-) PQQ-Stock solution was always added first, followed by MeOD-d_4 and then DMSO-d_6. Each NMR tube was shaked well and submitted for analysis. Measurements were conducted in a row by auto sampling and lasted approx. 3h in total.

Ratio – DMSO-d_6-MeOD-d_4 (vol%)	MeOD-d_4 (mol%)	(La-/Ca-) PQQ Stock 80 mM, MeOD-d_4 (µL)	DMSO-d_6 (µL)	MeOD-d_4 (µL)
0-100	99.9	50	0	450
10-90	94	50	50	400
20-80	87	50	100	350
30-70	80	50	150	300
40-60	72	50	200	250
50-50	63	50	250	200
60-40	54	50	300	150
70-30	43	50	350	100
80-20	30	50	400	50
90-10	16	50	450	0

8.2.3 UV-Vis Titrations with Methanol

Stock solutions of PQQ and its metal salts (3 equiv.) were each prepared in DMSO and MeOH (0.4 mM):

PQQ: PQQ (0.7 mg, 2 µmol) in DMSO/MeOH (5 mL).

Ca-PQQ: PQQ (0.7 mg, 2 µmol), $CaCl_2 \cdot 2H_2O$ (0.9 mg, 6 µmol) in DMSO/MeOH (5 mL).

La-PQQ: PQQ (0.7 mg, 2 µmol), $LaCl_3 \cdot 7H_2O$ (2.4 mg, 6 µmol) in DMSO/MeOH (5 mL).

Measurements were conducted on an Agilent 8453 Diode Array Spectrophotometer.

8.2.4 Increasing Methanol Concentrations and Influence of La and Ca

The stock solutions in DMSO were given in quartz suprasil cuvettes and were diluted in DMSO and MeOH according to Table VIII.5. Each mixture was directly measured after preparation.

Table VIII.5: Titration of PQQ in DMSO (0.4 mM) with or without $LaCl_3 \cdot 7H_2O$ or $CaCl_2 \cdot 2H_2O$ (1.2 mM) and increasing amounts of MeOH. Constant total volume of 1 mL (0.04 mM PQQ) in a quartz suprasil cuvette (d = 1 cm). The stock solution (PQQ or La-/Ca-PQQ) was filled in first, followed by DMSO, then MeOH. Mixing through inversion for 30 seconds prior to measurement.

Ratio – DMSO-MeOH (vol%)	MeOH (mol%)	V (La-, Ca-)PQQ in DMSO), 0.4 mM (µL)	V (DMSO) (µL)	V (MeOH) (µL)
100-0	0	100	900	0
90-10	16	100	800	100
80-20	31	100	700	200
70-30	43	100	600	300
60-40	54	100	500	400
50-50	64	100	400	500
40-60	72	100	300	600
30-70	80	100	200	700
20-80	88	100	100	800
10-90	94	100	0	900

8.2.5 Decreasing Methanol Concentrations and Influence of La and Ca

The stock solutions in MeOH were given in quartz suprasil cuvettes and were diluted in MeOH and DMSO according to Table VIII.6. Each mixture was directly measured after preparation.

Table VIII.6**:** Titration of PQQ in MeOH (0.4 mM) with or without $LaCl_3 \cdot 7H_2O$ or $CaCl_2 \cdot 2H_2O$ (1.2 mM) and increasing amounts of DMSO. Constant total volume of 1 mL (0.04 mM PQQ) in a quartz suprasil cuvette (d = 1 cm). The stock solution (PQQ or La-/Ca-PQQ) was filled in first, followed by MeOH, then DMSO. Mixing through inversion for 30 seconds prior to measurement.

Ratio – MeOH-DMSO (vol%)	MeOH (mol%)	V (La-, Ca-)PQQ in MeOH), 0.4 mM (µL)	V (DMSO) (µL)	V (MeOH) (µL)
100-0	99.99	100	0	900
90-10	94	100	100	800
80-20	88	100	200	700
70-30	80	100	300	600
60-40	72	100	400	500
50-50	64	100	500	400
40-60	54	100	600	300
30-70	43	100	700	200
20-80	31	100	800	100
10-90	16	100	900	0

8.2.6 UV-Vis-Titration with Controlled Ionic Strength

Stock solutions of PQQ and its metal salts (3 equiv.) were each prepared in DMSO (0.4 mM):

PQQ (3 equiv. NaCl): PQQ (0.7 mg, 2 µmol), NaCl (0.35 mg, 6 µmol) in DMSO (5 mL).
PQQ (100 equiv. NaCl): PQQ (0.7 mg, 2 µmol), NaCl (11.7 mg, 0.2 mmol) in DMSO (5 mL).

Ca-PQQ (3 equiv. NaCl): PQQ (0.7 mg, 2 µmol), NaCl (0.35 mg, 6 µmol),
$CaCl_2 \cdot 2H_2O$ (0.9 mg, 6 µmol) in DMSO (5 mL).
Ca-PQQ (100 equiv. NaCl): PQQ (0.7 mg, 2 µmol), NaCl (11.7 mg, 0.2 mmol),
$CaCl_2 \cdot 2H_2O$ (0.9 mg, 6 µmol) in DMSO (5 mL).

La-PQQ (3 equiv. NaCl): PQQ (0.7 mg, 2 µmol), NaCl (0.35 mg, 6 µmol),
$LaCl_3 \cdot 7H_2O$ (2.4 mg, 6 µmol) in DMSO (5 mL).
La-PQQ (100 equiv. NaCl): PQQ (0.7 mg, 2 µmol), NaCl (11.7 mg, 0.2 mmol),
$LaCl_3 \cdot 7H_2O$ (2.4 mg, 6 µmol) in DMSO (5 mL).

The stock solutions were given in quartz suprasil cuvettes and were diluted in DMSO and MeOH according to Table VIII.7. Each mixture was directly measured after preparation. Measurements were conducted on an Agilent 8453 Diode Array Spectrophotometer.

Table VIII.7: Titration of PQQ (**13**) in MeOH (0.4 mM) with NaCl (1.2 mM or 40 mM), with or without $LaCl_3 \cdot 7H_2O$ or $CaCl_2 \cdot 2H_2O$ (1.2 mM) and with increasing amounts of DMSO. Constant total volume of 1 mL (0.04 mM PQQ) in a quartz suprasil cuvette (d = 1 cm). The stock solution (PQQ or La-/Ca-PQQ) was filled in first, followed by DMSO, then MeOH. Mixing through inversion for 30 seconds prior to measurement.

Ratio –DMSO-MeOH (vol%)	MeOH (mol%)	V (La-, Ca-)PQQ in DMSO), 0.4 mM (µL)	V (DMSO) (µL)	V (MeOH) (µL)
100-0	0	100	900	0
90-10	16	100	800	100
80-20	31	100	700	200
70-30	43	100	600	300
60-40	54	100	500	400
50-50	64	100	400	500
40-60	72	100	300	600
30-70	80	100	200	700
20-80	88	100	100	800
10-90	94	100	0	900

8.2.7 PQQ Metal Titrations in MeOH

Stock solutions of PQQ (0.4 mM) and metal salts (0.8 mM) were each prepared in MeOH:

PQQ: PQQ (0.7 mg, 0.002 mmol) in MeOH (5 mL).

$LaCl_3$: $LaCl_3 \cdot 7H_2O$ (1.0 mg, 0.003 mmol) in MeOH (3.5 mL).

$EuCl_3$: $EuCl_3 \cdot 6H_2O$ (1.0 mg, 0.003 mmol) in MeOH (3.5 mL).

$CaCl_2$: $CaCl_2 \cdot 2H_2O$ (1.0 mg, 0.003 mmol) in MeOH (8.5 mL).

The stock solutions were given in quartz suprasil cuvettes and were diluted in MeOH according to Table VIII.8. Each mixture was directly measured after preparation. Measurements were conducted on an Agilent 8453 Diode Array Spectrophotometer.

Table VIII.8: Titration of PQQ in MeOH (0.4 mM) with increasing amounts of $CaCl_2 \cdot 2H_2O$, $LaCl_3 \cdot 7H_2O$ or $EuCl_3 \cdot 6H_2O$ in MeOH (0.8 mM). Constant total volume of 1 mL (0.04 mM PQQ) in a quartz suprasil cuvette (d = 1 cm). Mixing through inversion for 30 seconds prior to measurement.

Curve-Title / Ratio	V (PQQ) [µL]	V (metal salt) [µL]	V (MeOH) [µL]
PQQ	100	0	900
1 metal equiv.	100	50	850
2 metal equiv.	100	100	800
3 metal equiv.	100	150	750
4 metal equiv.	100	200	700
5 metal equiv.	100	250	650

8.3. Synthesis of PQQ-hemiketal

8.3.1 Synthesis of PQQ-hemiketal (**16**)

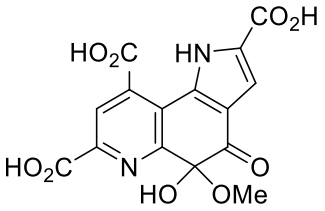

PQQ·H_2O (29 mg, 83.3 µmol) was completely dissolved in MeOH (2 mL) in an ultrasonic bath at 50°C and was allowed to cool down to room temperature afterwards. After one day, the received suspension was centrifuged and the orange colored supernatant was removed. To wash the received pellet, MeOH was added (1 mL) and the suspension was first vortexed and then centrifuged, followed by removal of the supernatant. This washing step was repeated two more times. The pellet was then transferred to a Schlenk flask and dried overnight under high vacuum, to afford a pale-yellow powder of the PQQ-hemiketal (**16**) (12 mg, 33.1 µmol, 40%).

^{13}C-ssNMR (500 MHz, CP–MAS): δ / ppm = 189.76, 167.41, 163.69, 159.40, 141.59, 136.41, 129.63, 125.61, 124.15, 121.36, 116.70, 92.37, 50.23.
Two carbon resonances are missing or probably overlap.

IR (Diamond-ATR, neat): $\tilde{\nu}$ / cm^{-1} = 3343 (w), 3257 (w), 3177-2676 (w, broad), 1724 (s), 1652 (s), 1558 (w), 1539 (w), 1506 (m), 1405 (m), 1364 (s), 1331 (m), 1257 (s), 1193 (s), 1167 (m), 1144 (m), 1112 (m), 1095 (m), 1057 (m), 1038 (m), 1008 (m), 976 (m), 921 (m), 883 (m), 865 (m), 806 (m), 755 (m), 721 (m), 691 (m).

Elemental Analysis (CHN): Found: C, 48.79; H, 2.93; N, 7.60. Calc. for **16**·0.59 MeOH [$C_{15}H_{10}N_2O_9$·0.59 CH_4O]: C, 49.13; H, 3.27; N, 7.35 or calc. for **16**·0.39 H_2O [$C_{15}H_{10}N_2O_9$ ·0.39 H_2O]: C, 48.79; H, 2.94; N, 7.59.

8.4. Kinetics of the Formation and Decay of PQQ-hemiketal

8.4.1 Reversibility of the C5-hemiketal Formation

Solid PQQ-hemiketal (**16**) (9 mg, 24.8 µmol) was given in an NMR-tube, DMF-d_7 (0.6 mL) was added and ^{1}H-NMR spectra were recorded immediately after on a Bruker Avance III (400 MHz) at 4°C. Measuring times and received integral values of the two species (PQQ and PQQ-hemiketal) are provided in Table VIII.9. Due to the locking process, the first ^{1}H-NMR spectrum was measured ~5 minutes after DMF-d_7 addition.

Table VIII.9: ^{1}H-NMR measuring times and integral values of PQQ-hemiketal (**16**) (9 mg, 24.8 µmol) in DMF-d_7 (0.6 mL). Due to the set-up of the NMR-device, the lock process had to be repeated each measurement, resulting in different measuring intervals. All spectra relative to the solvent singlet (8.03 ppm), which was set to an integral value of 1.00 and was used as reference for integral analysis of the 8H resonance of PQQ (**13**) and the PQQ-hemiketal (**16**).

#	minutes (total)	seconds (total)	Integral-Analysis	
			13	**16**
1	0	0	0.55	0.46
2	4:43	283	0.62	0.38
3	7:20	440	0.65	0.35
4	9:56	596	0.69	0.31
5	12:33	753	0.76	0.27
6	15:09	909	0.77	0.25
7	17:43	1063	0.81	0.21
8	20:20	1220	0.85	0.19
9	22:54	1374	0.86	0.17
10	25:30	1530	0.89	0.15
11	28:07	1687	0.91	0.14
12	30:44	1844	0.92	0.12
13	33:20	2000	0.93	0.11
14	35:56	2156	0.93	0.11
15	38:33	2313	0.95	0.09
16	41:08	2468	0.96	0.10
17	43:43	2623	0.96	0.08
18	46:20	2780	0.97	0.08
19	48:57	2937	0.99	0.07
20	51:32	3092	0.98	0.08

8.4.2 Kinetics of the PQQ-methanol Adduct Formation

Solid PQQ (**13**) (9 mg, 27.2 µmol) was given in an NMR-tube, MeOD-d_4 (0.5 mL) was added, the NMR tube was shaken and ^{1}H-NMR spectra were measured immediately after on a Bruker Avance III (400 MHz) at 0°C. ^{1}H-NMR spectra recorded roughly every 90 seconds (4 scans per measurement). Due to the locking process, the first ^{1}H-NMR spectrum was measured ~5 minutes after MeOD-d_4 addition. In a similar experiment, solid $LaCl_3$·7H_2O (9.6 mg, 27.2 µmol) was added to the solid PQQ (**13**) (9 mg, 27.2 µmol) before 0.5 mL of MeOD-d_4 were added.

9. Experimental Procedures for Chapter VII

9.1. Precursor Synthesis

9.1.1 Synthesis of 2-Bromo-6-carboxypyridine 1-oxide (**34**)

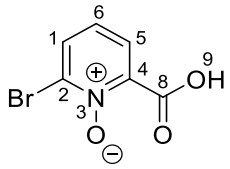

According to a literature procedure,[262] to a stirring solution of 6-bromopicolinic acid (**33**) (30.0 g, 0.149 mol) in trifluoroacetic acid (324 mL), hydrogen peroxide (30%, 65 mL) was added very slowly. The reaction mixture was heated to 80°C and stirred for 24 h. After cooling to room temperature, another 40 mL of hydrogen peroxide were added to the solution and the reaction mixture was stirred for another 2 days at 80°C. After completion of the reaction, the yellow solution was concentrated *in vacuo* and then poured into 1 L of water. The product was collected on a glass frit, washed with water (3 x 50 mL) and dried under high vacuum, to afford the title compound (**34**) (29.6 g, 0.136 mol, 91%) as a colorless powder.

^{1}H-NMR (400 MHz, DMSO-*d*$_6$): δ (ppm) = 8.31 (dd, *J* = 8.0 Hz, 1.9 Hz, 1H, 1), 8.26 (dd, *J* = 8.0 Hz, 1.9 Hz, 1H, 6), 7.71 (t, *J* = 8.0 Hz, 1H, 5).

^{13}C-NMR (100 MHz, DMSO-*d*$_6$): δ (ppm) = 160.5 (8), 138.4 (4), 134.7 (6), 132.6 (2), 131.4 (1), 127.8 (5).

Analytical data were consistent with those reported in the literature.[262]

9.1.2 Synthesis of 1,2-HOPO (**35**)

1-Hydroxy-6-oxo-1,6-dihydropyridine-2-carboxylic acid

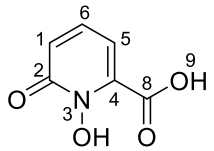

According to a literature procedure,[262] 2-bromo-6-carboxypyridine 1-oxide (**34**) (29.6 g, 0.136 mol) was dissolved in 600 mL aqueous potassium hydroxide solution (10%) and the reaction mixture was stirred for 3 days at 80°C. After cooling to room temperature, the yellow

solution was acidified with concentrated hydrochloric acid (300 mL) and the white precipitate was collected of a glass frit. The product was dried under high vacuum, to afford the title compound (**35**) (20.6 g, 0.133 mol, 98%) as a colorless powder.

^{1}H-NMR (400 MHz, DMSO-*d*$_6$): δ (ppm) = 7.46 (dd, *J* = 9.0 Hz, *J* = 7.0 Hz, 1H, 6), 6.74 (dd, *J* = 9.0 Hz, 1.7 Hz, 1H, 5), 6.66 (dd, *J* = 7.0 Hz, 1.7 Hz, 1H, 1).

^{13}C-NMR (100 MHz, DMSO-*d*$_6$): δ (ppm) = 161.8 (8), 157.2 (2), 138.9 (4), 136.8 (6), 120.3 (1), 106.5 (5).

Analytical data were consistent with those reported in the literature.[262]

9.1.3 Synthesis of 1,2-HOPOBn (**36**)

1-(Benzyloxy)-6-oxo-1,6-dihydropyridine-2-carboxylic acid

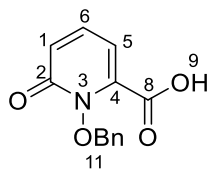

According to a literature procedure,[262] to a stirring solution of compound **35** (20.6 g, 0.133 mol, 1.0 equiv.) in methanol (350 mL), benzylchloride (20.4 g, 18.5 mL, 0.16 mol, 1.2 equiv.) and dry potassium carbonate (36.6 g, 0.265 mol, 2.0 equiv.) were added. After refluxing for 24 h, the mixture was filtered and the solvent was removed *in vacuo*. The residue was suspended in water (120 mL) and the pH was adjusted to pH 2 with 6 *M* HCl. The white precipitate was filtered on a glass frit and dried first in air than under high vacuum, to afford the title compound (**36**) (30.6 g, 0.125 mol, 94%) as a colorless powder.

^{1}H-NMR (400 MHz, DMSO-*d*$_6$): δ (ppm) = 7.51-7.40 (m, 6H, 11+6), 6.73 (dd, *J* = 9.3 Hz, 1.7 Hz, 1H, 5), 6.55 (dd, *J* = 6.8 Hz, 1.7 Hz, 1H, 1), 5.28 (s, 2H, 11-CH_2).

^{13}C-NMR (100 MHz, DMSO-*d*$_6$): δ (ppm) = 161.7 (8), 157.6 (2), 140.9 (arC), 138.7 (arC), 133.9 (arC), 129.6 (arC), 129.6 (arC), 129.0 (arC), 128.5 (arC), 128.5 (arC), 123.8 (arC), 106.0 (arC), 77.9 (11-CH_2).

Analytical data were consistent with those reported in the literature.[262]

9.1.4 Synthesis of 1,2-HOPO-thiaz (**38**)

1-(Benzyloxy)-6-(2-thioxothiazolidine-3-carbonyl)pyridin-2(1H)-one

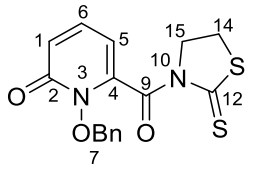

According to a literature procedure[263] and to GP II, 1,2-HOPO(Bn) (**36**) (3.0 g, 12.23 mmol) was transformed to its acyl chloride. The Acyl chloride was subsequently transformed to its acyl thiazolidine-2-thione, following GP III. The crude product was further purified by flash column chromatography (EtOAc / *i*-hexane = 6:4) to give the title compound (**38**) (1.76 g, 5.06 mmol, 41%) as a bright yellow solid.

^{1}H-NMR (400 MHz, $CDCl_3$): δ / ppm = 7.47 – 7.44 (m, 2H, 7), 7.41 – 7.37 (m, 3H, 7), 7.28 (dd, *J* = 9.3, 6.8 Hz, 1H, 6), 6.77 (dd, *J* = 9.3, 1.6 Hz, 1H, 5), 6.17 (dd, *J* = 6.8, 1.6 Hz, 1H, 1), 5.32 (s, 2H, 7-CH_2), 4.45 (t, *J* = 7.4 Hz, 2H, 14), 3.15 (t, *J* = 7.4 Hz, 2H, 15).

Analytical data were consistent with those reported in the literature.[263]

9.1.5 Synthesis of PDC-thiaz (**51**)

Methyl 6-(2-thioxothiazolidine-3-carbonyl)picolinate

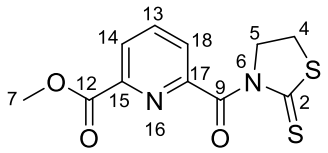

6-(methoxycarbonyl)picolinic acid (**40**) (0.15 g, 0.83 mmol) was transformed to its acyl chloride, following GP II. The Acyl chloride was subsequently transformed to its acyl thiazolidine-2-thione, following GP III. The crude product was further purified by flash column chromatography (DCM, pure) to give the title compound (**51**) (0.10 g, 0.35 mmol, 43%) as a yellow solid.

^{1}H-NMR (400 MHz, $CDCl_3$): δ / ppm = 8.19 (dd, J = 7.8, 1.1 Hz, 1H, 18), 7.93 (t, J = 7.8 Hz, 1H, 13), 7.73 (dd, J = 7.8, 1.1 Hz, 1H, 14), 4.62 (t, J = 7.3 Hz, 2H, 4), 3.98 (s, 3H, 7), 3.52 (t, J = 7.3 Hz, 2H, 5).

^{13}C-NMR (100 MHz, $CDCl_3$): δ / ppm = 202.06 (2), 168.48 (9), 165.07 (12), 152.90 (17), 147.35 (15), 138.06 (13), 127.04 (14), 126.95 (18), 55.68 (5), 53.19 (7), 29.85 (4).

HRMS (ESI +): *m/z* calc. for $[C_{11}H_{11}N_2O_3S_2]^+$: 283.0206; found: 283.0206.

IR (Diamond-ATR, neat): $\tilde{\nu}$ / cm^{-1} = 2953 (m), 2923 (m), 2853 (m), 1733 (s), 1686 (s), 1584 (m), 1473 (m), 1372, 1333 (m), 1286 (s), 1239 (s), 1164 (s), 1136 (s), 1057 (m), 980 (m), 837 (m), 811 (m), 738 (m), 697 (s).

9.2. Synthesis and Investigation of TREN-(1,2-HOPO)$_3$

9.2.1 Synthesis of TREN-(1,2-HOPOBn)$_3$ (**39**)

1-(Benzyloxy)-N-(2-(bis(2-((2-(formyl-l2-azaneyl)ethyl)amino)ethyl)amino)ethyl)-6-oxo-1,6-dihydropyridine-2-carboxamide

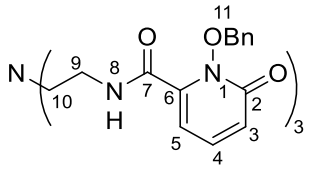

According to a literature procedure,[260] under nitrogen atmosphere, 1,2-HOPO(Bn)-thiaz (**38**) (1.5 g, 4.33 mmol 3.2 equiv.) was dissolved in dry DCM (30 mL) and Tris(2-aminoethyl)amine (0.20 g, 1.35 mmol, 1.0 equiv.) was added. The reaction mixture was stirred at room temperature for 60 h and was subsequently washed with KOH (1 *M*) and brine and dried over anhydrous Na_2SO4. After filtration, the solvent was evaporated *in vacuo*. The crude product was purified by column chromatography (DCM/MeOH 9.5:0.5 → 85:15) to give the title compound (**39**) (0.90 g, 1.09 mmol, 81%) as a colorless powder.

^{1}H-NMR (400 MHz, $CDCl_3$): δ / ppm = 7.47 – 7.42 (m, 6H, 11), 7.33 – 7.27 (m, 9H, 11), 7.15 (dd, *J* = 9.3, 6.8 Hz, 3H, 4), 7.06 (t, *J* = 5.7 Hz, 3H, 8), 6.43 (dd, *J* = 9.3, 1.7 Hz, 3H, 5), 6.06 (dd, *J* = 6.8, 1.7 Hz, 3H, 3), 5.25 (s, 6H, 11-CH_2), 2.94 (q, *J* = 5.7 Hz, 6H, 9), 2.31 (t, *J* = 5.5 Hz, 6H, 10).

Analytical data were consistent with those reported in the literature.[260]

9.2.2 Synthesis of TREN-(1,2-HOPO)$_3$ (**32**)

N-(2-(Bis(2-((2-(formyl-l2-azaneyl)ethyl)amino)ethyl)amino)ethyl)-1-hydroxy-6-oxo-1,6-dihydropyridine-2-carboxamide

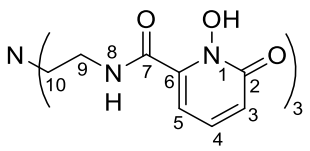

The benzyl group of TREN-[1,2-HOPO(Bn)]$_3$ (**39**) (0.9 g, 1.09 mmol) was deprotected, following a literature procedure[260] and GP I. The deprotection led to title compound (**32**) (0.8 g, quant.) as a colorless powder.

^{1}H-NMR (400 MHz, DMF-*d*$_7$): δ / ppm = 9.46 (t, *J* = 5.7 Hz, 3H, 8), 7.52 – 7.41 (m, 3H, 4), 6.72 – 6.71 (m, 3H, 5), 6.70 – 6.67 (m, 3H, 3), 4.00 (q, *J* = 6.0 Hz, 6H, 9), 3.74 (t, *J* = 6.2 Hz, 6H, 10).

^{13}C-NMR (100 MHz, DMF-*d*$_7$): δ / ppm = 160.92 (7), 157.67 (2), 140.98 (6), 136.74 (4), 119.57 (3), 106.07 (5), 52.30 (10), 34.55 (9).

IR (Diamond-ATR, neat): $\tilde{\nu}$ / cm^{-1} = 3204 (w), 3030 (w), 2596 (w), 2356 (w), 2145 (w), 1992 (w), 1632 (s), 1520 (m), 1498 (m), 1293 (s), 1217 (m), 1161 (m), 1068 (m), 1014 (m), 841 (m), 802 (s), 742 (s).

Elemental Analysis (CHN): Found: C, 41.84; H, 5.06; N, 14.13. Calc. for [$C_{24}H_{27}N_7O_9$·3.5HCl·1.5MeOH]: C, 41.97; H, 4.67; N, 13.98.

Analytical data were consistent with those reported in the literature.[260]

9.2.3 Complex Formation with TREN-(1,2-HOPO)$_3$ (**32**)

Mass Experiments

ESI-mass spectra were measured from solutions of *in situ* generated complexes of TREN-(1,2-HOPO)$_3$ (**32**) with lanthanum or calcium in methanol (3 mM). Pyridine was added to deprotonate the HOPO hydroxyl groups and promote complexation. Moreover, PDC (**40**) and PQQ (**13**) were added to show a possible co-complexation. Initially, all compounds were dissolved in appropriate solvents (0.1 mg per µL) and combined subsequently

A: TREN-(1,2-HOPO)$_3$ (1.5 mg, 2.7 µmol, methanol); $LaCl_3 \cdot 7H_2O$ (1.0 mg, 2.7 µmol, H_2O); PDC (0.5 mg, 2.7 µmol, methanol); pyridine (0.87 µL, 10.8 µmol); methanol (870 µL).

B: TREN-(1,2-HOPO)$_3$ (1.5 mg, 2.7 µmol, methanol); La(AcO)$_3$ (0.9 mg, 2.7 µmol, H_2O); PDC (0.5 mg, 2.7 µmol, methanol); methanol (871 µL).

A+B: HRMS (ESI ±): *m/z* calc. for [La (**32**) (**40**)] - $C_{32}H_{30}LaN_8O_{13}$, M=874.1074], found: 875.1171, calc. 875.1147 (ESI +), 873.0986, calc. 873.1001 (ESI −).

HRMS (ESI ±): *m/z* calc. for [La (**32**) (**40a**)] - $C_{33}H_{33}LaN_8O_{13}$, M=888.1231, found: 889.1322, calc. 889.1303 (ESI +), 887.1164, calc. 887.1158 (ESI −).

C: TREN-(1,2-HOPO)$_3$ (1.5 mg, 2.7 µmol, methanol); Ca(AcO)$_2$ (0.5 mg, 2.7 µmol, H_2O); PDC (0.5 mg, 2.7 µmol, methanol); methanol (875 µL).

HRMS (ESI ±): No complex formation was observed

D: TREN-(1,2-HOPO)$_3$ (1.5 mg, 2.7 µmol, methanol); La(AcO)$_3$ (0.9 mg, 2.7 µmol, H_2O); PQQ (0.9 mg, 2.7 µmol, 44.5 µL, 0.1 mg per 5 µL DMSO); methanol (831.5 µL).

HRMS (ESI ±): *m/z* calc. for [La (**32**)] - $C_{24}H_{24}LaN_7O_9$, M=693.0699], found: 694.07844, calc. 694.0772 (ESI +).

9.3. Synthesis and Investigation of TREN-(1,2-HOPO)$_2$-TAM-N1-PDA

9.3.1 Synthesis of TREN- (1,2-HOPOBn$_2$ (**45**)

1-(Benzyloxy)-N-(2-(bis(2-((2-(formyl-l2-azaneyl)ethyl)amino)ethyl)amino)ethyl)-6-oxo-1,6-dihydropyridine-2-carboxamide

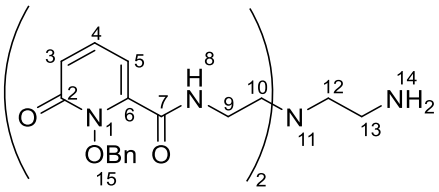

According to a literature procedure,[265] 1,2-HOPO(Bn)-thiaz (**38**) (1.35 g, 3.90 mmol, 2.0 equiv.) was dissolved in DCM (350 mL) and was added dropwise and under heavy stirring over 3 days to a solution of Tris(2-aminoethyl)amine (0.28 g, 1.95 mmol, 1.0 equiv.) and triethylamine (0.79 g, 7.79 mmol, 4.0 equiv.) in DCM (500 mL). The reaction mixture was stirred for another day at room temperature, before the solvent was evaporated *in vacuo*.

The crude product was purified by column chromatography (DCM/MeOH 97:03 → 88:12) to give the title compound (**45**) (0.83 g, 1.38 mmol, 71%) as a pale yellow foam.

^{1}H-NMR (400 MHz, $CDCl_3$): δ / ppm = 8.53 (s, 2H, 8), 7.62 – 7.56 (m, 4H, 15), 7.41 – 7.32 (m, 6H, 15), 7.31 – 7.27 (m, 2H, 4), 6.59 (dd, *J* = 9.2, 1.7 Hz, 2H, 5), 6.19 (d, *J* = 6.7 Hz, 2H, 3), 5.30 (s, 4H, 15-CH_2), 2.99 (brs, 4H, 9), 2.20 – 2.04 (m, 6H, 10+12), 1.41 (brs, 2H, 13).

^{13}C-NMR (100 MHz, $CDCl_3$): δ / ppm = 161.32 (2C, 7), 159.24 (2C, 2), 144.18 (2C, 6), 139.29 (2C, 4), 133.36 (2C, arC), 131.56 (4C, arC), 129.81 (2C, arC), 128.85 (4C, arC), 122.54 (2C, 3), 105.27 (2C, 5), 79.98 (2C, 15-CH_2), 54.15 (2C, 10), 52.15 (12), 37.23 (2C, 9), 35.64 (13).

HRMS (ESI +): *m/z* calc. for $[C_{32}H_{37}N_6O_6]^+$: 601.2769; found: 601.2773.

IR (Diamond-ATR, neat): $\tilde{\nu}$ / cm^{-1} = 2853 (w), 1644 (s), 1521 (m), 1295 (m), 1139 (m), 958 (w), 904 (w), 802 (w), 753 (s), 699 (s).

Analytical data were consistent with those reported in the literature.[265]

9.3.2 Synthesis of TAM-N1-thiaz (**47**)

Tert-butyl (3-(2,3-bis(benzyloxy)-4-(2-thioxothiazolidine-3-carbonyl)benzamido)-propyl)carbamate

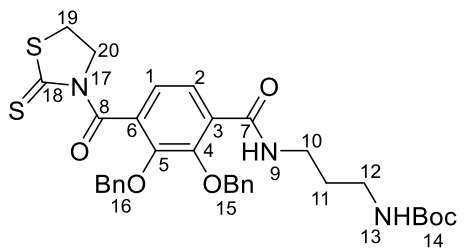

According to a literature procedure,[265] a solution of *N*-Boc-1,3-propanediamine (**N1**) (83 mg, 0.476 mmol, 1.0 equiv.) and triethylamine (59 mg, 0.08 mL, 0.583 mmol, 1.2 equiv.) in dichloromethane (250 mL) and isopropanol (4 mL) was added dropwise over a period of two days to a stirring solution of 2,3-dibenzyloxy-1,4-dicarbonyl(2-mercaptothiazolide) (**46**) (2.5 g, 4.31 mmol, 9.0 equiv.) in dichloromethane (600 mL). After stirring for another 24 h at room temperature, the solvent was evaporated. The crude product was purified by flash column chromatography (DCM/MeOH 100:0 → 95:5) to give the title compound (**47**) (249 mg, 0.392 mmol, 82%) as a yellow oil.

^{1}H-NMR (400 MHz, $CDCl_3$): δ (ppm) = 7.89 (d, J = 8.3 Hz, 1H, 2), 7.81 (br, 1H, 9), 7.39-7.31 (m, 10H, 15+16), 7.21 (d, J = 8.1 Hz, 1H, 1), 5.12 (s, 4H, 15-CH_2+16-CH_2), 5.02 (br, 1H, 13), 4.38 (t, J = 7.3 Hz, 2H, 19), 3.27 (q, J = 6.3 Hz, 2H, 10), 3.01 (q, J = 6.3 Hz, 2H, 12), 2.95 (t, J = 7.5 Hz, 2H, 20), 1.48 (p, J = 6.5 Hz, 2H, 11), 1.43 (s, 9H, 14).

^{13}C-NMR (100 MHz, $CDCl_3$): δ (ppm) = 201.5 (18), 167.0 (7/8), 150.2 (7/8), 149.3 (14-C=O), 137.1 (4/5), 135.9 (4/5), 133.7 (3/6), 130.0 (3/6), 129.1 (2C, 15/16), 129.0 (2C, 15/16), 128.8 (2C, 15/16), 128.6 (2C, 15/16), 128.1 (2C, 15/16), 127.0 (1/2), 124.5 (1/2), 79.2 (14), 76.3 (2C, 15-CH_2+16-CH_2), 55.7 (20), 37.6 (10/12), 36.8 (10/12), 30.1 (11), 28.8 (19), 28.6 (3C, 14-CH_3).

IR (Diamond-ATR, neat): $\tilde{\nu}$ / cm^{-1} = 3287 (w), 2975 (w), 1650 (m), 1520 (m), 1363 (m), 1310 (s), 1228 (s), 1166 (s), 1062 (m), 1001 (m), 735 (s), 698 (s).

Analytical data were consistent with those reported in the literature.[265]

9.3.3 Synthesis of TREN-(1,2-HOPOBn)$_2$-TAMBn-N1-Boc (**48**)

Tert-butyl (3-(2,3-bis(benzyloxy)-4-((2-(bis(2-(1-(benzyloxy)-6-oxo-1,6-dihydropyridine-2-carboxamido)ethyl)amino)ethyl)carbamoyl)benzamido)propyl)carbamate

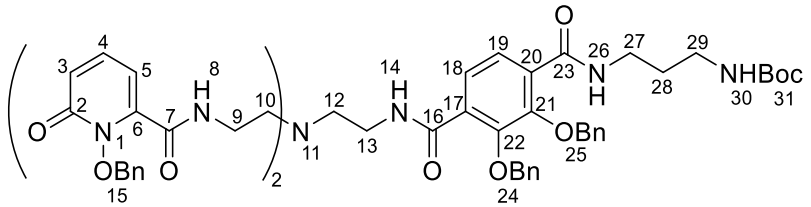

According to a literature procedure,[265] **45** (150 mg, 0.25 mmol, 2.0 eq) and **47** (80 mg, 0.126 mmol, 1.0 equiv.) were dissolved in dichloromethane (50 mL). Triethylamine (38.2 mg, 0.05 mL, 0.377 mmol, 3.0 equiv.) was added and the reaction mixture was stirred for three days at room temperature. After completion of the reaction, the solvent was removed *in vacuo*. The crude product was purified by flash column chromatography (DCM / MeOH 100:0 → 95:5) to give the title compound (**48**) (112 mg, 0.10 mmol, 80%) as a brown-yellow solid.

^{1}H-NMR (400 MHz, $CDCl_3$): δ (ppm) = 7.52-7.49 (m, 4H, 24/25), 7.42-7.28 (m, 11H, 24/25), 7.20-7.17 (m, 5H, 15), 7.03-7.01 (m, 2H, 4), 6.92 (d, J = 8.2 Hz, 1H, 18/19), 6.71 (d, J = 8.2 Hz, 1H, 18/19), 6.67 (dd, J = 9.3 Hz, J = 1.6 Hz, 2H, 5), 6.15 (dd, J = 6.8 Hz, J = 1.6 Hz, 2H, 3), 5.37 (s, 4H, 15-CH_2), 4.96 (s, 2H, 24/25-CH_2), 4.54 (s, 2H, 24/25-CH_2), 3.53 (q, J = 6.3 Hz, 2H, 27/29), 3.26-3.23 (m, 6H, 10+12), 3.05 (br, 2H, 27/29), 2.48-2.45 (m, 4H, 9), 2.09-2.07 (m, 2H, 13), 1.77 (p, J = 6.3 Hz, 2H, 28), 1.45 (s, 9H, 31).

^{13}C-NMR (100 MHz, $CDCl_3$): δ (ppm) = 166.4 (16/23), 165.9 (16/23), 161.1 (2C, 7), 159.0 (2C, 2), 151.3 (31-C=O), 149.5 (arC_q), 143.1 (2C, 6), 138.9 (2C, 4), 136.7 (arC_q), 133.9 (arC_q), 130.6 (arCH), 129.3 (arCH), 128.8 (arCH), 128.8 (arCH), 128.6 (arCH), 128.6 (arCH), 128.5 (arCH), 127.6 (18/19), 125.3 (18/19), 123.8 (2C, 3), 105.6 (2C, 5), 79.4 (2C, 15-CH_2), 78.3 (31), 76.7 (24/25-CH_2), 76.5 (24/25-CH_2), 55.6 (2C, 10), 52.9 (12), 39.5 (2C, 9), 37.3 (27/29), 36.8 (27/29), 29.9 (28), 28.7 (3C, 31-CH_3).

Several carbon resonances are missing or probably overlap.

IR (Diamond-ATR, neat): $\tilde{\nu}$ / cm^{-1} = 3264 (w), 3034 (w), 2934 (w), 1645 (s), 1521 (s), 1454 (m), 1365 (s), 1289 (m), 1216 (m), 1168 (m), 957 (m), 911 (m), 799 (m), 747 (s), 699 (s).

Analytical data were consistent with those reported in the literature.[265]

9.3.4 Synthesis of TREN-(1,2-HOPOBn)$_2$-TAMBn-N1 (**49**)

N1-(3-Aminopropyl)-2,3-bis(benzyloxy)-N4-(2-(bis(2-(1-(benzyloxy)-6-oxo-1,6-dihydropyridine-2-carboxamido)ethyl)amino)ethyl)terephthalamide

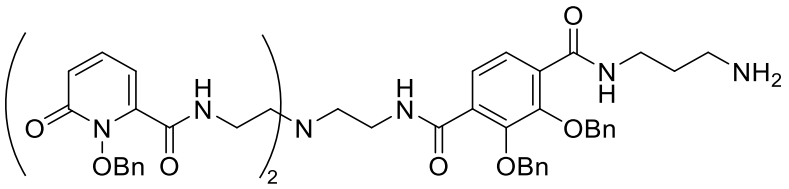

In order to remove the Boc-protecting group, starting material **48** (51.5 mg, 0.046 mmol) was dissolved in 20 mL hydrochloric acid (3M in ethyl acetate). The reaction mixture was stirred for 30 min at room temperature. After completion of the reaction, the mixture was evaporated to dryness under high vacuum. The product was not further purified and was directly used for the next reaction step.

9.3.5 Synthesis of PDC-N1-Boc (**52**)

Methyl 6-((3-((tert-butoxycarbonyl)amino)propyl)carbamoyl)picolinate

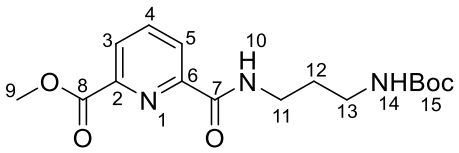

Under nitrogen atmosphere, a solution of N-Boc-1,3-propanediamine (**N1**) (0.17 g, 0.98 mmol, 1.2 equiv.) in dichloromethane (10 mL) and isopropanol (1 mL) was added to a stirring solution of PDC-thiaz (**51**) (0.23 g, 0.82 mmol, 1.0 equiv.) in dichloromethane (15 mL). Triethylamine (0.1 g, 0.14 mL, 0.98 mmol, 1.2 equiv.) was added and the reaction mixture was stirred at room temperature. The completion of the reaction was achieved after 72 h, stated by TLC-analysis of reaction aliquots. Subsequently, the solution was washed with 1M KOH (2 x 10 mL) and brine (1 x 10 mL) and dried over sodium sulfate. After filtration, the solvent was evaporated *in vacuo* and the crude product was purified by flash column chromatography (DCM / MeOH = 9.5:0.5) to give the title compound (**52**) (0.25 g, 0.74 mmol, 90%) as a colorless solid.

^{1}H-NMR (400 MHz, $CDCl_3$): δ / ppm = 8.34 (dd, *J* = 7.8, 1.2 Hz, 1H, 5), 8.19 (dd, *J* = 7.8, 1.2 Hz, 1H, 3), 7.98 (t, *J* = 7.8 Hz, 1H, 4), 3.98 (s, 3H, 9), 3.53 (q, *J* = 6.6 Hz, 2H, 11), 3.17 (q, *J* = 6.4 Hz, 2H, 13), 1.78 (p, *J* = 6.5 Hz, 2H, 12), 1.41 (s, 9H, 15).

^{13}C-NMR (100 MHz, $CDCl_3$): δ / ppm = 163.94 (7/8), 162.97 (7/8), 155.16 (15-C=O), 149.04 (6), 145.54 (2), 137.53 (4), 126.24 (3), 124.35 (5), 51.89 (9), 36.44 (11/13), 35.54 (11/13), 29.15 (12), 27.41 (15-CH_3).

HRMS (ESI +): *m/z* calc. for $[C_{16}H_{24}N_3O_5]^+$: 338.1710; found: 338.1718.

IR (Diamond-ATR, neat): $\tilde{\nu}$ / cm^{-1} = 3345 (w), 2975 (w), 1671 (s), 1523 (s), 1436 (m), 1365 (m), 1243 (s), 1160 (s), 1136 (s), 996 (m), 846 (w), 752 (s), 690 (m).

9.3.6 Synthesis of PDC-N1 (**53**)

Methyl 6-((3-aminopropyl)carbamoyl)picolinate

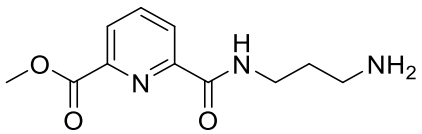

In order to remove the Boc-protecting group, starting material PDC-N1-Boc (**52**) (256 mg, 0.76 mmol) was dissolved in 30 mL hydrochloric acid (3*M* in ethyl acetate) and the reaction mixture was stirred for 1 h at room temperature. After completion of the reaction, the mixture was evaporated to dryness, solved in a small amount of water, and was again dried under high vacuum (3 x repetition). The product was not further purified and was directly used for the next reaction step.

9.3.7 Synthesis of PDC-N1-TAM (**54**)

Methyl 6-((3-(2,3-bis(benzyloxy)-4-(2-thioxothiazolidine-3-carbonyl)benzamido)propyl)-carbamoyl)picolinate

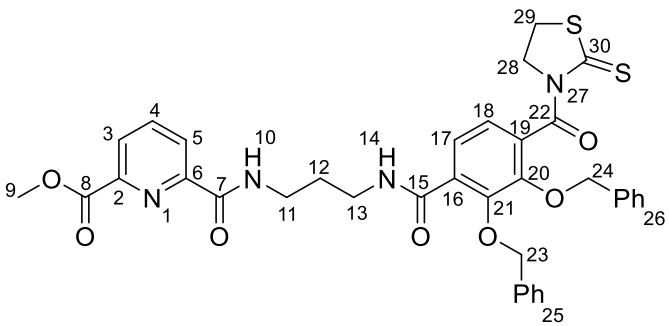

A solution of deprotected PDC-N1 (**53**) (180 mg, 0.76 mmol, 1.0 equiv.) and a few drops of triethylamine and isopropanol in dichloromethane (50 mL) was added over 5 h to a stirring solution of 2,3-dibenzyloxy-1,4-dicarbonyl(2-mercaptothiazolide) (2204 mg, 3.79 mmol, 5.0 equiv.) in dichloromethane (120 mL). The reaction mixture was stirred at room temperature for 3 days. After completion of the reaction, the solvent was evaporated *in vacuo* and the crude product was purified by flash column chromatography (DCM / MeOH 100:0 → 85:15) to give the title compound (**54**) (170 mg, 0.24 mmol, 32%) as a yellow solid.

^{1}H-NMR (400 MHz, $CDCl_3$): δ / ppm = 8.34 (ddd, *J* = 7.8, 2.8, 1.2 Hz, 1H, 5), 8.21 (ddd, *J* = 7.8, 2.5, 1.2 Hz, 1H, 3), 7.98 (td, *J* = 7.8, 2.8 Hz, 1H, 4), 7.91 (dd, *J* = 8.2, 1.5 Hz, 1H, 17), 7.40 – 7.33 (m, 10H, Ph), 7.20 (dd, *J* = 8.2, 1.0 Hz, 1H, 18), 5.14 (s, 2H, 23), 5.12 (s, 2H, 24), 4.38 (t, *J* = 7.3 Hz, 2H, 29), 3.35 (dq, *J* = 19.7, 6.6 Hz, 4H, 11+13), 2.95 (t, *J* = 7.3 Hz, 2H, 28), 1.65 (p, *J* = 6.8 Hz, 2H, 12), 1.20 (d, *J* = 6.1 Hz, 3H, 9).

^{13}C-NMR (100 MHz, $CDCl_3$): δ / ppm = 201.39 (30), 166.91 (22), 164.58 (8), 164.50 (15), 163.85 (7), 150.27 (2), 150.21 (21), 149.28 (20), 147.02 (6), 138.53 (4), 137.08 (Ph_q), 135.94 (Ph_q), 133.50 (19), 130.26 (PhH), 129.06 (PhH), 129.00 (PhH), 128.96 (PhH), 128.73 (PhH), 128.72 (PhH), 128.51 (PhH), 128.04 (PhH), 127.25 (3), 126.93 (17), 125.31 (5), 124.38 (18), 77.12 (23/24), 76.18 (23/24), 55.65 (29), 37.18 (13), 37.00 (11), 29.58 (12), 28.78 (28), 25.47 (9).

HRMS (ESI +): *m/z* calc. for $[C_{36}H_{35}N_4O_7S_2]^+$: 699.1942; found: 699.1965.

IR (Diamond-ATR, neat): $\tilde{\nu}$ / cm^{-1} = 3390 (w), 2941 (w), 1722 (m), 1661 (s), 1524 (s), 1425 (m), 1366 (m), 1311 (s), 1229 (s), 1171 (s), 1064 (s), 997 (s), 748 (s), 698 (s).

9.3.8 Synthesis of TREN-(1,2-HOPOBn)$_2$-TAM-N1-PDC (**55**)

Methyl 6-((3-(4-((2-((2-(1-methoxy-6-oxo-1,6-dihydropyridine-2-carboxamido)ethyl)(2-(6-oxo-1-(2-oxo-2-phenylethoxy)-1,6-dihydropyridine-2-carboxamido)ethyl)amino)ethyl)-carb-amoyl)-2,3-bis(2-oxo-2-phenylethoxy)benzamido)propyl)carbamoyl)picolinate

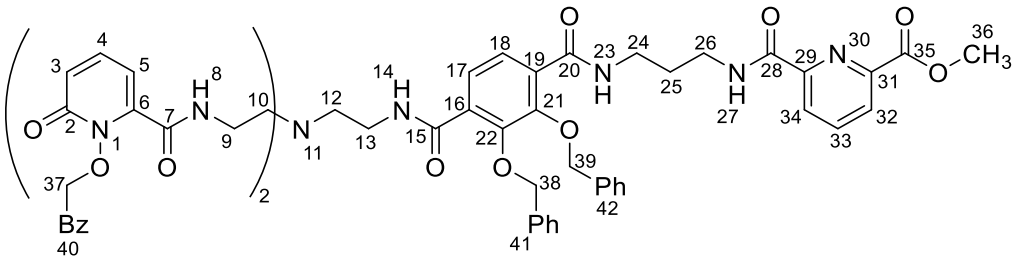

Under nitrogen atmosphere, TREN-bis-[1,2-HOPO(Bn)]$_2$ (**36**) (76 mg, 0.13 mmol, 1.0 equiv.), PDC-N1-TAM (**44**) (88 mg, 0.13 mmol, 1.0 equiv.) and trimethylamine (15 mg, 0.15 mmol, 0.02 mL) were dissolved in dry DCM (2 mL) and the mixture was stirred at room temperature. After six days, the mixture was diluted with DCM (10 mL), washed with 1M KOH (2 x 10 mL) and brine (2 x 10 mL) and dried over sodium sulfate. After filtration, the solvent was evaporated *in vacuo* and the crude product was purified by flash column chromatography (DCM / MeOH 100:0 → 87:13) to give the title compound (**45**) (95 mg, 0.08 mmol, 61%) as a colorless foam.

^{1}H-NMR (400 MHz, Methanol-*d*$_4$): δ / ppm = 8.30 (dt, *J* = 7.8, 1.1 Hz, 1H, 34), 8.25 (dt, *J* = 7.8, 1.1 Hz, 1H, 32), 8.12 (t, *J* = 7.8 Hz, 1H, 33), 7.50 – 7.45 (m, 4H, Ph), 7.41 (dd, *J* = 9.2, 6.8 Hz, 2H, 4), 7.37 (td, *J* = 8.1, 1.5 Hz, 2H, 17+18), 7.35 – 7.25 (m, 16H, Ph), 6.69 (dd, *J* = 9.2, 1.7 Hz, 2H, 3), 6.29 (dd, *J* = 6.8, 1.7 Hz, 2H, 5), 5.27 (s, 4H, 37), 5.09 (s, 2H, 38/39), 5.03 (s, 2H, 38/39), 3.46 (t, *J* = 6.8 Hz, 2H, 24), 3.41 (t, *J* = 6.8 Hz, 2H, 26), 3.27 (t, *J* = 6.1 Hz, 4H, 9), 3.20 (t, *J* = 6.2 Hz, 2H, 12), 2.55 (t, *J* = 6.1 Hz, 4H, 10), 2.42 (t, *J* = 6.2 Hz, 2H, 16), 1.84 (p, *J* = 6.8 Hz, 2H, 25).

^{13}C-NMR (100 MHz, Methanol-*d*$_4$): δ / ppm = 166.37 (15), 166.07 (35), 164.43 (28), 164.40 (20), 161.21 (7), 159.29 (2), 150.31 (21/22), 150.20 (31), 150.06 (21/22), 146.43 (d, 29), 143.39 (6), 139.17 (4), 138.98 (d, 33), 136.30 (Ph$_q$), 136.26 (Ph$_q$), 133.56 (Ph$_q$), 132.87 (16/19), 130.91 (16/19), 129.91 (PhH), 129.06 (PhH), 128.41 (PhH), 128.29 (PhH), 128.28 (PhH), 127.16 (d, 32), 125.31 (d, 34), 124.69 (17/18), 124.43 (17/18), 122.66 (3), 105.73 (5), 79.08 (37), 76.58 (38/39), 76.53 (38/39), 53.44 (10/12), 52.77 (10/12), 37.89 (24/26), 37.58 (24/26), 37.18 (9/13), 36.93 (9/13), 28.71 (25).

No resonance was found for the PDC methyl ester (**36**), which was most likely deprotected during the KOH treatment.

HRMS (ESI +): *m/z* calc. for $[C_{65}H_{66}N_9O_{13}]^+$: 1180.4775; found: 1180.4790.

IR (Diamond-ATR, neat): $\tilde{\nu}$ / cm^{-1} = 3390 (w), 3265 (w), 3033 (w), 2938 (w), 1725 (w), 1650 (s), 1523 (s), 1290 (s), 1215 (m), 1140 (m), 958 (m), 799 (m), 749 (s), 697 (s).

9.3.9 Synthesis of TREN-(1,2-HOPO)$_2$-TAM-N1-PDA (**43**)

6-((3-(4-((2-(Bis(2-(1-hydroxy-6-oxo-1,6-dihydropyridine-2-carboxamido)ethyl)-amino)ethyl)-carbamoyl)-2,3-dihydroxybenzamido)propyl)carbamoyl)picolinic acid

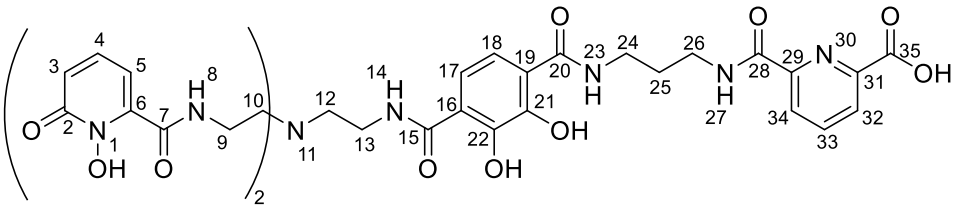

According to GP I, TREN-[1,2-HOPO(Bn)]$_2$-TAM-N1-PDC (**55**) (95 mg, 0.081 mmol) was deprotected, to afford the title compound (**43**) as a pale yellow foam (65 mg, quant.)

^{1}H-NMR (400 MHz, Methanol-*d*$_4$): δ / ppm = 8.30 (d, *J* = 7.7 Hz, 1H, 34), 8.23 (d, *J* = 7.3 Hz, 1H, 32), 8.13 (t, *J* = 7.8 Hz, 1H, 33), 7.40 (t, *J* = 8.0 Hz, 2H, 4), 7.11 (q, *J* = 8.6 Hz, 2H, 17+18), 6.82 (d, *J* = 8.8 Hz, 2H, 3), 6.78 (d, *J* = 7.1 Hz, 2H, 5), 3.98 – 3.85 (m, 6H, 9+13), 3.80 – 3.70 (m, 6H, 10+12), 3.55 (dt, *J* = 16.7, 6.5 Hz, 4H, 24+26), 1.99 (p, *J* = 6.0 Hz, 2H, 25).

^{13}C-NMR (100 MHz, Methanol-*d*$_4$): δ / ppm = 171.16 (15), 170.40 (20), 166.84 (35), 165.89 (28), 163.49 (7), 159.66 (2), 151.42 (31), 150.76 (21/22), 149.53 (21/22), 147.56 (29), 140.40 (33), 139.97 (6), 137.78 (4), 128.51 (32), 126.56 (34), 120.59 (3), 119.26 (16/19), 119.11 (16/19), 118.46 (17/18), 117.41 (17/18), 111.27 (5), 56.14 (10/12), 55.32 (10/12, 38.37 (24/26), 38.26 (24/26), 36.43 (9/13), 36.34 (9/13), 29.97 (25).

HRMS (ESI −): *m/z* calc. for $[C_{36}H_{35}\mathbf{Fe}N_9O_{13}]^-$: 857.1709; found: 857.1718.

IR (Diamond-ATR, neat): $\tilde{\nu}$ / cm^{-1} = 3238 (w), 3057 (w), 2946 (w), 2613 (w), 2356 (w), 1738 (w), 1641 (s), 1536 (s), 1434 (m), 1329 (s), 1237 (s), 1166 (m), 1029 (m), 804 (s), 742 (s), 680 (s).

Elemental Analysis (CHNS): Found: C, 47.53; H, 5.32; N, 12.97. Calc. for $[C_{36}H_{39}N_9O_{13}\cdot 2.4\ HCl\cdot 2.45\ CH_3OH]$: C, 47.52; H, 5.31; N, 12.97.

9.3.10 Mass experiments with TREN -(1,2-HOPO)$_2$-TAM-N1-PDA (**43**)

ESI-mass spectra were measured from solutions of *in situ* generated complexes of TREN -(1,2-HOPO)$_2$-TAM-N1-PDA (**43**) with lanthanum or europium in methanol (3 mM). Pyridine was added to deprotonate the HOPO and TAM hydroxyl groups and promote complexation. Initially, all compounds were dissolved in appropriate solvents (0.1 mg per µL) and combined subsequently.

A: TREN-(1,2-HOPO)$_2$-TAM-N1-PDA (1.3 mg, 1.6 µmol); $LaCl_3 \cdot 7H_2O$ (0.6 mg, 1.6 µmol); pyridine (0.4 mg, 0.4 µL, 5.1 µmol); methanol (600 µL).

B: TREN-(1,2-HOPO)$_2$-TAM-N1-PDA (1.4 mg, 1.7 µmol); $EuCl_3 \cdot 6H_2O$ (0.6 mg, 1.7 µmol); pyridine (0.4 mg, 0.4 µL, 5.1 µmol); methanol (600 µL).

Received mass spectra are provided in Figure IX.30 and Figure IX.31 and assigned mass peaks in Table VII.3.

9.3.11 UV-Vis Titrations with TREN -(1,2-HOPO)$_2$-TAM-N1-PDA (**43**)

Table VIII.10: Titration of TREN-(1,2-HOPO)$_2$-TAM-N1-PDA (**43**) or TREN-(1,2-HOPO)$_3$ (**32**) in methanol (6.20 mM, diluted to 0.310 mM) with increasing amounts of $LaCl_3 \cdot 7H_2O$ or $EuCl_3 \cdot 6H_2O$ in MeOH (14.6 mM). Constant total volume of 1 mL (0.292 mM **43** or **32**) in a quartz suprasil cuvette (d = 1 cm).

Components	V (**43**/**32**) [µL]	V (metal salt) [µL]	V (MeOH) [µL]
Ligand (**43**/**32**)	940	0	60
0.5 metal equiv.	940	10	50
1.0 metal equiv.	940	20	40
1.5 metal equiv.	940	30	30
2.0 metal equiv.	940	40	20
2.5 metal equiv.	940	50	10
3.0 metal equiv.	940	60	0

9.4. Synthesis and Investigation of PQQ-Aza-Crown Ether Complexes

9.4.1 Synthesis of PQQMe$_2$-aza-crown-6 (**58**) *via* PyBOP Coupling

Dimethyl 7-(1,4,7,10,13-pentaoxa-16-azacyclooctadecane-16-carbonyl)-4,5-dioxo-4,5-dihydro-1H-pyrrolo[2,3-f]quinoline-2,9-dicarboxylate

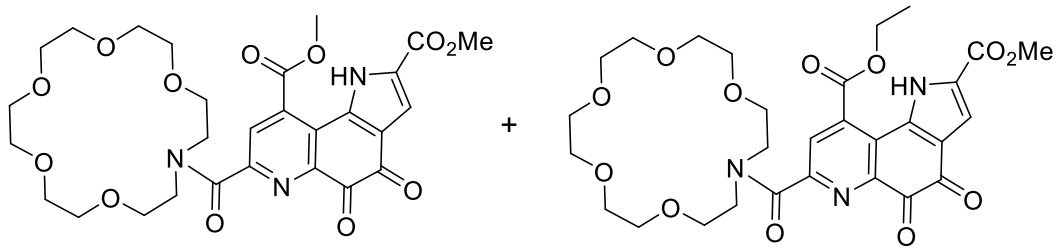

58 **59**

In a dry and nitrogen flushed Schlenk-Tube, $PQQMe_2$ (**19**) (1.0 equiv., 30 mg, 83.4 µmol) was dissolved in dry DMF (2 mL), together with 1-Aza-18-crown-6 (1.2 equiv., 26.5 mg, 100.5 µmol) and triethylamine (2.0 equiv., 16.9 mg, 23.38 µL, 167.5 µmol). PyBOP (1.2 equiv., 52.3 mg, 100.5 µmol) was added and the mixture was stirred at room temperature for 3 h. The solvent was removed in vacuo and the crude product was dissolved in H_2O (50 mL). The solution was extracted with DCM (3 x 30 mL) and the combined organic phases were washed thoroughly with water (3 x 50 mL) and brine (2 x 50 mL) to remove traces of DMF. The combined organic phases were dried with Na_2SO_4 and the solvent was removed in vacuo, to receive 77 mg of a dark-red viscous substance (PQQ-aza-crown-6). Since NMR showed large amounts of Triphenylphosphine oxide (residues of PyBOP), column chromatography was performed: Dry load with celite – rinse with DCM, until dryload is on the column – run column with 99:1 DCM/EtOH. Combination of the clean fractions and evaporation of the solvents gave PQQ-aza-crown-6-ethyl-ester (**59**) as a brown viscous substance (9 mg, 14.6 µmol, 17%) while the rest of the crude product could be regained after partly dissolving the silica with water and extraction with DCM.

PQQ-aza-crown-6 (**58**):

^{1}H-NMR (400 MHz, $CDCl_3$): δ / ppm = 12.85 (s, 1H, 1), 8.60 (s, 1H, 8), 7.41 (d, *J* = 2.3 Hz, 1H, 3), 4.11 (s, 3H, 9-Me), 4.03 – 3.96 (m, 2H, Crown18-a), 3.95 (s, 3H, 2-Me), 3.89 – 3.77 (m, 6H, Crown18-b), 3.70 – 3.55 (m, 16H, Crown18-c).

HRMS (ESI −): *m/z* found: 602.19905, calc. for $[C_{28}H_{32}N_3O_{12}]^-$: 602.19915.

PQQ-aza-crown-6-ethyl-ester (**59**):

^{1}H-NMR (400 MHz, $CDCl_3$): δ / ppm = 12.89 (s, 1H, 1), 8.62 (s, 0.09, 8x), 8.59 (s, 1H, 8), 7.43 (d, J = 2.3 Hz, 1H, 3), 4.59 (q, J = 7.1 Hz, 2H, 9-$\underline{CH_2}$-CH_3), 4.12 (s, 0.59, 9'x-Me), 4.00 (t, J = 5.8 Hz, 2H, Crown18-a), 3.96 (s, 0.48, 2'x-Me), 3.96 (s, 3H, 2-Me), 3.91 – 3.78 (m, 6H, Crown18-b), 3.73 – 3.56 (m, 16H, crown18-c), 1.50 (t, J = 7.2 Hz, 3H, 9-CH_2-$\underline{CH_3}$).

Residual PQQ-crown18 (**58**) resonances.

^{13}C-NMR (100 MHz, $CDCl_3$): δ / ppm = 179.57 (5), 173.18 (4), 167.14 (9'), 166.38 (7'), 160.37 (2'), 153.90 (5a), 145.92 (7), 134.38 (9), 134.17 (1a), 131.13 (8), 127.82 (2/3a), 126.24 (9a), 124.86 (2/3a), 115.67 (3), 70.96 (Crown18-c), 70.87 (Crown18-c), 70.75 (Crown18-c), 70.72 (Crown18-c), 70.57 (Crown18-c), 70.51 (Crown18-c), 70.42 (Crown18-a), 69.28 (Crown18-b), 64.62 (9-$\underline{CH_2}$-CH_3), 52.62 (2'-Me), 50.74 (Crown18-b), 48.32 (Crown18-b), 14.17 (9'-CH_2-$\underline{CH_3}$). Two missing carbon resonances from the aza-18-crown-6 residue, which most likely overlap with the other crown ether resonances.

HRMS (ESI −): *m/z* found: 616.21400, calc. for $[C_{29}H_{34}N_3O_{12}]^-$: 616.21480.

9.4.2 Synthesis of PQQMe$_2$-aza-crown-5 (**31**) *via* CDI Coupling

Dimethyl 7-(1,4,7,10-tetraoxa-13-azacyclopentadecane-13-carbonyl)-4,5-dioxo-4,5-dihydro-1*H*-pyrrolo[2,3-*f*]quinoline-2,9-dicarboxylate

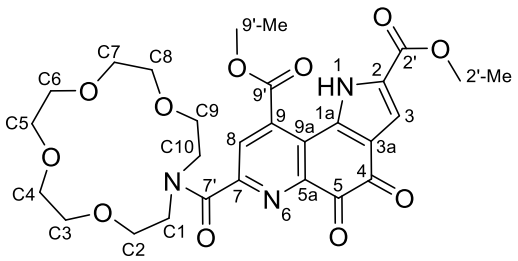

All glassware was given in an aqueous, EDTA containing bath overnight, to remove remaining metal ions from the surface, which could otherwise coordinate to the ligand.

Under nitrogen atmosphere, PQQMe$_2$·0.68 H_2O (**19**) (100 mg, 0.27 mmol, 1.00 equiv.) and CDI (54 mg, 0.33 mmol, 1.22 equiv.) were dissolved in dry DMF (5 mL). 1-Aza-15-crown-5 (74 mg, 0.33 mmol, 1.22 equiv.) was separately dissolved in a small amount of dry DMF (100 µL) under nitrogen atmosphere and was added along with dry TEA (77.4 µL, 0.56 mmol, 2.07 equiv.) under nitrogen atmosphere. The dark brown reaction mixture was stirred for 19 h at room temperature. DMF was removed *in vacuo*. To remove any remaining DMF from the sample, the residue was left under high vacuum for 24 h. The solid was dissolved in water (40 mL) and extracted with DCM (3 x 80 mL). The combined organic phases were washed with brine and dried over sodium sulfate. After filtration, the solvent was evaporated *in vacuo* and the crude product was further dried under high vacuum to afford the title compound (**31**) (84 mg, 0.15 mmol, 56%). as a light brown solid.

^{1}H-NMR (400 MHz, DMSO-*d*$_6$): δ / ppm = 8.20 (s, 1H, 8), 7.26 (s, 1H, 3), 4.03 (s, 3H, 9'-Me), 3.88 (s, 3H, 2'-Me), 3.78 – 3.49 (m, 20H, C1-C10).

^{13}C-NMR (100 MHz, DMSO-*d*$_6$): δ / ppm = 177.59 (5), 173.29 (4), 166.87 (9'), 166.74 (7'), 160.01 (2'), 152.79 (5a/7), 147.14 (5a/7), 134.30 (1a), 134.22 (9), 127.77 (8), 126.27 (2/3a), 124.51 (9a), 124.28 (2/3a), 113.92 (3), 70.19 (C1-C10), 70.14 (C1-C10), 69.60 (C1-C10), 69.56 (C1-C10), 69.51 (C1-C10), 69.38 (C1-C10), 69.34 (C1-C10), 67.82 (C1-C10), 54.06 (9'-Me), 52.25 (2'-Me), 50.67 (C1-C10), 48.61 (C1-C10).

Assignments based on 2D-NMR HMBC- and HMQC- spectra. Integral value for the crown ether corresponding multiplet is too high, since traces of unreacted 1-Aza-15-crown-5 are still present.

HRMS (ESI −): *m/z* calc. for $[C_{26}H_{28}N_3O_{11}]^-$: 558.1729, found: 558.1734.

IR (Diamond-ATR, neat): $\tilde{\nu}$ / cm^{-1} = 2861 (w, H_2O), 1715 (m, COOMe), 1682 (m, C=O), 1627 (m, C=O), 1435 (m, C=N), 1236 (s, C-O-C), 1205 (s, C-O-C), 1111 (s, C-O-C), 999 (s), 930 (m), 765 (m).

Elemental Analysis (CHN): Found: C 54.78; H 5.56; N 7.76. Calc. for $[C_{26}H_{29}N_3O_{11}\cdot 2.41\ H_2O\cdot 0.33C_{16}H_{10}N_2O_8\cdot 0.22C_3H_7NO]$: C, 54.78; H, 5.56; N, 7.76.

9.4.3 Synthesis of PQQMe$_2$-aza-crown-6 (**58**) *via* CDI Coupling

Dimethyl 7-(1,4,7,10,13-pentaoxa-16-azacyclooctadecane-16-carbonyl)-4,5-dioxo-4,5-dihydro-1*H*-pyrrolo[2,3-*f*]quinoline-2,9-dicarboxylate

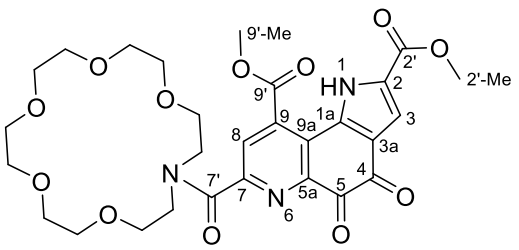

All glassware was given in an aqueous, EDTA containing bath overnight, to remove remaining metal ions from the surface, which could otherwise coordinate to the ligand.

Under nitrogen atmosphere, PQQMe$_2$·0.68 H_2O (**19**) (101 mg, 0.27 mmol, 1.00 equiv.) and CDI (54.4 mg, 0.34 mmol, 1.26 equiv.) were dissolved in dry DMF (5 mL). 1-Aza-18-crown-6 (88.3 mg, 0.33 mmol, 1.22 equiv.) was separately dissolved in a small amount of dry DMF

(100 µL) under nitrogen atmosphere and was added along with dry TEA (77.4 µL, 0.56 mmol, 2.07 equiv.). The dark brown reaction mixture was stirred for 24 h at room temperature. DMF was removed *in vacuo*. To remove any remaining DMF, the dark-brown solid was taken up in water (10 mL) and lyophilized (Christ Alpha) for 24 h. The received solid was dissolved in water (20 mL) and extracted with DCM (3 x 25 mL). After the second extraction, no phase separation occurred, whereby additional brine was added (10 mL). The organic phases were combined, washed with water (3 x 150 mL) and brine (3 x 10 mL) and dried over sodium sulfate. After filtration, the solvent was evaporated *in vacuo* and the crude product was further dried under high vacuum to afford the title compound (**58**) (99 mg, 0.16 mmol, 61%). as a light brown solid.

^{1}H-NMR (400 MHz, DMSO-d_6**):** δ / ppm = 8.18 (s, 1H, 8), 7.25 (s, 1H, 3), 4.02 (s, 3H, 9'-Me), 3.87 (s, 3H, 2'-Me), 3.78 – 3.43 (m, 24H, C1-C12).

^{13}C-NMR (100 MHz, DMSO-d_6**):** δ / ppm = 173.24 (4), 166.88 (9'), 166.66 (7'), 160.14 (2'), 152.68 (5a/7), 147.01 (5a/7), 134.57 (1a), 134.34 (9), 127.76 (8), 126.58 (2/3a), 124.71 (9a), 124.27 (2/3a), 114.01 (3), 70.02 (C1-C12), 69.97 (C1-C12), 69.94 (C1-C12), 69.89 (C1-C12), 69.85 (C1-C12), 69.76 (C1-C12), 69.61 (C1-C12), 69.30 (C1-C12), 68.09 (C1-C12), 67.83 (C1-C12), 54.02 (9'-Me), 52.20 (2'-Me), 49.26 (C1-C12), 46.81 (C1-C12).

Assignments based on 2D-NMR HMBC- and HMQC- spectra. Resonance for quinone C5 is missing. Resonances 134.57 (1a) and 126.58 (2/3a) only detectable *via* 2D coupling. Integral value for the crown ether corresponding multiplet is too high, since traces of unreacted 1-Aza-18-crown-6 are still present.

HRMS (ESI −): *m/z* calc. for $[C_{28}H_{32}N_3O_{12}]^-$: 602.1991; found: 602.1999.

IR (Diamond-ATR, neat): $\tilde{\nu}$ / cm^{-1} = 2867 (w, H_2O), 1714 (m, COOMe), 1683 (m, C=O), 1626 (m, C=O), 1434 (m, C=N), 1238 (s, C-O-C), 1204 (s, C-O-C), 1096 (s, C-O-C), 1002 (s), 935 (m), 767 (m).

Elemental Analysis (CHN): Found: C 52.92; H 5.73; N 7.41. Calc. for $[C_{28}H_{33}N_3O_{12}\cdot 1.53H_2O\cdot 0.40C_3H_7NO]$: C, 53.11; H, 5.93; N, 7.21.

9.5. Preparation of Dry Metal Perchlorate Solutions in Acetonitrile

9.5.1 General Procedure

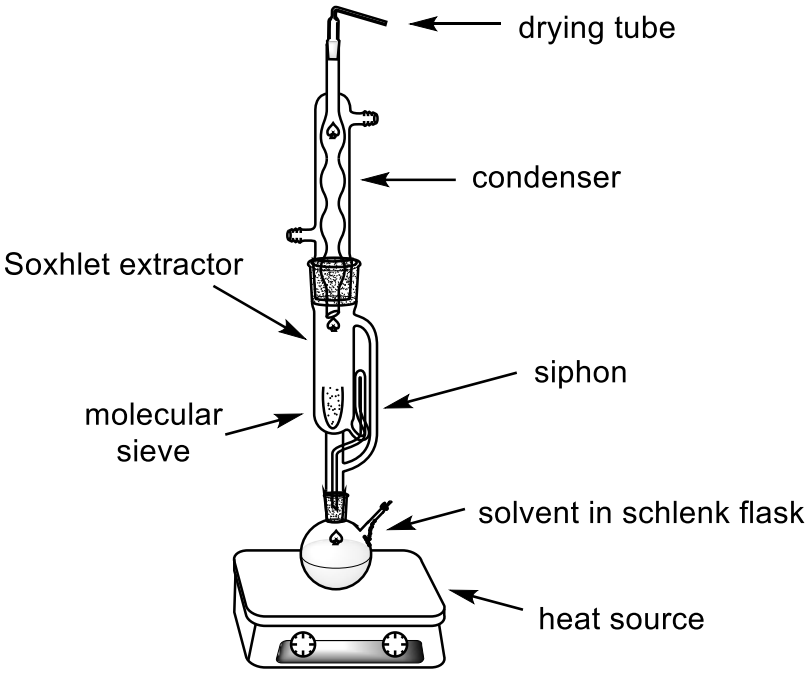

Figure VIII.3: Experimental set-up containing a Soxhlet extraction device for preparation of dry metal perchlorate solutions in acetonitrile.

To prepare dry acetonitrile solutions of perchlorate salts, a literature known procedure was performed.[300] The corresponding salt was placed in a dry and nitrogen flushed Schlenk flask and dissolved in dry acetonitrile. Activated molecular sieve (3 Å) was placed in a Soxhlet extraction device. The Schlenk flask was added to the Soxhlet device under nitrogen counterflow. The solution was heated to reflux (125°C) and stirred for 26 – 71 h at that temperature.

$Ca(ClO_4)_2 \cdot 4H_2O$ (118.7 mg, 0.382 mmol) was dissolved in acetonitrile (250 mL) under nitrogen atmosphere. The calcium perchlorate containing acetonitrile solution was refluxed for 26 h.

$La(ClO_4)_3 \cdot 6H_2O$ (259.6 mg, 0.476 mmol) was dissolved in acetonitrile (250 mL) under nitrogen atmosphere. The lanthanum perchlorate containing acetonitrile solution was refluxed for 71 h.

9.5.2 Determination of the Metal Content of $Ca(ClO_4)_2$ Containing Acetonitrile Solution

Eriochrome Black T is a known complexometric indicator, originally used for Ca^{2+} and Mg^{2+} determination,[301] but successfully applied for Ln^{3+} determination as well.[302] The calcium concentration of the dry $Ca(ClO_4)_2$ acetonitrile solution was determined spectrophotometrically by complexometric titration with Eriochrome Black T as indicator. For this purpose, Eriochrome Black T (10.1 mg, 21.8 µmol) was dissolved in aqueous CAPS buffer (10 mL, 20 mM, pH 10.45) resulting in a concentration of 2.19 mM. For the measurements, the Eriochrome Black solution (2.19 mM, 750 µL) was further diluted with Caps buffer (6750 µL, 10:1 dilution) resulting in a concentration of 0.219 mM.

$Ca(ClO_4)_2 \cdot 4H_2O$ (6.5 mg, 20.9 µmol) was dissolved in acetonitrile (10.45 mL) to obtain a stock solution with a known concentration of 2.0 mM.

An Epoch 2 Plate Reader from Biotek was used with a 96 well quartz microplate from Hellma, treated with EDTA solution prior to measurements, to remove any metal ions remaining on the well plate.

The volumes used for the respective measurements are summarized in Table VIII.11 and Table VIII.12. The received spectra are provided in Figure VIII.4.

Table VIII.11: UV-Vis titration of Eriochrome Black T with Ca^{2+} for the determination of a calibration line and determination of the calcium content of a calcium perchlorate solution of unknown concentration.

	Eriochrome Black T - Buffer Solution – 0.219 mM [µL]	Acetonitrile [µL]	Defined calcium perchlorate solution - 2 mM [µL]	Calcium concentration in 200 µL solution [µM]
1. Sample	190	10	0	0
2. Sample	190	9	1	10
3. Sample	190	8	2	20
4. Sample	190	7	3	30
5. Sample	190	6	4	40
6. Sample	190	5	5	50
7. Sample	190	4	6	60
8. Sample	190	3	7	70
9. Sample	190	2	8	80
10. Sample	190	1	9	90
11. Sample	190	0	10	100

Table VIII.12: UV-Vis titration of Eriochrome Black T with a calcium perchlorate solution of unknown concentration.

	Eriochrome Black T - Buffer Solution – 0.219 mM [µL]	Acetonitrile [µL]	Calcium perchlorate solution of unknown concentration [µL]
1. Sample	190	9	1
2. Sample	190	7	3
3. Sample	190	5	5
4. Sample	190	3	7
5. Sample	190	1	9

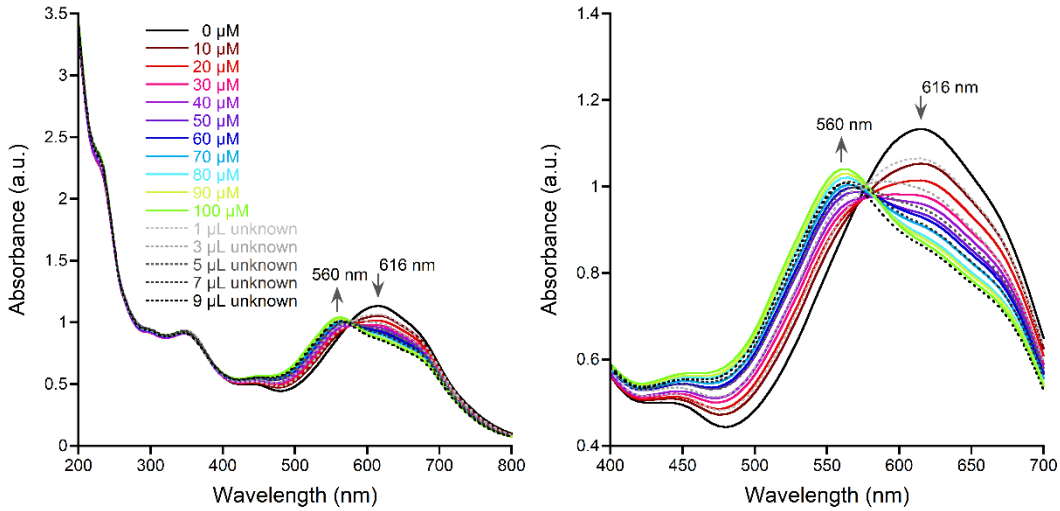

Figure VIII.4: Spectrophotometric titration of Eriochrome Black T (208 µM) in CAPS buffer (20 mM, pH 10.45) with solutions of $Ca(ClO_4)_2$ in acetonitrile. Known Ca^{2+} concentrations between 0 – 100 µM as solid colored lines for determination of a calibration line, unknown Ca^{2+} concentration with different volumina of the solution with unknown concentration as dottet line in shades of grey.

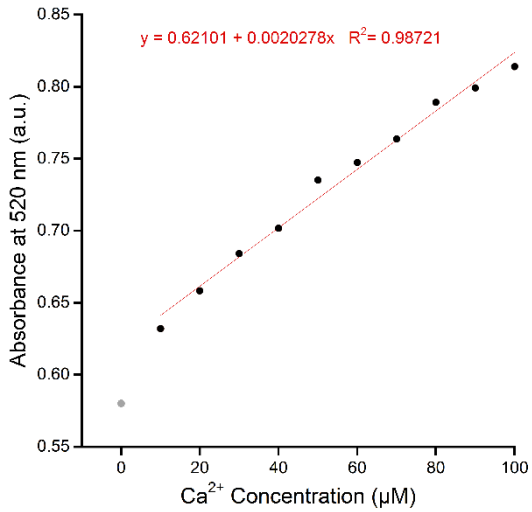

Figure VIII.5: Calibration line for the relation between Ca^{2+} concentration and the absorbance of Eriochrome Black T at 520 nm. The 0-value was not taken into account for calculation, as it would have caused large deviations.

The absorbance at 520 nm was used instead of the increasing maximum at 560 nm. Due to the close proximity to the isosbestic point, the absorption was subject to fluctuations, resulting in larger standard deviations than using the 520 nm absorbance. Table VIII.13 gives a summary over relevant values for absorbance at 520 nm and calculated concentrations.

Table VIII.13: Absorbance of Eriochrome Black T at 520 nm for different Ca^{2+} concentrations or after addition of different amounts of a $Ca(ClO_4)_2$ solution in acetonitrile with unknown concentration. Determined concentrations of the $Ca(ClO_4)_2$ solution in the 200 µL microplate well and resulting concentrations of the $Ca(ClO_4)_2$ solution itself.

Conc. (µM)	0	10	20	30	40	50	60	70	80	90	100
Absorbance at 520 nm (a.u.)	0.580	0.632	0.658	0.684	0.702	0.735	0.747	0.764	0.789	0.799	0.814
Solution with unknown Ca-concentration (µL)	1	3	5	7	9						
Absorbance at 520 nm (a.u.)	0.647	0.703	0.737	0.769	0.785						
Conc. in 200 µL well (µM)	13.01	40.38	57.35	72.93	80.72						
Conc. of solution with unknown Ca-conc. (mM)	2.60	2.69	2.29	2.08	1.79						

With the formula received from the calibration line given in Figure VIII.5, the concentration of the water-free $Ca(ClO_4)_2$ solution in acetonitrile was calulcated to be 2.3 mM with a standart deviation of 0.33 mM (2.29 ± 0.3 mM).

9.5.3 Determination of the Metal Content of $La(ClO_4)_3$ Containing Acetonitrile Solution

Similar to the procedure described above, also the lanthanum concentration of the dry $La(ClO_4)_3$ acetonitrile solution was determined spectrophotometrically.

Eriochrome Black T (10.3 mg, 22.3 µmol) was dissolved in aqueous CAPS buffer (10 mL, 20 mM, pH 10.45) resulting in a concentration of 2.23 mM. For the measurements, the Eriochrome Black solution (2.23 mM, 850 µL) was further diluted with Caps buffer (7650 µL, 10:1 dilution) resulting in a concentration of 0.223 mM.

$La(ClO_4)_2 \cdot 6H_2O$ (8.5 mg, 15.6 µmol) was dissolved in acetonitrile (7.79 mL) to obtain a stock solution with a known concentration of 2.0 mM.

An Epoch 2 Plate Reader from Biotek was used with a 96 well quartz microplate from Hellma, treated with EDTA solution prior to measurements, to remove any metal ions remaining on the well plate.

The volumes used for the respective measurements are summarized in Table VIII.14 and Table VIII.15. The received spectra are provided in Figure VIII.6

Table VIII.14: UV-Vis titration of Eriochrome Black T with La^{3+} for the determination of a calibration line and determination of the lanthanum content of a lanthanum perchlorate solution of unknown concentration.

	Eriochrome Black T - Buffer Solution – 0.223 mM [µL]	Acetonitrile [µL]	Defined lanthanum perchlorate solution - 2 mM [µL]	Lanthanum concentration in 200 µL solution [µM]
1. Sample	190	10	0	0
2. Sample	190	9	1	10
3. Sample	190	8	2	20
4. Sample	190	7	3	30
5. Sample	190	6	4	40
6. Sample	190	5	5	50
7. Sample	190	4	6	60
8. Sample	190	3	7	70
9. Sample	190	2	8	80
10. Sample	190	1	9	90
11. Sample	190	0	10	100

Table VIII.15: UV-Vis titration of Eriochrome Black T with a lanthanum perchlorate solution of unknown concentration.

	Eriochrome Black T - Buffer Solution – 0.223 mM [µL]	Acetonitrile [µL]	Lanthanum perchlorate solution of unknown concentration [µL]
1. Sample	190	9	1
2. Sample	190	7	3
3. Sample	190	5	5
4. Sample	190	3	7
5. Sample	190	1	9

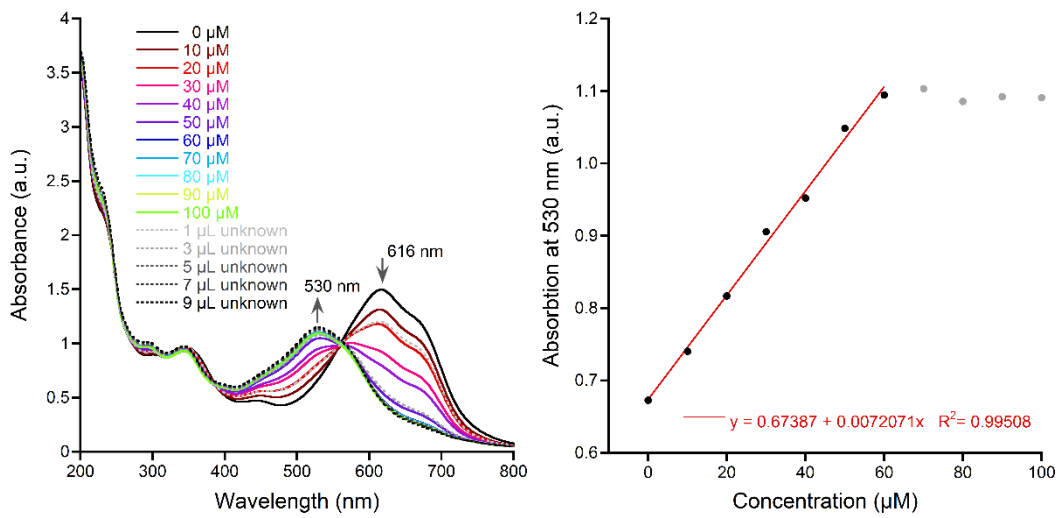

Figure VIII.6: Left: Spectrophotometric titration of Eriochrome Black T (212 µM) in CAPS buffer (20 mM, pH 10.45) with solutions of $La(ClO_4)_2$ in acetonitrile. Known La^{3+} concentrations between 0 – 100 µM as solid colored lines for determination of a calibration line, unknown La^{3+} concentration with different volumina of the solution with unknown concentration as dottet lines in shades of grey. Right: Calibration line for the relation between La^{3+} concentration and the absorbance of Eriochrome Black T at 530 nm. Saturation occurred after a La^{3+} concentration of approximately 60 µM. Values above that concentration were not considered for the calibration line (grey dots).

The increasing absorbance at 530 nm was used for the calibration line and for determination of the lanthanum content of the water-free $La(ClO_4)_3$ solution in acetonitrile. Table VIII.16 gives a summary over relevant values for absorbance at 530 nm and calculated concentrations.

Table VIII.16: Absorbance of Eriochrome Black T at 530 nm for different La^{3+} concentrations or after addition of different amounts of a $La(ClO_4)_3$ solution in acetonitrile with unknown concentration. Determined concentrations of the $La(ClO_4)_3$ solution in the 200 µL microplate well and resulting concentrations of the $La(ClO_4)_3$ solution itself. Saturation occurred for the $La(ClO_4)_3$ solution in acetonitrile with unknown concentration and titrations with 5 – 9 µL of this solution could not be taken into account.

Conc. (µM)	0	10	20	30	40	50	60	70	80	90	100
Absorbance at 530 nm (a.u.)	0.673	0.740	0.817	0.906	0.952	1.049	1.095	1.103	1.086	1.092	1.091
Solution with unknown La-concentration (µL)	1	3	5	7	9						
Absorbance at 530 nm (a.u.)	0.810	1.074	1.123	1.133	1.150						
Conc. in 200 µL well (µM)	18.87	55.46	-	-	-						
Conc. of solution with unknown La-conc. (mM)	3.77	3.70	-	-	-						

With the formula received from the calibration line given in Figure VIII.6, the concentration of the water-free $La(ClO_4)_3$ solution in acetonitrile was calulcated to be 3.7 mM with a standart deviation of 0.04 mM (3.74 ± 0.04 mM).

9.5.4 Spectrophotometric Titrations of **31** and **58** with Ca and La

Table VIII.17: Titration of aza-crown ether ligands **31** or **58** in dry acetonitrile (1.5 mM) with increasing amounts of $La(ClO_4)_3$ (3.74 ± 0.04 mM) or $Ca(ClO_4)_2$ (2.29±0.3 mM) in dry acetonitrile. Constant total volume of 3 mL (25 µM **31** or **58**) in a quartz suprasil cuvette (d = 1 cm) with a rubber septum. Cuvette was deaerated with N_2 for 3 min prior to each measurement.

Components	V (**31** or **58**)) [µL]	V (metal salt) [µL]	V (MeCN) [µL]
Ligand	50	0	2950
0.31 Ca^{2+} equiv.	50	10	2940
0.61 Ca^{2+} equiv.	50	20	2930
1.19 Ca^{2+} equiv.	50	39	2911
3.60 Ca^{2+} equiv.	50	118	2832
6.02 Ca^{2+} equiv.	50	197	2753
8.43 Ca^{2+} equiv.	50	276	2674
0.25 La^{3+} equiv.	50	5	2945
0.50 La^{3+} equiv.	50	10	2940
0.75 La^{3+} equiv.	50	15	2935
1.00 La^{3+} equiv.	50	20	2930
1.50 La^{3+} equiv.	50	30	2920
2.49 La^{3+} equiv.	50	50	2900
3.99 La^{3+} equiv.	50	80	2870
4.49 La^{3+} equiv.	50	90	2860
4.99 La^{3+} equiv.	50	100	2850
9.97 La^{3+} equiv.	50	200	2750

IX. APPENDIX

1. Supporting Information

1.1. Supporting Information of Chapter II.2

1.1.1 Experimental Section

DFT calculations. Structure optimizations were performed using Gaussian 09[79] and the B3LYP functional with the 6-31G(d) basis set for C, H, N, O.[80-84, 303] Quasi relativistic effective core potentials (ECP) were used for the central metal: MWB46 for La^{3+}, 47 for Ce^{3+}, 48 for Pr^{3+}, 52 for Eu^{3+}, 59 for Yb^{3+} (Figure II.1, Figure IX.1 and Figure IX.2).[86-88] Calculations were performed with 11 outer sphere electrons, as pseudo-singlets (f-electrons included in ECP) and restricted closed-shell calculations. None of the frequency calculations showed negative values. Starting point of the geometry optimization was the active site of the crystal structure of Ce-MDH isolated from SolV (4MAE) with exchange of Ce^{3+} with La^{3+}, Pr^{3+}, Yb^{3+} and Eu^{3+} respectively. Based on the method from Schelter *et al.* the amino acid residues and the polyethylene glycol, present in the crystal structure were truncated and the anchoring carbon atoms were frozen in their crystallographic position to mimic the sterics imposed by the protein.[76] For simplification only the cofactor PQQ and the amino acids directly coordinating to the metal ions were included in the calculations.

1.1.2 Supporting Information

Figure IX.1 Example input for Gaussian optimizations. -1 denotes a frozen carbon atom.

```
%chk=Eu(III)-aktives Zentrum-vereinfacht-singlet.chk
%mem=60GB
%nprocshared=8
#p opt freq rb3lyp/gen nosymm geom=connectivity 5d 7f pseudo=read

Eu(III) - aktives Zentrum-vereinfacht
Singulett

0 1
C      -1   -4.90400000   3.34400000   3.52500000
C       0   -4.43100000   2.75000000   2.21200000
O       0   -5.31600000   2.48300000   1.32700000
O       0   -3.21300000   2.47700000   2.02300000
C      -1   -7.59200000   1.55900000  -2.75400000
C       0   -6.78400000   1.98800000  -1.55100000
O       0   -5.53400000   1.90100000  -1.57100000
N       0   -7.44100000   2.47100000  -0.49176943
C      -1   -7.57000000  -2.04200000   0.45144469
C       0   -6.14900000  -1.61500000   0.75161945
O       0   -5.81500000  -0.46701986   0.29292243
O       0   -5.39000000  -2.35900000   1.42100000
C      -1   -3.16200000  -0.96440872  -4.27600000
C       0   -3.96500000  -0.84870079  -2.97500000
O       0   -5.10800000  -1.31100000  -2.91900000
O       0   -3.34000000  -0.27056742  -1.98200000
N       0    3.33000000  -0.81662988   1.47900000
C       0    3.61300000  -2.05900000   1.97300000
C       0    5.01500000  -2.49400000   2.20800000
O       0    5.88200000  -1.54200000   1.91200000
O       0    5.26800000  -3.61500000   2.62500000
C       0    2.41800000  -2.74800000   2.13600000
C       0    1.39400000  -1.87800000   1.71500000
C       0    1.99200000  -0.65850047   1.29400000
C       0   -0.03196565  -2.09600000   1.68300000
O       0   -0.65585683  -3.02200000   2.17600000
C       0   -0.80639866  -0.98447544   0.95671480
O       0   -1.97200000  -1.16300000   0.63270177
C       0   -0.13660882   0.31747211   0.63836618
N       0   -0.97622754   1.23100000   0.17358237
C       0   -0.50347008   2.43600000  -0.15877326
C       0   -1.51600000   3.38500000  -0.69429278
O       0   -2.68200000   3.07700000  -0.90161786
O       0   -1.02900000   4.60100000  -0.94685640
C       0    0.84871874   2.74100000  -0.04652754
C       0    1.77100000   1.78600000   0.39850560
C       0    3.21000000   2.20900000   0.35976671
O       0    3.37200000   3.51000000   0.13590368
O       0    4.17700000   1.46400000   0.47970217
C       0    1.28200000   0.49657896   0.78449450
O       0   -3.93300000  -0.32848794   2.35300000
C       0   -3.16200000  -0.45069210   3.55200000
C      -1   -4.04600000  -0.73580415   4.76200000
H       0   -7.34200000   2.20600000  -3.60200000
H       0   -7.28400000   0.54246200  -3.01600000
H       0   -8.67000000   1.59400000  -2.58300000
H       0   -7.70800000  -2.10900000  -0.63361256
H       0   -7.80300000  -3.00600000   0.90925659
H       0   -8.26700000  -1.28200000   0.82000108
H       0   -5.67800000   4.09600000   3.34900000
H       0   -5.35100000   2.54500000   4.12900000
H       0   -4.07300000   3.78100000   4.08500000
H       0   -4.78000000   0.06458975   4.90600000
H       0   -4.58800000  -1.67900000   4.63500000
H       0   -3.43600000  -0.81454479   5.67000000
H       0   -2.63900000   0.50250317   3.66600000
H       0   -2.41400000  -1.24600000   3.43300000
H       0   -2.74100000   0.00689772  -4.55900000
H       0   -2.32100000  -1.65000000  -4.12400000
H       0   -3.79400000  -1.34200000  -5.08200000
H       0    4.34900000   3.70100000  -0.00827955
H       0    1.19100000   3.72400000  -0.32958075
H       0    6.90200000  -1.87400000   1.98800000
H       0   -1.75500000   5.14900000  -1.30300000
H       0    4.02400000  -0.11676026   1.22800000
H       0    2.30000000  -3.76900000   2.46200000
H       0   -8.45000000   2.47400000  -0.46268410
H       0   -6.90800000   2.66300000   0.35974909
H       0   -4.37900000  -1.19400000   2.13400000
Eu      0   -3.90000000   0.86148825   0.01088327

1 2 1.0 50 1.0 51 1.0 52 1.0
2 3 1.5 4 1.5
3 70 1.0
4 70 1.0
5 6 1.0 44 1.0 45 1.0 46 1.0
6 7 2.0 8 1.5
7 70 1.0
8 67 1.0 68 1.0
9 10 1.0 47 1.0 48 1.0 49 1.0
10 11 1.5 12 1.5
11 70 1.0
12
13 14 1.0 58 1.0 59 1.0 60 1.0
14 15 1.5 16 1.5
15 70 1.0
16 70 1.0
17 18 1.5 24 1.5 65 1.0
18 19 1.0 22 1.5
19 20 1.5 21 2.0
20 63 1.0
21
22 23 1.5 66 1.0
23 24 1.5 25 1.5
24 40 1.0
25 26 2.0 27 1.0
26
27 28 2.0 29 1.0
28 70 1.0
29 30 1.5 40 1.5
30 31 1.5 70 1.0
31 32 1.0 35 1.5
32 33 2.0 34 1.5
33 70 1.0
34 64 1.0
35 36 1.5 62 1.0
36 37 1.0 40 1.5
37 38 1.5 39 2.0
38 61 1.0
39
40
41 42 1.0 69 1.0 70 1.0
42 43 1.0 56 1.0 57 1.0
43 53 1.0 54 1.0 55 1.0
44
45
46
47
48
49
50
51
52
53
54
55
56
57
58
59
60
61
62
63
64
65
66
67
68
69
70

C H N O 0
6-31G(d)
****
Eu 0
MWB52
****

Eu 0
MWB52
```

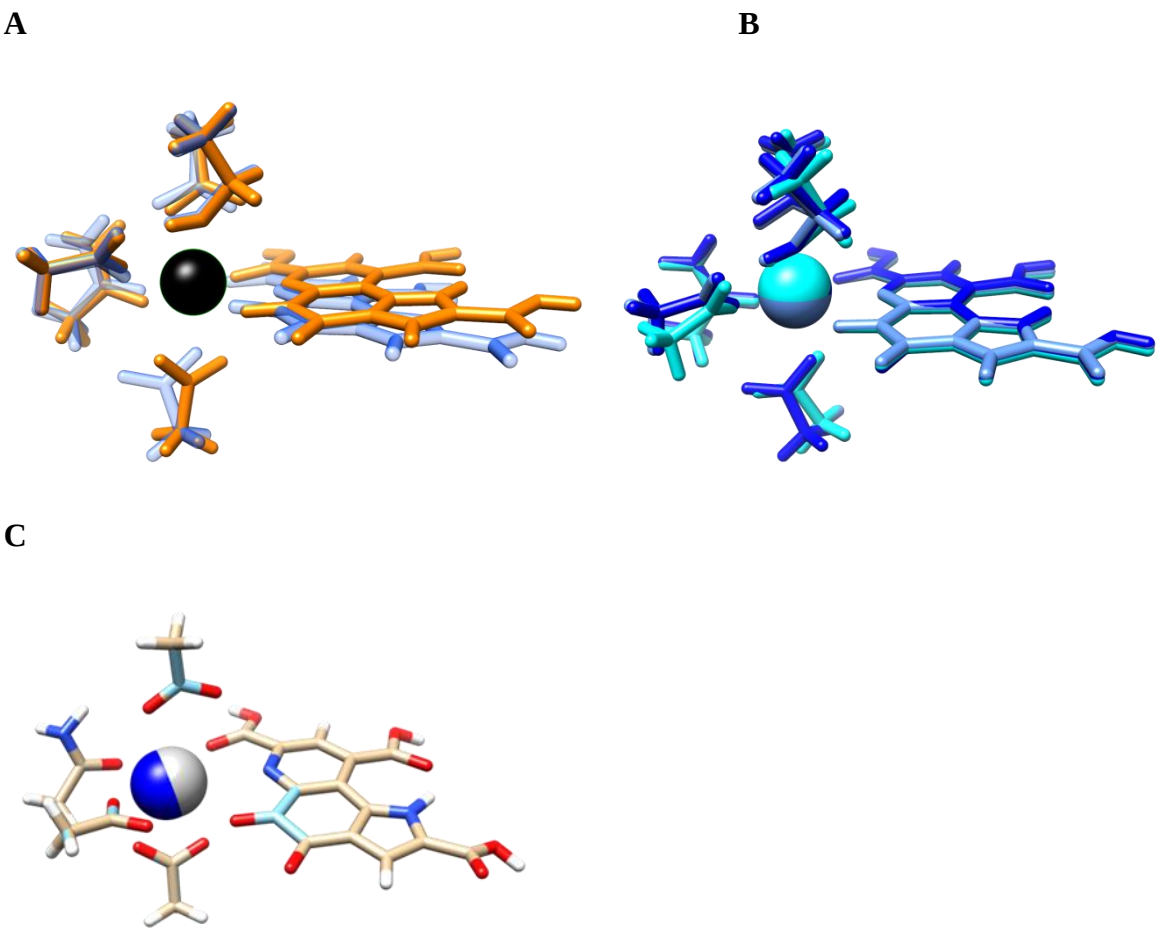

Figure IX.2: A Overlay of the Eu (blue) and Ce (orange) optimized structures (aligned by the frozen carbon atoms of the amino acids). The structures were obtained using the same level of theory as in Figure II.1. The most significant deviation observed was a shift of the PQQ residue and a change in coordination mode of Asp301. B Overlay of Eu structures where either all anchoring amino acid carbon atoms were frozen (dark blue), all but Asp301 (light blue) and none (cyan). The structures were obtained using the same level of theory as in Figure II.1. Starting point for the calculations was the crystal structure of Ce-MDH. In all optimized structures Asp301 is monodentate (when the substrate was included), demonstrating that the change in coordination mode from bidentate to monodentate is due to the central atom in the active site and not due to freezing the amio acid carbon atoms in their position. C Calculated active site structures (residues) superimposed, starting from the Eu crystal structure without substrate in the active site. All residue- and PQQ-atoms frozen but Eu was let to refine freely (Eu(III) in blue, Eu(II) in grey).

1.2. Supporting Information of Chapter II.3

1.2.1 Materials and Methods

DFT Calculations

Electronic-structure calculations for determination of the redox-cycling for the Ce^{3+} PQQ^0 and Ce^{3+} $PQQ^{\bullet-}$ species were performed with Gaussian 09[79] as described by Schelter *et al.*[76] Example input-files for all calculations are given in the SI (Figure IX.5,8,10 and 12-14). The B3LYP functional with the 6-31G(d) basis set for C, H, N, O was used.[94] 28 electron quasi relativistic effective core potentials (ECP) and segmented basis sets were used for the central metal: MWB28.[286-287] Starting point of the geometry optimization was the active site of the crystal structure of Ce-MDH isolated from SolV (4MAE). The present amino acids in the active site were truncated and the terminal carbon atoms were frozen to mimic the sterics imposed by the protein. The present polyethylenglycol was truncated as well and used as a substrate-model. The conductor-like polarizable continuum model (CPCM) was used for water, with the default settings for the universal force field (UFF) and a dielectric constant of 4, to reproduce the interior of the protein and the active site. For additional calculations with alternative Ln, the central metal in the input file was exchanged with La or Lu and the used ECP was changed accordingly. Structure optimizations for the preferred coordination number were performed in a similar manner, but with several simplifications for computational savings. Again, the B3LYP functional with the 6-31G(d) basis set for C, H, N, O was used, but larger ECPs for the central metal: MWB46+4f^n (e.g. 59 for Yb^{3+}). Calculations were performed with 11 outer-sphere electrons, as pseudo-singlets (f-electrons included in ECP) and restricted closed-shell calculations in the gas phase. The present amino acids in the active site were reduced to the actual coordinating ones (Glu172, Asn256, Asp299, Asp301), which were truncated and the terminal carbon atoms, as well as all of the PQQ-atoms were frozen. The present polyethylenglycol was truncated as well but not frozen. The cerium atom was then exchanged with every Ln in the series. In case of Gd, the Harris functional was not able to form the initial guess, therefore the core Hamiltonian was used instead, using “guess=(core,always)”. Test calculations with solvent model (CPCM=Water), with the right spin state (smaller ECP-MWB28) or unfrozen amino acids slightly influenced the overall structure, but had no influence on the coordination numbers. For additional active center calculations, the truncated polyethylene glycol residue was manually removed, and/or the PQQ-quinone part was manually converted to a quinol. For simplification, the added quinol protons were frozen as well in their position.

Kinetic Experiments

Protein purification, handling and concentration determination were conducted after a previously reported protocol.[94] *Plate-reader assay with different metal ions* (as shown in Figure II.4): A phenazine ethosulfate (PES, ≥ 95 %, Sigma-Aldrich) and 2,6-Dichlorophenolindophenol (DCPIP, sodium salt dihydrate, ≥ 90 %, Fluka) dye-coupled assay at 45°C was used for this experiment using 96 well microtiter plates and the Epoch2 plate reader from BioTek, Winooski, VT, USA. A commonly used protocol is shown in Figure IX.3. Each well contained 185 µL assay mix (20 mM PIPES (1,4-Piperazinediethanesulfonic acid, ≥ 99%, BioPerformance certified, Sigma) pH 7.2, 100 µM DCPIP, 1 mM PES and 1 mM KCN) and Eu-MDH enzyme (200 nM) and this mixture was incubated for 2 minutes at 45°C. The assay mix without enzyme had been previously incubated at 45°C for 15 minutes in the dark to alleviate background reactions. Then 10 µL of freshly prepared 0.4 mM stock solutions of each Ln^{3+} chloride salt were added to each well ($LaCl_3 \cdot 7H_2O$, $CeCl_3 \cdot 7H_2O$, $PrCl_3 \cdot 7H_2O$, $NdCl_3 \cdot 6H_2O$, $SmCl_3$, $EuCl_3 \cdot 6H_2O$, $GdCl_3 \cdot 6H_2O$, $TbCl_3 \cdot 6H_2O$, $DyCl_3$, $HoCl_3 \cdot 6H_2O$, $ErCl_3 \cdot 7H_2O$, $TmCl_3 \cdot 6H_2O$, $YbCl_3 \cdot 6H_2O$, $LuCl_3 \cdot 6H_2O$, all minimum of ≥ 99.9 % purity, ABCR). Water was added to one control well in each row. The consumption of residual MeOH which had to be added for storage of the protein, was monitored at 600 nm for 2 minutes before 10 µL of a 1M solution of MeOH (final concentration ~ 50 mM, HPLC grade, Fisher Chemical) were added for a final volume of 205 µL in each well and the oxidation reaction was monitored at 600 nm. An average of six measurements (three experimental replicates with two technical replicates each) was taken to calculate specific activities (SA) and an extinction coefficient of 18.5 $cm^{-1} \cdot mM^{-1}$ for DCPIP at pH 7.2 in PIPES buffer was used. Initial rates (the first 3 min of the slope after methanol addition) were used for the calculation of the SA. The SA of MDH without added metal ions was normalized to 1, while the SA of each of the assays with Ln was normalized by dividing through the activity of MDH without added metal ions. No background reaction of the assay mix (without enzyme) with added metal ions was observed. Metal titrations (shown in Figure II.3) with La^{3+}, Pr^{3+}, Nd^{3+} and Eu^{3+} were fit using the Michaelis-Menten equation (6).

$$\nu_0 = \frac{\nu_{max} \cdot [S]}{K_M + [S]} \tag{6}$$

with ν_0 being the initial velocity, ν_{max} being the maximum turnover speed, [S] being the substrate concentration and K_M being the Michaelis-Menten constant. But in the case of metal titrations K_M denotes K_{assoc}, the metal association constant and [S] not substrate but metal ion concentration. The SA was normalized by subtracting the activity without added metal ions

from the values. Here the same concentrations of assay components as above were used, however, the 10 µL of the metal stock solutions contained different concentrations of Ln to achieve the final concentrations of 0, 0.25, 1, 2, 5, 10 and 20 µM. Measuring specific activities of the mixtures of Lu and La, Nd and Eu respectively (Figure II.7), was done using the same plate reader assay as with the different metal ions (as shown in Figure II.4) but 100 denotes 100% of either La, Nd or Eu (20 µM), 75 (15 µM La, Nd or Eu + 5 µM Lu), 50 (10 µM La, Nd or Eu + 10 µM Lu), 25 (5 µM La, Nd or Eu + 15 µM Lu) and 0 (20 µM Lu). For the Michaelis-Menten kinetics, each well contained 185 µL assay mix (20 mM PIPES pH 7.2, 100 µM DCPIP, 1 mM PES and 1 mM KCN) and Eu-MDH enzyme (200 nM) as well as 10 µL $LnCl_3$ stock for a final concentration of 20 µM and incubated for 2 minutes at 45°C. Methanol concentrations varied from 0, 1, 2, 5, 10, 20, 50, 50000 µM. Here it was important to wait until background activity from storage methanol and endogenous substrate had ceased, hence a delay of 5 minutes was introduced until methanol was added.

$$\nu_0 = \frac{\nu_{max} \cdot [S]}{K_M + [S]} \tag{7}$$

The software KaleidaGraph 4.5 from synergy software was used to fit and plot all data.

1.2.2 Supporting Information

Read: (A) 600
Temperature: Setpoint 45 °C
Plate Out,In Add assay mix with enzyme
Shake: Linear for 0:10
Delay for 0:02:00
Plate Out,In Add 10uL 0.4mM metal stock solutions
Shake: Linear for 0:10
Start Kinetic [Run 0:02:00, Interval 0:00:11]
    Read: (A) 600
End Kinetic
Plate Out,In Add 10uL 1M methanol
Shake: Linear for 0:10
Start Kinetic [Run 0:03:00, Interval 0:00:11]
    Read: (A) 600
End Kinetic

Figure IX.3: Typical procedure for the Epoch 2 plate-reader assay with Eu-MDH and different lanthanide ions. The plate type used was a 96 well plate. A path length correction was applied (Path length Correction: 977 / 900, Absorbance at 1 cm: 0.18)

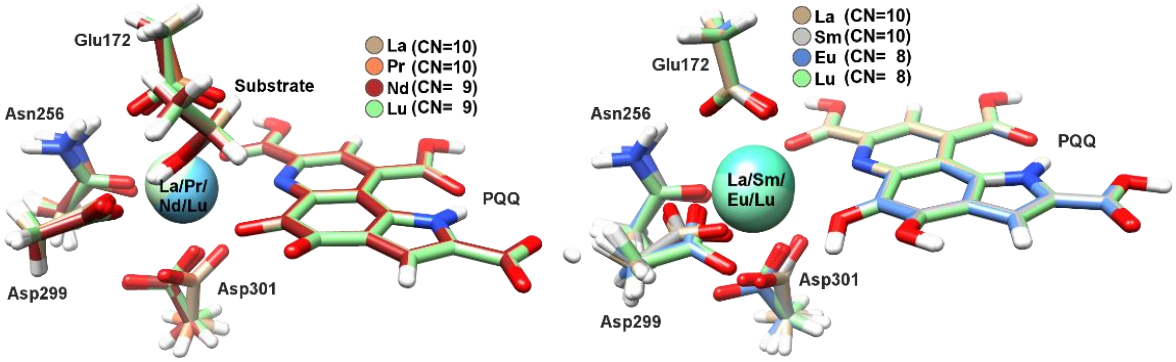

Figure IX.4: Left: Optimized Structures for the active center with PQQ^0, substrate and La (tan), Pr (light brown), Nd (brown) and Lu (green). Right: Optimized Structures for the active center with $PQQH_2$ and La (tan), Sm (grey), Eu (blue) and Lu (green) - Images generated with the UCSF Chimera package.[[41]] Structure optimizations were similar to a procedure described by Schelter *et al.*[[76]] and performed using Gaussian 09[[79]] and the B3LYP functional with the 6-31G(d) basis set for C, H, N, O.[[80-83, 85, 303]] Starting point was the crystal structure of the known Ce-MDH (PDB 4MAE).[[36]] The present amino acids in the active site were truncated and the terminal carbon atoms, as well as all of the PQQ-atoms were frozen, to mimic the sterics imposed by the protein. The present polyethylenglycol was truncated as well and used as a substrate-model. The cerium atom was then exchanged with every Ln in the series. Quasi relativistic effective core potentials (ECP) and segmented basis sets were used for the central metal: ECP-MWB46+$4f^n$.[[286-287, 304]] Calculations were performed with 11 outer sphere electrons, as pseudo-singlets (f-electrons included in ECP) and restricted closed-shell calculations.[89] Calculations were conducted in the gas phase. For additional active site calculations, the truncated polyethylene glycol residue was manually removed, and/or the PQQ-quinone part was manually converted to the quinol. For simplification, the added quinol protons were frozen as well in their position. In case of Gd, the Harris functional was not able to form the initial guess, therefore the core Hamiltonian was used instead, using “guess=(core,always)”. None of the calculations showed negative frequencies.

Figure IX.5: Example input for Gaussian optimizations (in this case La^{3+} PQQ with substrate). -1 denotes a frozen carbon atom.

```
%chk=57-LaIII-PQQ-with-Substrate.chk
%mem=64GB
%nprocshared=4
#p opt freq rb3lyp/gen geom=connectivity 5d 7f pseudo=read

La(III) - PQQ – with substrate

0 1
 C          -1  -4.90400000   3.34400000   3.52500000
 C           0  -4.43100000   2.75000000   2.21200000
 O           0  -5.31600000   2.48300000   1.32700000
 O           0  -3.21300000   2.47700000   2.02300000
 C          -1  -7.59200000   1.55900000  -2.75400000
 C           0  -6.78400000   1.98800000  -1.55100000
 O           0  -5.53400000   1.90100000  -1.57100000
 N           0  -7.44100000   2.47100000  -0.49176943
 C          -1  -7.57000000  -2.04200000   0.45144469
 C           0  -6.14900000  -1.61500000   0.75161945
 O           0  -5.81500000  -0.46701986   0.29292243
 O           0  -5.39000000  -2.35900000   1.42100000
 C          -1  -3.16200000  -0.96440872  -4.27600000
 C           0  -3.96500000  -0.84870079  -2.97500000
 O           0  -5.10800000  -1.31100000  -2.91900000
 O           0  -3.34000000  -0.27056742  -1.98200000
 N          -1   3.33000000  -0.81662988   1.47900000
 C          -1   3.61300000  -2.05900000   1.97300000
 C          -1   5.01500000  -2.49400000   2.20800000
 O          -1   5.88200000  -1.54200000   1.91200000
 O          -1   5.26800000  -3.61500000   2.62500000
 C          -1   2.41800000  -2.74800000   2.13600000
 C          -1   1.39400000  -1.87800000   1.71500000
 C          -1   1.99200000  -0.65850047   1.29400000
 C          -1  -0.03196565  -2.09600000   1.68300000
 O          -1  -0.65585683  -3.02200000   2.17600000
 C          -1  -0.80639866  -0.98447544   0.95671480
 O          -1  -1.97200000  -1.16300000   0.63270177
 C          -1  -0.13660882   0.31747211   0.63836618
 N          -1  -0.97622754   1.23100000   0.17358237
 C          -1  -0.50347008   2.43600000  -0.15877326
 C          -1  -1.51600000   3.38500000  -0.69429278
 O          -1  -2.68200000   3.07700000  -0.90161786
 O          -1  -1.02900000   4.60100000  -0.94685640
 C          -1   0.84871874   2.74100000  -0.04652754
 C          -1   1.77100000   1.78600000   0.39850560
 C          -1   3.21000000   2.20900000   0.35976671
 O          -1   3.37200000   3.51000000   0.13590368
 O          -1   4.17700000   1.46400000   0.47970217
 C          -1   1.28200000   0.49657896   0.78449450
 O           0  -3.93300000  -0.32848794   2.35300000
 C           0  -3.16200000  -0.45069210   3.55200000
 C          -1  -4.04600000  -0.73580415   4.76200000
 H           0  -7.34200000   2.20600000  -3.60200000
 H           0  -7.28400000   0.54246200  -3.01600000
 H           0  -8.67000000   1.59400000  -2.58300000
 H           0  -7.70800000  -2.10900000  -0.63361256
 H           0  -7.80300000  -3.00600000   0.90925659
 H           0  -8.26700000  -1.28200000   0.82000108
 H           0  -5.67800000   4.09600000   3.34900000
 H           0  -5.35100000   2.54500000   4.12900000
 H           0  -4.07300000   3.78100000   4.08500000
 H           0  -4.78000000   0.06458975   4.90600000
 H           0  -4.58800000  -1.67900000   4.63500000
 H           0  -3.43600000  -0.81454479   5.67000000
 H           0  -2.63900000   0.50250317   3.66600000
 H           0  -2.41400000  -1.24600000   3.43300000
 H           0  -2.74100000   0.00689772  -4.55900000
 H           0  -2.32100000  -1.65000000  -4.12400000
 H           0  -3.79400000  -1.34200000  -5.08200000
 H          -1   4.34900000   3.70100000  -0.00827955
 H          -1   1.19100000   3.72400000  -0.32958075
 H          -1   6.90200000  -1.87400000   1.98800000
 H          -1  -1.75500000   5.14900000  -1.30300000
 H          -1   4.02400000  -0.11676026   1.22800000
 H          -1   2.30000000  -3.76900000   2.46200000
 H           0  -8.45000000   2.47400000  -0.46268410
 H           0  -6.90800000   2.66300000   0.35974909
 H           0  -4.37900000  -1.19400000   2.13400000
 La          0  -3.90000000   0.86148825   0.01088327

1 2 1.0 50 1.0 51 1.0 52 1.0
2 3 1.5 4 1.5
3 70 1.0
4 70 1.0
5 6 1.0 44 1.0 45 1.0 46 1.0
6 7 2.0 8 1.5
7 70 1.0
8 67 1.0 68 1.0
9 10 1.0 47 1.0 48 1.0 49 1.0
10 11 1.5 12 1.5
11 70 1.0
12
13 14 1.0 58 1.0 59 1.0 60 1.0
14 15 1.5 16 1.5
15 70 1.0
16 70 1.0
17 18 1.5 24 1.5 65 1.0
18 19 1.0 22 1.5
19 20 1.5 21 2.0
20 63 1.0
21
22 23 1.5 66 1.0
23 24 1.5 25 1.5
24 40 1.0
25 26 2.0 27 1.0
26
27 28 2.0 29 1.0
28 70 1.0
29 30 1.5 40 1.5
30 31 1.5 70 1.0
31 32 1.0 35 1.5
32 33 2.0 34 1.5
33 70 1.0
34 64 1.0
35 36 1.5 62 1.0
36 37 1.0 40 1.5
37 38 1.5 39 2.0
38 61 1.0
39
40
41 42 1.0 69 1.0 70 1.0
42 43 1.0 56 1.0 57 1.0
43 53 1.0 54 1.0 55 1.0
44
45
46
47
48
49
50
51
52
53
54
55
56
57
58
59
60
61
62
63
64
65
66
67
68
69
70

C H N O 0
6-31G(d)
****
La 0
MWB46
****

La 0
MWB46
```

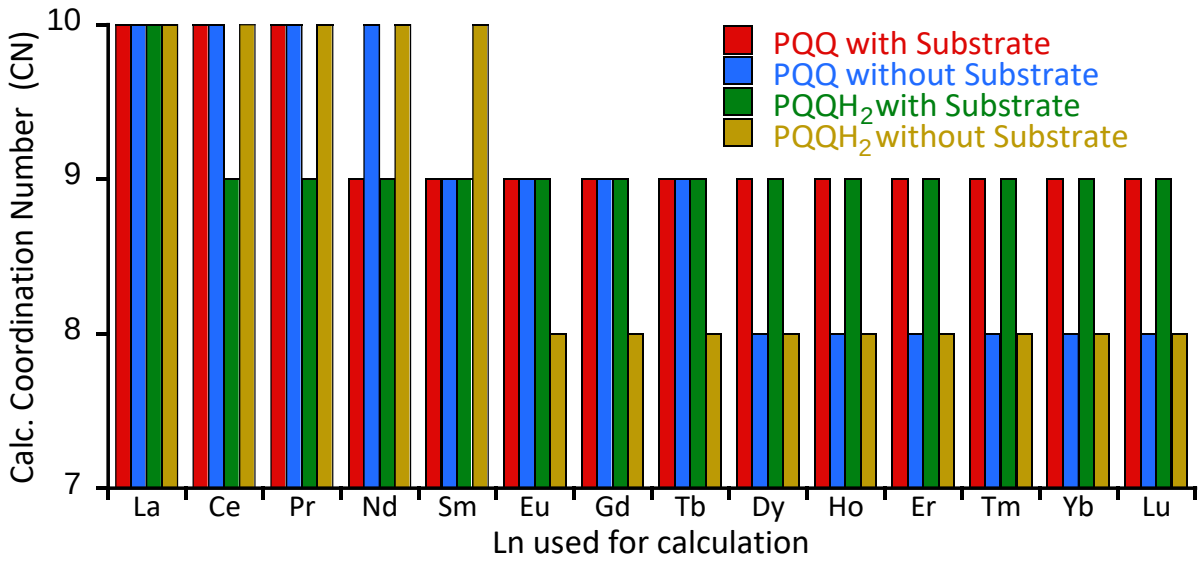

Figure IX.6: Calculated coordination numbers of the active site in MDH with oxidized (PQQ) or reduced ($PQQH_2$) cofactor with- and without substrate.

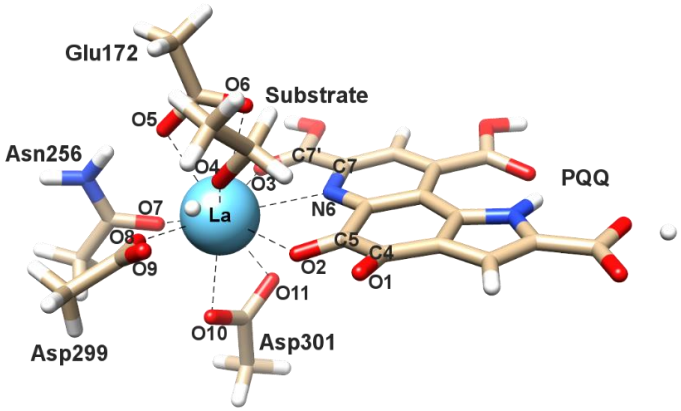

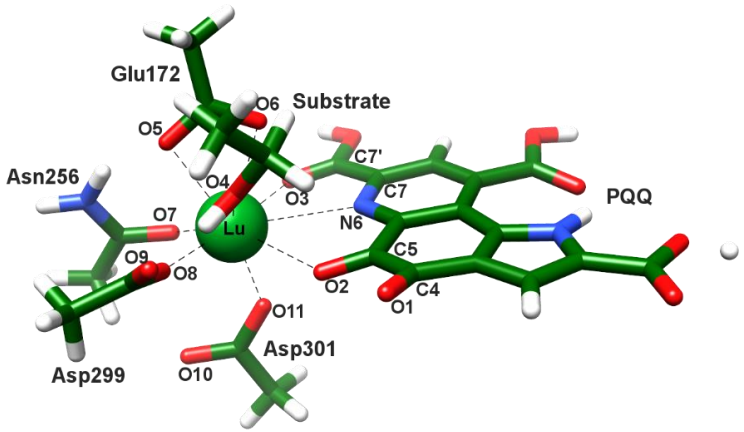

Table IX.1: Calculated bond lengths and angles of the structure optimizations for Ln^{3+} with PQQ^0 and substrate as described in Figure IX.4. Example structures of the La^{3+} and Lu^{3+} calculations are given above.

PQQ + S	Distance Substr.-O-C5	Distance Substr.-O-M	Distance C5(O)-M	Distance N6-M	Distance C7'(CO_2)-M	Distance O10-M	Distance O11-M	Bond angle O10-M-O11	Binding mode (ASP301)	Binding mode (ASP299)	CN	Atomic number
La	3.41871	2.66856	2.77142	2.89968	2.70271	2.64509	2.69935	48.99033	bidentate	monodentate	10	57
Ce	3.41485	2.66337	2.76197	2.89762	2.70936	2.63128	2.69154	49.14706	bidentate	monodentate	10	58
Pr	3.41219	2.65857	2.75417	2.89826	2.71734	2.61729	2.68469	49.29969	bidentate	monodentate	10	59
Nd	3.41778	2.61171	2.8574	2.99031	2.73730	3.49774	2.37672	39.70468	monodentate	monodentate	9	60
Sm	3.41537	2.59286	2.86013	3.00451	2.75280	3.59349	2.34644	37.85292	monodentate	monodentate	9	62
Eu	3.41492	2.58683	2.8639	3.01475	2.76106	3.60815	2.33595	37.51399	monodentate	monodentate	9	63
Gd	3.41444	2.58184	2.8679	3.02469	2.76871	3.61594	2.32783	37.31441	monodentate	monodentate	9	64
Tb	3.41577	2.57695	2.87418	3.03645	2.77646	3.62958	2.31973	37.00105	monodentate	monodentate	9	65
Dy	3.41595	2.57284	2.88008	3.04880	2.78509	3.63383	2.31230	36.86735	monodentate	monodentate	9	66
Ho	3.41630	2.56955	2.88679	3.06206	2.79398	3.63696	2.30498	36.75500	monodentate	monodentate	9	67
Er	3.41718	2.5667	2.89434	3.07614	2.80304	3.63804	2.29817	36.68542	monodentate	monodentate	9	68
Tm	3.41814	2.56512	2.90226	3.08903	2.81036	3.63908	2.29201	36.62292	monodentate	monodentate	9	69
Yb	3.41893	2.56333	2.9108	3.10398	2.81956	3.63864	2.2857	36.58582	monodentate	monodentate	9	70
Lu	3.41938	2.56218	2.91864	3.11756	2.82784	3.63362	2.28047	36.64844	monodentate	monodentate	9	71

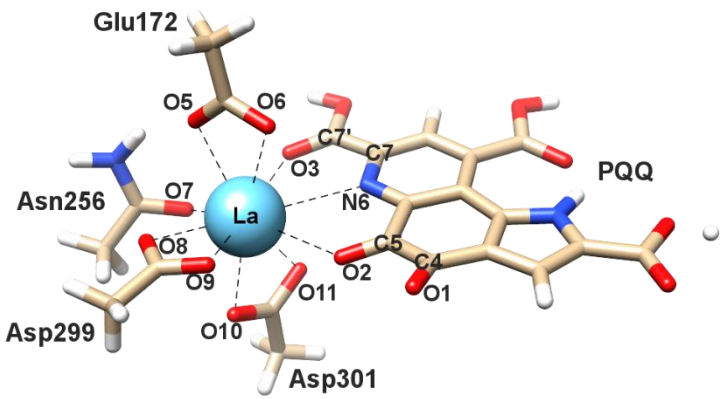

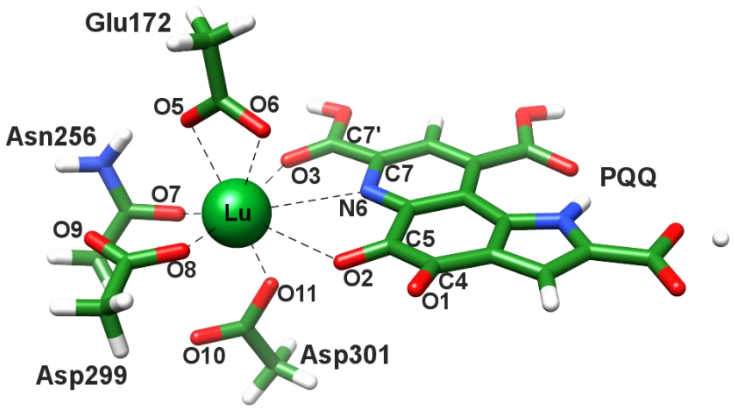

Table IX.2: Calculated bond lengths and angles of the structure optimizations for Ln^{3+} with PQQ^0 and without substrate as described in Figure IX.4. Example structures of the La^{3+} and Lu^{3+} calculations are given above.

PQQ - S	Distance C5(O)-M	Distance N6-M	Distance C7'(CO_2)-M	Distance O10-M	Distance O11-M	Bond angle O10-M-O11	Binding mode (ASP301)	Binding mode (ASP299)	CN	Atomic number
La	2.96030	3.20725	2.86410	2.63074	2.59339	50.21016	bidentate	bidentate	10	57
Ce	2.97706	3.22575	2.86963	2.62193	2.57966	50.37921	bidentate	bidentate	10	58
Pr	2.99437	3.24509	2.87580	2.61454	2.56625	50.53544	bidentate	bidentate	10	59
Nd	3.01204	3.26478	2.88222	2.60951	2.5525	50.67674	bidentate	bidentate	10	60
Sm	2.89771	3.03707	2.71801	2.55847	2.5967	50.68474	bidentate	monodentate	9	62
Eu	2.90947	3.04857	2.71891	2.54712	2.59047	50.82384	bidentate	monodentate	9	63
Gd	2.91986	3.05875	2.71977	2.53707	2.58482	50.94776	bidentate	monodentate	9	64
Tb	2.93182	3.07068	2.72104	2.52512	2.57823	51.10283	bidentate	monodentate	9	65
Dy	3.10597	3.18576	2.69915	3.42002	2.29714	40.74210	monodentate	monodentate	8	66
Ho	3.12665	3.20178	2.69759	3.46268	2.2822	39.91409	monodentate	monodentate	8	67
Er	3.14994	3.22022	2.69600	3.48318	2.2708	39.48094	monodentate	monodentate	8	68
Tm	3.19116	3.24933	2.68576	3.42667	2.26154	40.50209	monodentate	monodentate	8	69
Yb	3.21140	3.26725	2.68713	3.44662	2.25019	40.08331	monodentate	monodentate	8	70
Lu	3.22792	3.2828	2.68946	3.45084	2.24257	39.96807	monodentate	monodentate	8	71

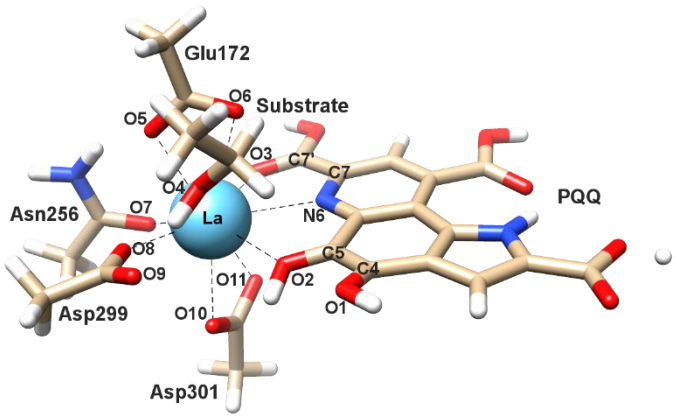

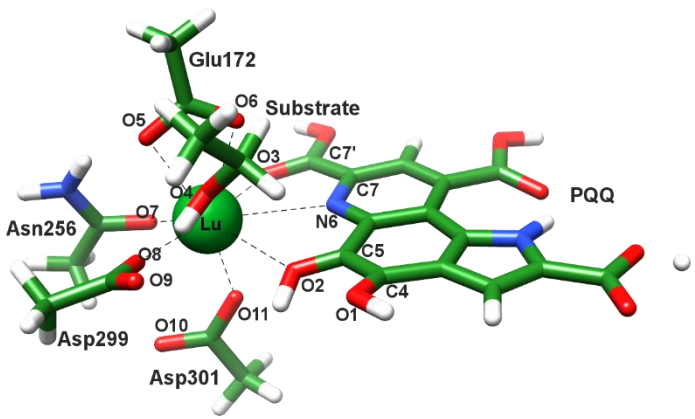

Table IX.3: Calculated bond lengths and angles of the structure optimizations for Ln^{3+} with reduced $PQQH_2$ and substrate as described in Figure IX.4. Example structures of the La^{3+} and Lu^{3+} calculations are given above.

$PQQH_2$ + S	Distance Substr.-O-C5	Distance Substr.-O-M	Distance C5(O)-M	Distance N6-M	Distance C7'(CO_2)-M	Distance O10-M	Distance O11-M	Bond angle O10-M-O11	Binding mode (ASP301)	Binding mode (ASP299)	CN	Atomic number
La	3.54092	2.70834	2.81254	2.86802	2.62451	2.71244	2.66632	48.64818	Bidentate	monodentate	10	57
Ce	3.54946	2.63521	2.91106	2.95102	2.64007	3.68944	2.40021	36.28487	Monodentate	monodentate	9	58
Pr	3.54064	2.63263	2.90953	2.95712	2.64814	3.69075	2.3828	36.19016	Monodentate	monodentate	9	59
Nd	3.5334	2.62958	2.91074	2.96688	2.65772	3.68653	2.36869	36.19823	Monodentate	monodentate	9	60
Sm	3.52661	2.62199	2.91926	2.98775	2.67306	3.69495	2.34789	35.9033	Monodentate	monodentate	9	62
Eu	3.52627	2.62008	2.92709	2.99971	2.67872	3.69484	2.33881	35.83736	Monodentate	monodentate	9	63
Gd	3.52663	2.61864	2.93476	3.01084	2.68363	3.69327	2.33143	35.81268	Monodentate	monodentate	9	64
Tb	3.52582	2.61692	2.94434	3.02416	2.68955	3.69751	2.32426	35.67653	Monodentate	monodentate	9	65
Dy	3.52649	2.61604	2.95369	3.03771	2.69576	3.69566	2.3173	35.65926	Monodentate	monodentate	9	66
Ho	3.52752	2.61594	2.96397	3.05224	2.70222	3.69367	2.31027	35.64429	Monodentate	monodentate	9	67
Er	3.52895	2.61629	2.97493	3.06762	2.70907	3.69064	2.30366	35.65323	Monodentate	monodentate	9	68
Tm	3.53062	2.61775	2.98598	3.08189	2.71457	3.68782	2.29767	35.66513	Monodentate	monodentate	9	69
Yb	3.53273	2.61924	2.99806	3.09834	2.72169	3.68425	2.29139	35.68734	Monodentate	monodentate	9	70
Lu	3.53428	2.62061	3.0085	3.11303	2.72844	3.67742	2.28598	35.78303	Monodentate	monodentate	9	71

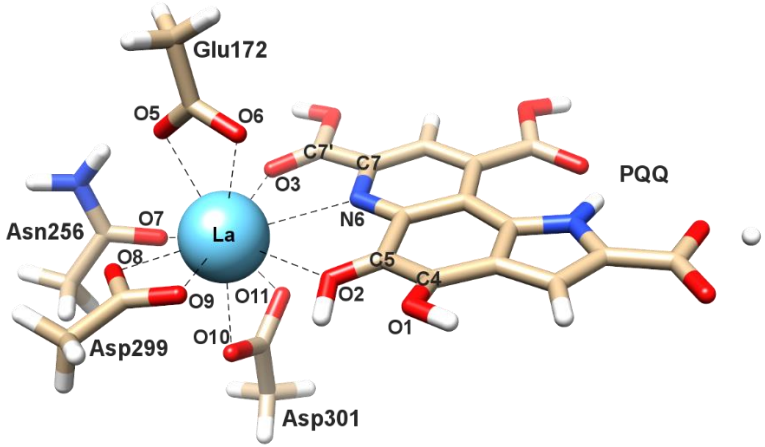

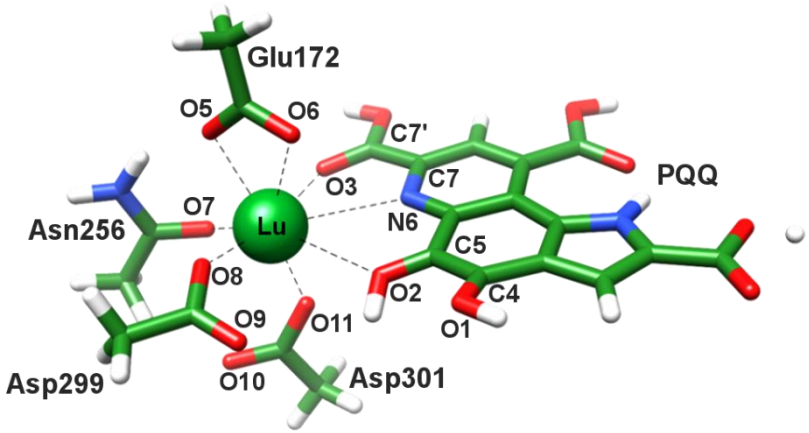

Table IX.4: Calculated bond lengths and angles of the structure optimizations for Ln^{3+} with reduced $PQQH_2$ and without substrate as described in Figure IX.4. Example structures of the La^{3+} and Lu^{3+} calculations are given above.

$PQQH_2$ - S	Distance C5(O)-M	Distance N6-M	Distance C7'(CO_2)-M	Distance O10-M	Distance O11-M	Bond angle O10-M-O11	Binding mode (ASP301)	Binding mode (ASP299)	CN	Atomic number
La	2.95742	3.13982	2.78158	2.63361	2.60395	50.02797	bidentate	bidentate	10	57
Ce	2.97215	3.15675	2.78697	2.62111	2.59302	50.20832	bidentate	bidentate	10	58
Pr	2.98586	3.17385	2.79371	2.61024	2.58227	50.37431	bidentate	bidentate	10	59
Nd	3.00095	3.19184	2.80022	2.6013	2.57175	50.52454	bidentate	bidentate	10	60
Sm	3.07479	3.2641	2.81502	2.63305	2.51598	50.66503	bidentate	bidentate	10	62
Eu	3.03114	3.09536	2.66574	3.4818	2.30303	39.60913	monodentate	monodentate	8	63
Gd	3.04624	3.10588	2.66276	3.52863	2.28762	38.66039	monodentate	monodentate	8	64
Tb	3.06665	3.12128	2.66008	3.56398	2.27436	37.90669	monodentate	monodentate	8	65
Dy	3.0875	3.13792	2.65814	3.57228	2.26438	37.68103	monodentate	monodentate	8	66
Ho	3.10862	3.15511	2.65662	3.57863	2.25469	37.49011	monodentate	monodentate	8	67
Er	3.12939	3.17266	2.65601	3.57974	2.24588	37.40832	monodentate	monodentate	8	68
Tm	3.14776	3.18799	2.65536	3.57983	2.23828	37.35706	monodentate	monodentate	8	69
Yb	3.16743	3.2055	2.65608	3.57884	2.2299	37.31814	monodentate	monodentate	8	70
Lu	3.18277	3.22011	2.6578	3.57202	2.22282	37.40757	monodentate	monodentate	8	71

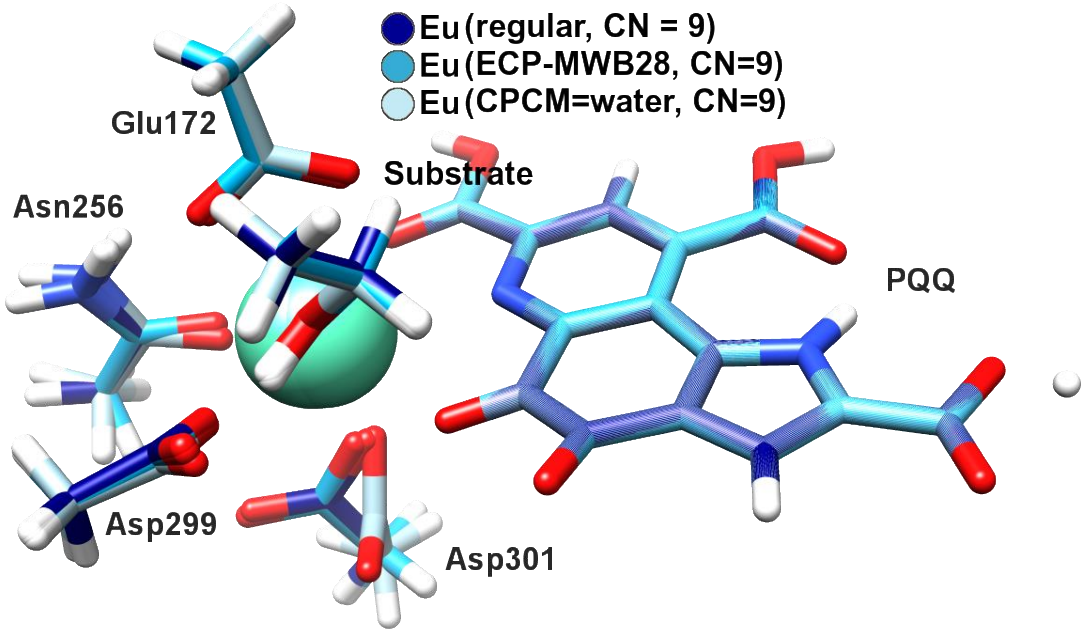

Figure IX.7: Optimized and superimposed structures for the active center with PQQ, substrate and Eu^{3+}. The regular calculation, as described in Figure IX.4 and Figure IX.5 is given in dark blue. An open shell calculation, using the smaller ECP-MWB28[[286-287, 304]] and taking the f-electrons into account is given in blue and a calculation, taking solvent effects into account, by using the CPCM method with water, is given in light blue. Input commands for the calculations are given below. The structures received from the calculations only differ slightly, with an exception of Asp301, which is tilted away under the influence of the solvent model (light blue). Since all calculations show the same coordination number – the property of interest - the simplified, "regular" calculations described above were used for every Ln and active site configuration. **None of the calculations showed negative frequencies**.

Figure IX.8: Example inputs of the calculations described in Figure IX.4. **Left**: Open shell calculation, using the smaller ECP-MWB28. **Right**: Closed-shell calculation, considering solvent effects by the use of CPCM with water.

Eu (ECP-MWB28)

```
#p opt freq ub3lyp/gen geom=connectivity
5d 7f pseudo=read

0 7

Atomic coordinates and
geometry specifications as in Figure IX.5

C H N O 0
6-31G(d)
****
Eu 0
MWB28
****
Eu 0
MWB28
```

Eu (CPCM=water)

```
#p opt freq rb3lyp/gen scrf=(cpcm,solvent=water)
geom=connectivity 5d 7f pseudo=read

0 1

Atomic coordinates and
geometry specifications as in Figure IX.5

C H N O 0
6-31G(d)
```

****
Eu 0
MWB52
****

Eu 0
MWB52

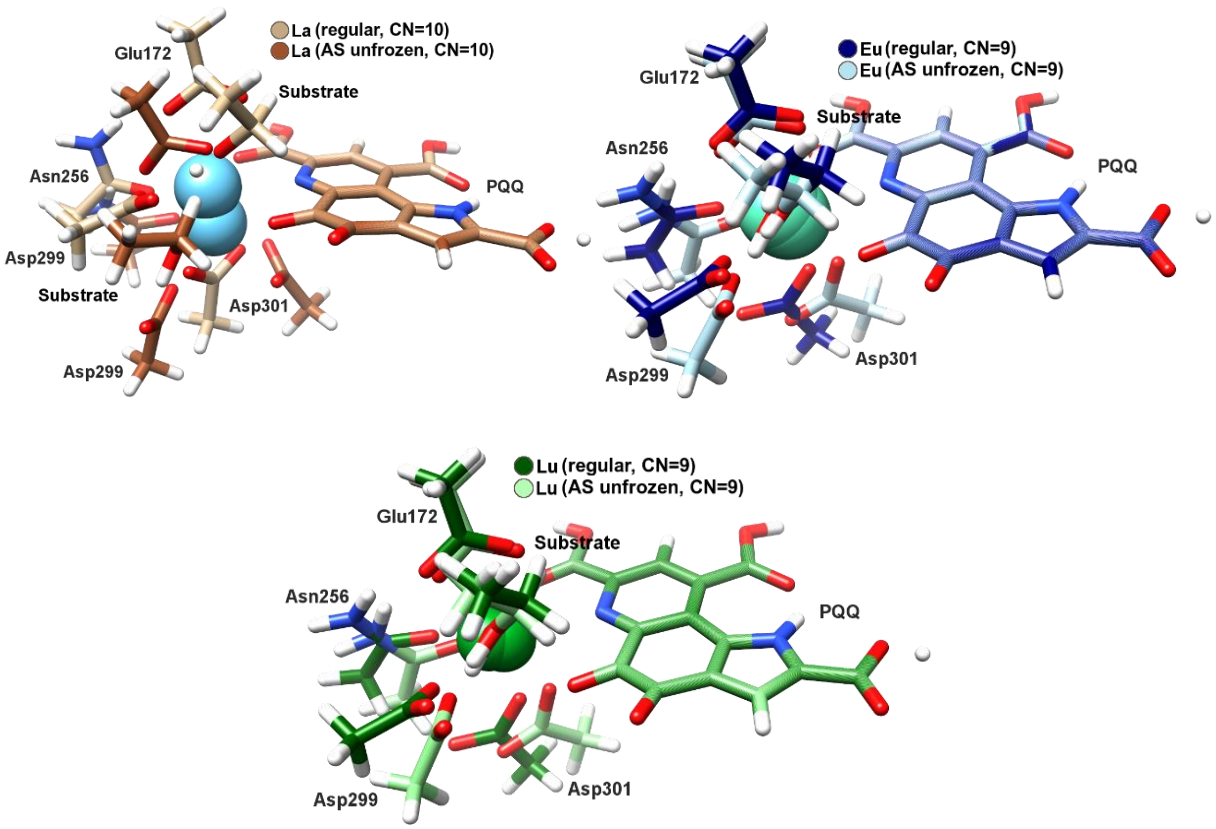

Figure IX.9: Optimized and superimposed structures for the active center with PQQ, substrate and La^{3+}, Eu^{3+} or Lu^{3+}. Calculations were performed exactly as the "regular" ones described in Figure IX.4 and Figure IX.5, but with all amino acid residues set to unfrozen. An example input command for the La^{3+} calculation is given below in Figure IX.10. Both Eu and Lu calculations only differ slightly from the regular ones. Glu172 and the substrate almost keep their position, while Asn256, Asp299 and Asp301 are shifted more significantly from their position. The unfrozen La calculation differs strongly from the regular one, with all amino acids, central metal and substrate rearranged. However, the coordination number for all three calculations does not differ from the respective regular calculation. The coordination number is therefore not forced by the frozen amino acids but only by the varying properties of the Ln. None of the calculations showed negative frequencies.

Figure IX.10: Example input for Gaussian optimizations with all amino acids set to unfrozen (while keeping all PQQ atoms frozen). -1 denotes a frozen carbon atom.

```
%chk=LaIII-PQQ-with-Substrate-not-frozen.chk
%mem=60GB
%nprocshared=8
#p opt freq rb3lyp/gen geom=connectivity 5d 7f pseudo=read

La(III) - PQQ - with Substrat
AS not frozen

0 1
 C      0  -4.90400000   3.34400000   3.52500000
 C      0  -4.43100000   2.75000000   2.21200000
 O      0  -5.31600000   2.48300000   1.32700000
 O      0  -3.21300000   2.47700000   2.02300000
 C      0  -7.59200000   1.55900000  -2.75400000
 C      0  -6.78400000   1.98800000  -1.55100000
 O      0  -5.53400000   1.90100000  -1.57100000
 N      0  -7.44100000   2.47100000  -0.49176943
 C      0  -7.57000000  -2.04200000   0.45144469
 C      0  -6.14900000  -1.61500000   0.75161945
 O      0  -5.81500000  -0.46701986   0.29292243
 O      0  -5.39000000  -2.35900000   1.42100000
 C      0  -3.16200000  -0.96440872  -4.27600000
 C      0  -3.96500000  -0.84870079  -2.97500000
 O      0  -5.10800000  -1.31100000  -2.91900000
 O      0  -3.34000000  -0.27056742  -1.98200000
 N     -1   3.33000000  -0.81662988   1.47900000
 C     -1   3.61300000  -2.05900000   1.97300000
 C     -1   5.01500000  -2.49400000   2.20800000
 O     -1   5.88200000  -1.54200000   1.91200000
 O     -1   5.26800000  -3.61500000   2.62500000
 C     -1   2.41800000  -2.74800000   2.13600000
 C     -1   1.39400000  -1.87800000   1.71500000
 C     -1   1.99200000  -0.65850047   1.29400000
 C     -1  -0.03196565  -2.09600000   1.68300000
 O     -1  -0.65585683  -3.02200000   2.17600000
 C     -1  -0.80639866  -0.98447544   0.95671480
 O     -1  -1.97200000  -1.16300000   0.63270177
 C     -1  -0.13660882   0.31747211   0.63836618
```

N	-1	-0.97622754	1.23100000	0.17358237
C	-1	-0.50347008	2.43600000	-0.15877326
C	-1	-1.51600000	3.38500000	-0.69429278
O	-1	-2.68200000	3.07700000	-0.90161786
O	-1	-1.02900000	4.60100000	-0.94685640
C	-1	0.84871874	2.74100000	-0.04652754
C	-1	1.77100000	1.78600000	0.39850560
C	-1	3.21000000	2.20900000	0.35976671
O	-1	3.37200000	3.51000000	0.13590368
O	-1	4.17700000	1.46400000	0.47970217
C	-1	1.28200000	0.49657896	0.78449450
O	0	-3.93300000	-0.32848794	2.35300000
C	0	-3.16200000	-0.45069210	3.55200000
C	0	-4.04600000	-0.73580415	4.76200000
H	0	-7.34200000	2.20600000	-3.60200000
H	0	-7.28400000	0.54246200	-3.01600000
H	0	-8.67000000	1.59400000	-2.58300000
H	0	-7.70800000	-2.10900000	-0.63361256
H	0	-7.80300000	-3.00600000	0.90925659
H	0	-8.26700000	-1.28200000	0.82000108
H	0	-5.67800000	4.09600000	3.34900000
H	0	-5.35100000	2.54500000	4.12900000
H	0	-4.07300000	3.78100000	4.08500000
H	0	-4.78000000	0.06458975	4.90600000
H	0	-4.58800000	-1.67900000	4.63500000
H	0	-3.43600000	-0.81454479	5.67000000
H	0	-2.63900000	0.50250317	3.66600000
H	0	-2.41400000	-1.24600000	3.43300000
H	0	-2.74100000	0.00689772	-4.55900000
H	0	-2.32100000	-1.65000000	-4.12400000
H	0	-3.79400000	-1.34200000	-5.08200000
H	-1	4.34900000	3.70100000	-0.00827955
H	-1	1.19100000	3.72400000	-0.32958075
H	-1	6.90200000	-1.87400000	1.98800000
H	-1	-1.75500000	5.14900000	-1.30300000
H	-1	4.02400000	-0.11676026	1.22800000
H	-1	2.30000000	-3.76900000	2.46200000
H	0	-8.45000000	2.47400000	-0.46268410
H	0	-6.90800000	2.66300000	0.35974909
H	0	-4.37900000	-1.19400000	2.13400000
La	0	-3.90000000	0.86148825	0.01088327

1 2 1.0 50 1.0 51 1.0 52 1.0
2 3 1.5 4 1.5
3 70 1.0
4 70 1.0
5 6 1.0 44 1.0 45 1.0 46 1.0
6 7 2.0 8 1.5
7 70 1.0
8 67 1.0 68 1.0
9 10 1.0 47 1.0 48 1.0 49 1.0
10 11 1.5 12 1.5
11 70 1.0
12
13 14 1.0 58 1.0 59 1.0 60 1.0
14 15 1.5 16 1.5
15 70 1.0
16 70 1.0
17 18 1.5 24 1.5 65 1.0
18 19 1.0 22 1.5
19 20 1.5 21 2.0
20 63 1.0
21
22 23 1.5 66 1.0
23 24 1.5 25 1.5
24 40 1.0
25 26 2.0 27 1.0
26
27 28 2.0 29 1.0
28 70 1.0
29 30 1.5 40 1.5
30 31 1.5 70 1.0
31 32 1.0 35 1.5
32 33 2.0 34 1.5
33 70 1.0
34 64 1.0
35 36 1.5 62 1.0
36 37 1.0 40 1.5
37 38 1.5 39 2.0
38 61 1.0
39
40
41 42 1.0 69 1.0 70 1.0
42 43 1.0 56 1.0 57 1.0
43 53 1.0 54 1.0 55 1.0
44
45
46
47
48
49
50
51
52
53
54
55
56
57
58
59
60
61
62
63
64
65
66
67
68
69
70

C H N O 0
6-31G(d)
****
La 0
MWB46
****

La 0
MWB46

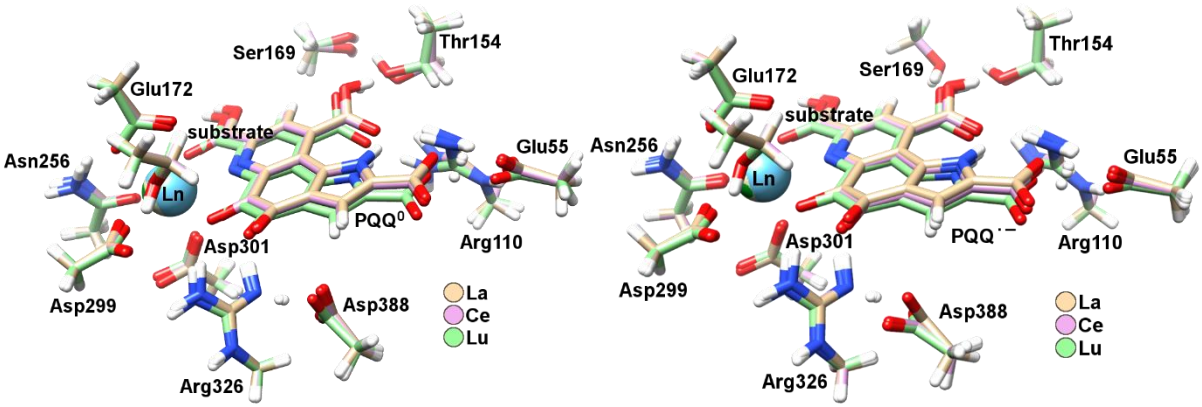

Figure IX.11: Optimized Structures for the extended active center with substrate and La (tan), Ce (purple) or Lu (green) with PQQ in the active quinone state (PQQ^0 – left) or the resting semiquinone state ($PQQ^{\bullet-}$ – right). Electronic-structure calculations were performed with Gaussian 09 and exactly as described by Schelter *et al.*[[76]] The B3LYP functional with the 6-31G(d) basis set was used for C, H, N and O. 28 electron quasi

relativistic effective core potentials (ECP) and segmented basis sets were used for each central metal respectively (La, Ce, Lu): ECP-MWB28.[[286-287, 304]] Starting point of the geometry optimization was the active site of the crystal structure of Ce-MDH isolated from SolV (4MAE).[[36]] The present amino acids in the active site were truncated and the terminal carbon atoms were frozen, to mimic the sterics imposed by the protein. The present polyethylenglycol was truncated as well and used as a substrate-model. The conductor-like polarizable continuum model (CPCM) was used for water, with the default settings for the universal force field (UFF) and a dielectric constant of 4, to reproduce the interior of the protein and the active site pocket. The charge and multiplicity for the quinone PQQ^0 state were set to "0 1" for La and Lu and to "0 2" for Ce. The additional electron for the semiquinone $PQQ^{\bullet-}$ state was taken into account, by changing the system to "−1 2" for La and Lu and to "−1 3" for Ce. None of the calculations showed negative frequencies. All structures differed only slightly, by changing the central metal or the PQQ state. The PQQ ligand moved closer to the central metal, especially in case of Lu, probably due to the decreased ionic radius. In contrast to the simplified calculations described in Figure IX.4 and Figure IX.5, Asp301 remained monodentate for all calculations and therefore the overall coordination number did not change over the exchange of La to Ce or Lu. Since the simplified system given in Figure IX.4 was also calculated with a smaller ECP and solvent effects as described in Figure IX.7, the binding mode of Asp301 is probably influenced during the optimization by the larger hydrogen bond network due to the additional amino acids and the change of the dielectric constant to 4.

Figure IX.12: Example input for Gaussian optimizations (in this case La^{3+} PQQ^0). -1 denotes a frozen carbon atom.

```
%chk=C:\Users\akdaumann\Desktop\La(III)-PQQ(0).chk
%mem=128GB
%nprocshared=12
#p opt=maxcycle=999 freq rb3lyp/gen scrf=(cpcm,solvent=water,read)
geom=connectivity pseudo=read scf=maxcycles=1024 formcheck

La(III) - PQQ(0)

0 1
C    -1  10.31100000  -2.74300000   0.91007048
C     0   8.93000000  -2.09500000   0.98227463
O     0   8.26200000  -2.29300000   2.04300000
O     0   8.55300000  -1.38000000   0.00969315
C    -1   8.18300000  -0.06179479  -3.80000000
N     0   7.90300000  -0.03453109  -2.37100000
C     0   7.07000000   0.82769766  -1.78300000
N     0   6.37600000   1.73100000  -2.50700000
N     0   6.93100000   0.79380766  -0.44848331
C     0   7.08000000   4.45200000  -0.35938247
O     0   5.73400000   4.21400000  -0.86097367
C    -1   7.09400000   5.43300000   0.80182198
C    -1   2.43900000   6.91600000  -0.75832705
O     0   3.32900000   5.98400000  -1.38600000
C    -1  -4.90400000   3.34400000   3.52500000
C     0  -4.43100000   2.75000000   2.21200000
O     0  -5.31600000   2.48300000   1.32700000
O     0  -3.21300000   2.47700000   2.02300000
C    -1  -7.59200000   1.55900000  -2.75400000
C     0  -6.78400000   1.98800000  -1.55100000
O     0  -5.53400000   1.90100000  -1.57100000
N     0  -7.44100000   2.47100000  -0.49176943
C    -1  -7.57000000  -2.04200000   0.45144469
C     0  -6.14900000  -1.61500000   0.75161945
O     0  -5.81500000  -0.46701986   0.29292243
O     0  -5.39000000  -2.35900000   1.42100000
C    -1  -3.16200000  -0.96440872  -4.27600000
C     0  -3.96500000  -0.84870079  -2.97500000
O     0  -5.10800000  -1.31100000  -2.91900000
O     0  -3.34000000  -0.27056742  -1.98200000
N     0   3.33000000  -0.81662988   1.47900000
C     0   3.61300000  -2.05900000   1.97300000
C     0   5.01500000  -2.49400000   2.20800000
O     0   5.88200000  -1.54200000   1.91200000
O     0   5.26800000  -3.61500000   2.62500000
C     0   2.41800000  -2.74800000   2.13600000
C     0   1.39400000  -1.87800000   1.71500000
C     0   1.99200000  -0.65850047   1.29400000
C     0  -0.03196565  -2.09600000   1.68300000
O     0  -0.65585683  -3.02200000   2.17600000
C     0  -0.80639866  -0.98447544   0.95671480
O     0  -1.97200000  -1.16300000   0.63270177
C     0  -0.13660882   0.31747211   0.63836618
N     0  -0.97622754   1.23100000   0.17358237
C     0  -0.50347008   2.43600000  -0.15877326
C     0  -1.51600000   3.38500000  -0.69429278
O     0  -2.68200000   3.07700000  -0.90161786
O     0  -1.02900000   4.60100000  -0.94685640
C     0   0.84871874   2.74100000  -0.04652754
C     0   1.77100000   1.78600000   0.39850560
C     0   3.21000000   2.20900000   0.35976671
O     0   3.37200000   3.51000000   0.13590368
O     0   4.17700000   1.46400000   0.47970217
C     0   1.28200000   0.49657896   0.78449450
O     0  -3.93300000  -0.32848794   2.35300000
C     0  -3.16200000  -0.45069210   3.55200000
C    -1  -4.04600000  -0.73580415   4.76200000
C    -1  -1.81800000  -5.63500000  -3.12600000
N     0  -2.49200000  -5.27000000  -1.87800000
C     0  -2.38200000  -4.05700000  -1.31700000
N     0  -1.38300000  -3.25400000  -1.70400000
N     0  -3.28000000  -3.66000000  -0.40296842
C    -1   2.04400000  -6.54300000  -1.24900000
C     0   1.30700000  -5.20800000  -1.01900000
O     0   0.91595122  -4.60900000  -2.08800000
O     0   1.10700000  -4.82700000   0.15045621
H     0  -7.34200000   2.20600000  -3.60200000
H     0  -7.28400000   0.54246200  -3.01600000
H     0  -8.67000000   1.59400000  -2.58300000
H     0  -7.70800000  -2.10900000  -0.63361256
H     0  -7.80300000  -3.00600000   0.90925659
H     0  -8.26700000  -1.28200000   0.82000108
H     0  -5.67800000   4.09600000   3.34900000
H     0  -5.35100000   2.54500000   4.12900000
H     0  -4.07300000   3.78100000   4.08500000
H     0  -4.78000000   0.06458975   4.90600000
H     0  -4.58800000  -1.67900000   4.63500000
H     0  -3.43600000  -0.81454479   5.67000000
H     0  -2.63900000   0.50250317   3.66600000
H     0  -2.41400000  -1.24600000   3.43300000
H     0  -2.74100000   0.00689772  -4.55900000
H     0  -2.32100000  -1.65000000  -4.12400000
H     0  -3.79400000  -1.34200000  -5.08200000
H     0  -2.14000000  -4.97600000  -3.94100000
H     0  -0.73347419  -5.57200000  -3.01300000
H     0  -2.10500000  -6.66000000  -3.36700000
H     0   2.70200000  -6.48700000  -2.12300000
H     0   2.62300000  -6.83100000  -0.36649540
H     0   1.30600000  -7.33200000  -1.44700000
H     0   8.60600000   0.88889236  -4.14600000
H     0   8.91800000  -0.84624694  -3.98300000
H     0   7.28400000  -0.29160738  -4.38300000
H     0   6.71300000   6.41500000   0.49706827
H     0   6.48200000   5.06400000   1.63100000
H     0   8.11900000   5.56800000   1.16300000
H     0   7.69900000   4.80800000  -1.19000000
H     0   7.44400000   3.46900000  -0.05527242
H     0   2.84700000   7.91400000  -0.93492756
H     0   1.43200000   6.86500000  -1.19300000
H     0   2.36900000   6.75000000   0.32496012
H     0  11.07300000  -1.98700000   1.13500000
H     0  10.40200000  -3.55600000   1.63300000
H     0  10.50600000  -3.11500000  -0.10037254
H     0   2.95500000   5.09900000  -1.25100000
H     0   4.34900000   3.70100000  -0.00827955
H     0   5.34500000   5.05500000  -1.17800000
H     0   5.98800000   2.54800000  -2.03600000
H     0   6.58800000   1.84500000  -3.48700000
H     0   6.08300000   1.18200000  -0.04770952
```

H	0	7.36600000	-0.01798868	0.02169258
H	0	8.34400000	-0.71492873	-1.74500000
H	0	1.19100000	3.72400000	-0.32958075
H	0	6.90200000	-1.87400000	1.98800000
H	0	-1.75500000	5.14900000	-1.30300000
H	0	4.02400000	-0.11676026	1.22800000
H	0	2.30000000	-3.76900000	2.46200000
H	0	-3.08300000	-2.86900000	0.19805491
H	0	-4.17200000	-4.11700000	-0.28136504
H	0	-1.44200000	-2.29500000	-1.39100000
H	0	-0.41936651	-3.68700000	-1.86600000
H	0	-3.17200000	-5.90700000	-1.49000000
H	0	-8.45000000	2.47400000	-0.46268410
H	0	-6.90800000	2.66300000	0.35974909
H	0	-4.37900000	-1.19400000	2.13400000
La	0	-3.90000000	0.86148825	0.01088327

1 2 1.0 101 1.0 102 1.0 103 1.0
2 3 1.5 4 1.5
3
4
5 6 1.0 90 1.0 91 1.0 92 1.0
6 7 2.0 111 1.0
7 8 1.0 9 1.0
8 107 1.0 108 1.0
9 109 1.0 110 1.0
10 11 1.0 12 1.0 96 1.0 97 1.0
11 106 1.0
12 93 1.0 94 1.0 95 1.0
13 14 1.0 98 1.0 99 1.0 100 1.0
14 104 1.0
15 16 1.0 73 1.0 74 1.0 75 1.0
16 17 1.5 18 1.5
17 125 1.0
18 125 1.0
19 20 1.0 67 1.0 68 1.0 69 1.0
20 21 2.0 22 1.0
21 125 1.0
22 122 1.0 123 1.0
23 24 1.0 70 1.0 71 1.0 72 1.0
24 25 1.5 26 1.5
25 125 1.0
26
27 28 1.0 81 1.0 82 1.0 83 1.0
28 29 1.5 30 1.5
29 125 1.0
30 125 1.0
31 32 1.5 38 1.5 115 1.0
32 33 1.0 36 1.5
33 34 1.0 35 2.0
34 113 1.0
35
36 37 1.5 116 1.0
37 38 1.5 39 1.0
38 54 1.0
39 40 2.0 41 1.0
40
41 42 2.0 43 1.0
42 125 1.0
43 44 1.5 54 1.5
44 45 1.5 125 1.0
45 46 1.0 49 1.5
46 47 2.0 48 1.0
47 125 1.0
48 114 1.0
49 50 1.5 112 1.0
50 51 1.0 54 1.5
51 52 1.0 53 2.0
52 105 1.0
53
54
55 56 1.0 124 1.0 125 1.0
56 57 1.0 79 1.0 80 1.0
57 76 1.0 77 1.0 78 1.0
58 59 1.0 84 1.0 85 1.0 86 1.0
59 60 2.0 121 1.0
60 61 1.0 62 1.0
61 119 1.0 120 1.0
62 117 1.0 118 1.0
63 64 1.0 87 1.0 88 1.0 89 1.0
64 65 1.5 66 1.5
65
66
67
68
69
70
71
72
73
74
75
76
77
78
79
80
81
82
83
84
85
86
87
88
89
90
91
92
93
94
95
96
97
98
99
100
101
102
103
104
105
106
107
108
109
110
111
112
113
114
115
116
117
118
119
120
121
122
123
124
125

C H N O 0
6-31G(d)
****
La 0
S 5 1.00
60228.6130000 0.000003
7142.4190000 0.000035
1034.3051000 0.000329
563.4427000 -0.000106
123.5532000 0.003280
S 1 1.00
34.5544000 1.0
S 1 1.00
24.6330000 1.0
S 1 1.00
11.2660000 1.0
S 1 1.00
2.9062000 1.0
S 1 1.00
1.5433000 1.0
S 1 1.00
0.5672000 1.0
S 1 1.00
0.2539000 1.0
S 1 1.00
0.0467000 1.0
S 1 1.00
0.0200000 1.0
P 6 1.00
3966.3547000 0.000004
1143.9280000 0.000033
446.9977000 0.000034
229.5466000 0.000362
27.3267000 -0.007136
19.4864000 0.206654
P 1 1.00
13.9024000 1.0
P 1 1.00
4.2361000 1.0
P 1 1.00
2.2936000 1.0
P 1 1.00
1.1258000 1.0
P 1 1.00
0.5279000 1.0
P 1 1.00
0.2292000 1.0
P 1 1.00
0.0800000 1.0
D 6 1.00
367.7157000 0.000074
113.5768000 0.000612
33.5588000 0.007687
14.4198000 -0.076510
7.3159000 0.151754
3.9483000 0.421873
D 1 1.00
2.0150000 1.0
D 1 1.00
0.9581000 1.0
D 1 1.00
0.3109000 1.0
D 1 1.00

```
0.0954000 1.0
F 5 1.00
124.7971000 0.001150
43.9427000 0.014333
19.2668000 0.062594
8.4893000 0.164000
3.7672000 0.285863
F 1 1.00
1.5902000 1.0
F 1 1.00
0.6098000 1.0
F 1 1.00
0.1973000 1.0
G 4 1.00
19.2668000 -0.002118
8.4893000 0.026709
3.7672000 -0.029667
1.5902000 0.282785
G 1 1.00
0.6098000 1.0
G 1 1.00
0.1973000 1.0
****

La 0
ECP28MWB 5 28
H-Komponente
1
2 1.000000 0.000000
S-H
1
2 19.441418 585.201953
P-H
1
2 16.016353 330.109510
D-H
1
2 15.128259 186.058232
F-H
1
2 23.103875 -49.433352
G-H
1
2 15.639020 -20.123020

stoichiometry=H2O1
solventname=water
eps=4.0
```

Figure IX.13: Input for the calculation of the La^{3+} $PQQ^{\bullet-}$ species.

For the semiquinone $PQQ^{\bullet-}$ species, following modification was implemented, while the rest of the input file was unchanged to Figure IX.12:

```
#p opt=maxcycle=999 freq ub3lyp/gen scrf=(cpcm,solvent=water,read)
geom=connectivity formcheck pseudo=read scf=maxcycles=1024

La(III) - PQQ(-1)

-1 2
```

Figure IX.14: Input for the calculation of the Ce^{3+} and Lu^{3+} variants of the PQQ^{0} species. For the semiquinone $PQQ^{\bullet-}$ species, the input files were exactly the same, but the charge and multiplicity were changed to −1 3 for Ce^{3+} and −1 2 for Lu^{3+}.

Ce^{3+} PQQ^{0}

```
#p opt(maxcycle=999) freq ub3lyp/gen scrf=(cpcm,solvent=water,read)
geom=connectivity scf=maxcycles=1024 pseudo=read

Ce(III) - PQQ(0)

0 2

Atomic coordinates and
geometry specifications as in Figure IX.12

C H N O 0
6-31G(d)
****
Ce 0
S 5 1.00
66920.6810000 0.000005
7142.4190000 0.000062
1149.2279000 0.000408
626.0474000 0.000080
137.2813000 0.003559
S 1 1.00
36.6434000 1.0
S 1 1.00
25.9742000 1.0
S 1 1.00
11.8859000 1.0
S 1 1.00
3.0284000 1.0
S 1 1.00
1.5664000 1.0
S 1 1.00
0.5937000 1.0
S 1 1.00
0.2630000 1.0
S 1 1.00
0.0490000 1.0
S 1 1.00
0.0207000 1.0
P 6 1.00
3813.8026000 0.000005
1216.9447000 0.000051
496.6641000 0.000053
212.5431000 0.000671
27.6306000 0.008805
19.6040000 0.150861
P 1 1.00
13.8918000 1.0
P 1 1.00
4.4389000 1.0
P 1 1.00
2.3374000 1.0
P 1 1.00
1.1067000 1.0
P 1 1.00
0.5287000 1.0
P 1 1.00
0.2305000 1.0
P 1 1.00
```

```
0.0800000 1.0
D 6 1.00
367.7157000 0.000120
109.8798000 0.000991
36.0211000 0.007778
14.7637000 -0.062958
7.3281000 0.180342
3.9441000 0.432529
D 1 1.00
2.0202000 1.0
D 1 1.00
0.9649000 1.0
D 1 1.00
0.3273000 1.0
D 1 1.00
0.1032000 1.0
F 5 1.00
123.4821000 0.001566
43.9881000 0.018101
19.4518000 0.076157
8.6013000 0.192683
3.8049000 0.324332
F 1 1.00
1.6176000 1.0
F 1 1.00
0.6364000 1.0
F 1 1.00
0.2164000 1.0
G 4 1.00
19.4518000 0.002199
8.6013000 0.037428
3.8049000 0.030378
1.6176000 0.355664
G 1 1.00
0.6364000 1.0
G 1 1.00
0.2164000 1.0
****

Ce 0
ECP28MWB 5 28
H-Komponente
1
2 1.000000 0.000000
S-H
1
2 20.137829 580.083457
P-H
1
2 15.998482 310.302833
D-H
1
2 14.974187 167.813944
F-H
1
2 23.402455 -49.390229
G-H
1
2 16.570553 -21.331879

stoichiometry=H2O1
solventname=water
eps=4.0
```

Lu^{3+} PQQ^{0}

```
#p opt=maxcycle=999 freq rb3lyp/gen scrf=(cpcm,solvent=water,read)
geom=connectivity pseudo=read scf=maxcycles=1024 formcheck

Lu(III) - PQQ(0)

0 1
Atomic coordinates and
geometry specifications as in Figure IX.12

C H N O 0
6-31G(d)
****
Lu 0
S 5 1.00
95169.7670000 0.000022
15488.4030000 0.000145
3776.2335000 0.000651
1079.0501000 0.002038
268.9538000 0.005127
S 1 1.00
63.4679000 1.0
S 1 1.00
45.1332000 1.0
S 1 1.00
21.4568000 1.0
S 1 1.00
5.3483000 1.0
S 1 1.00
2.6778000 1.0
S 1 1.00
1.0287000 1.0
S 1 1.00
0.4408000 1.0
S 1 1.00
0.0791000 1.0
S 1 1.00
0.0313000 1.0
P 6 1.00
4043.9748000 0.000294
958.8771000 0.002353
309.1220000 0.010441
114.2203000 0.025828
37.1091000 0.085047
20.4579000 -0.200371
P 1 1.00
14.5932000 1.0
P 1 1.00
6.527500 1.0
P 1 1.00
3.2448000 1.0
P 1 1.00
1.4504000 1.0
P 1 1.00
0.6635000 1.0
P 1 1.00
0.2858000 1.0
P 1 1.00
0.080000 1.0
D 6 1.00
484.5275000 0.002286
146.6655000 0.018629
56.3779000 0.074088
23.6711000 0.161554
9.4401000 0.308091
4.3712000 0.448334
D 1 1.00
1.9580000 1.0
D 1 1.00
0.7272000 1.0
D 1 1.00
0.2460000 1.0
D 1 1.00
0.0744000 1.0
F 5 1.00
175.1559000 0.004102
62.8909000 0.039086
28.3624000 0.147044
13.2478000 0.271092
6.1440000 0.345665
F 1 1.00
2.7623000 1.0
F 1 1.00
1.1574000 1.0
F 1 1.00
0.4244000 1.0
G 4 1.00
28.3624000 0.047905
13.2478000 0.150128
6.1440000 0.322911
2.7623000 0.444494
G 1 1.00
1.1574000 1.0
G 1 1.00
0.4244000 1.0
****

Lu 0
ECP28MWB 5 28
H-Komponente
1
2 1.000000 0.000000
S-H
1
2 35.162097 989.995584
P-H
1
2 19.464402 278.865652
D-H
1
2 10.006865 71.009178
F-H
1
2 23.517932 -47.405890
G-H
1
2 29.412238 -35.557146

stoichiometry=H2O1
solventname=water
eps=4.0
```

Table IX.5: Location of highest electron density and energy values of the calculated molecular orbitals (MO) for the calculations given in Figure IX.11.

Number	Orbital	Location of highest e^--density	Additional e^--density	Energy		
				Hartrees	eV	kJ/mol
La^{3+} PQQ^0						
265	HOMO-3	Asp388	Asp301 + Arg326	-0.23192	-6.31087	-608.906
266	HOMO-2	Asp301	Asp388	-0.23137	-6.29590	-607.462
267	HOMO-1	Asp388	Arg326	-0.22645	-6.16202	-594.544
268	HOMO	Asp388	-	-0.21038	-5.72473	-552.353
269	LUMO	PQQ	-	-0.14161	-3.85341	-371.797
270	LUMO+1	PQQ	-	-0.11693	-3.18183	-307.000
La^{3+} $PQQ^{\bullet-}$						
266-a	HOMO-3	PQQ	Asp388	-0.22487	-6.11903	-590.396
266-b	HOMO-2	Asp388	Arg326 + PQQ	-0.22295	-6.06678	-585.355
267-a	HOMO-2	Asp388	Arg326	-0.22282	-6.06324	-585.014
267-b	HOMO-3	PQQ	Arg326 + Asp388	-0.22212	-6.04420	-583.176
268-a	HOMO-1	Asp388	-	-0.20769	-5.65154	-545.290
268-b	HOMO-1	Asp388	-	-0.20768	-5.65126	-545.264
269-a	HOMO	PQQ	-	-0.17401	-4.73506	-456.863
269-b	LUMO	PQQ	-	-0.10397	-2.82917	-272.973
270-a	LUMO+1	PQQ	-	-0.10276	-2.79624	-269.796
Ce^{3+} PQQ^0						
266-b	HOMO-3	Asp388	Asp301	-0.23159	-6.30189	-608.040
266-a	HOMO-3	Asp388	Asp301	-0.23158	-6.30162	-608.013
267-b	HOMO-2	Asp388	Arg326	-0.22657	-6.16529	-594.860
267-a	HOMO-2	Asp388	Arg326	-0.22657	-6.16529	-594.860
268-b	HOMO-1	Asp388	-	-0.21046	-5.72691	-552.563
268-a	HOMO-1	Asp388	-	-0.21046	-5.72691	-552.563
269-a	SOMO	Ce^{3+}	-	-0.19763	-5.37779	-518.878
269-b	LUMO	PQQ	-	-0.14155	-3.85177	-371.640
270-a	LUMO	PQQ	-	-0.14155	-3.85177	-371.640
270-b	LUMO+1	PQQ	-	-0.11667	-3.17475	-306.317
271-a	LUMO+1	PQQ	-	-0.11671	-3.17584	-306.422
Ce^{3+} $PQQ^{\bullet-}$						
266-a	HOMO-3	PQQ	-	-0.22722	-6.18297	-596.566
266-b	HOMO-3	PQQ	-	-0.22373	-6.08801	-587.403
267-a	HOMO-2	Asp388	Arg326	-0.22237	-6.05100	-583.832
267-b	HOMO-2	Asp388	Arg326	-0.22235	-6.05045	-583.780
268-a	HOMO-1	Asp388	-	-0.20890	-5.68446	-548.467
268-b	HOMO-1	Asp388	-	-0.20885	-5.68310	-548.336
269-a	SOMO	Ce^{3+}	-	-0.18258	-4.96826	-479.364
270-a	HOMO	PQQ	Ce^{3+}	-0.17564	-4.77941	-461.143
269-b	LUMO	PQQ	-	-0.10564	-2.87461	-277.358
270-b	LUMO+1	PQQ	-	-0.09881	-2.68876	-259.426
Lu^{3+} PQQ^0						
272	HOMO-3	Asp388	Arg326 + PQQ	-0.23099	-6.28556	-606.464
273	HOMO-2	Asp388	Arg326 + Asp301	-0.22661	-6.16638	-594.965
274	HOMO-1	Asp301	-	-0.22574	-6.14270	-592.680
275	HOMO	Asp388	-	-0.21016	-5.71875	-551.775
276	LUMO	PQQ	-	-0.14311	-3.89422	-375.735
277	LUMO+1	PQQ	-	-0.11684	-3.17938	-306.763
Lu^{3+} $PQQ^{\bullet-}$						
273-a	HOMO-3	Asp388	Arg326	-0.22188	-6.03767	-582.546
273-b	HOMO-3	Asp388	Arg326	-0.22187	-6.03739	-582.520
274-a	HOMO-2	Asp301	-	-0.22005	-5.98787	-577.741
274-b	HOMO-2	Asp301	-	-0.21990	-5.98379	-577.347
275-a	HOMO-1	Asp388	-	-0.20811	-5.66296	-546.393
275-b	HOMO-1	Asp388	-	-0.20806	-5.66160	-546.262
276-a	HOMO	PQQ	-	-0.17618	-4.79410	-462.561
276-b	LUMO	PQQ	-	-0.10606	-2.88604	-278.461
277-a	LUMO+1	PQQ	-	-0.10285	-2.79869	-270.033

1 Hartree ~ 27.2114 eV ~ 2625.50 kJ·mol^{-1}.[305]

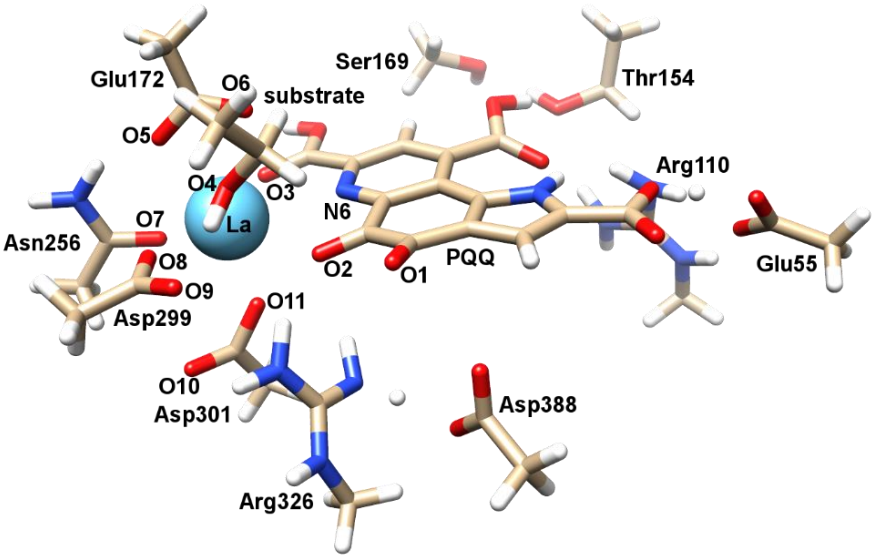

Table IX.6: Ln-ligand distances [Å] for the active site calculations given in Figure Figure IX.11.

	La-PQQ^0	La-PQQ$^{\cdot-}$	Ce-PQQ^0	Ce-PQQ$^{\cdot-}$	Lu-PQQ^0	Lu-PQQ$^{\cdot-}$
PQQ O2	2.88072	2.61357	2.86311	2.59050	2.72515	2.43018
PQQ N6	2.96958	2.85159	2.94383	2.81733	2.73335	2.63617
PQQ O3	2.71471	2.76245	2.69047	2.73264	2.49334	2.55311
Substrate O4	2.63346	2.65730	2.63014	2.66181	2.59689	2.57834
Glu172 O5	2.54295	2.56530	2.52417	2.55965	2.41993	2.44482
Glu172 O6	2.67813	2.71147	2.66758	2.65592	2.55701	2.67900
Asn256 O7	2.53227	2.61032	2.50117	2.58137	2.28928	2.39758
Asp299 O8	2.39335	2.44359	2.35205	2.38363	2.17319	2.21431
Asp301 O10	3.86233	4.08612	3.84750	3.98604	3.73898	3.80749
Asp301 O11	2.38081	2.36061	2.35938	2.33516	2.30894	2.28001

Table IX.7 Visualization of the frontier orbitals for the calculations given in Figure IX.11. In all cases, the LUMO of the PQQ^0 species and the HOMO of the $PQQ^{\bullet-}$ species seem to be the same PQQ related orbital. In case of La^{3+} and Lu^{3+}, the sign of the orbital wave function changes, probably due to the change from a closed- to an open shell system.

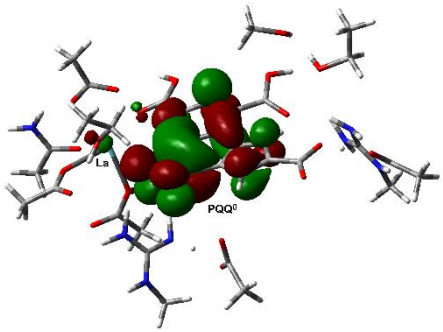 **La^{3+} PQQ^0 - 269 LUMO**	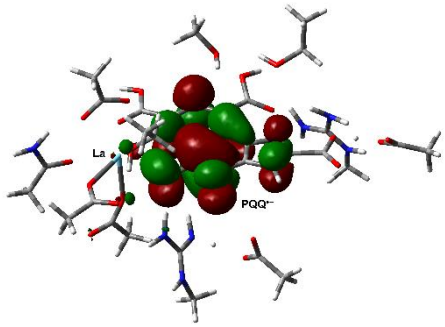 **La^{3+} $PQQ^{\bullet-}$ - 269-a HOMO**
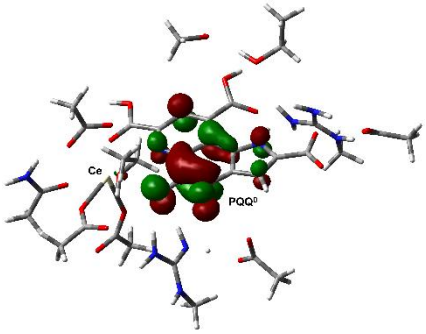 **Ce^{3+} PQQ^0 - 270-a LUMO**	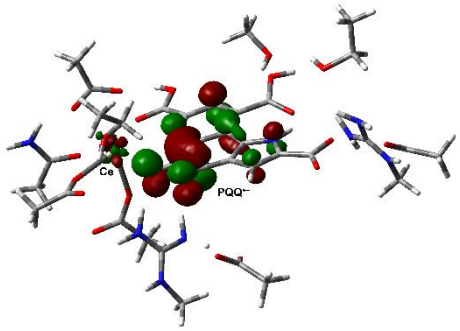 **Ce^{3+} $PQQ^{\bullet-}$ - 270-a HOMO**
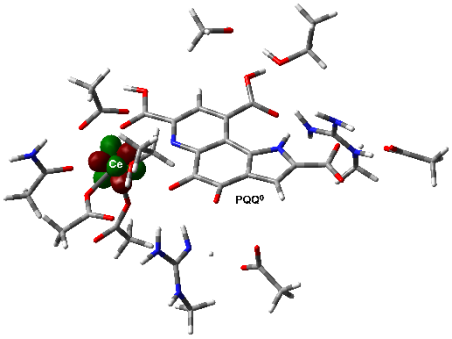 **Ce^{3+} PQQ^0 - 269-a SOMO**	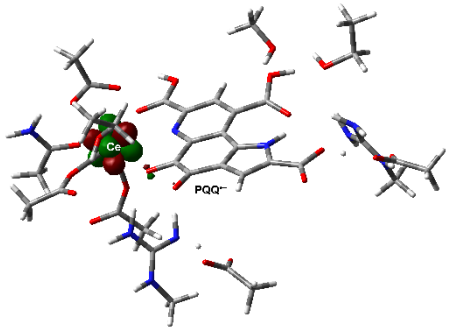 **Ce^{3+} $PQQ^{\bullet-}$ - 269-a SOMO**
Lu^{3+} PQQ^0 - 276 LUMO 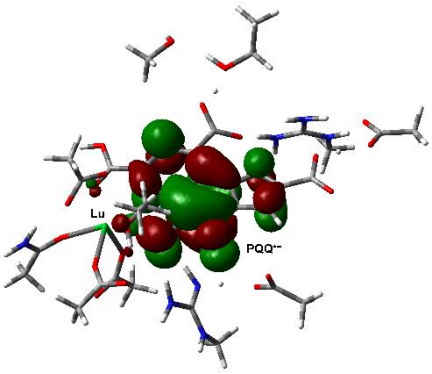	**Lu^{3+} $PQQ^{\bullet-}$ - 276-a HOMO** 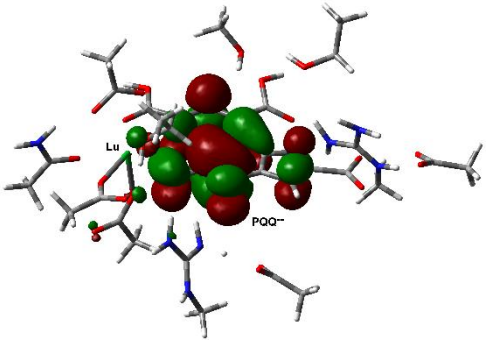

1.3. Supporting Information of Chapter IV.1

1.3.1 Experimental Section

Nuclear Magnetic Resonance (NMR) ^{1}H-NMR and ^{13}C-NMR spectra were recorded, unless otherwise stated, at room temperature or 0°C with Jeol ECP 270 (400 MHz), Jeol ECX 400 (400 MHz) and Bruker Avance III (400 MHz) spectrometers operating at 400 MHz for proton nuclei and 100 MHz for carbon nuclei. Low temperature measurements (-50°C) were performed on a Varian NMR System (400 MHz). ^{1}H-chemical shifts are reported in units of ppm relative to DMSO-d_6 (δ_H = 2.50) and DMF-d_7 (δ_H = 8.03). ^{13}C-NMR chemical shifts are given in units of ppm relative to DMSO-d_6 (δ_H = central line of septet: δ_C= 39.52) and DMF-d_7 (central line of triplet: δ_C= 163.15). The software used for data processing was MestReNova Version 11.0. Two-dimensional heteronuclear multiple quantum correlation (HMQC) and heteronuclear multiple bond connectivity (HMBC) experiments were used to assign each resonance in the spectra. Experiments were performed by default with 16 scans for ^{1}H-NMR and 4000 scans for ^{13}C-NMR experiments and were increased to up to 64 scans for ^{1}H-NMR and 10000 scans for ^{13}C-NMR for correct assignments and side-product analysis. Solid state NMR was performed at room temperature with a Bruker Avance III (500 MHz, 11,74 T) with Magic-Angle-Spinning (MAS) in 4-mm rotors. ^{1}H-NMR with single pulse excitation, ^{13}C-NMR with cross-polarization over ^{1}H. Scan delays (d1): ^{13}C: 16 s; ^{1}H: 128 s. Chemical shifts are reported in units of ppm relative to TMS, indirectly measured with 0.1% TMS in $CDCl_3$. All NMR spectra are included in the supporting information.

Stepwise addition of lanthanide(III) and calcium(II) salts to PQQ Metal induced NMR shifts were used in order to examine the position of coordinating metals to PQQ in solution. PQQ shows good solubility in polar solvents like H_2O (pH > 7), MeOH, DMSO and DMF but not in MeCN. While metal addition to aqueous solutions of PQQ lead to precipitation of a 1:1 complex, solutions in methanol give a hemiketal adduct as predominant species, which complicates analysis. In DMSO significant solvent complexation can also occur and is comparatively stronger than in other solvents ($[Ln(DMSO)_8]^{3+}$ - for a summary, see Cotton and Harrowfield).[123] Therefore, DMF-d_7 was the solvent of choice for coordination experiments. Unless otherwise noted, the NMR tube contained PQQ (9 mg, 27 µmol), which was dissolved by sonication at 50°C for 5 min. $LiClO_4$ (16 mg, 0.15 mmol) for controlled ionic strength and Ln/Ca-salts were always added as solids and were dissolved by sonication at 50°C for 5 min. In case of

very small amounts of metal (0.01 equiv.), a stock solution was prepared in DMF-d_7 (0.01 mg/µL) which was used for metal addition (0.01 equiv. equals around 10 µL of stock solution (Table IX.8). ^{1}H- and ^{13}C-NMR spectra were recorded within 1 h after the metal addition. Experiments with higher amounts of PQQ (50 mg, 151 µmol) in DMF-d_7 (0.6 mL) were performed in the same way, but higher temperatures (65°C) were necessary to ensure complete dissolution. All NMR experiment conditions can be found in Table IX.8, and shifts in Table IX.9-11. **FT-Infrared Spectroscopy (IR)** was carried out with a Jasco FT/IR-460Plus with an ATR Diamond Plate. IR data can be found in Table IX.12 and Figure IX.17-18. **UV-Vis spectroscopy** of the different PQQ derivatives was conducted with an Agilent 8453 Diode Array Spectrophotometer in a 1 cm pathlength quartz Suprasil® cuvette. The following stock solutions were prepared: PQQ in DMF or DMSO (4 mM). A blank was recorded with 990 µL solvent (DMF/DMSO/H_2O), followed by addition of 10 µL of the respective PQQ stock solution (4 mM) to yield a final concentration of 4 µM. For measurements in H_2O, the PQQ stock solution in DMF was used, leading to a total DMF concentration of 1% in the cuvette. Spectra were recorded instantly after mixing. UV-Vis spectra can be found in Figure IX.19. **UV-Vis spectroscopy** of PQQ (**13**) in DMF or water with lanthanide- and calcium chlorides was performed on an Epoch 2 Plate Reader from Biotek, using a 96 well quartz microplate from Hellma. In DMF, measurements included 190 µL of a PQQ stock solution in DMF (42.1 µM) and 10 µL of DMF or 10 µL of $LnCl_3 \cdot nH_2O$ (Ln=La-Lu – n=7 for La-Ce and n=6 for Pr-Lu, except Sm and Dy, where n=0) or $CaCl_2 \cdot 2H_2O$ in DMF (0.8 mM), to yield a final concentration of 40 µM for both PQQ and metal salts (1:1) (Figure IV.6). In a subsequent experiment, 2 µL of DMF, 2 µL of $LnCl_3 \cdot nH_2O$ (Ln=La-Lu, except Pm) or $CaCl_2 \cdot 2H_2O$ in DMF (40 mM) were added to the respective well, resulting in a final PQQ concentration of 39.6 µM and a PQQ to metal ratio of 1:11. A blank was recorded in pure DMF (200 µL) and the resulting absorbance was subtracted from the spectra. Additional UV-Vis spectra can be found in Figure IX.24 and Figure IX.25. Measurements in water included 180 µL of a PQQ stock solution in H_2O (278 µM) and 20 µL of H_2O or 18 µL of H_2O and 2 µL of $LnCl_3 \cdot nH_2O$ (Ln=La-Lu – n=7 for La-Ce and n=6 for Pr-Lu, except Sm and Dy, where n=0) or $CaCl_2 \cdot 2H_2O$ in H_2O (25 mM), to yield a final concentration of 250 µM for both PQQ and metal salts (1:1) (Figure IX.21). A solvent blank was recorded and subtracted from the respective spectrum. **Job's plot measurements** included PQQ, as well as $LuCl_3$ (anhydrous) stock solutions in DMF (200 µM) (Figure IX.23) or in water (250 µM) (Figure IX.22) and were

conducted using a plate reader (Epoch 2). For the PQQ stock solution in water, a concentrated DMF solution was prepared first (25 mM), which was diluted with water to the final 250 µM concentration (including 130 mM DMF). The $LuCl_3$ stock solution in water was treated with the same amount of DMF (130 mM). Both water and DMF based measurements included x µL PQQ & y µL $LuCl_3$ (x = 200; 190; 180; …; 0) (y = 200 − x) - total of 20 different ratios. For data processing the corrected extinction of PQQ was calculated at 343 nm (data analysis in water) or 435 nm (in DMF) and plotted against the mole fraction of added lutetium(III). **Stepwise addition** (0.2 equiv. steps) of metal salts to a fixed concentration of dissolved PQQ included stock solutions of PQQ (333.33 µM) in water and 5 mM stock solutions of $LaCl_3{\cdot}7H_2O$; $LuCl_3{\cdot}6H_2O$; or $CaCl_2{\cdot}2H_2O$ in water. Each well contained 200 µL total volume, including 150 µL PQQ + x µL metal salt + y µL water (x = 0; 2; 4; …; 50) (y = 50 − x), resulting in 250 µM PQQ with increasing amounts of metal salts (0.2 equiv. per 2 µL added) (Figure IV.5 and Figure IX.21).

Elemental Microanalyses (EA) (C, H, N) were performed with a vario EL element analyzer. **Inductively Coupled Plasma Optical Emission Spectroscopy (ICP-OES)** was conducted with a VARIAN-VISTA instrument with autosampler and was used for determining lanthanide and calcium contents of precipitates. Samples were digested in hot nitric acid and then diluted with Millipore water to a final HNO_3 concentration of 3%. The following wavelengths (nm) were used for metal content determination: La (333.749, 408.671), Eu (381.967, 397.197), Lu (291.139), Ca (393.366, 396.847). The values shown are averaged. **DFT Calculations** were performed with Gaussian 09, Revision D.01.[79] All calculations were performed using the B3LYP functional[80-83, 85, 303] and the 6–31g(d) basis set was used. Solvent effects were modeled using the conductor-like polarizable continuum model (CPCM) with the default setting for the universal force field (UFF).[288-289] Magnetic properties (NMR-shifts) were calculated by the gauge-independent atomic orbital (GIAO) method.[290-291] Calculated structures and shifts can be found in Table IX.6. **Thermogravimetric analysis** (TGA) was performed on a TGA 4000 system from PerkinElmer, using Al_2O_3 crucibles and plots can be found in Figure IX.27. **ESI mass** spectra of PQQ were recorded with a Thermo Finnigan LTQ FT Ultra Fourier Transform Ion Cyclotron Resonance mass spectrometer with acetonitrile/water as the carrier solvent.

Materials Metal salts were purchased from abcr Germany ($LnCl_3 \cdot nH_2O$ - Ln, 99,9% = Nd, Sm, Gd, Tb, Dy, Ho, Er, Tm, Yb, Lu; $Ln(NO_3)_3 \cdot nH_2O$ – Ln, 99.99% = La, Lu), Sigma-Aldrich ($LnCl_3 \cdot nH_2O$ - Ln, 99,99% = La, Ce, Pr, Eu) Alfa Aesar ($LiClO_4$, 99%; $Ca(NO_3)_3 \cdot 4H_2O$, 99.9995%) and VWR ($CaCl_2 \cdot 2H_2O$, 99%). The water of crystallization of the lanthanides (nH_2O) was analyzed by elemental microanalysis prior to experiments and is given in the respective experimental descriptions. Deuterated solvents were purchased from Sigma-Aldrich (DMF-d_7, 99.5%) and EurIsotop (DMSO-d_6, 99.8%). PQQ was either used from a commercial source (Fluorochem Ltd. Hadfield (97% purity, EA: Found: C, 47.81; H, 3.02; N, 7.98. Calc. for [$C_{14}H_6N_2O_8 \cdot 1.4\ H_2O$]: C, 47.31; H, 2.5; N, 7.88.) or conveniently (and cost-saving) extracted from Doctor's Best® Science-Based Nutrition™ BioPQQ® capsules, as described below, and transferred from its disodium salt to the fully protonated form, which gave PQQ in high purity. MilliQ-grade water (pH 5.5) was used for all experiments, received from a Millipore® Synergy® UV system from Merk (Darmstadt, Germany).

Isolation and purification of PQQ PQQ was extracted from Doctor's Best® Science-Based Nutrition™ BioPQQ® capsules containing PQQ (as PQQ disodium salt), cellulose and modified cellulose. The capsules (60 x 20 mg PQQ = 1.20 g, 3.21 mmol) were emptied and the powder suspended in water (250 mL). While the PQQ sodium salt was soluble in water, the cellulose which remained as a solid, was filtered off and washed several times with water, until the filtrate was colorless. The water was subsequently removed from the filtrate under reduced pressure to give the disodium salt of PQQ as a brown powder (1.12 g, 2.99 mmol, 93 %). ^{1}H-NMR (400 MHz, DMSO-d_6): δ / ppm = 8.61 (s, 1H, 8), 7.08 (d, J = 1.4 Hz, 1H, 3). IR (neat): $\tilde{\nu}$ / cm^{-1} = 3303, 2360, 2171, 1668, 1603, 1541, 1499, 1339, 1230, 905, 712. EA: Found C 35.72; H 3.39; N 5.93; calc. for $C_{14}H_4N_2Na_2O_8.5.5H_2O$ (PQQ disodium salt) (373.98): C 35.53; H 3.19; N 5.92. The isolated $PQQNa_2$ was converted to the fully protonated form according to a literature procedure.[154] In brief, crude $PQQNa_2$ (1.12 g, 2.99 mmol) was dissolved in water (500 mL) and heated to 70°C. Concentrated HCl (2.3 mL) was added and the mixture was stirred at 70°C for 24 h. The resulting precipitate was filtered, washed with 2 M HCl and dried *in vacuo*. The product (1.02 g, 3.09 mmol, 91 %) was isolated as a bright red solid. Total yield over two purification steps: 85%. IR (neat): $\tilde{\nu}$ / cm^{-1} = 1742 (m), 1699 (m), 1640 (s) (C=O); 1506 (m) (C=N); 1191 (s), 1263 (s), 1315 (s) (C=C); 865 (m) (C-N). EA: Found: C, 48.04; H, 2.50; N, 7.93. Calc. for [$C_{14}H_6N_2O_8 \cdot 1.15\ H_2O$]: C,

47.92; H, 2.38; N, 7.98. HRMS (ESI −, H_2O/MeCN): m/z calc. for $[C_{14}H_5N_2O_8]^-$: 329.0051; found: 329.0051.

PQQ-metal complex precipitation from water $PQQNa_2$ (**14**) (30 mg, 0.08 mmol - received from Doctor's Best® Science-Based Nutrition™ BioPQQ® capsules) was dissolved in H_2O (12 mL). $LaCl_3{\cdot}7H_2O$ (**A**: 0.5 equiv., 14.9 mg, 0.04 mmol /**B**: 1.0 equiv., 29.8 mg, 0.08 mmol/**C**: 2.0 equiv., 59.5 mg, 0.16 mmol) was added as a solid, resulting in an immediate turbidity and a color change from dark red to light-brown. The suspension was centrifuged (5 minutes at 4500 rpm in a Heraeus Megafuge 8R Benchtop Centrifuge with swinging bucket) and the colorless supernatant removed. To wash the resulting pellet, water was added (12 mL) and the suspension was first vortexed and then centrifuged (same configuration), followed by removal of the supernatant. This washing step was repeated two more times. The pellet was then transferred to a Schlenk flask and dried overnight under high vacuum, to afford A: 26 mg, B: 23 mg and C: 43 mg of a brown powder. EA (CHNLa): (**A**) Found C, 30.42; H, 2.44; N, 5.17; La, 25.94. (**B**) Found: C, 31.21; H, 2.34; N, 5.22; La 22.97. (**C**) Found: C, 30.14; H, 2.50; N, 5.19; La 25.18. Calc. for $PQQLa{\cdot}5H_2O$ $[C_{14}H_{13}LaN_2O_{13}]$: C, 30.23; H, 2.36; N, 5.04; La, 24.98. The experiments were repeated with $CaCl_2{\cdot}2H_2O$ (0.5; 1.0; 2.0; 3.0 equiv.), $EuCl_3{\cdot}6H_2O$ (1.0 and 3.0 equiv.) and $LuCl_3{\cdot}6H_2O$ (1.0 and 3.0 equiv.), each indicating a $PQQ{\cdot}M{\cdot}5H_2O$ complex as well (IR Data are available in the supporting information, Figure IX.18). We have attempted to obtain mass spectra of the M-PQQ complexes, however, we mostly observed PQQ (**13**) and the geminal diol (**15**, Figure IX.15B).

1.3.2 Supporting Information

Table IX.8: Compound composition of NMR-experiments. (-) indicates the same mixture as in the lane above and therefore no addition, (/) indicates no addition at all.

Experiment	Solvent	PQQ	Metal-salt	$LiClO_4$ & other additives
$LaCl_3$ (1 equiv.)	DMF-d_7 (0.6 mL)	9 mg (27.2 µmol)	$LaCl_3 \cdot 7H_2O$ 10.1 mg, 27.2 µmol	/
$LaCl_3$ (2 equiv.)	-	-	+10.1 mg $LaCl_3 \cdot 7H_2O$ (20.2 mg, 54.5 µmol)	/
$LaCl_3$ (3 equiv.)	-	-	+10.1 mg $LaCl_3 \cdot 7H_2O$ (30.4 mg, 81.7 µmol)	/
$LaCl_3$ (4 equiv.)	-	-	+10.1 mg $LaCl_3 \cdot 7H_2O$ (40.5 mg, 109.0µmol)	/
$LaCl_3$ (5 equiv.)	-	-	+10.1 mg $LaCl_3 \cdot 7H_2O$ (50.6 mg, 136.2 µmol)	/
$LiClO_4$	DMF-d_7 (0.6 mL)	9 mg (27.2 µmol)	/	16.0 mg (150 mmol, 250 mM)
$LaCl_3$ (0.5 equiv.) $LiClO_4$	-	-	+5.1 $LaCl_3 \cdot 7H_2O$ (5.1 mg, 13.6 µmol)	-
$LaCl_3$ (1 equiv.) $LiClO_4$	-	-	+10.1 mg $LaCl_3 \cdot 7H_2O$ (10.1 mg, 27.2 µmol)	-
$LaCl_3$ (5 equiv.) $LiClO_4$	-	-	+40.5mg $LaCl_3 \cdot 7H_2O$ (50.6 mg, 136.0 µmol)	-
$LaCl_3$ (10 equiv.) $LiClO_4$	-	-	+50.6 mg $LaCl_3 \cdot 7H_2O$ (101.2 mg, 272.1 µmol)	-
$La(NO_3)_3$ (0.25 equiv.) $LiClO_4$ (0°C+r.t.)	DMF-d_7 (0.6 mL)	9 mg (27.2 µmol)	$La(NO_3)_3 \cdot 6H_2O$ (2.9 mg, 6.8 µmol)	16.0 mg (150 mmol, 250 mM)
$La(NO_3)_3$ (0.50 equiv.) $LiClO_4$ (-50°C+0°C+r.t.)	-	-	+ 2.9 mg $La(NO_3)_3 \cdot 6H_2O$ (5.9 mg, 13.6 µmol)	-
$La(NO_3)_3$ (1.0 equiv.) $LiClO_4$ (r.t.)	-	-	+ 5.9 mg $La(NO_3)_3 \cdot 6H_2O$ (11.8 mg, 27.2 µmol)	-
$CaCl_2$ (1 equiv.)	DMF-d_7 (0.6 mL)	9 mg (27.2 µmol)	$CaCl_2 \cdot 2H_2O$ 4.0 mg, 27.2 µmol	/
$CaCl_2$ (2 equiv.)	-	-	+4.0 mg $CaCl_2 \cdot 2H_2O$ (8.0 mg, 54.5 µmol)	/
$CaCl_2$ (3 equiv.)	-	-	+4.0 mg $CaCl_2 \cdot 2H_2O$ (12.0 mg, 81.7 µmol)	/
$CaCl_2$ (4 equiv.)	-	-	+4.0 mg $CaCl_2 \cdot 2H_2O$ (16.0 mg, 109.0µmol)	/
$CaCl_2$ (5 equiv.)	-	-	+4.0 mg $CaCl_2 \cdot 2H_2O$ (20.0 mg, 136.2 µmol)	/
$CaCl_2$ (1 equiv.) $LiClO_4$	DMF-d_7 (0.6 mL)	9 mg (27.2 µmol)	$CaCl_2 \cdot 2H_2O$ 4.0 mg, 27.2 µmol	16.0 mg (150 mmol, 250 mM)
$CaCl_2$ (5 equiv.) $LiClO_4$	-	-	+ 16.0 mg $CaCl_2 \cdot 2H_2O$ (20.0 mg, 136.0 µmol)	-
$CaCl_2$ (10 equiv.) $LiClO_4$	-	-	+ 20.0 mg $CaCl_2 \cdot 2H_2O$ (40.0 mg, 272.1 µmol)	-
$CaCl_2$ (10 equiv.) $LiClO_4$ + H_2O	-	-	-	+ 9.8 µL H_2O (54.5 µmol, 20 equiv.
$Ca(NO_3)_3$ (1.0 equiv.) $LiClO_4$	DMF-d_7 (0.6 mL)	9 mg (27.2 µmol)	$Ca(NO_3)_2 \cdot 4H_2O$ (6.4 mg, 27.2 µmol)	16.0 mg (150 mmol, 250 mM)
$LuCl_3$ (1.0 equiv.)	DMF-d_7 (0.6 mL)	9 mg (27.2 µmol)	$LuCl_3 \cdot 6H_2O$ (10.6 mg, 27.2 µmol)	16.0 mg (150 mmol, 250 mM)
$LuCl_3$ (1.0 equiv.)	DMF-d_7 (0.6 mL)	9 mg (27.2 µmol)	$LuCl_3 \cdot 6H_2O$ (10.6 mg, 27.2 µmol)	/
$LuCl_3$ (5.0 equiv.)	-	-	+ 42.5 mg $LuCl_3 \cdot 6H_2O$ (53.1 mg, 27.4 µmol)	/
$LuCl_3$ (10.0 equiv.)	-	-	+ 53.1 mg $LuCl_3 \cdot 6H_2O$ (106.2 mg, 27.4 µmol)	/
$Lu(NO_3)_3$ (0.25 equiv.) $LiClO_4$ (0°C+r.t.)	DMF-d_7 (0.6 mL)	9 mg (27.2 µmol)	$Lu(NO_3)_3 \cdot 6H_2O$ (3.2 mg, 6.8 µmol)	16.0 mg (150 mmol, 250 mM)
$Lu(NO_3)_3$ (1.0 equiv.) $LiClO_4$ (r.t.)	-	-	+ 9.6 mg $Lu(NO_3)_3 \cdot 6H_2O$ (12.8 mg, 27.3 µmol)	-
$CeCl_3$ (0.5 equiv.)	DMF-d_7 (0.6 mL)	9 mg (27.2 µmol)	$CeCl_3 \cdot 7H_2O$ (4.8 mg, 13.7 µmol)	/
$CeCl_3$ (1.0 equiv.)	-	-	+ 5.1 mg $CeCl_3 \cdot 7H_2O$ (10.2 mg, 27.4 µmol)	/
$CeCl_3$ (1.5 equiv.)	-	-	+ 5.1 mg $CeCl_3 \cdot 7H_2O$ (15.3 mg, 41.1 µmol)	/
$CeCl_3$ (2.0 equiv.)	-	-	+ 5.1 mg $CeCl_3 \cdot 7H_2O$ (20.4 mg, 54.8 µmol)	/
$CeCl_3$ (2.5 equiv.)	-	-	+ 5.1 mg $CeCl_3 \cdot 7H_2O$ (25.5 mg, 68.4 µmol)	/

$CeCl_3$ (3.0 equiv.)	-	-	+ 5.1 mg $CeCl_3 \cdot 7H_2O$ (30.6 mg, 82.1 µmol)	/
$PrCl_3$ (0.5 equiv.)	DMF-d_7 (0.6 mL)	9 mg (27.2 µmol)	$PrCl_3 \cdot 6H_2O$ (4.8 mg, 13.6 µmol)	/
$PrCl_3$ (1.0 equiv.)	-	-	+ 4.8 mg $PrCl_3 \cdot 6H_2O$ (9.6 mg, 27.2 µmol)	/
$PrCl_3$ (1.5 equiv.)	-	-	+ 4.8 mg $PrCl_3 \cdot 6H_2O$ (14.4 mg, 40.9 µmol)	/
$PrCl_3$ (2.0 equiv.)	-	-	+ 4.8 mg $PrCl_3 \cdot 6H_2O$ (19.2 mg, 54.5 µmol)	/
$PrCl_3$ (2.5 equiv.)	-	-	+ 4.8 mg $PrCl_3 \cdot 6H_2O$ (24.0 mg, 68.1 µmol)	/
$PrCl_3$ (3.0 equiv.)	-	-	+ 4.8 mg $PrCl_3 \cdot 6H_2O$ (28.8 mg, 81.8 µmol)	/
$SmCl_3$ (0.5 equiv.)	DMF-d_7 (0.6 mL)	9 mg (27.2 µmol)	$SmCl_3$ (4.8 mg, 13.7 µmol)	/
$SmCl_3$ (1.0 equiv.)	-	-	+ 3.5 mg $SmCl_3$ (7.0 mg, 27.4 µmol)	/
$SmCl_3$ (1.5 equiv.)	-	-	+ 3.5 mg $SmCl_3$ (10.5 mg, 41.1 µmol)	/
$SmCl_3$ (2.0 equiv.)	-	-	+ 3.5 mg $SmCl_3$ (14.0 mg, 54.8 µmol)	/
$SmCl_3$ (2.5 equiv.)	-	-	+ 3.5 mg $SmCl_3$ (17.5 mg, 68.4 µmol)	/
$SmCl_3$ (3.0 equiv.)	-	-	+ 3.5 mg $SmCl_3$ (30.6 mg, 82.1 µmol)	/
$EuCl_3$ (0.5 equiv.)	DMF-d_7 (0.6 mL)	9 mg (27.2 µmol)	$EuCl_3 \cdot 6H_2O$ (5.0 mg, 13.6 µmol)	/
$EuCl_3$ (1.0 equiv.)	-	-	+ 5.0 mg $EuCl_3 \cdot 6H_2O$ (10.0 mg, 27.3 µmol)	/
$EuCl_3$ (1.5 equiv.)	-	-	+ 5.0 mg $EuCl_3 \cdot 6H_2O$ (15.0 mg, 40.9 µmol)	/
$EuCl_3$ (2.0 equiv.)	-	-	+ 5.0 mg $EuCl_3 \cdot 6H_2O$ (20.0 mg, 54.5 µmol)	/
$EuCl_3$ (2.5 equiv.)	-	-	+ 5.0 mg $EuCl_3 \cdot 6H_2O$ (25.0 mg, 68.1 µmol)	/
$EuCl_3$ (3.0 equiv.)	-	-	+ 5.0 mg $EuCl_3 \cdot 6H_2O$ (30.0 mg, 81.8 µmol)	/
$EuCl_3$ (0.05 equiv.)	DMF-d_7 (0.6 mL)	9 mg (27.2 µmol)	$EuCl_3 \cdot 6H_2O$ (0.5 mg, 1.4 µmol)	/
$TbCl_3$ (0.01 equiv.)	DMF-d_7 (0.6 mL)	9 mg (27.2 µmol)	$TbCl_3 \cdot 6H_2O$ (0.01 mg/µL DMF-d_7) (0.1018 mg, 10.18 µL, 0.2726 µmol)	/
$TbCl_3$ (0.02 equiv.)	-	-	+ 10.18 µL $TbCl_3 \cdot 6H_2O$ (0.2036 mg, 20.36 µL, 0.5453 µmol)	/
$ErCl_3$ (0.01 equiv.)	DMF-d_7 (0.6 mL)	9 mg (27.2 µmol)	$ErCl_3 \cdot 6H_2O$ (0.01 mg/µL DMF-d_7) (0.1040 mg, 10.40 µL, 0.2725 µmol)	/
$ErCl_3$ (0.02 equiv.)	-	-	+ 10.40 µL $TbCl_3 \cdot 6H_2O$ (0.2080 mg, 20.80 µL, 0.5449 µmol)	/
$TmCl_3$ (0.01 equiv.)	DMF-d_7 (0.6 mL)	9 mg (27.2 µmol)	$TmCl_3 \cdot 6H_2O$ (0.01 mg/µL DMF-d_7) (0.1058 mg, 10.58 µL, 0.2760 µmol)	/
$TmCl_3$ (0.02 equiv.)	-	-	+ 10.40 µL $TmCl_3 \cdot 6H_2O$ (0.2106 mg, 21.06 µL, 0.5519 µmol)	/
PQQ (50 mg)	DMF-d_7 (0.6 mL)	50 mg (143.2 µmol)	/	/

Table IX.9: Overview over all NMR experiments in DMF-d_7 with PQQ and diamagnetic metal salts, ^{1}H- and ^{13}C-NMR shifts in ppm, as well as additional signals from water adducts in blue. Resonances marked with a question mark appeared with higher amounts of metal salts and could not be satisfactorily assigned. The integral values of the PQQ resonances remained unchanged while the ones for the unknown resonances grew with higher amounts of metal salt and with addition of water. 2D-experiments did not show an interaction with carbon resonances from PQQ, meaning that the unknown resonances are unlikely PQQ or PQQ-adduct related.

Experiment / # PQQ	°C	1H	8H	3H	5	4	9'	7'	2'	5a	7	9	1a	8	2	9a	3a	3	1H	?	?	8H	?	3H
PQQ $LiClO_4$	r.t.	13.53	8.82	7.27	179.68	174.46	170.11	166.00	161.94	149.74	148.40	137.28	135.58	130.75	129.24	128.13	125.82	114.41	13.18 (s, 0.04)			8.73 (s, 0.05)		7.27
PQQ	0°C	13.57	8.81	7.26	179.32	174.43	170.23	166.10	162.06	149.88	148.21	137.23	135.49	130.78	129.08	128.03	125.83	114.39	13.26 (s, 0.07)			8.73 (s, 0.10)		7.26 (d, 0.06)
$CaCl_2$ (1.0 equiv.)	r.t.	-	-	-	179.94	174.57	170.03	166.11	162.00	149.76	148.53	138.17	135.92	130.91	129.42	128.14	125.78	114.52	-	-	-	-	-	-
$CaCl_2$ (2.0 equiv.)	r.t.	-	-	-	180.07	174.51	169.89	166.14	161.95	149.60	148.46	138.92	136.09	130.98	129.40	128.01	125.58	114.49	-	-	-	-	-	-
$CaCl_2$ (3.0 equiv.)	r.t.	14.19	8.80	7.29	180.12	174.44	169.78	166.15	161.88	149.48	148.40	139.32	136.14	130.99	129.38	127.90	125.45	114.45	13.57 (s, 0.12)	10.05 (s, 0.37)		8.69 (s, 0.12)		7.29
$CaCl_2$ (4.0 equiv.)	r.t.	14.40	8.80	7.28	-	-	-	-	-	-	-	-	-	-	-	-	-	-	13.71 (s, 0.13)	10.06 (s, 0.60)		8.68 (s, 0.12)		7.28
$CaCl_2$ (5.0 equiv.)	r.t.	14.62	8.80	7.27	180.34	174.30	169.64	166.31	161.83	149.18	148.32	140.66	136.44	131.13	129.28	127.64	125.13	114.42	13.89 (s, 0.16)	10.06 (s, 1.02)		8.68 (s, 0.15)		7.27
$CaCl_2$ (1.0 equiv.) $LiClO_4$	r.t.	13.89	8.81	7.28	179.85	174.41	169.86	166.00	161.88	149.55	148.34	138.32	135.86	130.81	129.24	127.96	125.57	114.39	13.36 (s, 0.06)	9.62 (s, 0.09)		8.71 (s, 0.06)		7.27 (s, 0.14)
$CaCl_2$ (5.0 equiv.) $LiClO_4$	r.t.	14.26	8.78	7.28	179.96	174.17	169.49	166.02	161.64	149.17	148.13	139.56	135.98	130.8	129.14	127.6	125.16	114.27	13.62 (s, 0.13)	9.98 (s, 0.23)		8.67 (s, 0.13)		7.27 (s, 0.09)
$CaCl_2$ (10.0 equiv.) $LiClO_4$	r.t.	14.47	8.75	7.26	179.91	173.86	169.2	166.19	161.4	148.81	147.86	140.40	135.88	130.71	128.91	127.2	124.83	114.11	13.84 (s, 0.23)	9.96 (s, 0.52)		8.63 (s, 0.17)		7.25 (d, 0.38)
$CaCl_2$ (10.0 equiv.) $LiClO_4 + H_2O$	r.t.	14.76	8.77	7.24	180.11	173.77	169.28	166.46	161.46	148.57	147.90	141.28	136.11	130.83	128.75	127.00	124.61	114.12	14.07 (s, 0.34)	9.78 (s, 1.46)		8.65 (s, 0.32)		7.24
$Ca(NO_3)_2$ (1.0 equiv.) $LiClO_4$	r.t.	13.80	8.83	7.27	179.80	174.41	170.04	166.04	161.93	149.60	148.32	138.02	135.79	130.83	129.20	128.03	125.65	114.39	13.32 (s, 0.06)			8.74 (s, 0.06)		7.27
$LaCl_3$ (1.0 equiv.)	r.t.	13.82	8.81	7.28	180.00	174.48	170.41	166.16	161.95	149.63	148.66	138.46	135.89	130.93	129.36	127.99	125.66	114.48	13.36 (s, 0.12)			8.70 (s, 0.11)		
$LaCl_3$ (2.0 equiv.)	r.t.	14.37	8.80	7.26	180.55	174.22	170.79	166.71	161.91	149.17	149.07	140.54	136.24	131.25	129.21	127.53	125.19	114.44	13.74 (s, 0.15)	12.27 (d, 0.07)	9.90 (s, 1.64)	8.68 (s, 0.14)	8.52 (s, 0.07)	7.21 (d, 0.11)
$LaCl_3$ (3.0 equiv.)	r.t.	14.45	8.79	7.26	180.69	174.03	170.84	167.09	161.82	149.01	149.34	141.01	136.13	131.27	129.09	127.26	125.02	114.37	13.83 (s, 0.18)	12.25 (d, 0.13)	9.91 (s, 2.31)	8.67 (s, 0.18)	8.50 (s, 0.12)	7.19 (d, 0.13)
$LaCl_3$ (4.0 equiv.)	r.t.	14.46	8.78	7.25	180.73	173.87	170.85	167.40	161.74	148.93	149.51	141.23	135.98	131.23	128.97	127.05	124.91	114.30	13.88 (s, 0.23)	12.24 (d, 0.17)	9.88 (s, 2.77)	8.66 (s, 0.22)	8.49 (s, 0.16)	7.18 (d, 0.17)
$LaCl_3$ (5.0 equiv.)	r.t.	14.56	8.78	7.24	180.97	173.68	170.93	167.99	161.71	148.80	149.89	141.82	135.89	131.30	128.84	126.77	124.75	114.25	14.00 (s, 0.25)	12.21 (d, 0.27)	9.85 (s, 4.14)	8.65 (s, 0.24)	8.47 (s, 0.25)	7.17 (d, 0.27)
$LaCl_3$ (0.5 equiv.) $LiClO_4$	r.t.	13.74	8.81	7.28	179.81	174.42	170.17	166.01	161.91	149.60	148.42	137.99	135.75	130.81	129.23	127.99	125.65	114.40	13.29 (s, 0.07)			8.72 (s, 0.08)		7.28
$LaCl_3$ (1.0 equiv.) $LiClO_4$	r.t.	13.83	8.80	7.28	179.86	174.33	170.18	166.00	161.82	149.46	148.42	138.35	135.77	130.81	129.19	127.86	125.50	114.35	13.35 (s, 0.10)			8.70 (s, 0.11)		7.28
$LaCl_3$ (5.0 equiv.) $LiClO_4$	r.t.	14.23	8.77	7.25	180.19	173.75	170.42	166.82	161.50	148.87	148.83	140.16	135.63	130.86	128.77	127.05	124.85	114.10	13.68 (s, 0.23)	9.79 (s, 1.03)		8.65 (s, 0.23)		7.25
$LaCl_3$ (10.0 equiv.) $LiClO_4$	r.t.	14.32	8.74	7.22	180.34	173.17	170.55	168.07	161.23	149.27	148.66	140.94	135.11	130.74	128.25	126.26	124.43	113.83	13.85 (s, 0.22)	9.63 (s, 2.55)		8.62 (s, 0.28)		7.21 (s, 0.27)
$La(NO_3)_3$ (0.25 equiv.) $LiClO_4$	r.t.	13.64	8.82	7.27	179.75	174.46	170.24	166.04	161.97	149.70	148.42	137.66	135.70	130.81	129.23	128.08	125.77	114.42	13.25 (s, 0.05)			8.73 (s, 0.05)		
$La(NO_3)_3$ (0.25 equiv.) $LiClO_4$	0°C	13.56	8.81	7.26	179.31	174.41	170.34	166.08	162.04	149.85	148.20	137.24	135.48	130.76	129.06	128.00	125.80	114.37	13.27 (s, 0.07)			8.73 (0.16)		7.27 (s, 0.09)
$La(NO_3)_3$ (0.5 equiv.) $LiClO_4$	r.t.	13.82	8.82	7.26	179.85	174.43	170.28	166.07	161.97	149.60	148.39	138.21	135.85	130.88	129.20	128.01	125.64	114.42	13.34 (s, 0.06)			8.73 (s, 0.06)		7.27 (s, 0.08)
$La(NO_3)_3$ (0.5 equiv.) $LiClO_4$	0°C	13.68	8.81	7.26	179.37	174.39	170.36	166.09	162.04	149.77	148.17	137.59	135.57	130.80	129.02	127.94	125.71	114.36	13.33 (s, 0.10)			8.73 (s, 0.10)		7.27 (s, 0.08)
$La(NO_3)_3$ (0.5 equiv.) $LiClO_4$	-50°C	13.65	8.75	7.22	178.52	174.37	170.52	166.17	162.19	150.00	147.66	-	135.25	130.76	128.68	127.63	125.66	114.27	13.42 (s, 0.11)			8.69 (s, 0.08)		7.25 (s, 0.11)
$La(NO_3)_3$ (1.0 equiv.) $LiClO_4$	r.t.	14.01	8.82	7.26	179.96	174.37	170.34	166.10	161.96	149.45	148.35	138.83	136.00	130.95	129.13	127.89	125.48	114.39	13.46 (s, 0.08)			8.73 (s, 0.07)		7.27 (s, 0.05)
$LuCl_3$ (1.0 equiv.) $LiClO_4$	r.t.	13.52	8.81	7.29	179.79	174.46	170.49	166.32	162.03	149.75	148.88	137.79	135.52	130.84	129.37	128.14	125.96	114.54	13.20 (s, 0.08)			8.72 (s, 0.04)		7.29
$LuCl_3$ (1.0 equiv.)	r.t.	13.54	8.81	7.29	179.75	174.44	170.47	166.40	162.02	149.74	148.93	137.88	135.48	130.81	129.34	128.1	125.94	114.54	13.21 (s, 0.08)			8.72 (s, 0.09)		7.29
$LuCl_3$ (5.0 equiv.)	r.t.	16.64	8.76	7.30	178.48	173.88	170.38	167.76	161.72	150.14	149.15	139.19	134.39	130.03	128.70	127.08	125.84	114.33	13.34 (s, 0.26)		9.72 (s, 0.28)	-		7.30
$LuCl_3$ (10.0 equiv.)	r.t.	13.77	8.71	7.27	177.79	173.56	170.57	168.47	161.44	150.24	148.68	139.99	133.87	129.47	128.07	126.34	125.58	113.99	-		9.61 (s, 0.60)	-		-
$Lu(NO_3)_3$ (0.25 equiv.) $LiClO_4$	r.t.	13.57	8.82	7.27	179.35	174.39	170.37	166.12	162.04	149.81	148.25	137.23	135.42	130.78	129.07	128.02	125.82	-	13.21 (s, 0.05)			8.73 (s, 0.05)		7.27
$Lu(NO_3)_3$ (0.25 equiv.) $LiClO_4$	0°C	13.53	8.80	7.26	179.79	174.43	170.30	166.09	161.96	149.65	148.51	137.60	135.61	130.82	129.24	128.11	125.80	-	13.25 (s, 0.08)			8.72 (s, 0.09)		7.26
$Lu(NO_3)_3$ (1.0 equiv.) $LiClO_4$	r.t.	13.69	8.81	7.26	179.96	174.32	170.48	166.16	161.94	149.44	148.56	138.15	135.64	130.88	129.18	128.02	125.67	-	13.29 (s, 0.09)			8.72 (s, 0.12)		7.26

Intensity reduced 5a and 7 change position due to metal induced shifts

Table IX.10: Overview over all NMR experiments in DMF-d_7 with PQQ and paramagnetic metal salts, ^{1}H- and ^{13}C-NMR shifts in ppm, as well as additional signals from water adducts in blue.

Experiment / # PQQ	°C	1H	8H	3H	5	4	9'	7'	2'	5a	7	9	1a	8	2	9a	3a	3	1H	8H	3H
PQQ	r.t.	13.40	8.82	7.28	179.94	174.57	170.03	166.11	162.00	149.76	148.53	138.17	135.92	130.91	129.42	128.14	125.78	114.52	-	-	-
$CeCl_3$ (0.5 equiv.)	r.t.	13.51	9.05	7.22	179.47	174.42	170.08	166.58	161.96	149.79	149.18	138.48	135.70	131.12	129.31	128.18	125.76	114.43	13.18 (s, 0.04)	-	-
$CeCl_3$ (1.0 equiv.)	r.t.	13.57	9.22	7.16	179.12	174.20	169.93	-	161.84	149.64	-	139.27	135.70	131.35	129.23	128.12	125.53	114.32	13.22 (s, 0.08)	-	-
$CeCl_3$ (1.5 equiv.)	r.t.	13.62	9.44	7.08	-	173.91	169.80	-	161.69	149.50	-	140.06	135.64	131.68	129.10	128.08	125.25	114.17	13.26 (s, 0.11)	9.84 (s, 0.23)	-
$CeCl_3$ (2.0 equiv.)	r.t.	13.69	9.81	6.97	-	173.52	169.73	-	161.57	149.37	-	141.19	135.60	132.24	128.94	128.11	124.94	114.03	13.32 (s, 0.12)	-	-
$CeCl_3$ (2.5 equiv.)	r.t.	13.73	9.78	6.86	-	173.14	169.68	-	161.43	149.26	-	141.91	135.51	132.70	128.78	128.16	124.65	113.87	13.35 (s, 0.15)	10.07 (s, 0.29)	-
$CeCl_3$ (3.0 equiv.)	r.t.	13.74	9.76	6.77	-	172.86	169.65	-	161.34	149.20	-	142.49	135.43	-	128.65	128.21	124.45	113.76	13.37 (s, 0.17)	10.31 (s, 0.40)	6.87 (s, 0.19)
$PrCl_3$ (0.5 equiv.)	r.t.	13.58	9.44	7.17	-	174.30	169.70	-	161.90	149.67	-	-	135.64	-	129.27	128.40	125.64	114.35	13.25 (s, 0.03)	-	-
$PrCl_3$ (1.0 equiv.)	r.t.	13.67	9.76	7.05	-	173.99	169.29	-	161.72	149.40	-	-	135.52	-	129.12	128.50	125.28	114.14	13.33 (s, 0.07)	-	-
$PrCl_3$ (1.5 equiv.)	r.t.	13.71	9.77	6.92	-	173.63	168.96	-	161.52	149.14	-	-	135.34	-	128.93	128.60	124.90	113.90	13.37 (s, 0.12)	10.35 (s, 0.53)	-
$PrCl_3$ (2.0 equiv.)	r.t.	13.80	9.76	6.74	-	173.23	168.72	-	161.36	148.84	-	-	135.17	-	128.72	-	124.46	113.65	13.46 (s, 0.12)	-	-
$PrCl_3$ (2.5 equiv.)	r.t.	13.82	9.73	6.56	-	172.89	168.54	-	161.16	148.58	-	-	134.94	-	128.48	-	124.03	113.36	13.51 (s, 0.10)	-	-
$PrCl_3$ (3.0 equiv.)	r.t.	13.82	9.69	6.37	-			-	160.95		-	-	134.61	-	128.24	-	123.61	113.10	13.53 (s, 0.09)	-	-
$SmCl_3$ (0.5 equiv.)	r.t.	13.59	8.87	7.27	179.84	174.50	170.67	166.46	162.05	149.83	148.94	137.75	135.76	130.94	129.41	128.13	125.88	114.53	13.23 (s, 0.02)	-	-
$SmCl_3$ (1.0 equiv.)	r.t.	13.67	8.9	7.26	179.84	174.38	170.79	166.70	162.00	149.72	149.15	138.05	135.76	130.97	129.40	128.03	125.77	114.50	13.28 (s, 0.04)	-	-
$SmCl_3$ (1.5 equiv.)	r.t.	13.72	8.93	7.25	179.83	174.25	170.89	166.92	161.94	149.64		138.27	135.75	130.97	129.39	127.92	125.66	114.47	13.31 (s, 0.05)	9.94 (s, 0.06)	-
$SmCl_3$ (2.0 equiv.)	r.t.	13.76	8.96	7.24	179.80	174.12	170.97		161.90	149.58		138.47	135.72	130.99	129.36	127.82	125.58	114.43	13.34 (s, 0.06)	9.98 (s, 0.14)	-
$SmCl_3$ (2.5 equiv.)	r.t.	13.79	8.99	7.23	179.76	173.97	171.06		161.85	149.52		138.64	135.67	130.99	129.33	127.72	125.49	114.39	13.37 (s, 0.07)	10.02 (s, 0.18)	-
$SmCl_3$ (3.0 equiv.)	r.t.	13.82	9.02	7.22	179.72	173.85	171.13		161.81	149.48		138.82	135.62	131.00	129.29	127.60	125.41	114.36	13.39 (s, 0.09)	10.03 (s, 0.20)	-
$EuCl_3$ (0.05 equiv.)	r.t.	13.44	8.74	7.3	179.88	174.52	171.35	166.09	162.15	149.87	148.55	-	135.65	130.73	129.42	-	126.08	114.59	-	-	-
$EuCl_3$ (0.5 equiv.)	r.t.	13.66	8.43	7.38	-	-	-	-	162.30	-	-	-	135.85	-	129.55	-	125.89	114.76	-	-	-
$EuCl_3$ (1.0 equiv.)	r.t.	13.78	-	7.46	-	-	-	-	162.47	-	-	-	135.94	-	129.64	-	125.70	114.91	13.30 (s, 0.05)	9.93 (s, 0.10)	-
$EuCl_3$ (1.5 equiv.)	r.t.	13.86	-	7.54	-	-	-	-	162.62	-	-	-	135.98	-	129.73	-	125.54	115.05	13.34 (s, 0.05)	10.02 (s, 0.24)	-
$EuCl_3$ (2.0 equiv.)	r.t.	13.98	-	7.65	-	-	-	-	-	-	-	-	136.00	-	129.79	-	-	115.22	13.41 (s, 0.09)	10.06 (s, 0.57)	-
$EuCl_3$ (2.5 equiv.)	r.t.	14.06	-	7.74	-	-	-	-	-	-	-	-	136.01	-	129.85	-	-	115.38	13.46 (s, 0.77)	10.08 (s, 0.77)	-
$EuCl_3$ (3.0 equiv.)	r.t.	14.10	-	7.83	-	-	-	-	-	-	-	-	136.00	-	129.93	-	-	115.52	13.49 (s, 0.09)	10.11 (s, 1.01)	-
$TbCl_3$ (0.01 equiv.)	r.t.	13.20	9.05	7.25	179.64	174.61	-	166.22	162.07	149.96	148.76	-	135.51	131.11	129.31	128.20	126.07	114.49	-	-	-
$TbCl_3$ (0.02 equiv.)	r.t.	13.11	9.21	7.22	-	-	-	-	162.04	149.91	-	-	135.47	131.33	129.25	-	-	114.47	-	-	-
$ErCl_3$ (0.01 equiv.)	r.t.	13.43	8.75	7.3	179.76	174.64	170.60	166.13	162.13	150.02	148.66	136.36	135.61	130.83	129.43	128.27	126.13	114.60	-	-	-
$ErCl_3$ (0.02 equiv.)	r.t.	13.49	8.7	7.32	-	174.59	-	166.10	162.15	-	-	-	135.64	-	129.44		126.13	114.63	-	-	-
$TmCl_3$ (0.01 equiv.)	r.t.	13.45	8.74	7.31	179.75	174.71	170.55	166.13	162.14	150.02	148.65	136.71	135.65	130.80	129.45	128.31	126.17	114.61	-	-	-
$TmCl_3$ (0.02 equiv.)	r.t.	13.53	8.68	7.32	179.72	174.80	170.66	166.11	162.16	149.99	148.66	136.57	135.70	130.80	129.48	128.32	126.20	114.66	-	-	-

medium intensity reduction significant intensity reduction hardly distinguishable from noise

Table IX.11: Overview of PQQ NMR-shifts, ^{1}H- and ^{13}C-NMR shifts in ppm. Resonances were assigned by 2D HMQC and HMBC experiments. In case of ^{13}C-NMR resonances 2 and 3a no determination was possible by 2D-NMR, so assignments are based on the reported DMSO-d_6 shifts by Houck *et al.*[67]

PQQ (**13**) (capsules)	PQQ (**13**) (capsules) 50 mg	PQQ-H_2O (**15**) (capsules) (50 mg) (~5% to PQQ)	PQQ·2DMF (crystals)	PQQ (**13**) (capsules)	PQQ (**13**) (Fluorochem)
DMF-d_7	DMF-d_7	DMF-d_7	DMF-d_7	DMSO-d_6	DMSO-d_6
13.40 (s, 1H, 1)	13.26 (s, 1H, 1)	13.09 (s, 1H, 1)	13.40 (s, 1H)	13.22 (s, 1H, 1)	13.68 (s, 1H, 1)
8.82 (s, 1H, 8)	8.77 (s, 1H, 8)	8.72 (s, 1H, 8)	8.83 (s, 1H)	8.60 (s, 1H, 8)	8.60 (s, 1H, 8)
7.28 (d, *J* = 2.1 Hz, 1H, 3)	7.19 (d, *J* = 2.2 Hz, 1H, 3)	7.24 (d, *J* = 2.3 Hz, 1H, 3)	7.29 (d, *J* = 2.3 Hz, 1H)	7.20 (d, J = 2.2 Hz, 1H, 3)	7.20 (d, *J* = 2.2 Hz, 1H, 3)
179.71 (5)	179.60 (5)	188.41 (4)	179.73 (5)	177.88 (5)	178.10 (5)
174.59 (4)	174.33 (4)	170.20 (9')	174.68 (4)	173.37 (4)	173.36 (4)
170.31 (9')	170.14 (9')	165.49 (7')	170.38 (9')	168.82 (9’)	168.52 (9')
166.10 (7')	165.90 (7')	162.03 (5a)	166.17 (7')	164.94 (7’)	165.01 (7')
162.07 (2')	161.85 (2')	161.76 (2')	162.13 (2')	160.88 (2’)	160.93 (2')
149.96 (5a)	149.69 (5a)	145.66 (7)	150.06 (5a)	148.77 (5a)	148.66 (5a)
148.59 (7)	148.46 (7)	136.35 (9)	148.67 (7)	146.86 (7)	146.78 (7)
136.97 (9)	136.60 (9)	134.27 (1a)	137.02 (9)	135.87 (9)	136.92 (9)
135.57 (1a)	135.27 (1a)	128.93 (2)	135.64 (1a)	134.14 (1a)	134.56 (1a)
130.82 (8)	130.83 (8)	127.38 (8)	130.83 (8)	129.09 (8)	129.27 (8)
129.37 (2)	129.29 (2)	122.86 (9a)	129.42 (2)	127.62 (2)	127.61 (2)
128.29 (9a)	128.17 (9a)	122.67 (3a)	128.33 (9a)	126.46 (9a)	126.39 (9a)
126.05 (3a)	125.87 (3a)	113.32 (3)	126.13 (3a)	124.59 (3a)	124.37 (3a)
114.54 (3)	114.41 (3)	91.07 (5)	114.58 (3)	113.51 (3)	113.54 (3)

Table IX.12: Collected IR-Data from different solid PQQ-species.

PQQ (**13**)				$PQQNa_2$ (**14**)		PQQ-La 1 : 0.5 (**A**)		PQQ-La 1 : 1 (**B**)		PQQ-La 1 : 2 (**C**)	
cm^{-1}	%T	cm^{-1}	%T	cm^{-1}	%T	cm^{-1}	%T	cm^{-1}	%T	cm^{-1}	%T
3540	106	980	79	1738	90	3192	87	3220	92	3094	94
3250	103	926	72	1709	86	1602	65	1604	75	1572	81
2941	97	866	63	1668	77	1575	63	1575	73	1559	81
2594	99	846	70	1627	67	1504	74	1504	80	1502	85
1743	70	805	68	1576	70	1348	52	1349	65	1344	74
1720	78	761	54	1495	76	1243	72	1242	78	1238	82
1699	79	725	52	1383	72	1192	77	1191	81	1191	84
1682	81	687	56	1353	55	1146	83	-	-	-	-
1639	61			1296	73	1117	83	1116	85	1116	86
1583	74			1239	69	975	86	-	-	-	-
1508	66			1147	79	787	74	784	80	786	83
1490	75			1085	81	723	66	725	73	723	76
1453	91			1048	84						
1397	81			976	86						
1359	80			944	86						
1315	55			810	73						
1284	55			797	73						
1263	55			756	69						
1225	59			725	70						
1193	45			695	70						
1151	62			668	71						
1122	70			657	71						
1075	69										

Table IX.13: Calculated ^{13}C-NMR shifts and referenced values to TMS for the two PQQ-H_2O species. Calculation was performed with Gaussian 09 – b3lyp, 6-31g(d), cpcm (DMF), NMR: giao-method. TMS was calculated in the same way and used as reference– TMS: 190.1627 ppm. Structurally optimized PQQ-H_2O species with diol formation in position 5 (left) and position 4 (right).

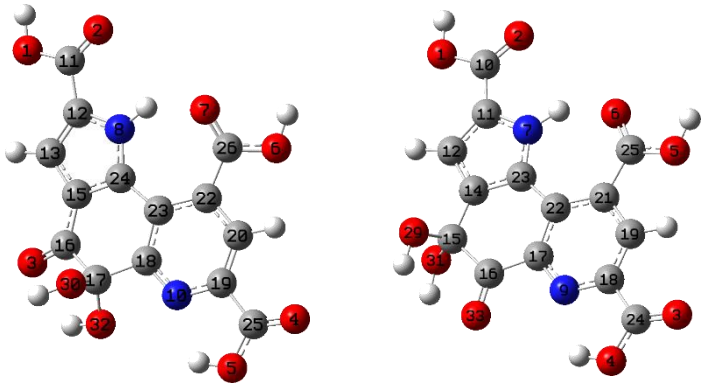

NMR	Position 5:				Position 4:			
PQQ-H_2O (3) in DMF-d_7	Gaussian #	PQQ #	Shielding (ppm)	Referred to TMS (ppm)	Gaussian #	PQQ #	Shielding (ppm)	Referred to TMS (ppm)
188.41 (4)	16	4	5.97	184.19	16	5	-2.72	192.89
170.20 (9')	26	9'	29.41	160.75	25	9'	31.31	158.85
165.49 (7')	25	7'	34.58	155.58	24	7'	35.57	154.59
162.03 (5a)	18	5a	35.73	154.43	10	2'	38.14	152.03
161.76 (2')	11	2'	38.45	151.71	17	5a	49.69	140.48
145.66 (7)	19	7	52.13	138.03	18	7	52.29	137.87
136.35 (9)	24	1a	59.92	130.24	22	9a	58.78	131.38
134.27 (1a)	22	9	60.64	129.52	19	8	61.73	128.44
128.93 (2)	20	8	66.54	123.62	21	9	62.72	127.45
127.38 (8)	12	2	67.53	122.64	14	3a	64.48	125.69
122.86 (9a)	23	9a	68.32	121.85	11	2	67.71	122.46
122.67 (3a)	15	3a	72.88	117.28	23	1a	69.99	120.17
113.32 (3)	13	3	78.79	111.38	12	3	78.48	111.69
91.07 (5)	17	5	100.40	89.77	15	4	104.78	85.39

Table IX.14: UV-Vis absorption maxima and shoulders (*) in nm and associated extinction coefficients (ε) in L · mol^{-1} · cm^{-1} of PQQ (**13**) in different solvents (4 µM).

DMF		DMSO		H_2O (1% DMF)	
λ	ε	λ	ε	λ	ε
277	214179	272	177104	249	256500
334	132396	338	112354	275*	170167
443	15229	436	14458	331	105417
				479	7521

A

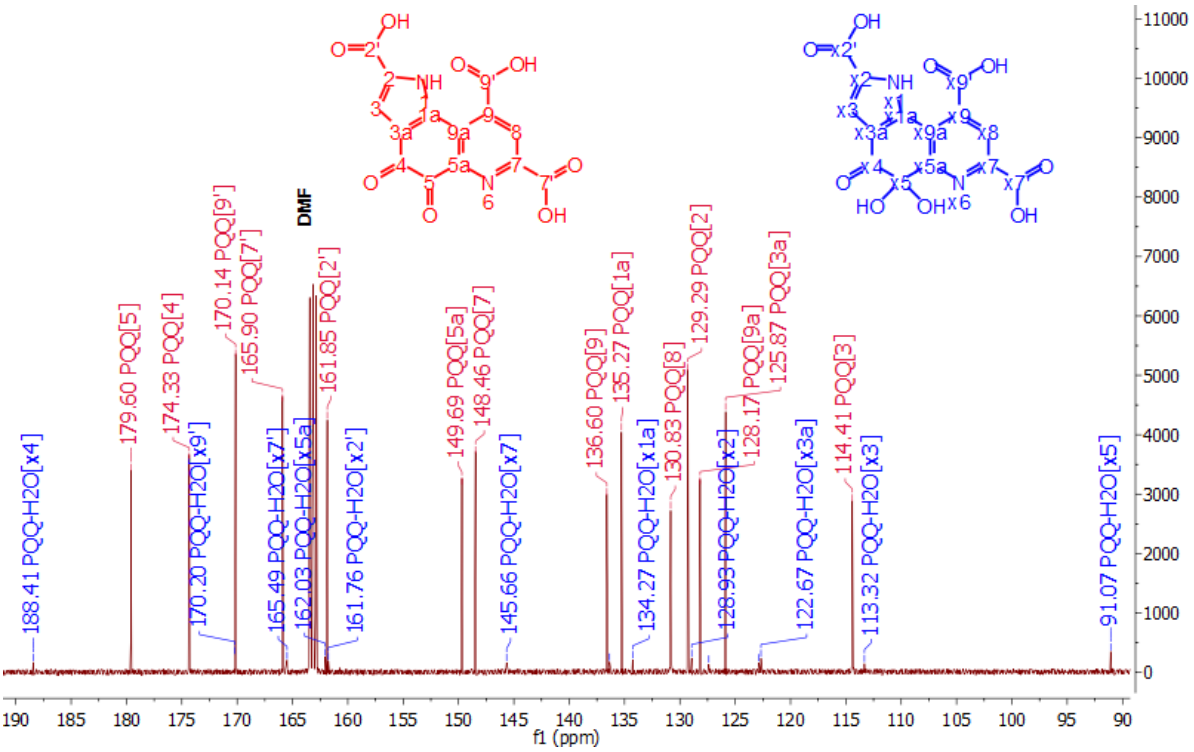

B

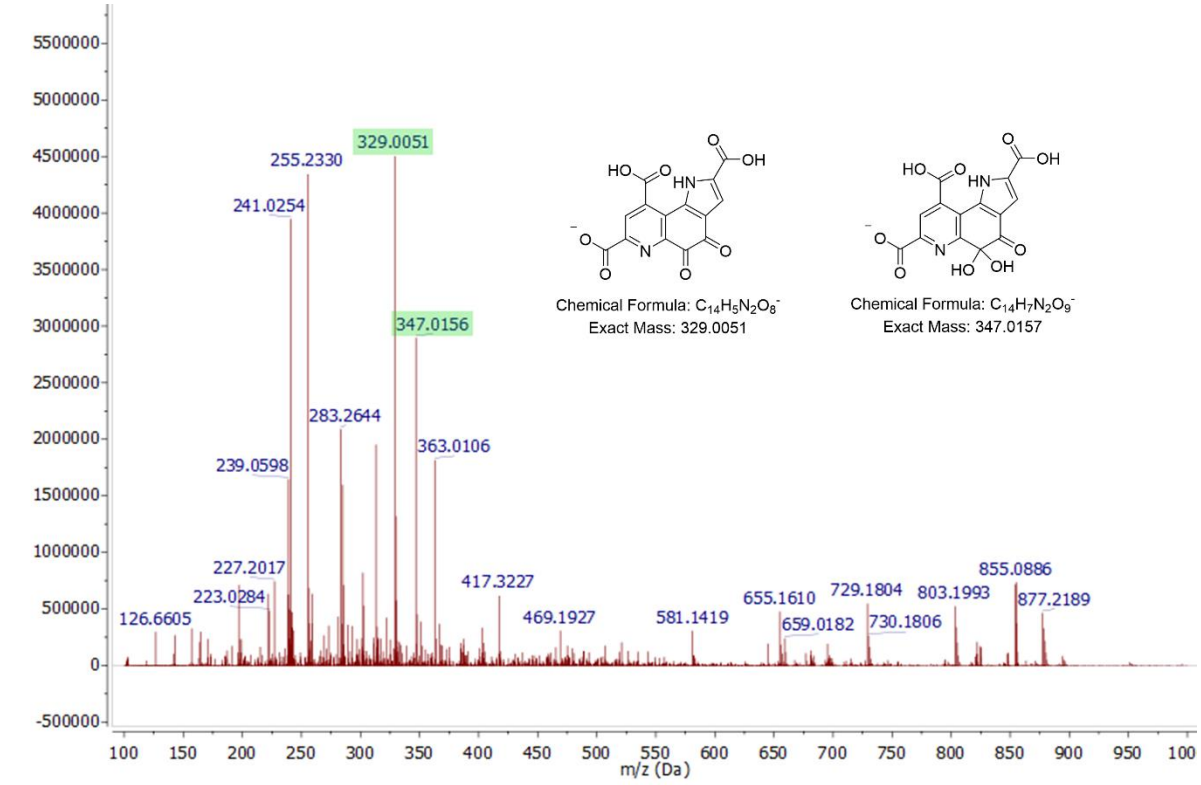

Figure IX.15: **A** ^{13}C-NMR spectrum of PQQ in DMF-d$_7$ (151 µM), showing resonances for PQQ (**13**, red) and the water adduct yielding the geminal diol (**15**, blue). **B** Negative ESI mass spectrum of solid PQQ-La complex that was redissolved in H_2O/MeCN with the masses of **13** and **15** highlighted in green.

A

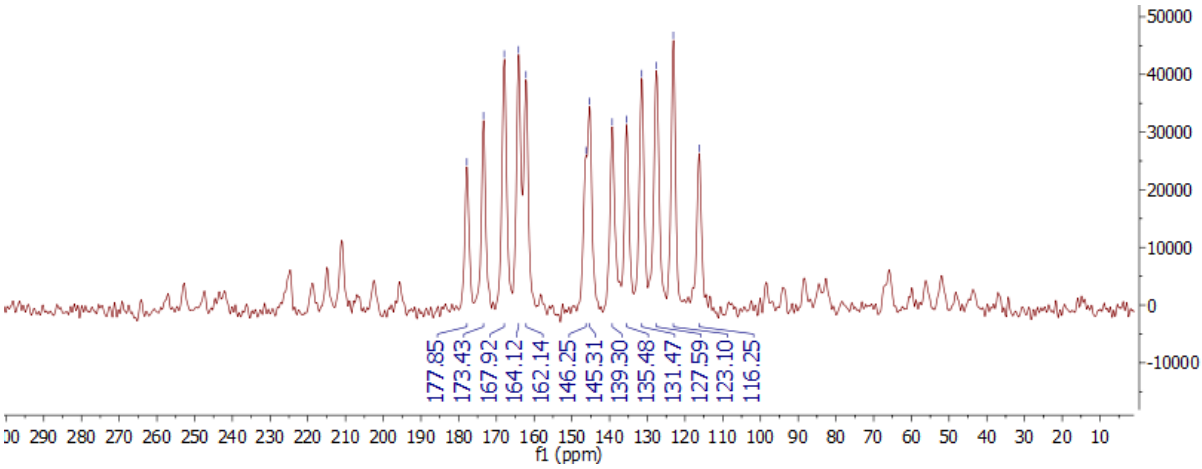

B

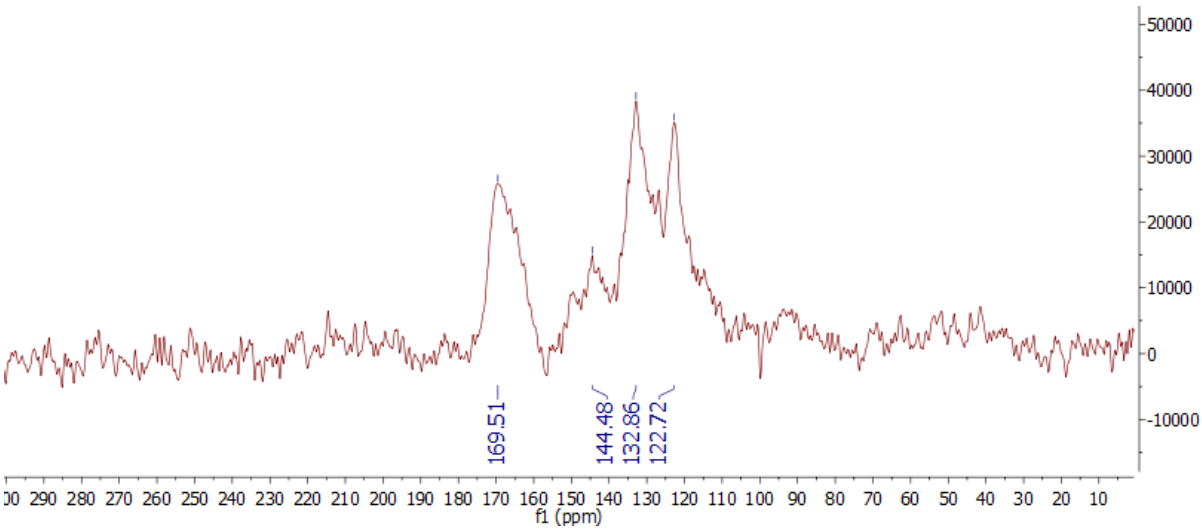

Figure IX.16: **A** ^{13}C-NMR spectrum of PQQ in the solid state, showing 13 resonances for PQQ and multiple spinning side bands in the high- and low field. **B** ^{13}C-NMR spectrum of the 1:1 PQQ-La complex in the solid state, showing overlapping, broadened PQQ resonances.

A

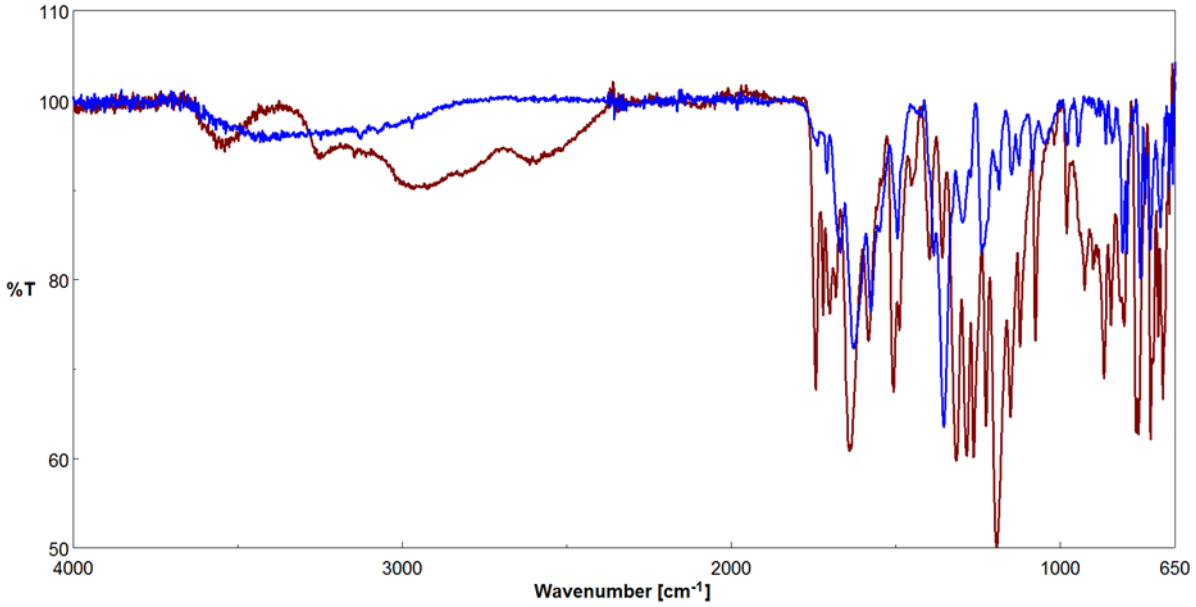

B

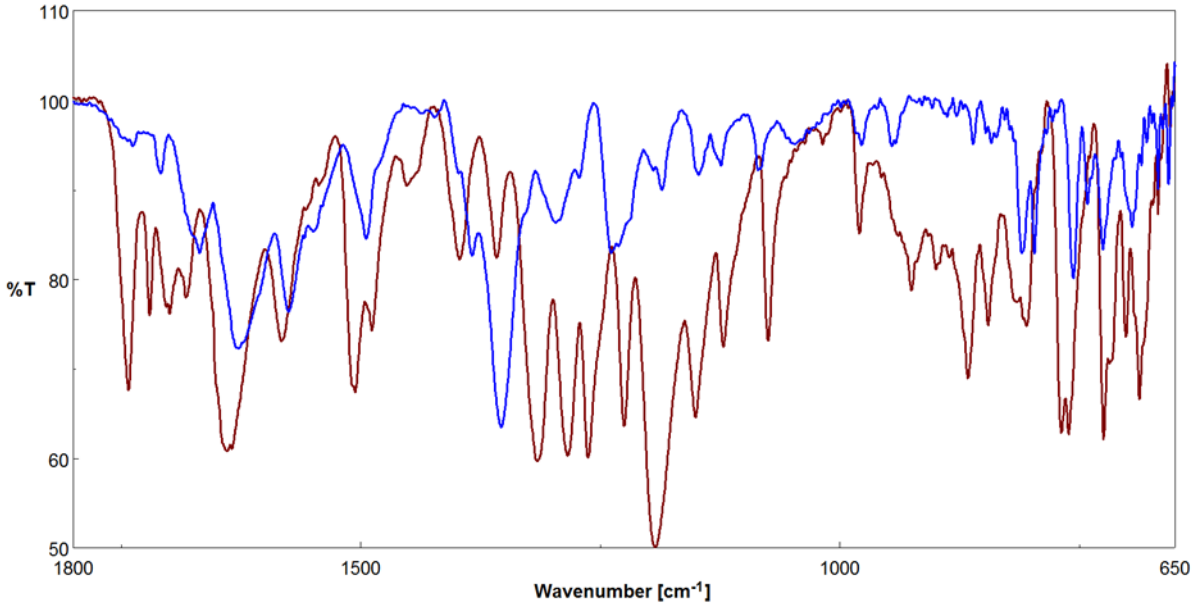

Figure IX.17: **A** Overlayed IR spectra of PQQ **13** (red) and $PQQNa_2$ **14** (blue). **B** Close-up between 1800-650 cm^{-1}.

A

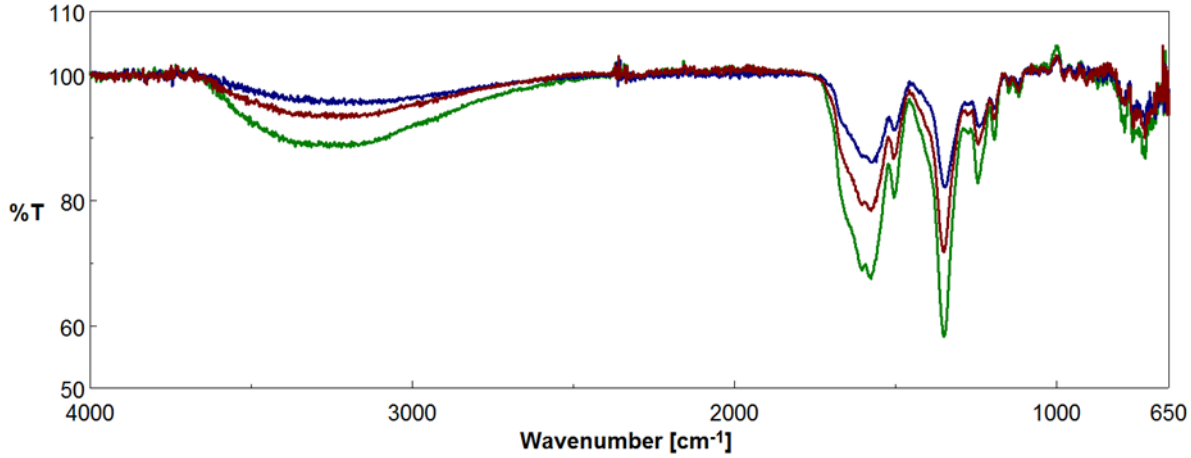

B

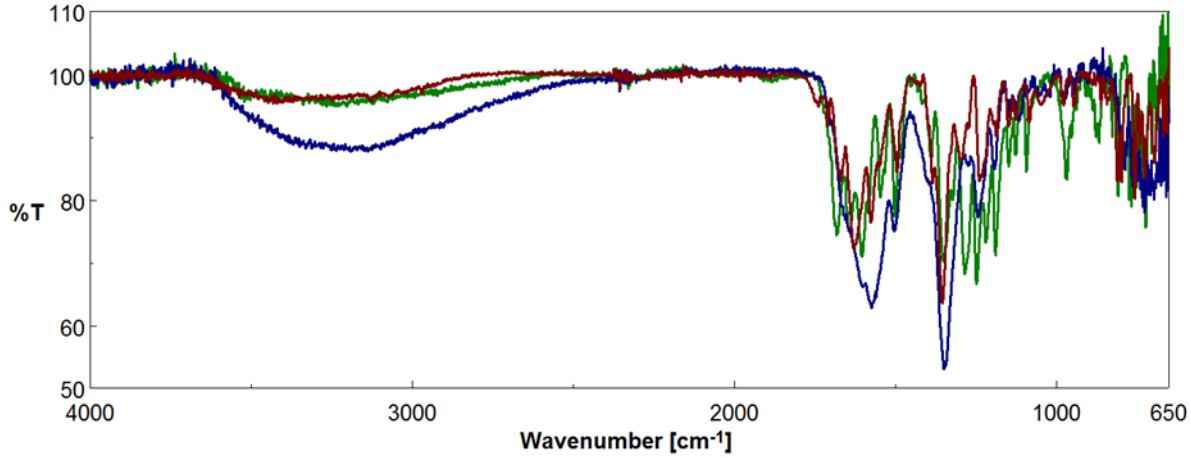

C

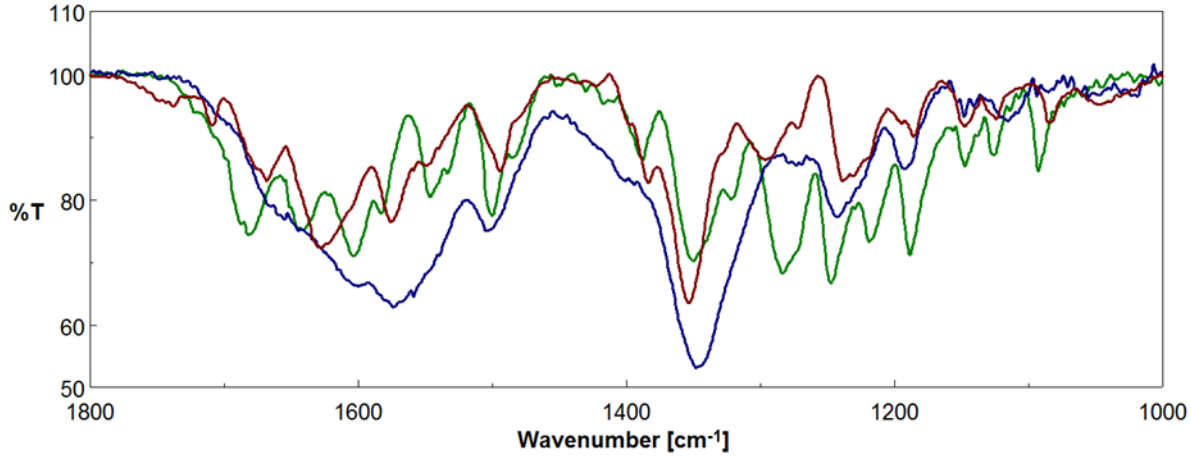

Figure IX.18: **A** IR-spectra of PQQ-La complexes A – 0.5 equiv. $LaCl_3$ (green), B – 1.0 equiv. $LaCl_3$ (red) and C – 2.0 equiv. $LaCl_3$ (blue). **B** IR-spectra of Na_2PQQ (red), PQQ-La complex C – 2.0 equiv. $LaCl_3$, (blue), and PQQ-Ca complex C – 2.0 equiv. $CaCl_2$ (green). **C** Close-up of B between 1800 – 1000 cm^{-1}.

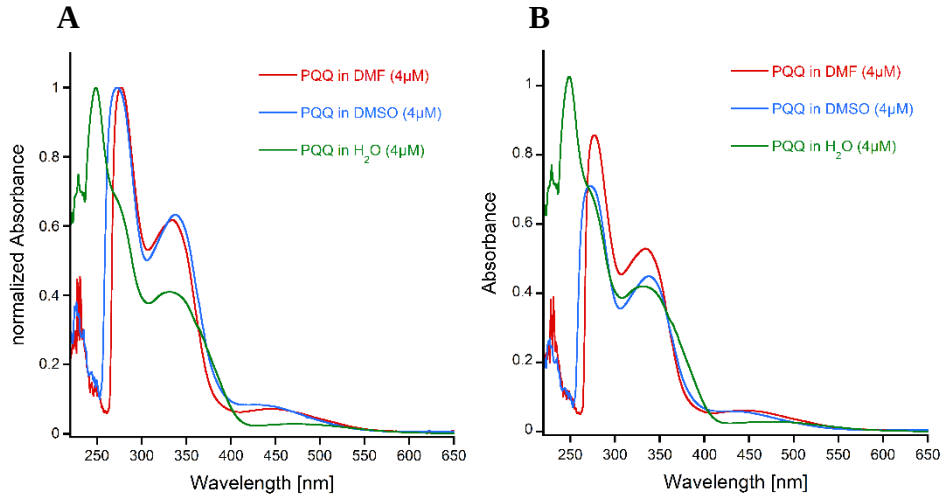

Figure IX.19: UV-Vis spectra of PQQ in different solvents (**A** normalized to highest absorption, **B** non-normalized).

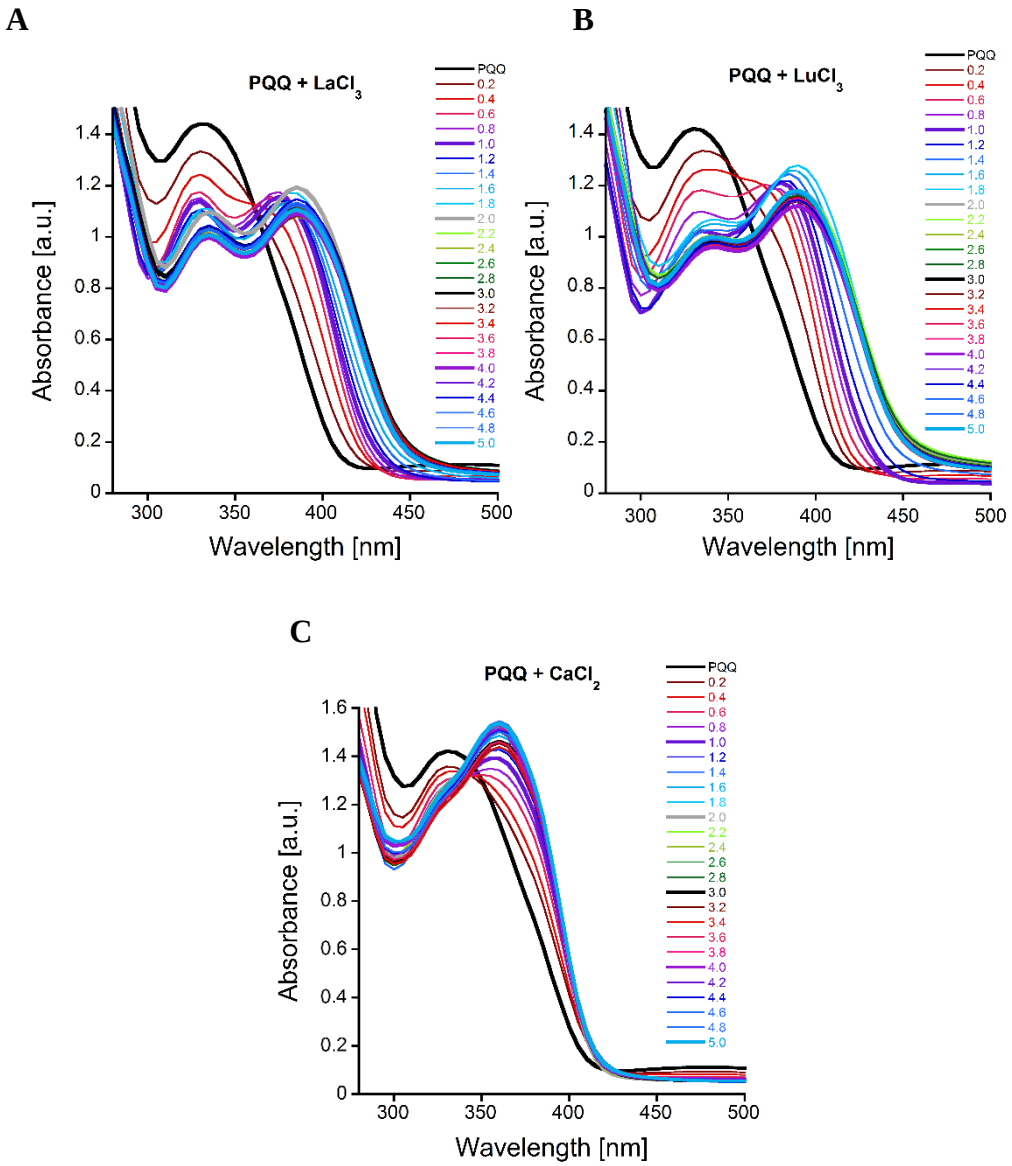

Figure IX.20: Sequential addition of metal chlorides (5 mM in water – 2 µL per 0.2 equiv.) to PQQ (250 µM) in water. **A** $LaCl_3 \cdot 7H_2O$, **B** $LuCl_3 \cdot 6H_2O$ or **C** $CaCl_2 \cdot 2H_2O$.

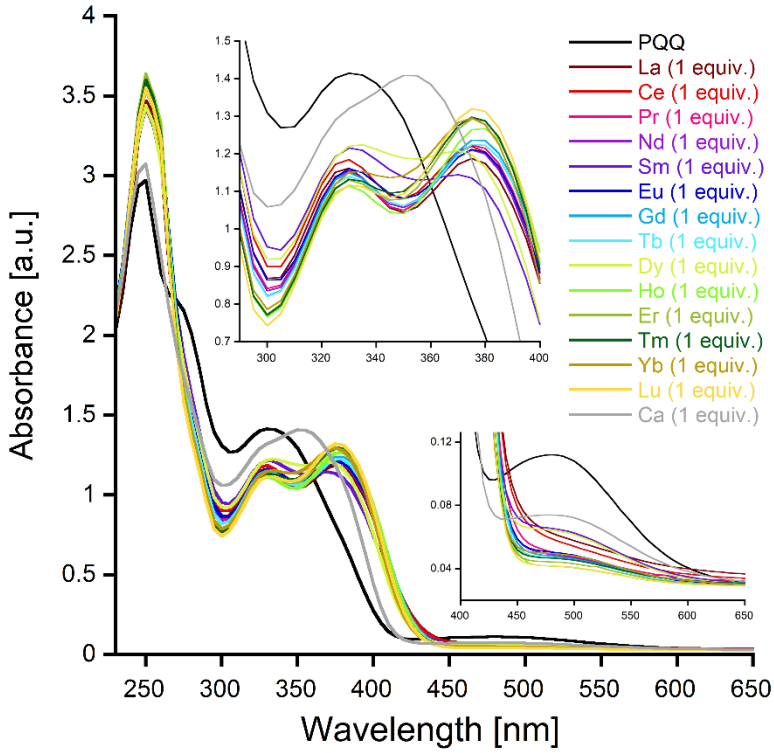

Figure IX.21: UV-Vis spectra of PQQ (250 µM) in water with 1 equiv. of $LnCl_3 \cdot nH_2O$ or $CaCl_2 \cdot 2H_2O$, directly measured after metal addition.

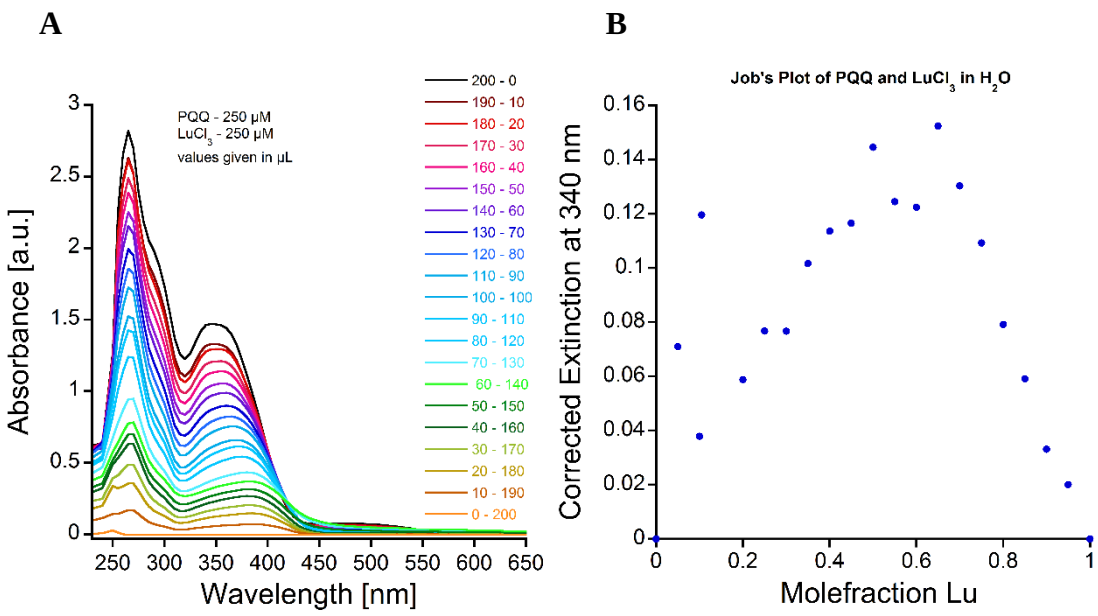

Figure IX.22: Method of continuous variation in water. **A** Raw data as obtained directly after mixing the components. **B** Job's plot of the corrected data from A, indicates the formation of a 1:1 complex. Note: Due to the presence of multiple PQQ species (**13**, **15**, and M-**13** and M-**15** complexes) the data from Job's plot has to be interpreted with caution.

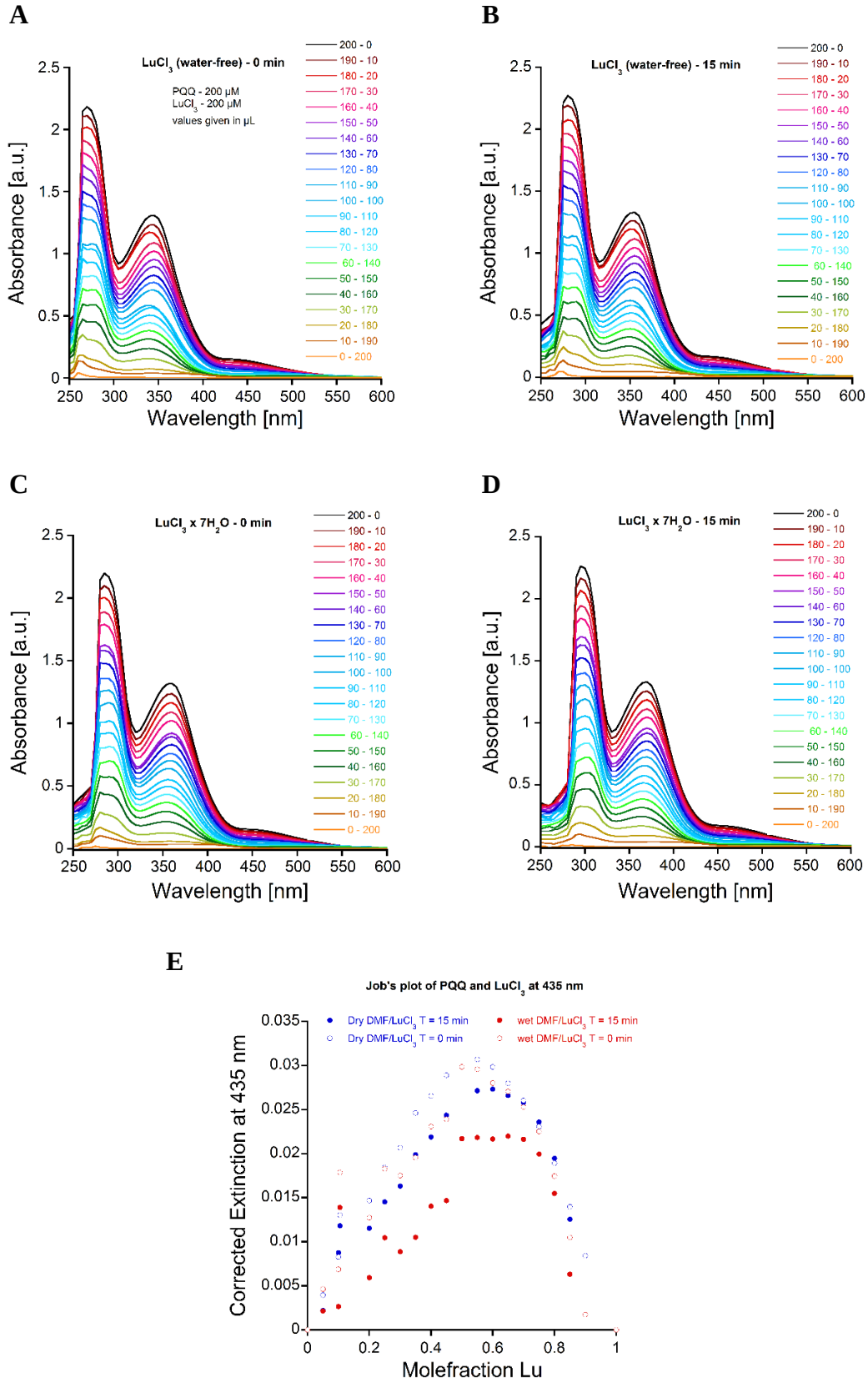

Figure IX.23: Method of continuous variation in DMF. **A** Raw data as obtained directly after mixing the components (PQQ and Lu^{3+}, anhydrous). **B** Raw data as obtained 15 minutes after mixing (PQQ and Lu^{3+}, anhydrous). **C** Raw data as obtained directly after mixing the components (PQQ and Lu^{3+}, wet DMF). **D** Raw data as obtained 15 minutes after mixing (PQQ and Lu^{3+}, wet DMF). **E** Job's plot of the corrected data from A-D. Slight curvature around a mole fraction of 0.55 Lu could indicate a 1:1 PQQ-Lu complex with low binding affinity, however this data should not be over interpreted due to more than two species present.

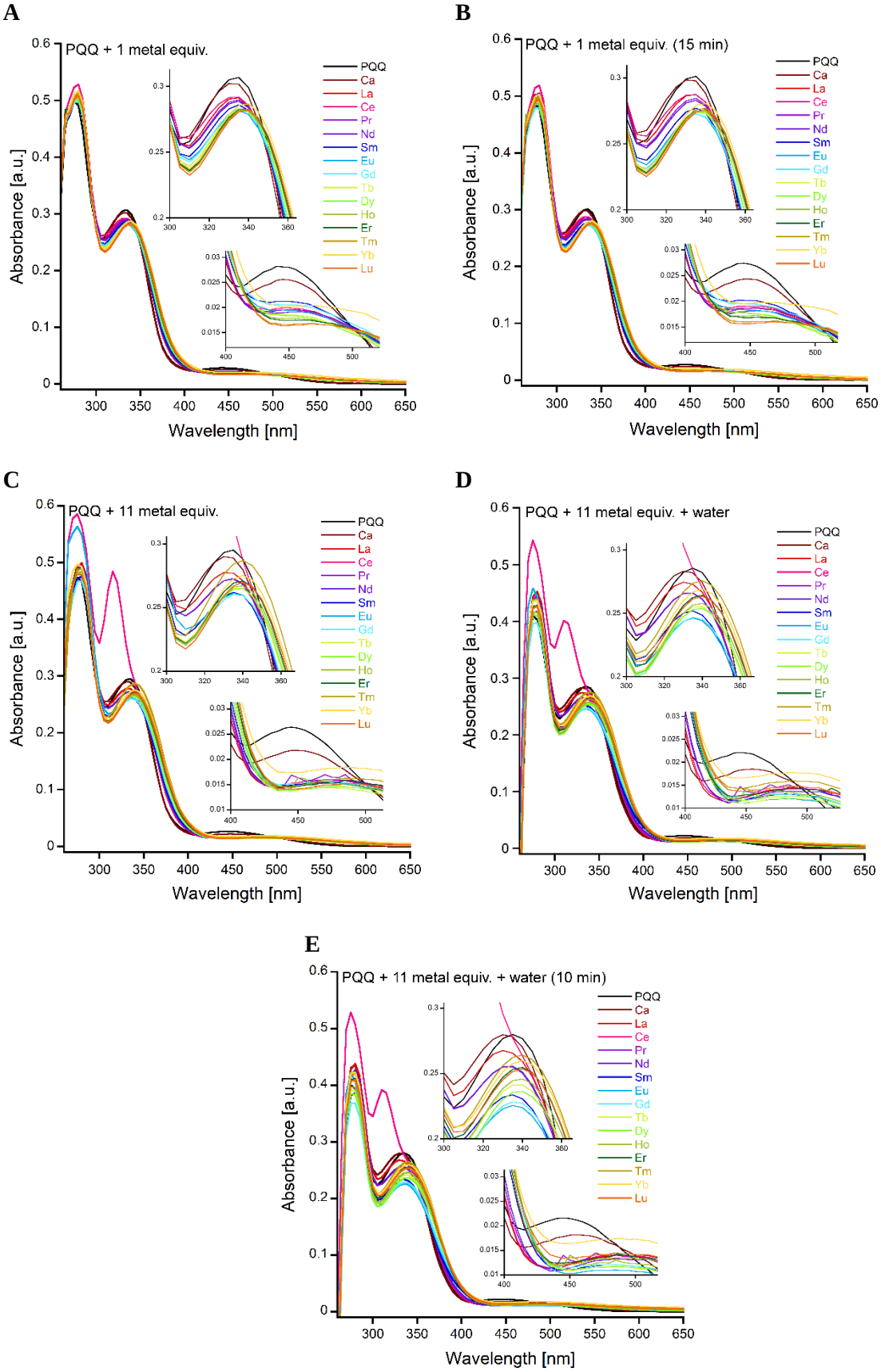

Figure IX.24: UV-Vis spectra of PQQ in DMF (40 µM). **A** 1 equiv. of $LnCl_3 \cdot nH_2O$ or $CaCl_2 \cdot 2H_2O$, directly measured after metal addition. **B** after 15 minutes. **C** 11 equiv. of $LnCl_3 \cdot nH_2O$ or $CaCl_2 \cdot 2H_2O$, directly measured after metal addition. **D** 11 equiv. of $LnCl_3 \cdot nH_2O$ or $CaCl_2 \cdot 2H_2O$ and 10 µL of H_2O (5 vol%), directly measured after water addition. **E** 10 minutes after water addition. The strong deviation from the Ce measurement is most likely caused by redox processes of the Ce^{III} – Ce^{IV} couple.

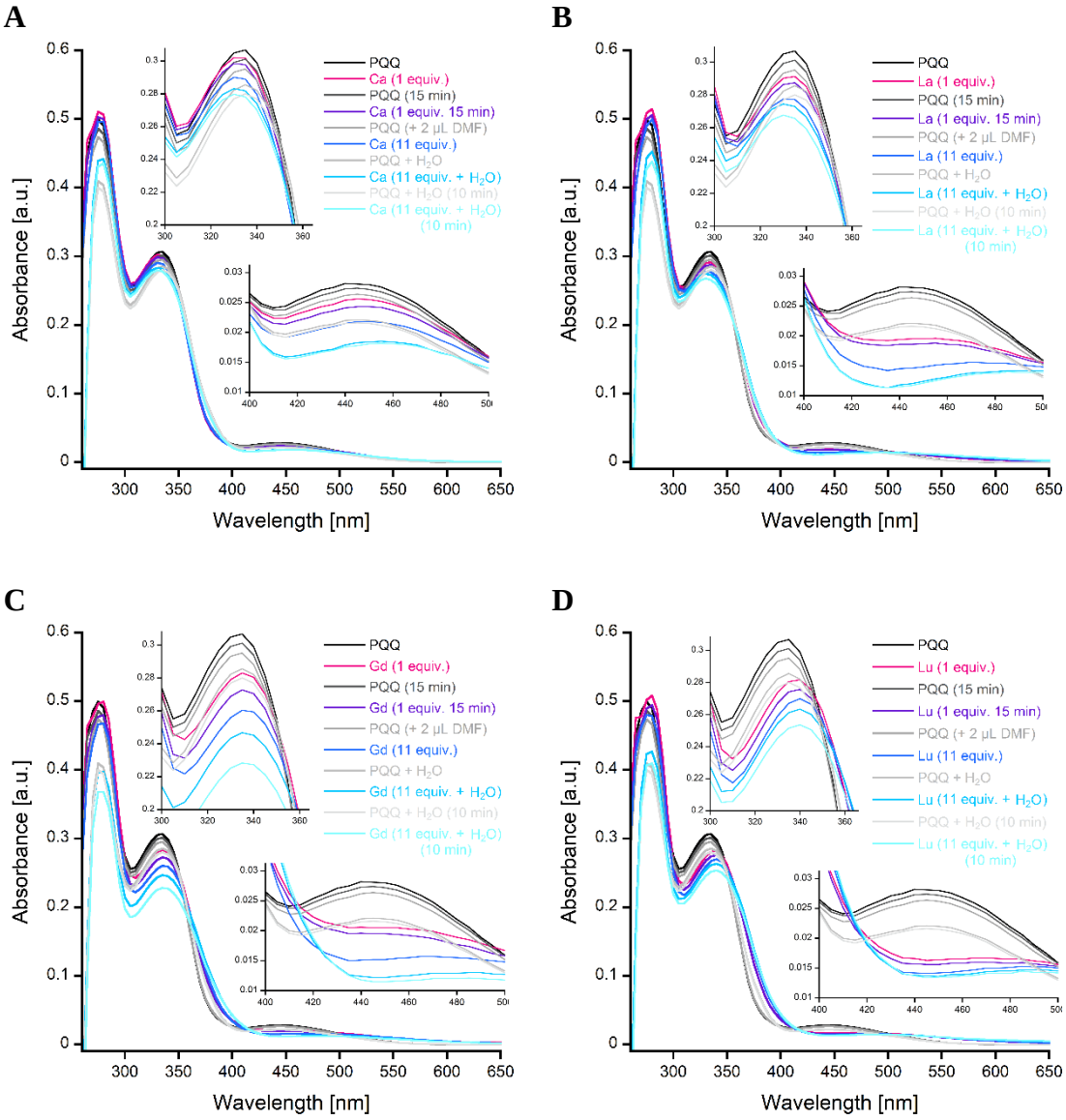

Figure IX.25: Combined UV-Vis spectra of Figure IX.24 A-E for Ca^{2+} (**A**), La^{3+} (**B**), Gd^{3+} (**C**) and Lu^{3+} (**D**). PQQ in DMF (40 µM) with 1 equiv. of $LnCl_3 \cdot nH_2O$ or $CaCl_2 \cdot 2H_2O$ (pink lines); PQQ in DMF (40 µM) with 1 equiv. of $LnCl_3 \cdot nH_2O$ or $CaCl_2 \cdot 2H_2O$ after 15 minutes (violet lines); PQQ in DMF (40 µM) with 11 equiv. of $LnCl_3 \cdot nH_2O$ or $CaCl_2 \cdot 2H_2O$ (dark blue lines), PQQ in DMF (40 µM) with 11 equiv. of $LnCl_3 \cdot nH_2O$ or $CaCl_2 \cdot 2H_2O$ and 10 µL of H_2O (5 vol%) (blue lines) and PQQ in DMF (40 µM) with 11 equiv. of $LnCl_3 \cdot nH_2O$ or $CaCl_2 \cdot 2H_2O$ and 10 µL of H_2O (5 vol%) after 10 minutes (light blue lines).

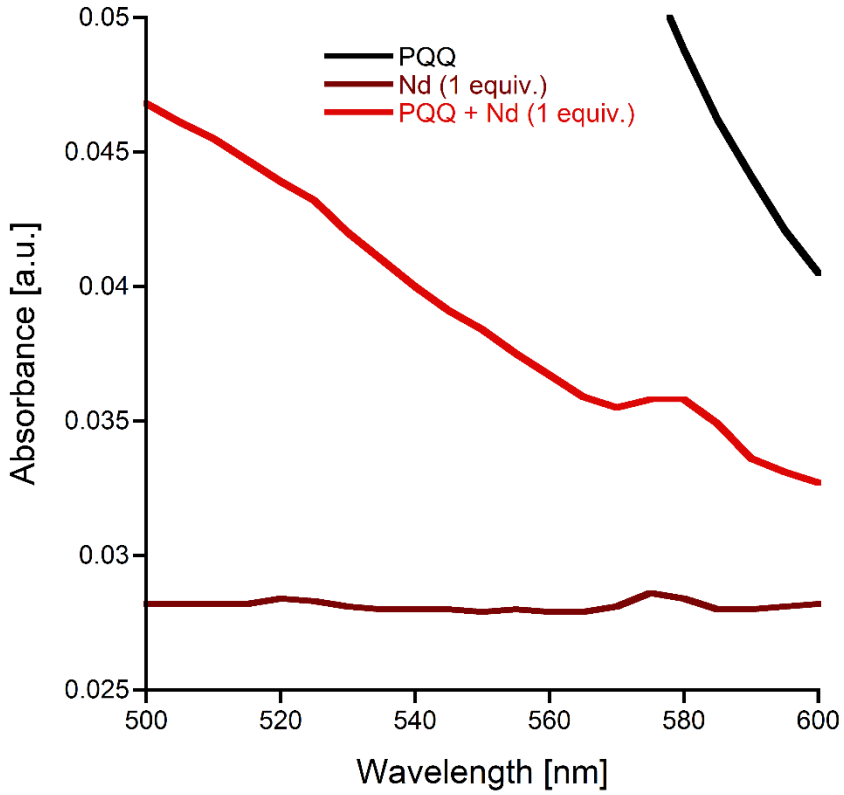

Figure IX.26: UV-Vis spectra of PQQ (250 µM), $NdCl_3 \cdot 6H_2O$ (250 µM) and PQQ + 1 equiv. $NdCl_3 \cdot 6H_2O$ in water, showing the hypersensitive transitions of Nd^{3+} at 578 nm, which are slightly influenced in the presence of PQQ.

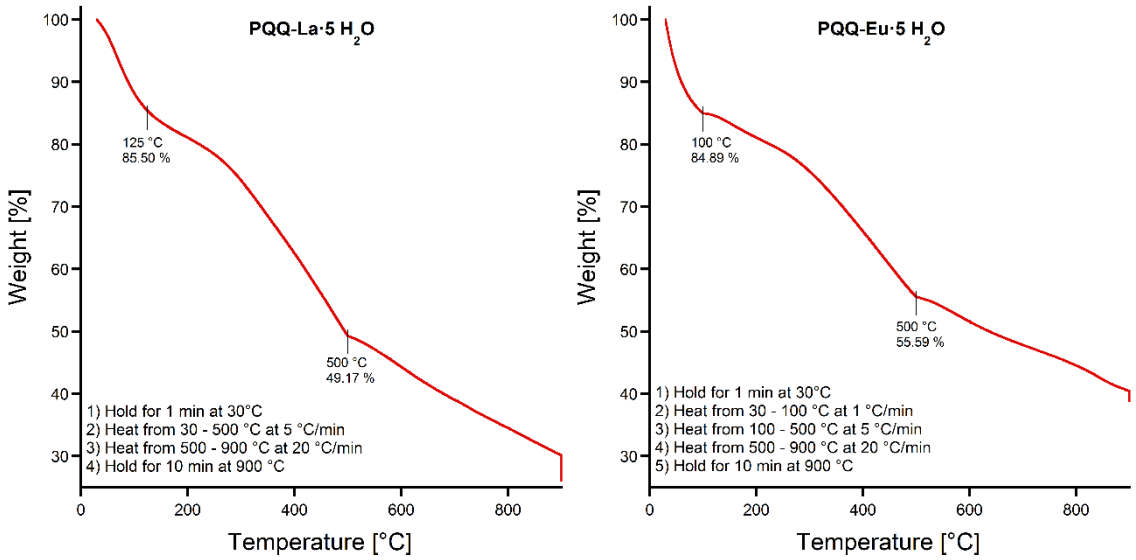

Figure IX.27: TGA analysis of the 1:1 PQQ:Ln (La or Eu) complexes.

1.3.3 Additional Experimental Procedures

Recrystallization of PQQ in DMF for water free PQQ

PQQ (55 mg, 0.167 mmol) was completely dissolved at 60°C in an ultrasonic bath (10 minutes) in DMF (1 mL). The solvent was removed *in vacuo* at 70°C, giving a viscous dark red thin layer. DMF (100 µL) was added and the vial with the concentrated solution was placed in a glass with *tert*-butyl methyl ether (3 mL), to slowly diffuse into the DMF solution to give small orange crystals after 2 hours. To complete crystallization, the reaction mixture was left overnight. The crystals were removed *via* pipette, dried on a filter paper and under high vacuum to give the product as small orange crystals (36 mg). Elemental analysis revealed two equivalents of DMF per PQQ, giving a total yield of 45%. The ^{1}H-NMR spectrum showed highly purified PQQ. A water adduct, which is normally visible as a second signal set, with integral values of up to 10% in comparison to free PQQ, is now only visible in very small traces.

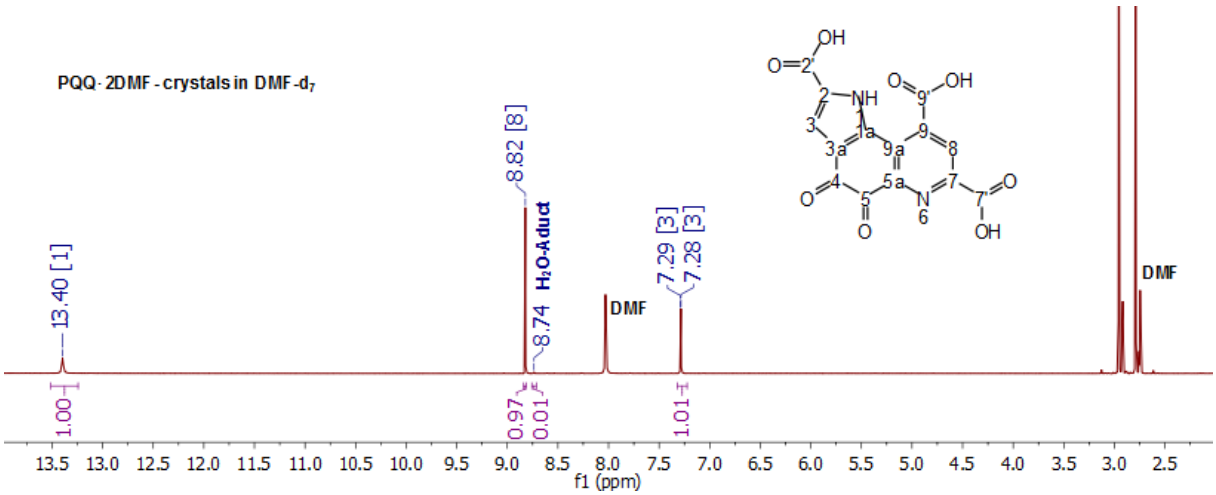

Figure IX.28: ^{1}H-NMR spectrum of PQQ·2DMF, dissolved in 0.6 mL of DMF-d_7.

^{1}H-NMR (400 MHz, DMF-d_7) δ 13.40 (s, 1H, 1), 8.83 (s, 1H, 8), 7.29 (d, J = 2.3 Hz, 1H, 3). ^{13}C-NMR (100 MHz, DMF-d_7) δ 179.73 (5), 174.68 (4), 170.38 (9'), 166.17 (7'), 162.13 (2'), 150.06 (5a), 148.67 (7), 137.02 (9), 135.64 (1a), 130.83 (8), 129.42 (3a), 128.33 (9a), 126.13 (2), 114.58 (3). Elemental Analysis (CHNS): Found: C, 50.32; H, 4.20; N, 11.76. Calc. for PQQ·2DMF [$C_{20}H_{20}N_4O_{10}$]: C, 50.42; H, 4.23; N, 11.76.

Coordination with Europium & Lutetium:

Experiments were performed in the same way, as described for lanthanum. Starting materials and outcome:

A: $PQQNa_2$ (50 mg, 0.13 mmol), $EuCl_3{\cdot}6H_2O$ (1.0 equiv., 49.0 mg, 0.13 mmol), H_2O (20 mL) → dark brown, almost black powder (53.5 mg, 0.09 mmol, 69%)

A: $PQQNa_2$ (30 mg, 0.08 mmol), $LuCl_3{\cdot}6H_2O$ (1.0 equiv., 31.2 mg, 0.08 mmol), H_2O (12 mL) → light brown powder (9.7 mg, 0.02 mmol, 25%)

B: $PQQNa_2$ (30 mg, 0.08 mmol), $EuCl_3 \cdot 6H_2O$ (3.0 equiv. 88.1 mg, 0.24 mmol), H_2O (12 mL) → dark brown, almost black powder (32.1 mg, 0.06 mmol, 75%)

B: $PQQNa_2$ (30 mg, 0.08 mmol), $LuCl_3 \cdot 6H_2O$ (3.0 equiv., 93.7 mg, 0.24 mmol), H_2O (12 mL) → light brown powder (31.8 mg, 0.05 mmol, 63%)

Elemental Analysis (CHNSEu): (**A**) Found C, 30.00; H, 2.25; N, 5.02; Eu, 27.82. (**B**) Found: C, 29.74; H, 2.22; N, 4.99; Eu 29.11. Calc. for PQQ-Eu·$5H_2O$ [$C_{14}H_{13}EuN_2O_{13}$]: C, 28.39; H, 2.21; N, 4.73; Eu, 26.70.

Elemental Analysis (CHNSLu): (**A**) Found C, 28.36; H, 2.08; N, 4.83; Lu, 31.42. (**B**) Found: C, 27.51; H, 2.06; N, 4.72; Lu 33.47. Calc. for PQQ-Lu·$5H_2O$ [$C_{14}H_{13}LuN_2O_{13}$]: C, 28.39; H, 2.21; N, 4.73; Lu, 29.54.

Coordination with Calcium:

$PQQNa_2$ (30 mg, 0.08 mmol - received from Doctor's Best® Science-Based Nutrition™ BioPQQ® capsules) was dissolved in H_2O (12 mL). $CaCl_2 \cdot 2H_2O$ (**A**: 0.5 equiv., 5.9 mg, 0.04 mmol /**B**: 1.0 equiv., 11.8 mg, 0.08 mmol/**C**: 2.0 equiv., 23.6 mg, 0.16 mmol /**D**: 3.0 equiv., 35.4 mg, 0.24 mmol) was added as a solid. The metal addition led to a precipitation as well, but unlike the lanthanum-experiment, the supernatant remained red-colored, regardless of the number of washing steps. Also centrifugation was only partly possible, and parts of the product remained in the supernatant. After 4 washing steps, only traces of a pellet remained for approach **A**. Approaches **B**-**D** were dried *in vacuo* and the Ca-amount was determined by ICP-OES. The amount of Ca was determined to be 10-13% by mass (B: 10%, C: 11%, D: 13%). Calculating a potential 1:1 PQQ-Ca complex with 3-6 water equivalents, the amount of Ca^{2+} would be between 8-9% by mass. A 2:1 complex would only contain around 5% Ca^{2+} by mass, while a 1:2 complex would contain around 16% Ca^{2+}. Taken the insufficient purification procedure into account (red-colored supernatant indicated free PQQ; even with 3 equiv. of $CaCl_2$), all three approaches indicate the formation of a 1:1 PQQ-Ca complex, similar to the experiment with lanthanum.

Elemental Analysis (Ca): (**B**) Found: Ca, 9.69. (**C**) Found: Ca, 10.56. (**D**) Found: Ca, 12.55. Calc. for $PQQ^{2-}Ca^{2+} \cdot 3H_2O$ [$C_{14}H_{10}CaN_2O_{11}$]: C, 39.82; H, 2.39; N, 6.63; Ca, 9.49.

1.4. Supporting Information of Chapter IV.2

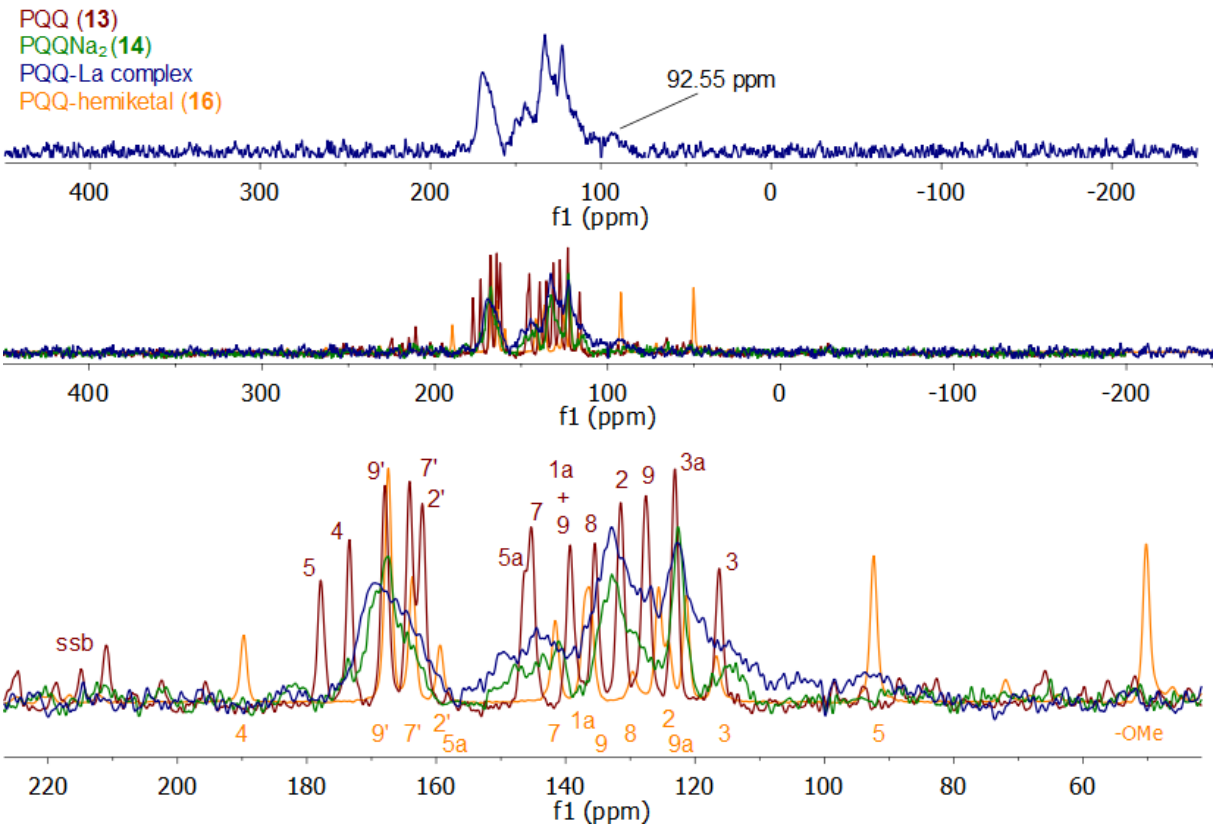

Figure IX.29: Superimposed ^{13}C-NMR spectra of PQQ (**13** - red), PQQNa$_2$ (**14** - green), PQQ-hemiketal (**16** - orange) and the 1:1 PQQ-La complex (blue) in the solid state. Assignments based on liquid NMR (Table VI.2). ssb = spinning side bands. The broad resonance at 92.55 ppm from the PQQ-La complex could stem from small amounts of the PQQ-water adduct (**15**) in the precipitated solid, since C5 shift of the related PQQ-hemiketal (**16**) (orange spektrum) is in the same range.

Table IX.15: Complex formation of $PQQNa_2$ with La/Ln or La/Ca couples. The given samples were digested in defined amounts of nitric acid (65%) and then diluted with the given amount of MilliQ water, to yield a concentration of 1.0256 mg/mL in 3% nitric acid for each sample. Values below the detection limit are marked with "-".

	Mass Fraction (%) (EA)			µg / L (ICP-MS)																		
	C	**H**	**N**	**Na**	**La**	**Ce**	**Pr**	**Nd**	**Sm**	**Eu**	**Gd**	**Tb**	**Dy**	**Ho**	**Er**	**Tm**	**Yb**	**Lu**	**Ca**	Yield (mg)	Weight of sample (mg)	Volume of added H_2O (mL)
La/Ln (1)	32.78	1.94	5.56	12.3	5.4	7.3														24.4	8.7	8.091
La/Ln (1)	32.67	1.86	5.46	13.1	5.7		7.5													25.4	6.3	5.859
La/Ln (1)	31.98	1.96	5.32	13.2	5.6			7.2												24.4	9.8	9.114
La/Ln (1)	32.60	1.93	5.38	12.9	7.5				5.8											26.0	7.9	7.347
La/Ln (1)	31.83	1.81	5.33	13.0	6.2					7.7										24.0	7.0	6.510
La/Ln (1)	29.68	2.22	4.95	12.0	7.1						6.5									22.9	8.4	7.812
La/Ln (1)	31.28	1.90	5.23	13.2	8.4							5.8								21.8	5.7	5.301
La/Ln (1)	31.79	2.05	5.23	14.2	9.0								3.9							18.1	7.6	7.068
La/Ln (1)	31.59	2.05	5.21	13.2	10.4									4.7						21.0	5.8	5.394
La/Ln (1)	32.32	1.90	5.36	12.9	9.8										4.1					25.5	6.4	5.952
La/Ln (1)	27.80	2.02	4.60	12.9	9.4											5.1				28.1	6.3	5.859
La/Ln (1)	27.59	2.02	4.59	11.1	9.1												5.1			28.3	6.9	6.417
La/Ln (1)	27.05	2.08	4.50	12.7	10.4													5.9		29.0	6.6	6.138
La/Ln (1)	27.55	2.03	4.63	12.2	11.6														-	29.2	6.7	6.231
La/Ln (2)	32.09	2.18	5.54	28.9	6.0	7.9														25.5	7.1	6.603
La/Ln (2)	30.99	2.41	5.76	30.0	6.6		8.6													25.9	7.4	6.882
La/Ln (2)	31.31	2.31	6.14	30.8	6.5			7.5												26.6	5	4.65
La/Ln (2)	30.9	2.29	5.87	28.4	6.5				6.0											25.3	5.2	4.836
La/Ln (2)	31.01	2.20	5.78	33.2	6.7					7.4										24.3	5.3	4.929
La/Ln (2)	31.10	1.87	5.38	29.8	7.0						7.1									25.0	8.4	7.812
La/Ln (2)	31.70	1.79	5.41	30.3	8.1							7.7								25.7	5.5	5.115
La/Ln (2)	31.81	1.79	5.41	35.3	9.0								5.8							25.3	9.2	8.556
La/Ln (2)	30.92	2.19	5.28	34.9	8.9									4.4						24.6	7.1	6.603
La/Ln (2)	30.68	2.34	5.24	35.3	9.8										3.7					25.6	7.7	7.161
La/Ln (2)	31.26	2.22	5.21	34.4	9.4											3.1				25.6	9.1	8.463
La/Ln (2)	31.41	2.19	5.29	34.4	9.8												3.3			25.4	6	5.580
La/Ln (2)	31.11	2.34	5.25	33.5	8.8													3.1		24.9	6.6	6.138
La/Ln (2)	31.78	2.34	5.27	26.2	12.3														9.2	24.4	8.1	7.533
La/Ln (3)	31.85	2.41	5.44	27.6	4.3	6.0														24.4	10.6	9.858
La/Ln (3)	32.24	2.17	5.44	28.2	4.5		6.5													22.3	4.8	4.464
La/Ln (3)	31.00	2.57	5.34	27.4	4.6			6.5												24.9	5.5	5.115
La/Ln (3)	30.35	2.65	5.22	29.4	6.5				6.7											25.5	6.1	5.673
La/Ln (3)	30.48	2.74	5.14	28.2	5.3					7.1										26.2	13.7	12.741
La/Ln (3)	29.57	2.77	5.10	28.3	6.2						6.3									25.3	8.2	7.626
La/Ln (3)	35.97	3.21	6.17	26.8	6.7							5.8								25.7	7.4	6.882
La/Ln (3)	31.15	2.58	6.20	25.6	8.4								4.4							24.4	6	5.580
La/Ln (3)	30.78	2.37	6.04	27.9	7.9									4.9						24.9	6.1	5.673
La/Ln (3)	31.08	2.48	6.16	32.8	9.4										4.9					25.5	8.3	7.719
La/Ln (3)	31.76	2.49	3.36	22.0	8.5											3.9				25.3	6.7	6.231
La/Ln (3)	31.69	2.51	6.51	21.0	9.2												4.2			25.7	5.2	4.836
La/Ln (3)	30.72	2.56	6.08	18.8	8.3													4.5		25.1	5.8	5.394
La/Ln (3)	31.11	2.68	5.59	20.5	13.1														9.2	23.4	5.5	5.115
La/Pr (digestion A)				-	5.3		7.1	-													6.3	5.859
La/Pr (digestion B)				-	5.5		7.3	-													6.2	5.766
La/Nd (digestion A)				-	5.3		-	6.9													9.8	9.114
La/Nd (digestion B)				-	4.9		-	6.3													6.0	5.580
HNO_3- MilliQ				21.2	-	-	-	-	-	-	-	-	-	-	-	-	-	-	-			
MilliQ				28.1	-	-	-	-	-	-	-	-	-	-	-	-	-	-	-			

1.5. Supporting Information of Chapter VII

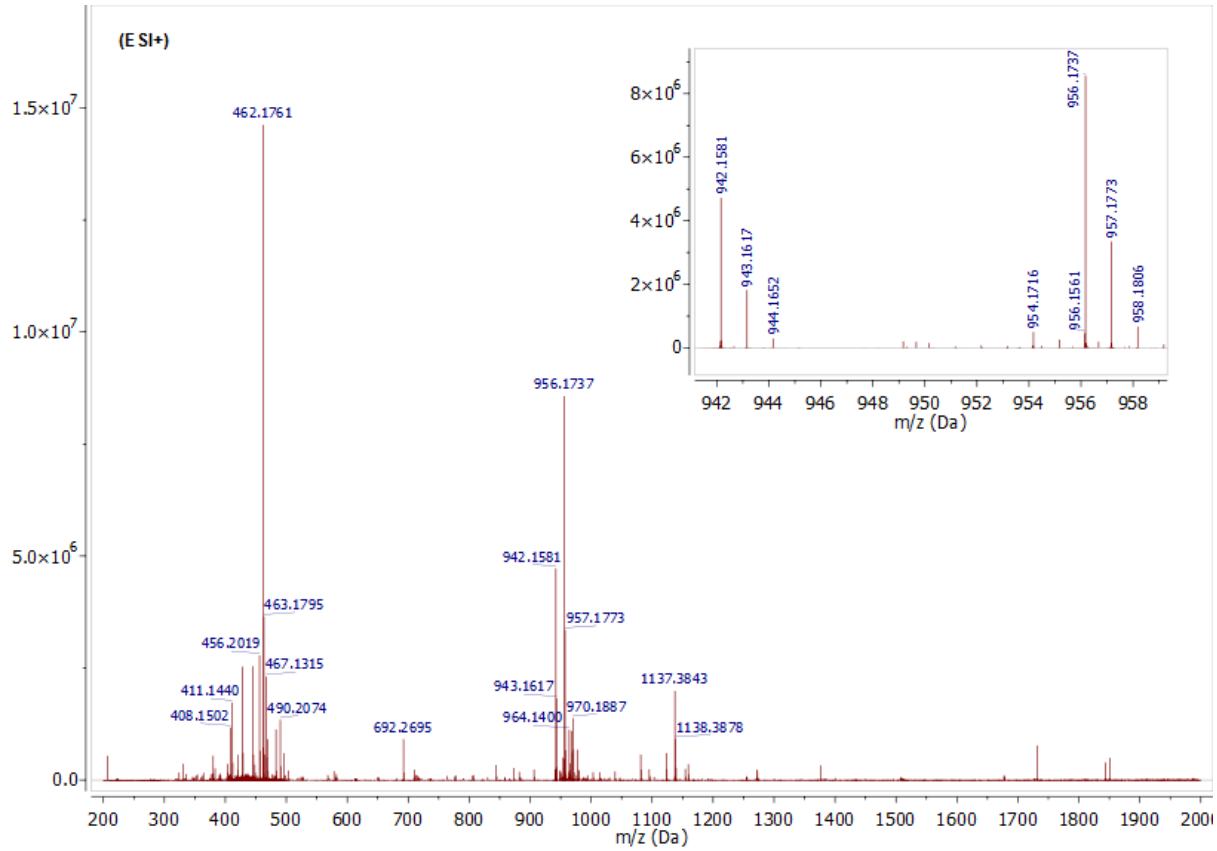

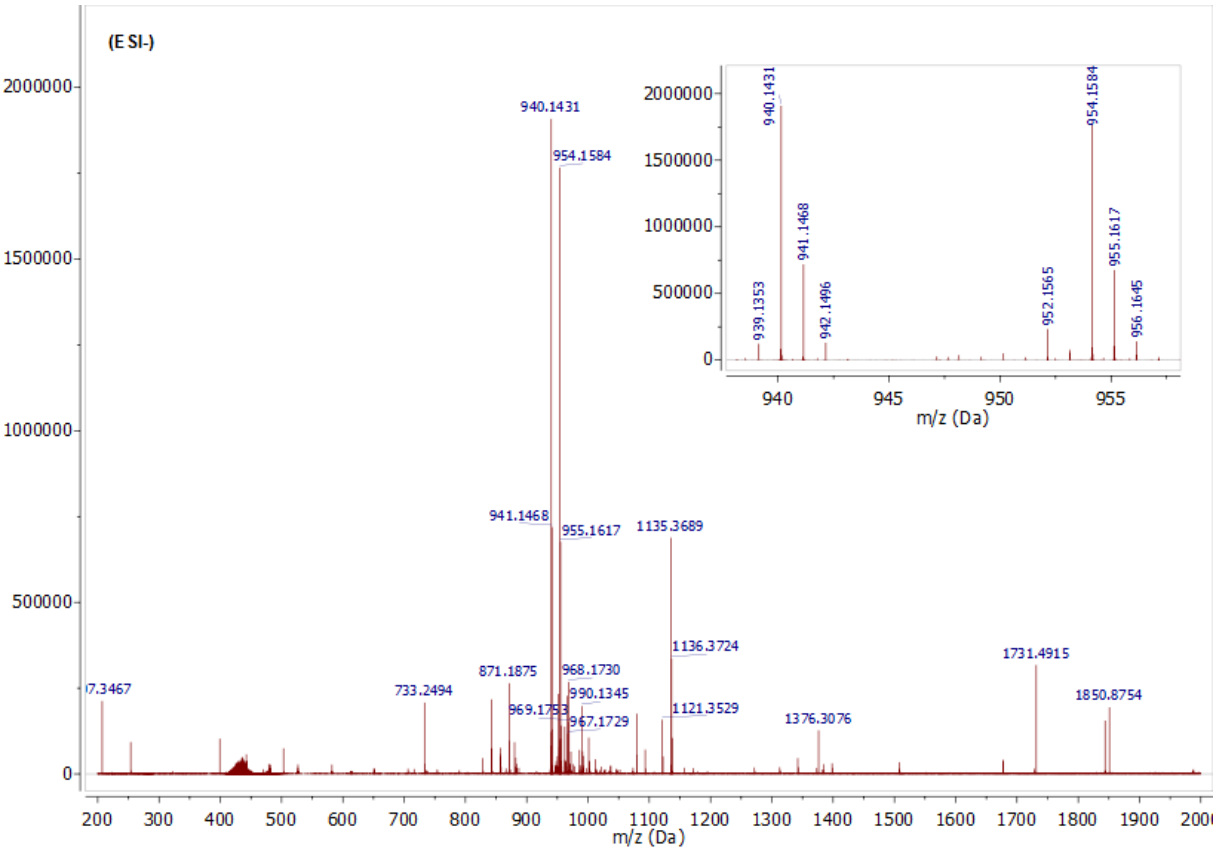

Figure IX.30: ESI mass spectra of La-TREN-(1,2-HOPO)$_2$-TAM-N1-PDA complex [La (**43**)].

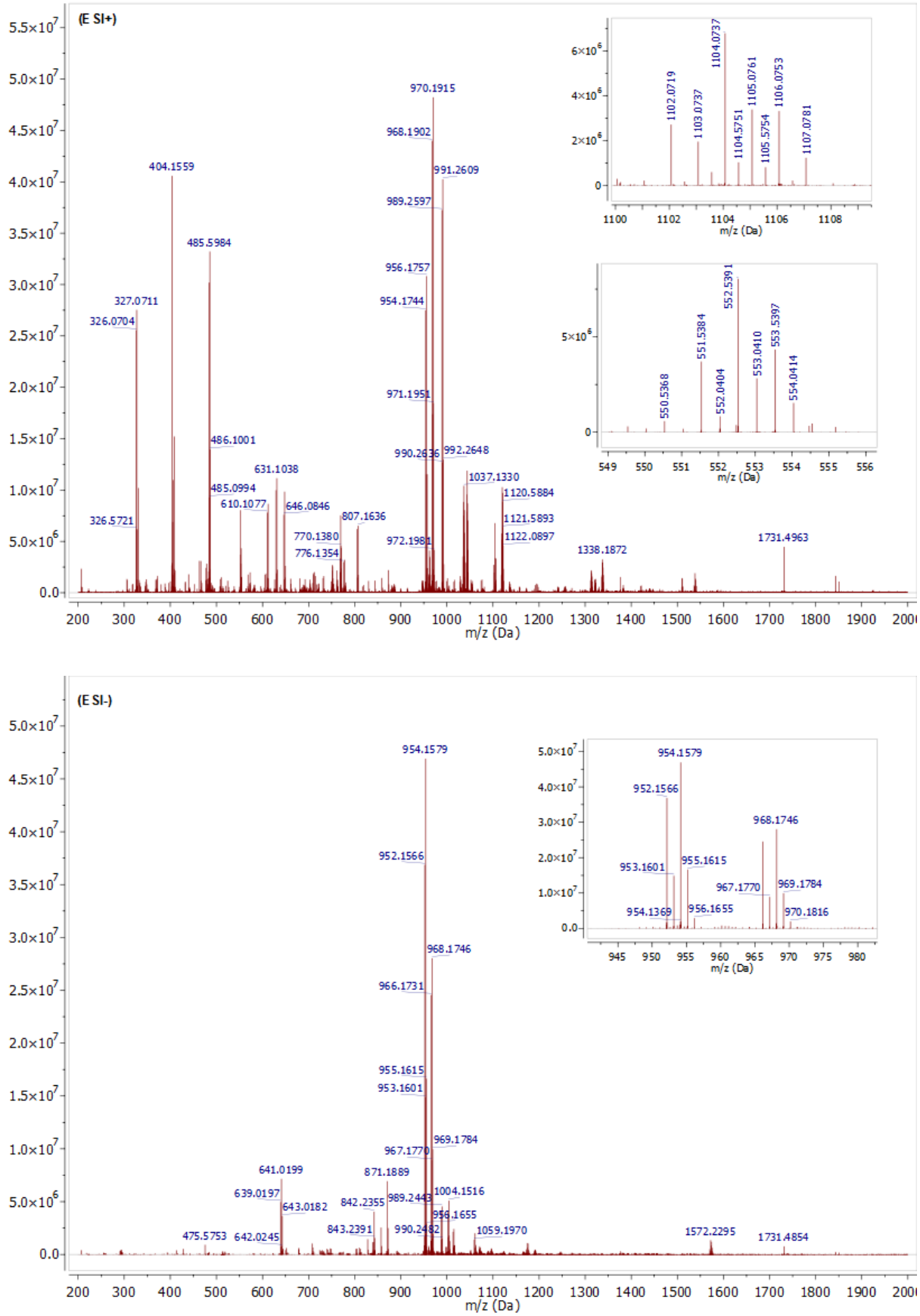

Figure IX.31: ESI mass spectra of Eu-TREN-(1,2-HOPO)$_2$-TAM-N1-PDA complex [Eu (**43**)].

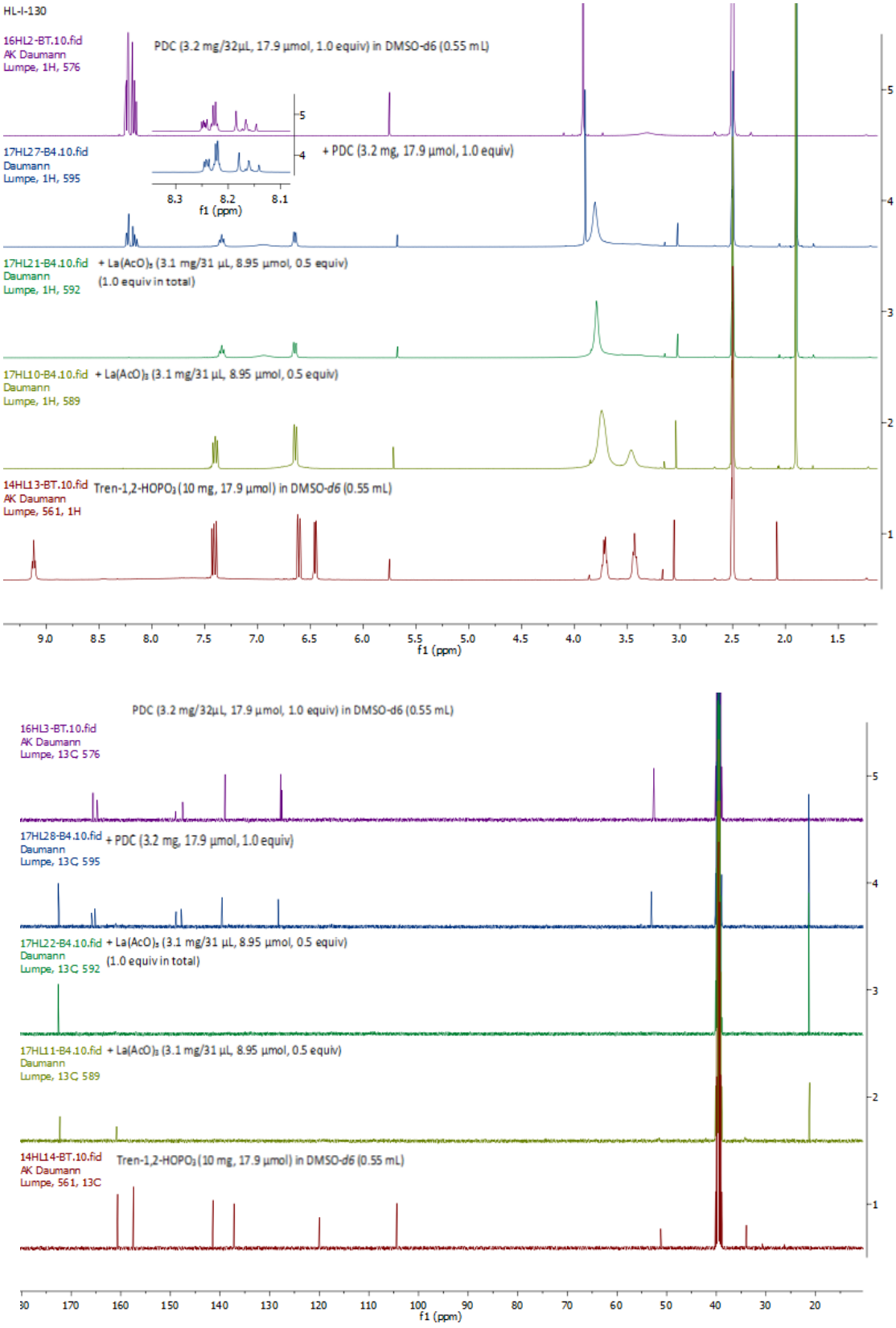

Figure IX.32: Stacked ^{1}H- and ^{13}C-NMR spectra of TREN-1,2-HOPO$_3$ (**32**) with increasing amounts of La(AcO)$_3$ and PDC (**40**).

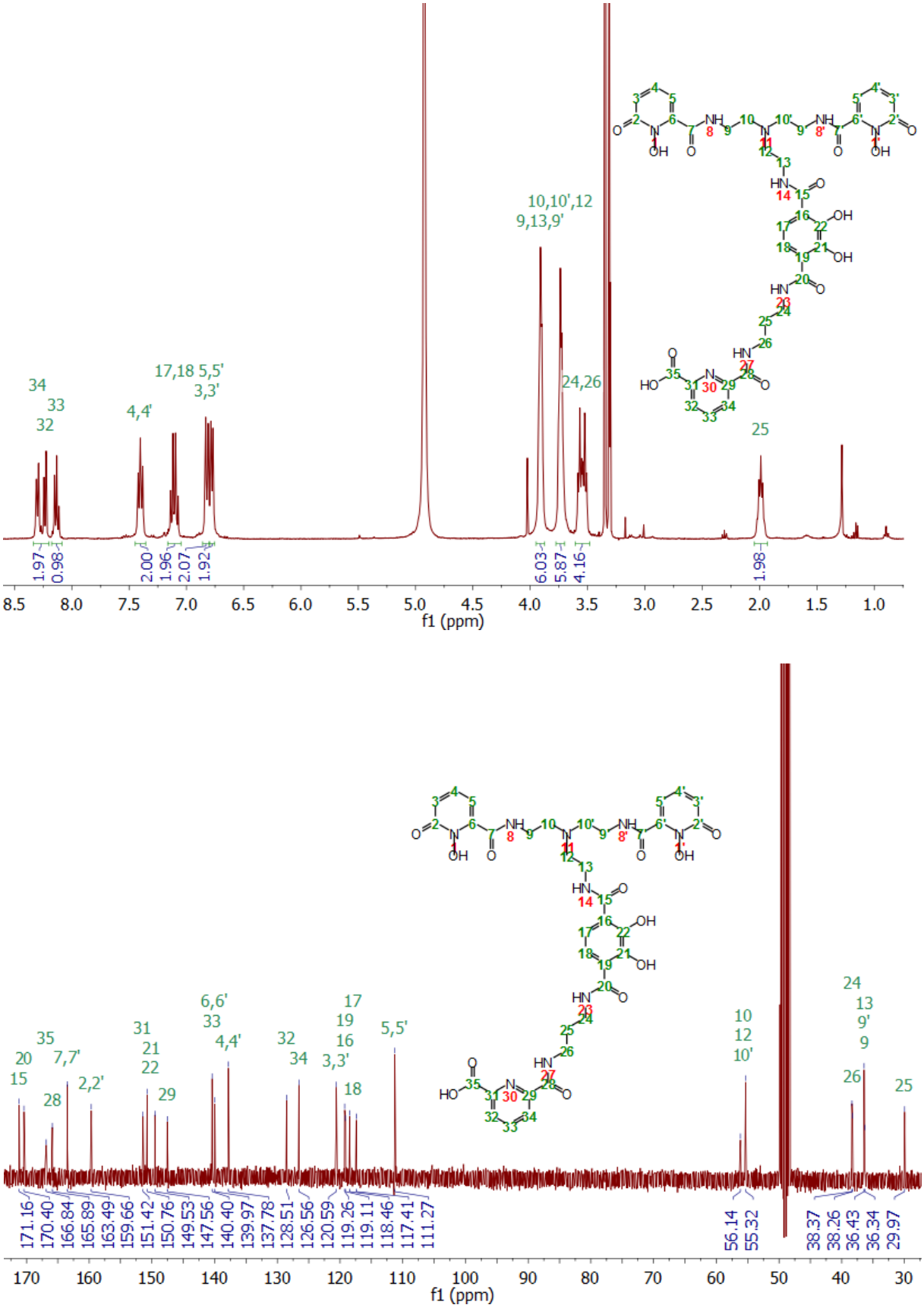

Figure IX.33: ^{1}H- and ^{13}C-NMR spectra of TREN-(1,2-HOPO)$_2$-TAM-N1-PDA (**43**) in MeOD-d_4 with assigned signals.

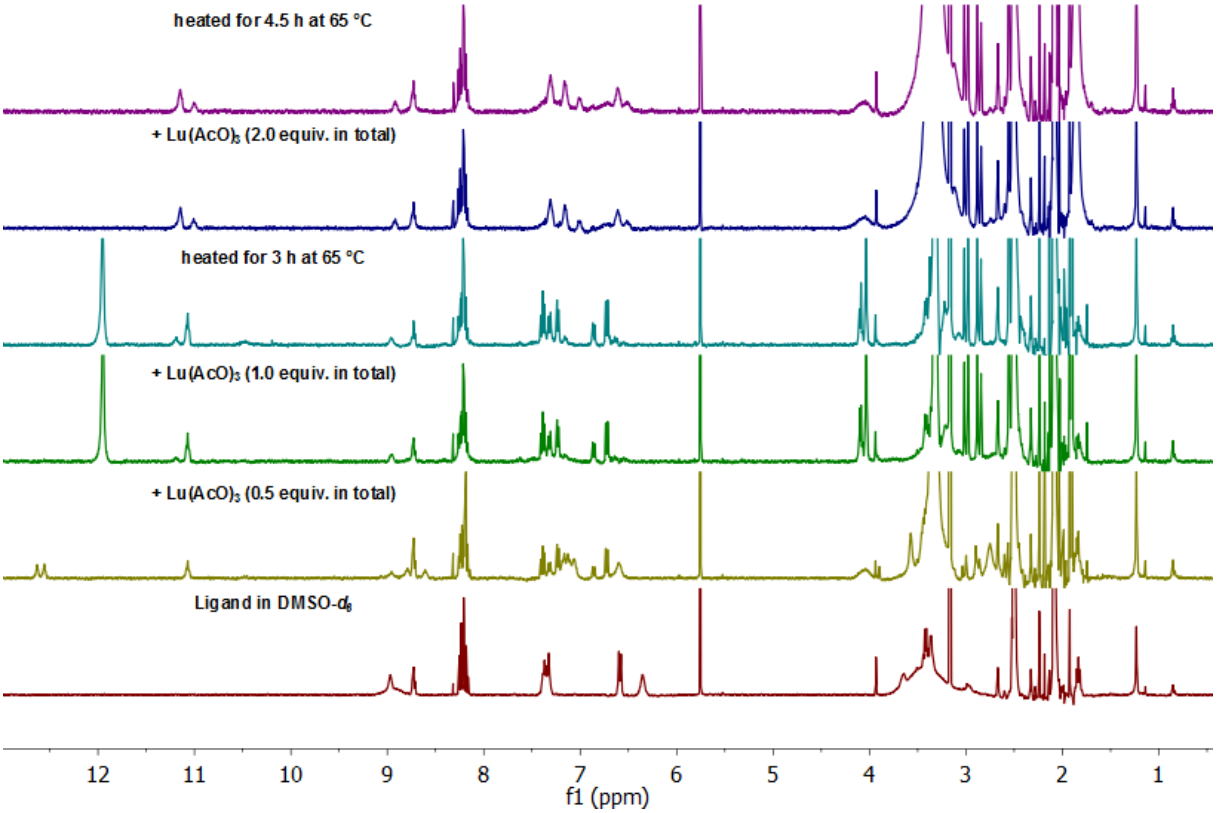

Figure IX.34: Stacked ^{1}H-NMR spectra of Tren-(1,2-HOPO)$_2$-TAM-N1-PDA (**43**, 5 µmol) in DMSO-d_6 (0.6 mL) and increasing amounts of Lu(AcO)$_3$.

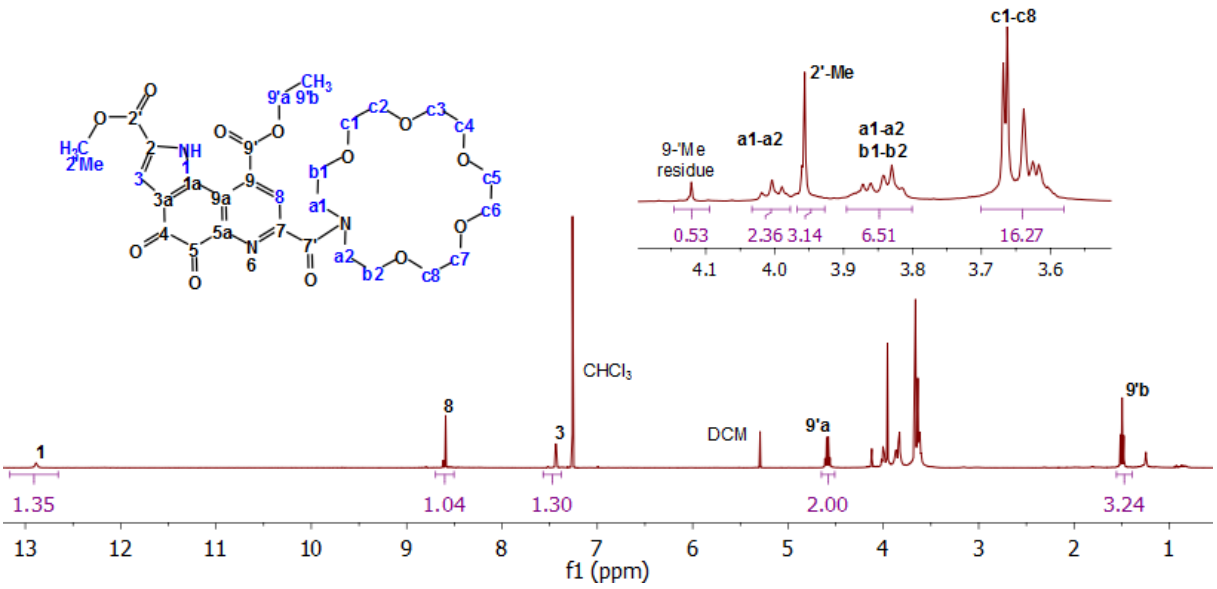

Figure IX.35: ^{1}H-NMR spectrum of PQQ-Crown-18 (**59**) with an ethyl-ester in C9 position in CDCl$_3$.

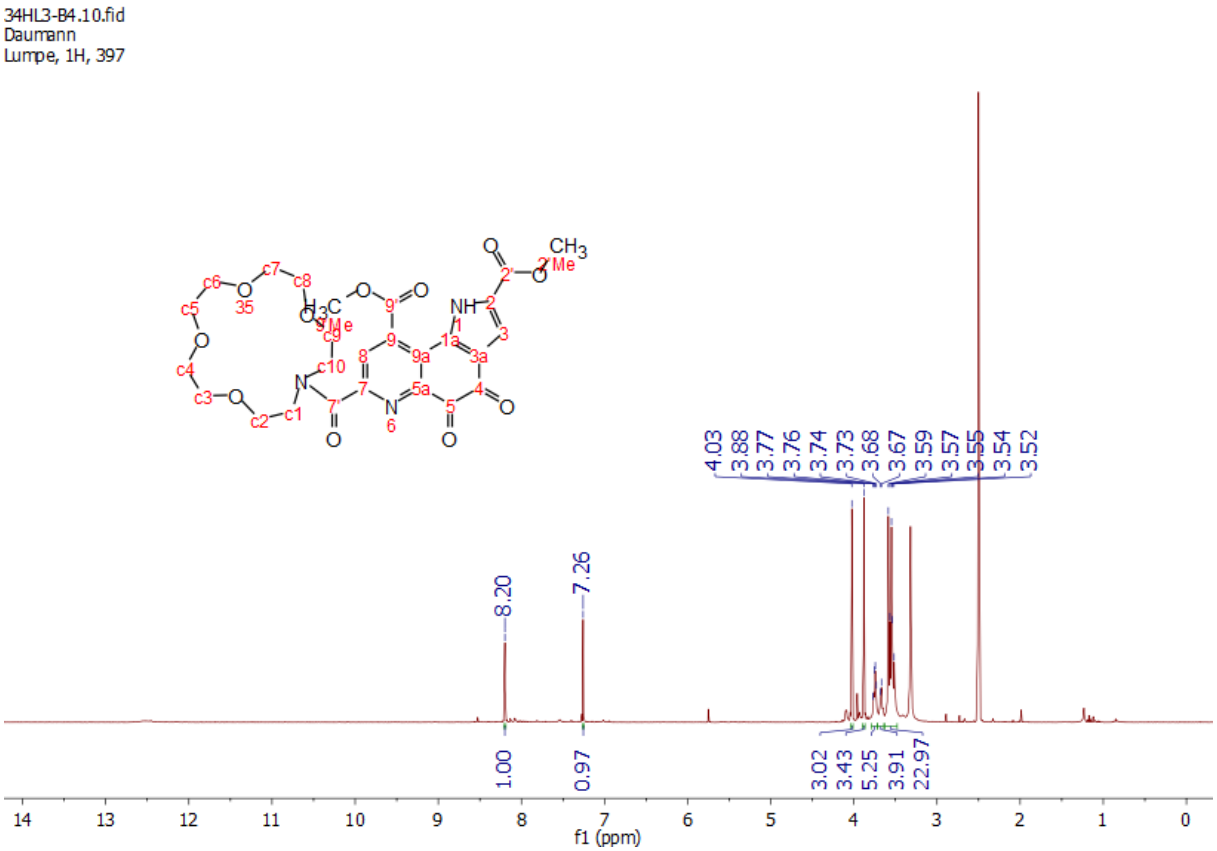

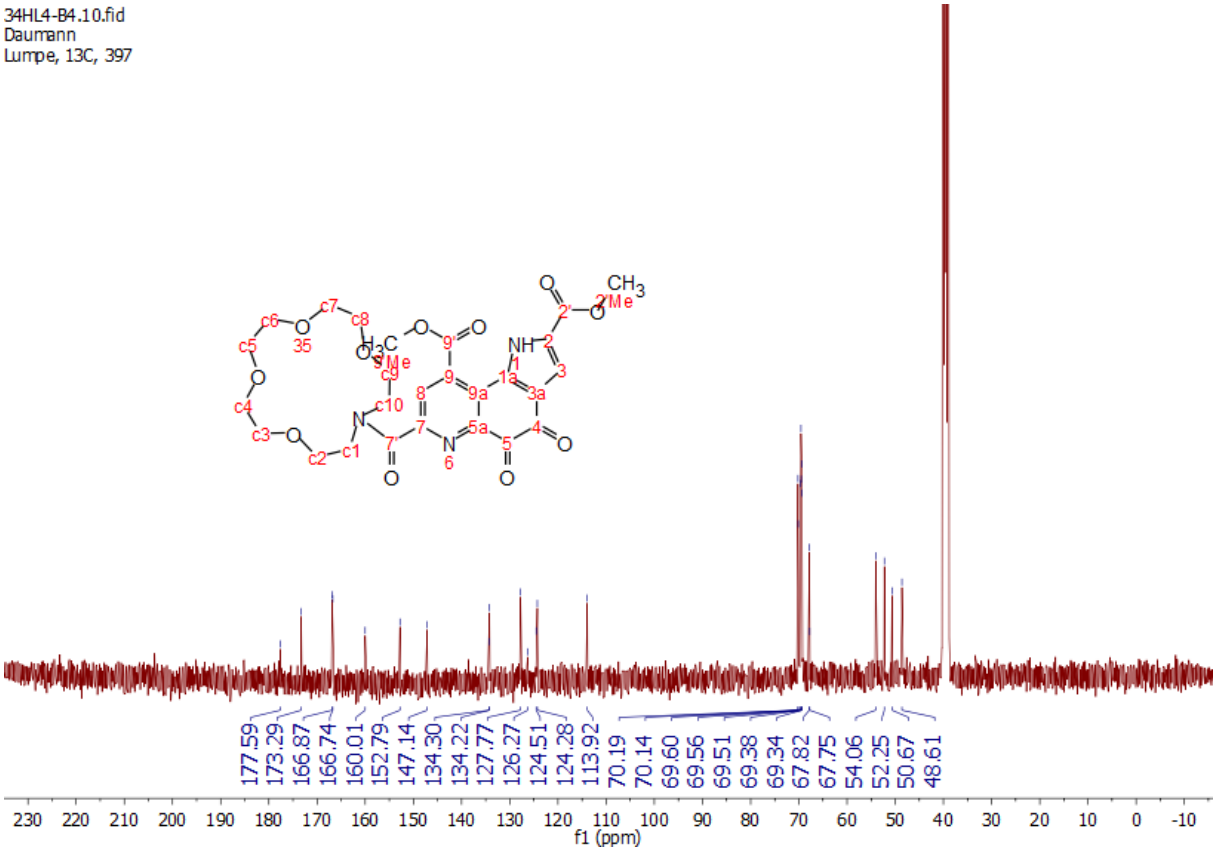

Figure IX.36: ^{1}H- and ^{13}C-NMR spectra of PQQ-Crown-15 (**31**) in DMSO-d_6.

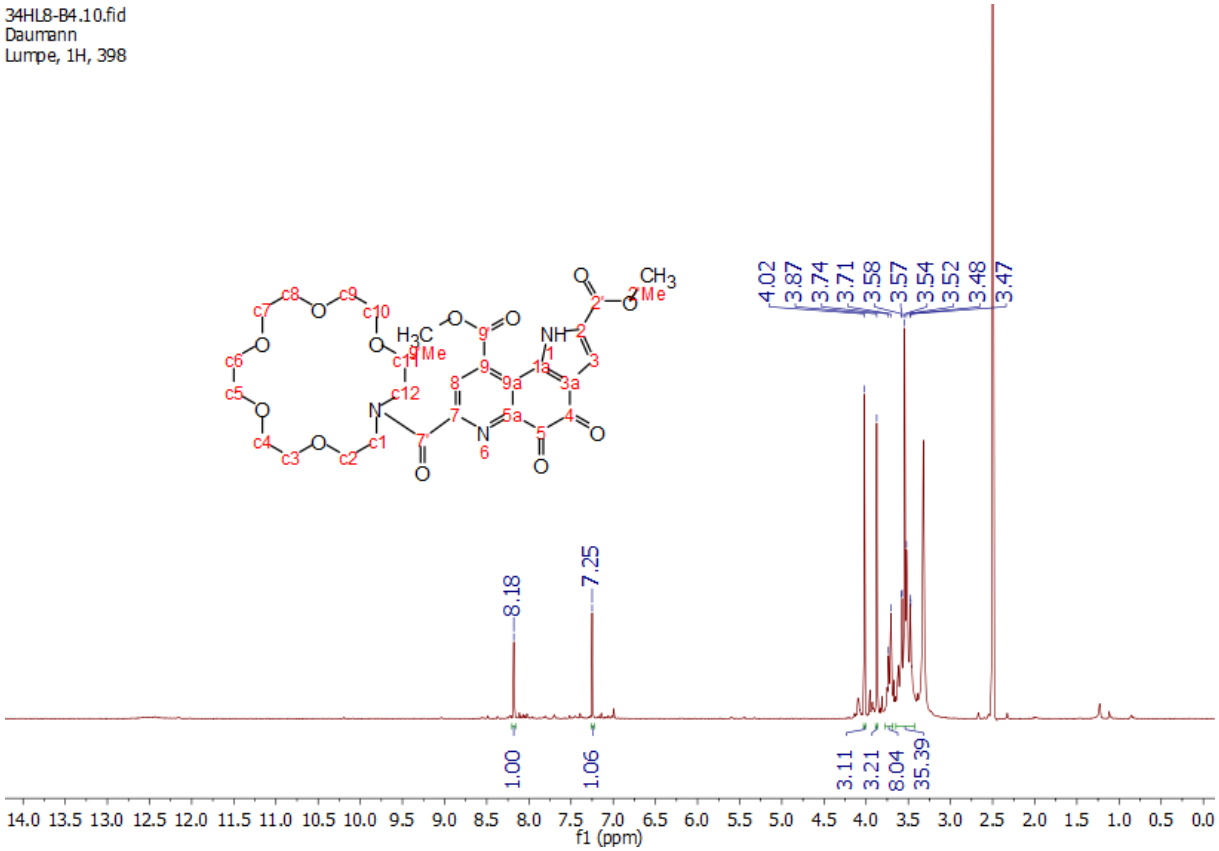

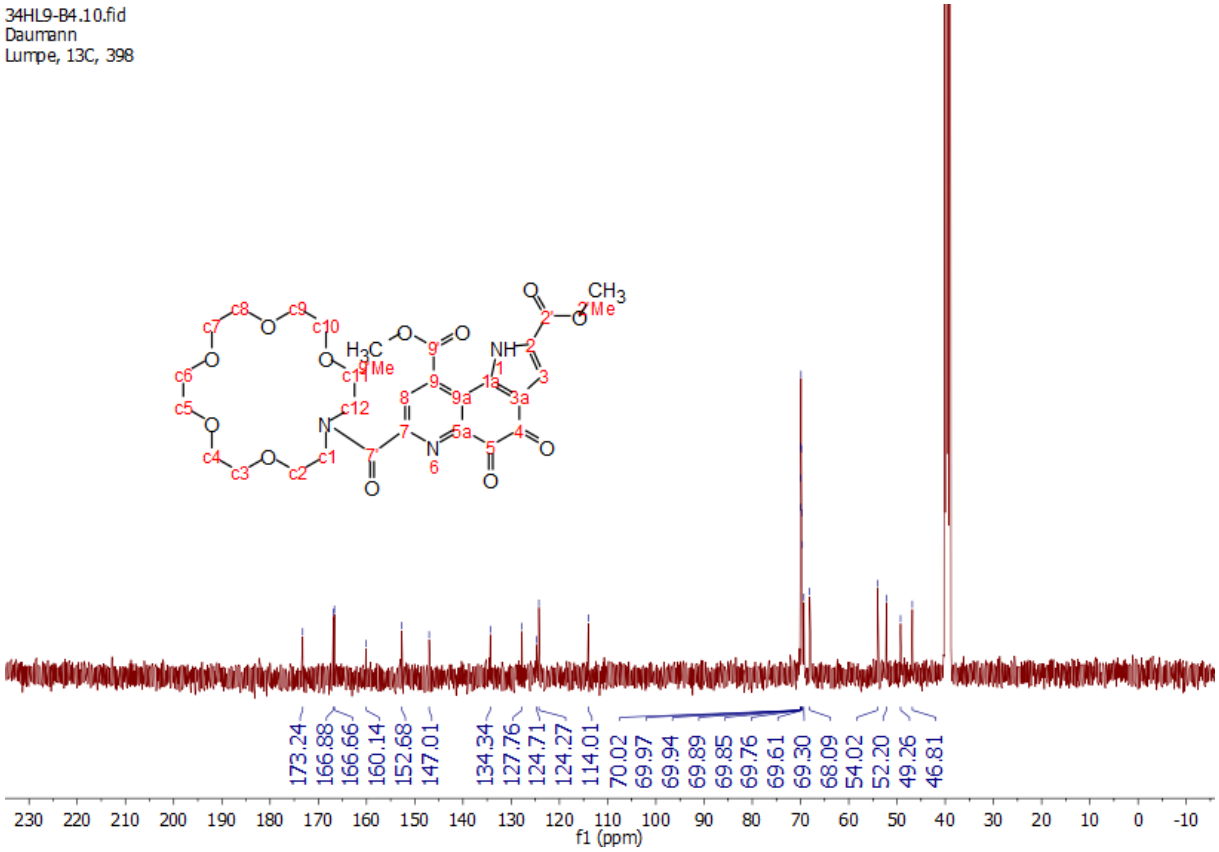

Figure IX.37: ^{1}H- and ^{13}C-NMR spectra of PQQ-Crown-18 (**58**) in DMSO-d_6

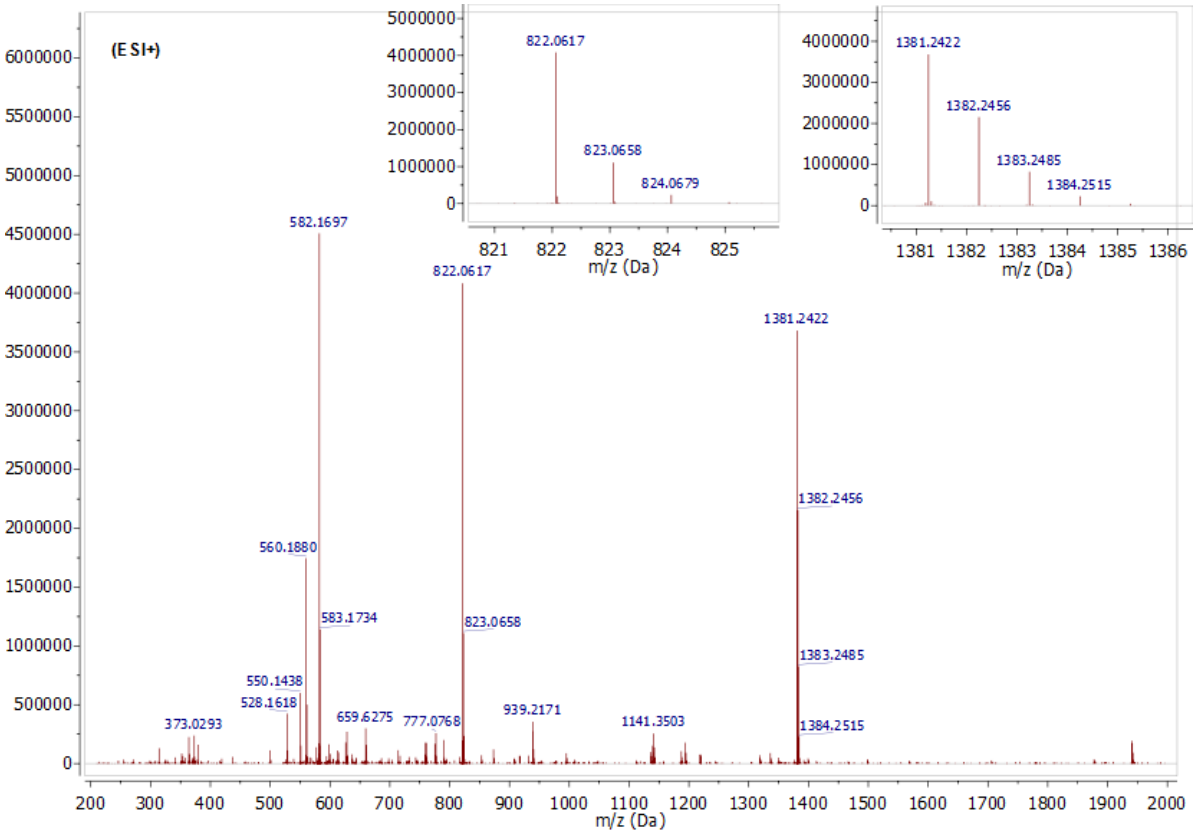

Figure IX.38: ESI mass spectrum of PQQ-Crown-15 (**31**) lanthanum complexes $[La(\mathbf{31})(NO_3)_2]^+$ and $[La(\mathbf{31})_2(NO_3)_2]^+$.

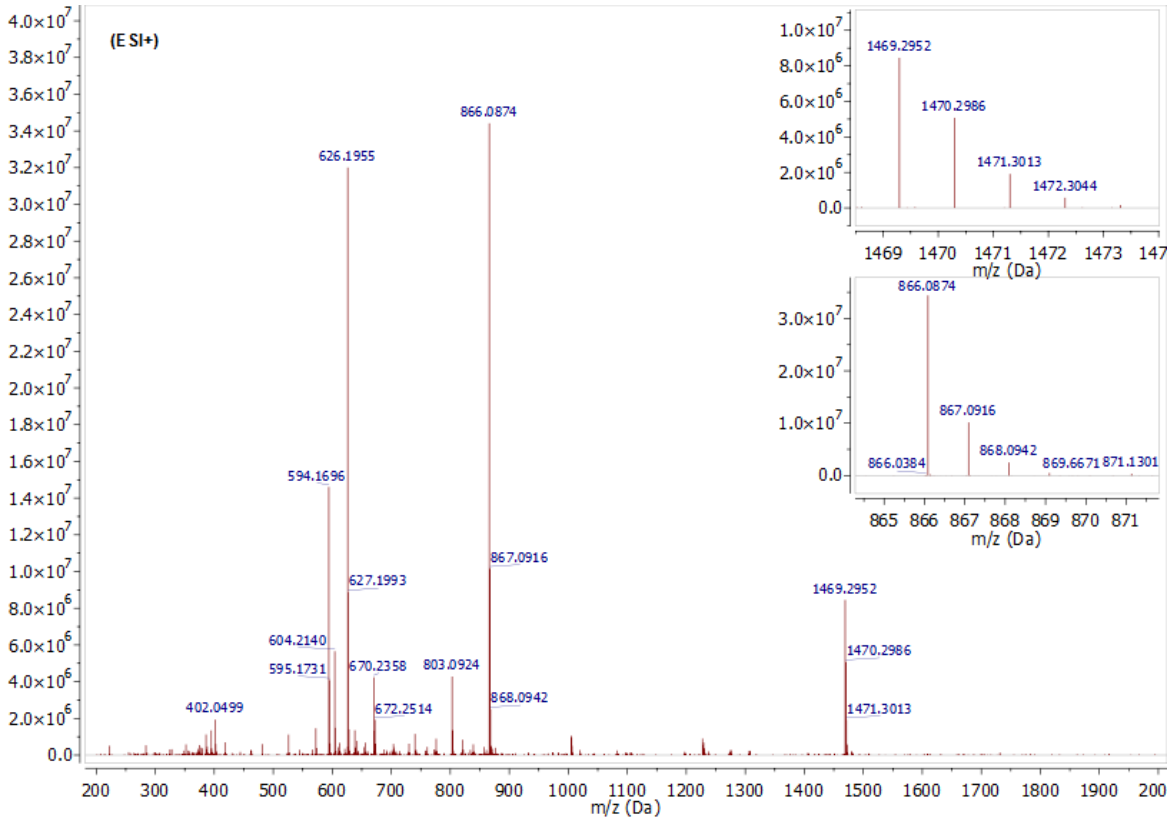

Figure IX.39: ESI mass spectrum of PQQ-Crown-18 (**58**) lanthanum complexes $[La(\mathbf{31})(NO_3)_2]^+$ and $[La(\mathbf{31})_2(NO_3)_2]^+$.

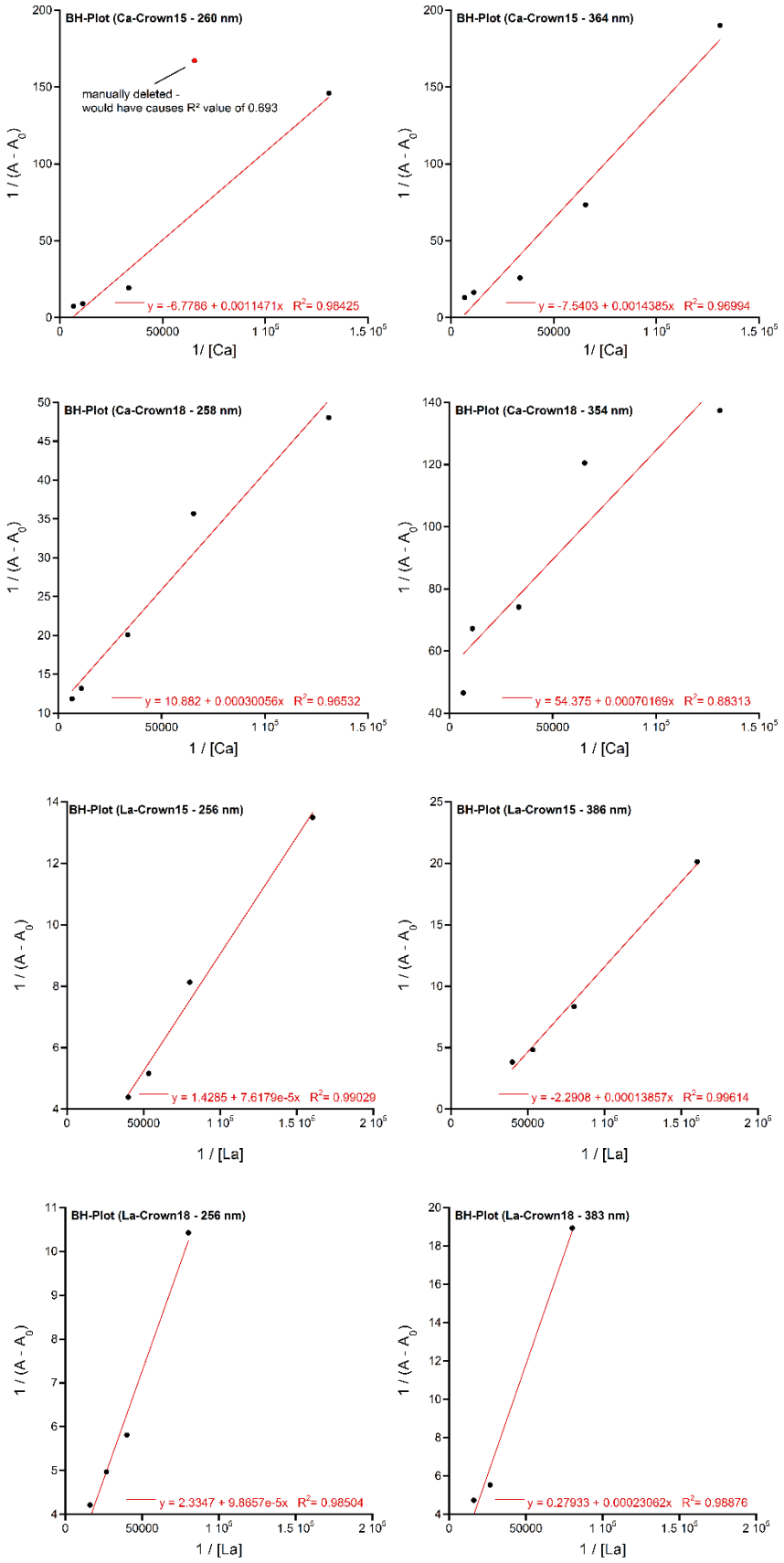

Figure IX.40: Benesi-Hildebrand plots for determination of binding constants K for complexes of PQQ-crown ether ligands **31** and **58** with La^{3+} or Ca^{2+}.

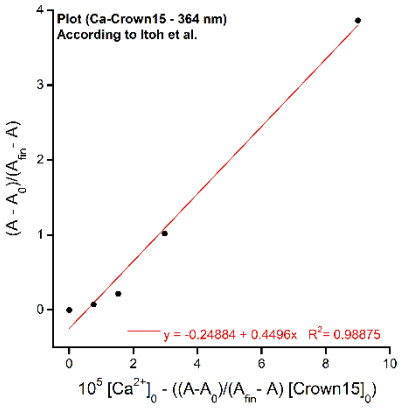

Figure IX.41: Determination of binding constant K for a [Ca (**31**)]$^{2+}$ complex, according to Itoh *et al.*[152]

2. List of Abbreviations

2D	two-dimensional
ATP	Adenosine Triphosphate
ATR	Attenuated Total Reflection
Å	Ångström
a.u.	arbitrary units
Bn	benzyl
boc	*tert*-Butyloxycarbonyl
calc.	calculated
CDI	1,1'-carbonyldiimidazole
CE	Counter Electrode
CN	Coordination Number
conc.	concentrated
COSY	Two-dimensional correlation spectroscopy
CPCM	Conductor-like polarizable continuum model
CV	Cyclic Voltammetry / Cyclic Voltammogram
DBN	1,5-Diazabicyclo[4,3,0]non-5-ene
DBU	1,8-Diazabicyclo[5,4,0]undec-7-ene
DCM	Dichloromethane
DCPIP	2,6-Dichlorophenolindophenol
DFT	Density Functional Theory
DMF	Dimethylformamide
DMSO	Dimethyl sulfoxide
DOTA	1,4,7,10-Tetraazacyclododecane-1,4,7,10-tetraacetic acid
dpa	2,6-Dipicolinic acid
DTPA	Diethylenetriaminepentaacetic acid
DWH	Deepwater Horizon
EA	Elemental Analysis
ECP	Effective Core Potentials
EDTA	Ethylenediaminetetraacetic acid
equiv.	equivalent
ESI	Electrospray Ionization
Et	ethyl
EtOAc	Ethyl Acetate
EURARE	EuRare-project, funded by the European Union for the development of a sustainable exploitation scheme for Europe’s Rare-Earth ore deposits.
eV	Electron Volt

GP	General Procedure
h	hour(s)
HMBC	Heterobinuclear Multiple Bond Correlation
HOMO	Highest Occupied Molecular Orbital
HOPO	1-Hydroxy-6-oxo-1,6-dihydropyridine-2-carboxylic acid
HRE	Heavy Rare-Earth Elements - ^{64}Gd – ^{71}Lu + ^{39}Y
HRMS	High-Resolution Mass Spectrometry
HSQC	Heteronuclear Single Quantum Coherence
ICP-MS	Inductively Coupled Plasma Mass Spectrometry
IR	Infrared
K	Binding Constant
K_M	Michaelis-Menten Constant
LC/MS	Liquid Chromatography–Mass Spectrometry
LED	Light-Emitting Diode
Ln	Lanthanide - ^{57}La – ^{71}Lu
Ln-MDH	Lanthanide Dependent Methanol Dehydrogenase
LRE	Light Rare-Earth Elements - ^{57}La – ^{63}Eu
LUMO	Lowest Unoccupied Molecular Orbital
M	mol/L
MAS	Magic-Angle-Spinning
MDH	Methanol Dehydrogenase
Me	methyl
MeCN	Acetonitrile
MeOH	Methanol
MHz	Megahertz
Milli-Q	System for water purification
mm	Millimeter
MO	Molecular orbital
nm	Nanometer
MxaF	Ca-dependent MDH enzyme
mxaF	Gene, which encodes MxaF
NMR	Nuclear Magnetic Resonance
NOTA	1,4,7-Triazacyclononane-1,4,7-triacetic acid
ORTEP	Oak Ridge Thermal Ellipsoid Plot
PCTA	3,6,9,15-tetraazabicyclo[9.3.1]pentadeca-1(15),11,13-triene-3,6,9-triacetic acid
PDB	Protein Database - followed by a four letter code
PDC	Pyridinedicarboxylic Acid Monomethyl Ester
PEG	Polyethylene Glycol

PES	Phenazine Ethosulfate
Ph	phenyl
PIPES	Piperazine-N,N′-bis(2-ethanesulfonic acid)
PMS	Phenazine Methosulfate
ppm	parts per million
PQQ	Pyrroloquinoline quinone
pTSA	p-Toluenesulfonic acid
PyBOP	Benzotriazol-1-yl-oxytripyrrolidinophosphonium hexafluorophosphate
r.t.	room temperature
RE	Reference Electrode
REE	Rare-Earth Element - ^{57}La – ^{71}Lu + ^{21}Sc and ^{39}Y
ssNMR	solid-state NMR
T	Tesla
TAM	benzyl-protected terephthalamide moiety
TCM	Trichloromethane / Chloroform
TEA	Triethylamine
THF	Tetrahydrofuran
TLC	Thin Layer Chromatography
TMS	Tetramethylsilane
TRIS	2-Amino-2-(hydroxymethyl)propane-1,3-diol
UFF	Universal Force Field
UV	Ultra Violet
V	Volt
$\tilde{\nu}$	Wavenumber
vis	visible
vs.	versus
WE	Working Electrode
XoxF	Ln-dependent MDH enzyme
xoxF	Gene, which encodes XoxF
δ	Chemical Shift

3. Table of Compounds

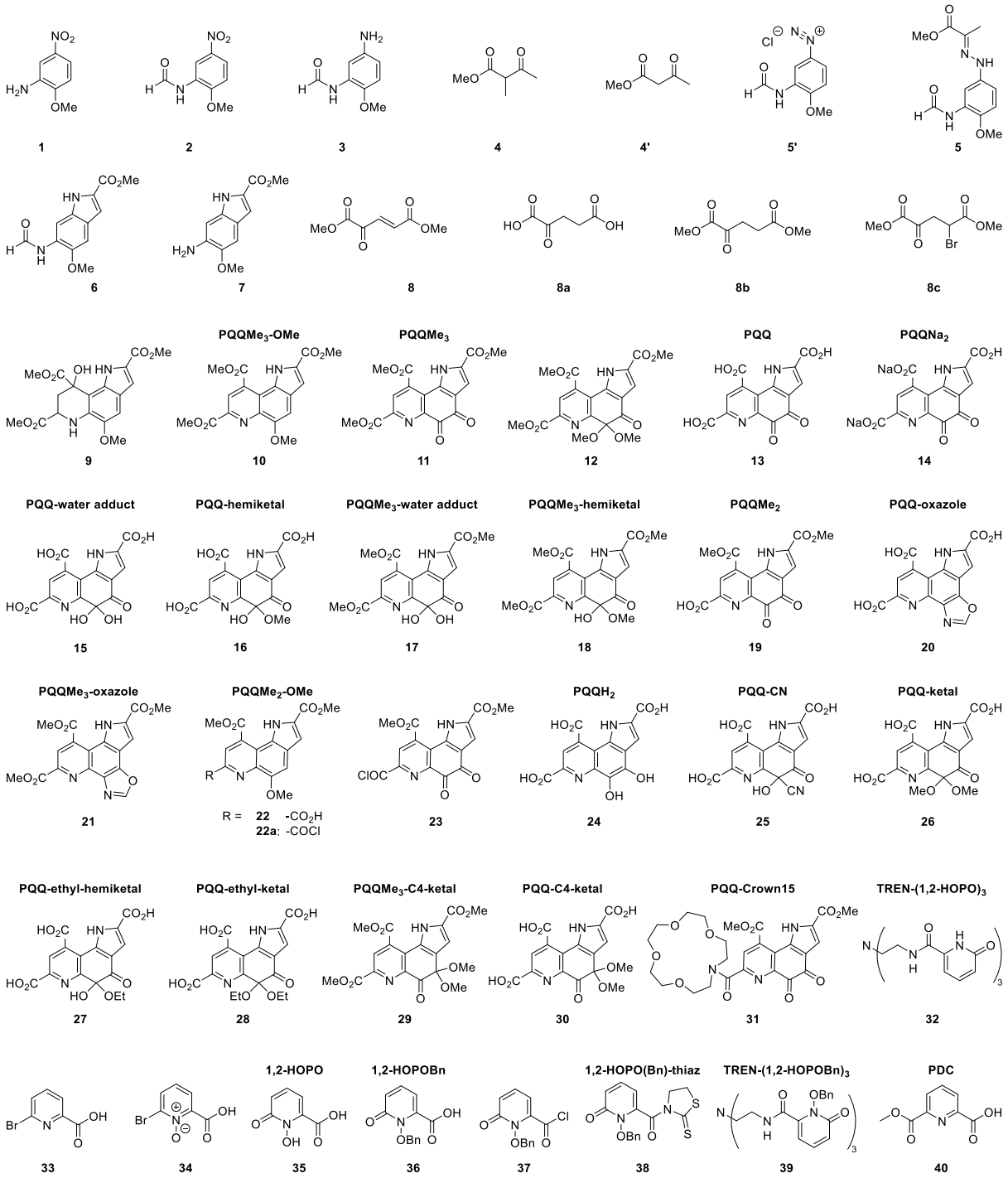

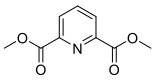

40a

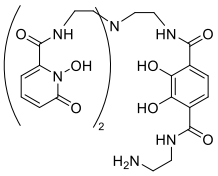

41

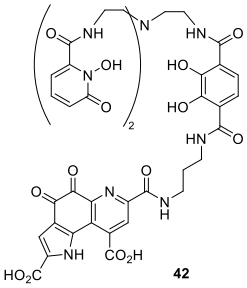

42

TREN-(1,2-HOPO)$_2$-TAM-N1-PDA

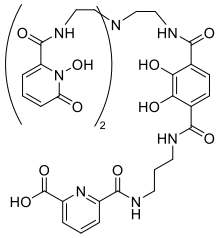

43

TREN-(1,2-HOPO)$_2$-TAM-N1-PDC

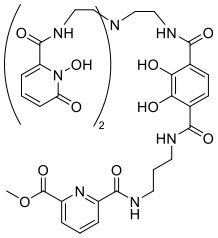

43a

PDA

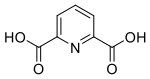

44

TREN-(1,2-HOPOBn)$_2$

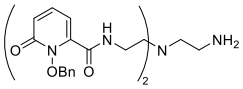

45

TAM-bis-thiaz

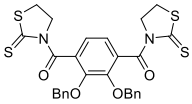

46

TAM-N1-thiaz

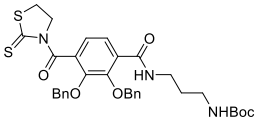

47

TREN-(1,2-HOPOBn)$_2$-TAMBn-N1-Boc

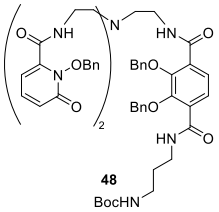

48

TREN-(1,2-HOPOBn)$_2$-TAMBn-N1

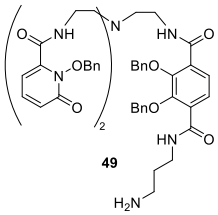

49

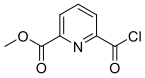

50

PDC-thiaz

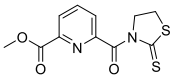

51

PDC-N1-Boc

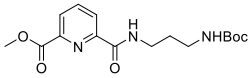

52

PDC-N1

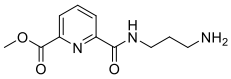

53

PDC-N1-TAM

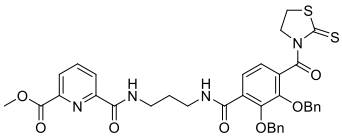

54

TREN-(1,2-HOPOBn)$_2$-TAM-N1-PDC

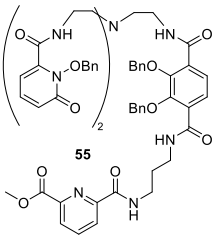

55

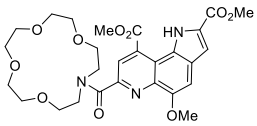

56

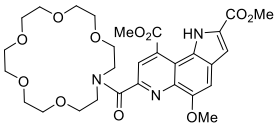

57

PQQ-Crown15

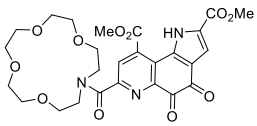

31

PQQ-Crown18

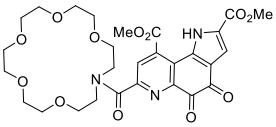

58

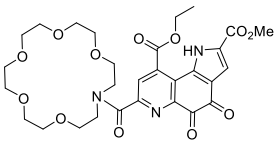

59

4. References

[1] Brief history is given on http://www.eoht.info/page/CHNOPS visited: Oct 06th 2019.
[2] S. Berry, *J. Chem. Educ.* **1997**, *74*, 950.
[3] J. Emsley, *Nature's Building Blocks: An A-Z Guide to the Elements*, Oxford University Press, Oxford, **2011**.
[4] W. Maret, *Int. J. Mol. Sci.* **2016**, *17*, 66.
[5] J. B. Vincent, *J. Trace Elem. Med Biol.* **2014**, *28*, 397-405.
[6] T. W. Lane, M. A. Saito, G. N. George, et al., *Nature* **2005**, *435*, 42-42.
[7] R. R. Crichton, *Biological Inorganic Chemistry - A New Introduction to Molecular Structure and Function, Second Edition*, Elsevier, Oxford, **2012**.
[8] https://www.nature.com/subjects/bioinorganic-chemistry visited: Oct 06th 2019.
[9] B. Bhushan, *Phil. Trans. R. Soc. A* **2009**, *367*, 1443–1444.
[10] N. Picone, H. J. M. Op den Camp, *Curr. Opin. Chem. Biol.* **2019**, *49*, 39-44.
[11] T. Cheisson, E. J. Schelter, *Science* **2019**, *363*, 489-493.
[12] L. Chistoserdova, *Mol. Microbiol.* **2019**, *111*, 1127-1131.
[13] L. J. Daumann, *Angew. Chem. Int. Ed.* **2019**, *58*, 12795-12802.
[14] J. A. Cotruvo, *ACS Cent. Sci.* **2019**, *9*, 1496-1506.
[15] K. H. Wedepohl, *Geochim. Cosmochim. Acta* **1995**, *59*, 1217-1232.
[16] D. N. Trifonov, *The rare-earth elements*, Pergamon Press [distributed in the Western Hemisphere by Macmillan, New York], **1963**.
[17] L. S. Ettre, in *Chapters in the Evolution of Chromatography* (Ed.: J. V. Hinshaw), Imperial College Press, London, **2008**, pp. 223-241.
[18] A. Walters, P. Lusty, A. Hill, *British Geological Survey: Rare Earth Elements*, Natural Environment Research Council, http://www.bgs.ac.uk/mineralsuk/, **2011**.
[19] http://www.eurare.eu/RareEarthElements.html visited: Oct 8th 2019. Reproduced with kind permission of the EURARE project.
[20] R. Shannon, *Acta Crystallogr. A* **1976**, *32*, 751-767.
[21] C. H. Evans, *Biochemistry of the Lanthanides*, Springer Science+Business Media, New York, **1990**.
[22] S. P. Fricker, *Chem. Soc. Rev.* **2006**, *35*, 524-533.
[23] V. M. Goldschmidt, T. F. W. Barth, *Isomorphie und Polymorphie der Sesquioxyde. Die Lanthaniden-Kontraktion und Ihre Konsequenzen*, Dybwad, Oslo, **1925**.
[24] S. Cotton, *Lanthanide and actinide chemistry*, John Wiley & Sons, Chichester, UK, **2006**.
[25] P. Pyykko, *Chem. Rev.* **1988**, *88*, 563-594.
[26] Z. Hu, H. Richter, G. Sparovek, et al., *J. Plant Nutr.* **2004**, *27*, 183-220.
[27] S. A. Abdelnour, M. E. Abd El-Hack, A. F. Khafaga, et al., *Sci. Total Environ.* **2019**, *672*, 1021-1032.
[28] K. Redling, *Rare Earth Elements in Agriculture with Emphasis on Animal Husbandry (Doctoral Thesis)*, Ludwig-Maximilians-University Munich, **2006**.
[29] https://www.biosciencewriters.com/Guidelines-for-Formatting-Gene-and-Protein-Names.aspx visited: Oct 27th 2019.
[30] D. Sadava, D. M. Hillis, H. C. Heller, et al., *Purves Biologie, german translation of the 11. original English edition "Life The Science of Biology", published by Sinauer Associated, Inc., Sunderland, USA, 2017, Vol. 10*, Springer Spektrum, Berlin, **2019**.
[31] S. Lim, S. J. Franklin, *Cell. Mol. Life Sci.* **2004**, *61*, 2184-2188.
[32] Y. Hibi, K. Asai, H. Arafuka, et al., *J. Biosci. Bioeng.* **2011**, *111*, 547-549.
[33] T. Nakagawa, R. Mitsui, A. Tani, et al., *PLoS One* **2012**, *7*, e50480.
[34] N. A. Fitriyanto, M. Fushimi, M. Matsunaga, et al., *J. Biosci. Bioeng.* **2011**, *111*, 613-617.
[35] A. Pol, K. Heijmans, H. R. Harhangi, et al., *Nature* **2007**, *450*, 874-878.
[36] A. Pol, T. R. M. Barends, A. Dietl, et al., *Environ. Microbiol.* **2014**, *16*, 255-264.
[37] M. Taubert, C. Grob, A. M. Howat, et al., *Environ. Microbiol.* **2015**, *17*, 3937-3948.
[38] J. Huang, Z. Yu, L. Chistoserdova, *Front. Microbiol.* **2018**, *9*, Article 1366.
[39] J. T. Keltjens, A. Pol, J. Reimann, et al., *Appl. Microbiol. Biotechnol.* **2014**, *98*, 6163-6183.
[40] E. R. Featherston, H. R. Rose, M. J. McBride, et al., *ChemBioChem* **2019**, *20*, 2360-2372.
[41] E. F. Pettersen, T. D. Goddard, C. C. Huang, et al., *J. Comput. Chem.* **2004**, *25*, 1605-1612.
[42] C. Anthony, L. J. Zatman, *Biochem. J.* **1964**, *92*, 609-614.
[43] C. Anthony, L. J. Zatman, *Biochem. J.* **1964**, *92*, 614-621.
[44] C. Anthony, in *Enzyme-Catalyzed Electron and Radical Transfer: Subcellular Biochemistry* (Eds.: A. Holzenburg, N. S. Scrutton), Springer US, Boston, MA, **2000**, pp. 73-117.
[45] C. Anthony, P. Williams, *Biochim. Biophys. Acta* **2003**, *1647*, 18-23.
[46] C. Anthony, *Arch. Biochem. Biophys.* **2004**, *428*, 2-9.
[47] Y.-J. Zheng, T. C. Bruice, *Proc. Natl. Acad. Sci. U. S. A.* **1997**, *94*, 11881-11886.
[48] A. Oubrie, B. W. Dijkstra, *Protein Sci.* **2000**, *9*, 1265-1273.
[49] Y.-J. Zheng, Z.-x. Xia, Z.-w. Chen, et al., *Proc. Natl. Acad. Sci. U. S. A.* **2001**, *98*, 432-434.
[50] S. Itoh, H. Kawakami, S. Fukuzumi, *J. Am. Chem. Soc.* **1997**, *119*, 439-440.
[51] A. Oubrie, H. J. Rozeboom, K. H. Kalk, et al., *EMBO J.* **1999**, *18*, 5187-5194.

[52] C. Anthony, *The Biochemistry of Methylotrophs*, Academic Press London, **1982**.
[53] L. Chistoserdova, M. G. Kalyuzhnaya, M. E. Lidstrom, *Annu. Rev. Microbiol.* **2009**, *63*, 477-499.
[54] J. D. Semrau, A. A. DiSpirito, W. Gu, et al., *Appl. Environ. Microbiol.* **2018**, *84*, e02289-02217.
[55] F. Chu, D. A. C. Beck, M. E. Lidstrom, *PeerJ* **2016**, *4*, e2435.
[56] F. Chu, M. E. Lidstrom, *J. Bacteriol.* **2016**, *198*, 1317-1325.
[57] N. M. Good, O. N. Walser, R. S. Moore, et al., *bioRxiv* **2018**, 329011.
[58] S. Masuda, Y. Suzuki, Y. Fujitani, et al., *mSphere* **2018**, *3*, e00462-00417.
[59] Y. Zheng, J. Huang, F. Zhao, et al., *mBio* **2018**, *9*, e02430-02417.
[60] B. Graham, W. K. Reilly, F. Beinecke, et al., *Deep Water: The Gulf Oil Disaster and the Future of Offshore Drilling*, National Commission on the BP Deepwater Horizon Oil Spill and Offshore Drilling, Washington DC, **2013**.
[61] M. C. Redmond, D. L. Valentine, *Proc. Natl. Acad. Sci. U. S. A.* **2012**, *109*, 20292-20297.
[62] A. M. Shiller, E. W. Chan, D. J. Joung, et al., *Sci. Rep.* **2017**, *7*, 10389.
[63] H. N. Vu, G. A. Subuyuj, S. Vijayakumar, et al., *J. Bacteriol.* **2016**, *198*, 1250-1259.
[64] M. Wehrmann, P. Billard, A. Martin-Meriadec, et al., *mBio* **2017**, *8*, e00570-00517.
[65] https://elizabethskovran.wixsite.com/skovranlab visited: Oct 8th 2019.
[66] J. J. A. Cotruvo, E. R. Featherston, J. A. Mattocks, et al., *J. Am. Chem. Soc.* **2018**.
[67] D. R. Houck, J. L. Hanners, C. J. Unkefer, *J. Am. Chem. Soc.* **1988**, *110*, 6920-6921.
[68] D. J. Cole, N. D. M. Hine, *J. Phys.: Condens. Matter* **2016**, *28*, 393001.
[69] N. B. Idupulapati, D. S. Mainardi, *J. Phys. Chem. A* **2010**, *114*, 1887-1896.
[70] M. Leopoldini, N. Russo, M. Toscano, *Chem. Eur. J.* **2007**, *13*, 2109-2117.
[71] P. Hothi, M. J. Sutcliffe, N. S. Scrutton, *Biochem. J.* **2005**, *388*, 123-133.
[72] X. Zhang, S. Y. Reddy, T. C. Bruice, *Proc. Natl. Acad. Sci. U. S. A.* **2007**, *104*, 745-749.
[73] S. Y. Reddy, T. C. Bruice, *Protein Sci.* **2004**, *13*, 1965-1978.
[74] N. B. Idupulapati, D. S. Mainardi, *J. Mol. Struc-THEOCHEM* **2009**, *901*, 72-80.
[75] S. Y. Reddy, T. C. Bruice, *J. Am. Chem. Soc.* **2003**, *125*, 8141-8150.
[76] J. A. Bogart, A. J. Lewis, E. J. Schelter, *Chem. Eur. J.* **2015**, *21*, 1743-1748.
[77] M. Prejanò, T. Marino, N. Russo, *Chem. Eur. J.* **2017**, *23*, 8652-8657.
[78] S. Tsushima, *PCCP* **2019**, *21*, 21979-21983.
[79] M. J. Frisch, G. W. Trucks, H. B. Schlegel, et al., *Gaussian 09, Revision A.02*, Gaussian, Inc., Wallingford CT, **2016**.
[80] A. D. Becke, *J. Chem. Phys.* **1993**, *98*, 5648-5652.
[81] C. Lee, W. Yang, R. G. Parr, *Phys. Rev. B* **1988**, *37*, 785-789.
[82] S. H. Vosko, L. Wilk, M. Nusair, *Can. J. Phys.* **1980**, *58*, 1200-1211.
[83] P. J. Stephens, F. J. Devlin, C. F. Chabalowski, et al., *J. Phys. Chem.* **1994**, *98*, 11623-11627.
[84] G. A. Petersson, A. Bennett, T. G. Tensfeldt, et al., *J. Chem. Phys.* **1988**, *89*, 2193-2218.
[85] G. A. Petersson, T. G. Tensfeldt, J. A. Montgomery Jr., *J. Chem. Phys.* **1991**, *94*, 6091-6101.
[86] N. N. Greenwood, A. Earnshaw, *Chemistry of the Elements, Vol. 2*, Butterworth Heinemann, Oxford, **1998**.
[87] M. Dolg, H. Stoll, A. Savin, et al., *Theor. Chim. Acta* **1989**, *75*, 173-194.
[88] M. Dolg, H. Stoll, H. Preuss, *Theor. Chim. Acta* **1993**, *85*, 441-450.
[89] M. Regueiro-Figueroa, D. Esteban-Gómez, A. de Blas, et al., *Chem. Eur. J.* **2014**, *20*, 3974-3981.
[90] S. A. Cotton, *C. R. Chim.* **2005**, *8*, 129-145.
[91] M. Seitz, A. G. Oliver, K. N. Raymond, *J. Am. Chem. Soc.* **2007**, *129*, 11153-11160
[92] S. A. Cotton, P. R. Raithby, *Coord. Chem. Rev.* **2017**, *340*, 220-231.
[93] A. Ramachandran, D. A. Walsh, *FEMS Microbiol. Ecol.* **2015**, *91*, fiv105-fiv105.
[94] B. Jahn, A. Pol, H. Lumpe, et al., *ChemBioChem* **2018**, *19*, 1147-1153.
[95] A. Jongejan, S. S. Machado, J. A. Jongejan, *J. Mol. Catal. B: Enzym.* **2000**, *8*, 121-163.
[96] P. R. Afolabi, F. Mohammed, K. Amaratunga, et al., *Biochemistry* **2001**, *40*, 9799-9809.
[97] J. M. Cox, D. J. Day, C. Anthony, *Biochim. Biophys. Acta, Protein Struct. Mol. Enzymol.* **1992**, *1119*, 97-106.
[98] N. M. Good, H. N. Vu, C. J. Suriano, et al., *J. Bacteriol.* **2016**, *198*, 3109-3118.
[99] N. C. Martinez-Gomez, H. N. Vu, E. Skovran, *Inorg. Chem.* **2016**, *55*, 10083-10089.
[100] E. Skovran, N. C. Martinez-Gomez, *Science* **2015**, *348*, 862-863.
[101] M. Farhan Ul Haque, B. Kalidass, N. Bandow, et al., *Appl. Environ. Microbiol.* **2015**, *81*, 7546-7552.
[102] W. Gu, M. Farhan Ul Haque, A. A. DiSpirito, et al., *FEMS Microbiol. Lett.* **2016**, *363*, fnw129.
[103] C. M. Reddy, J. S. Arey, J. S. Seewald, et al., *Proc. Natl. Acad. Sci. U. S. A.* **2012**, *109*, 20229-20234.
[104] T. B. Ryerson, R. Camilli, J. D. Kessler, et al., *Proc. Natl. Acad. Sci. U. S. A.* **2012**, *109*, 20246-20253.
[105] E. A. Solomon, *Nat. Geosci.* **2014**, *7*, 394.
[106] R. Ghosh, J. R. Quayle, *Anal. Biochem.* **1979**, *99*, 112-117.
[107] F. H. Firsching, S. N. Brune, *J. Chem. Eng. Data* **1991**, *36*, 93-95.
[108] V. L. Davidson, *Principles and Applications of Quinoproteins*, 1st ed., Marcel Dekker, Inc., New York, **1992**.
[109] P. Hothi, J. Basran, M. J. Sutcliffe, et al., *Biochemistry* **2003**, *42*, 3966-3978.
[110] J. Ma, P. K. Dasgupta, W. Blackledge, et al., *Environ. Sci. Technol.* **2010**, *44*, 3028-3034.
[111] P. D'Angelo, A. Zitolo, V. Migliorati, et al., *Inorg. Chem.* **2011**, *50*, 4572-4579.
[112] M. Laing, *J. Chem. Educ.* **2009**, *86*, 188.

[113] N. Kaltsoyannis, P. Scott, *The f elements*, Oxford University Press, Oxford, **1999**.
[114] A. McSkimming, T. Cheisson, P. J. Carroll, et al., *J. Am. Chem. Soc.* **2018**, *140*, 1223-1226.
[115] T. K. Harris, V. L. Davidson, *Biochem. J.* **1994**, *300*, 175-182.
[116] M. G. Goodwin, A. Avezoux, S. L. Dales, et al., *Biochem. J.* **1996**, *319*, 839-842.
[117] O. Adachi, K. Matsushita, E. Shinagawa, et al., *Agric. Biol. Chem.* **1990**, *54*, 2833-2837.
[118] J. M. Armstrong, *Biochim. Biophys. Acta* **1964**, *86*, 194-197.
[119] A. Ramirez-Solis, J. I. Amaro-Estrada, J. Hernández-Cobos, et al., *Inorg. Chem.* **2018**, *57*, 2843-2850.
[120] Z.-x. Xia, W.-w. Dai, Y.-f. Zhang, et al., *J. Mol. Biol.* **1996**, *259*, 480-501.
[121] M. Ghosh, C. Anthony, K. Harlos, et al., *Structure* **1995**, *3*, 177-187.
[122] P. A. Williams, L. Coates, F. Mohammed, et al., *Acta Crystallogr. D* **2005**, *61*, 75-79.
[123] S. A. Cotton, J. M. Harrowfield, *Lanthanides: Solvation, in Encyclopedia of Inorganic and Bioinorganic Chemistry*, John Wiley & Sons, Ltd, **2011**.
[124] R. H. Betts, O. F. Dahlinger, *Can. J. Chem.* **1959**, *37*, 91-100.
[125] N. Graeppi, D. Hugh Powell, G. Laurenczy, et al., *Inorg. Chim. Acta* **1995**, *235*, 311-326.
[126] S. A. Cotton, J. M. Harrowfield, *Lanthanides: Biological Activity and Medical Applications, in Encyclopedia of Inorganic and Bioinorganic Chemistry*, John Wiley & Sons, Ltd, **2011**.
[127] S. A. Cotton, J. M. Harrowfield, in *The Rare Earth Elements: Fundamentals and Applications* (Ed.: D. A. Atwood), John Wiley & Sons, Chichester, UK, **2012**, p. 65.
[128] S. A. Salisbury, H. S. Forrest, W. B. T. Cruse, et al., *Nature* **1979**, *280*, 843.
[129] E. J. Corey, A. Tramontano, *J. Am. Chem. Soc.* **1981**, *103*, 5599-5600.
[130] J. A. Gainor, S. M. Weinreb, *J. Org. Chem.* **1981**, *46*, 4317-4319.
[131] J. A. Gainor, S. M. Weinreb, *J. Org. Chem.* **1982**, *47*, 2833-2837.
[132] J. B. Hendrickson, J. G. DeVries, *J. Org. Chem.* **1982**, *47*, 1148-1150.
[133] A. R. MacKenzie, C. J. Moody, C. W. Rees, *J. Chem. Soc., Chem. Commun.* **1983**, 1372-1373.
[134] G. Buchi, J. H. Botkin, G. C. M. Lee, et al., *J. Am. Chem. Soc.* **1985**, *107*, 5555-5556.
[135] J. B. Hendrickson, J. G. De Vries, *J. Org. Chem.* **1985**, *50*, 1688-1695.
[136] A. Roderick Mackenzie, C. J. Moody, C. W. Rees, *Tetrahedron* **1986**, *42*, 3259-3268.
[137] J. A. Jongejan, R. P. Bezemer, J. A. Duine, *Tetrahedron Lett.* **1988**, *29*, 3709-3712.
[138] P. Martin, E. Steiner, K. Auer, et al., *Helv. Chim. Acta* **1993**, *76*, 1667-1673.
[139] J. Kempf, D. Gopal, W. Stalzer, WO 2006/102642 A1, **2006**.
[140] J. A. Lewis, J. C. DiNardo, A. S. Thompson, et al., WO 2012/170378 A1, **2012**.
[141] R. Gavara Govinda, G. Sambasivam, T. T. Puthiaparampil, et al., WO 2014/195896 A1, **2014**.
[142] C. M. Glinkerman, D. L. Boger, *J. Am. Chem. Soc.* **2016**, *138*, 12408-12413.
[143] M. Ameyama, M. Hayashi, K. Matsushita, et al., *Agric. Biol. Chem.* **1984**, *48*, 561-565.
[144] J. S. Velterop, E. Sellink, J. J. Meulenberg, et al., *J. Bacteriol.* **1995**, *177*, 5088-5098.
[145] Y.-Q. Shen, F. Bonnot, E. M. Imsand, et al., *Biochemistry* **2012**, *51*, 2265-2275.
[146] P. M. Goodwin, C. Anthony, in *Advances in Microbial Physiology, Vol. 40* (Ed.: R. K. Poole), Academic Press, **1998**, pp. 1-80.
[147] T. E. Stites, T. R. Sih, R. B. Rucker, *BBA - Gen Subjects* **2000**, *1524*, 247-252.
[148] X.-H. Xiong, Y. Zhao, X. Ge, et al., *Int. J. Mol. Sci.* **2011**, *12*, 8913-8923.
[149] M. Akagawa, M. Nakano, K. Ikemoto, *Biosci., Biotechnol., Biochem.* **2016**, *80*, 13-22.
[150] *https://www.mgc.co.jp/eng/products/nc/pqq.html visited: Oct 30th 2019.*
[151] *https://healthcare.evonik.com/product/health-care/en/products/health-ingredients/PentaQQ/ visited: Oct 30th 2019.*
[152] S. Itoh, H. Kawakami, S. Fukuzumi, *J. Mol. Catal. B: Enzym.* **2000**, *8*, 85-94.
[153] C. N. Carrigan, R. D. Bartlett, C. S. Esslinger, et al., *J. Med. Chem.* **2002**, *45*, 2260-2276.
[154] K. Ikemoto, S. Mori, K. Mukai, *Acta Crystallogr. B* **2017**, *73*, 489-497.
[155] N. Nakamura, T. Kohzuma, H. Kuma, et al., *Inorg. Chem.* **1994**, *33*, 1594-1599.
[156] S. Itoh, M. Ogino, Y. Fukui, et al., *J. Am. Chem. Soc.* **1993**, *115*, 9960-9967.
[157] M. A. G. van Kleef, J. A. Jongejan, J. A. Duine, *Eur. J. Biochem.* **1989**, *183*, 41-47.
[158] S. Itoh, M. Mure, A. Suzuki, et al., *J. Chem. Soc., Perkin Trans. 2* **1992**, 1245-1251.
[159] J. A. Duine, J. Frank, P. E. J. Verwiel, *Eur. J. Biochem.* **1980**, *108*, 187-192.
[160] L. J. Farrugia, *J. Appl. Crystallogr.* **2012**, *45*, 849-854.
[161] K. Mukai, A. Ouchi, S.-i. Nagaoka, et al., *Biosci., Biotechnol., Biochem.* **2016**, *80*, 178-187.
[162] H. Firouzabadi, N. Iranpoor, H. R. Shaterian, *Phosphorus, Sulfur, and Silicon and the Related Elements* **2000**, *166*, 71-81.
[163] Nomenclature Committee of the International Union of Biochemistry and Molecular Biology (NC-IUBMB). http://www.sbcs.qmul.ac.uk/iubmb/enzyme/EC1/ visited: Oct 16th 2018.
[164] J. A. Duine, J. Frank, J. A. Jongejan, in *Advances in Enzymology and Related Areas of Molecular Biology*, John Wiley & Sons, Inc., **2006**, pp. 169-212.
[165] C. Anthony, *Biochem. J.* **1996**, *320*, 697-711.
[166] C. C. F. Blake, M. Ghosh, K. Harlos, et al., *Nat. Struct. Biol.* **1994**, *1*, 102-105.
[167] N. C. Martinez-Gomez, E. Skovran, *Methane Biocatalysis: Paving the Way to Sustainability*, Kalyuzhnaya, M. G.; Xing, X.-H. , Springer International Publishing, Cham, **2018**.
[168] H. Lumpe, A. Pol, H. J. M. Op den Camp, et al., *Dalton Trans.* **2018**, *47*, 10463-10472.

[169] D. R. Houck, J. L. Hanners, C. J. Unkefer, et al., *Antonie Van Leeuwenhoek* **1989**, *56*, 93-101.
[170] C. Anthony, L. J. Zatman, *Biochem. J.* **1967**, *104*, 960-969.
[171] J. Westerling, J. Frank, J. A. Duine, *Biochem. Biophys. Res. Commun.* **1979**, *87*, 719-724.
[172] S. Itoh, H. Kawakami, S. Fukuzumi, *J. Am. Chem. Soc.* **1998**, *120*, 7271-7277.
[173] S. Itoh, H. Kawakami, S. Fukuzumi, *Biochemistry* **1998**, *37*, 6562-6571.
[174] J. A. Duine, *J. Biosci. Bioeng.* **1999**, *88*, 231-236.
[175] L. M. Felton, C. Anthony, *Nature* **2005**, *433*, E10.
[176] M. Wanner, T. Sixt, K.-W. Klinkhammer, et al., *Inorg. Chem.* **1999**, *38*, 2753-2755.
[177] H. Mitome, T. Ishizuka, Y. Shiota, et al., *Inorg. Chem.* **2013**, *52*, 2274-2276.
[178] K. Kano, K. Mori, B. Uno, et al., *Bioelectrochem. Bioenerget.* **1990**, *24*, 193-201.
[179] K. Kano, K. Mori, B. Uno, et al., *Bioelectrochem. Bioenerget.* **1990**, *23*, 227-238.
[180] Z. P. Zhang, L. M. V. Tillekeratne, J. R. Kirchhoff, et al., *Biochem. Biophys. Res. Commun.* **1995**, *212*, 41-47.
[181] J. A. Duine, J. Frank, P. E. J. Verwiel, *Eur. J. Biochem.* **1981**, *118*, 395-399.
[182] R. H. Dekker, J. A. Duine, J. Frank, et al., *Eur. J. Biochem.* **1982**, *125*, 69-73.
[183] Zhejiang Hisun Pharmaceutical Co. Ltd., https://www.fda.gov/downloads/Food/IngredientsPackagingLabeling/GRAS/NoticeInventory/ucm508141.pdf visited: Oct 30th 2019.
[184] K. Nakamoto, in *Infrared and Raman Spectra of Inorganic and Coordination Compounds, Part B: Applications in Coordination, Organometallic, and Bioinorganic Chemistry*, Sixth ed., John Wiley & Sons, Inc., Hoboken, New Jersey, **2009**.
[185] N. M. Dimitrijevic, O. G. Poluektov, Z. V. Saponjic, et al., *J. Phys. Chem. B* **2006**, *110*, 25392-25398.
[186] L. Tommasi, L. Shechter-Barloy, D. Varech, et al., *Inorg. Chem.* **1995**, *34*, 1514-1523.
[187] J. S. Renny, L. L. Tomasevich, E. H. Tallmadge, et al., *Angew. Chem. Int. Ed.* **2013**, *52*, 11998-12013.
[188] J. B. Noar, E. J. Rodriguez, T. C. Bruice, *J. Am. Chem. Soc.* **1985**, *107*, 7198-7199.
[189] S. Suzuki, T. Sakurai, S. Itoh, et al., *Inorg. Chem.* **1988**, *27*, 591-592.
[190] B. Schwederski, V. Kasack, W. Kaim, et al., *Angew. Chem.* **1990**, *102*, 74-76.
[191] T. Ishida, M. Doi, K. Tomita, et al., *J. Am. Chem. Soc.* **1989**, *111*, 6822-6828.
[192] M. R. VanEngelen, R. K. Szilagyi, R. Gerlach, et al., *Environ. Sci. Technol.* **2010**, *45*, 937-942.
[193] S. A. Cotton, J. M. Harrowfield, *Lanthanides: Coordination Chemistry, in Encyclopedia of Inorganic and Bioinorganic Chemistry*, John Wiley & Sons, Ltd, **2011**.
[194] P. Job, *Ann.di Chim. Appl.* **1928**, *9*, 113-203.
[195] D. E. Henrie, R. L. Fellows, G. R. Choppin, *Coord. Chem. Rev.* **1976**, *18*, 199-224.
[196] D. G. Karraker, *Inorg. Chem.* **1967**, *6*, 1863-1868.
[197] N. Ouali, B. Bocquet, S. Rigault, et al., *Inorg. Chem.* **2002**, *41*, 1436-1445.
[198] M. Vonci, K. Mason, E. A. Suturina, et al., *J. Am. Chem. Soc.* **2017**, *139*, 14166-14172.
[199] A. W. J. Poh, J. A. Aguilar, A. M. Kenwright, et al., *Chem. Eur. J.* **2018**, *24*, 16170-16175.
[200] E. A. Suturina, K. Mason, C. F. G. C. Geraldes, et al., *Angew. Chem. Int. Ed.* **2017**, *56*, 12215-12218.
[201] O. A. Blackburn, R. M. Edkins, S. Faulkner, et al., *Dalton Trans.* **2016**, *45*, 6782-6800.
[202] H. M. McConnell, R. E. Robertson, *J. Chem. Phys.* **1958**, *29*, 1361-1365.
[203] B. Bleaney, *J. Magn. Reson.* **1972**, *8*, 91-100.
[204] K. Ikemoto, H. Sakamoto, M. Nakano, *Chem. Cent. J.* **2012**, *6*, 57.
[205] R. G. Lacoste, G. V. Christoffers, A. E. Martell, *J. Am. Chem. Soc.* **1965**, *87*, 2385-2388.
[206] C. A. Chang, M. E. Rowland, *Inorg. Chem.* **1983**, *22*, 3866-3869.
[207] E. Brücher, B. Györi, J. Emri, et al., *J. Chem. Soc., Chem. Commun.* **1993**, 574-575.
[208] C. A. Chang, V. O. Ochaya, *Inorg. Chem.* **1986**, *25*, 355-358.
[209] A. Roca-Sabio, M. Mato-Iglesias, D. Esteban-Gómez, et al., *Dalton Trans.* **2011**, *40*, 384-392.
[210] J. A. Bogart, B. E. Cole, M. A. Boreen, et al., *Proc. Natl. Acad. Sci. U. S. A.* **2016**, *113*, 14887-14892.
[211] G. Tircsó, Z. Kovács, A. D. Sherry, *Inorg. Chem.* **2006**, *45*, 9269-9280.
[212] E. Toth, E. Brucher, I. Lazar, et al., *Inorg. Chem.* **1994**, *33*, 4070-4076.
[213] X. Zhu, S. Z. Lever, *Electrophoresis* **2002**, *23*, 1348-1356.
[214] E. Brucher, A. D. Sherry, *Inorg. Chem.* **1990**, *29*, 1555-1559.
[215] K. L. Nash, D. Brigham, T. C. Shehee, et al., *Dalton Trans.* **2012**, *41*, 14547-14556.
[216] B. Nowicka, J. Kruk, *Biochim. Biophys. Acta* **2010**, *1797*, 1587-1605.
[217] E. J. Son, J. H. Kim, K. Kim, et al., *J. Mater. Chem. A* **2016**, *4*, 11179-11202.
[218] C. Anthony, M. Ghosh, C. C. F. Blake, *Biochem. J.* **1995**, *304* 665-674.
[219] M. B. Davies, *Polyhedron* **1992**, *11*, 285-321.
[220] W. Brzyska, A. Krol, *Pol. J. Chem.* **1988**, *62*, 667.
[221] H. A. Tajmir-Riahi, *J. Inorg. Biochem.* **1990**, *40*, 181-188.
[222] H. A. Tajmir-Riahi, *J. Inorg. Biochem.* **1991**, *44*, 39-45.
[223] B. Zümreoglu-Karan, *Coord. Chem. Rev.* **2006**, *250*, 2295-2307.
[224] S. Jin Oh, Y.-S. Choi, S. Hwangbo, et al., *Chem. Commun.* **1998**, 2189-2190.
[225] A. E. Wendlandt, S. S. Stahl, *Angew. Chem. Int. Ed.* **2015**, *54*, 14638-14658.
[226] I. Shinobu, O. Yoshiki, A. Toshio, *Bull. Chem. Soc. Jpn.* **1986**, *59*, 1911-1914.
[227] P. S. Guin, S. Das, P. C. Mandal, *Int. J. Electrochem. Sci.* **2011**, *2011*, 22.

[228] C. M. H. Ferreira, I. S. S. Pinto, E. V. Soares, et al., *RSC Advances* **2015**, *5*, 30989-31003.
[229] B. I. Kharisov, M. A. Méndez-Rojas, A. D. Garnovskii, et al., *J. Coord. Chem.* **2002**, *55*, 745-770.
[230] E. R. Milaeva, Z. Szeverenyi, L. I. Simandi, *Inorg. Chim. Acta* **1990**, *167*, 139-141.
[231] I. L. Fedushkin, O. V. Maslova, E. V. Baranov, et al., *Inorg. Chem.* **2009**, *48*, 2355-2357.
[232] I. L. Fedushkin, O. V. Maslova, A. G. Morozov, et al., *Angew. Chem. Int. Ed.* **2012**, *51*, 10584-10587.
[233] E. J. Coughlin, M. Zeller, S. C. Bart, *Angew. Chem. Int. Ed.* **2017**, *56*, 12142-12145.
[234] C. F. Baes, R. S. Mesmer, *The Hydrolysis of Cations* John Wiley & Sons, New York, **1976**.
[235] C. W. Lange, C. G. Pierpont, *Inorg. Chim. Acta* **1997**, *263*, 219-224.
[236] C. G. Pierpont, C. W. Lange, in *Progress in Inorganic Chemistry, Vol. 41* (Ed.: K. D. Karlin), John Wiley & Sons, **1994**, pp. 331-442.
[237] S. Rondinini, *Anal. Bioanal. Chem.* **2002**, *374*, 813-816.
[238] L. N. Bykova, S. I. Petrov, *Russ. Chem. Rev.* **1972**, *41*, 975.
[239] I. M. Kolthoff, M. K. Chantooni, H. Smagowski, *Anal. Chem.* **1970**, *42*, 1622-1628.
[240] J. R. Aranzaes, M.-C. Daniel, D. Astruc, *Can. J. Chem.* **2006**, *84*, 288-299.
[241] V. V. Pavlishchuk, A. W. Addison, *Inorg. Chim. Acta* **2000**, *298*, 97-102.
[242] T. S. Eckert, T. C. Bruice, J. A. Gainor, et al., *Proc. Natl. Acad. Sci. U. S. A.* **1982**, *79*, 2533-2536.
[243] C. J. Unkefer, D. R. Houck, B. Mark Britt, et al., in *Methods in Enzymology, Vol. 258* (Ed.: J. P. Klinman), Academic Press, Cambridge, **1995**, pp. 227-235.
[244] T. K. Harris, V. L. Davidson, *Biochemistry* **1993**, *32*, 4362-4368.
[245] S. Y. Reddy, T. C. Bruice, *Proc. Natl. Acad. Sci. U. S. A.* **2004**, *101*, 15887-15892.
[246] E. J. Rodriguez, T. C. Bruice, *J. Am. Chem. Soc.* **1989**, *111*, 7947-7956.
[247] H. van Koningsveld, J. C. Jansen, J. A. Jongejan, et al., *Acta Crystallogr. C* **1985**, *41*, 89-92.
[248] H. Lumpe, L. J. Daumann, *Inorg. Chem.* **2019**, *58*, 8432-8441.
[249] A. Holzenburg, N. S. Scrutton, *Enzyme-Catalyzed Electron and Radical Transfer*, Springer Science+Business Media, New York, **2000**.
[250] H. B. Dunford, W. D. Hewson, *J. Phys. Chem.* **1979**, *83*, 3307-3307.
[251] R. W. Begland, D. R. Hartter, *J. Org. Chem.* **1972**, *37*, 4136-4145.
[252] J. V. Ho, J. A. Cotruvo, *Biochemistry* **2019**, *58*, 2665-2669.
[253] A. R. Dewanti, J. A. Duine, *Biochemistry* **2000**, *39*, 9384-9392.
[254] R. A. van der Meer, A. C. Mulder, J. A. Jongejan, et al., *FEBS Lett.* **1989**, *254*, 99-105.
[255] H. E. Gottlieb, V. Kotlyar, A. Nudelman, *J. Org. Chem.* **1997**, *62*, 7512-7515.
[256] K. Ikemoto, Y. Sakamoto, R. Tanaka, et al., *Crystal Growth & Design* **2017**, *17*, 4118-4123.
[257] K. N. Raymond, V. C. Pierre, *Bioconj. Chem.* **2005**, *16*, 3-8.
[258] E. J. Werner, A. Datta, C. J. Jocher, et al., *Angew. Chem. Int. Ed.* **2008**, *47*, 8568-8580.
[259] A. Datta, K. N. Raymond, *Acc. Chem. Res.* **2009**, *42*, 938-947.
[260] J. Xu, D. G. Churchill, M. Botta, et al., *Inorg. Chem.* **2004**, *43*, 5492-5494.
[261] C. J. Jocher, E. G. Moore, J. Xu, et al., *Inorg. Chem.* **2007**, *46*, 9182-9191.
[262] L. J. Daumann, D. S. Tatum, B. E. R. Snyder, et al., *J. Am. Chem. Soc.* **2015**, *137*, 2816-2819.
[263] L. J. Daumann, D. S. Tatum, C. M. Andolina, et al., *Inorg. Chem.* **2016**, *55*, 114-124.
[264] A. K. Katz, J. P. Glusker, S. A. Beebe, et al., *J. Am. Chem. Soc.* **1996**, *118*, 5752-5763.
[265] E. J. Werner, J. Kozhukh, M. Botta, et al., *Inorg. Chem.* **2009**, *48*, 277-286.
[266] C. Schmuck, U. Machon, *Chem. Eur. J.* **2005**, *11*, 1109-1118.
[267] M. K. Thompson, D. M. J. Doble, L. S. Tso, et al., *Inorg. Chem.* **2004**, *43*, 8577-8586.
[268] R. D. Rogers, J. Zhang, C. B. Bauer, *J. Alloys Compd.* **1997**, *249*, 41-48.
[269] J. A. Johnson, Z. Pi, J. X. Qiao, et al., *Vol. WO/2015/105749* (Ed.: B.-M. Squibb), USA, **2015**.
[270] H. A. Staab, *Angew. Chem.* **1956**, *68*, 754-754.
[271] J.-C. G. Bünzli, A. Milicic-Tang, C. Mabillard, *Helv. Chim. Acta* **1993**, *76*, 1292-1304.
[272] H. A. Benesi, J. H. Hildebrand, *J. Am. Chem. Soc.* **1949**, *71*, 2703-2707.
[273] S. Goswami, D. Sen, N. K. Das, et al., *Chem. Commun.* **2011**, *47*, 9101-9103.
[274] C. J. Pedersen, *J. Am. Chem. Soc.* **1970**, *92*, 386-391.
[275] G. W. Gokel, D. M. Goli, C. Minganti, et al., *J. Am. Chem. Soc.* **1983**, *105*, 6786-6788.
[276] Y. Liu, B.-H. Han, Y.-T. Chen, *Coord. Chem. Rev.* **2000**, *200-202*, 53-73.
[277] Y. Liu, T. Lu, M. Tan, et al., *J. Phys. Chem.* **1993**, *97*, 4548-4551.
[278] Y. Liu, T.-B. Lu, M.-Y. Tan, et al., *Acta Chim. Sin.* **1993**, *51*, 874.
[279] R. M. Izatt, J. D. Lamb, J. J. Christensen, et al., *J. Am. Chem. Soc.* **1977**, *99*, 8344-8346.
[280] B. Ammann, J.-C. G. Bünzli, in *Lanthanoid(III) Complexes with 18-Crown-6 Ether: Heat of Formation in Anhydrous Acetonitrile. In: Angewandte chemische Thermodynamik und Thermoanalytik: Vorträge des Rapperswiler TA-Symposiums* (Eds.: E. Marti, H. R. Oswald, H. G. Wiedemann), Birkhäuser, Basel, **1979**, pp. 49-53.
[281] Y. Liu, T.-B. Lu, M.-Y. Tan, et al., *J. Chin. Rare Earths* **1994**, *12*, 111.
[282] V. J. Gatto, G. W. Gokel, *J. Am. Chem. Soc.* **1984**, *106*, 8240-8244.
[283] *Bruker (2015). SAINT. Bruker AXS Inc., Madison, Wisconsin, USA.*
[284] *Bruker (2001). SADABS. Bruker AXS Inc., Madison, Wisconsin, USA.*
[285] G. Sheldrick, *Acta Crystallogr. A* **2015**, *71*, 3-8.
[286] X. Cao, M. Dolg, *J. Mol. Struc-THEOCHEM* **2002**, *581*, 139-147.

[287] M. Dolg, H. Stoll, H. Preuss, *J. Chem. Phys.* **1989**, *90*, 1730-1734.
[288] V. Barone, M. Cossi, *J. Phys. Chem. A* **1998**, *102*, 1995-2001.
[289] M. Cossi, N. Rega, G. Scalmani, et al., *J. Comput. Chem.* **2003**, *24*, 669-681.
[290] J. R. Cheeseman, G. W. Trucks, T. A. Keith, et al., *J. Chem. Phys.* **1996**, *104*, 5497-5509.
[291] K. Wolinski, J. F. Hinton, P. Pulay, *J. Am. Chem. Soc.* **1990**, *112*, 8251-8260.
[292] C. Adamo, D. Jacquemin, *Chem. Soc. Rev.* **2013**, *42*, 845-856.
[293] E. Runge, E. K. U. Gross, *Phys. Rev. Lett.* **1984**, *52*, 997-1000.
[294] J. M. Harrington, S. Chittamuru, S. Dhungana, et al., *Inorg. Chem.* **2010**, *49*, 8208-8221.
[295] A. H. Trotta, *Org. Lett.* **2015**, *17*, 3358-3361.
[296] S. Krishnamurthy, *Tetrahedron Lett.* **1982**, *23*, 3315-3318.
[297] S. Witzel, *Synthesis of ligands and cofactors for bioinspired complexes of rare earth element methanol dehydrogenase (Research Internship Report)*, Ruprecht-Karls-University Heidelberg, **2016**.
[298] *European Chemicals Bureau, European Union Risk Assessment Report: Dimethyl Sulfate, Luxembourg: Office for Official Publications of the European Communities, 2002, ISBN 92-894-1274-7.*
[299] T. Urakami, A. Tanaka, K. Yamaguchi, et al., *BioFactors* **1995**, *5*, 139-146.
[300] V. R. Sastri, J. R. Perumareddi, V. Ramachandra Rao, et al., in *Modern Aspects of Rare Earths and their Complexes*, Elsevier, Amsterdam, **2003**, p. 268.
[301] H. Diehl, F. Lindstrom, *Anal. Chem.* **1959**, *31*, 414-418.
[302] R. T. Gettar, E. A. Gautier, R. E. Servant, et al., *J. Chromatogr.* **1999**, *855*, 111-119.
[303] G. A. Petersson, M. A. Al-Laham, *J. Chem. Phys.* **1991**, *94*, 6081-6090.
[304] Taken from http://www.tc.uni-koeln.de/PP/clickpse.en.html visited: Oct 28th 2019.
[305] CODATA Recommended Values. National Institute of Standards and Technology. https://physics.nist.gov/cuu/Constants/ visited: Oct 28th 2019.

5. List of Publications and Statement of Contribution

5.1. Publications Published as Part of this Thesis

Similar but not the same: First Kinetic and Structural Analyses of a Methanol Dehydrogenase Containing a Europium Ion in the Active Site

Bérénice Jahn, Arjan Pol, Henning Lumpe, Thomas R. M. Barends, Andreas Dietl, Carmen Hogendoorn, Huub J. M. Op den Camp and Lena J. Daumann

Published in: *ChemBioChem* **2018**, *19*, 1147-1153. DOI: 10.1002/cbic.201800130

Press releases: https://q-more.chemeurope.com/news/1155696/the-biological-role-of-europium.html, https://www.bionity.com/de/news/1155696/erster-einblick-in-ein-europium-enzym.html, https://www.laborjournal.de/editorials/1540.php.

Henning Lumpe (Ludwig-Maximilians-University Munich, advisor: Prof. Dr. Lena Daumann) performed the DFT calculations, discussed the received results, wrote the respective part of the methods section and edited the related images and supporting information. Bérénice Jahn (Ludwig-Maximilians-University Munich, advisor: Prof. Dr. Lena Daumann) and Prof. Dr. Lena Daumann performed and interpreted all enzyme activity assays, which will be part of Bérénice Jahn's PhD thesis and wrote the main part of the manuscript together. Dr. Arjan Pol (Radboud University Nijmegen, the Netherlands, scientific staff in the group of Prof. Dr. Huub op den Camp) cultivated the microbe and purified the Eu-MDH enzyme together with Lena Daumann, who also conducted the UV-Vis measurements. Andreas Dietl (Max-Planck Institute for Medical Research, Heidelberg, advisor: Dr. Thomas R. M. Barends) grew the protein crystals, performed X-ray diffraction analysis and interpreted the data with the help of his supervisor. Carmen Hogendoorn (Radboud University Nijmegen, the Netherlands, advisor: Prof. Dr. Huub J. M. Op den Camp) performed growth experiments of the microbe under influence of different lanthanides. Each author also revised the manuscript.

Impact of the Lanthanide Contraction on the Activity of a Lanthanide-dependent Methanol Dehydrogenase – A Kinetic and DFT Study

Henning Lumpe, Arjan Pol, Huub op den Camp and Lena Daumann

Published in: *Dalton Trans.* **2018**, *47*, 10463-10472. DOI: 10.1039/c8dt01238e.

Henning Lumpe (Ludwig-Maximilians-University Munich, advisor: Prof. Dr. Lena Daumann) performed all DFT calculations, interpreted the results, generated the images of the calculated structures and the related tables and figures. He also contributed in the literature screening and wrote parts of the discussion section. Prof. Dr. Lena Daumann performed the enzyme activity essays, interpreted the results and wrote the main part of the manuscript. Arjan Pol (Radboud University Nijmegen, the Netherlands, scientific staff in the group of Prof. Dr. Huub op den Camp) cultivated the microbe and purified the europium MDH together with Lena Daumann. All authors contributed in revising the manuscript.

Studies of the Redox Cofactor Pyrroloquinoline Quinone and its Interaction with Lanthanides(III) and Calcium(II)

Henning Lumpe and Lena J. Daumann

Published in: *Inorg. Chem.* **2019**, *58*, 8432-8441. DOI: 10.1021/acs.inorgchem.9b00568.

Henning Lumpe (Ludwig-Maximilians-University Munich, advisor: Prof. Dr. Lena Daumann) wrote the main part of the manuscript, screened the literature, performed the experiments, did or commissioned the analysis and interpreted it and edited the images, figures and tables. In every aspect, Prof. Dr. Lena Daumann contributed in guidance and advice, wrote parts of the manuscript including a thorough revision and performed the analysis of the Job's plot measurements.

5.2. Publications Published as not Part of this Thesis

Lanthanoide – biologisch wichtig

Henning Lumpe and Lena J. Daumann

Published in: *Nachr. Chem*. **2018**, *66*, 945–948.

5.3. Publications Published Prior to this Thesis

Directed Zincation or Magnesiation of the 2-Pyridone and 2,7-Naphthyridone Scaffold Using TMP Bases

Dorothée S. Ziegler, Robert Greiner, Henning Lumpe, Laura Kqiku, Konstantin Karaghiosoff and Paul Knochel

Published in: *Org. Lett.* **2017**, *19*, 5760-5763. DOI: 10.1021/acs.orglett.7b02690.

6. Contributions to Conferences

The Surprising Bioinorganic Chemistry of Rare Earth Elements - Spectroscopic Models for the Characterization of REE-dependent Methanol Dehydrogenases (poster presentation)

Henning Lumpe, Bérénice Jahn , Violeta Vetsova, Patrick Grassl, Sina Witzel, Arjan Pol, Huub op den Camp and Lena Daumann

13. Koordinationschemie-Tagung in Potsdam (Germany), **2017**.
Travel grant from the Fonds der Chemischen Industrie

The Coordination Chemistry of Pyrroloquinoline Quinone, the Redox-Cofactor of Rare Earth Element Dependent Enzymes (oral presentation)

Henning Lumpe, Sabrina Kräh and Lena Daumann

14. Koordinationschemie-Tagung in Heidelberg (Germany), **2018**.

Studies of the Redox Cofactor Pyrroloquinoline quinone (PQQ) and its Interaction with Lanthanides(III) and Calcium(II) (poster presentation)

Henning Lumpe and Lena J. Daumann

SFB 749 Meeting, Venice International University (VIU), San Servolo (Italy), **2019**.

Danksagung

Zuallererst möchte ich Prof. Dr. Lena Daumann für die Betreuung meiner Doktorarbeit danken. Lena, Du hast mir das Vertrauen geschenkt, mich als ersten Doktoranden in Deine Gruppe aufzunehmen, hast mich gefordert und gefördert und hattest in den Jahren stets eine offene Tür für mich. Vielen Dank für die Möglichkeit der Konferenzteilnahmen und der Forschungsaufenthalte, die mich sogar bis ans andere Ende der Welt gebracht haben.

Herrn Prof. Dr. Hans-Christian Böttcher möchte ich für die freundliche Übernahme des Zweitgutachtens und dem damit verbundenen zeitlichen Aufwand danken.

Prof. Dr. Konstantin Karaghiosoff, Prof. Dr. Stefan Schwarzer, Dr. Dorian Didier und Dr. Constantin Hoch danke ich für die Mitwirkung in der Prüfungskommission.

Prof. Dr. Rainer Pöttgen und Theresa Block danke ich für den freundlichen Besuch in Münster und für die Einführung in die Mößbauer-Spektroskopie. Prof. Dr. Paul Bernhardt danke ich für den Aufenthalt an der University of Queensland und zusammen mit Jessica Bilyj für die Unterweisung in die Cyclovoltammetrie.

Bérénice Jahn, Niko Jonasson, Violeta Vetsova, Helena Singer, dem gesamten und stetig wachsenden AK Daumann, sowie auch allen ehemaligen Mitgliedern möchte ich für die angenehme Stimmung auch außerhalb der Universität danken und für die vielen Hilfestellungen und Diskussionsrunden für meine Arbeit, nicht zuletzt auch für das gründliche Korrekturlesen. Vor allem Violeta Vetsova, die mich erst als Praktikantin, dann als Masterandin und schließlich als Kollegin über weite Phasen dieser Arbeit unterstützt hat, möchte ich danken.

Lida Holowatyi-den Toom danke ich für die vielen kleinen und großen organisatorischen Dinge, die über die Jahre angefallen sind.

Für ihre gründliche und gewissenhafte Arbeit danke ich der gesamten Analytik Abteilung des Departments Chemie. Christine Neumann danke ich für ihre hilfsbereite Art und die stetige Versorgung mit Glasgeräten aller Art.

Meinen Praktikanten danke ich für die Unterstützung bei der praktischen Arbeit meiner Dissertation, namentlich Violeta Vetsova, Arthur Poliakow, Laura Schwabbauer, Sabrina Kräh, Pavlos Pelagias, Annika Menke und Marianne Friemert.

Allen Mitgliedern der Mittwochs- und Donnerstags-Fußballrunden, sowie der Ultimate-Frisbee Gruppe danke ich für den sportlichen Ausgleich während meiner Promotion.

Allen Freunden, die die bisherige Zeit in München so einzigartig gemacht haben, möchte ich meinen tiefen Dank aussprechen. Besonders Daniel, für Deine Mitwirkung an dieser Arbeit in Form der Einführung in die Welt der Theoretischen Chemie und für Deine Chauffeurdienste. Aber natürlich auch außerhalb der Uni für die epischen Schlachten und gediegenen Barabende. Veit, für die nicht ganz so gediegenen Barabende, die selbst meine Couch überlebt hat. Anne, für die unzähligen Film- und Serienabende; Debby und Andi, für entspannte Brettspielrunden; Leo und Carina für kulinarische Höchstleistungen, Judith und Nelli für die Ausrichtung gemeinsamer Betrachtung hochkarätiger TV Formate, Jens für Deine super Grill-Sessions und Hendrik und Laura, die stets für spontane Biergartenbesuche zu haben sind.

Meiner gesamten Familie danke ich für die immerwährende Unterstützung und die schöne Zeit mit Euch, die mich stets gern in die Heimat zurückkehren lässt. Sebastian, Dir danke ich für die vielen schönen Momente in München und dass man sich auf Dich verlassen kann, wenn es darauf ankommt.

Denise, Regine und Volker, ihr seid für mich wie eine zweite Familie geworden. Danke für die schöne Zeit mit Euch, sei es in Marbach, Gronsdorf oder auch auf einem Segelboot.

Meinen Eltern gebührt mein tiefe Dank. Ihr habt mich großgezogen und maßgeblich dazu beigetragen wer ich heute bin. Dabei durfte ich stets auf Eure vollumfängliche und bedingungslose Unterstützung vertrauen. Ich danke Euch für die Freiheit, die ihr mir bei der Wahl meines Lebenswegs gegeben habt.

Jeannine, Dir möchte ich für Deine unendliche Unterstützung danken, für den Ausgleich und die Motivation auch in schwierigen Phasen und für Dein Verständnis vor allem während der finalen Etappe dieser Arbeit. Vielen Dank für die wunderschöne Zeit die wir schon verbracht haben und die wir noch verbringen werden.

What we know is a drop, what we don't know is an ocean.

Sir Isaac Newton